Exploring particle populations and magnetic field structures in the relativistic jets of blazars

by

Callum McCall

A thesis submitted in partial fulfillment of the
requirements of Liverpool John Moores University
for the degree of Doctor of Philosophy

June 2025

Declaration

The work presented in this thesis was carried out at the Astrophysics Research Institute, Liverpool John Moores University. Unless otherwise stated, it is the original work of the author.

While registered as a candidate for the degree of Doctor of Philosophy, for which submission is now made, the author has not been registered as a candidate for any other award. This thesis has not been submitted in whole, or in part, for any other degree.

Callum McCall
Astrophysics Research Institute
Liverpool John Moores University
IC2, Liverpool Science Park
146 Brownlow Hill
Liverpool
L3 5RF
UK

June 2025

Abstract

Well-sampled optical photo-polarimetric observations are paramount to understanding emission mechanisms and particle populations within the inner, highly collimated acceleration region of relativistic jets. This thesis presents the results of multiwaveband photo-polarimetric monitoring of a sample of γ-ray bright blazars. This includes the development and implementation of reduction pipelines used to calibrate and analyse data from the Liverpool Telescope RINGO3 and MOPTOP instruments.

The Python pipelines developed in this work incorporated standard differential photometry techniques, alongside instrument-specific calibration methods such as determining non-standard waveband reference star magnitudes for RINGO3, accounting for telescope mirror degradation, and deriving polarimetric coefficients for MOPTOP. A novel approach was developed to correct for the 180° electric vector position angle (EVPA) ambiguity, reducing the need for manual intervention and accounting for measurement uncertainties.

Long-term optical and γ-ray photometric correlations were observed across most sources, with trends suggesting that low-synchrotron peak (LSP) blazars demonstrate more scattered relationships than high-synchrotron peak (HSP) sources. These results support a predominantly leptonic emission scenario in blazar jets while allowing for the possibility of additional hadronic contributions, particularly in LSP sources where greater scatter in optical–γ-ray flux-flux space was identified. Spectral analysis of optical variability revealed logarithmic colour evolution trends, implying the presence of spectral variability stabilisation during increased optical photometric activity. These trends, classified as bluer-stable-when-brighter and redder-stable-when-brighter, require a two-component emission model, with contributions from both thermal (disk) and non-thermal (jet) emission.

Photo-polarimetric analysis revealed significant correlations and anti-correlations between optical and γ-ray flux and polarisation degree, consistent with emission mechanisms such as relativistic shocks and magnetic field kink instabilities. Frequency-dependent polarisation variability was detected, with LSP sources dominating the sample of objects exhibiting bluer- and redder-when-brighter polarisation trends. Optical EVPA rotations were identified across multiple sources, primarily during heightened photometric states. By analysing the accompanying polarimetric states, distinct rotation mechanisms were inferred, further supporting shock propagation and kink instabilities within blazar jets in addition to stochastic variability.

The 2015 OJ287 binary black hole impact outburst was examined in detail, confirming a dual-peak flaring episode. The first flare was attributed to thermal bremsstrahlung originating from the primary accretion disk while the second flare was attributed to synchrotron emission from the jet. These data were corroborated with multi-frequency observations and supported the formation of a knot propagating along the jet's helical magnetic field.

Intranight monitoring of PKS 0735+178 during heightened γ-ray activity uncovered an intranight, red-leading temporal lag in the optical wavebands, suggestive of second-order Fermi acceleration processes such as magnetic reconnection. Multiple epochs of significant intranight variability were detected across the sample, with statistical tests confirming variability in OJ287 and PKS 0735+178. Colour trends were also observed during some of the variable nights, with both redder- and bluer-when-brighter behaviours detected in PKS 0735+178.

Long-term photo-polarimetric monitoring of blazars allows one to determine the dominant emission mechanisms occurring within the jet, leading to a better understanding of the structure and evolution of the involved magnetic field structures. These results collectively contribute to the understanding of multiwaveband blazar variability and jet emission mechanisms, while providing new insights into the connections between photometric, polarimetric, and spectral behaviours.

Publications

In the course of completing the work presented in this thesis, its contents have been submitted and/or accepted for publication in a refereed journal:

1. 'Detection of an intranight optical hard-lag with colour variability in blazar PKS 0735+178'

Callum McCall, Helen Jermak, Iain Steele, Shiho Kobayashi, Johan Knapen & Pablo M. Sánchez-Alarcón, **2024**, *Monthly Notices of the Royal Astronomical Society*, 528, 3, 4702-4719.

2. 'Distinguishing radiation mechanisms and particle populations in blazar jets through long-term multi-band monitoring with RINGO3 and Fermi'

Callum McCall, Helen Jermak, Iain Steele, Iván Agudo, Ulisses Barres de Almeida, Talvikki Hovatta, Gavin Lamb, Elina Lindfors & Carole Mundell, **2024**, *Monthly Notices of the Royal Astronomical Society*, 532, 2, 2788-2819.

Acknowledgements

Thank you to my friends: K, Izzy, Gemma, Lucy (Rolo), Becki (Bowie), Rebecca, Sean, Cara, Matt, Lauren, Jacob, Reka, and Peter. Thank you all for your years of support and encouragement, and for distracting me with coffee trips, dinners, drinks, and weekends away when I needed them most.

Thank you to my supervisors, Helen and Iain. You have been instrumental right from the beginning with my MPhys project and the PVC scholarship, through to the (many) applications and feedback requests. I could not have done this without your unwavering support. We got there in the end!

Thank you to my fellow ARI PGRs. I hope you will keep my badminton legacy alive without me, and make good use of my amazing spreadsheet skills. I wish you all the best of luck with your work and whatever comes next.

Thank you to my family. Thank you for helping with the house move and the endless questions that followed. It has been a difficult few years for us all, and I hope I have made you proud.

Thank you, Jason, for putting up with everything from start to finish. Thank you for keeping me grounded and sane. Most of all, thank you for caving and letting me get our pup, Arlo. I *think* he helped more than he hindered...

Callum McCall June 2025

Contents

List of Figures

List of Tables

Abbreviations

AGN	**A**ctive **G**alactic **N**ucleus
AU	**A**stronomical **U**nits
BLR	**B**road **L**ine **R**egion
BLRG	**B**road **L**ine **R**adio **G**alaxy
BSWB	**B**luer-**S**table **W**hen **B**righter
BWB	**B**luer **W**hen **B**righter
CD	**C**ompton **D**ominance
DEC	**D**eclination
EVPA	**E**lectric **V**ector **P**osition **A**ngle
EW	**E**quivilent **W**idth
EC	**E**xternal **C**ompton
FoV	**F**ield **o**f **V**iew
FR	**F**anaroff **R**iley
FSRQ	**F**lat **S**pectrum **R**adio **Q**uasar
GRB	**G**amma-**R**ay **B**urst
HBL	**H**igh synchrotron peaked **BL** Lac
HSP	**H**igh **S**ynchrotron **P**eaked
HWP	**H**alf **W**ave **P**late
IBL	**I**ntermediate synchrotron peaked **BL** Lac
INOV	**Intra** **N**ight **O**ptical **V**ariability
ISM	**I**nter**s**tellar **M**edium
ISP	**I**ntermediate **s**ynchrotron **p**eaked
kpc	**k**ilo**p**arse**c**
LAT	**L**arge **A**rea **T**elescope
LBL	**L**ow synchrotron peaked **BL** Lac

LSP	**l**ow **s**ynchrotron **p**eaked
LT	**L**iverpool **T**elescope
$M_\odot$	Solar **M**asses
MAD	**M**edian **A**bsolute **D**eviation
MeV	**M**ega **e**lectron **V**olts
MJD	**M**odified **J**ulian **D**ate
MOPTOP	**M**ulticolour **OPT**imised **O**ptical **P**olarimeter
Mpc	**M**ega**p**arse**c**
MWL	**M**ulti-**W**ave**L**ength
NLR	**N**arrow **L**ine **R**egion
NLRG	**N**arrow **L**ine **R**adio **G**alaxy
PWB	**P**olarised **W**hen **B**righter
PWF	**P**olarised **W**hen **F**ainter
QPO	**Q**uasi-**P**eriodic **O**scillation
RA	**R**ight **A**scension
RL	**R**adio **L**oud
RQ	**R**adio **Q**uiet
RSWB	**R**edder-**S**table **W**hen **B**righter
RWB	**R**edder **W**hen **B**righter
SMBH	**S**uper **M**assive **B**lack **H**ole
SNR	**S**ignal to **N**oise **R**atio
SSC	**S**ynchrotron-**S**elf **C**ompton
SWB	**S**table **W**hen **B**righter
Sy	**Se**y**f**ert
TCS	**T**elescopio **C**arlos **S**ánchez
TDE	**T**idal **D**isruption **E**vent
ToO	**T**arget **o**f **O**pportunity
VHE	**V**ery **H**igh **E**nergy
WCS	**W**orld **C**oordinate **S**ystem

Chapter 1

Introduction

1.1 Active galactic nuclei

It is widely accepted that at the centre of all massive galaxies resides one or more supermassive black holes (SMBHs) (Kormendy & Richstone, 1995). SMBHs exist within a range of masses. Generally, the smallest SMBHs have masses of approximately 10^5 $M_\odot$ with the largest going up to the model-predicted theoretical maximum at a few 10^{10} $M_\odot$ (King, 2016). They are referred to as an active galactic nucleus (AGN) if subject to the accretion of dust and gas via an accretion disk around the black hole. Figure 1.1 shows a generalised schematic of an AGN, with the different structural components labelled. These will be explored throughout this section. Table 1.1 shows a summary of the different AGN components with approximate values for the radius, electron density, and electron column density for each. The column density describes the total number of electrons integrated along a line of sight through a particular region. Accretion disks are typically sized at roughly 10^{13} m in radius (Guo et al., 2022; Jha et al., 2022) and consist of material spiralling inwards towards the black hole through the loss of angular momentum, primarily driven by friction and magnetic turbulence within the disk (Shakura & Sunyaev, 1976; Balbus & Hawley, 1991; Abramowicz & Fragile, 2013). Bremsstrahlung emission is thought to be a key cooling mechanism within the disk (Yarza et al., 2020; Gopal-Krishna, 2024), whereby the deceleration of charged particles during Coulomb interactions causes the production of thermal photons (Rybicki & Lightman, 1986). The rate of accretion onto the compact object varies with the type of source, but on average is relatively high; up to a few tens of solar masses of material can be accreted per year (Bian

& Zhao, 2003). Surrounding the accretion disk at radii of approximately 10^{14-16} m sit high density, large column density gas clouds moving with velocities $\geq 10^3\,\mathrm{km\,s^{-1}}$. These clouds produce strong, broad emission lines, with equivalent width (EW) of 10^{1-2} Å due to their high velocities. The EW of an emission line is the width of the continuum that would contain the same energy as the emission line. The emission lines observed at optical frequencies in AGN spectra primarily include hydrogen Balmer lines (e.g., Hα, Hβ, Hγ), as well as lines from other ions such as carbon (e.g., C III], C IV), magnesium (e.g., Mg II) (Peterson, 1997) This component of the AGN structure is known as the broad line region (BLR). Further out from the central engine, at roughly $10^{16} - 10^{17}$ m, resides the torus consisting of dusty clouds with high column density. The torus is optically thick (i.e. a short photon mean free path), showing a large temperature gradient along its cross-section. Situated around 10^{17-18} m from the central black hole is the narrow line region (NLR). This region consists of slower moving, $10^2\,\mathrm{kms^{-1}}$, low density, low column density clouds. The clouds can be optically thin (i.e. a long photon mean free path), showing emission lines with much smaller EW than the BLR (Urry & Padovani, 1995; Netzer, 2006).

TABLE 1.1: Table showing the properties of the different components of an AGN. The distance from the central SMBH, and electron densities and column densities for each component are also given. r_g, gravitational radius, $= \frac{GM}{c^2}$. Table taken from Netzer (2006).

Component	Radius [m]	Density [$\mathrm{e^-cm^{-3}}$]	Column Density [$\mathrm{e^-cm^{-2}}$]
Accretion disk	10^{13}	10^{15}	$10^{10-100} r_\mathrm{g}$
BLR	10^{14-16}	10^{10}	10^{23}
Torus	10^{16-17}	10^{3-6}	$\geq 10^{25}$
NLR	10^{18-19}	10^{3-5}	10^{20-21}

An additional feature of some AGN are the jets emanating perpendicular to the accretion plane of the SMBH. These objects are known as quasars (Chiu, 1964). The jets themselves are highly collimated, forming very close to the black hole, and composed of charged particles that are accelerated through radiation and magnetic fields at speeds close to the speed of light (i.e. mildly-relativistic to relativistic) depending on factors that will be explored in this chapter. They extend out on vast scales; from a few astronomical units (AU) up to several megaparsecs (Mpcs) into the intergalactic medium where the jets form large radio lobes (Blandford et al., 2019). It is this feature that differentiates the two main classes of AGN; the radio-loud (RL), "jetted", AGN and the radio-quiet (RQ), "non-jetted", AGN (Padovani, 2016).

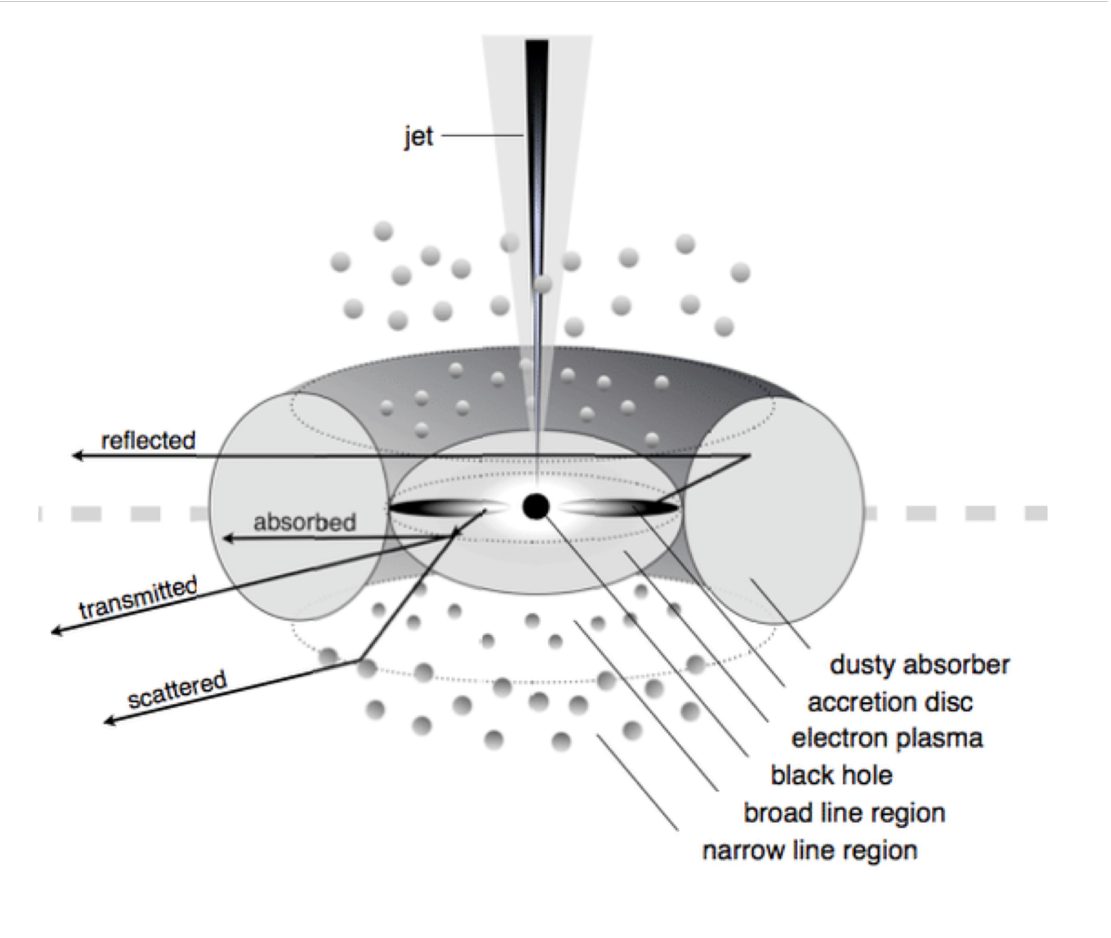

FIGURE 1.1: A structural overview of AGNs, cropped and taken from Beckmann & Shrader (2012). The various components that characterise AGNs include the accretion disk, torus, emission regions and relativistic jets.

Non-jetted AGN make up the majority of the population, comprising $\geq 90\%$ of all known AGN sources (Padovani, 2011). The Seyfert galaxies were first identified by Carl Seyfert in 1943 as resolvable, high-surface-brightness galaxies with "stellar appearing cores". Today, they are defined by their strong, high-ionisation emission lines and almost exclusively exist in spiral galaxies, implying likely young, low-mass central engines (Peterson, 1997). In general, spiral galaxies have not undergone large-scale galactic mergers, which typically lead to the formation of larger elliptical galaxies with a combined SMBH (Kormendy & Ho, 2013).It was Khachikian & Weedman (1974) who differentiated the class into type I and II Seyfert galaxies given the presence of broad and/or narrow emission lines, with type Is showing both broad and narrow lines and type IIs showing only narrow lines. From a morphological perspective, this can be explained if the two types are the same system, viewed from different angles. If the type II Seyfert galaxies are those viewed "edge-on", the dusty torus obscures the view of the central engine and BLR so

only the narrow lines would be visible. Conversely, if the source was observed at some angle away from the plane of the accretion disk/torus, the emission from the BLR would become visible and both broad and narrow lines would be observed, as in type I Seyfert galaxies. Recent studies however suggest some Seyfert I-type galaxies (around 16%; Varglund, I. et al., 2022) may also host a jetted AGN on account of high-energy γ-rays (Abdo et al., 2009) and superluminal motion at radio frequencies (Brunthaler et al., 2000; Lister et al., 2016). Superluminal motion refers to the phenomenon whereby parsec-scale regions within jets appear to move with apparent velocities faster than the speed of light (Cohen et al., 1977). In practice, this is a geometric effect arising from the relative velocity between the observer and region rest frames (Xiao et al., 2022). While Seyfert I-type jet powers are relatively weak, these sources would help populate the low-mass ($< 10^8\ M_\odot$) quasar distribution (Foschini et al., 2015; Foschini, 2017).

Despite being the minority of AGN sources, jetted AGN still show many different features and characteristics that require the population to be sub-classified. Fanaroff & Riley (1974) classified jetted AGN based on the ratio, $R_{\rm FR}$, of the distance between the brightest regions on either side of the core to the size of the whole system. Setting a threshold of 0.5, they split the jetted AGN population into two classes, FR Is and FR IIs. FR I sources have $R_{\rm FR} < 0.5$ and become fainter as distance increases further from the central core, known as "edge-darkened". FR II sources have $R_{\rm FR} > 0.5$ and have bright hotspots in their radio lobes, known as "edge-brightened". A diagram showing the observable difference between FR I and II sources is shown in Figure 1.2. A possible reason for the differences comes from the interaction between the jet and the surrounding environment. Assuming the central engines of FR I and II sources are the same and the jets always emerge at relativistic speeds, a denser inner interstellar medium (ISM) core can decelerate the jets of FR II sources to less energetic supersonic or subsonic speeds (De Young, 1993). While these initial jet–environment interactions and subsequent sub-sonic jet speeds would explain the differences between the two FR classes and are the most likely theory, alternative suggestions have been put forward to explain the differences. An alternative includes intrinsic differences in the properties of the central SMBHs, such as the accretion rate and the spin parameter (Baum et al., 1995).

As shown in Figure 1.1, jets are generally believed to be oriented perpendicular to the accretion disk, which is itself surrounded by a torus and aligned with the black hole's spin axis (Drouart et al., 2012). However, both observations and simulations have

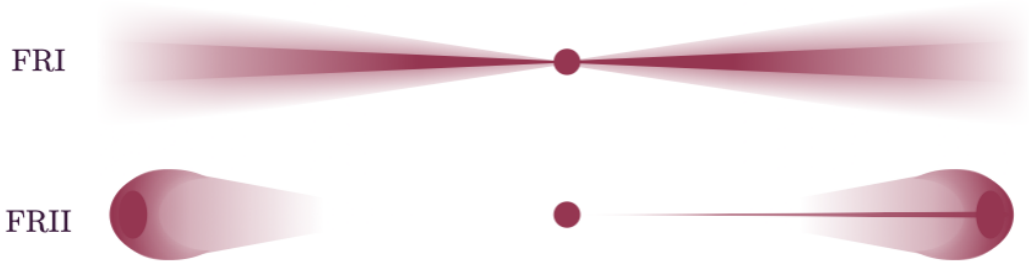

FIGURE 1.2: Diagram showing the observational difference between FR I and FR II sources. The jets of FR I sources become fainter away from the core, whereas FR II sources show bright lobes away from the core.

demonstrated that this alignment is not always maintained. A misalignment between the black hole spin and the accretion disk can occur, as the infalling gas that forms the disk is not immediately influenced by the black hole's spin (Chatterjee et al., 2020). Over timescales much shorter than the typical lifetime of a jet (i.e. $\ll 10^8$ years; Natarajan & Pringle, 1998), the black hole spin first aligns the inner regions of the accretion disk, leading to a warped disk structure before the outer disk also aligns. This warping alters the orientation of the jets, causing them to appear misaligned with the accretion plane on parsec scales. Similarly, the torus retains its original angular momentum for longer before aligning with the angular momentum of the disk, leading to potential misalignments between the torus, the disk, and the jet (Greenhill et al., 1996; Hopkins et al., 2012).

Furthermore, outflows from AGN are not limited to relativistic jets. Winds originating from the accretion disk, composed of matter and radiation, also play a significant role in shaping AGN structure and influencing both the host galaxy and the surrounding interstellar medium (ISM). For example, X-ray photons can be absorbed by the surrounding torus and subsequently re-emitted as ultraviolet radiation, contributing to the ionisation and heating of the ISM (Murray et al., 1995; Giustini & Proga, 2019). Additionally, magnetically driven winds can extract angular momentum and mass from the disk, facilitating both accretion and outflows (Pelletier & Pudritz, 1992; Wang et al., 2022). These outflows are a key component of AGN feedback, halting star formation and the growth of the host galaxy, which in turn lessens the rate of accretion and black hole growth (Fabian, 2012).

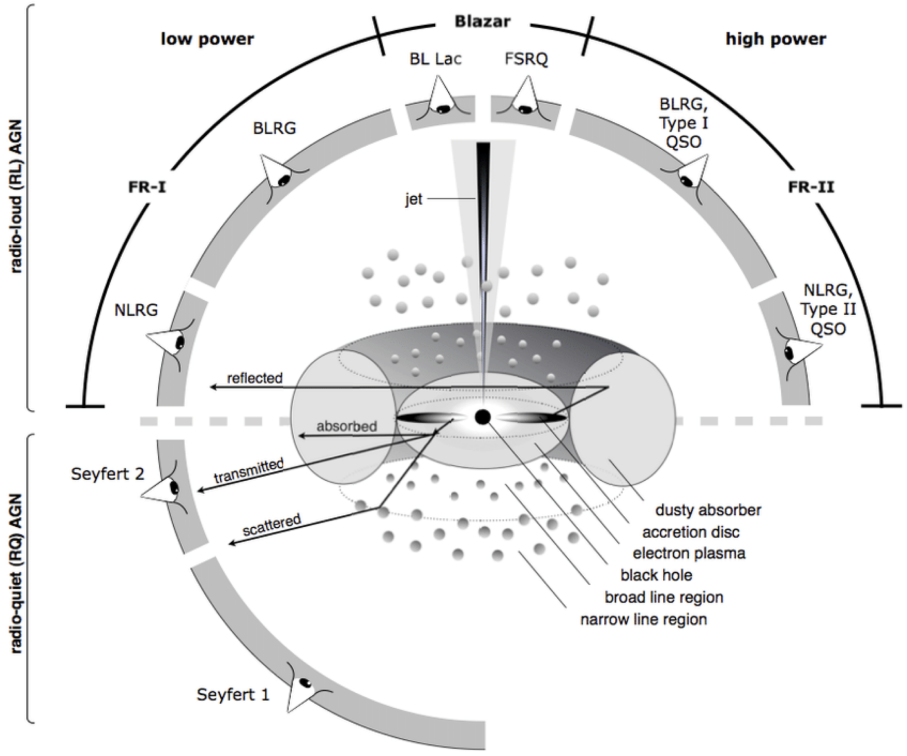

FIGURE 1.3: As Figure 1.1 but with source classification shown around the AGN structure. This figure is taken from Beckmann & Shrader (2012) and highlights how viewing the system from different angles changes how the object is classified.

Urry & Padovani (1995) produced a unified scheme for AGN, tying together decades of research categorising their various features, using the presence of any broad and narrow line emission, and the jet. Figure 1.3 shows the unified AGN model, with each structural component also labelled. The classification of the object depends on two things: the orientation of the system, and the presence of jets. When viewed edge-on, the torus obscures BLR emission, resulting in type II Seyferts (non-jetted) and Narrow-line Radio Galaxies (NLRG; jetted), with the latter being populated by FR I and II sources. As the angle with respect to the plane of the accretion disk increases and BLR emission becomes prevalent, one can expect to observe type I Seyferts (non-jetted) and Broad-line Radio Galaxies (BLRG; jetted), with the latter, again, being populated by FR I and II sources. Figure 1.3 also shows an additional class of AGN, observed at very small viewing angles with respect to the relativistic jet; blazars.

1.2 Blazars

Blazars are a subclass of jetted AGN whose relativistic jet is oriented along the observer's line of sight to within $\lesssim 15°$ (Hovatta et al., 2009). As a result of this, the jet emission is strongly Doppler boosted. Doppler boosting, or relativistic beaming, is the phenomenon whereby radiation emitted from a region travelling at speeds comparable to the speed of light appears brighter and more concentrated along the direction of travel. This has the effect of transforming small changes in the intrinsic luminosity of the jet into large changes in the observed (apparent) brightness. This makes blazars highly variable sources from radio to very high energy (VHE) γ-ray frequencies, and at a variety of timescales from minutes to years.

While the relativistic jet can be probed at all frequencies, and most often dominates the total flux, the emission from other structures can contribute significantly depending on the observation wavelength and general activity state of the blazar. At sub-GHz frequencies, one can observe the extended structure of blazar jets, namely the radio lobes and hotspots. The contribution from any dusty torus is evident at infrared frequencies, and at optical one can observe thermal emission from the accretion disk and BLR, as well as the host galaxy emission (Prandini & Ghisellini, 2022).

As seen in Figure 1.3, blazars can be split into two classes: BL Lacs and Flat Spectrum Radio Quasars (FSRQs). These classes can be distinguished by the size of any emission lines in their optical spectra originating from the BLR and NLR. Specifically, FSRQs have lines with EW $> 5\,$Å and in BL Lacs these lines are weaker or altogether absent (Stickel et al., 1991). Morphological differences between blazars might explain the reasoning for this difference. FSRQs have been found to have significantly higher accretion rates than BL Lacs (Cavaliere & D'Elia, 2002), implying a greater thermal emission contribution and stronger emission lines (Boroson & Green, 1992). The lack of any observed thermal emission in BL Lacs is not only suggestive of radiatively inefficient accretion but also the absence of any significant torus and BLR (Chiaberge et al., 1999). The increased thermal emission from FSRQs is further supported by the presence of the "blue-" or "UV-bump" seen in the optical region of the spectral energy distributions of FSRQs (more on this in Section 1.2.1), given thermal emission is intrinsically bluer than non-thermal emission.

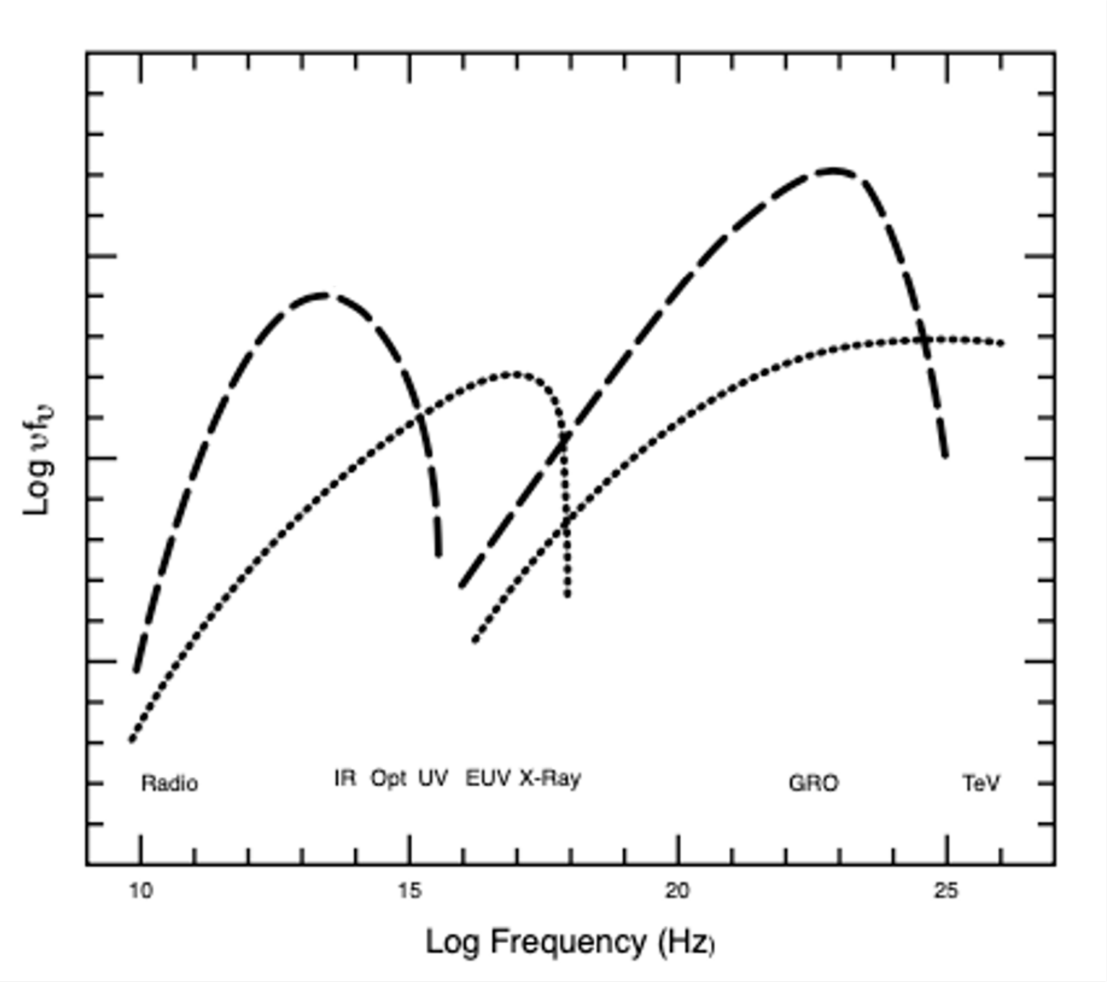

FIGURE 1.4: A generalised blazar spectral energy distribution (SED) showing its double-peak structure. The different lines show different source classifications, but in general the shape is the same. Figure taken from Ulrich et al. (1997).

1.2.1 Spectral energy distribution

A spectral energy distribution (SED) describes the energy output of an object at a given frequency. In general, blazar SEDs show a distinct double-peak structure. The first peak is found at infrared to X-ray frequencies, while the second peak is at γ-ray frequencies. These are referred to as the lower- and higher-energy peaks, respectively.

The lower-energy peak in blazar SEDs is generally accepted to be the result of non-thermal synchrotron emission in the jet and is the dominant source of emission at optical frequencies (Prandini & Ghisellini, 2022). As mentioned previously in Section 1.2, emission from the host galaxy and thermal contributions from the accretion disk and BLR also peak at optical frequencies, however these are most often outshone by the jet

by several orders of magnitude (Olguín-Iglesias et al., 2016). In the synchrotron scenario, relativistic electrons spiral through the magnetic fields within the jet, causing the emission of photons due to their transverse acceleration relative to velocity (Hofmann, 2004). It follows that this peak is often referred to as the synchrotron peak.

The origin of the higher-energy peak in blazar SEDs is more uncertain. The emission can be explained through leptonic or hadronic modelling, with the nomenclature of the latter evolving to "lepto-hadronic" modelling to better emphasise the possibility of a combination of emission mechanisms (Reimer, 2012). The fundamental difference between these two models is the population of particles producing the emission. Leptons (electrons, muons, taus, neutrinos, and their antiparticles) are elementary particles which do not interact with the strong nuclear force, whereas hadrons, namely baryons and mesons, do. Baryons refer to those particles which are made up of three quarks (protons, neutrons, and their antiparticles), while mesons are made up of two quarks (pions, kaons and their antiparticles).

In the leptonic model, it is inverse-Compton processes that are responsible for the high-energy emission, where lower-energy seed photons are upscattered through interactions with relativistic electrons. The location of the origin of the seed photon fields describes the exact process, with synchrotron-self Compton emission (SSC; Maraschi et al., 1992) referring to the same relativistic electrons that produce the lower energy synchrotron emission upscattering the synchrotron photons, and external Compton emission (EC; Dermer & Schlickeiser, 1993) referring to thermal photons travelling into the jet from the accretion disk and BLR which are instead the seeds for upscattering.

Conversely, in hadronic modelling, it is processes completely independent of lower-energy variability that produce the higher-energy emission. This can be achieved through the decay and emission from products of proton-photon interactions, or by the Synchrotron Proton Blazar model (SPB; Mücke & Protheroe, 2001). Here, protons are accelerated to relativistic energies producing synchrotron emission as they spiral through the magnetic field of the jet, and collide with soft photons. Soft photons are those with lower energy and frequency and populate the synchrotron SED peak, while hard photons are those with higher energy and frequency and populate the high-energy SED peak. These collisions produce other particles, including electrons, which in turn generate additional synchrotron emission. The presence of proton-photon interactions also allows for the

photo-meson channel, where the interaction between any nucleon and photon produces mesons, including charged and neutral pions (Mücke et al., 2003; Reimer, 2012). It is the decay of charged pions that produces leptons and, more importantly, neutrinos (Cerruti, 2020). It follows that neutrino emission is the smoking gun signature of hadronic emission mechanisms (proton-synchrotron) in relativistic jets. While many neutrino detections have error circles containing no flaring blazars, neutrino emission has been detected coinciding with several flaring blazars (Plavin et al., 2023), with the first detection in 2017 associated with the blazar TXS 0506+056 while in a γ-ray flaring state (IceCube Collaboration et al., 2018).

To demonstrate the differences between blazar classes, the SEDs of two sources, 3C 454.3 and MRK 501 (an FSRQ and BL Lac, respectively) are shown in Figure 1.5. In the SED of 3C 454.3 the superposition of the jet emission is shown, represented by the two peaks at optical and γ-ray frequencies, in addition to components from the accretion disk, dusty torus, and X-ray corona. These additional features slightly alter the shape when compared to a BL Lac type such as that of MRK 501. This additional thermal emission is particularly prevalent at optical frequencies (10^{15} Hz), where a small bump is seen in the SED. This will be explored further in Section 1.5.2. The SED of MRK 501 only shows the contributions from the jet and the host galaxy (Prandini & Ghisellini, 2022). This further supports the idea of a lack of dusty torus and BLR associated with BL Lac types as their contributions are not observed in their SEDs. In both figures, the different lines correspond to the fit of the SED at different epochs, showing how the shape of the SED changes with variability of the source.

1.2.2 The Blazar Sequence

The unification of jetted AGN was first proposed by Fossati et al. (1998) as "The Blazar Sequence". This was updated by Ghisellini et al. (2017) who detail the observational differences between blazar classes from their SEDs. Prandini & Ghisellini (2022) present a recent review of the current state of the Blazar Sequence. Figure 1.6 shows some of the results from this work. The left figure shows the γ-ray luminosity as a function of redshift. From this, one can see a general trend in that FSRQs tend to show higher γ-ray luminosities and are located at higher redshifts, whereas BL Lac sources tend to dominate the lower γ-ray luminosity–lower redshift regime. This data is then binned,

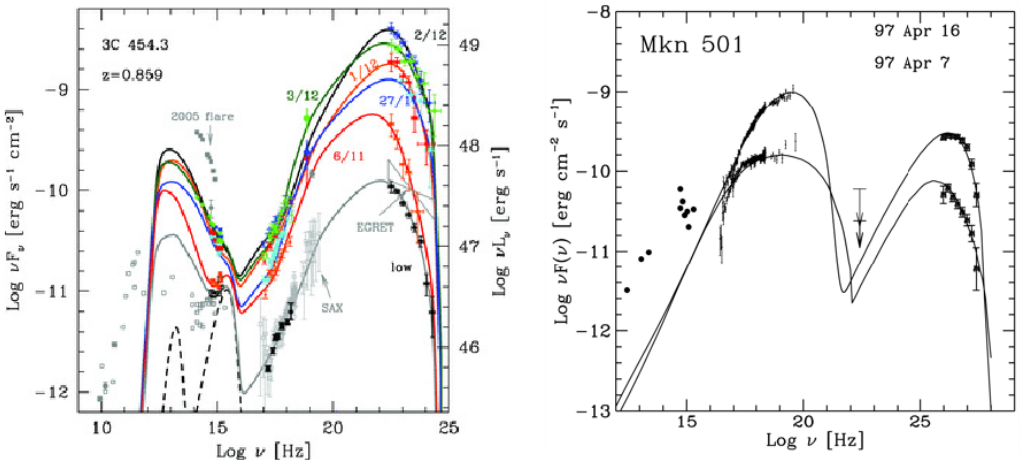

FIGURE 1.5: Plots highlighting the differences in the SEDs of BL Lac and FSRQ type objects. The SED of 3C 454.3, an FSRQ, is seen on the left, and of MRK501, a BL Lac, on the right. Plot taken from Prandini & Ghisellini (2022).

shown by the horizontal lines, and SEDs computed (Figure 1.6 right) to highlight inter- and intra-class differences. Here, one can see a dependence on the SED higher- and lower-energy peaks on γ-ray luminosity (i.e. class), most prevalent in BL Lacs where the peak frequencies increase for lower γ-ray luminosity objects. Furthermore, the Compton dominance (CD), that is the ratio between the peaks of the luminosities attributed to Compton and synchrotron emission (i.e. the higher-energy peak luminosity divided by the lower-energy peak luminosity), increases with γ-ray luminosity for FSRQs but does not change for BL Lacs. It is important to note, however, that binning the data into groups like that which has been described above masks any intra-class differences. Blazars are highly variable sources, and at times may appear more similar to other (sub)classes. This will be explored further in Section 1.5.

It is these works that support the need for subclassification of blazars. Abdo et al. (2010b) suggests a method of subclassifying blazars, expanding on the work of Padovani & Giommi (1995). This method is based on the location of the lower-energy synchrotron SED peak, ν_s, of the object. Low synchrotron peaked sources (LSPs) have $\nu_s < 10^{14}$ Hz, corresponding to IR emission. High synchrotron peaked sources (HSPs) have $\nu_s > 10^{15}$ Hz in UV or X-ray. Those with a synchrotron peak frequency in the optical regime between $10^{14} \leq \nu_s \leq 10^{15}$ Hz are classed as intermediate synchrotron peaked sources (ISPs). While both FSRQs and BL Lacs populate the LSP regime, only BL Lac sources show synchrotron peak frequencies corresponding to ISP and HSP classification. For

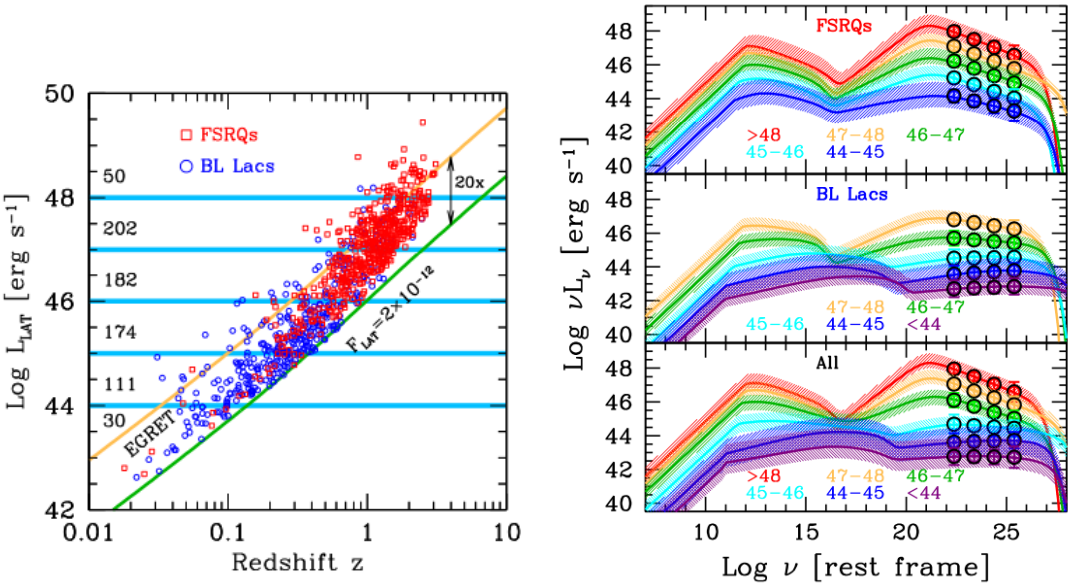

FIGURE 1.6: Left: blazar γ-ray luminosity as a function of redshift. Right: SEDs of different blazar classes for the bins are highlighted by the solid horizontal lines in the figure on the left. Both plots are taken from Ghisellini et al. (2017).

this reason, in this work, LSP, ISP, and HSP BL Lac objects will be referred to as LBL, IBL, and HBL objects, respectively.

Population statistics across blazar classes can help to reveal intrinsic differences in their observational properties. Liodakis & Pavlidou (2015) shows that FSRQs typically exhibit faster jets with higher bulk Lorentz factors (Γ) than BL Lac objects. Furthermore, FSRQs also show a trend of increasing luminosity with redshift, indicating they are intrinsically brighter at higher redshift (i.e. younger). Despite this, BL Lac and FSRQ beaming characteristics are comparable, supporting the idea that the differences observed in classes are intrinsic, rather than due to any geometric-related relativistic effects such as differences in Lorentz factors or viewing angles. (Kügler et al., 2014) showed that BL Lacs are hosted by massive elliptical galaxies, suggestive of older galaxies with larger SMBH masses. In their sample, synchrotron peak frequency distribution across all sources spanned $13.5 \leq \nu_{\rm peak} \leq 16$, peaking at 14.5 (indicating an IBL-dominated sample). While a potential high-redshift BL Lac population was noted, the large redshift uncertainties associated with BL Lac objects limited conclusions. Mingaliev et al. (2017) found LBLs generally exist at slightly higher redshifts than IBLs and HBLs, and show higher radio flux densities with greater variability.

It is important to note that not all blazars fit nicely into these classes and some "extreme"

sources have been found. Ultraluminous FSRQs or "MeV blazars" (PKS 0201+113, S4 0642+449, PKS 1351-018, PKS 2126-158; Marcotulli et al., 2020) have their SED shifted to lower energies, with their higher-energy peak at hard X-rays. In addition to this, some HBLs known as "extreme synchrotron" or "TeV" blazars have their lower- and higher-energy peaks at X-ray and TeV ($\geq 10^{26}$ Hz) frequencies, respectively (Prandini & Ghisellini, 2022). Such TeV sources include MRK 421 and 1ES 1959+650 (see Krawczynski, 2004; Prandini & Ghisellini, 2022, and references therein).

Furthermore, recent studies have suggested an additional population of transitional blazars (Ghisellini et al., 2011). These objects, also known as masquerading BL Lacs, show Eddington ratios much more similar to that of FSRQs than other BL Lacs, but are classified as BL Lacs due to emission from the broad line region being overpowered by the jet continuum, diluting or obscuring emission lines (Ruan et al., 2014). The Eddington ratio is given by $\lambda = L/L_{\rm Edd}$ where L is the accretion-related observed luminosity, and $L_{\rm Edd}$ is the Eddington luminosity. The Eddington luminosity for a given object is given by $L_{\rm Edd} = 1.26 \times 10^{38} (\frac{M}{M_\odot})\,{\rm erg\,s^{-1}}$ where $\frac{M}{M_\odot}$ is the mass of the SMBH expressed in solar masses. The Eddington luminosity, or Eddington limit, refers to the maximum rate of accretion onto the black hole before outwards radiative pressure balances the black hole's gravitational pull, halting further accretion. In FSRQs (and masquerading BL Lacs), this ratio is higher than BL Lac objects, implying a brighter thermal contribution due to a higher accretion rate and a more radiatively efficient accretion flow (Padovani et al., 2019).

In general, masses of SMBH, notably blazars, can be measured through reverberation mapping. Reverberation mapping is the process of measuring the time delay between variations in the emission from the accretion disk and a response in the broad emission lines originating from the BLR. This time lag, combined with the velocity dispersion of the gas in the BLR, allows for an estimation of the central black hole mass using the virial theorem (Wandel et al., 1999; Greene & Ho, 2005; Castignani et al., 2013). However, similarly to redshift, BL Lac type blazars often have weak or absent emission lines (see Section 1.2), making reverberation mapping techniques difficult. As a result, alternative statistical methods, such as correlations between black hole mass and host galaxy properties or black hole luminosity, can be used to give blazar mass estimates (Rakshit et al., 2020).

1.3 Jets

The relativistic jets of blazars can be observed across the electromagnetic spectrum from low-frequency radio waves to VHE γ-rays. At most frequencies, the jet appears highly collimated and cannot be spatially resolved, except for low-frequency radio and millimetre waves (GHz frequencies), which are capable of resolving the radio lobe structure (e.g. Hovatta & Lindfors, 2019). It follows that launching, structure, and acceleration mechanisms are debated features of relativistic jets.

There exists a disparity between theory and simulations on the launching of AGN jets. Current models suggest jets form as a result of the spectral state of the accretion disk and the direction of the surrounding magnetic field lines originating from the disk plasma. The action of the plasma accretion flow along with the mass of the disk and subsequent gravitational pull causes an accumulation of the magnetic flux around the black hole, twisting it around the axis of disk rotation and launching jets at perpendicular angles. This is described by the magnetically-arrested disk (MAD; Narayan et al., 2003) and would result in the formation of jets capable of extracting the spin energy of the black hole at high efficiencies. The requirement in this scenario is a radiatively inefficient (i.e. a short photon mean free path) thick disk at sub- or super-Eddington accretion rates (Tchekhovskoy, 2015). Sub- and super-Eddington accretion rates refer to $\lambda < 1\%$ and $\approx 100\%$ respectively. A thick disk has height, H, comparable to the radial distance to the black hole, R, ($H \sim R$) whereas a thin disk has height smaller than the radial distance to the black hole ($H \ll R$) (Frank et al., 2002). In contrast, recent simulations suggest that jets may be more resilient to accretion disk spectral state, thickness, and inclination angle than theory suggests. Davis & Tchekhovskoy (2020) present a simulation review on possible jet launching from different disk parameters. They show jets can form from both thin and thick disks, with initial toroidal (horizontal around a torus) or poloidal (vertical around a torus) magnetic field lines, and with or without large disk tilts relative to the black hole spin plane. In either case, the magnetic fields at the base of the jet are strong and likely twisted into a helical structure (Marscher et al., 2008; Tchekhovskoy et al., 2011).

Using low-frequency VLBA observations, Attridge et al. (1999) resolved the outer jet structure and found that the central core region showed a polarisation angle perpendicular to the jet axis, whereas the outer regions surrounding the core showed polarisation

angles parallel to the jet axis. This was the first observational evidence for a spine–sheath jet structure (Ghisellini et al., 2005). The spine of the jet is equivalent to the jet core, consisting of high particle velocities and Lorentz factors. The edges of the jet correspond to the sheath, where the jet slows due to interaction with the surrounding medium (Laing, 1996; Georganopoulos & Kazanas, 2003). Logically, this region consists of slower particles and lower Lorentz factors. Figure 1.7 shows a diagram of the spine-sheath jet structure, comprising regions with different Lorentz factors. This "two-flow" model fits well into the leptonic scenario, where the seed photons for SSC processes can originate from both the spine and sheath. It is believed that the "active" zone, where emission from both the spine and sheath originates, lies between 1/2 and 3/2 black hole radii along the jet. This model fails, however, to explain γ-ray flares without a lower-energy optical counterpart (orphan flares). Despite this, a spine–sheath configuration remains the most widely accepted jet structure.

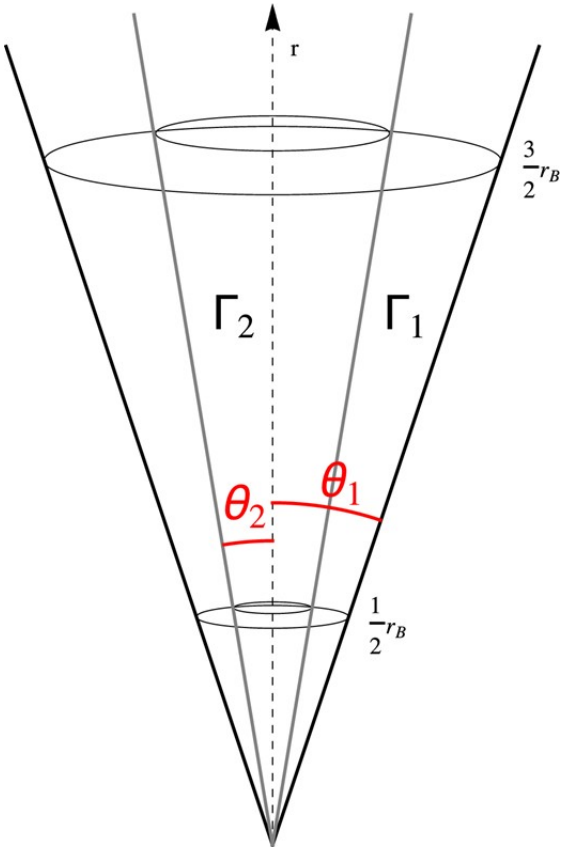

FIGURE 1.7: Figure showing the spine-sheath relativistic jet structure. Figure taken from Sikora et al. (2016).

The most probable mechanism behind particle acceleration in blazars is through the propagation of shocks through the jet (Guetta et al., 2004; Liodakis et al., 2022b).

Shocks form as a result of flow rate changes in the jet outflow, producing plasma waves or "plasmoids" of density inhomogeneities in the jet structure, each with differing velocities, Lorentz factors, and masses Cantó et al. (2013); Angelakis et al. (2016). It follows that faster propagating plasmoids are capable of catching up to slower ones and then interacting. The result is the dissipation of bulk motion kinetic energy into the magnetic field and radiated electron random energy, known as shocks (also referred to as shock-in-jet in this work). This process is described by Spada et al. (2001) as the Internal Shock Model.

First-order Fermi acceleration, also known as diffusive shock acceleration (DSA), describes the mechanism by which charged plasma particles gain energy through repeated crossings of magnetised shock fronts. As particles scatter across the shock, they interact with magnetic irregularities on either side, resulting in a net energy gain and efficient acceleration (Baring, 1997). In contrast, second-order Fermi acceleration does not require a shock front; instead, particles are accelerated through stochastic interactions with randomly moving magnetic fields in a turbulent medium, leading to slower and less efficient energy gains (Petrosian, 2012).

However, the internal shock model for particle acceleration in relativistic jets struggles to explain the speed of variability at TeV energies (Ghisellini et al., 2005). Emission regions would require bulk Lorentz factors much larger ($\Gamma \gtrsim 50 - 100$) than those which have been observed within the jet ($\Gamma \lesssim 10$) (Begelman et al., 2008) unless, after the TeV emission, efficient deceleration occurs on sub-parsec scales. Giannios et al. (2009) suggests an alternative "jet-in-jet" explanation, whereby the emission arises from regions or "blobs" with higher bulk Lorentz factors than the surrounding jet plasma and is dissipated through magnetic reconnection. Relativistic magnetic reconnection is another acceleration model that shows promise in replicating observed blazar emission (Giannios et al., 2009; Sironi et al., 2015; Petropoulou et al., 2016). In this scenario, oppositely directed magnetic field lines within jet plasma rearrange and release significant energy, resulting in particle acceleration (Zhang et al., 2022b).

MacDonald et al. (2015) suggests an emission mechanism involving a blob propagating through the jet spine, interacting with a shocked region of the sheath. The sheath provides a localised "ring" of seed photons for upscattering by the blob, resulting in orphan γ-ray flares but still aligning with the structured jet model.

The location and mechanisms behind particle acceleration in blazars are widely debated and are important questions given their connection to γ-ray emission. From Figure 1.5 one can see that the SED of an FSRQ becomes more Compton-dominated during a flaring state. This implies a disproportionate increase in γ-ray emission and therefore an excess of seed photons outside of those generated through synchrotron emission alone. The implication of this is that external seed photons are required to make up this deficit. It has been proposed that BLR emission is the most promising candidate for this emission (Ghisellini & Madau, 1996; Ghisellini et al., 2010; Marscher et al., 2010), but requires the accelerating region of the jet to be within the BLR, given the fast decrease in photon density away from the BLR. It follows that the acceleration region must be located within the radius of the BLR, or no more than 10^{16} m (1 pc) from the central engine (Hovatta & Lindfors, 2019, and references therein). This implies that the synchrotron (optical) and high-energy (γ-ray) emission, probed in this work, originates from the inner jet region of the blazar where particle acceleration must occur. Optical and γ-ray variability trace the evolution of acceleration zones and associated magnetic field structures in the highly-collimated jet regions.

1.4 Polarisation

As previously discussed in Section 1.2.1, the dominant source of emission at optical frequencies is non-thermal synchrotron emission originating from the jet. Strong evidence for this comes from the detection of high polarisation levels of radio to X-ray emission. Polarisation can be described as the preferential oscillation of the electric field of electromagnetic radiation. Two quantities can be obtained in order to describe the polarisation of the incoming light: The proportion (degree) of light that is polarised, and the angle of the electric field plane.

The degree of polarisation is the proportion of polarised light in the incident beam and is generally expressed as a percentage. It can refer to several types of polarisation, including linear, circular, and elliptical. Linear polarisation describes the oscillation of the electric field in a fixed, non-rotating plane, where as circular polarisation describes the electric field plane rotating about 360° as the wave travels. Elliptical polarisation is a more general case, where the electric field traces out an ellipse rather than a straight line or circle. It can be seen as a combination of linear and circular polarisation, where

the circular motion is stretched along one axis. Circular polarisation has rarely been detected in blazars. This is due to a suppression factor which scales roughly with $1/\gamma_e$ where γ_e is the Lorentz factor of the emitting electrons. For blazars and their large Lorentz factors, this suppression is typically large (Toma, 2021). This, however, has not stopped attempts to measure circular polarisation in blazars, but currently it is only constrained by upper limits (Liodakis et al., 2022a). The degree of polarisation, or just polarisation, henceforth refers to the fraction of linearly polarised light only in this work.

The electric vector position angle (EVPA) gives the orientation of the electric field of linearly polarised light relative to an arbitrarily fixed plane. While individual measurements of this angle provide little information, successive measurements over a given timeframe provide useful clues into the evolution of the emission region and its magnetic fields.

The optical polarisation variability in blazars is extreme. They are capable of showing some of the highest levels of polarisation of any astrophysical object, up to around 50% (Zhang, 2019, and references therein), and can vary significantly down to minute timescales (Covino et al., 2015). This is close to the theoretical maximum polarisation degree from synchrotron emission, around 70%. The maximum value of synchrotron polarisation for a population of electrons with energy distribution following a power law of index p can be derived as

$$\Pi = \frac{p+1}{p+\frac{7}{3}} \tag{1.1}$$

where the power law index of the electrons is typically between 2 and 3 (Rybicki & Lightman, 1979; Nalewajko & Sikora, 2012; Nava et al., 2016).

Like the degree of linear polarisation, the polarisation angle can be equally variable. During optical observations of γ-ray bright blazars, the EVPA has been observed to undergo large swings in excess of 90° over a variety of timescales ranging from hours to years, showing a rotation in the polarisation plane (Blinov et al., 2015).

Synchrotron emission has a natural polarisation signature originating from the preferential oscillation of the charged particles perpendicular to the magnetic field (Rybicki & Lightman, 1986). Figure 1.8 [1] shows the process of synchrotron emission, detailing the emission of photons from an electron travelling helically through a uniform magnetic

[1] https://emmaalexander.github.io/resources.html

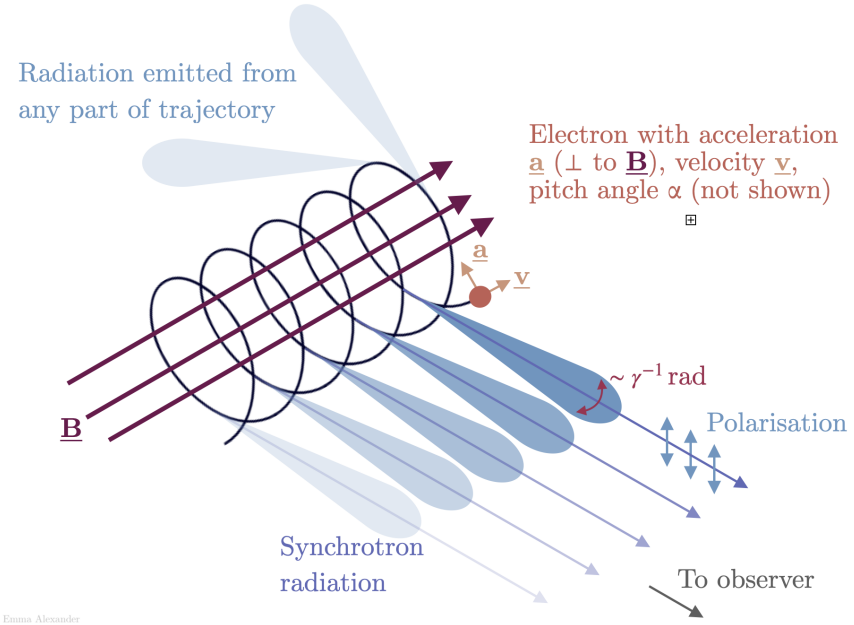

FIGURE 1.8: Schematic of the emission of synchrotron radiation and the direction of its preferential polarisation plane perpendicular to the magnetic field. Figure from [1].

field, with the direction of the preferential polarised plane perpendicular to the surrounding magnetic field. Consequently, the optical polarisation properties and variability of blazar emission can provide valuable information on the magnetic field properties and evolution of the emitting regions within the jet.

1.4.1 Stokes parameters

As discussed previously, the electric vector of polarised light traces an ellipse on a 2D plane. This ellipse is shown in Figure 1.9. The electric field components in the X and Y direction are denoted by E_{ox} and E_{oy}, respectively. ξ and η represent the major and minor principal axes of the ellipse, respectively, with the former offset from the X axis by angle ψ. The ellipticity, χ, can be calculated by $\tan\chi = \frac{\eta}{\xi}$. Not shown is the chirality of the ellipse, which denotes the rotation direction of the electric field; clockwise (right-handed) or counterclockwise (left-handed).

It is also important to note an inherent ambiguity in the angle ψ which arises due to the symmetrical nature of the ellipse about the minor axis. Since the ellipse is identical under a 180° rotation, the angle ψ and $\psi + 180°$ describe the same orientation of the major axis. When only intensity measurements are made, as is relevant to the work

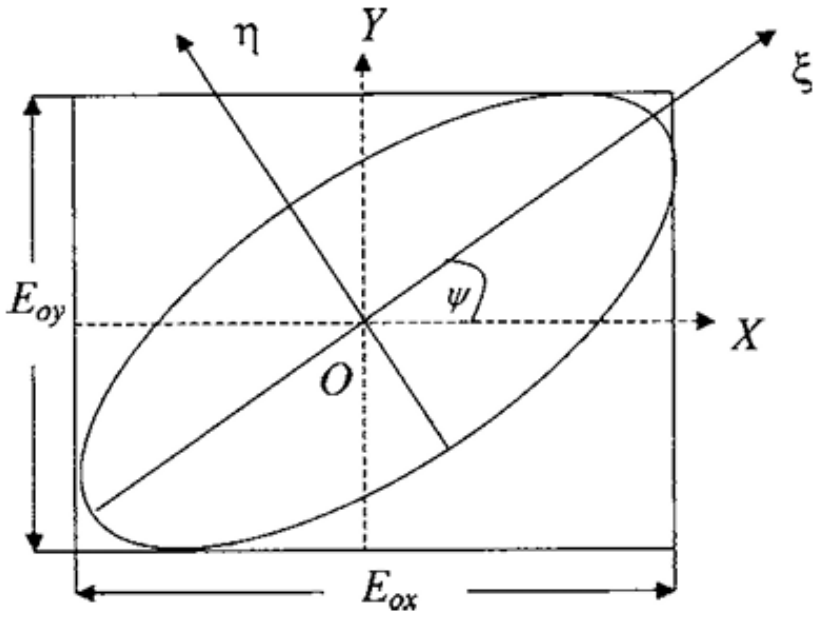

FIGURE 1.9: Diagram showing the elliptical path traced by the electric field vector of polarised light. Figure from Schaefer et al. (2007).

presented in this thesis, there is no way to distinguish between these two cases. This phenomenon will be explored further in Section 2.4.1.

The Stokes parameters (Stokes, 1851) are able to fully characterise the polarisation properties of an incident beam of light. There are four parameters, traditionally given as $IQUV$ but more modernly known as $S_1S_2S_3S_4$ or $S_0S_1S_2S_3$. In this work, the traditional $IQUV$ and $S_1S_2S_3S_4$ will be used interchangeably to align with the nomenclature in Clarke & Neumayer (2002). A visual depiction of the Stokes parameters and how they characterise the polarisation of the incident light beam is given in Figure 1.10 [1]. The I parameter is simply the total flux density (intensity) of the beam, including the polarised and unpolarised light. Q and U measure the intensity of linearly polarised light in the 0° and 90° planes, and 45° and 135° planes, respectively. Finally, the V parameter measures the intensity of both left- and right-handed circular polarisation. Equations 1.2 – 1.5 from Jermak (2016) summarise how one can calculate the Stokes parameters using the intensity, S, of the beam at different angles of a rotating polarising filter. The detectors in this work do not measure circularly polarised light so the V parameter is not used. Whilst attempts have been made to measure circular polarisation from blazars, this work focuses on linear polarisation.

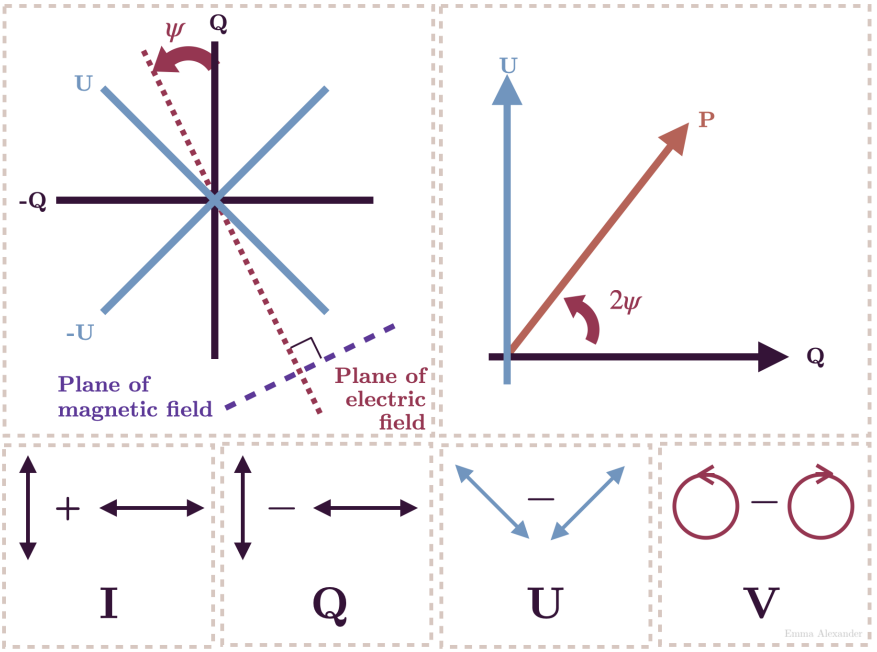

FIGURE 1.10: Schematic providing a visual representation of the Stokes parameters and how the intensity of the incident light beam at different angles is combined to produce them. Figure from [1].

$$I = S_0 = S_{0^\circ} + S_{90^\circ} \tag{1.2}$$

$$Q = S_1 = S_{0^\circ} - S_{90^\circ} \tag{1.3}$$

$$U = S_2 = S_{45^\circ} - S_{135^\circ} \tag{1.4}$$

$$V = S_3 = S_{RCP} - S_{LCP} \tag{1.5}$$

If one considers that the polarisation ellipse shown in Figure 1.9 collapses into a straight line along the major axis when considering linear polarisation only, the Stokes Q and U parameters can be read directly as the X and Y coordinates.

1.5 Variability overview

Table 1.2 shows a summary of the observable variability for various models explored throughout the remainder of this chapter and relevant to this thesis.

Zhang et al. (2015b)

TABLE 1.2: Observable variability properties of different blazar emission models. [1]Marscher (2014), [2]Shablovinskaya et al. (2023), [3]Böttcher (2016), [4]Böttcher & Dermer (2010), [5]Zhang et al. (2022b), [6]Acharya et al. (2023), [7]Dong et al. (2020), [8]Zhang et al. (2017), [9]Zhang et al. (2020), [10]Bachev et al. (2023).

Model	Variability					
	Optical	γ-ray	Polarisation	Polarisation angle	Lags	Timescales
Shocks	chromatic[1]	yes[1]	chromatic[2]	yes[3]	variable[4]	days/weeks[5]
Kink instabilities	chromatic[6]	yes[7]	anticorrelation[7]	yes[7]	no[8]	weeks/months[7]
Magnetic reconnection	chromatic[5]	yes[8]	chromatic[9]	yes[5]	no[5]	hours/days[5]
Doppler factor changes	achromatic[3]	-	yes[10]	yes[10]	no[10]	minutes/hours[10]

1.5.1 Flux

In Section 1.2.1, Figure 1.4 showed the double peak structure of blazar SEDs with emission peaks around optical and γ-ray frequencies. It follows that the behaviour of blazars' optical and γ-ray flux may give valuable insight into the locations of emitting regions and the underlying emission mechanisms occurring within the jet. Strongly correlated behaviour between the two fluxes suggests the emission may originate from linked processes within the jet, favouring leptonic models. Specifically, an increase in synchrotron photons leads to an increase in the seed photons available for inverse-Compton upscattering (Böttcher & Dermer, 2010). On the other hand, a lack of correlated behaviour including orphan optical and γ-ray flares could favour both leptonic and hadronic (lepto-hadronic) models (Sol & Zech, 2022).

Hovatta et al. (2014) analysed the correlations in the optical and γ-ray flux–flux space and found a tighter connection between the correlation of ISP and HSP objects over LSPs (both BL Lacs and FSRQs). If one assumes leptonic modelling, a tighter correlation is expected where the γ-rays are produced via SSC due to the same level of Doppler boosting in the emitting regions. Conversely, Dermer (1995) showed the inverse-Compton emission arising from external photons is more strongly boosted, meaning the linear flux–flux dependence breaks when EC emission occurs. For sources with higher disk, BLR, or torus (thermal) contributions, like the LSP subclass discussed in Section 1.2, one would expect greater EC contributions and therefore a more scattered optical–γ-ray flux correlation.

Some blazars have also been shown to demonstrate periodicity in their light curves. OJ287 is the best-known candidate for hosting a nanohertz gravitational wave emitting SMBH in the present observable universe, with observations dating back to 1888 (Sillanpaa et al., 1988; Valtonen et al., 2021). It has been a target of extensive multi-facility

observation campaigns (Sillanpaa et al., 1988; Valtonen et al., 2016, 2019), particularly over the past 20 years, resulting in the discovery of quasi-periodic doublet flares separated by a few years following a roughly 12 year cycle (Sillanpaa et al., 1988), along with a longer 60 year periodicity (Valtonen et al., 2006). These features are best interpreted as an eccentric binary system where the secondary SMBH "impacts" and crosses through the accretion disk of the primary twice during the 12 year orbital period. Such collisions are likely to significantly disturb the disk, resulting in detectable changes to jet outflow (producing shocks) or directly perturbing the base of the jet (Jormanainen et al., 2025). The longer approximately 60 year period can be interpreted as the advance of the periastron by approximately 36° per orbit. If one assumes the precession effects are asymmetric about the accretion disk plane, after roughly 60 years the periastron would be exactly halfway through its orbit whereby the variability cycle repeats (Dey et al., 2019). Lehto & Valtonen (1996) first proposed the binary SMBH model to explain the variability of OJ287, with subsequent refinements to the model over the subsequent decades (Valtonen et al., 2011, 2023).

While binary SMBHs are a good model for explaining periodic emissions in blazars, it is not the only possibility. Jet precession, or jet wobbling, has been invoked numerous times to explain the long-term periodic variability observed in some blazars (PG 1553+113; Ackermann et al. 2015, OJ287; Britzen et al. 2018, A0 0235+164; Escudero Pedrosa et al. 2024). In this scenario, periodic flares can be the result of geometric changes to the system, rather than any intrinsic luminosity variability (Britzen et al., 2023). During the precession, the apparent Doppler factor of the emission would change, arising from the small but significant changes in the jet angle (Sobacchi et al., 2017). Furthermore, Britzen et al. (2019) suggests jet precession may be responsible for the neutrino emission in TXS 0506+056. In their model, the neutrino emission arises from the interaction between crossing jet features on parsec scales, causing a large increase in high-energy and photo-hadronic interactions, the process that generates neutrinos.

1.5.2 Colour

A frequent optical photometric feature of blazars is their colour evolution during various levels of jet activity. The colour of a source is given by the difference between the magnitude observed in different wavebands. It can take a positive or negative value,

with positive implying the source is brightest/coloured more in the first waveband in the subtraction, while negative implies the opposite. In general, BL Lac type sources tend to exhibit "bluer-when-brighter" (BWB) trends where their spectral index at optical frequencies flattens during periods of higher flux. While some FSRQs also show this, a larger fraction show the opposite behaviour, a "redder-when-brighter" (RWB) trend where their SED at optical frequencies steepens during periods of higher flux (Zhang et al., 2015a). Negi et al. (2022) present a study into the colour variability of 897 blazars (455 BL Lacs and 442 FSRQs), finding 18.5% of BL Lacs display BWB trends and just 9% show RWB trends. For FSRQs, 10.2% of sources showed BWB trends and 17.6% RWB trends. In any case, the colour changes of blazars can be used to determine the origin of the emission and refine emission mechanisms.

BWB behaviour can be explained through different models. One proposed mechanism is synchrotron cooling of internal shock accelerated electrons, where higher-energy electrons cool faster making bluer light appear more variable than redder light (Kirk et al., 1998). Synchrotron cooling refers to the energy loss of accelerated particles via synchrotron emission. Alternatively, the one-component synchrotron model implies an injection of fresh electrons into the jet with a hard energy distribution. These subsequently cool, resulting in increased radiation that is naturally bluer in colour. However, these fail to explain the RWB trend in FSRQs, which requires additional components.

As the name suggests, two-component modelling suggests two underlying components to the observed flux. One of these components would be more intrinsically stable, with a larger spectral index (α_{const}) and the other variable with a flatter spectral index (α_{var}) such that $\alpha_{\text{const}} > \alpha_{\text{var}}$ (spectral index is defined in equation 3.3 and will be explored further in Chapter 3). When the variable component flares, the composite spectrum becomes flatter, showing a BWB trend (Fiorucci et al., 2004). The stable component would consist of thermal emission from the accretion disk and broad line regions (BLR), and the variable originating from non-thermal synchrotron emission. This model can also be adopted to explain the RWB behaviour in FSRQs. If the thermal contribution from BLR and disk emission is significantly larger, the composite spectrum would be flatter than the variable, non-thermal component. In this case, the composite spectrum would therefore steepen during a flare (Gu et al., 2006). Observationally, this is supported by the "blue-bump", sometimes called the "UV-bump", which is a thermal emission excess in FSRQ SEDs at optical and near-UV frequencies (Paltani et al., 1998).

In some cases, RWB behaviour has been observed in BL Lac objects. Where this is the case, the majority of sources tend to be host-galaxy-dominated (Negi et al., 2022), implying an increase in thermal emission. In other cases, this can come from more intrinsically luminous accretion disks than seen in the general BL Lac population, alluding to the masquerading BL Lac type objects.

Moreover, some objects display more complex optical colour behaviour. A stable-when-brighter (SWB) trend has been observed in some objects (Ghosh et al., 2000; Zhang et al., 2015a), where the colour of the source remains constant during flux increases. Additionally, some objects have been observed to display RWB during low states but BWB during high states (Ikejiri et al., 2011; Bonning et al., 2012). The analysis of Zhang et al. (2022a) showed that blazar colour variability could be modelled purely non-linearly whereby source colour follows a logarithmic trend, changing rapidly in lower flux states and remaining constant, or relatively stable, during heightened optical activity. The behaviour can be briefly named bluer-stable-when-brighter (BSWB) and redder-stable-when-brighter (RSWB). This model can reproduce both linear BWB and RWB colour trends as well as SWB behaviour if the source was only sampled during a high or low state, resulting in an apparent linear trend.

1.5.3 Polarisation

Correlations, or a lack thereof, comprising polarimetric quantities can provide valuable insight into emission locations and the jet's local magnetic field morphology.

Plasmoids are regions of relativistic particle density inhomogeneities and enhanced magnetic fields with slowing changing direction. If accelerating, the plasmoid can produce small rotations in the polarisation angle ($< 180°$) and can show a slight frequency dependence in polarisation degree across the optical waveband (Marscher & Jorstad, 2021). Petropoulou et al. (2016) suggest plasmoids may be the direct result of the magnetic reconnection processes in relativistic jets, with the timescale of variability correlated to the size and speed of the plasmoid. Giannios (2013) suggest that the combination of multiple plasmoids can produce fast-evolving TeV flares (notably in the case of PKS 1222+216).

One of the most widely accepted acceleration and emission mechanisms in blazar jets is shocks (Guetta et al., 2004; Liodakis et al., 2022b) (see Section 1.3 for more details on shocks). Depending on the shock speed and magnetic field strength in the emission region, one can expect to observe different polarisation variability. Assuming a weakly magnetised region, one would expect to see prolonged periods of high polarisation (roughly 40%) without any decay phase. This is due to the shock (faster or slower in speed) permanently changing the magnetic field topology. This type of behaviour has not been observed in blazars, so one can presume the variability does not originate from weakly magnetised regions. Conversely, a strongly magnetised emission region can temporarily alter the local larger-scale magnetic field topology as it passes through the jet, after which it returns to its initial state. A slower-moving shock is incapable of producing any large flares or structured polarisation degree/angle variability and only erratic variability is seen. Conversely, for a faster shock, the magnetic field at the shock front becomes more ordered producing flares in the photo-polarimetric data, with smooth rotations in the polarisation angle (Zhang et al., 2014, 2016; Liodakis et al., 2022b). These describe behaviours more typical of observed blazar variability.

It is also through shocks that one may observe frequency-dependent polarisation behaviour (Liodakis et al., 2022b; Shablovinskaya et al., 2023). Across the relatively small optical regime, this effect is only minor and very difficult to observe. However, through well-sampled observations of flaring blazars, the phenomenon has been possible to detect at optical frequencies (Smith & Sitko, 1991; Sillanpää et al., 1993; Tommasi et al., 2001). Most detections are of polarisation variability increasing with decreasing frequency (i.e. polarisation is stronger in redder wavelengths than bluer ones) but this could also be interpreted as dilution of the bluer polarised blazar emission from the host galaxy (Tommasi et al., 2001). It follows that polarimetric variability increasing with frequency (i.e. the polarisation being stronger in bluer wavelengths than redder ones) is much more certain evidence of frequency-dependent polarisation behaviour. Coincidently, this trend is also a signature of shock acceleration in relativistic jets (Angelakis et al., 2016; Liodakis et al., 2022b).

Ordering of the local emitting region's magnetic field however is not necessary to explain some blazar variability. Plasma blobs contain randomly tangled magnetic fields which can be modelled as a number of magnetic cells. In this case, the mean polarisation degree would be low and would fluctuate over time. The polarisation angle would be capable

of varying significantly, showing large ($> 180°$) clockwise and anticlockwise rotations (Marscher & Jorstad, 2021) arising from the stochastic magnetic fields.

Jet kinks (or kink instabilities) refer to current-driven plasma instabilities which cause twists in the jet magnetic field and the transverse displacement of plasma (Dong et al., 2020). These kinks are proposed to be an efficient mechanism to dissipate magnetic energy resulting in particle acceleration through magnetic reconnection (Begelman, 1998). Kink instabilities can cause quasi-periodic oscillations (QPOs) in the optical and γ-ray light curves, with characteristic timescales of weeks to months (Zhang et al., 2017). Interestingly, the photometric flares are anti-correlated with increases in polarisation. Also during the flares, the polarisation angle can undergo large rotations ($> 180°$) (Dong et al., 2020). This low polarisation alongside γ-ray flares during EVPA rotations has been observed in the RoboPol and Liverpool Telescope samples (Blinov et al., 2015; Jermak et al., 2016a). Furthermore, recent simulations have shown shocks can form at the kinked region where subsequent cooling is dominated by EC processes giving rise to multi-wavelength (MWL) flares Acharya et al. (2023). This scenario is one such possibility to explain the recent shorter time-scale (less than a few days) variability observed in BL Lac (Raiteri et al., 2023).

As mentioned in Section 1.3, it is theorised that the larger-scale magnetic field structure of the jet follows a helical trajectory. This structure arises as a direct consequence of the twisting of the accretion disk's magnetic field by the SMBH gravitational pull (Gabuzda, 2021). A strongly magnetised emitting region (i.e. shock) travelling through the jet would have a unique polarisation signature in that throughout long timescale monitoring, one would expect many smooth EVPA rotations, each in the same direction. These rotations would be followed by a "restoring" or "plateau" phase, where the disturbed large-scale magnetic field restores itself after the interaction (Zhang et al., 2016). In this model, rotations are accompanied by polarisation and MWL flares (Zhang et al., 2016). A helical magnetic field paired with the shock-in-jet model has been successfully applied to explain the observed photo-polarimetric emission of several flaring blazars (MRK 501; Villata & Raiteri, 1999) (BL Lac; Marscher et al., 2008) (PKS 1510-089; Marscher et al., 2010) (OJ287; Jormanainen et al., 2025)

Section 1.4 introduced a key feature of the optical polarisation angle variability in γ-ray bright blazars which is the tendency to display large swings/rotations. How and why

these rotations occur have been the focus of dedicated campaigns. Blinov et al. (2015) and Jermak et al. (2016a) found that a significant fraction of optical EVPA rotations were associated with γ-ray flares, indicating a likely connection. They also showed that EVPA rotations were a feature of all blazar subclasses, but more prevalent in LSP sources (Blinov & Pavlidou, 2019). Blinov et al. (2016) also showed that the polarisation degree is generally lower during EVPA rotations. Blinov et al. (2015) showed that not all rotations could be explained by random walk processes and that an alternative mechanism is required. Shishkina et al. (2024) showed a preferred rotation direction across a small sample of blazars, likely caused by the direction of the helical magnetic field structure in the jet.

1.5.4 Time lags

When discussing models for observed blazar variability, it is important to consider a temporal separation between flares on both inter- and intra-waveband scales. A time lag between different frequencies can provide useful information into the mechanisms and locations of the emitting particles, as well as determining true orphan flares from those that are just separated in time from other emission counterparts. Optical and γ-ray flare time lags have been the focus of many recent works (Chatterjee et al., 2008; Gaur et al., 2012; Liodakis et al., 2018). In the leptonic scenario, time lags between optical and γ-ray emission can constrain the locations of seed photons for inverse-Compton upscattering. Seed photons produced in the BLR must travel to the acceleration and synchrotron emitting regions within the jet, whereas synchrotron photons are already produced within the jet. Taking the distance as 10^{15} m from Table 1.1 and assuming $\tau \simeq d/c$, the timescales here are of the order of days to weeks. For this reason, one may expect an observable delay in the higher energy γ-ray emission compared to the optical.

While inter-band lags have been observed with relatively low uncertainties (Marscher et al., 2004; Cohen et al., 2014; Liodakis et al., 2019), intra-band lags are much less commonly observed. Wu et al. (2009) proposed the first detection of an approximately 2 minute intra-band time lag within the optical waveband (B and R bands). The internal shock model predicts time lags across all synchrotron emission frequencies, and therefore within the optical waveband. The rate of synchrotron cooling is frequency dependent, meaning variability at higher-energy precedes that at lower energies thus producing a

time lag (Kirk et al., 1998). Irregularly sampled data and limited time resolution make intra-band time lags difficult to detect, especially across the optical waveband which makes up only a very small part of the electromagnetic spectrum.

One of the biggest uncertainties around the detection of both inter- and intra-band time lags is their timescales. While the internal shock model predicts optical and γ-ray lags, the leading emission and the temporal separation can vary drastically depending on several parameters, producing lags on timescales of minutes to hours. For example, increasing external photon densities (more EC emission) increases the rate of cooling and decreases the γ-ray leading time lags. Decreasing external photon densities reveals SSC emission, producing optical-leading lags. As the size of the shell radius increases, its density decreases along with the magnetic field strength, increasing the Compton dominance. The size of any lags between optical and higher frequency emission increases with shell radius likely due to an increasing synchrotron cooling timescale. The relative Lorentz factor of the colliding shells ($\Gamma_{\rm rel}$) also affects the timescale of interband lags. A larger $\Gamma_{\rm rel}$ decreases the cooling timescales (i.e. more radiatively efficient) and subsequently any time lags Böttcher & Dermer (2010).

1.5.5 Intranight variability

Blazars can show variability on a variety of timescales, from years down to minutes, with the latter being referred to as intranight variability. While intranight variability campaigns predominantly focus on optical frequencies, successful efforts have been made to study the phenomenon at infrared (Gupta et al., 2008) and UV frequencies (Chand et al., 2021). For the remainder of this work, intranight variability will refer to that at optical frequencies only (intranight optical variability; INOV). The intranight variability of blazars has been the focus of numerous campaigns over the past 30 years (Miller et al., 1989; Sagar et al., 2004; Chand et al., 2021), but it is still not a well-understood characteristic of their emission.

Variability on intranight timescales can include quasi-periodic oscillations (QPOs) (Jorstad et al., 2022), micro-flares (Bhatta et al., 2015), and gradual flux changes (Subbu Ulaganatha Pandian et al., 2022), observed over minute- to hour-long timescales. Many models have been proposed to explain the different types of variability, and these predict time lags between different wavebands, colour evolution, and polarisation degree and

angle changes. Geometric changes correspond to the evolution of the physical features of the jet and its structure. When an emitting region traverses through the relativistic jet and around any helical magnetic field, it may be possible to detect photometric variability arising from the changing Doppler factor (Gopal-Krishna & Wiita, 1992). Variability intrinsic to the jet emission implies changes to its energy output. Changes to particle energy distributions can arise from shock propagation and magnetic reconnection which are associated with spectral trends and intra-band time lags (Urry et al., 1997; Tavecchio et al., 1998; Bachev et al., 2012; Bachev, 2015). It is also possible that variability is caused by reasons extrinsic to the blazar system. One such example includes microlensing from objects outside the blazar system along our line of sight and is associated with large, individual apparent flaring events (Paczynski, 1996).

There has been substantial recent progress in obtaining intranight or high cadence data through the use of dedicated facilities (ROBOPOL; Blinov & Pavlidou, 2019) or by combing efforts across different telescopes (Whole Earth Blazar Telescope (WEBT); Villata et al. 2002, NOn-stop Polarisation Experiment (NOPE); Liodakis et al. 2024).

1.6 Blazars in a wider context

1.6.1 Multiwavelength variability

While this thesis focuses on the variability of blazars in optical (photopolarimetric) and γ-ray (photometric), studies at radio and X-ray frequencies can provide further valuable insights. Similar to optical observations, radio observations are generally agreed to probe non-thermal synchrotron emission originating from the relativistic jet. The difference between optical and radio observations, however, is that optical frequencies probes the sub-parsec scale (collimated inner jet) and radio frequencies probe the parsec scale (less collimated outer jet). X-ray observations are capable of probing both the lower- and higher-energy (Böttcher, 2019) SED peaks, depending on the classification of the source; The synchrotron peak extends more into the X-ray regime for HBL sources, whereas the higher-energy peak emission dominates in X-rays for LSP objects (Abdo et al., 2010b).

Radio monitoring of blazars has long been used to trace jet activity, particularly through flux and polarisation variability with typical timescales of days to years. Long-term monitoring programmes such as the Owens Valley Radio Observatory (OVRO) 40m blazar monitoring programme (Richards et al., 2011) and the MOJAVE project (Lister et al., 2019) have provided high-cadence radio light curves and VLBI imaging, respectively, enabling detailed studies of parsec-scale jet kinematics, Doppler factors, and the correlation of radio variability with flaring at higher energies. Polarisation variability in the radio band also helps constrain magnetic field structures and the evolution of the energy density in the jet. Conclusions from radio photopolarimetric studies include: higher frequency radio observations show more polarisation variability than those observations at lower frequencies, and that the polarisation and radio spectral index are correlated, suggesting synchrotron emission from the jet (Fan et al., 2008); BL Lac objects display significantly larger variability amplitudes, but FSRQs vary more strongly (Richards et al., 2011); The shapes of some blazar jets suggest the switching on and off of the jet, or the realignment between the disk and jet (Baghel et al., 2023).

In the X-ray domain, instruments such as Swift-XRT and XMM-Newton have contributed extensively to time-domain studies, revealing flaring episodes and spectral changes indicative of particle acceleration processes (Piconcelli & Guainazzi, 2005; D'Ammando & Orienti, 2013; Giommi et al., 2021). Perhaps the most significant advancement in blazar observations in recent times has been the launch of the Imaging X-ray Polarisation Explorer (IXPE), which began science operations in January 2022. This observatory is the first X-ray polarisation telescope and has begun to make valuable contributions to the field of MWL photopolarimetric blazar observations, supported by simultaneous MWL observations, including those presented in this work. Observations of the blazar MRK 501, a HBL with synchrotron peak emission at X-ray frequencies, revealed a polarisation degree higher than those at optical wavelengths, and variability suggesting an increasingly turbulent plasma with distance from the core, with shocks being the dominant particle acceleration mechanism (Liodakis et al., 2022b). Furthermore, time lags between the different X-ray energy bands are a useful tool to detect cooling timescales of X-ray particle populations, with results suggesting the presence of soft lags of order minutes to hours (Zhang et al., 2002).

1.6.2 Other jetted sources

It is important to recognise that astrophysical relativistic jets are not restricted to blazars and AGN, but also appear in other transient or time-variable sources such as gamma-ray bursts (GRBs; Piran 2004), microquasars (X-ray binaries; Mirabel & Rodríguez 1999), and tidal disruption events (TDEs; Burrows et al. 2011). While the timescales, energies, and scales of these systems are vastly different, they do share several physical characteristics, such as the presence of collimated, relativistic jets thought to be powered by accretion onto compact objects and launched via magnetohydrodynamic processes (De Young, 1991; Tordella et al., 2011).

The benefit of studying blazars lies in their large size and longer variability timescales. In contrast, many other jetted transients, such as GRBs, exhibit extremely rapid variability, often evolving on timescales of seconds to minutes. This variability can arise due to similar mechanisms to blazars, such as jet outflow variability (shocks) (Ziaeepour, 2009), jet instabilities (Kylafis et al., 2012), or jet precession (Huang & Liu, 2024). Such short-duration behaviour on small scales poses significant challenges for acquiring detailed photopolarimetric data, which are required for probing the magnetic field structure and refining emission mechanisms in the jets (Toma et al., 2009; Gill et al., 2021; Bernardini & Cackett, 2014).

Blazars serve as a unique laboratory for exploring jet physics. Their extended activity and variability over longer timescales make them ideal for testing theoretical models and inferring properties that are likely applicable to more quickly evolving jetted sources. Furthermore, improved understanding of blazar jets can inform the design of observational campaigns and multiwavelength follow-up for GRBs, TDEs, and X-ray binaries.

1.7 Summary and thesis overview

The purpose of this thesis is to better understand the emission mechanisms across a large sample of γ-ray bright blazars of different classifications through the analysis of Liverpool Telescope photo-polarimetric data. Fermi-LAT γ-ray data have also been obtained to identify any related multi-wavelength behaviour. Together, the optical photometric,

polarimetric, and γ-ray data allow the investigation into the structure and evolution of emitting regions and magnetic fields within the inner jets of blazars.

The photopolarimetric data presented in this work comprise regular monitoring across multiple optical wavebands over an 11 year period, from 2013 to 2024. Although similar datasets exist, such as RINGO2/DIPOL (Jermak et al., 2016b), Tuorla/KVA (Nilsson et al., 2018), and RoboPol (Blinov & Pavlidou, 2019), few provide (quasi-)simultaneous multiwaveband observations of a large sample of sources over such extended timescales. This dataset captures blazar variability across low, high, and quiescent states, enabling unbiased and statistically robust conclusions regarding the origins of the observed behaviour. While higher-cadence monitoring could have been achieved by reducing either the sample size or the number of wavebands, as effectively demonstrated in other campaigns, the approach taken here allows for meaningful inferences about trends across and within blazar subclasses, while also providing insight into the wavelength-dependent nature of photopolarimetric variability, key to constraining emission models and jet physics.

Some of the open questions surrounding blazar science that this thesis aims to contribute towards can be summarised as follows:

- Where is the location of high energy emission, and what particles are responsible? - Is the emission leptonic or hadronic in origin?
- What are the mechanisms associated with particle acceleration?
- What is the magnetic field structure of the relativistic jets?
- Are there any differences between observed trends in different classes of blazars?
- What are the causes of periodic variability observed in some blazars?

This work aims to help answer these questions through the analysis of multi-band, long-term photo-polarimetric monitoring of a sample of blazars observed with Liverpool Telescope polarimeters from 2013 to 2024. Flux, colour, polarisation degree and polarisation angle changes in addition to both intra- and inter-band lags will be explored, providing insight into both long- and short-term behaviours. Table 1.3 summarises emission mechanisms and the possible observable channels (optical/γ-ray, neutrino, and polarised emission) explored in this chapter.

TABLE 1.3: Summary of emission mechanisms and their associated variability across different observational channels. [1]Maraschi et al. (1992), [2]Rybicki & Lightman (1979), [3]Bloom & Marscher (1996), [4]Sikora et al. (1994), [5]Mücke & Protheroe (2001), [6]Gopal-Krishna (2024).

Emission	Variability			
	Optical	γ-ray	Neutrino	Polarisation
Synchrotron	yes[1,3]	no	no	yes[2]
Synchrotron-self Compton	no	yes[1,3]	no	no
External Compton	no	yes[4]	no	no
Proton synchrotron	yes[5]	yes[5]	yes[5]	yes[5]
Bremsstrahlung	yes[6]	no	no	no

The findings from the previous generation RINGO3 polarimeter inform the decisions for the continuation of the Liverpool Telescope blazar monitoring program with the new generation polarimeter, MOPTOP. Observations with MOPTOP allow for more efficient source follow-up and investigation of fainter objects. These new observations will benefit from optical data with increased sensitivity and improvements to the observing cadence. This will allow a deeper investigation into the observed relationships and enable the identification of any new behaviour associated with individual sources and across the blazar population.

The thesis is organised as follows. Chapter 2 discusses the facilities and instrumentation used in this work, including the development of any data reduction pipelines. Chapter 3 details the photometric analysis and results from both the RINGO3 and MOPTOP polarimeters, in addition to comparison to γ-ray data. Chapter 4 details the polarimetric analysis and results from both the RINGO3 and MOPTOP polarimeters, which again includes comparison to γ-ray data. Chapter 5 presents an intranight monitoring campaign of a small sample of blazars. Chapter 6 concludes the thesis and discusses future work to be explored following on from the findings presented in previous chapters.

Chapter 2

Instrumentation and Data Reduction

2.1 Liverpool Telescope

The Liverpool Telescope (LT) is a 2-metre class, fully robotic telescope located at the Observatorio del Roque de los Muchachos in La Palma. First light for the telescope was achieved in July 2003, with science operations from January 2004. Since October 2004, operations have been fully autonomous (Steele et al., 2004). The main scientific goals of the LT consist of rapid target-of-opportunity (ToO) follow-up such as with gamma-ray bursts, supernovae, electromagnetic gravitational wave counterparts etc, and the monitoring of variable targets or small-scale surveys.

The LT is a fully robotic telescope with no permanent on-site astronomers. Instead, the telescope is controlled by a scheduling algorithm that is capable of planning observations based on a variety of constraints and variables, such as the observing program priority, current weather and atmospheric conditions, and the current location and trajectory of the source on the sky with respect to its zenith. Additionally, the scheduler can override current observations using ToO mode if triggered by short duration, high variability time-domain science.

The telescope itself has an $f/10$ Ritchey-Chrétien optical configuration, consisting of a 0.62 m secondary mirror reflecting light back through the primary. In addition to an

instrument located at the Cassegrain focus (straight-through port), a rotating tertiary fold mirror can be placed before the focus which allows up to eight instruments to sit at side ports. The field-of-view (FOV) at these side ports reduces from 42 arcminutes at the straight-through port to 7.5 arcminutes. During its lifetime, there have been many instruments situated on LT for a variety of scientific purposes, such as optical and infrared imaging, low- and high-resolution spectra, and polarimetry. LT instruments relevant to this work and their data reduction processes are detailed in the following sections.

2.1.1 RINGO3

The RINGO3 polarimeter operated on the Liverpool Telescope from January 2013 until it was decommissioned in January 2020. The instrument utilised a polaroid which rotated every 2.3 seconds to produce eight separate exposures synchronised to the phase of the polaroid. Specific phase positions can be stacked to calculate the polarimetric and photometric values. Stacking corresponding frames from multiple runs was used to increase signal-to-noise. Before reaching the detector, the light was split by two dichroic mirrors into red (770-1000 nm), green (650-760 nm), and blue (350-640 nm) light and detected by three separate cameras, d, f and e respectively. For the remainder of this work, these non-standard filters will be referred to as $r*$, $g*$, and $b*$ for red, green, and blue light respectively. This configuration allowed for simultaneous photo-polarimetric measurements of a given source across the entire optical spectrum (Arnold et al., 2012; Słowikowska et al., 2016).

Soon after its commission, it was discovered that the interaction between the polarised beam and dichroic mirror coatings was not as expected. Instead of a constant rate of depolarisation, the coatings caused depolarisation correlated with the polarisation of the source. This was seen in the q–u plots of polarised standard stars which were expected to show a circle around $q = 0$, $u = 0$ for each filter when observing at different sky angles (the rotation of the sky relative to the instrument), but instead showed circles with differing origins. For variable sources, there would therefore be a degeneracy between the actual q–u of the source and the instrumental q–u plane [1]. To correct for this, in December 2013 a depolarising Lyot prism was fitted before the collimator as after the

[1] https://telescope.livjm.ac.uk/TelInst/Inst/RINGO3/

polaroid, only the intensity of light is needed for any photo-polarimetric measurements (Słowikowska et al., 2016). Photometric data remained unaffected by this interaction, but only polarimetric measurements after the prism was fitted to RINGO3 could be used. The structure of the instrument can be seen in Figure 2.1.

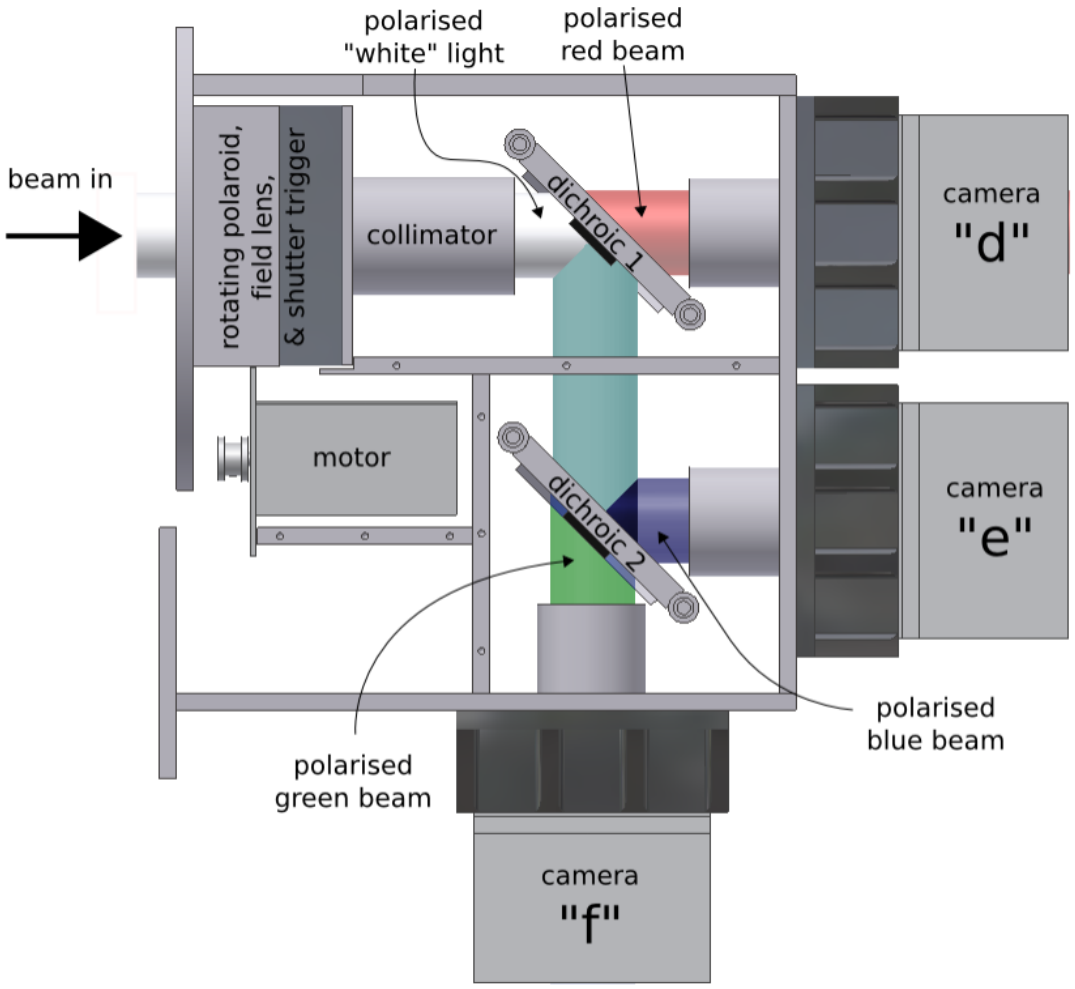

FIGURE 2.1: Structural overview of the RINGO3 polarimeter from Arnold et al. (2012). Light enters the instrument and passes through the rotating polaroid before being depolarised by a Lyot prism (not shown). Two dichroic mirrors split the light which is then detected by three cameras. The instrument was located on one of the telescope side ports.

2.1.1.1 Photometric reduction

The initial reduction of each frame is performed via the LT automated reduction pipeline which performs de-biasing, dark subtraction, flat fielding, and world coordinate system (WCS) fitting. Respectively, these remove the signal added to ensure the analogue-to-digital converter always receives a positive count value, remove the thermal noise

generated by the detector, account for the three detectors differing pixel-to-pixel sensitivities, and assign right ascension (RA, α) and declination (Dec, δ) coordinates to each pixel in the frame.

The photometric information was extracted using differential photometry. In this way, the apparent instrumental magnitude of an object in the frame with a known magnitude was used to calibrate the instrumental magnitude of the source. This is done using Equation 2.2 where the instrumental magnitude of an object is given by Equation 2.1. The errors on apparent and instrumental magnitudes are given by Equations 2.3 and 2.4 respectively.

$$inst = -2.5 \log_{10} (S_1) \tag{2.1}$$

$$mag_{src} = inst_{src} + mag_{cal} - inst_{cal} \tag{2.2}$$

$$\Delta mag_{src} = \sqrt{(\Delta inst_{src})^2 + (\Delta inst_{cal})^2} \tag{2.3}$$

$$\Delta mag_{inst} = \frac{2.5}{\ln(10)} \times \frac{\Delta S_1}{S_1} \tag{2.4}$$

An advantage to calculating the magnitude of variable sources in this way is that the nightly variability induced by seeing and airmass is negated due to the observation of both the source and in-frame calibration star occurring at the same time. This technique, however, requires a known magnitude for the calibration star in the respective waveband. This is difficult for RINGO3 observations given the non-standard waveband ranges of the three detectors. It was therefore necessary to devise a method to calculate the magnitude of the calibration star in each filter before performing differential photometry.

During the lifetime of RINGO3, observations of A0V stars were performed during various photometric nights. A0V stars have a unique property in any Vega-referenced magnitude system which is that their magnitude is consistent across all wavebands, implying that these stars have neutral colour (i.e. $V = b^* = g^* = r^*$) and also exhibit very little variability (Pecaut & Mamajek, 2013). These A0V star observations will therefore have

a known magnitude in the RINGO3 photometric system. Ideally, the observations of the A0V star will be taken on the same night as the observations of the blazar to negate the effects of mirror degradation changing the zero point over time. Unfortunately, this was not the case, so by adjusting the counts from the objects to account for mirror degradation, one can use these observations to calculate a zero point for a fixed date to then be used to calculate the magnitude of the calibration star in the RINGO3 waveband.

To find the rate of mirror degradation, one can use the nightly observations of polarimetric standards taken with RINGO3. The rate was calculated using data from the period MJD 57202 to 58296 for 3 standard stars, BD+64 106, BD+25 727, and HILT 960 and averaged across all sources. The rate was calculated as $4.65 \pm 0.13 \times 10^{-4}$ day^{-1} relative to the initial counts measured from the object at "day zero". The rate was also found to be consistent between cameras. This specific interval to calculate the degradation rate was chosen as the longest period between mirror cleans, which causes a large increase in throughput not consistent with the degradation rate.

The observations of the A0V stars spanned two mirror cleaning intervals: MJD 57202-58296 (primary mirror re-coating on 29/06/2015 and tertiary feed mirror clean on 27/06/2018 respectively) and MJD 58296-58862 (tertiary feed mirror clean on 27/06/2018 and decommissioning on 14/01/2020 respectively). The A0V stars used and the dates of observation under photometric conditions are detailed in Table 2.1. These data were reduced and the counts were calibrated to the beginning of the respective cleaning interval using Equation 2.5 where R is the mirror degradation rate ($4.65 \pm 0.13 \times 10^{-4}$ day^{-1}) and Δmjd was the number of days elapsed since the beginning of the cleaning period.

$$c_{after} = \frac{c_{before}}{1 - (R \times \Delta mjd)} \tag{2.5}$$

After calibration, the zero point at the beginning of each cleaning epoch was calculated for each observation for all A0V stars. The zero points for each camera at the start of each epoch are shown in Table 2.2. The error on each value has been calculated as the standard error from all the calculated values ($\frac{STDDEV}{\sqrt{N}}$). All the calculated zero points for each epoch are shown in Figures 2.2 and 2.3 for epochs beginning MJD 57202 and 58296 respectively.

TABLE 2.1: Table showing a list of A0V stars observed with RINGO3 with RA, DEC, magnitude ([1] Høg et al. (2000)), and the dates of observation.

Source	RA	DEC	Magnitude (V)	Observation Dates
HD50188	06:52:04.953	-00:18:18.256	9.509[1]	30/01/2016
-	-	-	-	31/01/2016
-	-	-	-	30/01/2019
-	-	-	-	31/01/2019
HD24083	03:49:08.835	-27:25:37.171	10.783[1]	30/01/2016
-	-	-	-	31/01/2016
-	-	-	-	10/02/2016
-	-	-	-	30/01/2019
-	-	-	-	31/01/2019
-	-	-	-	01/02/2019
HD27166	04:16:27.542	-27:01:18.629	10.022[1]	30/01/2016
-	-	-	-	31/01/2016
-	-	-	-	10/02/2016
-	-	-	-	30/01/2019
-	-	-	-	31/01/2019
-	-	-	-	01/02/2019
HD92573	10:42:07.669	+45:50:54.171	10.091[1]	30/01/2016
-	-	-	-	30/01/2019
-	-	-	-	31/01/2019
HD96781	11:08:56.367	+13:21:11.258	10.086[1]	13/06/2019
-	-	-	-	14/06/2019
-	-	-	-	15/06/2019
HD208368	21:56:08.041	-12:36:01.827	10.592[1]	13/06/2019
-	-	-	-	14/06/2019
-	-	-	-	15/06/2019
BD+30 2355	13:01:52.962	+29:34:57.159	10.580[1]	13/06/2019
-	-	-	-	14/06/2019
-	-	-	-	15/06/2019
BD+67 675	10:58:58.943	+67:03:29.652	10.451[1]	13/06/2019
-	-	-	-	14/06/2019
-	-	-	-	15/06/2019
BD+25 2478	12:16:33.885	+24:36:33.740	10.706[1]	13/06/2019
-	-	-	-	14/06/2019
-	-	-	-	15/06/2019
-	-	-	-	15/06/2019

TABLE 2.2: Table showing the zero points calculated for finding the calibration star magnitudes in the RINGO3 photometric system. These zero points have been calculated for the beginning of each mirror cleaning epoch where observations of A0V stars were taken.

	zero point		
Epoch MJD	$r*$	$g*$	$b*$
57202 - 58295	23.695±0.019	24.423±0.029	25.799±0.046
58296 - 58862	23.382±0.013	24.045±0.014	25.342±0.024

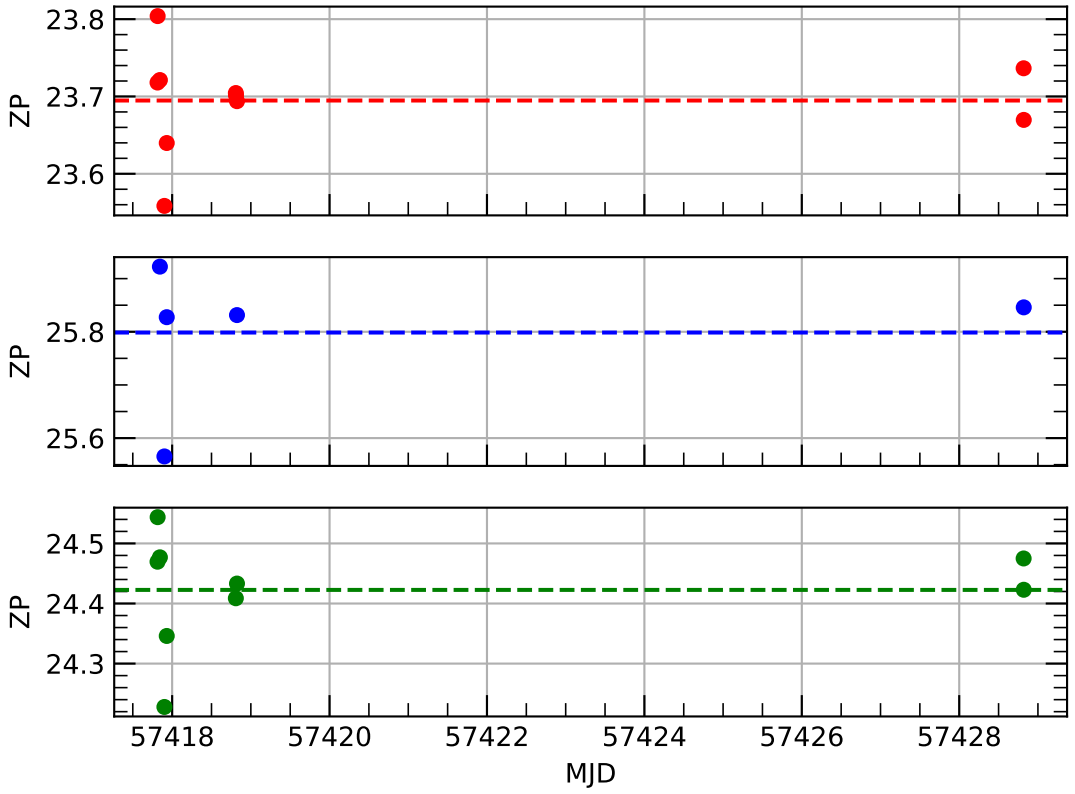

FIGURE 2.2: Zero points calculated with RINGO3 A0V star data calibrated for mirror degradation at MJD 57202.

With the calibrated zero points, reference magnitudes of the in-frame calibration star for each filter were obtained. This was done by taking the science observations from within either epoch and adjusting the counts for mirror degradation in the same way as previously described by equation 2.5. By doing this, the counts were calibrated to the same dates as the zero points. The magnitude of the calibration star was found by summing the associated zero point and instrumental magnitude. The average magnitude across both epochs using all available observations was used as the final calibration star magnitude.

2.1.1.2 Optimum aperture size

A procedure to calculate each source's optimum reduction aperture size was produced to obtain the best quality data for each source in the RINGO3 sample. This pipeline took a small sample of frames for each object and computed the SNR of the source for different aperture pixel radii ranging from 1 to 20 in increments of 0.1 pixels. Plotting the SNR vs. pixel size and identifying the pixel size value corresponding to the average

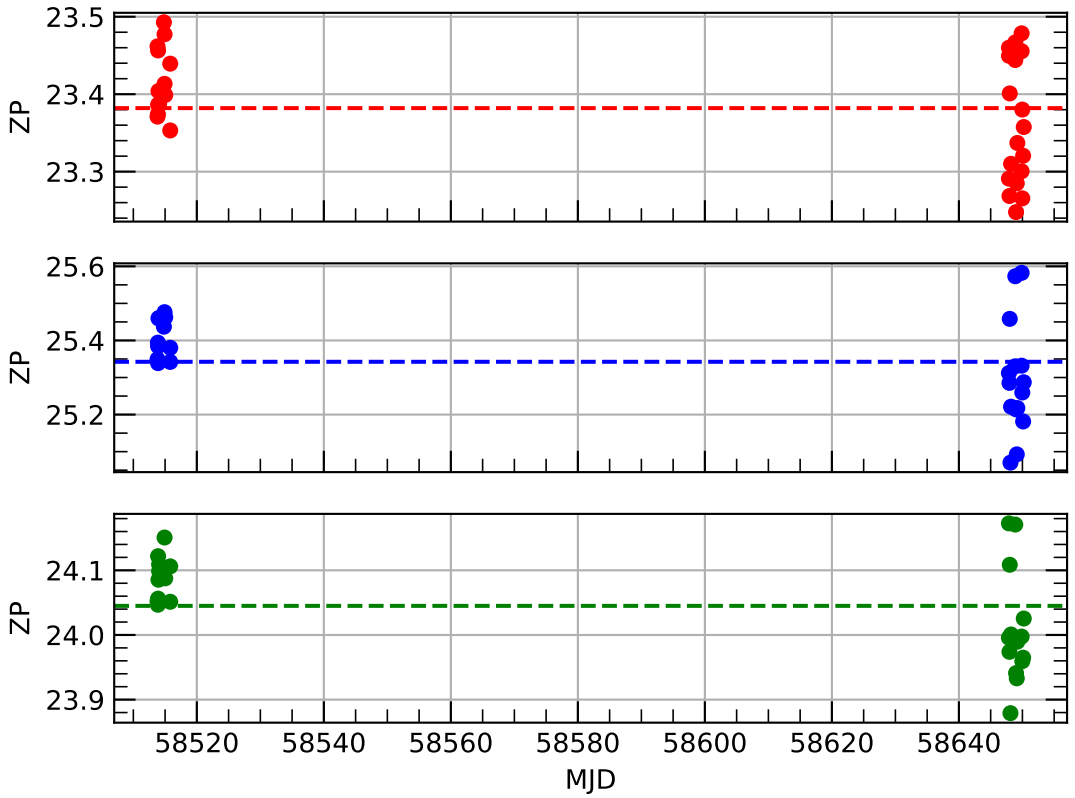

FIGURE 2.3: Zero points calculated with RINGO3 A0V star data calibrated for mirror degradation at MJD 58296.

peak SNR gave the aperture size used for reduction. Those sources whose plots produced an irregularly shaped curve were inspected. This irregularity was found to be due to a coincident foreground star entering the background annulus , the size of which was set by some multiples of the aperture radius. These multiples were adjusted to remove any objects from within the annulus. Figure 2.4 shows a plot of the different SNR vs. aperture size curves for the r^*-band data of OJ287. Each line represents a different frame and the vertical dotted line shows the average peak value. The same procedure was carried out for g^*- and b^*-band data and the final three aperture sizes were averaged to give the final value used in the reduction.

2.1.1.3 Polarimetric reduction

As described previously, RINGO3 observations consisted of a set of eight successive exposures taken with each camera as the polaroid rotated every 45°. Each observation, therefore, consisted of $N \times 24$ frames where N is the number of consecutive rotations.

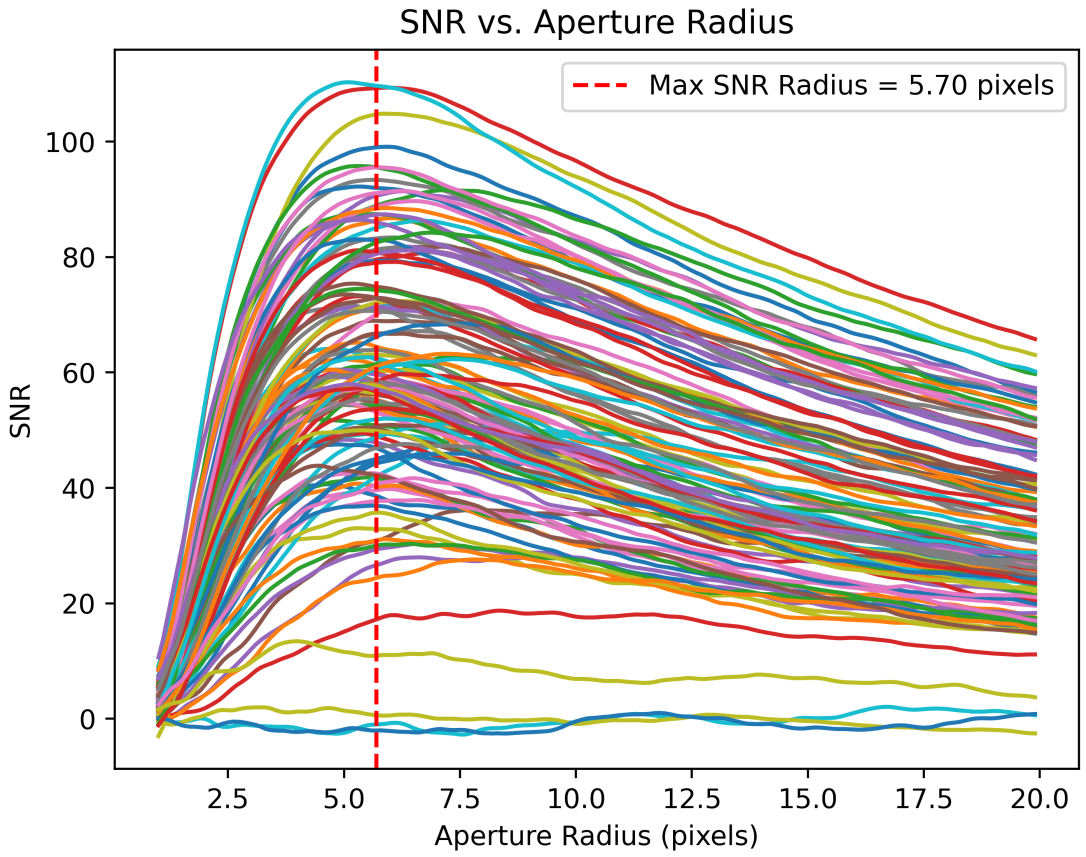

FIGURE 2.4: Plot showing the calculation of the optimum aperture size for the RINGO3 data of OJ287. Each line shows the SNR at a given aperture radius for different frames. The dotted vertical line shows the average peak, the value of which is given in the legend. This plot is for the r^*-band data, but the same procedure was carried out for g^*- and b^*-band data and the three optimum sizes were averaged to give the final value used in the reduction.

The complete reduction of all RINGO3 data including the extraction of relevant photo-polarimetric data was performed in Python. In this pipeline, the source extraction and basic polarimetric calculations were written by Dr. Manisha Shrestha using the ASTROPY package (Bradley, 2023) and followed the procedure detailed in Clarke & Neumayer (2002) to calculate three of the four Stokes polarisation parameters: I, Q, U.

Through the summation of the counts from the source at specific polaroid positions, one can calculate Stokes I, Q, and U parameters which, in turn, can be used to calculate the magnitude, degree of linear polarisation, and electric vector position angle (EVPA) of the source. Figure 2.5 from Clarke & Neumayer (2002) shows each polaroid position as different segments of a ring over 360°, where rotation positions 180° apart are detecting light in the same polarisation plane at both positions. The summations required to calculate Stokes parameters are detailed in Equations 2.6, 2.7 and 2.8 below with errors

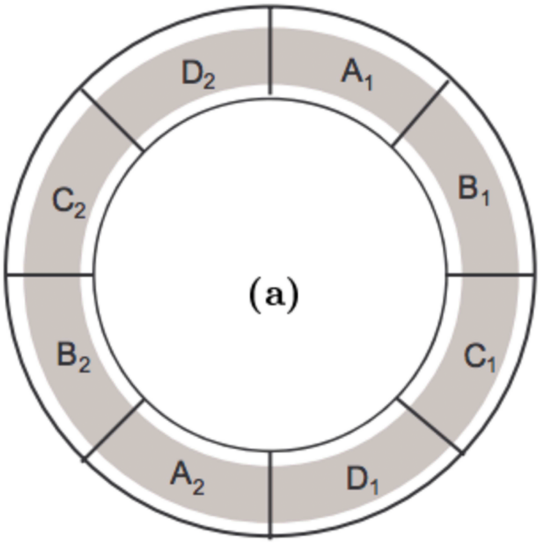

FIGURE 2.5: A schematic from Clarke & Neumayer (2002) of the RINGO3 polaroid positions. The counts received from each of the eight polaroid positions can be combined and used as described in Section 2.1.1.3.

in Equations 2.9, 2.10 and 2.11. The counts per rotor position are obtained through aperture photometry and the respective errors from the background in each frame.

$$S_1 = A_1 + A_2 + B_1 + B_2 + C_1 + C_2 + D_1 + D_2 \tag{2.6}$$

$$S_2 = A_1 + A_2 + B_1 + B_2 \tag{2.7}$$

$$S_3 = B_1 + B_2 + C_1 + C_2 \tag{2.8}$$

$$\Delta S_1 = \sqrt{\Delta A_1^2 + \Delta A_2^2 + \Delta B_1^2 + \Delta B_2^2 + \Delta C_1^2 + \Delta C_2^2 + \Delta D_1^2 + \Delta D_2^2} \tag{2.9}$$

$$\Delta S_2 = \sqrt{\Delta A_1^2 + \Delta A_2^2 + \Delta B_1^2 + \Delta B_2^2} \tag{2.10}$$

$$\Delta S_3 = \sqrt{\Delta B_1^2 + \Delta B_2^2 + \Delta C_1^2 + \Delta C_2^2} \tag{2.11}$$

The stokes q–u parameters normalised for the total intensity can be calculated using the $S_{1,2,3}$ summations as follows in Equations 2.12 and 2.13

$$q_{measured} = \frac{Q}{I} = \pi \left(\frac{1}{2} - \frac{S_3}{S_1} \right) \tag{2.12}$$

$$u_{measured} = \frac{U}{I} = \pi \left(\frac{S_2}{S_1} - \frac{1}{2} \right) \tag{2.13}$$

To calculate the final normalised Stokes q–u values, one must account for instrumental depolarisation in the form of the q_0, u_0 values detailed in Equations 2.14 and 2.15. The propagated errors are shown in Equations 2.16 and 2.17. These can be calculated by observing zero-polarised standard stars and measuring their apparent q–u values induced by the instrument. By observing many times and averaging results, more precise estimates of these values are obtained. In the case of RINGO3, these values were calculated by Dr. Manisha Shrestha. The corrective factor of 1.14 on the q value accounts for the elongation of the q–u circle in the q plane, correcting the angular dependence of instrumental depolarisation (Arnold, 2017). While no error is given on this value for RINGO3, the same method was employed to determine the characteristic ellipse of RINGO2 observations, where after correction, the ellipticity of all rings was less than 0.05. This is therefore assumed to be the error on the ellipticity correction value for RINGO3.

$$q = (q_{measured} - q_0) \times 1.14 \tag{2.14}$$

$$u = u_{measured} - u_0 \tag{2.15}$$

$$\Delta q = \pi \sqrt{\left(\frac{\Delta S_3}{S_1} \right)^2 + \left(\frac{S_3 \Delta S_1}{S_1^2} \right)^2} \tag{2.16}$$

$$\Delta u = \pi \sqrt{\left(\frac{\Delta S_2}{S_1} \right)^2 + \left(\frac{S_2 \Delta S_1}{S_1^2} \right)^2} \tag{2.17}$$

The degree of polarisation can be calculated from the normalised Stokes q–u values as the ratio of polarised light observed to unpolarised light. This is shown in Equation 2.18. Its propagated error is shown in Equation 2.19, in agreement with Naghizadeh-Khouei & Clarke (1993) and Clarke & Neumayer (2002).

$$P = \frac{\sqrt{Q^2 + U^2}}{I} = \sqrt{q^2 + u^2} \tag{2.18}$$

$$\Delta P = \frac{\sqrt{q^2(\Delta q)^2 + u^2(\Delta u)^2}}{P} \tag{2.19}$$

The uncorrected EVPA, θ, can be calculated as shown in Equation 2.20. There exists an ambiguity in the detection of the angle of the polarised light plane as it is not possible to distinguish planes rotated 180°. To account for this, one restricts the value to between 0° and 180°, and performs an unwrapping algorithm to best find the true value with respect to the previous value. The algorithm finds the true angle by adjusting points by any multiple of $N \times 180°$ greater or less than the detected value. This procedure is described in more detail in Section 2.4.1.

$$\theta = \frac{1}{2} tan^{-1}\left(\frac{u}{q}\right) \tag{2.20}$$

When calculating the EVPA, one must account for the position of the telescope on the sky and the position of the instrument on the telescope. This is shown in Equation 2.21 with its propagated error shown in Equation 2.22, in agreement with Naghizadeh-Khouei & Clarke (1993). The former of these positions are given in the fits headers of each observation as ROTSKYPA, which describes the observations' angle of rotation East of North on the sky. The latter is calculated using observations of polarised standard stars with known EVPA values and Equation 2.21 rearranged for k. Taking many observations of these standard stars, one can better constrain the k values for each camera.

$$EVPA = \theta + ROTSKYPA + k \tag{2.21}$$

$$\Delta EVPA = \frac{180}{\pi} \frac{\sqrt{u^2 (\Delta q)^2 + q^2 (\Delta u)^2}}{2P} \tag{2.22}$$

Importantly, all calibration values (q_0, u_0 and k) for each camera had to be recalculated after any mirror cleaning or instrument reintegration. This was due to non-uniform changes in the telescope throughput and a differing instrument orientation with respect to the telescope respectively.

2.1.1.4 Data vetting

After reduction, the data were subject to various quality checks in order to remove poor-quality (high uncertainty) data arising from poor weather and atmospheric effects, telescope problems, and incorrectly configured observing sequences. It was also important to ensure any automated vetting procedure was tailored to each source given the amount of data and average signal-to-noise (i.e. the average photometric and polarimetric uncertainty) would be different for each source. The following section describes the processes used to vet the data. In total, approximately 246,000 frames were reduced resulting in the vetting of around 10,000 *r*g*b** epochs.

The first of these checks was to remove data where the WCS could not be fitted, likely due to cloud cover obscuring all or part of the frame. Without this, the apertures during reduction will have been placed incorrectly, if at all, and the reduction will have produced inaccurate data. On average, across all sources in the RINGO3 sample, observations with WCS errors made up around 4.5% of all observations.

Next, it was noticed that some of the poor-quality data originated from frames where light cloud cover and/or poor seeing was present yet the WCS could still be fitted. To automatically remove these frames, the ratio of the calibration star counts to its error was taken, and those data where the ratio was smaller than the median ratio minus three median absolute deviations (MADs) were removed. This condition is shown in Equation 2.23 where $\left\langle \frac{S_1}{\Delta S_1} \right\rangle$ is the median S_1 to ΔS_1 ratio.

$$\frac{S_1}{\Delta S_1} < \left\langle \frac{S_1}{\Delta S_1} \right\rangle - 3 \times \mathrm{MAD}\left(\frac{S_1}{\Delta S_1}\right) \tag{2.23}$$

Across all sources in the sample, around 1.6% of data were removed due to a low calibration star counts to error ratio. Figure 2.6 shows the full light curve for the source S50716+714 including EVPA, pol and magnitude data for each RINGO3 band. The black points show the data removed by the vetting pipeline due to small calibration star ratios. It can be seen that these points make up a large proportion of the data with the largest photo-polarimetric uncertainties. It is noted that the vetting takes place before correcting for the 180° ambiguity in EVPA so the EVPA data is unwrapped in this plot.

Following this, data were removed based on the quality of the final polarimetric quantities: degree of polarisation and EVPA. This was done in a similar way to the calibration

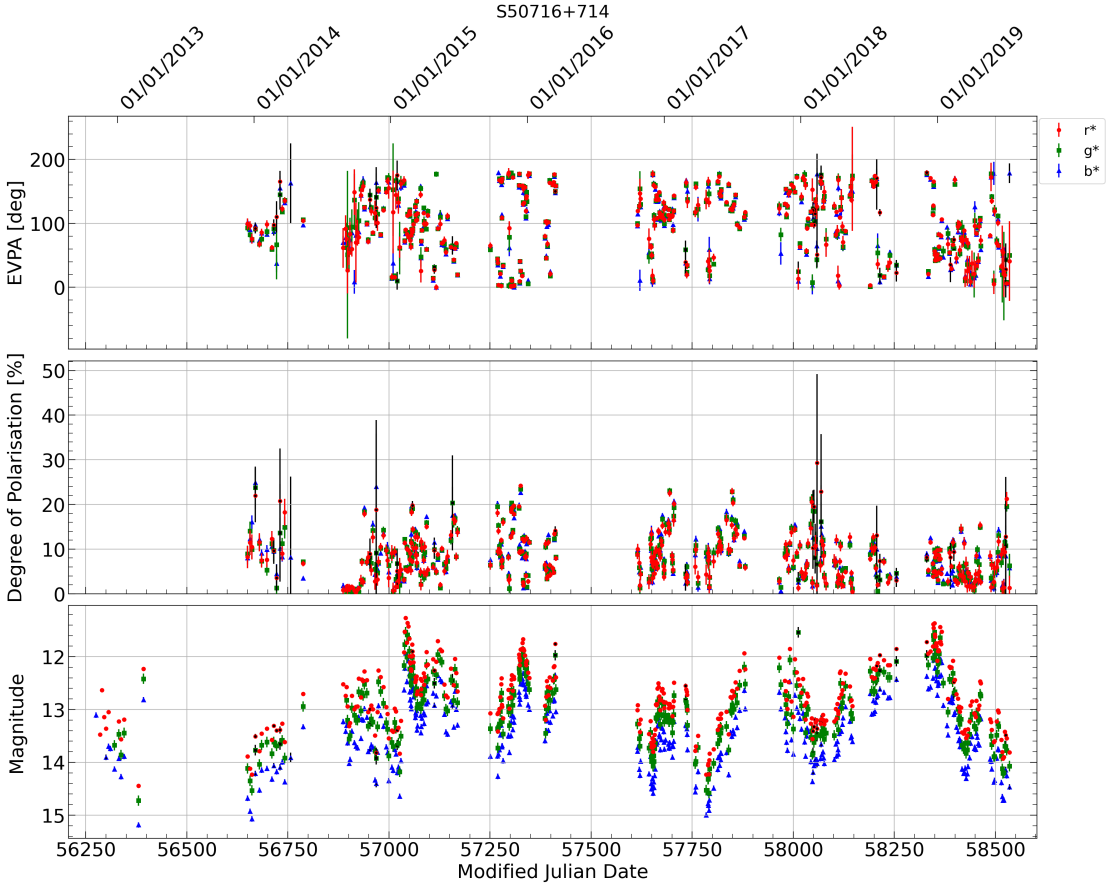

FIGURE 2.6: Figure showing the full photo-polarimetric light curve for the source S50716+714 where the black points have been flagged as poor quality based on the ratio of the calibration star counts to its error. They are therefore removed as a part of the vetting procedure.

star ratio where the median error and MAD were calculated and any point with an error value greater than the median plus ten MADs was removed. This is shown in Equation 2.24 where x_{err} is the error on any pol or EVPA data point. Like before, $\langle x_{err} \rangle$ represents the median of all the errors. Ten MADs was used here as this threshold was large enough to only remove the poor-quality data. This ensured as little data as possible were vetted for each source.

$$\Delta x_{err} > \langle x_{err} \rangle + 10 \times \mathrm{MAD}\,(x_{err}) \tag{2.24}$$

The removal of data based on the errors on the degree of polarisation data made up around 1.4% and errors on EVPA data around 2.8%. Figures 2.7 and 2.8 show the full photo-polarimetric light curves for S50716+714 after vetting data via the calibration star ratio condition (equation 2.23), where the black points highlight the data identified as poor polarisation degree quality and poor EVPA quality respectively. Additionally,

Figure 2.8 which shows the data removed due to large EVPA errors has the poor quality data identified in Figure 2.7 removed. It can be seen that together, these data make up the vast majority of points with the largest uncertainties, resulting in much cleaner data. Again, it is noted that the vetting takes place before the 180° ambiguity correction so the EVPA data is contained between 0° and 180° in these plots.

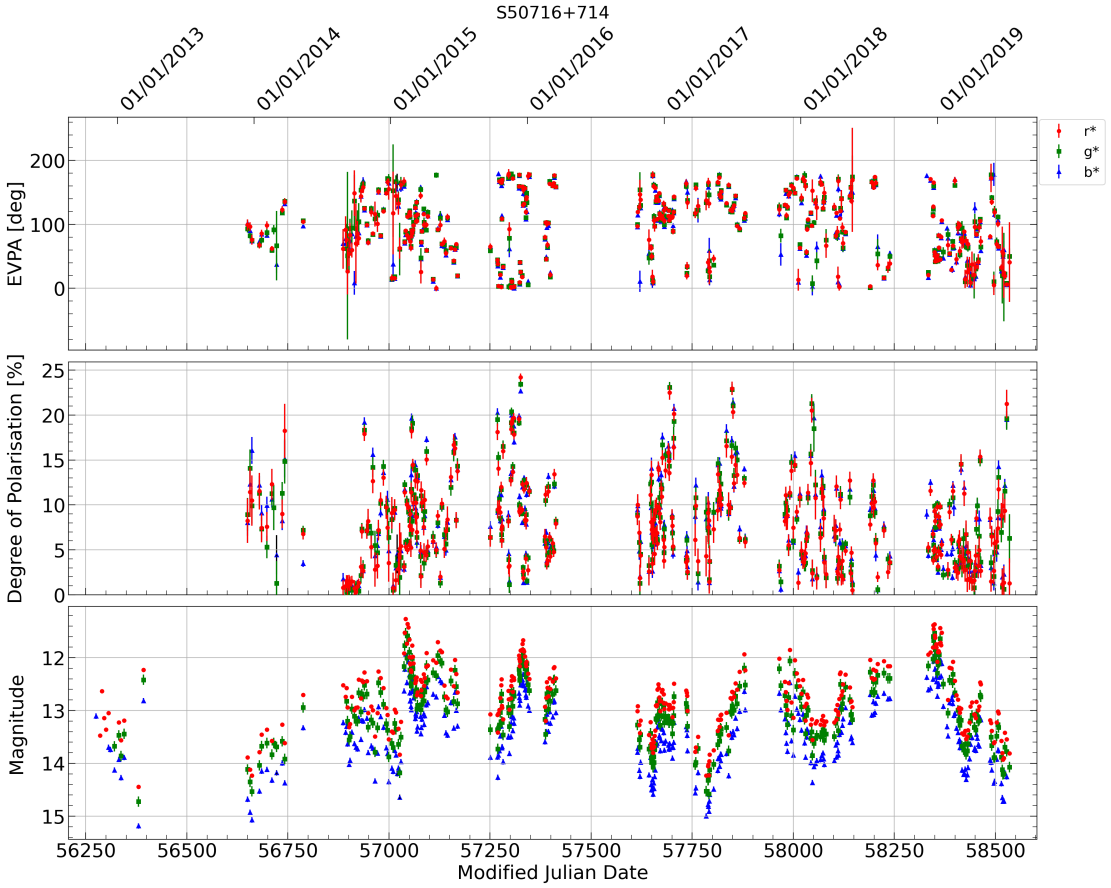

FIGURE 2.7: Figure showing the full photo-polarimetric light curve for the source S50716+714 where the black points have been flagged as poor quality based on the size of the polarisation degree error bars. They are therefore removed as a part of the vetting procedure.

Finally, sigma clipping was performed based on the colour information (b^*-r^*, b^*-g^*, g^*-r^*) of a given source. By performing this iterative process, data are clipped if more than three times the standard deviation of the data away from the median. After removing any outliers, the standard deviation and median are calculated again and the process repeats until no new data are clipped. Anomalous pixel values and the disproportionate increase in one colour over another are exaggerated as the colour takes out general variability. Subsequently, computing a difference between magnitudes, as with the colour index, would allow the anomalous data to be picked out more easily,

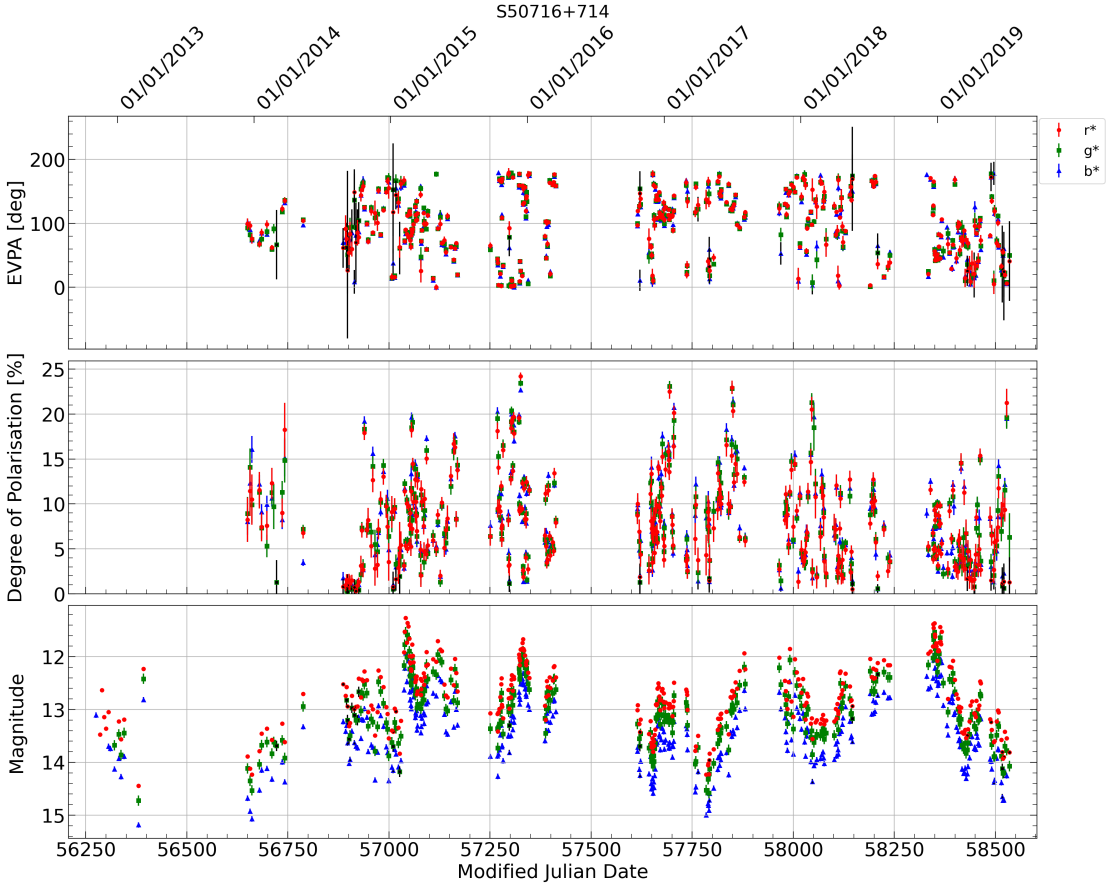

FIGURE 2.8: Figure showing the full photo-polarimetric light curve for the source S50716+714 where the black points have been flagged as poor quality based on the size of the EVPA error bars. They are therefore removed as a part of the vetting procedure.

given the colour index behaviour in blazars is approximately linear over long timescales (Zhang et al., 2022a). For S50716+714, the data removed by sigma clipping on the colour values for each colour permutation is shown in Figure 2.9. However, for this particular data set, the sigma clipping has very little effect on the correlation statistics as seen by the before and after ("..." and "- - -" respectively) Spearman rank correlation strength, c, and significance, p, coefficients (see Section 2.4.2 and Table 2.8 for their explanation) above each plot. The black points show those which have been removed by the process. To show the effect sigma clipping can have, Figure 2.10 shows the colour-magnitude diagrams for 4C 11.69 which shows several points to be much bluer than the rest, shown in black. These points are also displayed in black in Figure 2.11, which shows the full photo-polarimetric light curve for 4C 11.69. Removing these points has a large impact on the Spearman rank correlation statistics shown above each colour-magnitude diagram, increasing both the significance and the strength values.

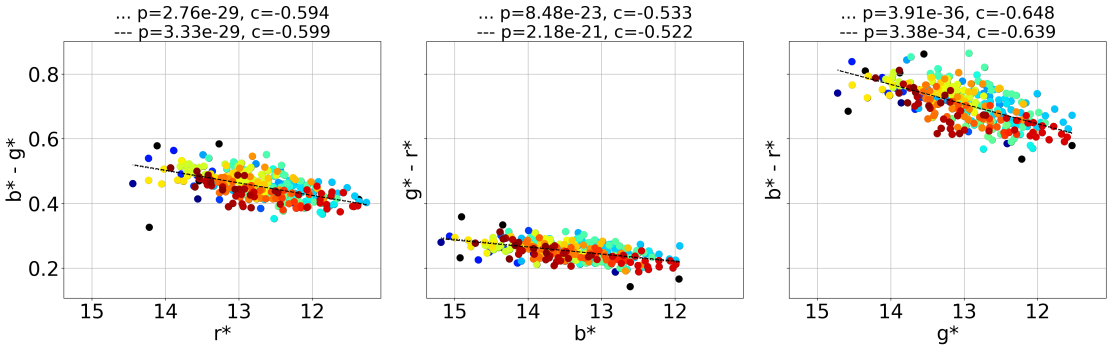

FIGURE 2.9: Figure showing colour-magnitude plots for the RINGO3 from S50716+714. The colour gradient from red to blue indicates time, and the black points highlight the data removed by sigma clipping on the colour values. The dotted line, and "..." correlation statistics, correspond to pre-vetted data and the dashed line, and "- - -" correlation statistics, correspond to the post-vetted data.

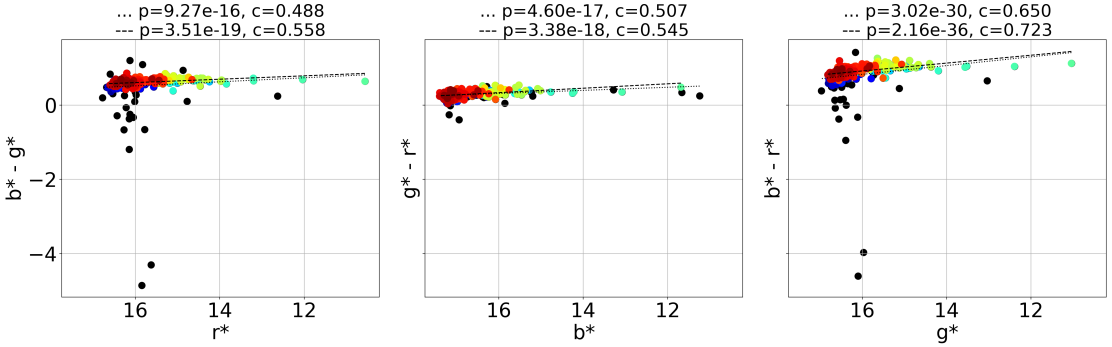

FIGURE 2.10: Figure showing colour-magnitude plots for the RINGO3 from 4C 11.69. The colour gradient from red to blue indicates time, and the black points highlight the data removed by sigma clipping on the colour values. The dotted line, and "..." correlation statistics, correspond to pre-vetted data and the dashed line, and "- - -" correlation statistics, correspond to the post-vetted data.

Across all forms of vetting, it was ensured that the remaining data was consistent between cameras. That is if a specific epoch was removed from the data from one camera, it was also removed from the remaining two regardless of whether it met the various vetting thresholds or not. This ensured the simultaneity of the data was preserved for intraband cross-correlations, such as photo-polarimetric colour analysis.

Of the sources selected for inclusion in the RINGO3 sample (see Table 3.1 in Section 3.1.1), the cumulative amount of data removed on average totalled 8%. This did, however, vary between sources based on the quality and volume of data. The highest amount of data removed was 11% and the lowest 4%. This proportion of lost data was comparable to the amount of downtime expected associated with poor weather during an observing semester on La Palma (around 10%; Gaug et al., 2024).

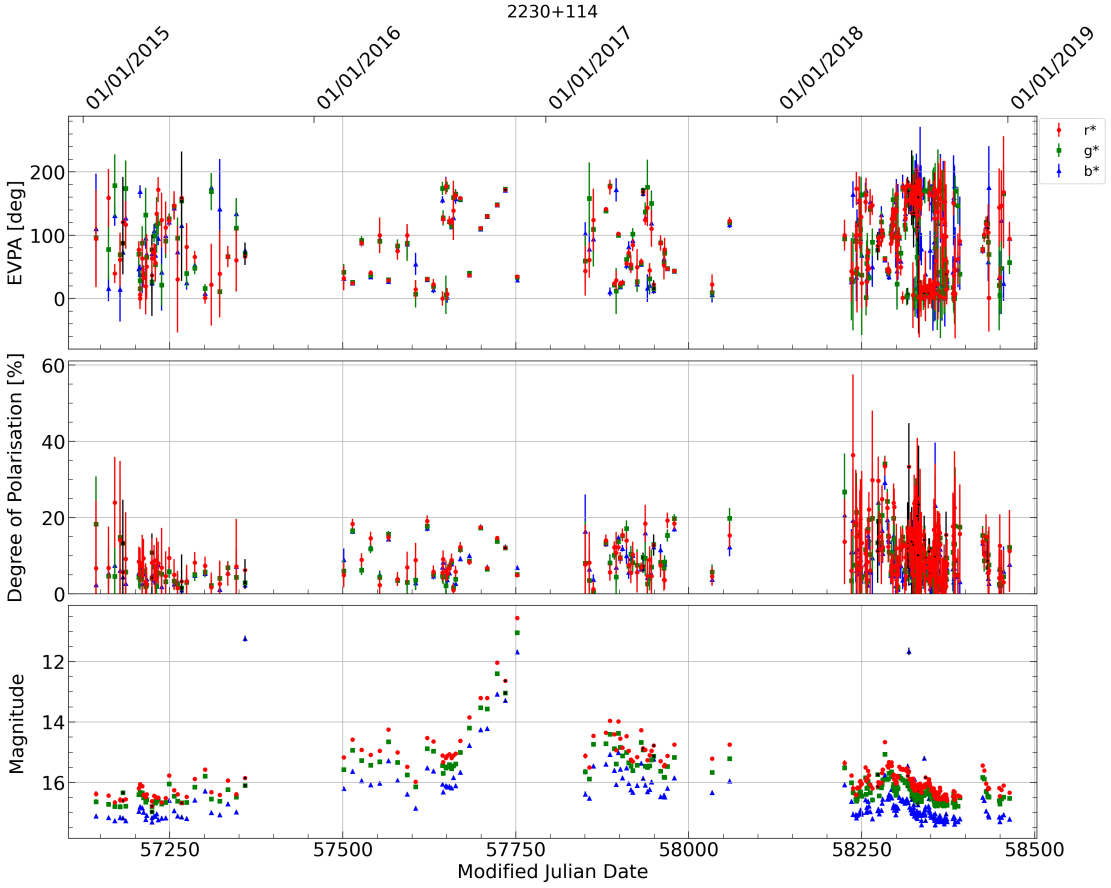

FIGURE 2.11: Figure showing the full photo-polarimetric light curve for the source 4C 11.69 where the black points have been flagged as poor quality by sigma clipping on the colour information of the source. They are therefore removed as a part of the vetting procedure.

2.1.2 MOPTOP

The Multicolour OPTimised Optical Polarimeter (MOPTOP) was installed onto the Liverpool Telescope for calibration in March 2020 and began robotic commissioning in October 2020. MOPTOP's design results in high sensitivity measurements ($< 0.1\%$) using a dual camera configuration that minimises systematic errors. MOPTOP also benefits from a fast rotating half-wave plate element to allow high time resolution (around 10 seconds), and a pair of low-noise fast-readout imaging cameras allowing a unique optimisation of the post data acquisition signal-to-noise ratio (Jermak et al., 2016b). Multi-colour quasi-simultaneous observations are achieved using a five-colour, BVRIL filter wheel. A summary of the waveband ranges associated with each filter is shown in Table 2.3. The cadence of successive observations (i.e. the delay in observations between filters) is around 30 seconds. Given that the required blazar monitoring timescale (days)

TABLE 2.3: Summary of the filters and wavelength ranges of MOPTOP filters. The wavelength cutoff of the MOP-I filter is determined by the quantum efficiency of the detector, and MOP-L is a broadband luminosity filter. QE cutoff refers to the quantum efficiency of the detector, where the sensitivity sharply falls.

Filter Name	Colour	λ range
MOP-B	"Blue"	380–520 nm
MOP-V	"Green"	490–570 nm
MOP-R	"Red"	580–695 nm
MOP-I	"Infrared"	695 nm – QE cutoff
MOP-L	"Luminosity"	400–700 nm

was much larger than the delay in successive observations (seconds), it did not affect the campaign.

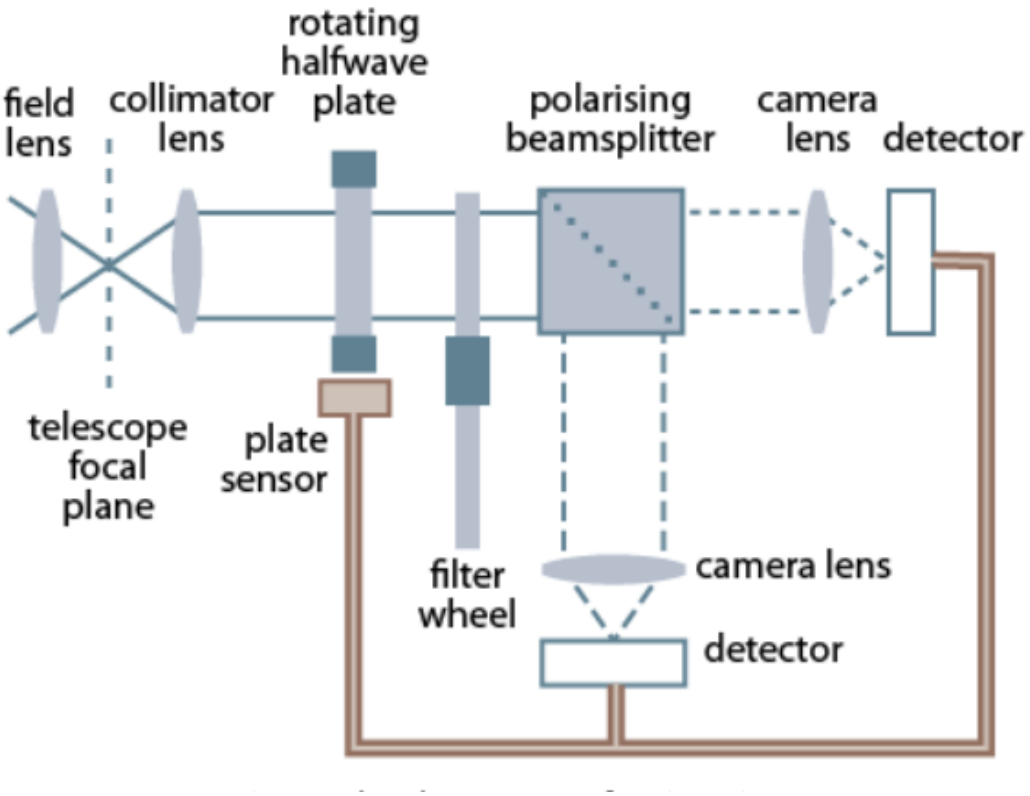

FIGURE 2.12: Structural overview of the MOPTOP polarimeter from Shrestha et al. (2020). The instrument is located on one of the telescope side ports.

The structure of MOPTOP can be seen in Figure 2.12. Collimated light enters the instrument and passes through the halfwave plate (HWP). The polarised light beam can be described as two orthogonal state vectors, one parallel (state p) to the plane of incidence and one perpendicular (state s). As the beam passes through the HWP, the two states will experience different phase delays resulting from the orientation of the fast and slow axes of the HWP's crystalline structure (light travelling along the

fast axis experiences a lower refractive index and thus can travel faster, whereas light travelling along the slow axis with a higher refractive index travels slower). This causes the state along the slow axis state to become half a wavelength out of phase with the other, having the effect of rotating the angle of the incident polarisation vector by 2θ where θ is the angle between the incoming polarised vector and the fast axis. After passing through a filter wheel, the modulated beam is split into the p and s states by a wire-grid beamsplitter before incident on two CMOS detectors.

After this initial exposure, the HWP rotates by 22.5° and another observation takes place, repeating a total of 16 times for a full 360° rotation of the HWP. Rotating the HWP has the effect of changing the angle between the incoming polarised vector and the HWP fast axis, changing the angle of the incident polarisation vector by a factor of two (45°). This, in effect, swaps the q and u parameters. The difference between the counts in the p and s state images with the HWP in the initial position equals the Stokes Q parameter, then the exposure taken after rotating by the HWP 22.5° gives the Stokes U parameter. The subsequent two HWP rotations result in the negation of Q and U (-Q and -U), respectively. The summation of all eight images gives the Stokes I parameter. After these four HWP rotations, the sequence of obtaining Stokes parameters from the p and s state images using respective HWP positions begins again until the HWP has rotated a full 360°. This gives a total of 8 values for Stokes Q and U values, and 4 Stokes I values, which can be averaged, respectively, to reduce systematic uncertainties given the standard error on an average scales with the inverse of the square root of the number of values within the average ($\mathrm{SE} = \frac{\sigma}{\sqrt{\mathrm{N}}}$). Repeatedly observing the Stokes parameters in this fashion also eliminates unwanted transmission effects, such as pleochroism. Pleochroism describes wavelength-dependent transmission variability through the HWP when rotating its angle with respect to the EVPA of the incoming light beam. This is caused by the axial symmetry of the crystalline structure of the HWP. Observing sets of Stokes parameters over multiple HWP angles can strongly reduce this effect, leading to more accurate polarisation values and smaller uncertainties (Patat & Romaniello, 2006; Wiersema et al., 2022).

The dual camera configuration allows MOPTOP to operate in a similar capacity to a single RINGO3 camera, so a filter wheel to enable multicolour measurements is located before the beamsplitter. It also means that in its current configuration, MOPTOP

is only capable of quasi-simultaneous, multi-waveband photo-polarimetric observations (successive observations in each filter).

Despite the absence of simultaneity, this configuration provides many benefits compared to the RINGO series of instruments. Firstly, MOPTOP boasts increases sensitivity by utilising 100% of the incoming beam of light compared to 50% with RINGO3 due to transmission through the polariod. Additionally, the systematic errors that arise from seeing and atmospheric variations over the course of each observation are eliminated, given the polarimetric Q and U parameters are calculated via a differencing image technique. Furthermore, any uneven transmittance of the p and s states via the beamsplitter is overcome in the measurement of successive $|Q|$ and $|U|$ values (Jermak, 2016).

The processes and methods used to calibrate and reduce MOPTOP data are outlined in the following sections and are publicly available on GitHub [2]. It is noted that there are alternative methods of deriving polarisation from MOPTOP frames, such as is reported in Wiersema et al. (2022).

2.1.2.1 Data reduction

The counts of a given object were calculated through the summation of pairs of frames taken with each camera. If m_N and n_N are the counts at rotor position N for cameras 1 and 2 respectively, the counts for two HWP rotations can be calculated as

$$\text{counts}_N = m_N + m_{N+1} + n_N + n_{N+1} \tag{2.25}$$

where N is any odd integer from 1 to 16, inclusive. Accounting for all 16 rotor positions, this produced eight estimates for the counts which were then averaged, before being used to find the instrumental magnitude of the target. This was done using equation 2.1 where *S1* is equal to the averaged counts. The error on the instrumental magnitude was calculated using equation 2.4 where, again, *S1* is equal to the averaged counts, and $\Delta S1$ is equal to the standard error on all eight count estimates.

Given the difference between the first, second, third, and fourth pairs of frames is equal to Stokes Q, U, -Q and -U parameters the following equations will detail the calculation

[2] https://github.com/clmccall/MOPTOP_reduction_pipeline.git

of the normalised q–u parameters for the first four rotor positions. Repeating the process for the remaining three sets of four positions results in four sets of normalised q–u values in total, which can be averaged to reduce the uncertainty in the polarimetric quantities.

In order to calculate the normalised Stokes q–u parameters, one must first account for the sensitivity differences between the two cameras. This can be done by calculating a sensitivity factor, f, and adjusting the counts in camera 2. These factors for the Q and U frames are given by the following equations.

$$f_q = \sqrt{\frac{n_1 n_3}{m_1 m_2}} \tag{2.26}$$

$$f_u = \sqrt{\frac{n_2 n_4}{m_2 m_4}} \tag{2.27}$$

One can correct the sensitivity difference in the camera 2 counts by dividing the counts by the f values. This is shown in the following equations.

$$\bar{n}_{1,3} = \frac{n_{1,3}}{f_q} \tag{2.28}$$

$$\bar{n}_{2,4} = \frac{n_{2,4}}{f_u} \tag{2.29}$$

Two estimates can be obtained for the Q, U, and I parameters using the following equations.

$$Q_1 = m_1 - \bar{n}_1 \tag{2.30}$$

$$U_1 = m_2 - \bar{n}_2 \tag{2.31}$$

$$Q_2 = -(m_3 - \bar{n}_3) \tag{2.32}$$

$$U_2 = -(m_4 - \bar{n}_4) \tag{2.33}$$

$$I_1 = \frac{m_1 + m_2 + \bar{n}_1 + \bar{n}_2}{2} \tag{2.34}$$

$$I_2 = \frac{m_3 + m_4 + \bar{n}_3 + \bar{n}_4}{2} \tag{2.35}$$

Following this, two estimates for the normalised q and u values were obtained by

$$q_{1,2} = \frac{Q_{1,2}}{I_{1,2}} \tag{2.36}$$

$$u_{1,2} = \frac{U_{1,2}}{I_{1,2}} \tag{2.37}$$

which were averaged. As previously described, this process was repeated four separate times, utilising all positions of the HWP. The resulting q–u pairs and I values were averaged to reduce uncertainties.

The increased sensitivity of MOPTOP allows for low polarisation signals to be more accurately detected compared to RINGO3. This means much more data with a low polarisation degree but still non-zero within errors could be obtained. In general, the true polarisation degree (P_0) of an object can be estimated using equation 2.18 and will be associated with uncertainty (σ). It follows that the measured polarisation degree can take any value inside a probability contour expressed as $\sqrt{P_0^2 + \sigma^2}$ (see Figure 1 in Plaszczynski et al., 2014). The Q and U values are normally distributed due to noise in their measurement, and when used in equation 2.18, the errors are always added in the positive direction (i.e. Rician statistics Rice, 1944), implying that the measured polarisation is likely overestimating the true value (Patat & Romaniello, 2006; Wiersema et al., 2022). The asymptotic estimator aims to obtain the true polarisation by subtracting σ from the measured polarisation. This however begins to fail at low flux SNR *or* low polarisation due to polarisation bias, where the uncertainty can become larger than the measured polarisation, thus estimating the true polarisation degree to be negative. This is true even when flux SNR is high but polarisation is low. Plaszczynski et al. (2014) describe a modified asymptotic (MAS) estimator, which aims to address this negative polarisation problem at low SNR by transforming the polarisation distribution from Gaussian at higher SNR to Rayleigh-like at low SNR (< 2). The MAS estimator is defined as

$$P_{\mathrm{MAS}} = P - b^2 \frac{1 - e^{-P^2/b^2}}{2P} \tag{2.38}$$

where P is the linear polarisation as calculated by equation 2.18 and b^2 is the noise bias which is calculated by

$$b^2 = \frac{q^2 \Delta u^2 + u^2 \Delta q^2}{q^2 + u^2} = \Delta P^2. \tag{2.39}$$

The confidence intervals, P_{min} and P_{max} (also given by Plaszczynski et al. (2014)), are defined by

$$P_{min} = P_{MAS} - \sigma_\alpha P_\alpha \left(1 + \beta e^{-\gamma P_{MAS}/\sigma_\alpha} \sin\left(\omega P_{MAS}/\sigma_\alpha + \phi\right)\right) \tag{2.40}$$

and

$$P_{max} = P_{MAS} + \sigma_\alpha P_\alpha \left(1 - \beta e^{-\gamma P_{MAS}/\sigma_\alpha}\right) \tag{2.41}$$

where

$$\sigma_\alpha = \sqrt{\frac{\Delta q^2 + \Delta u^2}{2}} \tag{2.42}$$

and P_α, β, γ, ω, and ϕ are parameters of the analytical approximation dependent on the required confidence level. In this work, the $\alpha = 0.68$ (1σ) confidence level is chosen. Given the expected variability of the polarisation data, a 1σ was chosen as a suitable representation of the data without being overly restrictive.

TABLE 2.4: Parameters for the MAS estimator confidence intervals for different significance, α, levels. Table taken from Plaszczynski et al. (2014).

Bound	α	P_α	β	γ	ω	ϕ
P_{min}	0.68	1	0.72	0.60	-0.83	4.41
P_{max}	0.68	1	0.97	2.01	-	-
P_{min}	0.90	1.64	0.88	0.68	2.03	-0.76
P_{max}	0.90	1.64	0.31	2.25	-	-
P_{min}	0.95	1.95	0.56	0.48	1.79	-1.03
P_{max}	0.95	1.95	0.22	2.54	-	-

2.1.2.2 Single-camera reduction

Despite being a dual-beam polarimeter, MOPTOP is also capable of collecting data with just a single camera at the expense of SNR. While this is not important under normal operations, MOPTOP has been subject to maintenance work, such as camera upgrades, which means at times it has operated with a single camera. Such a period occurred when camera 2 went offline on 20/09/2021 before both were replaced on 16/03/2022. During this time, polarimetric values could not be obtained using the standard differential technique, so the data were reduced following a similar process as the RINGO3 data (see Section 2.1.1.3) according to the equations detailed in (Shrestha et al., 2020). Importantly, a single MOPTOP camera produces twice the amount of frames as a RINGO3

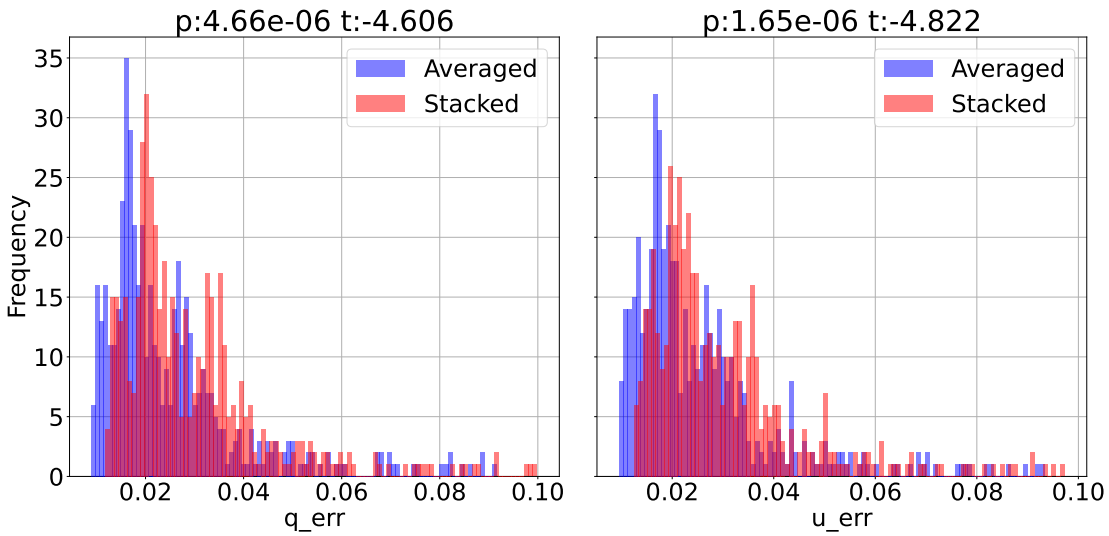

FIGURE 2.13: Histograms comparing the distribution of q–u uncertainties after reducing the data by averaging q–u estimates and stacking frames. T-test coefficients are given above each plot to quantify the difference between the distributions.

camera, meaning two methods could be employed to increase the sensitivity of the MOPTOP data during single-camera operations: compute two estimates of the q–u values using frames 1–8 followed by 9–16, or stack corresponding frames (1 and 9, 2 and 10... 8 and 16) and compute one set of q–u values. These methods were tested on the full set of single-camera data for OJ287 and the results are shown in Figure 2.13. This figure shows histograms of the errors on the q and u values calculated by both the averaging and stacking methods. A clear difference in the distributions is seen for both q_{err} and u_{err}, with the averaging method showing generally less polarimetric uncertainty. To quantify this, a T-test was performed and the results are shown above each plot in Figure 2.13. In both cases, the p-value is less than 0.05 implying the distributions' means are significantly different, and the t-statistics of -4.61 and -4.82 for the q_{err} and u_{err} distributions, respectively, indicate a large difference between the means (4.61σ and 4.82σ, respectively). Based on these results, during single-camera operations, the data were reduced to extract two q–u estimates with individual uncertainties which were subsequently averaged. The uncertainty on these final values was calculated through standard quadrature error propagation.

2.1.2.3 Polarimetric calibration

Calibration values characterising the levels of instrumental polarisation, depolarisation, and its mount angle relative to the telescope are required for all science data and were

calculated as a part of this work. These values would be needed for all periods following changes in the observing mode (single or dual camera operations) or detectors. This required 3 sets of q_0, u_0, k, and instrumental depolarisation to be found for each filter for the data presented in this work. Set 1 covers epoch 1 (dual-camera; 01/10/20 - 19/09/21), set 2 covers epoch 2 (single-camera; 20/09/21 - 19/03/22), and set 3 covers epoch 3 (single-camera; 20/03/22 - present). The data corresponding to each epoch was reduced with the appropriate reduction pipeline (single- or dual-camera), and one expects the coefficients to differ between each epoch on account of the change to the optics and/or the detectors.

A list of zero-polarised standard stars, with coordinates, observed regularly with MOPTOP is shown in Table 2.5. These stars have a unique feature in that their degree of polarisation is very low ($\approx 0\%$). Observations of these sources reveal the instrumental polarisation effects of the instrument, through q_0 and u_0 calibration values, as any detected polarised light must not come from the object but rather through the optics of the telescope and instrument. It is therefore important to subtract the q_0 and u_0 values from all subsequent science and calibration data in order to remove the induced instrumental polarisation.

TABLE 2.5: Table showing the names and coordinates of the zero-polarised standard stars observed with MOPTOP.

Name	α(2000)	δ(2000)
HD14069	02:16:45.194	07:41:10.637
GD319	12:50:04.526	55:06:01.800
BD+32 3739	20:12:02.149	32:47:43.693
HD212311	22:21:58.583	56:31:52.718
G191B2B	05:05:30.618	52:49:51.919
BD+28 4211	21:51:11.022	28:51:50.368

Figures C.1-C.3 and C.4-C.6 in the appendix show the q and u values for each observing epoch calculated using the data from each of the zero-polarised standards respectively. The dotted lines show the median values, with an error calculated as the standard error. The values for each filter at each epoch are summarised in Table 2.7.

Once q_0 and u_0 values had been determined, one could account for the mount angle of the instrument relative to the telescope in the form of k values. To do this, one can observe polarised standard stars which have known and constant polarisation values, and calculate an observed θ using equation 2.20. One can then extract k values using

Equation 2.21 and known EVPA values from the literature. As with the q_0 and u_0, these must be calculated for each filter, and for each observing epoch. Table 2.6 shows the polarised standard stars observed with MOPTOP, with their known EVPA values (θ_{act}) for each MOPTOP filter.

TABLE 2.6: Table showing the names and coordinates of the polarised standard stars observed with MOPTOP. Also shown are the θ_{act} and pol_{act} values obtained from the literature. [1]Schmidt et al. (1992), [2]Whittet et al. (1992), [3]HPOL (http://www.sal.wisc.edu/HPOL/pbotgtnam.html), *Value is obtained by averaging the source's *BVRI* values.

Name	α(2000)	δ(2000)	Filter	θ_{act}	pol_{act}
BD+64 106	00:57:36.689	+64:51:34.907	*B*	97.15[1]	5.506[1]
-	-	-	*V*	96.63[1]	5.687[1]
-	-	-	*R*	96.74[1]	5.150[1]
-	-	-	*I*	96.89[1]	4.696[1]
-	-	-	*L*	96.85*	5.44*
HD251204	06:05:05.667	+23:23:38.533	*B*	154.83[3]	4.46[3]
-	-	-	*V*	153.26[3]	4.72[3]
-	-	-	*R*	152.87[3]	4.78[3]
-	-	-	*I*	153.70[3]	4.37[3]
-	-	-	*L*	153.67*	4.58*
HD155197	17:10:15.747	-04:50:03.657	*B*	103.06[1]	4.112[1]
-	-	-	*V*	102.84[1]	4.320[1]
-	-	-	*R*	102.88[1]	4.274[1]
-	-	-	*I*	103.18[1]	3.906[1]
-	-	-	*L*	102.99*	4.24*
HILT 960	20:23:28.531	+39:20:59.037	*B*	55.06[1]	5.720[1]
-	-	-	*V*	54.79[1]	5.663[1]
-	-	-	*R*	54.54[1]	5.210[1]
-	-	-	*I*	53.96[1]	4.455[1]
-	-	-	*L*	54.59*	5.262*
VI Cyg12	20:32:40.957	+41:14:29.279	*B*	119[2]	9.67[2]
-	-	-	*V*	115.03[1]	8.947[1]
-	-	-	*R*	116.23[1]	7.893[1]
-	-	-	*I*	117[2]	7.06[2]
-	-	-	*L*	117*	8.84*
BD+57 2615	22:47:49.571	+58:08:49.516	*B*	42[2]	1.91[2]
-	-	-	*V*	42[2]	2.00[2]
-	-	-	*R*	41[2]	2.02[2]
-	-	-	*I*	41[2]	1.71[2]
-	-	-	*L*	42*	1.91*

Figures C.7–C.9 in the appendix show the k values for each observing epoch calculated using the data from each of the polarised standards. The dotted lines show the median values, with an error calculated as the standard error. The values for each filter at each epoch are summarised in Table 2.7.

TABLE 2.7: MOPTOP polarisation constants. The epoch and filter are given, followed by the q_0, u_0, k, and depolarisation values with uncertainties. Epoch 1: 01/10/20 - 19/09/21, Epoch 2: 20/09/21 - 19/03/22, Epoch 3: 20/03/22 - present

Epoch	Filter	q_0	u_0	k	depol
1	*B*	0.00189±0.00038	-0.01147±0.00022	31.88±0.84	0.856±0.016
1	*V*	0.00581±0.00013	-0.02141±0.00016	32.68±0.47	0.836±0.007
1	*R*	0.01071±0.00037	-0.02911±0.00016	31.54±0.33	0.873±0.007
1	*I*	0.01147±0.00025	-0.03162±0.00025	32.38±0.44	0.743±0.023
1	*L*	0.00727±0.00030	-0.01818±0.00022	31.85±0.70	0.880±0.010
2	*B*	0.00834±0.00055	-0.00857±0.00108	12.53±1.62	0.959±0.043
2	*V*	0.01946±0.00077	-0.01136±0.00178	9.26±1.60	0.967±0.056
2	*R*	0.02794±0.00077	-0.01558±0.00195	11.94±1.66	0.989±0.051
2	*I*	0.03056±0.00150	-0.01536±0.00154	9.48±2.50	0.836±0.043
2	*L*	0.01731±0.00147	-0.00884±0.00162	11.50±2.09	0.972±0.049
3	*B*	0.00127±0.00016	-0.01219±0.00019	123.77±0.33	0.913±0.010
3	*V*	0.00601±0.00015	-0.02326±0.00013	122.08±0.23	0.888±0.005
3	*R*	0.01163±0.00017	-0.03140±0.00019	123.55±0.13	0.901±0.005
3	*I*	0.01135±0.00015	-0.03401±0.00012	123.68±0.15	0.786±0.008
3	*L*	0.00787±0.00018	-0.01979±0.00028	124.85±0.35	0.920±0.007

Using the polarised standards, q_0, and u_0 values, one can also calculate the filter-/epoch-dependent instrument-induced depolarisation. By calculating a degree of polarisation from instrumental depolarisation corrected q–u values, one can plot them against known values obtained from the literature and compute the rate of change of known polarisation with respect to observed polarisation. This gradient is the instrumental depolarisation.

Figures C.10 - C.12 in the appendix show the measured polarisation vs. known polarisation for the polarised standards in Table 2.6 along with a linear fit. It is important to note that the data is fitted such that the linear regression passes through the origin. This is because the instrumental depolarisation linearly scales as a function of the polarisation of the object, and a zero-polarised object should measure as 0%. The values for each filter at each epoch are summarised in Table 2.7.

It is noted that these polarisation coefficients are subject to variation across the frame, an effect known as field-position-dependent instrumental polarisation. This arises due to the use of a 45° tertiary fold mirror to direct the incoming light beam into the instrument located on the side port. Preliminary investigations into this effect indicate a potential polarisation variation of a few percent across the frame (Bernardes et al., 2024a).

2.2 Telescopio Carlos Sánchez

The Carlos Sánchez Telescope (TCS) is a 1.52 m observatory located at the Observatorio del Teide, Tenerife. The TCS boasts a Dall-Kirkham configuration, similar to the Ritchey-Chrétien configuration but with ellipsoidal primary and spherical secondary mirrors. It has a focal length of $f/13.8$ and has been operational since 1972.

Five nights of observing time were allocated in January 2023, with the purpose of using intra-night, multicolour variability of blazars to constrain emission models and jet dynamics. To do this, observations would be taken with the four-colour simultaneous imager, MuSCAT2 (Narita et al., 2019).

2.2.1 MuSCAT2

MuSCAT2 was mounted at the Cassegrain focus of the TCS, producing pixel scales of 0.44 arcsec/pixel across each band and a field of view (FOV) of $7.4 \times 7.4\,\mathrm{arcsec}^2$ in all filters (Narita et al., 2019). Four-colour simultaneous observations are achieved using dichroic mirrors. Three mirrors are used in total to split the light into bands g (400–550 nm), r (550–700 nm), i (700–820 nm), z_s (820–920 nm) where the subscript "s" in this case denotes the "shorter" waveband range to the traditional z band filter). Four fast-readout PIXIS CCD cameras recorded the light, each controlled independently by the operator to ensure optimal SNR in each waveband.

2.2.1.1 Data reduction

The data were reduced by standard reduction and differential photometry techniques using the Python packages CCDPROC and ASTROPY. The data first required bias/dark subtraction, flat fielding, and WCS coordinate fitted for the reasons described in Section 2.1.1.1. The science frames and flat-field frames were first corrected for bias current and dark counts by subtracting dark frames taken each night with exposure times equal to that of the uncalibrated frames. Following this, the flat-field frames were divided into the science frames to correct for the pixel-to-pixel sensitivities. Finally, the WCS fitting was performed using the *Astrometry.net* application programming interface (API; Lang et al., 2010).

To calibrate the science data for analysis, five in-frame calibration stars were used to calculate the zero point of the telescope in each frame. To do this, the zero point for each star was calculated separately using the difference between each star's known and instrumental magnitude. These were subsequently averaged, with each value weighted by the size of the instrumental magnitude error. Known magnitudes in *griz* bands were obtained via the SDSS, Pan-STARRS and APASS catalogues (Abdurro'uf et al., 2022; Flewelling et al., 2020; Henden et al., 2018). Averaging the zero points in this way ensured those values with higher uncertainties contributed less to the final value. The averaged value was then used to calibrate the magnitude of the source in each image.

As a final quality control before applying statistical methods, the data were subject to the same sigma clipping techniques as described in Section 2.1.1.4. The amount of data clipped using this process equated to less than 10% (and in most cases less than 5%) per source per epoch.

2.3 Fermi Gamma-ray Space Telescope

The Fermi Gamma-ray Space Telescope, hereafter referred to as Fermi, is a γ-ray observatory launched into low Earth orbit in June 2008. Its primary goal is to survey the high-energy γ-ray sky, and therefore trace environments of particle acceleration, on a variety of timescales (McEnery et al., 2012). This is possible with the primary instrument, the Large Area Telescope (LAT), which is responsible for the detection and monitoring of γ-ray sources in the 20–300 MeV energy range (Atwood et al., 2009). The observatory also benefits from the secondary instrument, the Gamma-ray Burst Monitor (GBM), which takes spectra of transients, notably GRBs, at lower energies than can be observed with the LAT, from a few keV up to 40 MeV (hard X-rays to γ-rays). It also provides burst localisations for HE γ-ray follow-up with the LAT (Meegan et al., 2009).

2.3.1 Large Area Telescope

The LAT is a wide FOV imaging telescope covering the 20 MeV–300 GeV energy range, capable of observing the entire sky in just two orbits with a FOV at any given time of over 2.4 steradians (one-fifth of the sky). The main structure of the LAT is shown in Figure 2.14. Unlike lower energy photon regimes and their telescopes, HE γ-ray photons

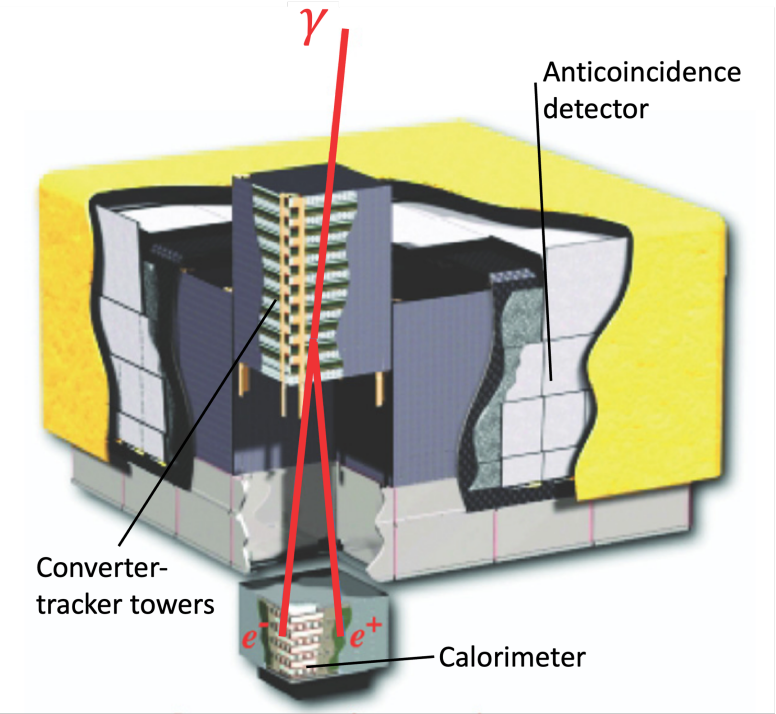

FIGURE 2.14: Schematic from Atwood et al. (2009) showing the structure of the LAT on the Fermi Gamma-ray Space Telescope.

cannot be reflected or refracted onto a detector. The LAT detects γ-ray photons by first converting them to electron–positron pairs, before measuring the energy deposited by the subsequent electromagnetic shower. Sky localisation is also obtained by tracking the paths of the electron–positron pairs (Atwood et al., 2009).

2.3.1.1 Data

The LAT records individual photons from a given source continuously when present in the FOV. This is advantageous for monitoring purposes as the data for a given source over the entire mission can be broken down into whichever time bins are most useful for the analysis (McEnery et al., 2012). The data used in this work comes from the Fermi LAT Light Curve Repository[3] (LCR; Abdollahi et al., 2023). This database consists of flux-calibrated light curves from over 1500 variable sources (Kocevski et al., 2021) with variability indexes > 21.67. The data can be downloaded at different binning intervals: three days, one week, and one month. Data binned over three days was used in this work, allowing for increased sensitivity over daily observations without compromising on cadence or losing short-timescale variability.

[3] https://fermi.gsfc.nasa.gov/ssc/data/access/lat/LightCurveRepository/

To account for the differing cadence of optical and γ-ray observations and allow the direct correlation of the two data sets, the temporally closest γ-ray data point was assigned to each of the optical observations.

2.4 Additional analytical methods

2.4.1 EVPA ambiguity correction

The 180° ambiguity arising from the measurement of the EVPA was introduced in Section 2.1.1.3. The need for an unwrapping pipeline to automatically adjust individual points by adding or subtracting 180° becomes apparent when looking at the raw EVPA data after reduction. Figure 2.15 shows the EVPA data for the source PG 1553+113 where very little structure is seen and it is not possible to trace the evolution of the angle through virtually any length of time.

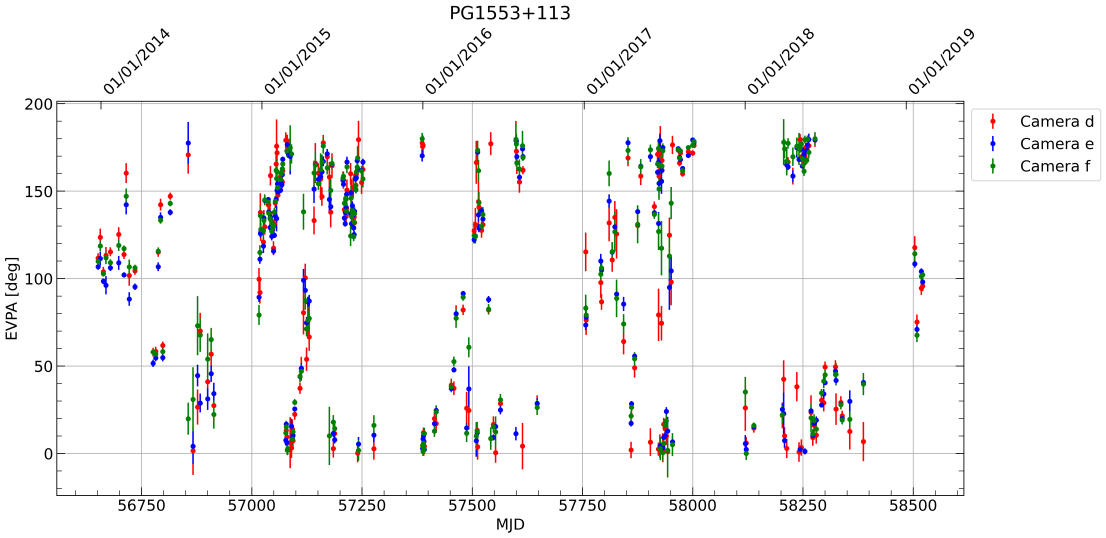

FIGURE 2.15: Figure showing the raw EVPA data for the source PG 1553+113 after reduction before subject to any unwrapping. Very little structure and few trends can be seen across any length of time.

The simplest unwrapping procedure to extract the true EVPA behaviour, and the first experimented with, takes a given point, x_i, and finds the difference between it and the previous point, x_{i-1}. If the difference is less than $-90°$ one must add 180° to point x_i, and if the difference is greater than 90° one must subtract 180° from point x_i. The aim of performing this is to minimise the difference between neighbouring points by shifting point x_i by 180°. These conditions are shown in Equations 2.43, 2.44, and 2.45. This

simple technique has been successfully utilised numerous times to unwrap the optical EVPA of astrophysical objects (Marscher et al., 2008; Larionov et al., 2008; Abdo et al., 2010a).

$$-90^\circ < (x_i - x_{i-1}) < 90^\circ \implies x_i = x_i \tag{2.43}$$

$$(x_i - x_{i-1}) \leq -90^\circ \implies x_i = x_i + 180^\circ \tag{2.44}$$

$$(x_i - x_{i-1}) \geq 90^\circ \implies x_i = x_i - 180^\circ \tag{2.45}$$

Subjecting the same data to these conditions results in what is shown in Figure 2.16. Generally, the simple method performs quite well and features over a range of timescales begin to become prevalent in the plot, such as rotations and periods of relative stability. There are, however, several problems that any upgraded pipeline may be able to account for or mitigate to some degree. Firstly, the simple method does not account for the error in each EVPA measurement. Points with large errors have more uncertainty and where the magnitude of the difference between it and the previous point is close to 90°, this method may incorrectly adjust data. It is therefore important to account for additional data, rather than just one previous point when deciding if point x_i needs adjusting. This will allow one to weigh the data points based on the confidence in its value before adjusting another. Secondly, the method cannot account for large amounts of time between subsequent observations. The EVPA can evolve in excess of 90° on a variety of timescales from days to weeks and, in some cases, can vary significantly over a single night (Bachev et al., 2023). It follows that the probability of a missed or incorrect rotation by the unwrapping pipeline increases as the time between observations increases. This is something that cannot be accounted for fully without the addition of new data either by merging both sets and unwrapping together or by comparing to plots in the literature.

Based on these problems, the method was adapted to account for the uncertainties on each measurement along with incorporating a weighted average of multiple successive data points to try and account for data with large uncertainties and mitigate the effects

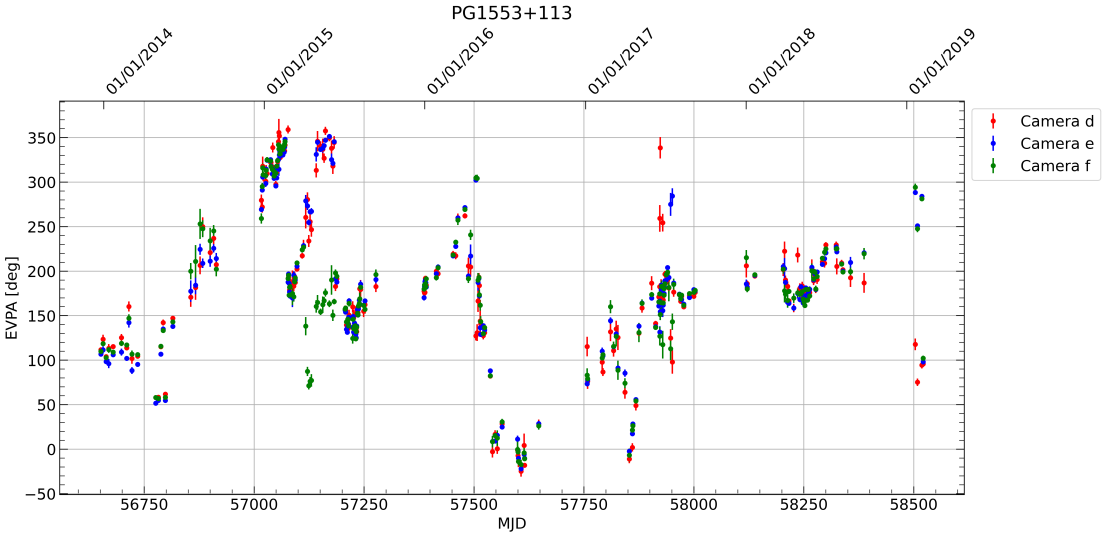

FIGURE 2.16: Figure showing the results of unwrapping the EVPA data from PG1553+113 with the simple method. Structure and trends within the data are beginning to be seen but the method doesn't perform well with points with large error bars or after when there is a large break in the observing cadence. This method also does not account for multiple 180° shifts.

of irregular cadence and sampling gaps. Equations 2.46 and 2.47 were discussed in Kiehlmann et al. (2013), Sasada et al. (2011) and Sorcia et al. (2013) and formed the basis of the adapted unwrapping procedure.

$$\Delta x = |x_i - x_{i-1}| - \sqrt{\sigma_i^2 + \sigma_{i-1}^2} \tag{2.46}$$

$$\Delta x = |x_i - x_{av,i-1,i-2\ldots i-n}| \tag{2.47}$$

Equation 2.46 is similar to the original method where the magnitude of the difference between neighbouring points is taken, but a factor incorporating the errors on the two points in question is subtracted. Here, if the resulting value was greater than 90°, then 180° must be added or subtracted, depending on the non-absolute value of $x_i - x_{i-1}$. Equation 2.47 is, again, similar to the original method where the difference between two values determines the adjustment, but this time the average of the previous "n" points is taken from point i. As with Equation 2.46, if the resulting value was greater than 90° then the method tells us that 180° must be added or subtracted, depending on the non-absolute value. Unlike Equation 2.46, Equation 2.47 does not account for uncertainties. This is likely to be problematic as points with higher uncertainties may

cause an unnecessary shift in subsequent data. Because of this, a factor similar to that included in Equation 2.46 was still needed in the final procedure. However, averaging the previous 'n' points proved to be a valuable tool when testing as it appeared to unwrap the data better than the previous methods.

The following sets of equations were generated to combine the three procedures and more accurately unwrap the data:

$$|x_i - \overline{x}_{i-1,i-2\ldots i-n}| - \overline{\sigma} > 90 \tag{2.48}$$

$$x_i - \overline{x}_{i-1,i-2\ldots i-n} \gtrless 0 \implies x_i \mp (N \times 180) \tag{2.49}$$

$$N = \text{round}(\frac{|x_i - \overline{x}_{i-1,i-2\ldots i-n}| - \overline{\sigma}_{i,i-1\ldots i-n}}{180}) \tag{2.50}$$

$$\overline{x} = \frac{\sum_{-n}^{i-1}[x \times x(P)]}{\sum_{-n}^{i-1} x(P)} \tag{2.51}$$

$$x(P) = 1 - \frac{\sigma}{\sum_{-n}^{i-1} \sigma} \tag{2.52}$$

$$\overline{\sigma} = \frac{\sum_{-n}^{i}[\sigma \times \sigma(P)]}{\sum_{-n}^{i} \sigma(P)} \tag{2.53}$$

$$\sigma(P) = 1 - \frac{\sigma}{\sum_{-n}^{i} \sigma} \tag{2.54}$$

Equation 2.48 shows the main condition for the upgraded unwrapping method which, if met, indicates some shift equal to $N \times 180°$ is required where N is any positive or negative integer. Whether this shift should be positive or negative, and the magnitude

of N is given by Equations 2.49 and 2.50 respectively. How to calculate the weighted average on the previous n points, $\overline{x}_{i-1,i-2...i-n}$, is given by Equations 2.52 and 2.54. The weight each previous observation is given is determined by the error on each observation, σ. An EVPA measurement with a larger error is given less weight when computing the weighted average given the larger uncertainty in the true value. Similarly, $\overline{\sigma}$ is given by Equations 2.53 and 2.54 where a weighted average error is calculated but this time including all data points used, including x_i.

Figure 2.17 shows the results of this new upgraded method when applied to the data from PG 1553+113. A large improvement is seen over the simple method as almost all of the correct structure is revealed from the data. Additionally, incorporating the N factor allows us to unwrap large, continuous rotations that exceed 180°. There are however still small interband deviations present in the data which almost exclusively occur after a small break in the observation cadence, sometimes just as short as a few days. Given this, if manually rotating individual points by $N \times 180°$ produces consistent trends between the wavebands, it is likely that the deviations are not intrinsic to the behaviour of the source and are likely a systematic error directly resulting from the observing cadence. One is therefore required to manually rotate a small number of data points in order to display the true EVPA behaviour of the source.

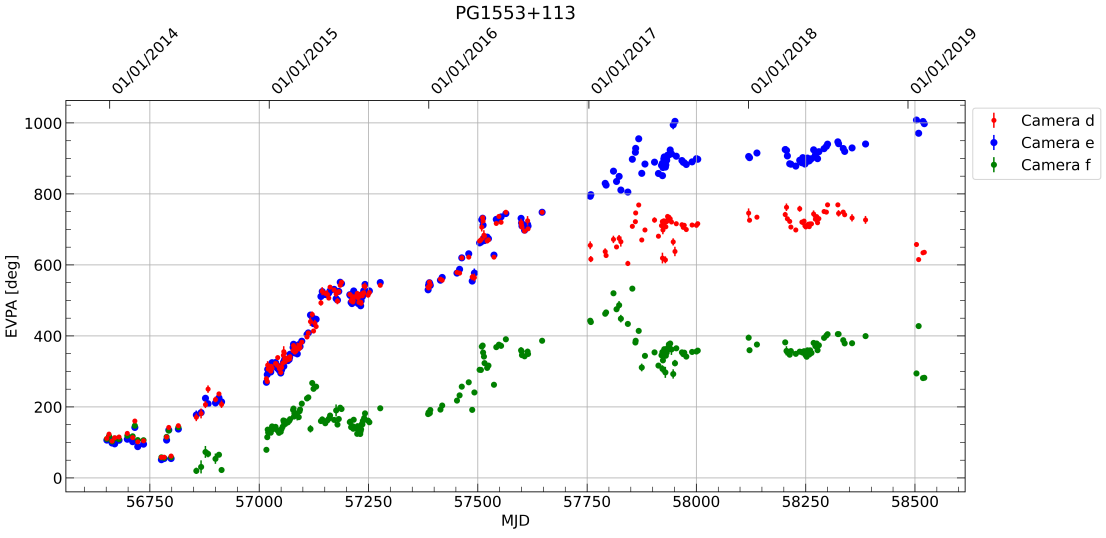

FIGURE 2.17: Figure showing the results of unwrapping the EVPA data from PG1553+113 with the upgraded method. By mitigating the effects of large breaks in cadence and larger EVPA errors by computing weighted averages, the evolution of the EVPA can be displayed very well with only a few deviations between wavebands. Additionally, the points are allowed to shift by any multiple of 180°.

The EVPA data for PG1553+113 after being fully unwrapped, including the inspection and adjustment of interband differences, are shown in Figure 2.18. After having manually corrected the remaining data points and compared them to data in the literature, the EVPA data can be used alongside the other post-reduction photo-polarimetric data.

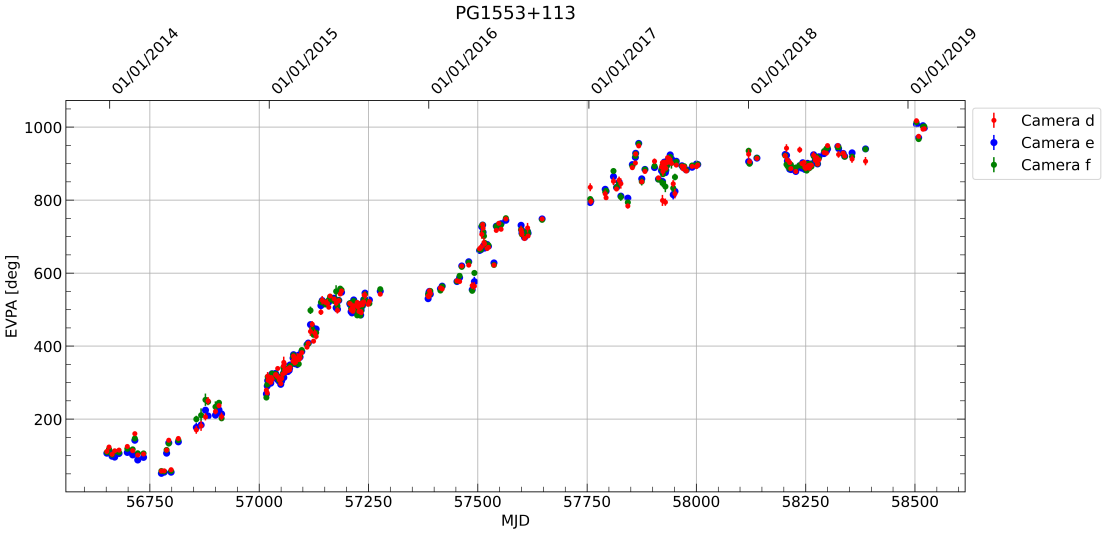

FIGURE 2.18: Figure showing the true EVPA evolution for PG1553+113 after being unwrapped by the upgraded method and after manually adjusting a small number of points which did or did not rotate due to cadence breaks.

2.4.2 Spearman rank

Throughout this work, the Spearman rank coefficient is used to test the strength and significance of monotonic relationships within the data in a non-parametric way. This test provides a coefficient for significance (p; how likely the data are to be correlated by chance) and strength (c; strength of the positive or negative correlation). Table 2.8 shows all the possible correlation strength coefficient values (c) and the qualitative interpretation used in this analysis when and only when $p \leq 0.05$ ($\alpha \leq 0.05$), implying a 2σ significance level for a Gaussian distribution.

2.5 Conclusions

This chapter has detailed the observatories, instruments, and reduction processes used to obtain and calibrate the photo-polarimetric data presented in the following analysis chapters.

TABLE 2.8: Qualitative interpretations of the quantitative Spearman rank strength correlation coefficients.

Value	Correlation Degree
$c = 0$	no correlation
$0 \leq \lvert c \rvert < 0.2$	very weak
$0.2 \leq \lvert c \rvert < 0.4$	weak
$0.4 \leq \lvert c \rvert < 0.6$	moderate
$0.6 \leq \lvert c \rvert < 0.8$	strong
$0.8 \leq \lvert c \rvert < 1$	very strong
$c = 1$	monotonic

The majority of the data was obtained using two instruments on the Liverpool Telescope; the RINGO3 and MOPTOP polarimeters. The RINGO3 reduction pipeline originates from work completed by Dr. Manisha Shrestha, using standard differential photometry techniques with the addition of calibration star magnitude calculations for the non-standard wavebands, and an optimum aperture size calculation for each source to maximise the SNR and data quality. Normalised Stokes q–u values were obtained following the procedures set out in Clarke & Neumayer (2002). The MOPTOP dual-camera reduction pipeline also originated from work completed by Dr. Manisha Shrestha, consisting of photometric and normalised Stokes q–u parameter calculations, accounting for the sensitivity differences between the two cameras (Shrestha et al., 2020). This work was adapted, adding procedures for downloading data directly from the Liverpool Telescope's "recent data" webpage, frame stacking, no WCS reduction, single and dual camera reduction, background subtraction, and simultaneous multi-object reduction.

Further optical photometric data were obtained using the MuSCAT2 imager on Telescopio Carlos Sánchez. The data were calibrated using dark and flat field frames obtained on-site, and a WCS was fitted using the *Astrometry.net* API (Lang et al., 2010). Following this calibration, the data were reduced using standard differential photometry techniques, with a pipeline being created using the photometric calculations from the MOPTOP pipeline.

The Large Area Telescope on the Fermi Gamma-ray Space Telescope collected flux data in the $1 - 100\,\mathrm{GeV}$ energy range and was accessed via the Fermi Gamma-ray Light Curve Repository (LCR; Abdollahi et al., 2023). This provides an opportunity to obtain a quasi-simultaneous multi-wavelength snapshot of all objects in the samples, as well as probing both emission peaks seen in blazar SEDs.

Chapter 3

Photometric Analysis

The photometric analysis of blazars refers to the changes in intrinsic and apparent brightness over time. In this work, the analysis comprises the comparison of fluxes at optical and γ-ray frequencies, identifying correlated interband behaviour and their temporal separation, in addition to searching for optical spectral and colour index variability. By conducting statistical correlation tests on these different observables, one can begin to characterise the emission processes occurring from the blazar system, whether they are from within the relativistic jet or from external regions such as the accretion disk or BLR.

Interband flux correlations, particularly those at optical and γ-ray frequencies, allow one to determine the dominant particle population within blazar emission regions. Should such a correlation exist, this could be indicative of leptonic emission processes, whereby lepton (particularly electron) acceleration is responsible for both lower- and higher-energy emission (optical and γ-ray, respectively) through synchrotron emission and inverse-Compton scattering (Maraschi et al., 1992; Dermer & Schlickeiser, 1993). A lack of correlation could suggest a disconnect between the optical and γ-ray emission and therefore separate emission mechanisms. This could be explained through hadronic modelling, whereby hadrons (protons) and their emission make up a significant contribution to the total particle population (Mücke & Protheroe, 2001; Mücke et al., 2003).

Changes in the jet's intrinsic energy output are explored through colour or spectral index evolution. Many objects repeatedly demonstrate linear colour changes during different flux states, becoming redder (steeper composite spectrum) or bluer (flatter composite

spectrum) during increased flux states (Zhang et al., 2015a; Negi et al., 2022). While this has been observed in numerous sources, other behaviours such as colourless flares and non-linear colour changes do not neatly fit into the currently accepted models (Ghosh et al., 2000; Ikejiri et al., 2011; Zhang et al., 2022a).

It is important to note that it is possible to observe different behaviour based on the classification of the object, which is in part related to the distance from the observer (Ghisellini et al., 2017) and the strength of host galaxy emission (Negi et al., 2022). One can also correct for the redshift differences between objects and perform the same tests to get a distance-independent look at the different source behaviours. This will also be explored in this chapter.

The results of Section 3.1 are published in McCall et al. (2024b).

3.1 RINGO3

3.1.1 Source catalogue

Table C.1 shows the complete catalogue of 49 sources observed with the RINGO3 polarimeter. The table includes the source name, RA/Dec coordinates (α_{2000} and δ_{2000}), redshift, spectral classification, the range of observation dates, and the number of observations within that timeframe. The data were obtained during separate monitoring campaigns orchestrated by Dr. Ivan Agudo, Dr. Helen Jermak, and Dr. Carole Mundell. The full photo-polarimetric light curves including γ-ray flux and optical $r^*g^*b^*$ EVPA, polarisation, and magnitude for each of these objects are shown in Appendix A.

A minimum of 60 observations was required for the source to be a part of the final sample to allow the measurement of long-term variability characteristics. An exception was made for any object where observations were taken with a density greater than once every ten days, given that at this observation density correlations may have been detectable. Applying these conditions resulted in a final total of 31 objects in the sample. These consist of objects across all blazar classes and subclasses; 18 BL Lacs (9 HBLs, 3 IBLs, 6 LBLs) and 13 FSRQs. While these sources will be used to infer inter-class and subclass trends, it is important to note the biased nature of the sample in that all these sources are γ-ray bright and so are generally active blazars.

TABLE 3.1: The RINGO3 blazar sample with source classification, redshift, r^*-band optical magnitude range, γ-ray flux range, and observation MJD range for each source shown. MRK 421 lacks comparison stars within the RINGO3 FOV, so calibrating photometry was not possible. IC 310 and 1ES 1426+428 do not have γ-ray data within the Fermi LAT LCR due to low variability indices.

[a]:De Jaeger et al. (2023),[b]:NASA Extragalactic Database.

Name	Type	z	r^* mag. range	Fermi range (erg cm^{-2} s^{-1})	Observational Period (MJD)
IC 310	HSP	0.0189[b]	13.137 - 12.873	-	56317.842 - 57989.231
1ES 1011+496	HSP	0.212[a]	15.408 - 14.676	2.16×10^{-11} - 3.46×10^{-10}	56321.963 - 58521.050
MRK 421	HSP	0.03[a]	-	1.12×10^{-10} - 1.09×10^{-9}	56272.275 - 58526.096
MRK 180	HSP	0.045[a]	14.752 - 14.241	9.98×10^{-12} - 9.58×10^{-11}	56321.980 - 58521.079
PG 1218+304	HSP	0.184[a]	16.125 - 14.962	3.24×10^{-11} - 3.28×10^{-10}	56268.274 - 58519.227
1ES 1426+428	HSP	0.129[b]	16.157 - 15.503	-	56322.127 - 58521.280
PG 1553+113	HSP	0.36[a]	14.106 - 13.006	2.61×10^{-11} - 5.78×10^{-10}	56318.196 - 58521.292
MRK 501	HSP	0.033[a]	12.817 - 12.594	1.60×10^{-11} - 3.86×10^{-10}	56318.203 - 58535.199
1ES 1959+650	HSP	0.047[a]	13.843 - 13.365	4.34×10^{-11} - 5.14×10^{-10}	57509.122 - 57975.920
3C 66A	ISP	0.444[a]	14.905 - 13.539	2.32×10^{-11} - 3.59×10^{-10}	56321.954 - 58496.939
S5 0716+714	ISP	0.127[a]	14.444 - 11.263	2.45×10^{-11} - 1.04×10^{-9}	56331.918 - 58527.891
ON 231	ISP	0.102[a]	15.460 - 13.488	1.89×10^{-11} - 1.99×10^{-10}	57206.950 - 58535.117
A0 0235+164	LSP	0.94[a]	18.473 - 14.618	1.81×10^{-11} - 7.39×10^{-10}	57051.876 - 58394.129
TXS 0506+056	LSP	0.336[a]	14.249 - 13.731	8.35×10^{-11} - 2.48×10^{-10}	58339.233 - 58360.174
OJ 287	LSP	0.306[a]	15.096 - 12.456	1.59×10^{-11} - 3.70×10^{-10}	56316.033 - 58759.242
S4 0954+65	LSP	0.367[a]	16.689 - 14.065	1.24×10^{-11} - 8.54×10^{-10}	57051.117 - 58535.055
4C 09.57	LSP	0.322[a]	17.301 - 14.384	2.24×10^{-11} - 1.24×10^{-9}	57090.231 - 58540.284
BL Lac	LSP	0.069[a]	13.900 - 11.967	3.33×10^{-11} - 8.25×10^{-10}	56407.184 - 58460.905
PKS 0502+049	LSP (FSRQ)	0.954[a]	18.206 - 15.126	3.41×10^{-11} - 1.48×10^{-9}	56652.997 - 57983.222
PKS 0736+01	LSP (FSRQ)	0.189[a]	16.274 - 14.384	2.63×10^{-11} - 6.68×10^{-10}	57007.998 - 57881.871
PKS 1222+216	LSP (FSRQ)	0.435[b]	15.223 - 13.018	1.68×10^{-11} - 8.92×10^{-10}	56332.163 - 58258.923
3C 279	LSP (FSRQ)	0.536[a]	15.339 - 12.818	3.43×10^{-11} - 1.01×10^{-8}	56322.115 - 58541.195
PKS 1510-089	LSP (FSRQ)	0.361[b]	16.023 - 13.260	4.60×10^{-11} - 2.47×10^{-9}	56304.292 - 58542.260
OS 319	LSP (FSRQ)	1.399[a]	17.918 - 16.381	1.87×10^{-11} - 9.95×10^{-11}	57110.113 - 58542.276
PKS B1622-297	LSP (FSRQ)	0.815[a]	18.629 - 16.057	1.94×10^{-11} - 3.73×10^{-10}	57090.217 - 58542.282
4C +38.41	LSP (FSRQ)	1.814[a]	17.531 - 15.202	2.45×10^{-11} - 7.05×10^{-10}	57128.155 - 58534.294
3C 345	LSP (FSRQ)	0.593[a]	17.629 - 15.750	1.11×10^{-11} - 4.76×10^{-10}	57083.139 - 58540.272
PKS B1730-130	LSP (FSRQ)	0.902[a]	17.643 - 16.315	4.15×10^{-11} - 2.37×10^{-10}	57085.216 - 58519.275
3C 446	LSP (FSRQ)	1.404[a]	18.272 - 17.361	1.62×10^{-11} - 7.18×10^{-11}	57175.149 - 58408.836
4C 11.69	LSP (FSRQ)	1.037[a]	16.658 - 10.560	4.29×10^{-11} - 8.25×10^{-9}	57143.229 - 58463.794
3C 454.3	LSP (FSRQ)	0.859[a]	15.795 - 13.346	8.36×10^{-11} - 6.65×10^{-9}	57143.225 - 58408.847

Table 3.1 shows details of the redshift, spectral peak (emission) classification, r^* band magnitude range and Fermi γ-ray flux range for the given observational period for each of the 31 objects in the sample. It is made up of the 15 sources in the combined KVA DIPOL (Tuorla blazar monitoring program) and RINGO2 (Liverpool Telescope blazar monitoring program) sample (Jermak et al., 2016a), with additional sources selected for γ-ray activity.

The photometric data for the majority of these sources are presented in this chapter with the following exceptions. MRK 421 lacks usable comparison stars in its field (due in part to the presence of a bright foreground star that causes ghosting in the frame). For this reason, differential photometry was not possible and it has been disregarded in this chapter, but will be included in the polarisation analysis presented in Chapter 4. IC310 and 1ES 1426+428 do not have data in the Fermi LAT LCR as their variability

indices are less than the defined threshold (see Section 2.3.1.1). These sources will be omitted from any γ-ray analysis.

In the RINGO3 dataset, the median difference in MJD between optical and γ-ray observations across all sources in the sample was 1.12 days. 96% of observations had a corresponding Fermi γ-ray observation within 12 days (the average cadence between optical observations across all sources). As described in Section 2.3.1.1, the differing cadence between optical and γ-ray observations was accounted for by assigning the temporally closest γ-ray data point to each of the optical observations. The γ-ray activity level of each source was determined by computing the median flux over the RINGO3 observation timescale. Any group of two or more points above three times the median absolute deviation (including lower error limits) are considered to be in a flaring state.

It is noted that no host galaxy corrections have been performed on the data. In general, blazars outshine their host galaxies by several orders of magnitude so no correction is required (Otero-Santos et al., 2022). Some sources in the sample within the HSP BL Lac class, such as IC 310, MRK 421 and MRK 180, do have resolvable host galaxies but these are not variable. This means that for a small amount of data, a change in position on magnitude/flux axes would occur following host correction, but the correlations observed would remain unchanged. This approach might not be appropriate for multi-facility analysis, especially in the presence of significantly variable seeing, but is appropriate for the work presented here.

3.1.2 Optical–gamma-ray flux

Studying correlated behaviour between optical and γ-ray flux allows the exploration of emission processes within blazar jets. Leptonic models predict a close connection between the wavebands, given the same population of electrons would be responsible for the lower and higher energy emissions. Conversely, in hadronic models, the higher energy emission is produced independently of the synchrotron electron population, thus resulting in much less correlated behaviour (Böttcher et al., 2013).

Furthermore, it was discussed in Chapter 1.2.2 through the work of Ghisellini et al. (2017) that in general, FSRQs tend to be located at higher redshifts than that of BL Lac type sources and are thus distanced further away from the observer. When investigating

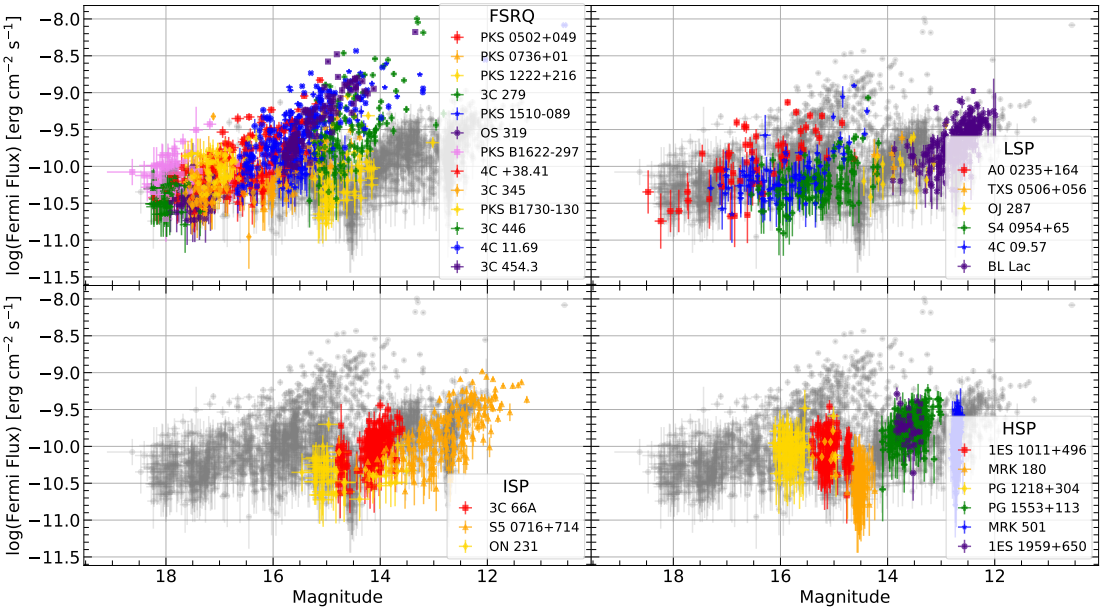

FIGURE 3.1: Fermi γ-ray flux vs. optical r^* magnitude for the sample. Each panel highlights the data for the different blazar subclasses separately with the upper left, upper right, lower left, and lower right highlighting data for FSRQs, BL Lac LSPs, ISP BL Lacs, and HSP BL Lacs respectively. In each panel, the data for the other subclasses is shown as faint grey circles.

the characteristics of different blazar classes, it is important to account for this factor, to ensure the observed behaviour is intrinsic to the group, and not induced by significant differences in distance.

The γ-ray fluxes vs. r^*-band magnitudes are shown in Figure 3.1, with each panel showing sources of different classifications (i.e. high-, intermediate-, low- synchrotron peak BL Lac types and FSRQs) and each colour within the panel showing different sources. The data from other object classifications are shown as grey points. There is a clear distinction between the BL Lac and FSRQ sources, with some overlap between the FSRQs and BL Lac LSPs. The FSRQ sources generally have higher γ-ray fluxes; however, this may just be due to the biased nature of the sample selection (sources were added to the observing campaign if they showed high levels of γ-ray activity with Fermi).

Using the redshifts from Table 3.1, the γ-ray fluxes and optical magnitudes can be calibrated for distance. To do this, the luminosity distance, $d_{\rm L}$, was calculated for each object using the WMAP9 COSMOLOGY module in ASTROPY. This module assumes a flat universe, with a Hubble constant of $H_0 = 69.32\,{\rm km\,s^{-1}\,Mpc^{-1}}$ and the matter density parameter set at $\Omega_{\rm m} = 0.2865$ (Hinshaw et al., 2013).

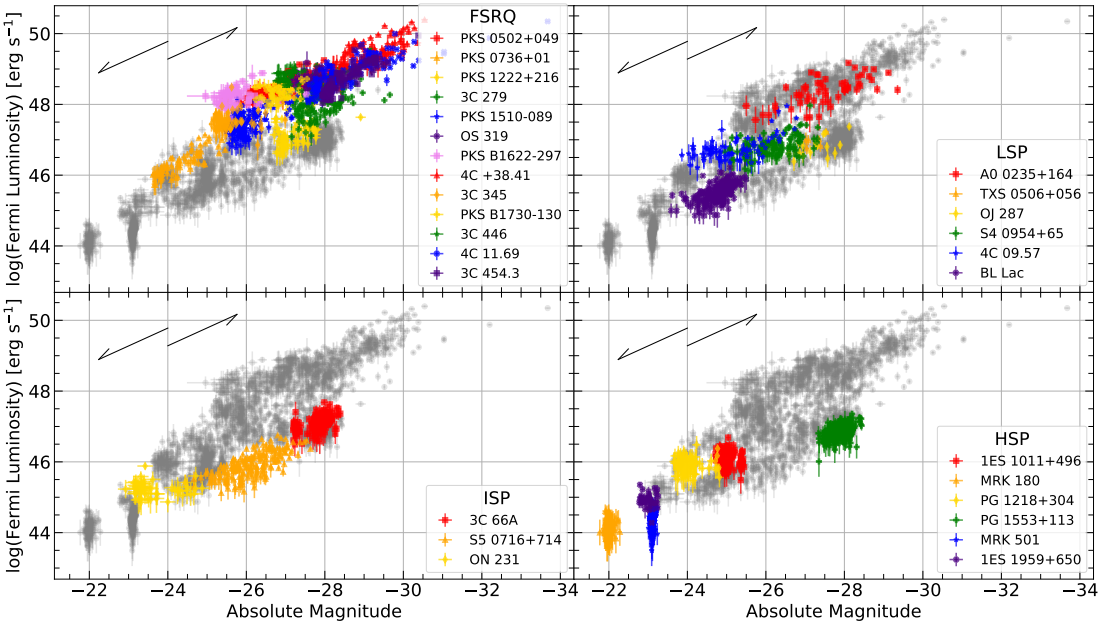

FIGURE 3.2: As Figure 3.1, but with Fermi γ-ray flux and r^* magnitude calibrated for distance (γ-ray luminosity and r^* absolute magnitude respectively). Additionally, redshift vectors are included to show the direction and distance the data for a given source would move if the redshift value given in Table 3.1 was incorrect. The decreasing line indicates the redshift has been overestimated by double and the increasing underestimated by half.

The γ-ray luminosity was calculated by

$$L = (\Gamma - 1)\, 4\pi F d_L^2 (1+z)^{\Gamma} \tag{3.1}$$

from Hovatta et al. (2014) where Γ is the photon power-law index (taken from the Fermi LCR), F is the γ-ray flux given in erg cm^{-2} s^{-1} in the 1–100 GeV photon energy range, and $d_{\rm L}$ is the luminosity distance given in cm. The absolute magnitude was calculated by

$$M = m - 5 \log d_{\rm L} + 5 \tag{3.2}$$

where m is the apparent magnitude, and $d_{\rm L}$ is the luminosity distance in pc.

The resulting distance-calibrated data are shown in Figure 3.2. As in Figure 3.1 the data are displayed in each panel according to subclass (e.g. FSRQ, LSP BL Lac, ISP BL Lac, HSP BL Lac), with grey points showing the other subclasses. Similarly to Figure 3.1, the distance-calibrated FSRQs are generally brighter at γ-ray frequencies but also dominate at the brightest optical absolute magnitudes.

It is noted that by definition, there is great difficulty determining the redshifts of BL Lac objects due to the small (or absent) emission lines in their optical spectra. This means the calculation of absolute magnitude and γ-ray luminosity is subject to this uncertainty. To account for this, one can fit how the average absolute magnitude and γ-ray luminosity vary as a function of redshift. This fit can be plotted alongside the data to visualise the direction and scale of shifting needed should the redshift value be incorrect by an arbitrary factor. 1000 redshift values between $\frac{z}{2} < z < 2z$ (where z is the redshift value stated in Table 3.1) were used to distance-calibrate the average γ-ray and optical magnitude data for each source in the sample. The resulting values were fitted, showing a linear relationship of the form $y = Ax + B$ where $A = -0.504 \pm 0.012$ and $B = 33.90 \pm 0.20$. Furthermore, the vector distance the data shifted was the same for redshift values of $\frac{z}{2}$ and $2z$ at 1.971 ± 0.023 units in Figure 3.2. From this, one could show redshift vectors in the upper left corner of each panel of Figure 3.2. These vectors show the distance and direction the data for a given source would shift for a 50% reduction ($\frac{z}{2}$) and a 100% increase ($2z$) in the redshift value stated in Table 3.1. If the true redshift were half the stated value, implying an overestimation, the object would be intrinsically fainter and so would shift in the direction of the decreasing vector, towards the point (0, 33.90), in Figure 3.2. Conversely, if the true redshift was double the stated value, implying an underestimation, the object would be intrinsically brighter and would shift in the direction of the increasing vector, away from the point (0, 33.90), in Figure 3.2.

Table C.2 in the appendix shows the Spearman rank significance (p) and strength (c) coefficients for correlations between the RINGO3 wavebands and γ-ray flux for each source in the sample, excluding IC310, 1ES 1426+428, and MRK421 for the reasons discussed previously. Of these 28 sources, 21 showed significant correlations between γ-ray flux and each optical $b^*g^*r^*$ magnitude. All significant correlations were positive. Breaking these correlations down by subclassification it is found that 33% of HSP BL Lac sources showed significant correlations, increasing to 66% for ISP BL Lac sources. All BL Lac LSP sources showed significant correlations between the optical and γ-ray fluxes, along with 85% of FSRQs.

3.1.3 Optical colour

The colour of an astronomical source refers to the difference in magnitude of measurements taken in two wavebands. When the colour is plotted as a function of the magnitude for multiple observations, it shows the spectral changes exhibited by a source with time. This can provide information into the changes in relative abundances of flux from different regions of the sources (i.e. increased non-thermal jet emission over thermal disk emission), or the underlying processes causing the variability (shock cooling producing bluer emission on a count of higher energy frequencies cooling faster than lower energy frequencies (Fiorucci et al., 2004)). It is noted that for colour analysis, it is important to use more than 2 wavebands to avoid introducing false correlations between the same uncertainties on both the x and y axes. This has been discussed in detail in Jermak (2016) and McCall et al. (2024b).

Figure 3.3 shows the b^*-g^* vs. r^*, b^*-r^* vs. g^* and g^*-r^* vs. b^* colour-magnitude plots for each source, with the colour denoting the camera used on the x-axis. The corresponding correlation coefficients and linear fit gradients are shown in Table C.3.

Of the 17 BL Lac types (8 HSPs, 3 ISPs and 7 LSPs), 15 show significant long-term b^*-r^* vs. g^* colour-magnitude relationships; all with negative correlation coefficients and gradients. Two BL Lac type sources did not display significantly correlated behaviour in b^*-r^* vs. g^*: 1ES 1959+650 (HSP) and A0 0235+164 (LSP). All 13 FSRQ sources show significant long-term colour-magnitude behaviour.

All significantly correlated BL Lac type objects, along with three FSRQs, show long-term bluer-when-brighter behaviour (negative correlations), i.e. when the magnitude of the source increases its colour becomes bluer. The remaining ten FSRQs show the opposite trend (positive correlations); they become redder as the magnitude increases (redder-when-brighter behaviour).

Exploration of the colour–magnitude behaviour as a function of the RINGO3 wavebands showed that the colour behaviour does not always remain consistent across the three wavebands, with some sources showing significant BWB and RWB behaviour depending on the chosen colour index. 3C 120 shows significant BWB in r^* vs. b^*-g^* and in g^* vs. b^*-r^* but a RWB correlation in b^* vs. g^*-r^*. Similarly, 3C 345 shows significant BWB correlations in g^* vs. b^*-r^* and b^* vs. g^*-r^* but RWB r^* vs. b^*-g^*. Furthermore in

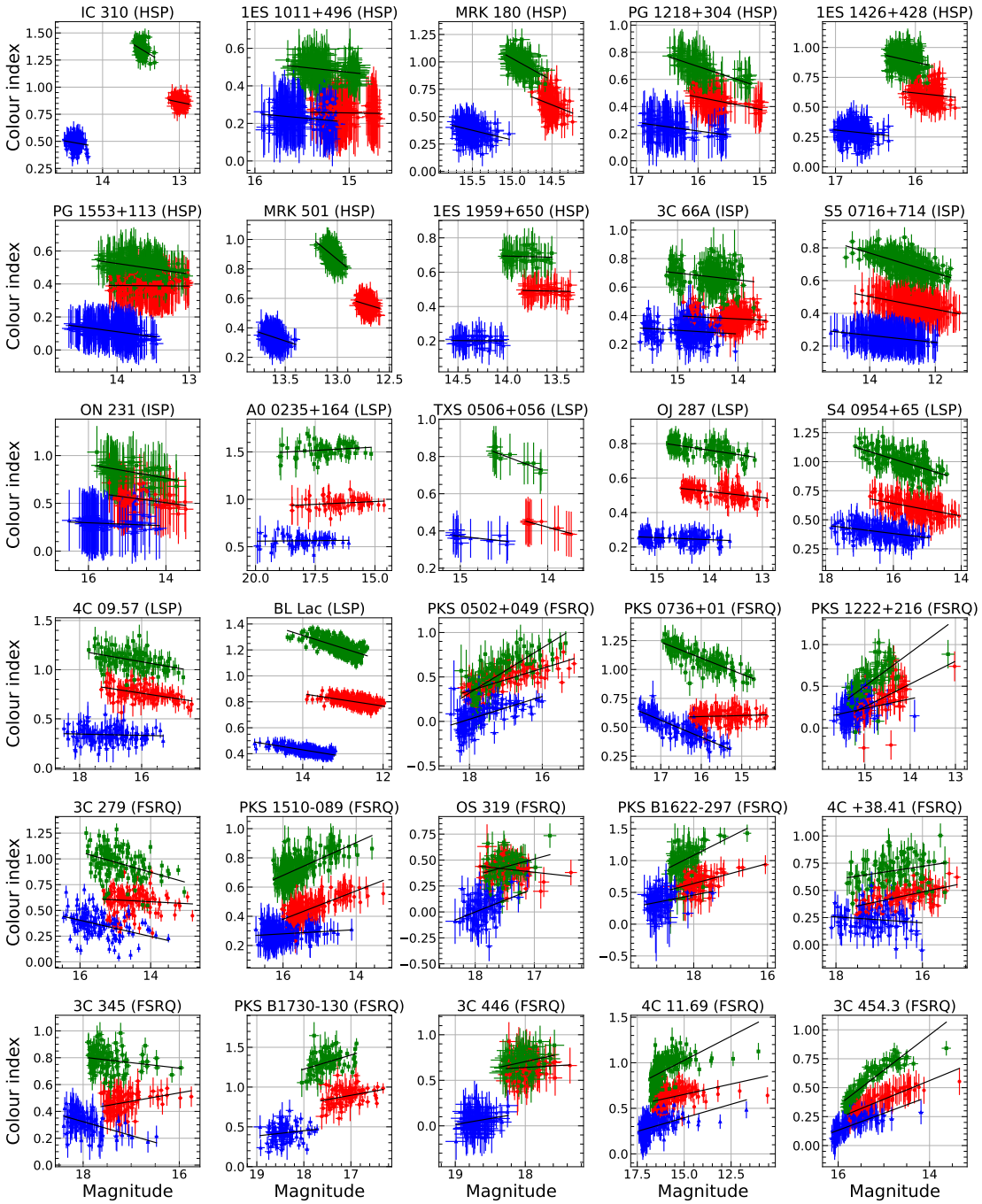

FIGURE 3.3: Colour–magnitude plots for each source in the RINGO3 sample. Each plot shows the three colour permutations (b^*-r^*, b^*-g^*, and g^*-r^*) plotted against the remaining magnitude (g^*, r^*, and b^*, respectively). A fit line is also shown.

some FSRQ objects, like 3C 454.3 and 4C 11.69, one could argue the linear fit doesn't describe the observed behaviour very well, and that a non-linear fit might be more appropriate.

To explore this potential non-linear feature further, one can consider the spectral changes of the objects in the sample, and compare the spectral state at each epoch to the flux. The spectral index was calculated assuming a single power law as defined by

$$\mathrm{F}_\nu \propto \nu^{-\alpha} \tag{3.3}$$

where F_ν is the flux at wavelength ν, ν is the central wavelength of the RINGO3 bands, and α is the spectral index. The gradient of log flux vs. log frequency gives $-\alpha$. This was done using the r^* and b^* data, and by fitting a linear least-squares regression. Like with the colour-magnitude analysis, it was important not to include the g^* band data in the y-axis colour calculation so as not to induce false correlations in the subsequent analysis (Jermak, 2016; McCall et al., 2024b). The uncertainty of the spectral index at each epoch was calculated using Monte Carlo resampling where, at each epoch, 1000 pairs of randomly generated r^* and b^* flux values within the respective error limits were generated and the spectral index was calculated. The standard error on these 1000 values was taken as the error on the spectral index.

From the data presented in Figure 3.4, it is clear that in many cases, a linear fit is not well suited to describe the relationship between optical spectral index and flux. For this reason, the spectral index and g^*-band flux were fitted with a linear least-squares regression and logarithmic function of the form

$$\alpha = A \ln\left(F_{\mathrm{g}*}\right) + B \tag{3.4}$$

where A and B are free parameters. A logarithmic functional form was selected after manually testing multiple alternative fits through trial and error, and finding the logarithmic from represented the data the most accurately. For both the linear and logarithmic fits, an Akaike Information Criterion (AIC; Akaike, 1974) and Bayesian Information Criterion (BIC; Schwarz, 1978), were calculated to quantify the quality of the fits on the data. The number of free parameters for both fits was two, and lower AIC and BIC values indicated better fits. Furthermore, Spearman rank correlation coefficients

were calculated for each dataset. For those data that were better fitted logarithmically, the alpha values were logged before the Spearman rank calculations to make the data linear.

Table C.4 in the appendix shows the results of the above analysis, with the 'Fit' column describing which model fits the data better according to the AIC and BIC values. There were no cases with conflicting AIC and BIC values. The 'Trend' column describes the colour relationship observed given the obtained preferred fit and sign on the Spearman rank strength coefficient, c. Negative strengths indicate bluer-when-brighter (BWB) behaviour, implying the spectral index flattens during periods of heightened flux. Conversely, positive strength coefficients indicate redder-when-brighter (RWB) behaviour implying the spectral index steepens during periods of heightened flux. In both cases where a log fit is preferred over a linear one, the behaviour becomes more stable as brightness increases. This means the rate at which the colour changes decreases, or altogether flattens. This can be referred to as bluer-stable-when-brighter (BSWB) and redder-stable-when-brighter (RSWB) behaviour. The preferred fit for each source is included in Figure 3.4. A dotted line indicates the linear fit and a solid line indicates a logarithmic fit.

Of the 17 BL Lac types (8 HSPs, 3 ISPs and 6 LSPs), 15 show significant long-term colour–flux relationships; all with negative correlation coefficients. Two BL Lac type sources did not display significantly correlated behaviour: 1ES 1959+650 (HSP) and A0 0235+164 (LSP). In most cases, these significant correlations are best fitted linearly, but six objects show the BSWB relationship, meaning their colour becomes more stable during high flux periods. All 13 FSRQ sources show significant long-term colour–flux behaviour. Two sources show a BWB trend, and one shows the BSWB trend. Eight show the RSWB, while only two FSRQs show linear RWB colour relationships.

3.1.4 Optical colour – gamma-ray

Blazar variability at optical frequencies consists of emission from different parts of the system including the jet, accretion disc, and, in periods of quiescence, the host galaxy (Goldoni et al., 2021). In order to study the jet variability it is important to separate out the emission from different parts of the AGN. One way to achieve this is to compare the optical colour to the γ-ray emission. Assuming leptonic modelling, if the optical

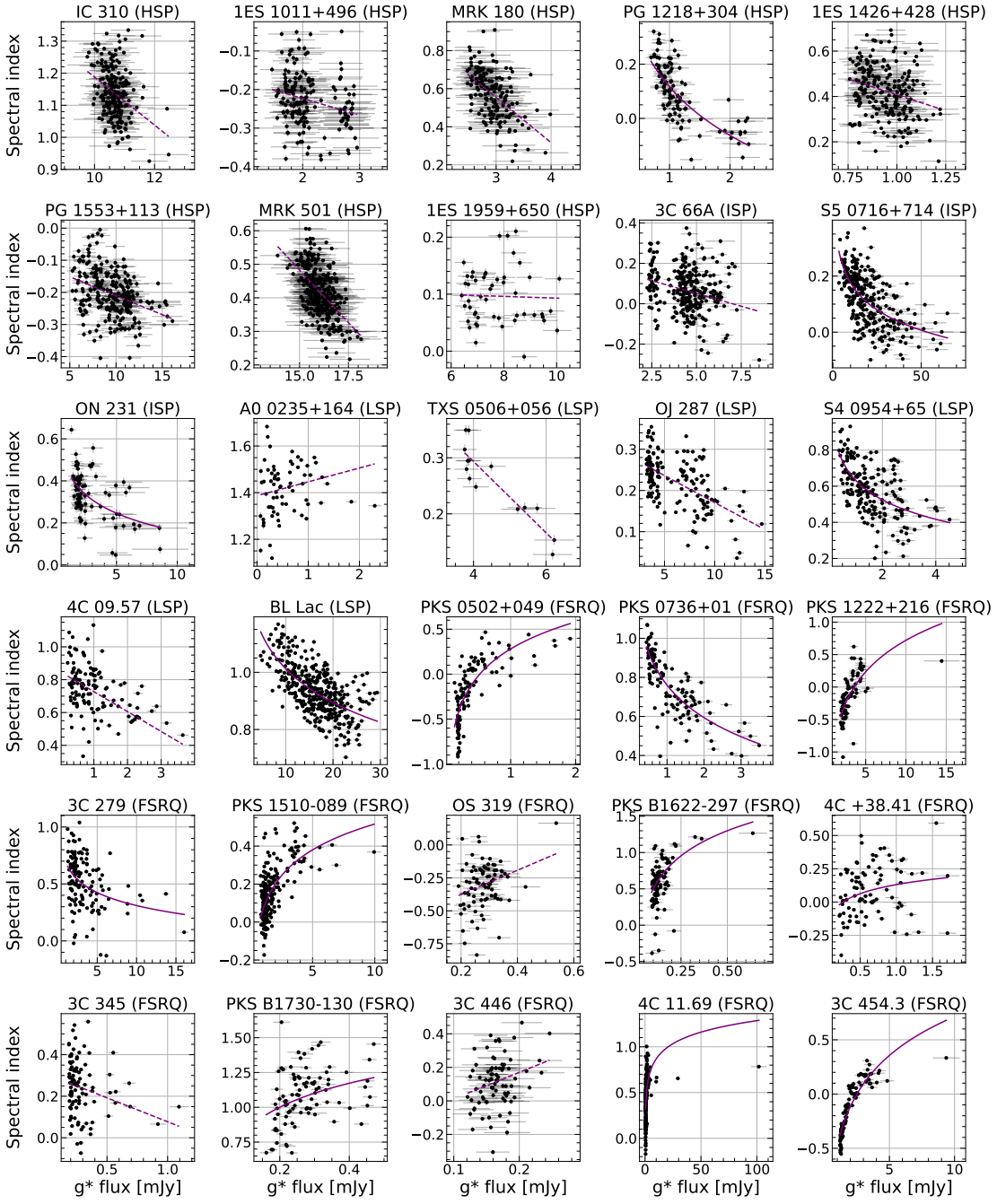

FIGURE 3.4: Spectral index vs. optical g^*-band flux for each object in the sample. A best-fit line is fitted to each set of data after having linear and logarithmic fits qualitatively assessed using AIC and BIC coefficients. A preferential linear fit is shown by a dotted fit line, while a logarithmic fit is shown by a solid line. The Spearman rank correlation coefficients associated with each correlation (linearised in the case of a logarithmic fit) are given in Table C.4.

and γ-ray emission originates from the same population of synchrotron electrons in the jet, colour changes resulting from shocks or otherwise increased jet emission will be correlated with changes to the γ-ray emission.

Figure 3.5 shows the γ-ray flux vs. optical colour index correlations with Table C.5 showing the correlation strengths and significances. Of the 29 sources with Fermi γ-ray data and calibrated optical magnitude, 19 (66%) show significant correlations with the optical b^*-r^* colour. The strengths of these correlations range from very weak (|0.128|) to very strong (|0.901|) with both positive and negative linear fit gradients.

Of the 15 BL Lac types, 10 showed significant behaviour (3 HSPs, 1 ISP, and all 6 LSPs). Additionally, all but two of the significantly correlated sources were negative in strength, implying an increase in γ-ray emission correlated with a decreasing optical spectral index (i.e. the sources became optically bluer when γ-ray brighter). Two sources, namely A0 0235+164 (LSP) and OJ287 (LSP), showed the opposite trend; these objects became optically redder when brighter in γ-rays. For the 13 FSRQs, nine showed correlated behaviour between the optical b^*-r^* colour and γ-ray flux. Two of these correlations indicated bluer when γ-ray brighter trends while the remaining seven showed redder when γ-ray brighter.

Like with the optical colour–magnitude analysis, the optical spectral index was calculated in order to investigate its evolution with the γ-ray flux, and to better identify any non-linear relationships. Figure 3.6 shows the optical spectral index vs. γ-ray flux for each object in the sample, and Table C.6 in the appendix shows their correlation strengths and significances. The γ-ray flux data is independent of the optical, meaning the optical spectral index could be calculated using all three optical flux colours ($b^*g^*r^*$). The error calculation for the spectral index per epoch, and the determination of linear/logarithmic fit preference was the same as detailed in Section 3.1.3. To reduce the chance of false correlations, the repeated instances where the γ-ray flux has been assigned to multiple optical epochs have been removed.

Of the 28 sources, 15 show significant correlations between the optical spectral index and γ-ray flux. The strengths of these correlations range from very weak (|0.164|) to very strong (|0.897|) with both positive and negative correlation strengths.

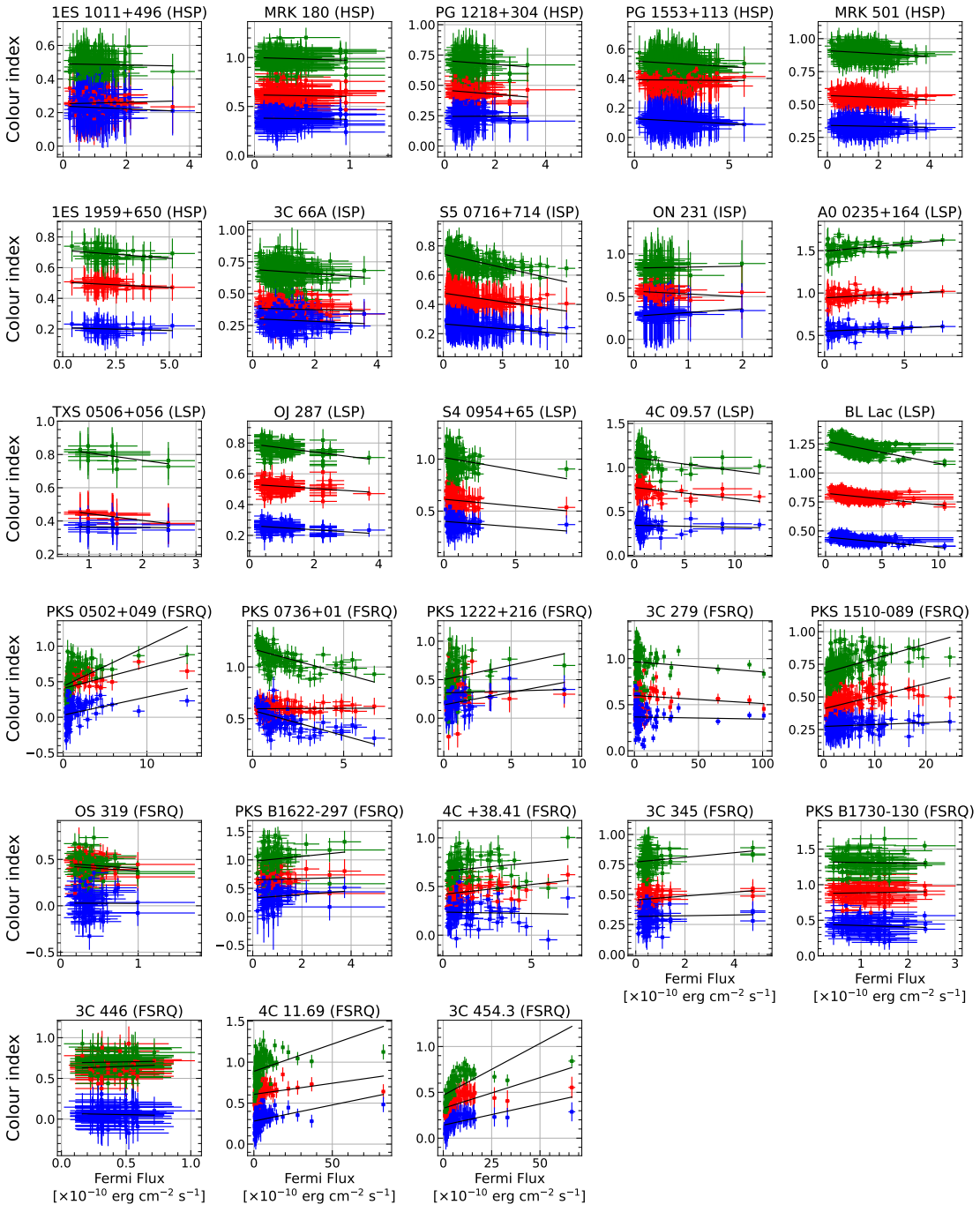

FIGURE 3.5: As Figure 3.3 but for optical colour index vs. γ-ray flux. The Spearman rank coefficients associated with each correlation are given in Table C.5.

Of the 15 BL Lac type sources, eight showed significant behaviour (2 HSPs, 1 ISP, and all 5 LSPs). Additionally, all but two of the significantly correlated sources were negative in strength, implying an increase in γ-ray emission correlated with a decreasing optical spectral index (i.e. the sources became optically bluer when γ-ray brighter). Furthermore, five objects demonstrated the BSWB trend. Two sources, namely A0 0235+164 (LSP) and OJ287 (LSP), showed the opposite trend; these objects became optically redder when brighter in γ-rays, but followed the linear relationship. For the 13 FSRQs, seven showed correlated behaviour between the optical spectral index and γ-ray flux. When brighter in γ-rays one of these correlations showed the BSWB trend, while the remaining six showed the RSWB trend.

3.1.5 Optical–gamma-ray time lags

If the variability observed is assumed to be leptonic in origin, time lags between optical and γ-ray emission can provide constraints on the location of the inverse Compton seed photons relative to the synchrotron emission region, differentiating inverse Compton and SSC emission (Cohen et al., 2014).

The Discrete Correlation Function (DCF; Edelson & Krolik, 1988) was used to explore time lags between the optical and γ-ray data. This process is fully described in Section 5.1.3 and in McCall et al. (2024a). The DCF points are fitted using the GaussianProcessRegressor module and the Rational Quadratic kernel from scikit-learn in Python (Pedregosa et al., 2011a). The maximum absolute value from this fit is chosen as the lag. The optical r^*-band flux is shifted with respect to the γ-ray flux, meaning a negative lag implies the γ-ray emission is leading the optical, and a positive lag implies the optical emission is leading the γ-ray.

The results are shown in Table C.7 in the appendix. If a lag is inconsistent with zero at the 3σ level and has a strength coefficient of greater than 0.40 (see Table 2.8) it is labelled as potentially significant (yes*). The "ΔPeak" column shows the error on the peak value, given as the average cadence between successive optical observations. In all cases, this value was larger than the error associated with the calculation of the DCF. The sources that meet these criteria are 1ES 1959+650, ON231, PKS 1510-089, and PKS B1622-297. To determine whether the measured lags were real, they were applied to the optical data and the correlation was re-tested using the Spearman rank coefficient. The

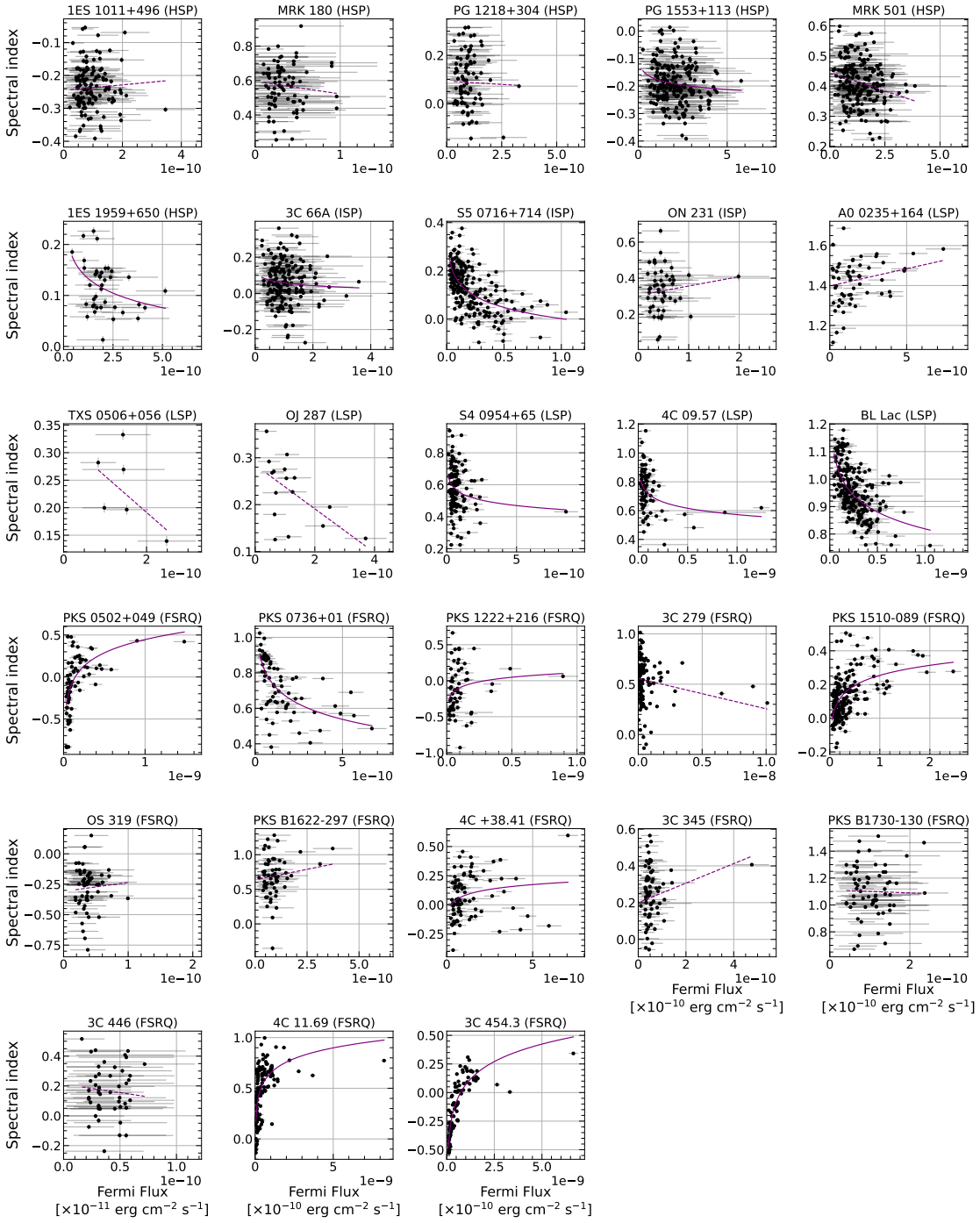

FIGURE 3.6: As Figure 3.3 but for spectral index vs. γ-ray flux. The Spearman rank coefficients associated with each correlation are given in Table C.6.

TABLE 3.2: Spearman rank correlation coefficients before and after application of the detected interband time lag between the optical and γ-ray fluxes.

Source	Lag [days]	ΔLag [days]	p		c	
			Before	After	Before	After
1ES 1959+650	29.75	9.34	0.197	4.87×10^{-05}	-0.185	-0.542
ON 231	118.09	16.20	0.250	7.65×10^{-03}	-0.128	0.293
PKS 1510-089	-55.41	9.44	2.34×10^{-21}	1.28×10^{-11}	0.565	0.421
PKS B1622-297	-129.82	17.29	0.012	7.46×10^{-02}	0.272	0.196

assumption is made that if the lags were real, the optical and γ-ray fluxes would become, or remain, significantly correlated with a larger strength value. These results are shown in Table 3.2 where the Spearman rank correlation statistics before and after applying the detected lags are shown. The correlations for PKS 1510-089 and PKS B1622-297 did not increase in strength after shifting, whereas for both 1ES 1959+650 and ON231, the optical–γ-ray correlations became significantly correlated. The coefficients suggested an inverse correlation for 1ES 1959+650, and direct for ON231.

The following caveats to the lag analysis results are noted. The 1ES 1959+650 light curve shows that from MJD 57500–57560 (while in an optically fainter state) the data were obtained at a much higher cadence (one observation every two days) than the rest of the observations (one observation every two weeks). After correcting for the potential lag, this period then aligns with an active state in the γ-ray light curve. Outside this period there is no correlated behaviour. Given this, it is concluded that the lag is likely a false detection caused by irregular sampling dominating the correlation statistics. In the case of ON231, the variability in the γ-ray light curve is consistent with noise, so the correlation results for this source are dubious. It is therefore determined that no significant long-term time lags between the optical and Fermi γ-ray fluxes in the data.

3.1.6 Discussion

Correlations were explored using the Spearman rank test and were considered significant at the 95% confidence interval, where $p \leq 0.05$. Those sources which did not have data accessible in the Fermi LAT LCR (IC 310, 1ES 1426+428) or did not have calibratable optical magnitude data (MRK 421) were omitted. Table 3.3 shows the results of all four correlation tests performed in this work. The table gives a "Yes" or "No" describing whether or not a significant correlation was detected, or the observed colour trend for those significantly correlated.

TABLE 3.3: Results of the different correlations explored in this work. The source name and subclass are given, along with 'Yes' or 'No' to describe whether or not the given correlation was statistically significant. The asterisk in the 3σ lag column indicates the potential significance of the detected lag, warranting further analysis.

Source	Type	opt flux – γ-ray flux	α – opt flux	α – γ-ray flux	3σ Lag
IC 310	HSP	-	BWB	-	-
1ES 1011+496	HSP	No	BWB	No	No
MRK 421	HSP	-	-	-	-
MRK 180	HSP	No	BWB	No	No
PG 1218+304	HSP	No	BSWB	No	No
1ES 1426+428	HSP	-	BWB	-	-
PG 1553+113	HSP	Yes	BWB	No	No
MRK 501	HSP	Yes	BWB	BWB	No
1ES 1959+650	HSP	No	No	BSWB	Yes*
3C 66A	ISP	Yes	BWB	No	No
S5 0716+714	ISP	Yes	BSWB	BSWB	No
ON 231	ISP	No	BSWB	No	Yes*
A0 0235+164	LSP	Yes	No	RWB	No
TXS 0506+056	LSP	Yes	BWB	No	No
OJ 287	LSP	Yes	BSWB	RWB	No
S4 0954+65	LSP	Yes	BSWB	BSWB	No
4C 09.57	LSP	Yes	BWB	BSWB	No
BL Lac	LSP	Yes	BSWB	BSWB	No
PKS 0502+049	LSP (FSRQ)	Yes	RSWB	RSWB	No
PKS 0736+01	LSP (FSRQ)	Yes	BSWB	BSWB	No
PKS 1222+216	LSP (FSRQ)	Yes	RSWB	RSWB	No
3C 279	LSP (FSRQ)	Yes	BSWB	No	No
PKS 1510-089	LSP (FSRQ)	Yes	RSWB	RSWB	Yes*
OS 319	LSP (FSRQ)	Yes	RWB	No	No
PKS B1622-297	LSP (FSRQ)	Yes	RSWB	No	Yes*
4C +38.41	LSP (FSRQ)	Yes	RSWB	RSWB	No
3C 345	LSP (FSRQ)	No	BWB	No	No
PKS B1730-130	LSP (FSRQ)	No	RSWB	No	No
3C 446	LSP (FSRQ)	Yes	RWB	No	No
4C 11.69	LSP (FSRQ)	Yes	RSWB	RSWB	No
3C 454.3	LSP (FSRQ)	Yes	RSWB	RSWB	No

3.1.6.1 Optical–gamma-ray analysis

Figures 3.1 and 3.2 show the optical and γ-ray correlations of the RINGO3 sample (both for the whole sample and separated by blazar subclasses) as functions of both apparent and absolute magnitude. 21 out of 28 (i.e. 75%) of sources showed significant positive correlations ranging in strength from $0.217 \leq c \leq 0.891$. Exploring the correlated behaviour between optical and γ-ray flux allows the exploration of emission processes within the jets. In the leptonic scenario, higher-energy γ-ray emission is a result of inverse-Compton upscattering of lower energy seed photons via relativistic particles in the jet (Maraschi et al., 1992; Bloom & Marscher, 1996; Böttcher et al., 2013). If the seed photons are from the same population of photons responsible for lower-energy

synchrotron emission, one could expect changes at optical and γ-ray wavelengths to be positively correlated over long timescales. Conversely, in hadronic models, the high-energy emission is likely produced through proton synchrotron emission, proton-proton interactions or other hadronic processes. In this case, long-term correlations between optical and γ-ray emission would be less likely (Mannheim & Biermann, 1992; Aharonian, 2000; Böttcher et al., 2013). In this work, significant positive correlations between optical and γ-ray flux were found for the majority of sources. It can therefore be concluded that the dominant jet emission mechanism within the blazar sample is likely leptonic.

Sources with high synchrotron peaks showed fewer significant correlations (33% for HSPs). The number of optical–γ-ray correlations increases to 67% of ISP sources and 89% of LSP objects (which includes all BL Lac objects and 85% of FSRQs). Jermak et al. (2016a) explored optical–γ-ray correlations for a sample of 15 blazars from the Liverpool Telescope and Tuorla blazar monitoring programs, using the RINGO2 and KVA DIPOL polarimeters, respectively. Significant positive correlations were found in 68% of sources. When considering object sub-classes, they found 43%, 50%, 88%, and 60% of HBL, IBL, LBL, and FSRQ sources, respectively, showed positively correlated behaviour. The overall results are therefore similar between the RINGO2 and RINGO3 analyses. The decrease in the strength of optical–γ-ray emission correlations on increasing synchrotron peak frequency (blazar subclass) can be understood as host-galaxy contamination in the case of HSPs. The host-galaxy emission would dilute the optical behaviour of the jet and, as such, result in weaker correlations with the γ-ray flux (Gaur, 2014; Chang et al., 2019; Otero-Santos et al., 2022). However, one cannot rule out the possibility that the intrinsic properties of HSPs differ from those of ISP and LSP objects, leading to weaker correlations.

Based on the optical and γ-ray flux properties, most sources in this sample occupied one of two regions in Figures 3.1 and 3.2. These regions are attributed to the FSRQ/BL Lac classification of blazars; with FSRQs typically displaying brighter γ-ray fluxes than BL Lacs. There are three sources, however, that appear to occupy the region in between these two blazar subclasses: A0 0235+164, S4 0954+64 and 4C 09.57. A0 0235+164 was originally classified as a BL Lac LSP source by Spinrad & Smith (1975) due to its featureless spectrum, however, Ruan et al. (2014) indicated that A0 0235+164 may belong to the FSRQ transitional class of blazars. This supports the conclusions of Ackermann et al. (2012) who model the A0 0235+164 SED during a flaring episode in

2008-2009 and find that the source's isotropic luminosity is more indicative of FSRQs than BL Lacs, and the dominant mechanism for the high energy emission is more likely to be external Compton processes; a signature of FSRQs, rather than synchrotron self-Compton. Similar to A0 0235+164, S4 0954+65 was also originally classified as a BL Lac object (Stickel et al., 1991). Ghisellini et al. (2011) classify this source as a low-frequency peaked blazar (LBL) due to the absence of prominent emission lines and the appearance of its SED. However, Hervet et al. (2016) classify the sources as an FSRQ by analysing the kinematic features of its radio jet. Furthermore, MAGIC Collaboration et al. (2018) model the multiwavelength emission of S4 0954+65 and compare it to other sources, concluding that it shows many behavioural similarities to FSRQs and other suspected transitional/masquerading BL Lac objects. Ghisellini et al. (2011) classify 4C 09.57 as a BL Lac LSP object based on the shape of its SED, however, they also observe emission lines with equivalent widths up to 12.5 Å. 4C 09.57 may also be a transitional object between the two subclasses (Uemura et al., 2017).

The correlations presented in Figures 3.1 and 3.2 agree with the results of Hovatta et al. (2014) in that the flux-flux correlations appear tighter for HSP and ISP sources compared to that of LSP objects (BL Lacs and FSRQs). In the SSC case, the low- and high-energy emission originates from the same region of the blazar jet so the emission is subject to the same level of Doppler boosting. This would mean those sources which have γ-ray production dominated by SSC emission should show tight correlations between the optical and γ-ray fluxes. Any EC emission should be more strongly boosted, obscuring any linear dependence between the low- and high-energy emission (Dermer, 1995). In this EC case, the flux-flux correlations would appear more scattered. The results support HSP and ISP sources having SSC as the dominant γ-ray emission mechanism, whereas LSP sources would show significant EC emission (Hovatta et al., 2014).

3.1.6.2 Spectral analysis (vs. optical and gamma-ray)

Figure 3.4 shows the spectral index vs. optical flux diagrams for all sources in the sample. Significant correlations were found for 28 of the 30 sources (15 BL Lacs and all 13 FSRQs). For the BL Lac objects, all 15 showed BWB behaviour with six (40%) displaying a logarithmic trend, indicating the stabilisation of the colour at higher fluxes (bluer-stable-when-brighter; BSWB). Of the FSRQs, two showed linear RWB trends and

one showed a linear BWB relationship. The rest (85%) showed stable trends. One of the stable trends was BSWB, while the remaining eight were RSWB. The Spearman rank strengths of all significant correlations ranged from roughly |0.195|–|0.953| (weak–very strong).

The exact mechanisms behind the optical colour behaviour of blazars are still debated and can be explained by both one and two-component synchrotron models. In the one-component model energy injection into the emitting regions increases the number of high-energy electrons, shifting the synchrotron SED peak to higher energies. This shift makes the object appear bluer (Ikejiri et al., 2011). The most accepted reasoning for this energy injection would be internal shocks travelling through the jet (Mastichiadis & Kirk, 2002; Guetta et al., 2004). In the two-component model, the total emission comprises radiation from different regions of the blazar, notably an underlying thermal contribution originating from the accretion disk and a more variable, non-thermal contribution from the jet (Fiorucci et al., 2004). If the flare component has a higher synchrotron peak frequency than that of the thermal emission, BWB trends would be observed. An observed feature in the SED of FSRQs is the UV bump (Gu et al., 2006), an excess of thermal emission which flattens the thermal/non-thermal composite spectrum at optical wavelengths. The increase in the thermal emission likely originates from the accretion disk and BLR. It follows that when the source brightens and the non-thermal emission increases, the spectrum steepens resulting in RWB trends (Ramírez et al., 2004; Gu et al., 2006).

This work shows more complex behaviour than a linear relationship between colour and flux, where colour changes stall, or become altogether absent, during heightened optical activity. Zhang et al. (2022a) suggest a unified model to explain observed blazar colour behaviour based on a two-component scenario made up of a less-variable thermal emission component from the accretion disk, and a highly variable non-thermal component from the jet synchrotron emission. They model the observed changes to the spectral index first by using a continuous segmented linear function, before generalising to a logarithmic relation given by

$$\alpha_{\rm obs} = 2.67 \ln \left[a + \frac{b}{F_{\rm obs,R}} \right] \tag{3.5}$$

where a and b are free parameters, and $F_{\mathrm{obs,R}}$ is the observed flux in R band. For a given source the spectral index, α_{obs}, depends only on $F_{\mathrm{obs,R}}$. This is based on the assumption that the two spectral index components (thermal and less variable, non-thermal and highly variable) are constant.

The results agree with the work by Zhang et al. (2022a) and Zhang et al. (2023): non-linear fits can better describe the relationship between the spectral index and flux in some sources, and the spectral index flattens during high states in all blazar classes. Where this is the case, the data can be fitted well by a single logarithmic curve with two free parameters. For those sources where no SWB features are observed, a lack of observations during high or low states may explain the seemingly linear trend.

This same analysis was used to look for non-linear relationships between the optical spectral index and γ-ray flux, the results of which are shown in Figure 3.6 with best fits and correlation statistics shown in Table C.6. 15 sources were found to have significant correlations (54%), eight BL Lacs (two HSP, one ISP, and five LSP) and seven FSRQs. Only three of the BL Lac objects displayed linear relationships (one BWB and two RWB), while the remaining five BL Lacs and all seven FSRQs showed stable features (all BSWB for the BL Lacs types and one FSRQ, and six RSWB for the remaining FSRQs).

Taking the leptonic scenario as the dominant source of high energy emission, the γ-ray emission from blazars originates from inverse-Compton processes occurring within the jet. While the optical emission can seed the γ-ray, causing the relationships observed in Section 3.1.2, it can also be composed of accretion disk variability or host galaxy emission. It follows that if the γ-ray emission is correlated with changes in the optical spectral index, then both emissions are more likely to be a result of jet activity, rather than coinciding disk and jet processes.

3.1.6.3 Time lag analysis

Leptonic modelling of blazar jet emission requires the high-energy γ-ray emission to be a result of inverse-Compton scattering of photons from the lower-energy synchrotron electrons. The seed photons may come from two locations; either the synchrotron photons from within the jet (synchrotron-self Compton; Maraschi et al., 1992) or photons

from outside the jet (external Compton; Dermer & Schlickeiser, 1993). It follows that temporal lags between the optical and γ-ray emission may allow the distinction between the two high-energy emission processes given the difference in separation between the low- and high-energy emitting regions (Cohen et al., 2014).

Time lags were tested for all sources with optical and γ-ray data. As summarized in Table 3.3, little evidence was found to show significantly lagged behaviour. Although four sources showed a potential lag based on the discrete correlation function, further analysis showed that all were likely false correlations. This included re-correlating the optical and γ-ray fluxes after applying the detected lag to the optical data, and inspecting the light curves for irregularities in cadence which could dominate the time lag correlation statistics. In summary, no evidence of long-term time lags with high confidence was found in the sample.

This analysis differs from that of related work in that long-term lag behaviour between the optical and γ-ray bands was searched for, rather than individual flares. However, this analysis is in agreement with recent work (Cohen et al., 2014; Liodakis et al., 2019; De Jaeger et al., 2023) in that the data show little evidence for temporal lags between the optical and γ-ray bands that are not consistent with zero days at the 3σ level. This means the data are suggestive of SSC processes dominating the jet flux, but further analysis into the characteristics of individual optical flares, and any gamma-ray correlations, could reveal more detail.

3.1.6.4 Correlations summary

Table 3.3 shows the results of all statistical tests performed in this work for each object in the sample. The majority of sources show the same relationships across tests, which could be used to infer the dominant radiation mechanisms over long timescales.

13 sources show significant correlations between the spectral index and optical flux but not between the spectral index and γ-ray flux. Of these 13, six (three HSPs, one ISP, and two FSRQs) do not show optical and γ-ray flux correlations, possibly due to relatively inactive or indiscernible γ-ray behaviour during these observations. The remaining seven sources (one HSP, one ISP, one LSP, and four FSRQs) do show significant optical and γ-ray flux correlations with no detected time lag. This implies their γ-ray brightening

episodes are optically colourless; a possible indication of γ-ray emission originating from seed photon fields outside the jet and a signature of EC processes.

12 sources (one HSP, one ISP, three LSPs, and seven FSRQs) show significant correlations between the optical and γ-ray fluxes with no detectable time lag, along with significant spectral index correlations for both optical and γ-ray flux, with matching spectral trends (i.e. both B(S)WB or both R(S)WB). This implies a strong connection between the jet's higher- and lower-energy behaviour in these sources, likely an indication of SSC-dominated emission.

Two objects (1ES 1959+650; HSP, and A0 0235+164; LSP) demonstrate significant spectral index vs. γ-ray flux correlations, but not spectral index vs. optical flux correlations. Furthermore, 1ES 1959+650 shows no significant correlation between the optical and γ-ray fluxes whereas A0 0235+164 does. In the case of 1ES 1959+650, the correlations may indicate a temporal separation between the spectral index and optical and γ-ray fluxes, explaining the lack of their correlations in this work. The time lag result for this source hinted at such behaviour but was ultimately disregarded due to unevenly sampled optical data. More observations of this object with regular sampling need to be obtained, ideally during a range of activity states, in order to make more definitive conclusions. For A0 0235+164, the majority of the observations occurred during a prolonged optical and γ-ray heightened state. It is possible that the optical observations only detected the flat region of a logarithmic RSWB colour trend and therefore appeared colourless, as not enough data were obtained during quiescent and/or low states. Furthermore, it has been previously reported that this object has a much brighter accretion disk than other LSP BL Lacs, and is more comparable to that of FSRQs (Ghisellini et al., 2010; Zhang et al., 2022a). This could explain why RWB spectral index vs. γ-ray flux behaviour was observed, in contrast to the generally accepted, almost exclusively BWB behaviour of BL Lac type blazars.

Finally, one object (OJ287; LSP) showed significantly correlated optical and γ-ray fluxes, but conflicting trends in the spectral index vs. optical flux (BSWB) and spectral index vs. γ-ray flux (RWB). It is noted that spectral index vs. γ-ray flux is very weakly correlated, and may also be slightly skewed on account of the expected accretion disk impact flare by a hypothesised secondary SMBH companion (Lehto & Valtonen, 1996).

TABLE 3.4: MOPTOP blazars used in this analysis with classification type, redshift, source type, optical R band magnitude range, Fermi γ-ray range, and observation range. [a]:De Jaeger et al. (2023),[b]:NASA Extragalactic Database.

Name	Type	z	R mag. range	Fermi range (ergs cm^{-2} s^{-1})	Observational Period (MJD)
PG1553+113	HSP	0.36[a]	14.228 - 13.134	9.97×10^{-11} - 6.04×10^{-10}	59938.287 - 60490.078
TXS 0506+056	LSP	0.336[a]	15.672 - 14.071	2.31×10^{-11} - 3.06×10^{-10}	59800.232 - 60394.903
OJ287	LSP	0.306[a]	16.011 - 14.028	1.44×10^{-11} - 3.38×10^{-10}	59478.259 - 60435.970
BL Lac	LSP	0.069[a]	14.549 - 11.192	6.10×10^{-11} - 4.37×10^{-9}	59113.834 - 60492.175
PKS1510-089	LSP (FSRQ)	0.361[b]	16.990 - 15.848	2.95×10^{-11} - 2.37×10^{-10}	59948.289 - 60488.964
4C 11.69	LSP (FSRQ)	1.037[a]	17.501 - 15.027	3.99×10^{-11} - 7.82×10^{-10}	59762.163 - 60492.120
3C 454.3	LSP (FSRQ)	0.859[a]	16.239 - 13.906	5.46×10^{-11} - 1.33×10^{-9}	59762.183 - 60492.127

This will be explored in more detail utilising the full RINGO3 photo-polarimetric data set in the next chapter.

3.2 MOPTOP

3.2.1 Source catalogue

Table 3.4 shows the catalogue of seven blazars observed as a part of the MOPTOP monitoring program. As Table 3.1, this table includes the source name, RA/DEC coordinates, redshift, spectral classification, the range of observation dates, and the number of observations within that timeframe. The full photo-polarimetric light curves including γ-ray flux and optical BVR EVPA, polarisation, and magnitude for each of these objects are shown in Appendix B.

These sources were chosen for continued observations with MOPTOP after preliminary analysis of the RINGO3 data showed high levels of variability. This sample is therefore a much more biased view of blazar variability, and given the small number of objects, inter-class and subclass trends are less likely to be statistically meaningful.

3.2.2 Optical–gamma-ray flux correlations

Fig 3.7 shows the γ-ray vs. R band flux correlations for the MOPTOP blazar sample. Like with the RINGO3 correlations, the data are grouped by their subclasses. Again, a clear distinction between the FSRQs and BL Lac type (all subclasses) is seen with the FSRQs generally dominating the higher γ-ray flux space at fainter optical magnitudes.

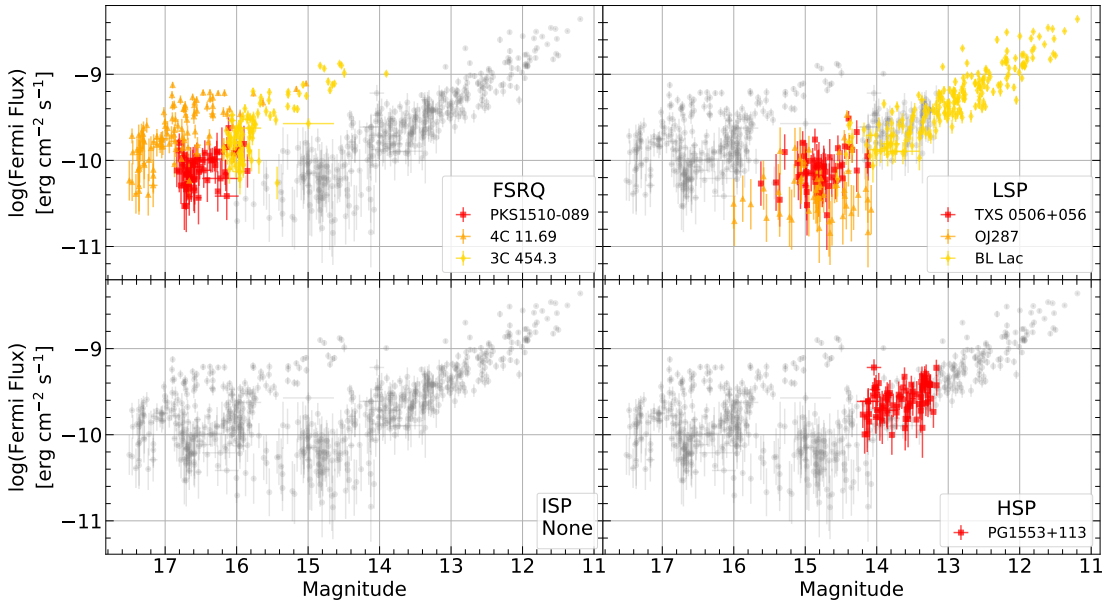

FIGURE 3.7: Fermi γ-ray flux vs. optical R magnitude for the MOPTOP sample. Each panel highlights the data for the different blazar subclasses separately with the upper left, upper right, lower left, and lower right highlighting data for FSRQs, BL Lac LSPs, ISP BL Lacs, and HSP BL Lacs respectively. In each panel, the data for the other subclasses is shown as faint grey circles.

The γ-ray and optical magnitude data were calibrated for distance as described in Section 3.1.2 using the redshifts shown in Table 3.4. The resulting data are shown in Figure 3.8. Again, to highlight uncertainty around redshift determination, redshift vectors are included to show the direction and distance data would shift if the redshift was overestimated by double and underestimated by half. The data followed a linear relationship of the form $y = Ax + B$ where $A = -0.494 \pm 0.016$ and $B = 34.17 \pm 0.26$ across all sources. Furthermore, the vector distance the data shifted was the same for redshift values $\frac{z}{2}$ and $2z$ at 1.972 ± 0.037 units in Figure 3.8. These values are consistent with those shown in Section 3.1.2.

The Spearman rank coefficients for each BVR filter magnitude vs. γ-ray flux are shown in Table C.8. The results show five out of seven sources demonstrate significant long-term correlations across all wavebands, with a further source (PKS 1510-089) showing a significant correlation in R band only. OJ287 is the only source with no significant correlations likely due to relatively inactive γ-ray behaviour over the course of MOPTOP observations.

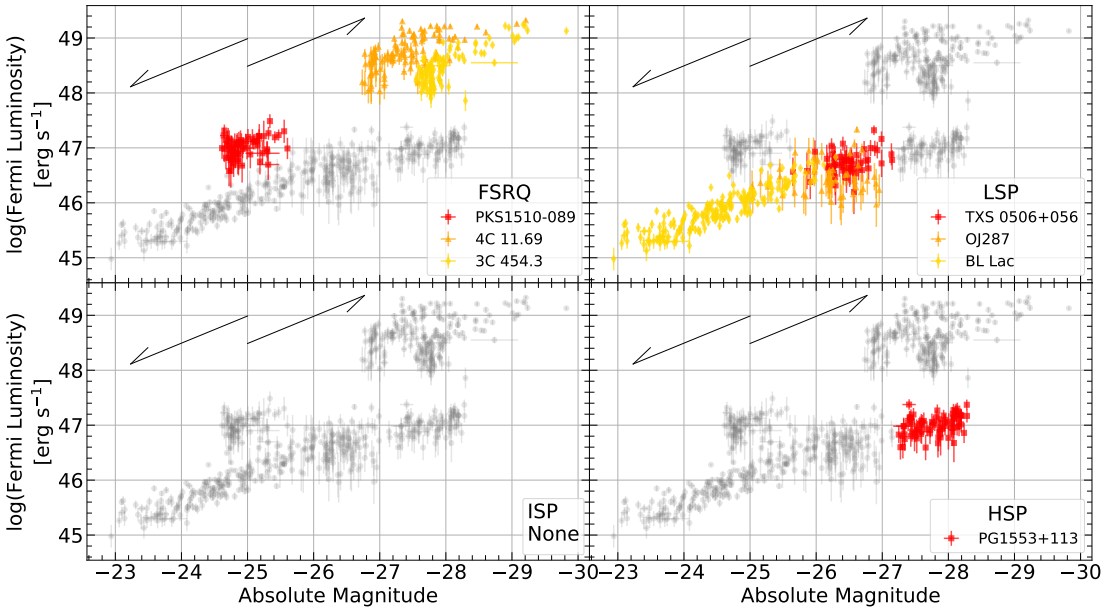

FIGURE 3.8: As Figure 3.7, but with Fermi γ-ray flux and R magnitude calibrated for distance (γ-ray luminosity and r^* absolute magnitude respectively). Additionally, redshift vectors are included to show the direction and distance the data for a given source would move if the redshift value given in Table 3.1 was incorrect. The decreasing line indicates the redshift has been overestimated by double and the increasing underestimated by half.

3.2.3 Optical spectral analysis

Given the results of Section 3.1.3, the spectral evolution was deemed a more effective probe into the colour behaviour of a given object than the colour index. This is because the same linear relationship can be obtained through computing the spectral index, but also the logarithmic trend. For that reason, the spectral evolution is the only metric presented in this section. Figure 3.9 shows the spectral evolution of each blazar in the MOPTOP sample. The Spearman rank correlation coefficients (calculated after linearising any logarithmic fit) are shown in Table C.9 in the appendix.

Five sources show the colour-SWB trend, consisting of three LBL BSWB trends and two FSRQ RSWB trends. There is only one source (PG 1553+113; HBL) that shows a significant linear trend, and one further source (PKS 1510-089; FSRQ) that shows no significant behaviour. The strength coefficients vary from $|0.541|$–$|0.794|$ which implies all significant correlations are moderate to strong in strength.

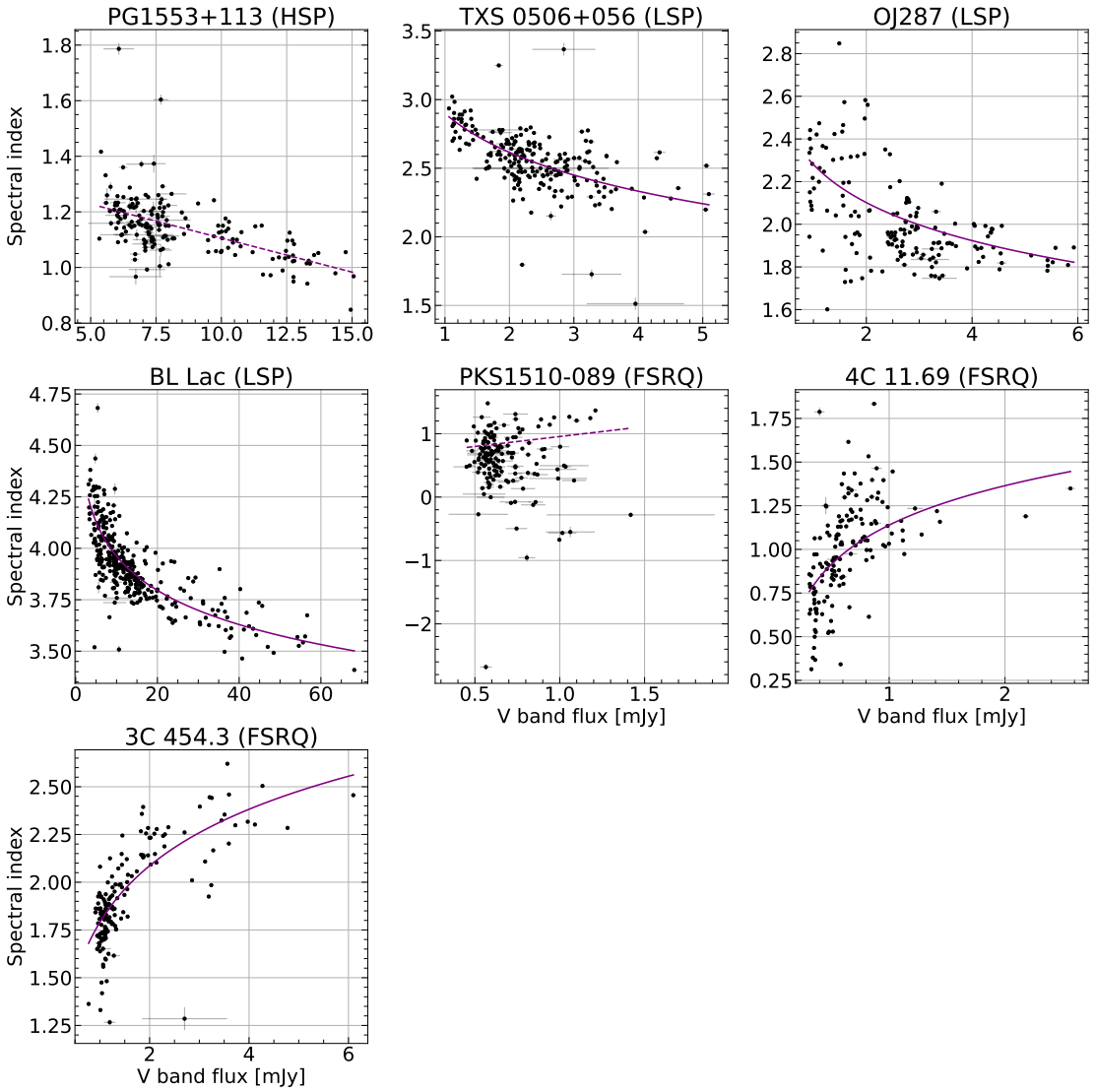

FIGURE 3.9: Spectral index vs. optical V band flux for each object in the sample. A best-fit line is fitted to each set of data after having linear and logarithmic fits qualitatively assessed using AIC and BIC coefficients. A preferential linear fit is shown by a dotted fit line, while a logarithmic fit is shown by a solid line. The Spearman rank correlation coefficients associated with each correlation (linearised in the case of a logarithmic fit) are given in Table C.9.

3.2.4 Optical spectral – gamma-ray analysis

Figure 3.10 shows the optical spectral index vs. γ-ray flux trends. The Spearman rank correlation coefficients are given Table C.10. Five sources (one HBL, one LBL, and all three FSRQs) show significant spectral index vs. γ-ray flux correlations. Just one source, BL Lac, shows the logarithmic trend (BSWB) with the other four showing linear relationships. PG 1553+113 (HBL) shows a BWB trend and all three FSRQs show RWB trends. TXS 0506+056 and OJ287 (both LBLs) show no significant relationship.

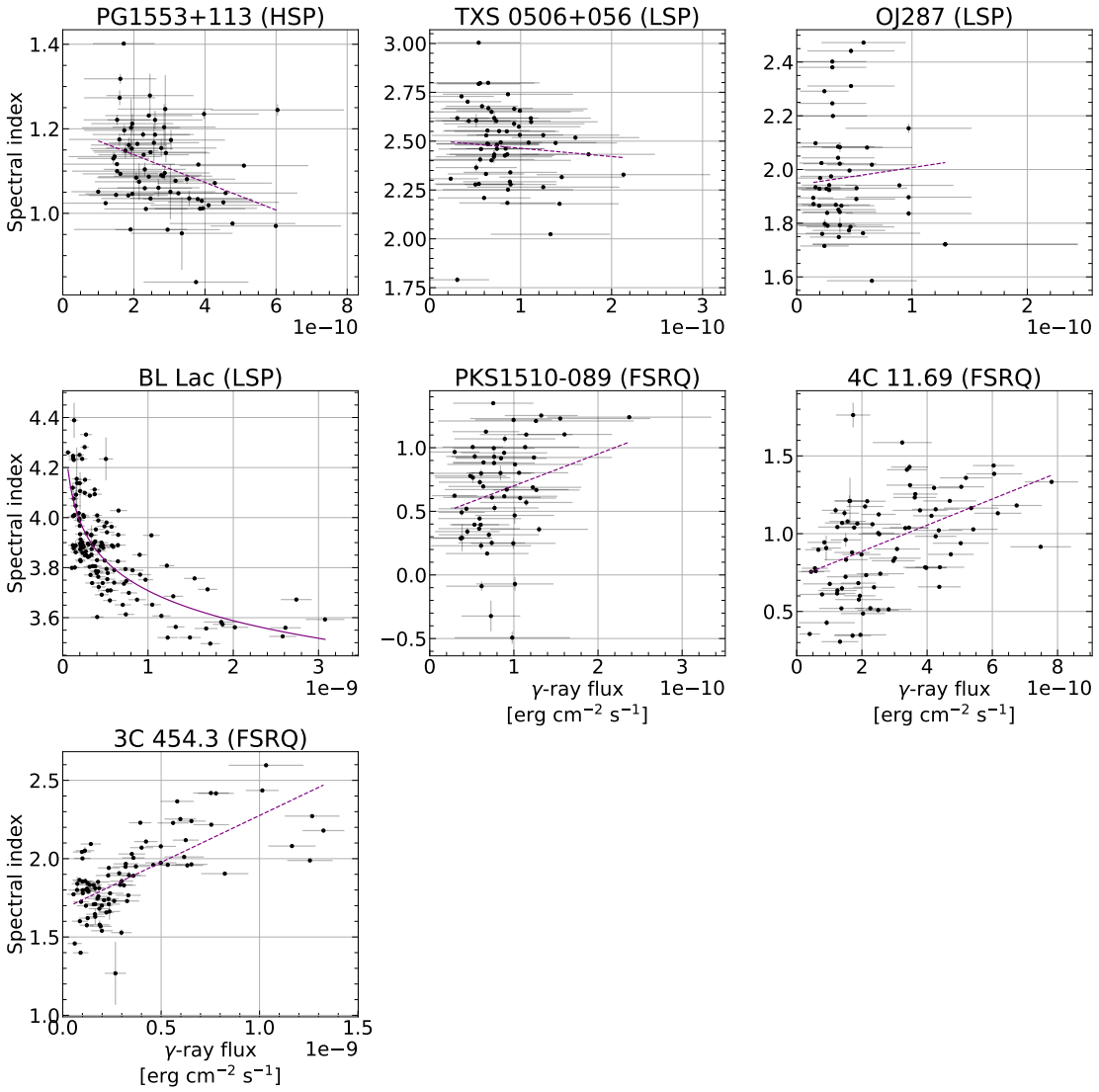

FIGURE 3.10: As Figure 3.9 but for spectral index vs. γ-ray flux. The Spearman rank coefficients associated with each correlation are given in Table C.10.

3.2.5 Optical–gamma-ray time lags

Interband time lags between the optical R band and γ-ray data were calculated as described in section 3.1.5 using the DCF (Edelson & Krolik, 1988) as described in McCall et al. (2024a). The detected lags and strength correlation coefficient are shown in Table C.11.

Potential lags are found in four sources, meeting the criteria of a lag larger than three times its error. For this data, unlike with RINGO3, there is no constraint on correlation strength for lag significance. This decision was made due to the increase in cadence and sensitivity of the MOPTOP data over RINGO3 data. This meant the alignment

TABLE 3.5: Results of the different correlations explored in this work. The source name and subclass are given, along with 'Yes' or 'No' to describe whether or not the given correlation was statistically significant. The asterisk in the 3σ lag column indicates the potential significance of the detected lag, warranting further analysis.

Source	Type	opt flux - γ flux	opt colour - opt flux	opt colour - γ flux	3σ Lag
PG 1553+113	HSP	Yes	BWB	BWB	Yes*
TXS 0506+056	LSP	Yes	BSWB	No	No
OJ 287	LSP	No	BSWB	No	No
BL Lac	LSP	Yes	BSWB	BSWB	Yes*
PKS 1510-089	LSP (FSRQ)	No	No	RWB	Yes*
4C 11.69	LSP (FSRQ)	Yes	RSWB	RWB	No
3C 454.3	LSP (FSRQ)	Yes	RSWB	RWB	Yes*

between optical and γ-ray points was more accurate. The median difference in MJD between optical and γ-ray points across the MOPTOP data sets was 0.65 days, almost half that of the RINGO3 data (Section 3.1). 81% of sources had matching optical and γ-ray data within 2.52 days (the average cadence between MOPTOP optical observations across all sources). This figure rises to 97% when using the RINGO3 observation cadence threshold of 12 days.

As with the RINGO3 data, the significance of a detected lag was assessed by applying the lag to the optical data, shifting it in time, and re-correlating the optical and γ-ray fluxes. If the correlation became or remained statistically significant, while simultaneously increasing in strength, the lag was more likely to be real rather than a stochastic feature. In doing this, two sources (BL Lac and 3C 454.3) were ruled out, leaving PG 1553+113 and PKS 1510-089. The optical R-band vs. γ-ray flux strength correlation for PG 1553+113 increased from 0.441 to 0.601 (moderate to strong) and for PKS 1510-089 the strength coefficient increased from 0.269 to 0.370 (increased but remained weak).

3.2.6 Discussion

Table 3.5 shows the results of all correlation tests performed on the MOPTOP data. As with Table 3.3, the table gives a "Yes" or "No" to indicate a significant correlation, or the observed colour trend for those significantly correlated.

3.2.6.1 Optical–gamma-ray analysis

Five out of seven sources showed significant correlations between the optical and γ-ray flux. All significant correlations were positive in strength and varied from approximately

0.28–0.91 (weak to very strong) across all filters. Generally, these correlations observed with MOPTOP were consistent with the RINGO3 results when looking at correlation strength and direction. It is noted however that BL Lac shows a much stronger relationship within the MOPTOP data and TXS 0506+056. For the latter, this is likely due to the large difference in number of observations. BL Lac could show a stronger correlation for a number of reasons including the source being in a more generally active state during the MOPTOP monitoring campaign, the increase in detector sensitivity, and the increase in observing cadence of the MOPTOP observations.

The two objects that did not show significant long-term behaviour were OJ287 (LBL) and PKS 1510-089 (FSRQ). Both of these sources demonstrated significant positive relationships in the RINGO3 sample. While the results for OJ287 previously were weak, PKS 1510-089 previously showed a moderate to strong relationship between optical and γ-ray flux. Possible reasons for the discrepancies could include the timeframe and number of observations being smaller during the MOPTOP observation campaign. In the case of OJ287, the correlation seen in the RINGO3 data may be caused by flaring behaviour resulting from the predicted disk impact event, a type of periodic event that was not expected to be observed with MOPTOP. This will be explored further in Chapter 4 when utilising the full photo-polarimetric datasets.

Given most sources showed significant, positive correlations, the results suggest the variability may be leptonic in origin. As previously discussed in Section 1.5.1 and 3.1.6.1, the signature of leptonic emission in blazar jets is correlated optical and γ-ray emission with little to no temporal separation. This is due to the SSC upscattering process, whereby optical synchrotron photons interact with relativistic particles in the jet, upscattering to γ-ray energies (Maraschi et al., 1992).

3.2.6.2 Spectral analysis (optical and gamma-ray)

Significant colour behaviour was observed in six out of seven sources in the MOPTOP sample. Of the six significant sources, one showed a linear trend (PG 1553+113; HBL) while the remaining five showed logarithmic trends. All three LBLs showed BSWB trends, and two FSRQs showed RSWB trends. PKS 1510-089 (FSRQ) was the only object to not show significant long-term colour behaviour.

The results of the optical spectral index vs. flux correlations mostly align with what was observed with RINGO3 with a few exceptions. For PG 1553+113, the linear but significant optical spectral index vs. flux correlation observed with MOPTOP is consistent with what was observed with RINGO3. The reason for the apparent linear trend observed may stem from both intrinsic and systematic properties. PG 1553+113 is a HBL and is the only HSP object in the MOPTOP sample. As previously discussed in Sections 1.2 and 3.1, HBLs are the blazar types most often associated with resolvable host galaxies and therefore, significant host galaxy emission. This emission has been shown to dilute blazar jet emission, especially masking optical variability during jet quiescence (Valtonen et al., 2022). It is possible that low-state jet emission has not been observed over both observation campaigns, resulting in the spectrally steeper BWB regime being difficult to detect.

Observations of TXS 0506+056 were much more numerous with MOPTOP than with RINGO3. The source was deemed an interesting candidate for inclusion in the MOPTOP sample due to its association with a neutrino flare in 2017 (IceCube Collaboration et al., 2018). Longer baselines may allow the source to demonstrate a wider range of activity states, so it is perhaps unsurprising that a linear trend was detected with RINGO3 and a logarithmic with MOPTOP. Conversely, observations of PKS 1510-089 were less numerous with MOPTOP compared to RINGO3 so one may expect the opposite to hold true (i.e. logarithmic behaviour from RINGO3 and linear with MOPTOP).

When considering the optical colour vs. γ-ray flux correlations, the MOPTOP results show 5 sources with significant correlations. Just one object (BL Lac; LBL) shows the logarithmic trend (BSWB), while four objects show linear trends. These are made up of one HBL (BWB) and all three FSRQs (all RWB). TXS 0506+056 and OJ287 show no significant optical colour vs. γ-ray flux trends.

BL Lac is the most densely observed object in the sample in addition to having the longest baseline of observations. The previous work in Chapter 3.1 details that many observations over many activity states are required in order to observe the SWB logarithmic feature. It is therefore unsurprising that the only observed logarithmic trend is seen in this source. This result also aligns with what was observed with RINGO3.

For all three FSRQs, RWB trends were observed with MOPTOP whereas RSWB trends were observed with RINGO3. In the case where the stable feature (logarithmic trend)

holds true, the most likely explanation for the differences is a lack of observations at the highest or lowest jet states at optical and γ-ray frequencies.

PG 1553+113 and OJ287 show different trends when comparing the results of RINGO3 and MOPTOP. PG 1553+113 shows no significant relationship in the RINGO3 correlations while it does in the MOPTOP correlations (BWB). The opposite is true for OJ287, where a RWB trend was observed with RINGO3 and no correlation was observed with MOPTOP. In the case of OJ287, it is possible that the RINGO3 correlations were affected by the predicted disk impact event mentioned in Sections 1.5.1 and 3.1.6.4. This will be explored further in Chapter 4 utilising the full RINGO3 and MOPTOP photopolarisation data sets.

Figure 3.11 shows a comparison of the range of optical and γ-ray fluxes observed with RINGO3 and MOPTOP. In the case of all FSRQs, RINGO3 observed a wider or similar range of both optical and γ-ray fluxes. Assuming logarithmic behaviour can be more easily seen when a given source is observed over a wider range of states, one could expect to find logarithmic trends in the RINGO3 FSRQ data over the MOPTOP data. This is what is seen in this data. In the case of OJ287, there is very little difference in the range of γ-ray flux observed with RINGO3 and MOPTOP, but the range of optical flux observed with RINGO3 is larger than with MOPTOP. Interestingly, the γ-ray flux is where a significant RWB trend was observed in the RINGO3 data, compared to MOPTOP where one sees no significant trend. In order to comment on the validity of this result, one must consider the contribution of the predicted disk impact event. As said previously, this can be more easily achieved with the full photo-polarimetric data sets and so will be explored further in Chapter 4. For two sources, PG 1553+113 and TXS 0506+056, one sees very similar optical and γ-ray flux ranges observed over both RINGO3 and MOPTOP. For PG 1553+113, the γ-ray flux trend agrees between instruments, with a very similar range of fluxes observed. Additionally, uncertainties on magnitude associated with this source were on average 5–10 times smaller with MOPTOP while the median magnitude observed with MOPTOP was 0.36 magnitudes fainter. It is possible that the increased sensitivity of MOPTOP allowed for the detection of PG 1553+113 in a fainter state which made it possible to observe a spectral trend. It is also important to remember that TXS 0506+056 was observed far less with RINGO3, so its RINGO3 ranges are very limited (i.e. no long-term trends observed) and can be disregarded.

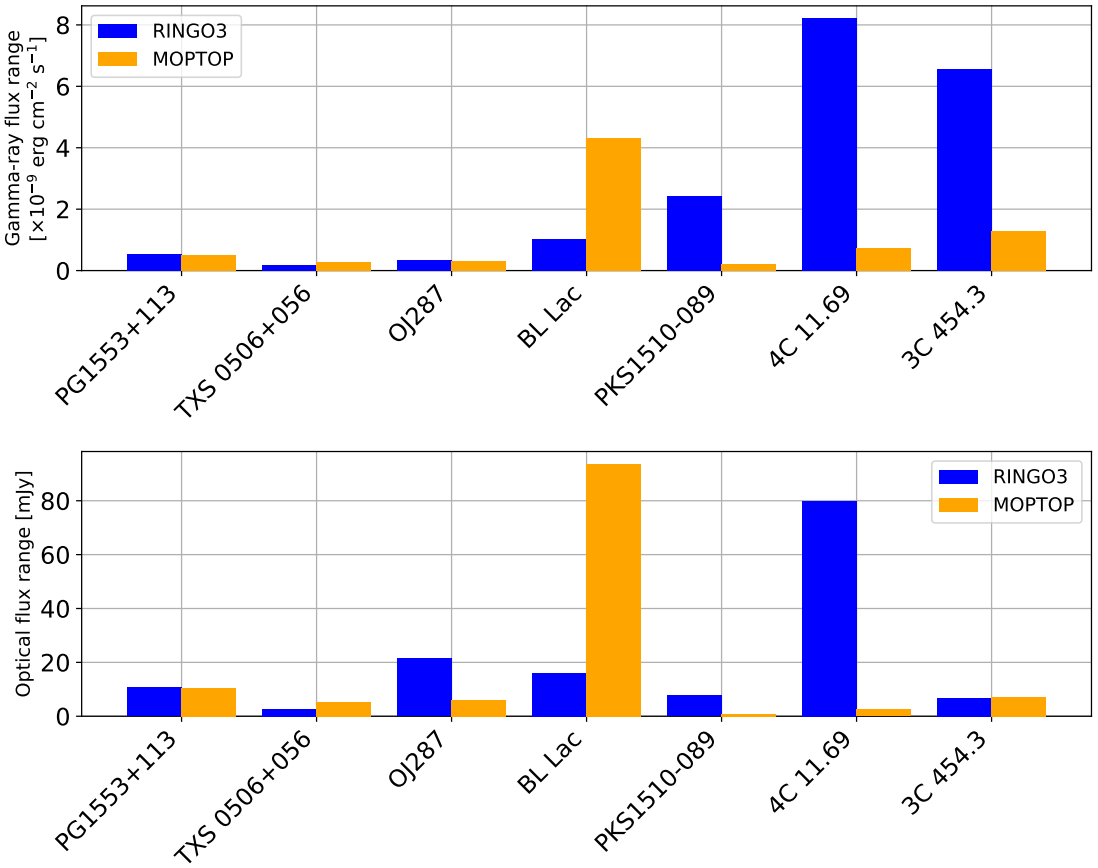

FIGURE 3.11: Comparison of the RINGO3 and MOPTOP optical and γ-ray flux ranges for the sources in the MOPTOP sample. The left of each pair of bars corresponds to the range observed with RINGO3 for that source, while the right is the range with MOPTOP.

3.2.6.3 Time lag analysis

The lag values and strength correlation coefficients on interband, optical–γ-ray time lags for all sources in the MOPTOP sample are shown in Table C.11. While four sources show potential lags, meeting the criterion of a lag value at least three times the size of the uncertainty, two are disregarded on account of their weaker correlation strength after adjusting for the lag. The two remaining sources were PG 1553+113 and PKS 1510-089, with optical–γ-ray lags of -20.64 ± 1.96 days and -40.62 ± 2.47 days, respectively. A negative lag implies the γ-ray emission is leading the optical. Given the long baseline of observations, this result could be interpreted as several delayed flaring episodes across the campaign.

Interestingly, both of these objects also had detected lags in the RINGO3 dataset but were ultimately disregarded (either due to a large uncertainty in the lag value or the

application of the lag not increasing the strength of the correlation). The lags in the RINGO3 dataset were -20.91 ± 8.54 days and -55.41 ± 9.44 days for PG 1553+113 and PKS 1510-089, respectively. These are both consistent with those lags detected by MOPTOP. Assuming $d \simeq c\tau$, then the distance travelled by the initial γ-ray photons in both lags is of the order 10^{14-15} m which is approximately equal to the distance from the central engine to the BLR (see Table 1.1).

Interband optical–γ-ray flux lags have been previously detected for PG 1553+113. Cohen et al. (2014) find a optical–γ-ray lag of -37.0 ± 5.8 days (optical leading in their nomenclature). Similarly, Ackermann et al. (2015) find an optical leading lag of 75 ± 27 days (a positive lag denotes an optical leading lag in their nomenclature) reducing to 28 ± 27 days when binning their optical data. Like the RINGO3 data, these are also consistent with those observed with MOPTOP.

For PKS 1510-089, a lag consistent with around 40 days has not been observed in the literature. Both Castignani et al. (2017) and Yuan et al. (2023) detect no significant lag between the optical and γ-ray emission. It is noted that the difference between the literature and this work is the observing cadence, with optical observations taken at a much higher frequency (roughly every 2.5 days with MOPTOP compared to 9 days in Castignani et al. (2017)). Abdo et al. (2010c) detect a γ-ray leading lag of 13 ± 1 days using optical R-band *GASP* data with a more similar cadence (roughly every 1.5 days). This trend is opposite to that detected with MOPTOP in this work.

3.3 Conclusions

In this chapter, the photometric properties of a sample of γ-ray bright blazars have been explored through the use of data collected with the RINGO3 and MOPTOP polarimeters on the Liverpool Telescope. Fermi data was also obtained to assess the multi-wavelength properties of the sample over the same time period from 2013-2024.

It was shown that, in general, the optical and γ-ray fluxes were correlated over long timescales. Those sources with low synchrotron peaks were more likely to show significant correlations, with this probability decreasing as synchrotron peak frequency increased (inferred from source classification). It was shown that in the optical–γ-ray flux–flux plane, two distinct populations exist corresponding to BL Lac and FSRQ source

classes. Where sources sit between these two groups, the literature suggests these may belong to a transitional class of blazars which blurs the lines between BL Lacs and FSRQs on account of their overlapping properties.

One of the principle findings of the work presented in this chapter is the non-linear optical spectral properties of blazars of all subclasses. This work showed that the spectral behaviour was better fit logarithmically rather than linearly, which was only the second time such a result was reported in the literature, and the first over a large blazar sample. Where a logarithmic trend was not found, this was proposed to be a lack of observations across enough activity states. The implication of this result was that during high optical activity states, these blazars tended to show colourless behaviour. The RSWB behaviour was unique to the FSRQ class and is therefore supportive of a distinction between the two classes. This distinction likely arises from additional thermal emission compared to BL Lac objects, caused by more efficient or a larger rate of accretion. This has the effect of flattening the composite spectrum of FSRQs in the optical regime, which then steepens during flaring episodes. This is in contrast to BL Lac objects whose composite spectrum flattens during heightened flux. When comparing the optical spectral behaviour to the γ-ray flux, one could also expect to see logarithmic behaviour over sufficient observations of activity states.

Long-term interband time lags were not a frequently observed phenomenon in this sample. While this was expected on account of the likely different processes occurring within the blazar jets over such a long period, there are instances of long-term, γ-ray leading lags.

The results presented in this chapter are indicative of leptonic emission within these blazar jets. This is due to the strong correlation between the optical and γ-ray fluxes across the majority of objects, with little evidence of lagged behaviour. While the results do not rule out hadronic emission, leptonic is likely dominant. Hadronic emission may become a significant contributor to the composite emission spectrum for some LSP objects on account of the increased scatter in the optical–γ-ray flux–flux space for LSP objects. Generally, this implies a connection between low- and high-energy emission, resulting from a single population of photons as opposed to multiple populations and unconnected emission processes.

Chapter 4

Polarimetric Analysis

The polarisation metrics explored in this work consist of changes in the degree of polarisation (the amount of detected light that is linearly polarised) and the evolution of the EVPA (angle of the polarised beam). These will be compared to the photometric quantities explored in Chapter 3 (optical magnitude and γ-ray flux) in order to characterise the non-thermal photo-polarimetric emission from the blazar jet in addition to any prevalent external emission from the disk and BLR.

As discussed in Section 1.3, optical emission from the jet must originate from the highly collimated acceleration region close to the SMBH. The polarisation properties of this light allow one to trace the magnetic field structure of this unresolved region. Correlated flares between the optical flux and linear polarisation imply the ordering of the field lines, indicative of a temporary magnetic field structure in a post-shocked medium (Zhang et al., 2016). Conversely, a lack of correlated behaviour could reveal the nature of the mechanism to be thermal rather than synchrotron, like emission originating from events in the accretion disk (Valtonen et al., 2019).

To distinguish between models, frequency-dependent polarisation (or polarimetric colour/chromatism) can provide useful insight. In shock acceleration, one could expect to observe a larger polarimetric variability at higher energy optical frequencies than at lower (Angelakis et al., 2016; Liodakis et al., 2022b). Put simply, polarisation in bluer wavebands increases more than in redder wavebands during an optical polarisation flare. Shock acceleration requires the injection of energy into the post-shocked medium,

such as second-order Fermi acceleration and magnetic reconnection (Begelman, 1998; Kalita et al., 2023).

Additionally, rotations in the electric vector plane, EVPA, can give indications into the larger structure of the local magnetic field. Magnetised emitting regions travelling around a helical field structure would produce large rotations in the EVPA (Marscher & Jorstad, 2021). If also associated with a kink in the jet, these rotations would be followed by a plateau phase in the EVPA light curve where the larger field structure restores itself after the emitting region passes (Zhang et al., 2016).

The sources analysed in this chapter are the same as those explored in Chapter 3. See Section 3.1 and 3.2.1 for details on object selection and source information for RINGO3 and MOPTOP sources.

4.1 RINGO3

4.1.1 Magnitude–polarisation

Figure 4.1 shows the long-term optical polarisation vs. normalised magnitude correlations for each waveband in the RINGO3 data. The data were normalised using z-score normalisation,

$$x_{\text{norm}} = \frac{x - \overline{x}}{\sigma},$$

where x is the observation, $\overline{x}$ is the mean observation, and σ is the standard deviation of the data. Normalising the data clarifies the plots by making the data in different bands overlap. This better highlights any trends while leaving the statistical correlation values unaffected. The Spearman rank correlation coefficients for each band are shown in Table C.12.

The b^* band was chosen as a representative of optical data as the average SNR was highest in this band across all sources, corresponding to generally lower uncertainties in magnitude and polarisation. Therefore, considering the b^* band only, 19 sources show significant long-term magnitude–polarisation correlations. Eight of these are BL Lac objects (six HSP and three LSP) while the remaining ten are FSRQs. The associated absolute strength coefficients range from $|0.146|$ to $|0.608|$ with significant correlations

in both the positive and negative direction. 13 of the significant correlations are positive implying an increase in optical polarisation with magnitude while six show an opposite, negative correlation.

If one requires all three filters to show significant trends in order to label the source as showing significant behaviour, the number of significantly correlated sources decreases to ten objects (one HBL, two LBLs, and seven FSRQs) with absolute strength coefficients ranging from |0.236| to |0.608|.

4.1.2 Gamma-ray–polarisation

Figure 4.2 shows the long-term optical polarisation vs. γ-ray flux correlations with the RINGO3 data. The Spearman rank correlation coefficients for each band are shown in Table C.13.

Looking at the $b*$ band only, 10 sources show significant long-term γ-ray–polarisation correlations. Three of these are BL Lac objects (one HSP, one ISP, and one LSP) while the remaining seven are FSRQs. As in Section 4.1.1, the $b*$ band was chosen as a representative of all correlations as the average SNR meant generally lower uncertainties in polarisation. The associated absolute strength coefficients range from |0.117| to |0.568| with significant correlations in both the positive and negative direction. Seven of the significant correlations are positive implying an increase in optical polarisation with γ-ray flux while three show an opposite, negative correlation.

4.1.3 Polarisation colour

Polarisation colour, or polarimetric chromatism, refers to the polarisation variability as a function of wavelength, implying different behaviour at different wavelengths. Such behaviour is generally attributed to synchrotron emission (from electrons or protons) in the jet, given its dominance over the blazar spectrum (Shablovinskaya et al., 2023). In terms of non-jet emission, polarimetric chromatism is seldom associated with thermal bremsstrahlung emission on account of its lack of polarisation, but can arise from electron scattering, which itself is frequency dependent, within the accretion disk (Agol, 1997). This, however, is not a major source of emission in blazar spectra and contributes minimally to the observed polarimetric properties.

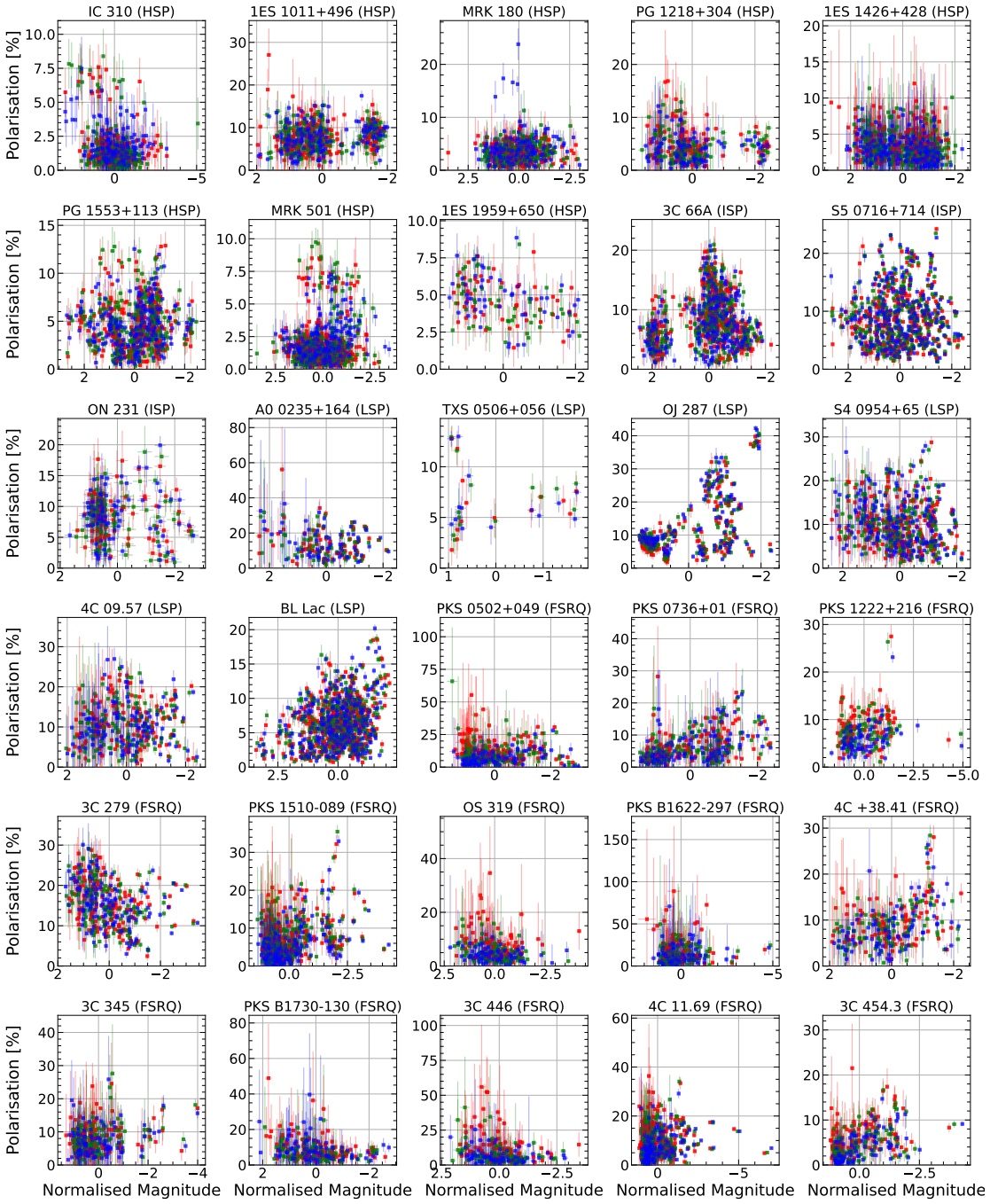

FIGURE 4.1: Optical magnitude vs. polarisation trends observed with RINGO3 for each source in the sample. the trends associated with each waveband are shown as a different colour. The data are normalised to better aid the clarity of any trends.

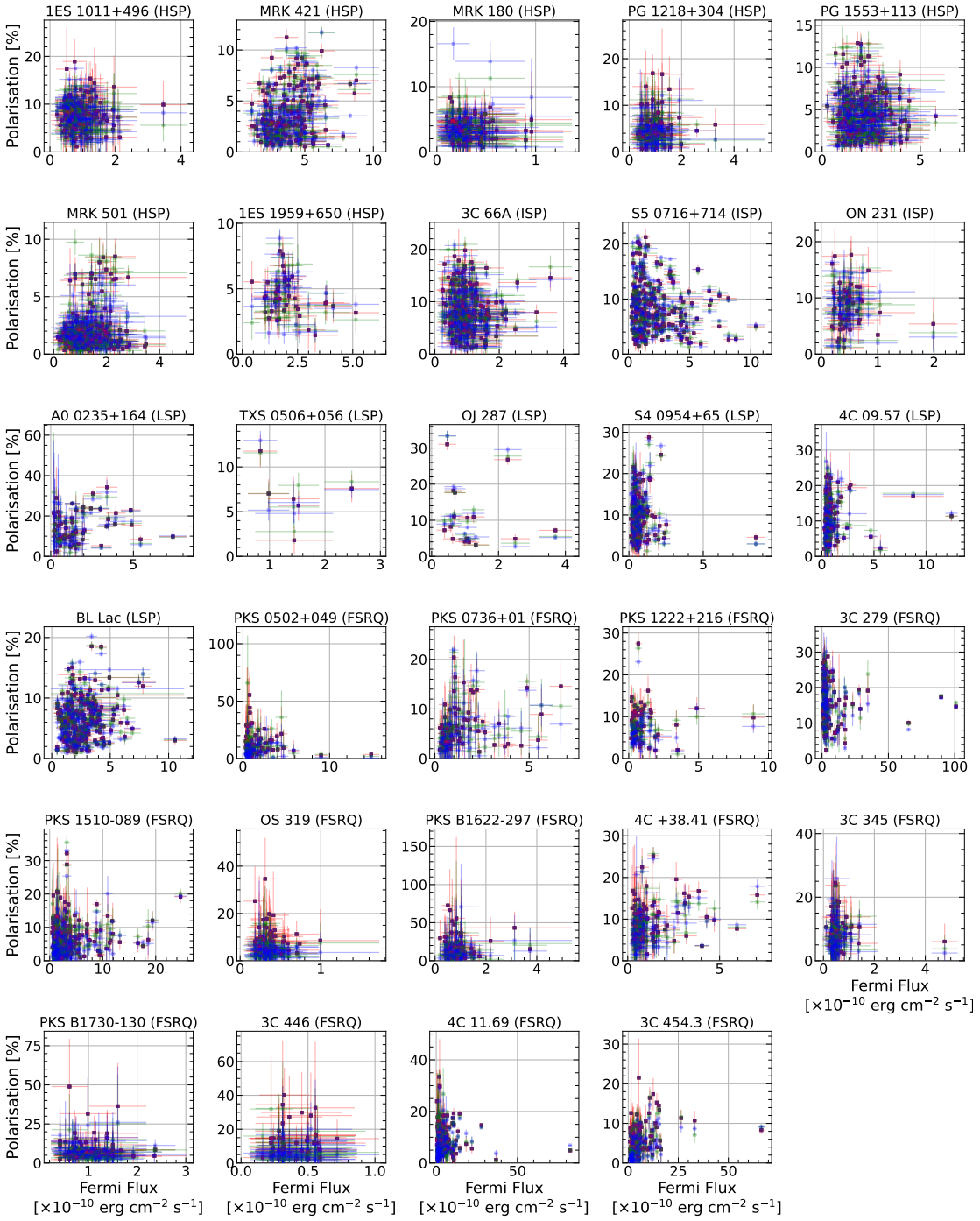

FIGURE 4.2: Fermi γ-ray flux vs. polarisation observed with RINGO3 for each source in the sample.

Figure 4.3 shows the polarisation colour plots for the RINGO3 data. Only the b^* pol – r^* pol vs. g^* pol is shown. This permutation offers the largest waveband difference on the colour axis and so one would expect, in general, the correlation significance to be the most prominent. This is supported by the results presented in Figure C.3. The Spearman rank correlation coefficients are shown in Table C.14. These results show 8 sources with significant long-term polarisation colour correlations. The strength correlations range from |0.126| to |0.256|, implying all correlations are very weak.

4.1.4 EVPA

As discussed in Section 1.4, an EVPA rotation is generally defined as a change over time in the angle of the electric vector. Given a rotation event may be made up of several observed epochs, a "swing" can be defined as the difference between EVPA measurements, with multiple swings constituting a rotation. Blinov et al. (2015) define a significant EVPA swing by consecutive EVPA measurements,

$$\Delta\theta = |\theta_{i+1} - \theta_i|,$$

which satisfy the condition

$$\Delta\theta > \sqrt{\sigma_{i+1}^2 + \sigma_i^2}$$

where σ_{i+1} and σ_i are the associated errors of the EVPA measurements. They define a rotation as 3 or more of these consecutive swings (totalling at least four measurements) in the same direction and in excess of 90° from beginning to end. A rotation larger than 90° is less likely to be the result of noise in the data and less ambiguous. The start and end points of the rotation are defined by a change in the EVPA curve gradient ($\Delta\theta_i/\Delta t_i$) by a factor of 5, or by the negation of the swing direction. They state while this definition of a rotation is rather conservative, it is generally consistent with reported rotations.

This work mostly adopts the definition of an EVPA rotation from (Blinov et al., 2015), ignoring the gradient change condition in favour of directional changes in the EVPA. This is due to the differing cadences between the samples. Comparatively, the RINGO3 data set had a much lower cadence at times so the gradient change condition was deemed too restrictive for this dataset. The EVPA rotation light curves in the RINGO3 dataset

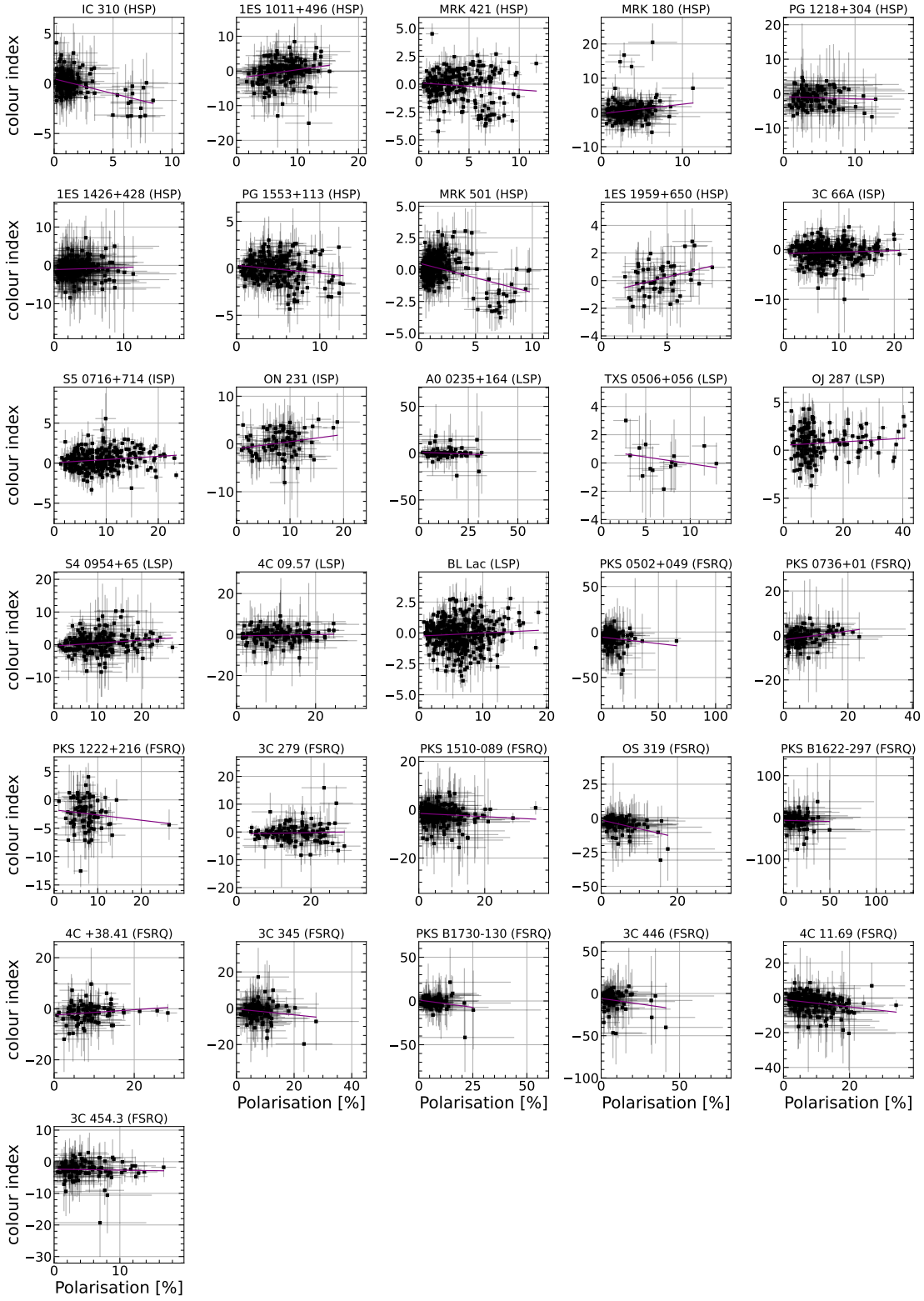

FIGURE 4.3: RINGO3 polarisation colour correlations. Only the b^*-r^* vs. g^* data is shown as this permutation offered the largest waveband difference and so better emphasises any frequency-dependent behaviour.

are shown in Figures C.13 – C.41 in the appendix. These plots show the γ-ray flux, polarisation and magnitude variability during the timeframe of each detected EVPA rotation. Also shown are the average γ-ray flux, polarisation, and magnitude over the full observation campaign to assess the states of the source during the rotation. Table 4.1 describes each rotation as well as a comparison of the state of the object during the rotation to its average behaviour observed across all RINGO3 observations. The exact values comparing the different activity states are shown in Table C.15 in the appendix.

The results show 29 EVPA rotations occurring over periods of approximately 3–92 days and rotation angles of 90°–180°. The rotations are detected for both FSRQs and BL Lacs covering each of the HSP, ISP, and LSP subclasses. 12/31 sources showed rotations, with several objects displaying multiple rotations across their light curves.

TABLE 4.1: EVPA rotations found in the RINGO3 dataset. Shown are the starts of the rotations as MJD and EVPA, and the duration and size of the rotation. Also shown are the γ-ray flux and optical polarisation and magnitude states during the rotation event compared to the full monitoring campaign (higher or lower).

Source	Type	MJD Start	ΔMJD [days]	EVPA Start [°]	ΔEVPA [°]	γ-ray State	Pol State	Opt State
MRK 421	HSP	56712.14	3.89	131.47	-91.83	Higher	Higher	-
...	...	56998.15	10.02	159.54	-101.72	Higher	Higher	-
MRK 180	HSP	57120.94	31.93	118.63	-183.27	Lower	Higher	Lower
MRK 501	HSP	56867.89	5.02	121.64	-154.16	Higher	Lower	Higher
S5 0716+714	ISP	56979.09	27.93	82.49	113.72	Higher	Lower	Lower
...	...	57078.94	7.01	25.66	90.25	Higher	Higher	Higher
...	...	57275.20	3.96	21.36	-92.57	Lower	Higher	Lower
...	...	57324.11	7.15	40.89	-90.57	Higher	Higher	Higher
...	...	57391.89	7.11	67.95	133.12	Higher	Lower	Higher
...	...	57653.21	3.97	10.28	-93.87	Lower	Higher	Lower
...	...	57702.27	34.88	-90.86	125.74	Lower	Higher	Lower
...	...	58030.24	12.97	-20.50	138.82	Higher	Higher	Lower
...	...	58334.22	13.02	200.71	144.91	Higher	Lower	Higher
OJ 287	LSP	57428.07	23.88	150.84	-103.51	Higher	Lower	Lower
...	...	57511.86	13.01	126.76	-128.76	Lower	Lower	Higher
S4 0954+65	LSP	57051.12	91.86	93.50	-113.55	Higher	Higher	Lower
...	...	57336.12	7.16	347.19	-175.67	Higher	Higher	Higher
...	...	58213.90	24.56	144.10	107.26	Higher	Higher	Higher
...	...	58425.23	4.97	131.40	-100.41	Lower	Lower	Higher
BL Lac	LSP	57150.21	30.92	192.94	-157.56	Higher	Lower	Lower
...	...	57205.19	2.92	-0.92	92.36	Higher	Lower	Lower
...	...	57620.08	16.92	177.69	-119.79	Lower	Lower	Lower
...	...	58342.52	5.99	195.81	-112.02	Higher	Lower	Higher
...	...	58373.12	10.34	180.38	-100.60	Lower	Lower	Higher
3C 279	LSP (FSRQ)	58123.21	15.02	104.87	125.94	Higher	Lower	Higher
PKS B1622-297	LSP (FSRQ)	57207.90	15.99	56.18	-126.38	Higher	Lower	Higher
4C +38.41	LSP (FSRQ)	57604.87	40.01	-88.68	177.82	Lower	Higher	Lower
4C 11.69	LSP (FSRQ)	57698.93	52.91	-68.67	103.53	Higher	Lower	Higher
3C 454.3	LSP (FSRQ)	57527.17	38.92	128.63	-140.08	Higher	Higher	Higher

4.1.5 Discussion

4.1.5.1 Flux–polarisation analysis

Table 4.3 shows a summary of the optical $b*$ and γ-ray fluxes vs. $b*$ polarisation correlations explored in this work. A statistically significant correlation and its behaviour is shown by polarised-when-brighter ("PWB") and polarised-when-fainter ("PWF") labels, and its absence by "No". Also shown is the optical flux vs. γ-ray flux correlations shown in Table 3.3. Nine sources show significant correlations between γ-ray flux and polarisation: one IBL, one LBL, and seven FSRQs. Eight of these are associated with significant optical flux and polarisation correlations (seven with the same behaviour and one with the opposite) with just one source (S5 0716+714) displaying no corresponding optical trend. In total, 18 sources (five HBL, three LBL, and ten FSRQs) show significant optical flux and polarisation correlations.

In nine sources (32%) there is no evidence for correlated flux (optical and γ-ray) and polarisation. Of these nine, there are one HBL, two IBLs, three LBLs, and three FSRQs. In three sources, there are also no correlations between the optical and γ-ray fluxes, possibly a result of relative inactivity during the monitoring campaign with respect to the general behaviour of the source, or the quality of the optical data (i.e. high photometric and/or polarimetric uncertainties). In six sources, however, the optical and γ-ray fluxes are correlated, implying a lack of significant polarised emission during correlated photometric activity. This could be intrinsic to the source, but also a reflection of the associated polarisation uncertainties.

In six sources (21%) there are PWB correlations for both the optical and γ-ray fluxes. Furthermore, all six also show positive correlations between the optical and γ-ray fluxes. These results imply a connection between the flaring episodes and the ordering of the magnetic field structure within the jet. This is indicative of shocks propagating through the jet, ordering the local magnetic field and producing MWL photo-polarimetric flares (Zhang et al., 2016; Liodakis et al., 2022b). One source (3C 279; FSRQ) shows the opposite behaviour: that is, PWF correlations for both the optical and γ-ray fluxes and positively correlated optical and γ-ray fluxes. An anti-correlation between the fluxes and polarisation while retaining photometric correlations may be indicative of kink instabilities in the jet (Dong et al., 2020), but also of a shock of relatively low Lorentz factor travelling down a spiral jet (Gaur et al., 2014).

In an additional six sources, the results show correlated optical flux – polarisation emission in a PWB trend but not γ-ray flux – polarisation. Two of these objects also show no significant correlation between the fluxes, implying no connection between the optical and γ-ray emission. In the remaining four sources, the optical and γ-ray flux is correlated. This is peculiar, given statistically one would expect a third metric to show a correlation if the other two showed correlations. The optical flux vs. polarisation correlations are, at most, weak for these sources so it must be considered that these results may be a statistical fluctuation.

Four sources show PWF trends between the optical flux and polarisation, but no significant correlation between the γ-ray emission and polarisation. Just two of these four objects demonstrate significantly correlated optical and γ-ray flux. The remaining two objects show no significant correlation between the optical and γ-ray emission. One

object (S5 0716+714; IBL) shows correlated optical and γ-ray flux but the polarisation is only correlated with the γ-ray emission following the PWF trend. It is important to note that the data quality for some of these sources is limited and may affect the correlations obtained.

OJ287 is the only object in the sample to display two significant correlations with opposite trends. The results show the source becomes more polarised when optically brighter but less polarised during heightened γ-ray activity. It is important to note that the statistics associated with this object may be skewed by abnormal behaviour arising during the predicted disk impact event in the binary SMBH model (Lehto & Valtonen, 1996). One can therefore separate the flaring epochs and recompute the statistics to show the trends observed during the different activity phases. Table 4.2 summarises these statistics for the optical–γ-ray flux, optical flux–spectral evolution, γ-ray flux–spectral evolution, optical flux–polarisation, and γ-ray flux–polarisation correlations. It can be seen that during the first flare, the optical and γ-ray emission is very strongly correlated, with no correlation between optical flux and polarisation. The likely implication of this is the addition of an unpolarised thermal bremsstrahlung emission component arising directly from the impact of the secondary black hole with the primary accretion disk (Dey et al., 2019). In the second flare, a correlation is seen between the optical flux and polarisation, implying the synchrotron nature of the emission. Supporting this is a significant spectral evolution trend. Given the timescales associated with the flares, it is unlikely that this emission originates from perturbed matter travelling through the jet. Valtonen et al. (2019) show the impact radius is approximately 17,500 Au or 10^{15} m. Assuming this is the distance to the jet acceleration region responsible for synchrotron photon upscattering, then it would take 38.5 days for any photons to reach it ($\tau \simeq \frac{r_{\rm impact}}{c}$). In Figure C.59, there are roughly 19 days between the optical and γ-ray peaks. It is important to note that the sampling of the 2015 flares was irregular in optical and sparse in γ-rays. These initial results provide valuable insight into the mechanisms behind the emissions, but more data sampled more regularly is needed during future flares for more certain conclusions.

Jormanainen et al. (2025) compiled recently published MWL photo-polarimetric data, including those presented in this work, and revisited the 2015 disk impact event. They described a new model, starting with the thermal impact flare in December 2015, where the impact event directly produces turbulence at the jet base resulting in the formation

TABLE 4.2: Correlation statistics for OJ 287 during the 2015 impact flares and the full data set with impact flares removed to show the general behaviour of the source.

	Optical–γ-ray flux		Colour–magnitude		Colour–γ-ray flux		Flux–polarisation		γ-ray flux–polarisation	
Epoch	p	c	p	c	p	c	p	c	p	c
Flare 1	4.54×10^{-4}	0.964	0.083	-0.397	0.535	-0.286	0.077	-0.405	0.285	-0.600
Flare 2	0.667	-0.500	0.031	-0.496	0.667	-0.500	1.90×10^{-4}	0.754	0.667	-0.500
General	0.019	0.174	1.13×10^{-39}	-0.545	0.053	0.144	1.28×10^{-10}	0.286	0.551	-0.045

of a moving component (knot) originating from the core region. The initial optical EVPA rotation, observed in this and other work, subsequent chaotic rotations, and synchrotron flare could be the formation of this component and its travelling through a helical magnetic field (Myserlis et al., 2018). The knot model is also more likely given the timescale is too fast for the synchrotron emission to be from matter travelling through the jet (see the previous paragraph for the discussion on timescales). The knot travels through a quasi-stationary feature first identified in (Lico et al., 2022) originating 10.0 pc from the de-projected radio core, producing turbulence in its wake and triggering a VHE γ-ray event in 2017.

4.1.5.2 Polarisation colour analysis

Table C.14 shows the Spearman rank coefficients for the long-term RINGO3 g^* vs. b^*-r^* polarisation colour correlations. The corresponding plots are shown in Figure 4.3. The results show eight sources with significant correlations: two HBLs, one IBL, two LBLs, and three FSRQs. Three sources (one HBL and two FSRQs) show negative correlations, implying a RWB polarimetric chromatism. This means in general, as the polarisation of the source increases, the lower energy redder band becomes more polarised than the bluer band. The remaining five (one HBL, one IBL, two LBLs, and one FSRQ) show an opposite positive correlation whereby the higher energy bluer band becomes more polarised than the redder band when the polarised state of the source increases (i.e. BWB polarimetric chromatism). Across all significant correlations, the strength coefficients range from |0.126| to |0.297|, or very weak to weak. These correlations and the apparent frequency dependence of polarisation may indicate relativistic shocks as a dominant source of emission in these sources (Angelakis et al., 2016; Liodakis et al., 2022b).

As with Section 4.1.5.1, one can break down the light curve of OJ287 during the 2015 impact flare event to check its effect on the long-term correlation behaviour. Table 4.4

TABLE 4.3: Results of the optical and γ-ray flux vs. polarisation correlations explored in this work. The source name and subclass are given, along with the optical flux vs. γ-ray flux correlation results from Table 3.3. The observed statistically significant polarisation trends "PWB" and "PWF" refer to polarised-when-brighter and polarised-when-fainter behaviour, respectively, and "No" implies no significant correlation was detected.

Source	Type	opt flux/γ-flux	opt flux/pol	gamma flux/pol
IC 310	HSP	-	No	-
1ES 1011+496	HSP	No	PWB	No
MRK 421	HSP	-	-	PWB
MRK 180	HSP	No	PWB	No
PG 1218+304	HSP	No	No	No
1ES 1426+428	HSP	-	PWF	-
PG 1553+113	HSP	Yes	PWB	No
MRK 501	HSP	Yes	PWB	No
1ES 1959+650	HSP	No	PWF	No
3C 66A	ISP	Yes	No	No
S5 0716+714	ISP	Yes	No	PWF
ON 231	ISP	No	No	No
A0 0235+164	LSP	Yes	No	No
TXS 0506+056	LSP	Yes	No	No
OJ 287	LSP	Yes	PWB	PWF
S4 0954+65	LSP	Yes	PWF	No
4C 09.57	LSP	Yes	No	No
BL Lac	LSP	Yes	PWB	No
PKS 0502+049	LSP (FSRQ)	Yes	PWB	PWB
PKS 0736+01	LSP (FSRQ)	Yes	PWB	PWB
PKS 1222+216	LSP (FSRQ)	Yes	PWB	No
3C 279	LSP (FSRQ)	Yes	PWF	PWF
PKS 1510-089	LSP (FSRQ)	Yes	PWB	PWB
OS 319	LSP (FSRQ)	Yes	No	No
PKS B1622-297	LSP (FSRQ)	Yes	No	No
4C +38.41	LSP (FSRQ)	Yes	PWB	PWB
3C 345	LSP (FSRQ)	No	No	No
PKS B1730-130	LSP (FSRQ)	No	PWF	No
3C 446	LSP (FSRQ)	Yes	PWF	No
4C 11.69	LSP (FSRQ)	Yes	PWB	PWB
3C 454.3	LSP (FSRQ)	Yes	PWB	PWB

TABLE 4.4: As Table 4.2 but for the polarisation colour correlations.

	Polarisation colour	
Epoch	p	c
Flare 1	0.104	0.374
Flare 2	0.904	0.030
General	0.077	0.084

shows the Spearman rank correlation coefficients for the flaring epochs as the general behaviour outside this time period. One can see that the removal of the flaring epoch results in the general polarisation colour behaviour of the source becoming uncorrelated, in disagreement with Table C.14. Both flares individually are also uncorrelated, which is perhaps expected due to the short timescales and small amounts of data within each correlation. The correlation found in the full dataset may therefore be a systematic feature arising from the increased cadence during the high-cadence flare monitoring campaign.

4.1.5.3 EVPA analysis

Given the three additional observables analysed in this work (γ-ray flux, polarisation, and magnitude), and that each rotation can take on two activity states when compared to the full light curve (higher or lower), there are a total of $2^3 = 8$ permutations of all states. Figure 4.4 shows the number of rotation events that correspond to each activity state. Each bin corresponds to a different state permutation, with "H" and "L" corresponding to the higher and lower states, respectively. The order of the parameters corresponds to the order of the state of the three observables during the detected rotation event: γ-ray flux, polarisation, and magnitude. Given MRK 421 does not have calibrated magnitude data, its two rotations could belong to either the HHH or HHL bins, or a combination of both. This is shown by the error bars on these bins.

Figure 4.4 shows that 70% (20/29) of optical EVPA rotations occur within heightened γ-ray states. Of these, 65 ± 5 ($13 \pm 1/20$)% occur during heightened optical states (the error here arising from the uncertainty regarding the optical magnitude state of MRK421 across RINGO3 observations) and 45% (9/20) during heightened polarisation states.

48% (14/29) of rotations occur during heightened optical polarisation states. Of these, 64% (9/14) occur within a heightened γ-ray state and 43 ± 7% (6±1/14) occur within a heightened optical state.

55±3% (16±1/29) of rotations occur during heightened optical states. Of these, 81±8% ($13 \pm 1/16 \pm 1$) occur within a heightened γ-ray state and 38 ± 6% ($6 \pm 1/16 \pm 1$) occur within a heightened polarisation state.

The combination with the most amount of observed rotations (7) is the HLH state, implying high photometric activity levels but low polarisation activity levels. Rotations occurring while in this photo-polarimetric state is likely indicative of jet kinks, whereby plasma instabilities cause twists in the jets magnetic field. The observational evidence for such a mechanism consists of MWL flaring (Acharya et al., 2023) in addition to an inverse correlation between optical flux and polarisation (Dong et al., 2020). Furthermore, one may expect to see multiple rotations as a result of a kinked jet, causing repeated flaring and rotation events. It could therefore be expected that one would observe a significant proprtion of rotations to be a result of this magnetic field structure.

It is worth noting that if the two rotations observed for MRK421 were also in high optical flux states, then the HHH state permutation would have the same number of rotations as the HLH state. This would imply rotations occurring during high states across all photo-polarimetric observables, as would be expected during fast shocks propergaing through a strongly magnetised region (Zhang et al., 2014, 2016; Liodakis et al., 2022b).

4.2 MOPTOP

4.2.1 Magnitude–polarisation

Figure 4.5 shows the normalised optical magnitude vs. polarisation plots for each source in the MOPTOP sample. Spearman rank correlation significance and strength values are shown in Table C.16. In this table, correlation coefficients are given for each MOPTOP waveband, but as MOPTOP photo-polarimetric uncertainties are generally lower in R-band, the coefficients from this band are used to determine if a source demonstrated significant behaviour. It is however worth noting that in this case, correlations across wavebands are consistent, albeit varying in strength.

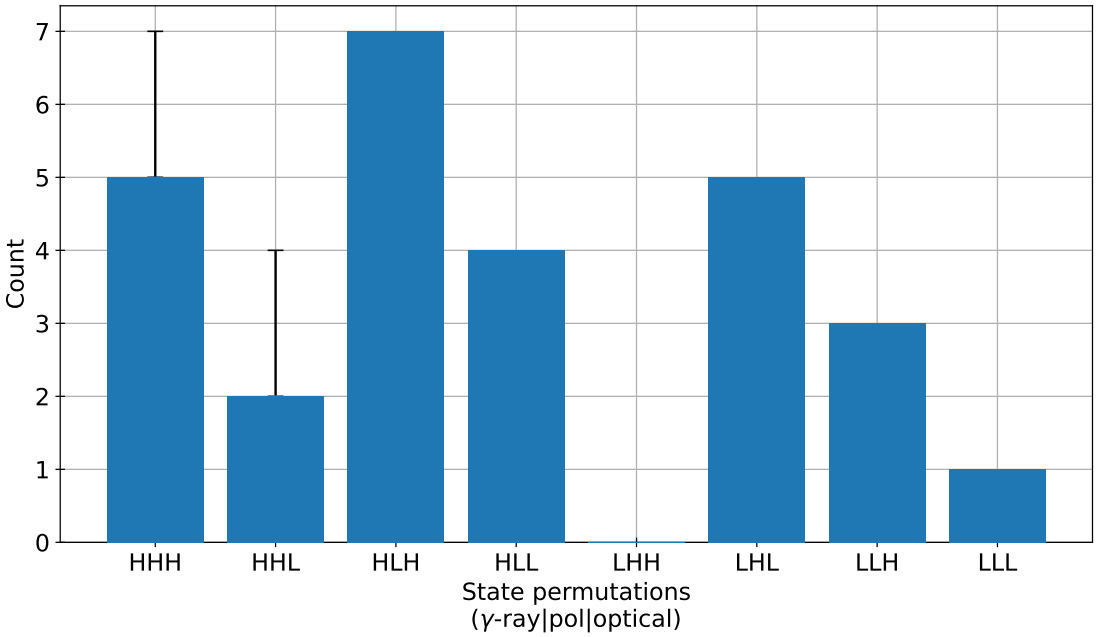

FIGURE 4.4: Breakdown of the frequency of different activity states during EVPA rotations in the RINGO3 dataset. There are two activity states (higher; H or lower; L) depending on the activity level during the rotation when compared to the entire light curve for the three observables (γ-ray flux, polarisation, and magnitude). The state permutations refer to the states of the three observables in the given order (i.e. "HHH" refers to higher-higher-higher for γ-ray flux–polarisation–magnitude, respectively). The error bars on states HHH and HHL arise from the uncalibrated magnitude data for MRK 421. Given the γ-ray and polarisation states are brighter and higher respectively, the two rotations observed for MRK 421 could be added to either bin.

The results show that all sources demonstrate significant optical magnitude vs. polarisation behaviour. Two sources (PG 1553+113; HBL, and BL Lac; LBL) show negative correlations with strength values of 0.226 and 0.212 (both weak) respectively, implying when the source becomes brighter its polarisation decreases. The remaining sources (two LBLs and 3 FSRQs) all show positive correlations with strength values ranging from 0.211 (weak) to 0.500 (moderate), implying polarisation increases with flux. The source with the highest correlation strength (0.500) was 4C 11.69 (FSRQ).

4.2.2 Gamma-ray–polarisation

The γ-ray vs. optical polarisation trends are shown in Figure 4.6 with the Spearman rank correlation coefficients shown in Table C.17. As before, coefficients have been calculated for each MOPTOP waveband, but as the R-band SNR is generally highest it will be used to determine if a source showed significant behaviour.

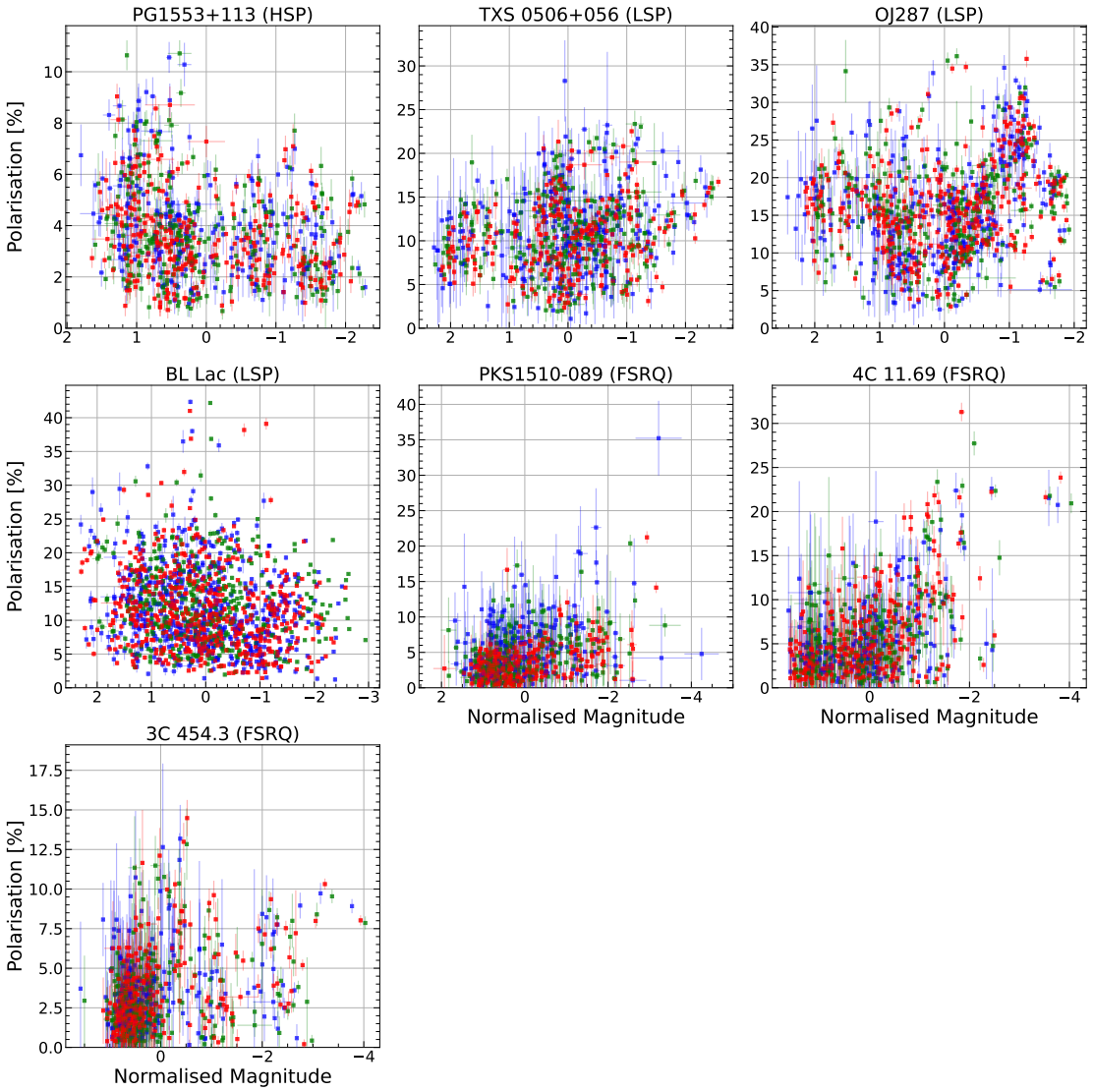

FIGURE 4.5: Optical magnitude vs. polarisation observed with MOPTOP for each source in the sample.

These results show four sources with significant correlations. All three FSRQ objects (PKS 1510-089, 3C 454.3 and 4C 11.69) show positive correlations (polarimetrically stronger when γ-ray brighter) with strength values ranging from 0.259 to 0.395 (weak). BL Lac (LBL) is the only object to show a negative correlation (polarimetrically weaker when γ-ray brighter) and has an associated strength value of -0.260 (weak).

4.2.3 Polarisation colour

Plots indicating any long-term wavelength dependence on polarisation are shown in Figure 4.7 for all sources in the MOPTOP sample. The corresponding Spearman rank correlation coefficients for all colour permutations are shown in Table C.18, but the

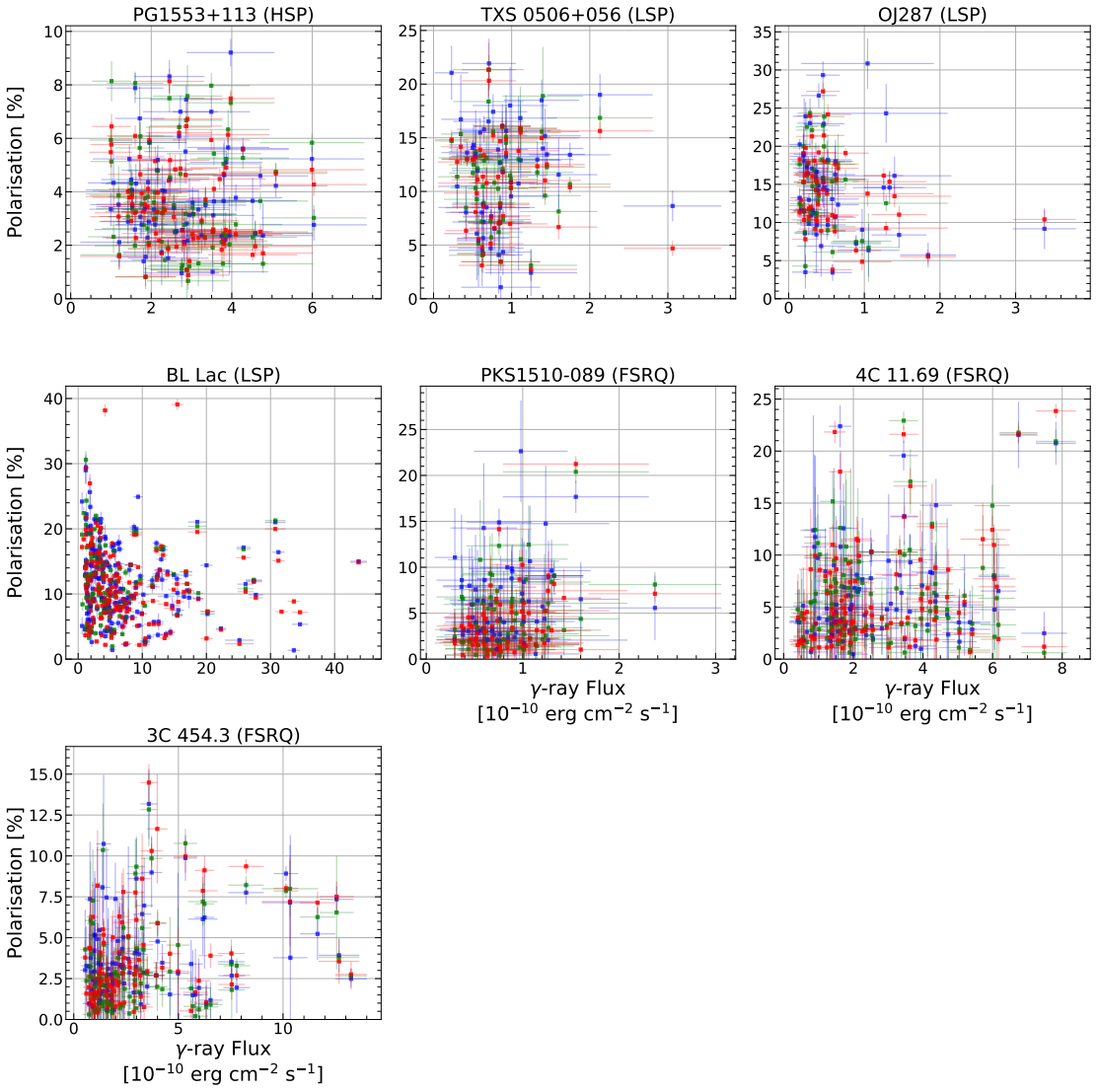

FIGURE 4.6: Fermi γ-ray flux vs. polarisation observed with MOPTOP for each source in the sample.

coefficients associated with the B-R vs. V-band data are used to determine significant behaviour for the source. This is due to this permutation having the largest wavelength difference in the polarisation colour and so is most likely to show polarimetric chromatism across the optical spectrum if it is present.

Three sources show significant chromatic polarisation trends: BL Lac, 4C 11.69, and 3C 454.3. While BL Lac shows a positive correlation of strength 0.280 (weak), both 4C 11.69 and 3C 454.3 show negative trends of strengths -0.393 and -0.230 (also both weak) respectively. A positive correlation implies the source became more polarised in the B-band when generally more polarised (BWB polarisation trends) across the optical

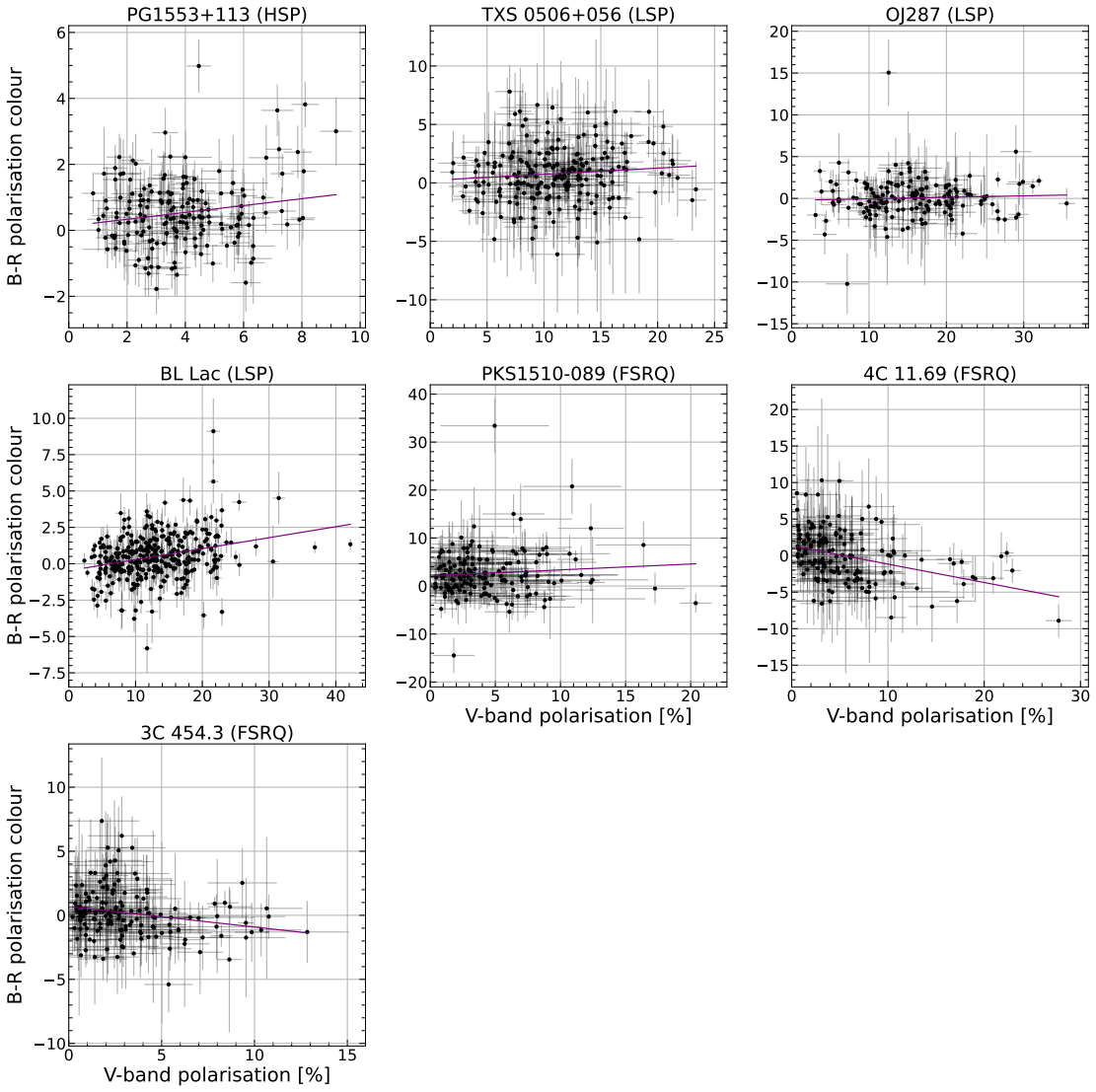

FIGURE 4.7: MOPTOP polarisation colour correlations. Only the *B*-*R* vs. *V* data is shown as this permutation offered the largest waveband difference and so better emphasises any frequency-dependent behaviour.

regime. Conversely, a negative correlation implies the source became more polarised in the *R*-band when generally more polarised (RWB polarisation trends).

4.2.4 EVPA

As with Section 4.1.4, EVPA rotations are detected using the methodology described by Blinov et al. (2015). The EVPA rotation light curves from the MOPTOP dataset are shown in Figures C.42 – C.57 in the appendix.

Included in these plots are the γ-ray flux, polarisation and magnitude variability during and around the rotation event. The average γ-ray flux, polarisation, and magnitude over

TABLE 4.5: EVPA rotations found in the MOPTOP dataset. Shown are the starts of the rotations as MJD and EVPA, and the duration and size of the rotation. Also shown are the γ-ray flux and optical polarisation and magnitude states during the rotation event compared to the full monitoring campaign (higher or lower).

Source	Type	MJD Start	ΔMJD [days]	EVPA Start [°]	ΔEVPA [°]	γ-ray State	Pol State	Opt State
PG1553+113	HSP	59963.29	43.84	31.25	245.67	Higher	Lower	Higher
...	...	60364.26	16.87	360.96	186.80	Higher	Higher	Lower
BL Lac	LSP	59684.24	18.93	-430.80	112.15	Higher	Lower	Higher
...	...	59797.98	10.04	-590.17	127.18	Lower	Lower	Lower
...	...	59932.82	18.00	-436.43	169.22	Higher	Lower	Higher
...	...	60196.93	47.89	-250.52	-112.31	Lower	Higher	Higher
PKS1510-089	LSP (FSRQ)	60047.15	3.86	33.97	115.49	Higher	Higher	Higher
...	...	60368.25	5.97	207.27	-182.51	Lower	Higher	Higher
...	...	60436.04	5.12	14.27	134.18	Lower	Lower	Lower
4C 11.69	LSP (FSRQ)	59936.84	123.39	47.84	-162.19	Higher	Higher	Higher
...	...	60150.16	4.96	-81.57	211.49	Higher	Higher	Higher
3C 454.3	LSP (FSRQ)	59800.11	6.96	157.46	-155.70	Lower	Lower	Lower
...	...	59872.92	10.94	76.11	-226.22	Higher	Higher	Higher
...	...	59883.86	5.98	-150.10	136.07	Higher	Higher	Higher
...	...	59936.85	139.35	119.24	218.53	Higher	Higher	Higher
...	...	60127.10	4.95	302.97	113.60	Higher	Higher	Lower

the full observation campaign is also shown to assess the states of the source during the rotation. A comparison of the average observed behaviour to that of during the rotation event is shown in Table 4.5, with the exact values comparing the different activity states in Table C.19 in the appendix.

The results show 16 EVPA rotations occurring over periods of approximately 4–140 days and rotation angles of 112°–245°. The rotations are detected for both FSRQs and HSP/LSP BL Lac classes. 5/7 sources showed rotations, with each object displaying multiple rotations across their light curves.

4.2.5 Discussion

4.2.5.1 Flux–polarisation analysis

A summary of the correlation statistics for the optical R-band and γ-ray flux vs. polarisation data are shown in Table 4.6. The correlations are summarized by their significance and observed trend, with "PWF" and "PWB" denoting significant polarised-when-fainter and polarised-when-brighter behaviour respectively. Similarly to Section 4.1.5.1 and Table 4.3, the optical vs. γ-ray flux correlations are also shown from Table C.8.

Two sources (PG 1553+113; HBL and BL Lac; LBL) show significant PWB behaviour when looking at their optical flux vs. polarisation correlations. When considering their γ-ray flux vs. polarisation correlations, BL Lac shows the same PWB trend while no significant trend is observed for PG 1553+113. Both of these sources show significant optical vs. γ-ray flux correlations. These results suggest that over the full duration of the MOPTOP campaign, the dominant source of emission was from relativistic shocks and the leptonic scenario (SSC or EC emission) (Maraschi et al., 1992; Dermer & Schlickeiser, 1993; Guetta et al., 2004; Liodakis et al., 2022b). This is due to the presence of long-term correlated MWL photo-polarimetric flaring. The absent γ-ray flux vs. polarisation correlation for PG 1553+113 is likely a result of the combination of generally lower polarisation, a common feature among HBL sources, and relative inactivity in γ-ray flux (see Figure 3.11).

Five sources show significant PWF optical R-band magnitude vs. polarisation correlations. Three of these (all three FSRQs) also show PWF trends when considering the γ-ray flux vs. polarisation trends. Two of these sources (4C 11.69 and 3C 454.3) show significant optical vs. γ-ray flux behaviour and PKS 1510-089 does not. Dong et al. (2020) suggest an inverse correlation between photometric and polarimetric emission is indicative of kink instabilities in the jet. If one assumes the origin of the emission is leptonic, it may be expected that both optical and γ-ray flux correlate inversely with polarisation. The remaining two (TXS 0506+056; LBL and OJ 287; LBL) do not show any significant γ-ray flux vs. polarisation trends. Furthermore, while TXS 0506+056 does show significant optical vs. γ-ray flux behaviour, OJ 287 does not.

One can compare Table 4.6 to its RINGO3 equivalent, Table 4.3, on a source-by-source basis to check for similar, gained, or lost trends. In all three FSRQs (PKS 1510-089, 4C 11.69, and 3C 454.3), the same trends are observed across all three flux metrics: positively correlated optical vs. γ-ray flux, and PWB optical/γ-ray flux vs. polarisation. Furthermore, these are the only three sources to display only consistent behaviour in both observation campaigns.

Compared to the RINGO3 results presented in Table 3.3 for those sources in the MOPTOP sample, four show long-term behaviour consistent between instruments, namely PKS 1510-089, 4C 11.69, 3C 454.3, and TXS 0506+056. It is noted that these consist of all three FSRQs and significant correlations were detected across all three measures.

TABLE 4.6: As Table 4.3 but for the MOPTOP sample.

Source	Type	opt flux/γ-flux	opt flux/pol	gamma flux/pol
PG 1553+113	HSP	Yes	PWF	No
TXS 0506+056	LSP	Yes	PWB	No
OJ 287	LSP	No	PWB	No
BL Lac	LSP	Yes	PWF	PWF
PKS 1510-089	LSP (FSRQ)	Yes	PWB	PWB
4C 11.69	LSP (FSRQ)	Yes	PWB	PWB
3C 454.3	LSP (FSRQ)	Yes	PWB	PWB

While TXS 0506+056 is classified as consistent, it is also worth noting that a correlation in optical flux vs. polarisation was gained in the MOPTOP dataset over RINGO3, likely in part due to the much larger quantity of data, and no correlation was detected in either dataset between γ-ray flux and polarisation. Both PG 1553+113 and BL Lac showed consistent behaviour in their optical vs. γ-ray fluxes (both a significant trend) and in their γ-ray flux vs. polarisation (no detection and a significant detection, respectively). The final source, OJ 287, was the only object to show a loss in observed long-term trends in the MOPTOP data over RINGO3. When comparing the MOPTOP dataset to the full RINGO3 dataset, both previously observed γ-ray vs. optical flux and γ-ray flux vs. polarisation trends do not re-occur. However, it may be more useful to compare the MOPTOP data to the flare-removed RINGO3 data given no such flare was observed during the MOPTOP campaign. When doing so, the same significant trend was observed in the optical vs. γ-ray flux correlation, and the γ-ray flux vs. polarisation trend observed in the RINGO3 data disappeared, consistent with the MOPTOP data. A loss in any observed optical vs. γ-ray flux correlation is still apparent.

4.2.5.2 Polarisation colour analysis

The results of the polarisation colour correlations for the MOPTOP sample are given in Table C.18, with plots shown in Figure 4.7. A significant trend is determined using the *B-R* colour permutation as this gives the largest waveband separation in the MOPTOP data and therefore a better likelihood of detecting significant correlations. A significant BWB polarisation trend was observed for BL Lac while both 4C 11.69 and 3C 454.3 showed significant RWB trends. In this measure, BWB chromatism implies the source becomes more polarised at higher-energy optical frequencies when the source brightens,

while the source becoming more polarised at lower-energy optical frequencies during periods of increased flux implies RWB chromatism. All the observed significant trends were weak in strength, with coefficients ranging from |0.230|–|0.393|. The polarimetric colour trend observed in BL Lac could be explained through a shock region travelling along a helical magnetic field (Shablovinskaya et al., 2023) with the frequency-dependent polarisation arising from the rotation of the shocked region and its turbulent magnetic field. Assuming the same scenario for 4C 11.69 and 3C 454.3, a post-shock energy injection would be required to overcome cooling and produce the RWB frequency dependence. Alternatively, the frequency dependence (BWB vs. RWB) may be an intrinsic property of the different blazar subclasses given both FSRQs show RWB behaviour and the BL Lac object shows a BWB trend.

Comparing these trends to those observed with RINGO3, only one source shows consistent behaviour, 4C 11.69. Across both campaigns, negative trends were observed, and this is indicative of a RWB polarimetric chromatism trend. Both BL Lac and 3C 454.3 showed no significant correlations in the RINGO3 data. Figure 4.8 shows a comparison of the polarisation ranges observed with both RINGO3 and MOPTOP. Larger polarisation ranges were observed with MOPTOP for BL Lac and TXS 0506+056, while OJ287 showed a larger range of states during the RINGO3 observations. The other sources showed a similar range across both campaigns. One would expect a vast difference in the activity states observed in TXS 0506+056 given the small number of observations with RINGO3.

It is important to note that the likelihood of observing different activity states increases with the duration and cadence of the monitoring campaign (i.e. more observation epochs over a longer baseline gives a better chance of observing variability). The duration of the RINGO3 campaign was longer than that of MOPTOP but also had a lower cadence. It is therefore likely that the differences presented in Figure 4.8 (and Figure 3.11) are reflections of the activity of the objects rather than a result of slightly different observing methods between the RINGO3 and MOPTOP campaigns.

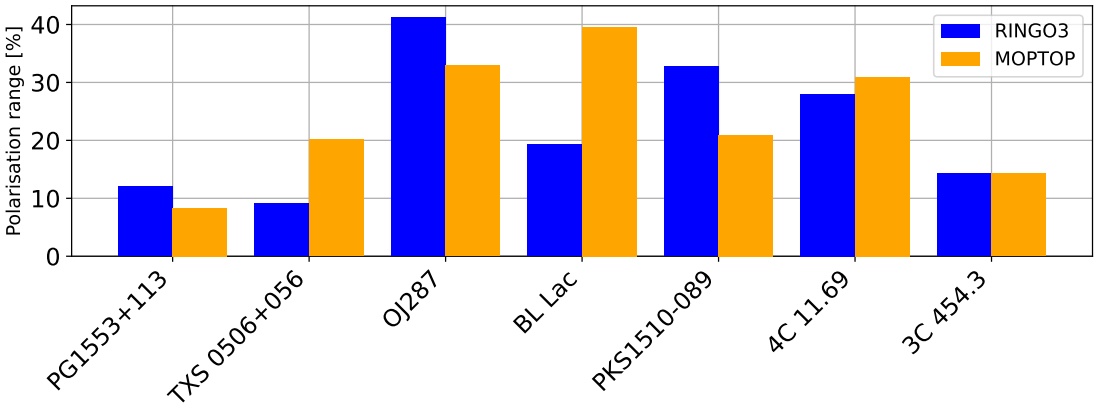

FIGURE 4.8: Comparison of the RINGO3 and MOPTOP polarisation ranges for the sources in the MOPTOP sample. The left of each pair of bars corresponds to the range observed with RINGO3 for that source, while the right is the range with MOPTOP.

4.2.5.3 EVPA analysis

During the MOPTOP campaign, a total of 16 EVPA rotations were detected following the procedure outlined in Section 4.1.4 and Blinov et al. (2015). Rotations were observed in five out of seven sources, with TXS 0506+056 and OJ 287 (both LBL sources) displaying no rotations. The light curves of each rotation are shown in Figures C.42 – C.57 and a table detailing the parameters of each rotation as well as the associated R-band magnitude, polarisation, and γ-ray activity states is given in Table C.19.

A breakdown of the activity states associated with each rotation is shown in Figure 4.9. Each bar represents one of all possible activity state permutations as either higher (H) or lower (L) than the campaign average for the source with the order of the observables being γ-ray flux, polarisation, and magnitude respectively.

The activity state permutation with the most detected EVPA rotations in the MOPTOP sample was the HHH state, implying most of the rotations occurred during simultaneous increased γ-ray, polarisation, and optical magnitude activity.

The majority of rotations, 69% (11/16) occurred when the source was in a heightened γ-ray state. Of these rotations, 73% (8/11) occurred during heightened polarisation states. Additionally, 82% (9/11) rotations occurred during heightened γ-ray activity.

When the objects were in heightened polarisation states, 63% (10/16) of rotations were observed. Of these, 80% (8/10) were coincident with increased γ-ray flux and 80% were detected alongside increase optical magnitude.

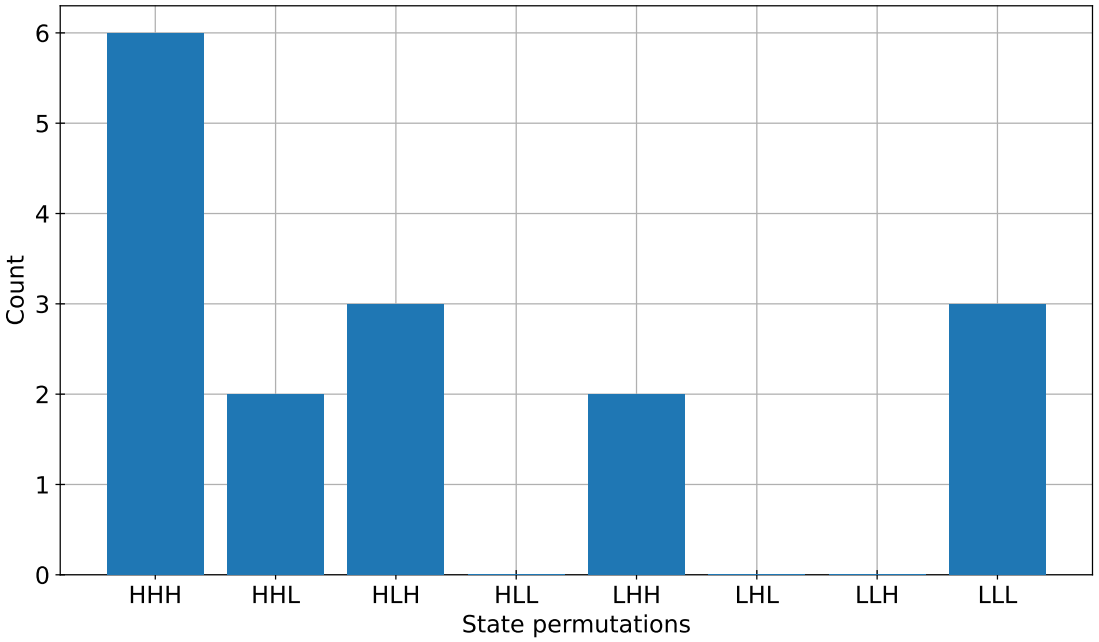

FIGURE 4.9: Breakdown of the frequency of different activity states during EVPA rotations in the MOPTOP dataset. There are two activity states (higher; H or lower; L) depending on the activity level during the rotation when compared to the entire light curve for the three observables (γ-ray flux, polarisation, and magnitude). The state permutations refer to the states of the three observables in the given order (i.e. "HHH" refers to higher-higher-higher for γ-ray flux–polarisation–magnitude, respectively).

When in increased optical magnitude states, 69% (11/16) of rotations were observed. Of these, 82% (9/11) and 73% (8/11) were associated with increased γ-ray flux and polarisation activity, respectively.

To give a more robust assessment of the likelihood of observing rotations in differing activity state permutations, one can aggregate the results of the RINGO3 and MOPTOP campaigns in order to obtain a larger sample. This is shown in Figure 4.10. The spread of these aggregated results across the different activity states is similar to those separated by instrument, which is unsurprising given the similarities between Figures 4.4 and 4.9.

The results are similar across both campaigns. The majority of rotations, 65% (30/46), occur during heightened γ-ray activity. This proportion is dominated by rotations occurring during heightened photometric activity in addition to a high or low polarised state. The individual state with the most observed rotations is the HHH state, followed closely by HLH. These two states account for approximately half ($22 \pm 1/46$) of all rotations.

As discussed in Section 4.1.5.3, the HHH and HLH states could be interpreted as originating from shock and jet kink instabilities, respectively. Over long timescales, these

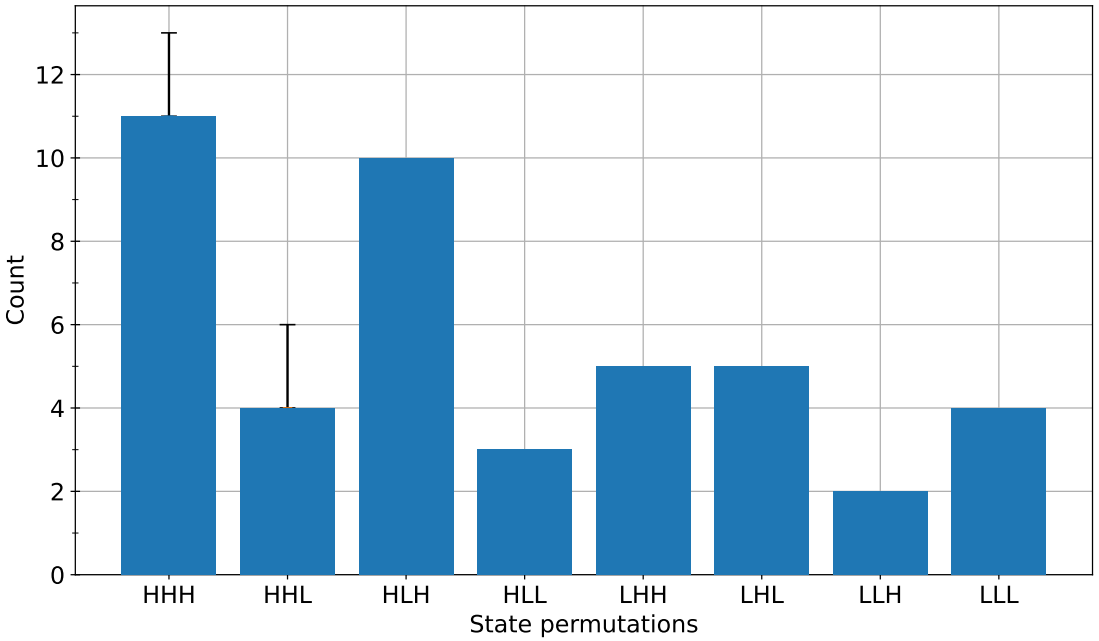

FIGURE 4.10: EVPA rotation activity state breakdown combining those observed with both RINGO3 and MOPTOP. The underlying data for this figure is the aggregation of those data observed in Figures 4.4 and 4.9.

mechanisms appear to dominate the observed behaviour. It is, however, important to note that some rotations will also occur as a result of stochastic variability of randomly tangled magnetic fields, rather than any field ordering. This is described by the passage of a plasma blob travelling through the jet, which shows erratic polarisation variability, including EVPA rotations (Marscher & Jorstad, 2021).

4.3 Conclusions

In this chapter, the polarimetric properties of a sample of γ-ray bright blazars have been explored through the use of data collected with the RINGO3 and MOPTOP polarimeters on the Liverpool Telescope. Fermi data was also obtained to assess the multi-wavelength properties of the sample over the same time period from 2013-2024.

There are numerous examples of both correlated and anticorrelated long-term behaviour in the optical and γ-ray fluxes vs. polarisation trends. Correlated behaviour between the optical flux and polarisation is suggestive of the ordering of the local magnetic field structure resulting from shock propagation through the jet. Where γ-ray emission is also correlated, the MWL activity likely suggests the leptonic nature of the emission.

Anti-correlated optical flux vs. polarisation trends are possible through kink instability emission. A large proportion of such trends were observed across both monitoring campaigns. Optical and γ-ray flux vs. polarisation trends generally appear consistent across the RINGO3 and MOPTOP monitoring campaigns. Both correlated and anticorrelated trends appear across all blazar subclassifications. As a result, one could conclude that relativistic shocks and jet kink instabilities, the mechanisms this work associates with the observed emission, are indiscriminate of blazar class. In other words, these emission mechanisms can occur in all blazar classes (FSRQs and BL Lacs) and all subclasses (HBLs, IBLs, and LBLs).

Frequency-dependent optical polarisation behaviour is predicted in the shock-in-jet model but is difficult to detect given the small width of the optical frequency regime. It was possible to detect such behaviour in a small number of sources, displaying increased variability at both redder and bluer frequencies. To explain increased polarisation at larger frequencies, post-shock acceleration would be required to overcome cooling. The large majority of sources displaying either trend were LSP sources, belonging to both FSRQ and BL Lac groups. While this could indicate a distinct property of LSP objects, the more probable scenario is that LSP sources were more likely to display some form of polarimetric variability. It is possible that further high-cadence monitoring observing ISP and HSP sources over long timeframes would reveal further frequency-dependent optical polarisation behaviour.

Across both campaigns, the majority of optical EVPA rotations occurred during simultaneously heightened γ-ray and optical flux states. A similar number of rotations occurred during higher and lower polarisation states alongside heightened photometric states. Rotations during these two state permutations could also be explained through shocks within a helical magnetic field and kink instabilities in the relativistic jets.

Chapter 5

Intranight Variability

The intranight variability of blazars refers to the behaviour observed over timescales of minutes to hours. While the phenomenon is prevalent across the blazar population, it is not a well-understood phenomenon and has only recently been the subject of dedicated observation campaigns (Sagar et al., 2004; Bachev, 2015; Liodakis et al., 2024). Observing significant variability outside of general noise allows one to better understand short-timescale acceleration and emission processes in relativistic jets. Such processes include those intrinsic to the jet's energy output, like the helical motion of emitting regions travelling through the jet's magnetic field (Gopal-Krishna & Wiita, 1992) or the cooling of shock-accelerated electrons (Bachev et al., 2012), but some theories suggest more exotic ideas such as microlensing (Paczynski, 1996). High-cadence, multiband, observations of blazars can provide valuable insights into the emission processes, such as colour changes of the jet synchrotron emission and any temporal separation of individual lightcurve events.

This chapter presents the results of a five-night intranight optical variability (INOV) monitoring campaign executed over the period 2023 January 15-19 on four blazars: TXS 0506+056, OJ287, PKS 0735+178 and OJ248. These sources were chosen due to a combination of their historic degrees of INOV and their observability during the campaign. The sample was kept small to ensure the data were sufficient to observe hour-long variability timescales with high sampling.

The results of this chapter are published in McCall et al. (2024a).

TABLE 5.1: List of the blazars used in this analysis including the source Right Ascension (α), Declination (δ), type, redshift (z), TCS observation date, hours observed (H), and the number of observations (N) in g, r, i, z_s bands.

Name	α (J2000)	δ (J2000)	Type	z	Date	H	N
TXS 0506+056	$05^h09^m25^s.96$	$+05°41'35''.333$	LSP	0.337	2023 Jan 15	5.15	121
...	...	...	...	...	2023 Jan 16	1.43	157
...	...	...	...	...	2023 Jan 18	0.87	100
OJ287	$08^h54^m48^s.875$	$+20°06'30''.640$	LSP	0.306	2023 Jan 15	7.95	216
...	...	...	...	...	2023 Jan 18	2.62	294
...	...	...	...	...	2023 Jan 19	0.29	17
PKS 0735+178	$07^h38^m07^s.394$	$+17°42'18''.998$	ISP	0.45	2023 Jan 15	3.22	77
...	...	...	...	...	2023 Jan 16	0.63	25
...	...	...	...	...	2023 Jan 17	7.24	313
OJ248	$08^h30^m52^s.086$	$+24°10'59''.820$	FSRQ	0.939	2023 Jan 16	0.61	29
...	...	...	...	...	2023 Jan 17	7.33	250
...	...	...	...	...	2023 Jan 19	0.74	66

5.1 TCS

A summary of the TCS observations is presented in Table 5.1. Each source was observed on three separate nights and, in general, observations were interleaved for two sources with a typical observing sequence of 10 frames per source with a 30 second exposure time (the longest that could be executed without autoguiding; imposed by an autoguider failure). For details on the Carlos Sánchez Telescope (TCS), MuSCAT2 instrument, and reduction methods employed, see Section 2.2. These sources were chosen for this campaign due to being visible from Tenerife for the majority of the night, as well as being within the declination limits of the telescope.

5.1.1 Temporal variability

The $griz_s$ light curves for each source on a given night are shown in Figure C.58, C.59, C.60 and C.61 for TXS 0506+056, OJ287, PKS 0735+178 and OJ248 respectively. The source name and night of observation are given above each plot.

In order to quantify variability in the light curves and to disentangle intrinsic variability from noise, one can employ several statistical tests to determine the variability likelihood. Specifically, calculation of the variability amplitude and fractional variability and perform chi-squared and enhanced F-test analyses. These tests are detailed in Sections 5.1.1.1, 5.1.1.2, 5.1.1.3, and 5.1.1.4.

5.1.1.1 Variability amplitude

Variability amplitude is defined in Heidt & Wagner (1996) as

$$\mathrm{VA} = \sqrt{(x_{\max} - x_{\min})^2 - 2\langle x_{\mathrm{err}}\rangle^2} \tag{5.1}$$

where $x_{\max}$ and $x_{\min}$ are the maximum and minimum observed values, and $\langle x_{\mathrm{err}}\rangle$ is the median measurement error. The percentage variability amplitude, $\mathrm{VA}_{\mathrm{per}}$ is given in Romero et al. (1999) as

$$\mathrm{VA}_{\mathrm{per}} = \frac{100}{\langle x\rangle}\sqrt{(x_{\max} - x_{\min})^2 - 2\langle x_{\mathrm{err}}\rangle^2} \tag{5.2}$$

where $\langle x\rangle$ is the average observed value. Its error, $\Delta\mathrm{VA}_{\mathrm{per}}$, is given in Singh et al. (2018) as

$$\Delta\mathrm{VA}_{\mathrm{per}} = 100 \times \left(\frac{x_{\max} - x_{\min}}{\langle x\rangle \times \mathrm{VA}}\right) \times \sqrt{\left(\frac{x_{\mathrm{err,max}}}{\langle x\rangle}\right)^2 + \left(\frac{x_{\mathrm{err,min}}}{\langle x\rangle}\right)^2 + \left(\frac{\langle x_{err}\rangle}{x_{\max} - x_{\min}}\right)^2 \mathrm{VA}^4} \tag{5.3}$$

where $x_{\mathrm{err,max}}$ and $x_{\mathrm{err,min}}$ are the errors on the maximum and minimum values, respectively. The variability amplitude quantifies the absolute range of variability of a given source by looking at the range of magnitude values outside of the scatter from the measurement errors.

The values obtained via the variability amplitude calculations can be seen in column four in Table C.20. The results show variability amplitudes ranging from 0.167% up to 1.456% across all sources, dates and filters. The ratio between the error and percentage variability amplitude shows that in 12/48 cases the percentage variability amplitudes are associated with large errors (where the ratio is greater than 3). It's noted that nine of these cases are attributed to the source OJ248; likely due to it being the faintest of the sample.

5.1.1.2 Fractional variability

Fractional variability, described fully in Schleicher et al. (2019), is a method of quantifying variability intensity while accounting for measurement uncertainties. It differs from

the variability amplitude by considering the variability relative to the mean brightness level. It is defined in Edelson et al. (2002) as

$$F_{\rm var} = \sqrt{\sigma^2_{\rm NXS}} = \sqrt{\frac{S^2 - \langle\sigma^2_{\rm err}\rangle}{\langle x\rangle^2}} \tag{5.4}$$

where S^2 is the variance of the data set, $\langle\sigma^2_{\rm err}\rangle$ is the median square error, and $\langle x\rangle$ is the median value. It can also be given as the square root of the normalised excess variance ($\sigma^2_{\rm NXS}$). Its associated error is given in Poutanen et al. (2008) as

$$\Delta F_{\rm var} = \sqrt{\mathrm{F}^2_{\rm var} + \Delta\sigma^2_{\rm NXS}} - F_{\rm var} \tag{5.5}$$

where $\Delta\sigma^2_{NXS}$ is the error on the normalised excess variance. This error is given in Vaughan et al. (2003) as

$$\Delta\sigma^2_{\rm NXS} = \sqrt{\left(\sqrt{\frac{2}{N}}\frac{\langle\sigma^2_{\rm err}\rangle}{\langle x\rangle^2}\right) + \left(\sqrt{\frac{\langle\sigma^2_{\rm err}\rangle}{N}}\frac{2F_{\rm var}}{\langle x\rangle}\right)^2} \tag{5.6}$$

where N is the number of data points in the sample. It follows that if the variance is less than the average square error, $S^2 < \langle\sigma^2_{\rm err}\rangle$, a real value cannot be computed and will be denoted as < 0, indicating a detection of insignificant variability. These values are shown in column five in Table C.20. Where sources had $F_{\rm var} > \Delta F_{\rm var}$, this test is deemed to show that an object has shown significant variability.

12/48 instances across all sources, dates and filters show significant levels of variability have been detected. These detections correspond to OJ287 on 2023 January 15, and PKS 0735+178 on 2023 January 15 and 17 across all filters, with the most significant detections corresponding to PKS 0735+178 on 2023 January 17.

5.1.1.3 Chi-squared

Chi-squared (χ^2), as used in Zeng et al. (2017), is given by

$$\chi^2 = \sum_i^N \left(\frac{x_i - \langle x\rangle}{x_{{\rm err},i}}\right)^2 \tag{5.7}$$

where x_i and $x_{{\rm err},i}$ are the individual values and errors respectively within the data set, and $\langle x\rangle$ is the median value. Its critical value was determined at the 99.9% confidence

level ($\alpha = 0.001$) with the degrees of freedom being equal to the number of data points. The χ^2 values together with critical values are shown in column six in Table C.20. Where the value is greater than the critical value, significant variability has been detected. χ^2 is a useful metric as it quantifies the levels of variability about the median values. Incorporating the critical value allows us to determine the significance of the value.

The χ^2 test shows significant variability in 27/48 instances across all sources, dates and filters. In most cases, non-detection is consistent across filters per source per date. Variability detections are consistent across all filters for TXS 0506+056 on 2023 January 15, OJ287 on 2023 January 15 and 18, and PKS 0735+178 on 2023 January 15 and 17.

5.1.1.4 Enhanced F-test

The enhanced F-test ($F_{\rm enh}$) is given in De Diego (2014) and aims to quantify the variability of a target while incorporating the variability of multiple reference stars (Subbu Ulaganatha Pandian et al., 2022). It is given as

$$F_{\rm enh} = \frac{S^2_{\rm blazar}}{S^2_{\rm star}} \tag{5.8}$$

where $S^2_{\rm blazar}$ is the variance of the blazar and $S^2_{\rm star}$ is the combined variance of the comparison stars. $S^2_{\rm star}$ is defined as

$$S^2_{\rm star} = \frac{1}{(\sum_{j=1}^{k} N_j - k)} \sum_{j=1}^{k} \sum_{i=1}^{N_j} \sigma_{j,i} \tag{5.9}$$

where N_j is the number of observations of the j^{th} comparison star, k is the number of comparison stars and $\sigma_{j,i}$ is the scaled square deviation. $\sigma_{j,i}$ is given as

$$\sigma_{j,i} = s_j (m_{j,i} - \langle m_j \rangle)^2 \tag{5.10}$$

where $m_{j,i}$ is the magnitudes of each comparison star, $\langle m_j \rangle$ is the mean magnitude of the comparison star and s_j is the scaling factor to account for the different SNRs of the comparison stars. s_j is given as

$$s_j = \frac{\langle \sigma^2_{\rm blazar} \rangle}{\langle \sigma^2_{sj} \rangle} \tag{5.11}$$

where $\langle\sigma^2_{\text{blazar}}\rangle$ and $\langle\sigma^2_{sj}\rangle$ are the average square errors of the blazar and comparison star magnitudes respectively. Its critical value was determined at the 99.9% confidence level ($\alpha = 0.001$) with the degrees of freedom for the blazars being one less than the number of observations, and the degrees of freedom for the comparison stars being the sum of one less than the number of observations for each comparison star.

The F_{enh} values with critical values are shown in column seven in Table C.20. They show significant detections of variability in 15/48 instances across all sources, dates and filters. 12 of these detections correspond to observations in all filters of OJ287 on 2023 January 15, and PKS 0735+178 on 2023 January 15 and 17.

5.1.1.5 Temporal variability summary

To summarise the results of each test shown in Table C.20 and determine epochs of variability, one can look at the results of the fractional variability, χ^2, and enhanced F-test analyses and determine variable epochs if all three tests are passed. If one or fewer tests were met, it can be argued that there is no statistical evidence for intranight variability in these sources/epochs.

All TXS 0506+056 and OJ248 epochs display no significant levels of intranight variability. There is possible variability from TXS 0506+056 on 2023 January 16. Given that this possible variability only occurs in the i band, this can likely be considered as a result of scatter in the data. OJ287 shows one epoch of significant variability on 2023 January 15. PKS 0735+178 shows two epochs of significant variability on 2023 January 15 and 17 and one of possible significant variability on 2023 January 16. The latter consists of very few observations due to poor observing conditions so, based on the light curve, it is possible that this is a false detection.

The light curves with statistically significant variability for OJ287 and PKS 0735+178 are shown in Figure 5.1, 5.2, and 5.3. Further sections will detail the additional analysis of only these variable epochs: full tables and plots for the other epochs can be found in the appendix.

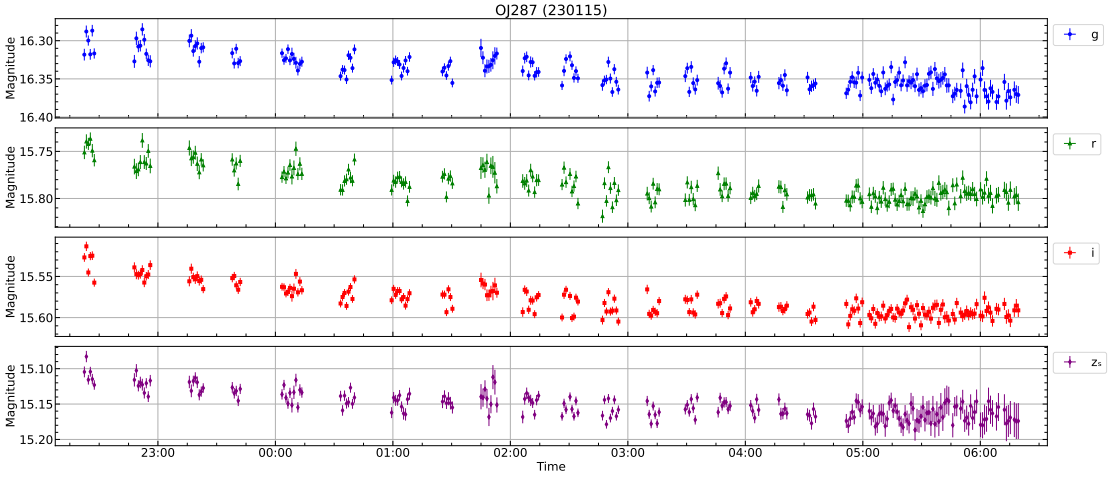

FIGURE 5.1: Light curves for OJ287 on the night of 2023 January 15. Panels correspond to g, r, i, z_s data separately, from top to bottom.

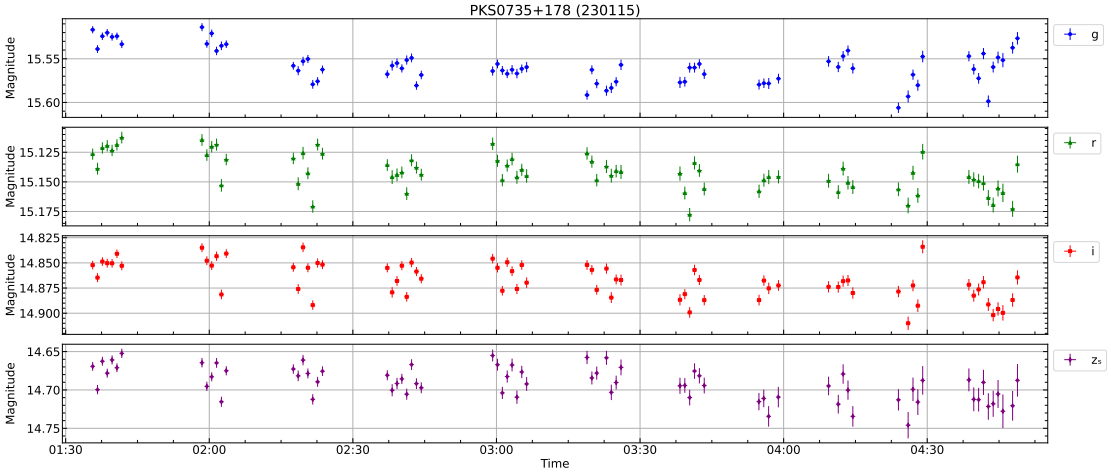

FIGURE 5.2: As Figure 5.1, but for PKS 0735+178 on the night of 2023 January 15.

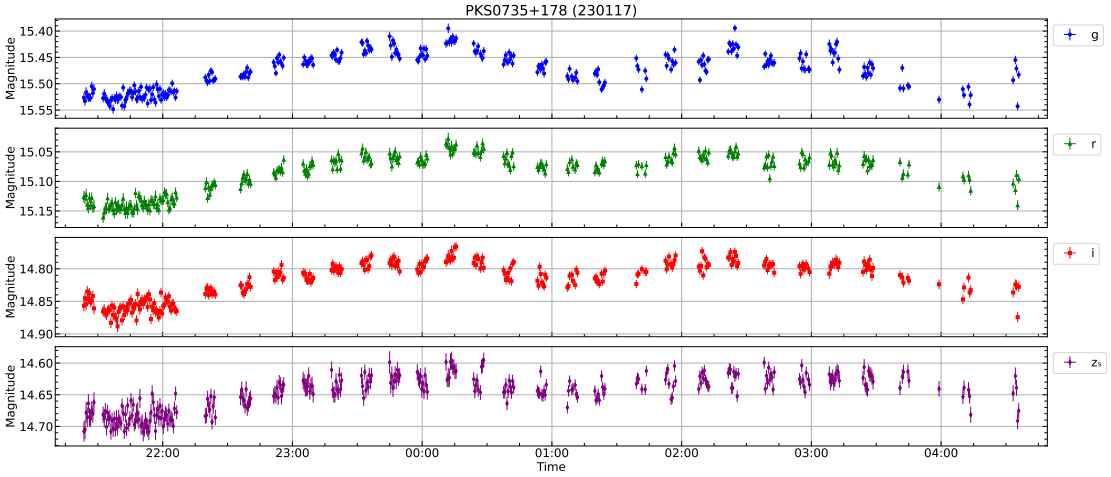

FIGURE 5.3: As Figure 5.1, but for PKS 0735+178 on the night of 2023 January 17.

TABLE 5.2: Colour variability statistics for variable sources on a given night. p and c refer to the Spearman rank correlation coefficients (significance and strength respectively), $F_{\rm enh}$ is the enhanced F-test value with the critical value as described in section 5.1.1.4, and the final column describes whether or not the colour of the source was deemed variable on the given night. If $p < 0.05$ and $F_{\rm enh} > F_{\rm crit}$ the source was deemed variable (V), otherwise not variable (NV).

Source	Date	p	c	$F_{\rm enh}$ ($F_{\rm crit}$)	Variable?
OJ287	2023 Jan 15	0.07	-0.12	0.88 (1.53)	NV
PKS 0735+178	2023 Jan 15	4.6×10^{-3}	0.33	4.66 (1.72)	V
...	2023 Jan 16	0.7	-0.08	1.84 (2.40)	NV
...	2023 Jan 17	3.9×10^{-10}	-0.35	3.13 (1.31)	V

5.1.2 Colour variability

Colour variability can be tested by investigating how the g-$z_{\rm s}$ colour changes with respect to r band magnitude and with time. The Spearman rank correlation coefficients is used to quantify the level of monotonic variability observed in each source on a given night. $\alpha = 0.05$ is set as the significance coefficient, p, implying a 95% confidence interval and one assigns the strength of the correlation, c, by the ranges specified in Table 2.8. The enhanced F-test is also utilised to account for the variability of the reference stars as previously described.

The Spearman rank correlation coefficients and enhanced F-test values for each set of g-$z_{\rm s}$ vs. r data are shown in Table 5.2 (full table for all epochs available in Table C.21 with the corresponding plots in Figure C.62 in the appendix). There are two epochs that show significant colour variability during observations; PKS 0735+178 on the nights of 2023 January 15 and 17. The former shows a positive correlation with a strength of 0.33, indicating a weak correlation. The positive nature of this correlation implies as the source gets brighter, it also gets redder in colour. Conversely, the latter date shows a negative correlation with a strength of 0.35, again indicating a weak correlation, although the negative nature this time indicates as the source gets brighter it also gets bluer.

The SED variability of each source on a given night can be seen by calculating the gradient of a straight line fitted through the g, i, and $z_{\rm s}$ band magnitudes at each epoch, and correlating it against the corresponding r band magnitude. These plots are shown in Figure 5.4 where Spearman rank correlation coefficients and significance values are given above each plot. The results align very closely with what is seen in the colour-magnitude diagrams in Figure C.62, showing the same significance values for each source with very similar correlation strengths.

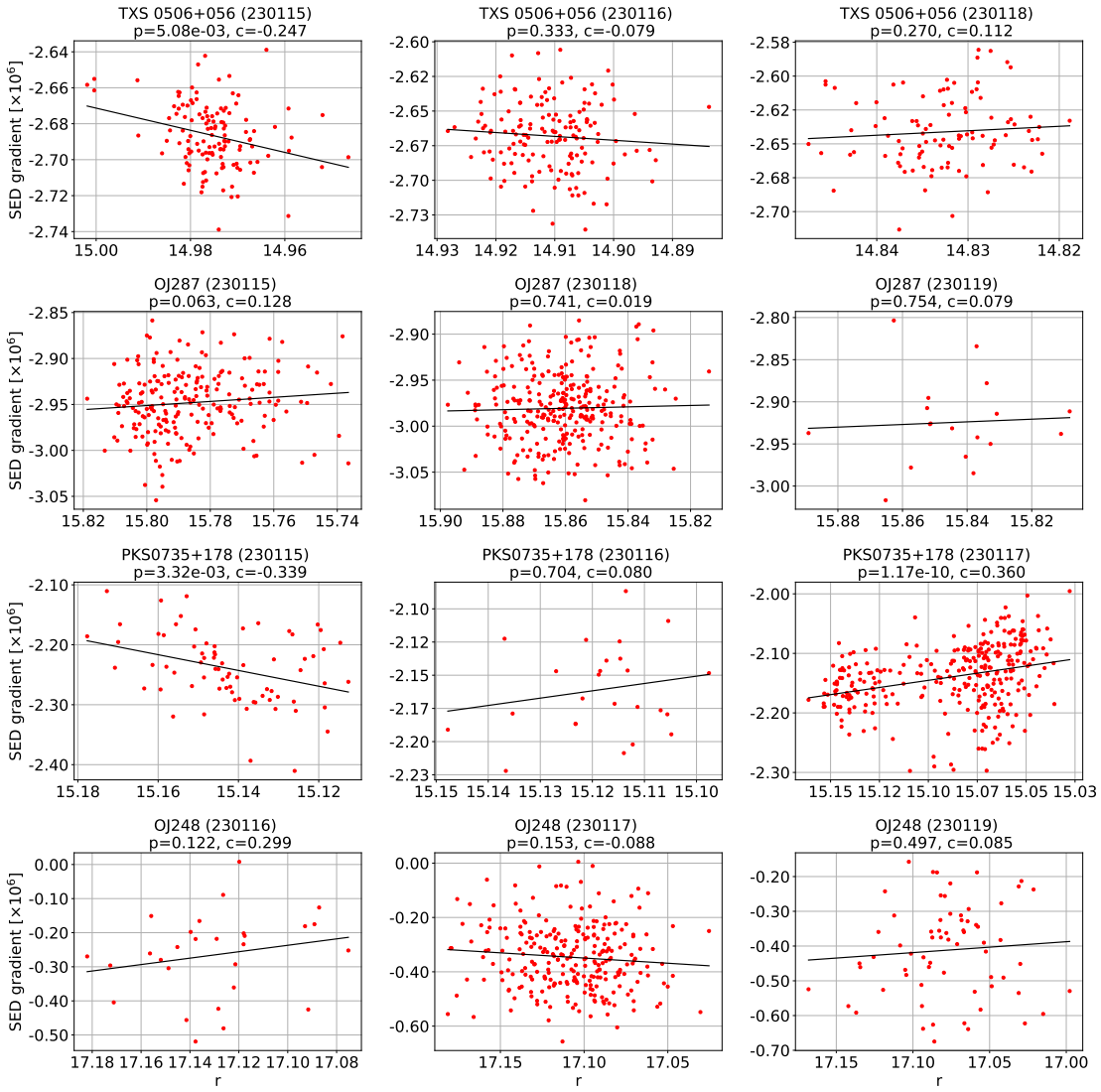

FIGURE 5.4: SED gradient using g, i, and z_s band magnitudes against r band magnitude for each of the four blazars (different rows) on different nights (different columns) as indicated above each plot. Spearman rank correlation coefficients and significance values are also shown above each plot.

5.1.3 Time lag analysis

Time lag between $griz_s$ bands can be tested for on the nights where sources show statistically significant variability. An intra-band time lag would be indicative of the evolution of the energy density within the relativistic jet, as is predicted by synchrotron cooling of accelerated electrons; higher energy electrons cool faster than lower energy electrons (Fiorucci et al., 2004). Observing such variability would allow one to rule out processes such as Doppler factor variability of emitting regions spiralling through the jet, in favour of those involving the acceleration and cooling of electrons (i.e. shocks). The variability

must occur over timescales less than the duration of the observations (minima and maxima within the lightcurves), which allows us to match up light curve features between bands and test for intra-band lags. Only one source and night fit these criteria, PKS 0735+178 on 2023 January 17. To perform the lag analysis, the Discrete Correlation Function (DCF) was used, which provides an estimate for the time lag between two unevenly sampled time series without the need for interpolation, while accounting for the effects of correlated errors (Edelson & Krolik, 1988). It is defined by

$$\mathrm{UDCF}_{ij} = \frac{(x_i - \langle x \rangle)\,(y_j - \langle y \rangle)}{\sqrt{(\sigma_x^2 - \langle \Delta x \rangle^2)\,(\sigma_y^2 - \langle \Delta y \rangle^2)}}, \tag{5.12}$$

where (x_i, y_j) are the observations, $(\langle x \rangle, \langle y \rangle)$ are the mean value from each light curve, (σ_x, σ_y) are the standard deviation of each light curve, and $(\langle \Delta x \rangle, \langle \Delta y \rangle)$ are the median error values (Liodakis et al., 2018). To find the DCF value associated with each time shift, τ, one averages over the number of (x_i, y_j) pairs, N, where $\tau - \frac{\Delta\tau}{2} < \Delta t_{ij} < \tau + \frac{\Delta\tau}{2}$ or in this case, the mean UDCF_{ij} value

$$\mathrm{DCF}(\tau) = \frac{\sum \mathrm{UDCF}_{ij}}{N} = \langle \mathrm{UDCF}_{ij} \rangle. \tag{5.13}$$

What also sets the DCF apart from other correlation methods is that a standard error on $\mathrm{DCF}(\tau)$ can be given by

$$\Delta\mathrm{DCF}(\tau) = \frac{1}{N-1}\left(\sqrt{\sum \left(\mathrm{UDCF}_{ij} - \mathrm{DCF}(\tau)\right)^2}\right), \tag{5.14}$$

assuming the individual $\mathrm{UDCF}_{\mathrm{ij}}$ values within a bin are uncorrelated.

Lags are tested for within a ± 60 min period. This period was chosen to capture any lags of order minutes in the data. The data spanned 7.24 hours, but due to the observing gaps, only 2.6 hours of on-source data were obtained. A lag of order hours was therefore deemed unlikely to be detectable or physically meaningful. While analysing the data using the DCF, its limitations in accounting for regularly unevenly sampled data became apparent. The data consists of an observing sequence over roughly 5 minutes before an approximately 10 minute break whilst observing a second target. When performing the DCF, this periodically resulted in a large decrease in the number of overlapping bins, zero in some instances, within $\frac{\Delta\tau}{2}$. This is seen in the correlation curves (Figure 5.5) as periodic peaks and drops in the coefficient values.

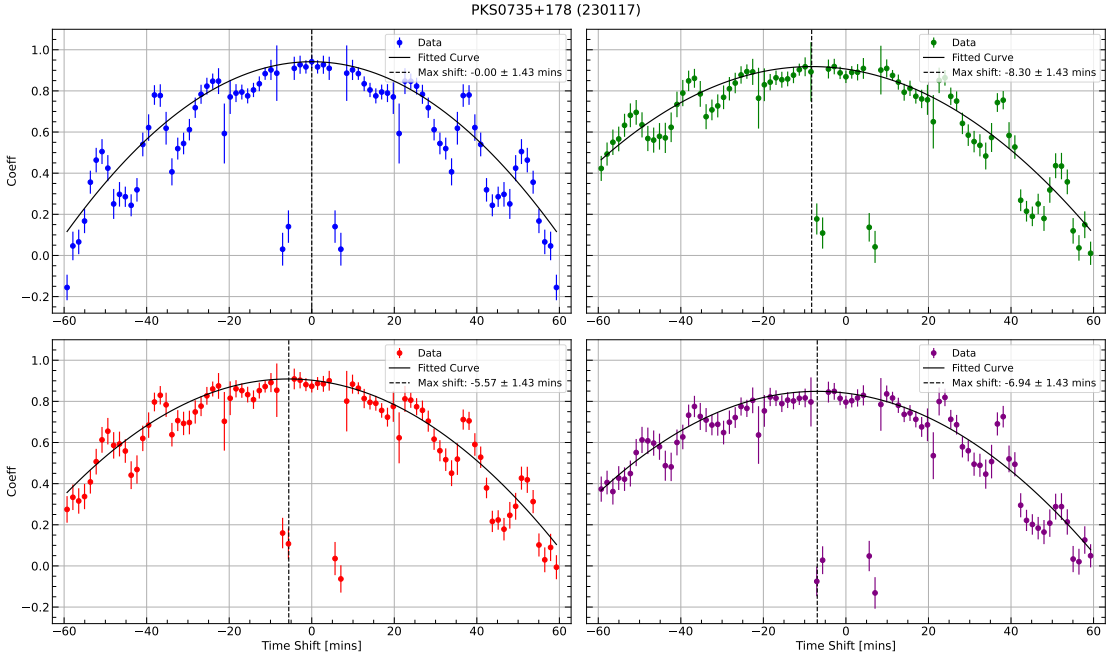

FIGURE 5.5: DCF coefficients testing for a lag on the data from PKS 0735+178 on the night of 2023 January 17. The coefficients (blue, green, red, and purple points for filters g, r, i, z_s respectively) are fitted with a Gaussian (black line) to find the peak. This peak value (vertical dotted line) is shown in the legend with an uncertainty.

Figure 5.5 shows the results of the DCF on the data from PKS 0735+178 on the night of 2023 January 17 on each $griz_s$ light curve with respect to the g light curve. In this configuration, a positive lag implies g leading the other bands and a negative lag implies g lagging the other bands. The solid curve shows a Gaussian fit to the DCF correlation values, calculated to offset the structure induced by the periodic number of overlapping bins. The dotted line shows the peak of the Gaussian curve, and therefore the lag value. It shows a significant non-zero lag in each riz_s light curve with respect to g. Between the three bands, the lags are all consistent, with a mean value of -6.94 ± 1.43 minutes. The uncertainty of 1.43 minutes is the average cadence of the observations and was chosen as the larger value of average cadence and error on the Gaussian peak.

In order to check the significance of the induced correlation curve structure, and to mitigate the scatter in the light curves, the DCF was also calculated after fitting a curve to the data. Each light curve is fitted using the GAUSSIANPROCESSREGRESSOR module from SCIKIT-LEARN in Python (Pedregosa et al., 2011a) using the Rational Quadratic kernel. Calculating the DCF on this fitted curve and following the same steps as outlined previously, one obtains the results shown in Figure 5.6. The uncertainties are kept the same (1.43 minutes) to reflect the original data cadence. The results for g and i are

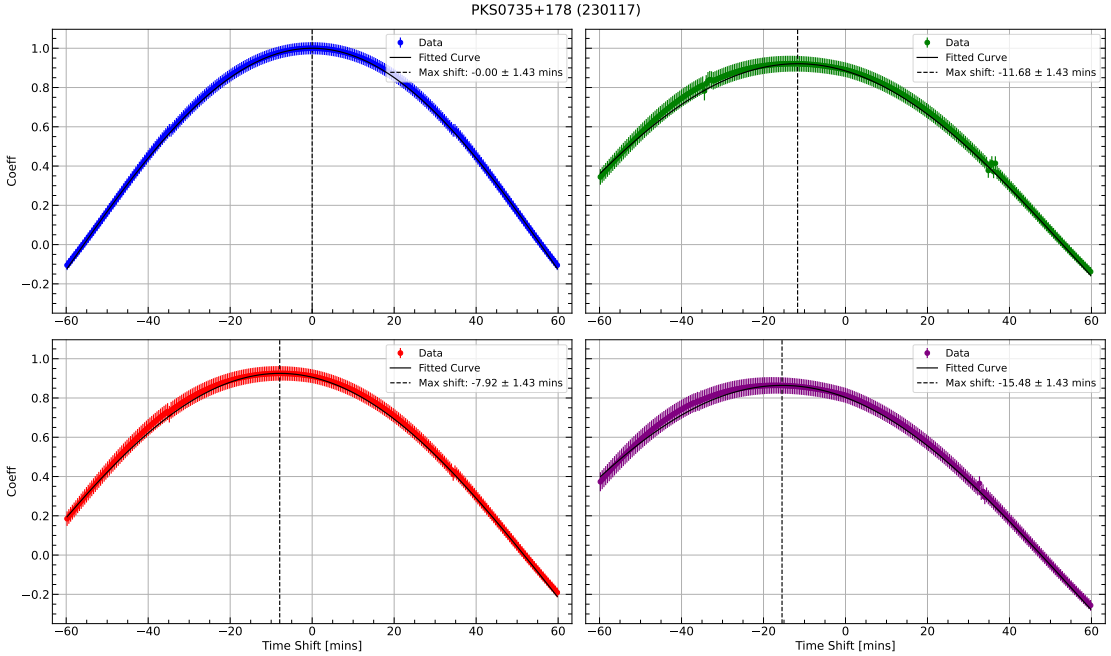

FIGURE 5.6: As Figure 5.5 but with the fitted data from PKS 0735+178 on the night of 2023 January 17.

consistent with the values obtained previously, but the lags obtained in r and z_s are significantly larger at -11.68 ± 1.43 minutes and -15.48 ± 1.43 minutes, respectively.

5.1.4 Discussion

Blazar intranight variability is thought to arise from geometric changes within the blazar jet; such as the Doppler factor variability of an emitting region travelling in a helical motion in the jet (Bachev et al., 2023), from the evolution of an emitting region through the jet (Gopal-Krishna & Wiita, 1992) or from the acceleration/cooling of particles (Bachev et al., 2012; Bachev, 2015). Additionally, it is entirely possible for the observed behaviour to be a combination of multiple emitting regions or different processes occurring simultaneously.

The mechanism behind Doppler factor variability involves an emitting region, or "blob", of density inhomogeneity travelling helically along the jet. This causes quasi-periodic oscillations (QPOs) in the light curve resulting from the apparent changing Doppler factor and subsequent bulk Lorentz factor (Camenzind & Krockenberger, 1992; Mohan & Mangalam, 2015; Bachev et al., 2023). On intranight timescales, this behaviour would present across the optical regime as multiple brightness peaks, depending on the number

of blobs, where individual peaks would be observed with no colour changes or time lags (Papadakis et al., 2004; Bachev, 2015). If the origin of the variability was many emitting blobs, each with differing SEDs, then one might expect the emission of different blobs to dominate at different times and subsequently cause rapid colour changes in addition to the brightness changes (Bachev et al., 2023). This variability, however, is a relativistic effect rather than any change in the emission output of the source.

Changes in the intrinsic luminosity of the source on intranight timescales can be attributed to processes such as shocks or magnetic reconnection in the jet. These processes involve a uniform injection of fresh, more energetic electrons which evolve as a function of their energy distribution, where harder electrons cool faster (Urry et al., 1997). This may produce intra- and inter-band time lags, which can determine cooling times and constrain the homogeneous synchrotron model (Tavecchio et al., 1998). An evolving energy distribution may also produce colour variability (Papadakis et al., 2004). Additionally, emission at optical frequencies can trace slightly different parts of the SED depending on the location of the synchrotron peak. For LSP sources (three of the sources), optical frequencies trace the falling region of the synchrotron peak which means redder frequencies map higher-energy emission and may produce faster-evolving variability, causing colour variability and time lags between wavebands. Conversely, for HSP blazars, optical frequencies trace the rising part of the SED so one would expect the bluer frequencies to evolve faster (Subbu Ulaganatha Pandian et al., 2022).

In this work, TXS 0506+056 and OJ248 showed no evidence of variability in the epochs studied. OJ248 is the faintest object in the sample and would have benefitted from longer exposure times for better signal-to-noise had the autoguider on the TCS been available. TXS 0506+056 showed significant, weak, colour variability on 2023 January 15, which may be due to the scatter in the data.

OJ287 showed evidence of significant flux variability on the night of 2023 January 15, but no significant changes in colour. There are no significant short-timescale features in the light curve, and the observed variability consists of a gradual decrease in the brightness over the roughly 6 hours of observing.

PKS 0735+178 displayed significant variability on two out of three nights, including significant colour correlations showing both redder-when-brighter and bluer-when-brighter

behaviour. Additionally, on the night when BWB colour variability was observed, a hard-lag of order 10 minutes was detected.

If the hard-lags observed in PKS 0735+178 are caused by the evolution of the electron energy distribution, different shock-in-jet processes can be examined to explain the variability. When the shock-accelerated population of electrons are given sufficient time to cool, the cooling timescales will be much longer than the acceleration timescales such that $t_{\rm acc} \ll t_{\rm cool}$. In this case, one may expect to observe a soft-lag where the higher-energy electrons show variability before the lower-energy electrons as a result of synchrotron cooling. Conversely, when the cooling timescale is comparable to the acceleration timescale, such that $t_{\rm acc} \approx t_{\rm cool}$, then the opposite (i.e. a hard-lag) may be observed (Zhang et al., 2002). In order to achieve this hard-lag, and produce comparable acceleration and cooling timescales, an energy injection is required to accelerate electrons after the shock has passed, rather than allowing the shocked particles to cool, which results in soft lags (Mastichiadis & Moraitis, 2008). Injecting energy into the post-shocked medium can be achieved using second-order Fermi acceleration processes. Kalita et al. (2023) describe how turbulent magnetic fields built behind a shock travelling through an inhomogeneous medium can produce these processes, resulting in the acceleration of the post-shock particles via magnetic reconnection. In this scenario, energy is released to the surrounding particles through the interaction of magnetic field lines with opposite polarity.

While a firm conclusion cannot be made as to the nature of the detected INOV in PKS 0735+178, the detection of a hard-lag favours changes to the electron energy distributions and the internal shock model over any geometric changes. It is also important to consider that the detected lag is around the same timescales as the break in observing cadence. While it is unlikely the sampling gaps could have caused the lag, given it's presence in the fitted and unfitted DCF curves, they will have had an impact on the value of the detected lag (i.e. the lag for each waveband could change slightly if a more regularly sampled dataset was obtained).

5.1.5 Conclusions

Simultaneous $g, r, i, z_{\rm s}$ photometric observations were performed using MuSCAT2 on the Carlos Sánchez Telescope to study the intranight optical variability of four γ-ray bright

blazars. The analysis consisted of employing several statistical methods to test for the presence of variability on timescales of a few hours. Additionally, the DCF was used to test for intra-band time lags between bands r, i, and z_s with respect to band g. The results show:

- TXS 0506+056 and OJ248 showed no evidence for intranight variability on any night.
- OJ287 showed evidence for intranight variability on 2023 January 15. The nature of this variability was a gradual change, around 0.1 magnitudes over 7 hours, and was not accompanied by any significant changes in colour.
- PKS 0735+178 showed evidence for intranight variability on two occasions along with changes in colour; showing both a redder-when-brighter and a bluer-when-brighter correlation on different dates.
- PKS 0735+178 showed a time lag where the g band lags the r, i, z_s bands by around 10 minutes. This suggests the variability may arise from changes in the electron energy-density distribution. It is possible that the observing cadence has had an effect on the fitting of the light curves causing the lag values to not progress in order of waveband.

Further observations of blazars during all activity states at high cadences can confirm whether intra-band hard-lags across optical frequencies are a more common feature than previously thought. This would provide strong evidence for changes in the jet's energy density as the cause for INOV in blazars.

Chapter 6

Conclusions

6.1 Thesis summary

This chapter will summarise the results and discussions detailed across Chapters 2, 3, 4, and 5 while relating to the theoretical and observational models and mechanisms explored in Chapter 1. This will include a summary of the production and maintenance of various reduction and analytical pipelines, and the results of both long-term and intranight multiwaveband photo-polarimetric blazar monitoring campaigns.

Future work will be detailed and contextualised through the potential significance of the work presented in this thesis.

6.1.1 Data calibration and reduction results

Reduction pipelines were created to calibrate the blazar data obtained by the RINGO3 polarimeter from 2013 to 2019 and the MOPTOP polarimeter from 2020 to the present. While adaptations to each pipeline were implemented, standard differential photometry techniques underpinned both pipelines using Python and the ASTROPY package (Bradley, 2023).

The main challenge arising from the RINGO3 calibration process resulted from non-standard wavebands and the need for inframe reference stars to calibrate flux/magnitude. To overcome this, a method was devised to calculate zero points for each RINGO3 camera, calculated and averaged over many epochs by calibrating for the telescope mirror

degradation. The mirror degradation was calculated using the LT archive's vast sample of polarisation standards, while the zero points were found using archived A0 star observations. Calibrating the inframe reference star to the same degradation epoch as the zero points and averaging over many observation epochs resulted in reference magnitudes that could be used to calibrate the photometric data obtained with RINGO3.

At the start of this PhD and work presented in this thesis, the MOPTOP polarimeter was still in its commissioning phase, meaning the characteristics of the instrument were not yet fully understood. In addition to producing a robust and effective reduction pipeline expanding on the work presented in Shrestha et al. (2020), it was necessary to determine the polarimetric coefficients required to calibrate any data taken with the instrument. This was achieved through the monitoring of polarised and zero-polarised objects, and by reducing this data through an additional Python pipeline created as a part of this work. Throughout this PhD, numerous developments to the pipeline were made. These included automating the process of stacking any required frames, differentiating between single and dual camera operations and reducing with appropriate respective techniques, integrating an API (application programming interface) to download the latest data from the archive, accounting for and correcting poor or unfitted WCS coordinates, and optimising the signal-to-noise in each frame through determining the optimum aperture size.

The 180° ambiguity associated with measurements of EVPA makes its interpretation difficult. A process was developed in this work to minimise the need for manual manipulation of the data, accounting for cadence irregularities and EVPA uncertainties. This method was unique in that it computed a weighted average, with weights defined by the uncertainties on the data, before adjusting points by ±180° where necessary to minimise the difference between subsequent data to be less than 90°.

Since their creation during this PhD, the RINGO3 and MOPTOP pipelines and calibration procedures have contributed significantly to both the field of blazar science and other photo-polarimetric studies. Contributions include Komossa et al. (2022); Steele et al. (2023); Valtonen et al. (2023); Bernardes et al. (2024a,b); Liodakis et al. (2024); Koljonen et al. (2024); Kravtsov et al. (2024); Kouch et al. (2024); Liodakis et al. (2024); Jormanainen et al. (2025); Shrestha et al. (2025); Agudo et al. (2025); Liodakis et al. (2025) with several additional submitted works pending peer review or in preparation.

An additional photometric reduction pipeline was produced for the reduction of data obtained by MuSCAT2 during an intranight monitoring campaign in January 2023. This pipeline consisted of the same techniques employed for the RINGO3 and MOPTOP pipelines while fitting a WCS to the frames through the ASTROMETRY.NET API (Lang et al., 2010).

6.1.2 Photometric results

Photometric correlations were explored within the optical waveband and between optical and γ-ray frequencies. Long-term correlated optical and γ-ray flux emission was apparent in the majority of sources in both the RINGO3 and MOPTOP samples. In the RINGO3 sample, with its larger sample of sources, the proportion of sources significantly correlated seemed to increase with decreasing synchrotron peak frequency. In other words, a higher proportion of low synchrotron peak sources (FSRQs and LBLs) showed significantly correlated optical–γ-ray flux behaviour than intermediate synchrotron peak sources (IBLs), which in turn showed a higher proportion of significantly correlated sources than that of high synchrotron peak sources (HBLs). It is interesting to note those sources with high synchrotron peaks are most often associated with resolvable host galaxies contributing significantly to the blazar composite spectrum (Prandini & Ghisellini, 2022). Quenching of the blazar variability could therefore be expected, which would make variability at optical frequencies less apparent without host-galaxy subtraction. Given the majority of sources showed significant long-term correlations between optical and γ-ray flux, these results generally indicate that emission originating from a leptonic particle population is more prevalent in blazar jets than that of hadronic particles. However, that is not to say no evidence for hadronic emission was detected. This work produced a detailed breakdown of optical vs. γ-ray flux by source classification. It was shown that LSP objects (FSRQs and BL Lacs) show more scatter in the flux-flux space compared to ISP or HSP objects. This is likely evidence for EC emission over SSC (Hovatta et al., 2014) but also for an additional high-energy emission mechanism, uncorrelated to the optical synchrotron emission (i.e. hadronic emission). It was also shown that FSRQs are generally brighter at γ-ray frequencies than BL Lacs but comparatively fainter at optical frequencies. This trend remained consistent when accounting for the source redshifts.

A comparison between the computation of colour and spectral index (magnitude difference and optical spectrum fitting, respectively) was performed, where it was found that the spectral index was a more informative metric when analysing blazar colour evolution. The main reason for this was the discovery of non-linear relationships in the spectral index vs. magnitude behaviour. Such trends were much more subtle when using the colour index, and not possible to detect. Logarithmic spectral evolution trends were found in numerous sources, implying a stabilisation in the spectral (colour) variability during periods of heightened optical activity. Fits to the data were tried both linearly and logarithmically, each allowing for two free parameters (one multiplicative and one additive), before quantifying the quality of the fit using Akaike Information Criterion (Akaike, 1974) and Bayesian Information Criterion (Schwarz, 1978). Logarithmic trends were observed across all source classifications, following both bluer- and redder-when-brighter trends. Such trends were given the names bluer-stable-when-brighter (BSWB) and redder-stable-when-brighter (RSWB), respectively. These trends indicated that as the levels of photometric activity increased, the colour of the source became bluer/redder but at a continuously slowing rate (i.e. at the highest levels of flux barely any colour changes were detected). It is possible that where such behaviour was not observed in individual sources, distinct photometric activity states were not sufficiently observed either systematically due to cadence or physically due to source behaviour. Missing activity states in the data would make it difficult to determine a logarithmic trend from a linear one. Non-linear trends are indicative of two-component emission, with a variable, underlying thermal component and a variable non-thermal synchrotron component (Zhang et al., 2022a). This is further supported when looking at the trends observed by different classes of blazar. The RWB/RSWB trend was observed only in FSRQs, while BWB/BSWB was observed across both FSRQs and BL Lacs. This can be explained by an additional thermal contribution in FSRQs over BL Lacs, flattening the optical region of the quiescent composite spectrum. During flaring, the spectrum steepens in FSRQs rather than flattens as in BL Lacs. This could imply a physical difference between the classes; additional or more efficient accretion in FSRQs.

To assess the mechanisms and locations of the observed emission, the optical spectral variability was tested against the γ-ray flux. Any correlation would suggest the higher γ-ray energy emission was related to the optical spectral variability, alluding the to synchrotron nature of the emissions; synchrotron-self Compton (SSC; Maraschi et al., 1992)

or external Compton (EC; Dermer & Schlickeiser, 1993) processes. Significant trends were observed in the majority of sources, with sources again displaying the high flux stable (logarithmic) behaviour. The RWB/RSWB feature was detected predominately in FSRQ objects, and trends across all metrics were compared to determine the likely emission mechanism behind the variability. Combining the results/trends observed across the MWL photometric and optical spectral data, a particle population dominated by leptons was deemed most likely and responsible for most of the observed variability. This was determined by the number of observed trends suggestive of leptonically dominated emission, either SSC or EC.

The temporal separation between optical and γ-ray emission (inter-band time lags) was tested using the discrete correlation function (Edelson & Krolik, 1988). Long-term inter-band photometric time lags were not as apparent in the data as some of the other metrics, with no significant detections during the RINGO3 campaign. However, lags for two sources, PG 1553+113 and PKS 1510-089, were found in the MOPTOP data and were consistent with the lags deemed insignificant observed with RINGO3. These lags were approximately 21 days and 41 days, respectively, with the higher energy γ-ray emission leading the optical. Lags of this duration correspond to distances of 10^{14-15} m, consistent with the distance from the central engine (approximately the acceleration zone) and the broad-line region. These in turn support the presence of significant, likely reoccurring (on account of the trends observed over long timescales) EC emission in these sources. Correlated optical and γ-ray behaviour with no temporal separation is indicative of a radiatively efficient SSC emitting particle population (Böttcher & Dermer, 2010; Cohen et al., 2014; Liodakis et al., 2018). Temporally distinct flaring episodes where higher- and lower-energy behaviour are observed separately (i.e. orphan flaring) have not yet been tested for in the RINGO3 and MOPTOP data, but would be an informative metric to test for hadronic emission episodes.

6.1.3 Polarimetric results

The observed optical linear polarisation was tested for correlations against the photometric values (optical and γ-ray flux) to quantify the strength of any polarisation–flux relationships. Significant correlated and anti-correlated trends were observed between polarisation and both the optical magnitude and γ-ray flux across the RINGO3 and

MOPTOP samples. Trends were apparent in a higher proportion of FSRQ objects than BL Lacs, including that of LSP BL Lacs. The direction of the trend (i.e. polarised-when-brighter or polarised-when-fainter) did not appear unique to any classes or subclasses within the sample. Correlated optical, γ-ray and polarised emission are indicative of a leptonic particle population and ordering of the magnetic field within the emitting region. This behaviour is predicted through shocks within the relativistic jets (Zhang et al., 2016; Liodakis et al., 2022b) and so one can conclude that in a large number of sources, this mechanism is the main driver of the observed variability. However, numerous sources showed long-term anti-correlated photo-polarimetric behaviour was observed; that is repeated MWL photometric flaring in temporal coincidence with decreased polarisation emission. Such behaviour has been predicted as kink instabilities within the jet (Dong et al., 2020), whereby plasma instabilities cause disruption to the magnetic field ordering, reducing polarisation.

The frequency dependence of polarisation is suggested to be a signature of the variability of particle energy distributions within blazar jets, and as such can be a valuable observable to distinguish emission mechanisms. It is however difficult to detect across the optical regime given its small width within the wider electromagnetic spectrum, and the requirement of high cadence, low uncertainty polarimetric data. Long-term frequency-dependent polarisation trends were observed in a small number of sources. The results across both campaigns show the majority of objects indicating such behaviour are LSP sources (FSRQs and BL Lacs), and that all classes of objects show both bluer- and redder-when-brighter polarisation trends. It was noted that while frequency-dependent polarisation trends could therefore be an intrinsic characteristic of LSP sources, these objects also display more polarisation variability generally so it may be that it is just easier to detect in these sources. The most probable mechanism behind changes to a region's particle energy distribution is the acceleration and cooling periods expected around shocks. While both BWB and RWB polarisation variability trends are indicative of the shock-in-jet model (Angelakis et al., 2016; Liodakis et al., 2022b), redder-when-brighter polarisation variability requires an additional energy injection into the shocked medium to reverse the bluer-when-brighter trend. Such injection is possible during second-order Fermi acceleration processes, namely magnetic reconnection (Begelman, 1998; Zhang et al., 2022b; Kalita et al., 2023).

Optical EVPA rotations were observed across numerous sources, spanning all classes and

subclasses. This work produced a detailed breakdown of the photo-polarimetric states associated with each rotation. It was found that the majority of rotations occurred during high states across optical and γ-ray frequencies, indicating a clear preference for EVPA rotations to occur during photometric flares. Furthermore, it was found that rotations occurred irrespective of polarimetric state (i.e. rotations were observed during high and low polarisation states). However, it is the differences in the polarisation states that allow one to determine the likely mechanisms behind the rotations. Simultaneously heightened photopolarimetric activity is likely the result of shock propagation through the jet and subsequent cooling of particles (Zhang et al., 2014; Liodakis et al., 2022b). It has been predicted that for a relatively fast-moving magnetised region passing through a helical magnetic field, one could observe many EVPA rotations separated by a plateau phase, where the larger magnetic field restores itself following perturbation (Zhang et al., 2016). MWL photometric quasi-periodic oscillations inversely correlated with polarisation could be associated with kink instabilities within the relativistic jet and are likely responsible for large EVPA rotations. While it is not certain what would cause the decrease in polarisation, it could be due to the emission of non-polarised thermal photons at the kinked region (Dong et al., 2020). Recent works have also suggested that kink instabilities may be responsible for the formation of shocks at the kinked region and the production of helical magnetic fields within the relativistic jets (Acharya et al., 2021, 2023). It is also important to consider that a significant proportion of rotations could be the result of stochastic variability within the jet (Marscher & Jorstad, 2021).

The supermassive binary black hole blazar candidate OJ287 was predicted to enter a flaring state during the RINGO3 monitoring campaign. This state was to be one of a pair of outburst phases within a 12 year cycle, arising from the impact of the secondary black hole with the primary's accretion disk. During this event, the observation cadence was increased to better sample the expected photopolarimetric variability. These observations sampled two flares during the outburst roughly 19 days apart. The first flare was found to be consistent with multi-wavelength emission arising from thermal bremsstrahlung processes. This was due to a lack of any correlation between optical flux and polarisation, implying an initial increase in non-polarised emission during the flare. The optical and γ-ray emission were also very strongly correlated, implying little to no temporal separation. The lack of any colour correlations with the photometric values suggests a lack of jet emission during this flare, also supporting the emission's origin

as the accretion disk. The second flare showed strongly correlated behaviour between the optical flux and polarisation, consistent with a synchrotron (jet) origin. This is supported by the presence of a bluer-when-brighter colour change when considering the optical flux. Unlike the first flare, this one did not coincide with any changes in γ-ray activity. This data was combined with additional multi-frequency photo-polarimetric observations by Jormanainen et al. (2025), producing a more complete picture of the outburst. It was shown that the impact event and subsequent variability are indicative of the formation of a knot and its movement around a helical magnetic field within the relativistic jet (Myserlis et al., 2018).

6.1.4 Intranight variability results

The most significant takeaway from the intranight monitoring campaign conducted in January 2023 was the detection of an intranight hard lag in the optical data of γ-ray flaring blazar PKS 0735+178. This result implies a temporal separation between the lower- and higher-energy (leading and lagging, respectively) emission. A hard lag of this nature is likely the result of changes to the particle energy distribution with the jet (i.e. the energy output of the jet was higher during the observing campaign) rather than any geometric effects, such as the passage of blob/emitting region through a helical magnetic field and subsequent Doppler boosting variability. Specifically, the trend is suggestive of second-order Fermi acceleration processes preventing the cooling of a post-shocked medium in the relativistic jet; magnetic reconnection (Mastichiadis & Moraitis, 2008; Zhang et al., 2002).

Several epochs of significant intranight variability were detected across the sample. The significance of variable behaviour was determined by using several statistical tests, resulting in statistically variable intranight light curves for OJ287 and PKS 0735+178. The tests employed included variability amplitude (Heidt & Wagner, 1996), fraction variability (Schleicher et al., 2019), chi-squared (Zeng et al., 2017), and the enhanced F test (De Diego, 2014). Furthermore, weak colour trends were observed in both PKS 0735+178 variable lightcurves, one redder-when-brighter and the other bluer-when-brighter. PKS 0735+178 is an intermediate synchrotron peaked BL Lac type object so the redder-when-brighter trend detected is unusual given this is a characteristic of some FSRQs rather than BL Lacs on account of additional thermal emission. Despite this, the result

supports the two-component modelling of composite blazar spectra, with an underlying thermal component and variable non-thermal (synchrotron) component. The bluer-when-brighter trend occurred on the same night as the hard lag. Assuming again the two-component spectral scenario, this is intuitive. If the hard lag were a result of an increase in the jet's particle energy distribution, one would expect an increase in the non-thermal emission relative to the thermal, flattening the composite spectrum in the optical regime and thus making the object appear bluer during the increased flux.

6.2 Future work

This section will present some discussion on additional observations obtained during this PhD, and assess the initial feasibility of novel analysis techniques that have been developed in this work. These data and methods could be used to provide further insight into the questions addressed in the thesis.

6.2.1 Ultra-high cadence blazar observations with HiPERCAM on GTC

As discussed in Section 1.5.5 and Chapter 5, blazars show variability on a variety of timescales, from years to minutes. The minute–hour timescale intranight optical variability (INOV) has been the focus of numerous campaigns over the past 30 years (Miller et al., 1989; Sagar et al., 2004; Negi et al., 2022), but is still not well understood. Many models propose to explain the different levels of variability observed over the approximately hour-long time scales which predict time lags between different wavebands, colour evolution, and polarisation degree and angle changes. These include geometric changes related to the jet angle and Doppler factors of emitting blobs (Gopal-Krishna & Wiita, 1992), intrinsic changes relating to particle energy distributions (Bachev, 2015), and extrinsic changes including microlensing from objects outside the blazar system along our line of sight (Paczynski, 1996).

In early 2024, five hours of observations were awarded using the five-band simultaneous imager HiPERCAM on the 10.4 m Gran Telescopio Canarias (GTC) in La Palma. This time was executed during the night of 11/03/2024 to study the intranight optical

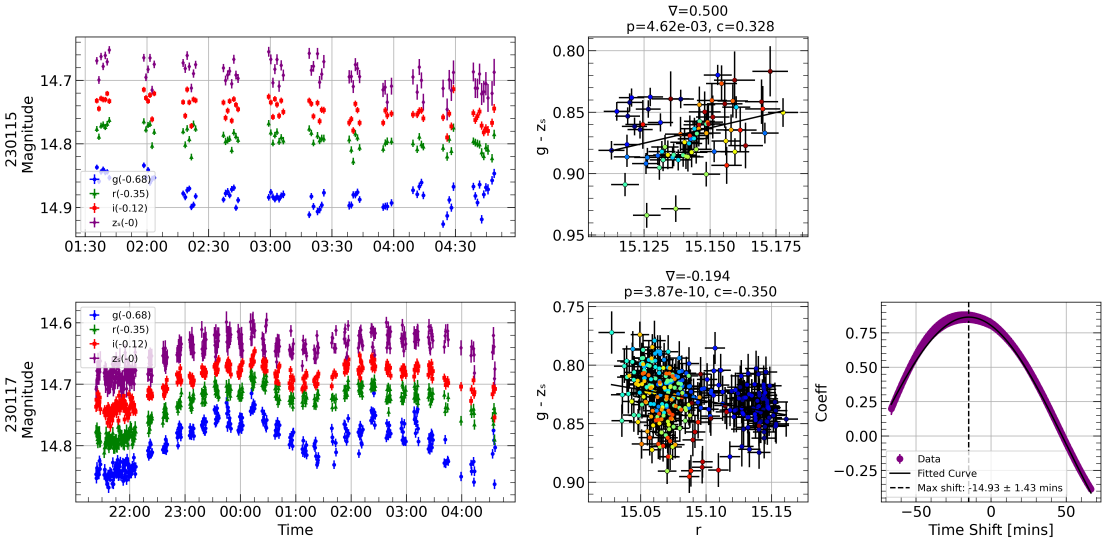

FIGURE 6.1: Plots showing the variability of PKS 0735+178 observed on 15/17 January 2023. Shown are the light curves and colour evolution (with correlation statistics) from each night. Additionally, a time lag analysis was performed on the data from the night of the 17th where a lag between the g and z_s bands was detected.

variability of blazar PKS0735+178 over a continuous five-hour period with ultra-high cadence; 7.60 seconds in u band, 3.04 seconds in g band, and 1.52 seconds in riz bands.

PKS 0735+178 is an ISP BL Lac type object (IBL), which may belong to a subclass of blazars named masquerading BL Lacs, or blue FSRQs (Padovani et al., 2019), where the Doppler-boosted synchrotron radiation in the relativistic jet is bright enough to outshine the broad line region thus making the FSRQ appear as a BL Lac object due to the apparent lack of emission lines. In 2021 December, PKS 0735+178 underwent its largest multiwavelength flaring event in spatial coincidence with several reported neutrino events (Savchenko et al., 2021; IceCube Collaboration, 2021).

Due to its highly variable nature, PKS 0735+178 was included in the sample of objects for an intranight observational campaign using MuSCAT2 on the Carlos Sánchez Telescope (TCS) in January 2023. These results were presented in Chapter 5. The high cadence, simultaneous multiwavelength data probed the colour evolution and the presence of intra-band time lags. Figure 6.1 shows results from this observing campaign: the upper row shows the light curve and colour evolution of the source on the night of 15 January 2023 and the lower row shows the light curve, colour evolution, and g, z_s lag analysis results from the night of 17 January 2023 (McCall et al., 2024a).

Although limited by SNR and the resultant achievable cadence, we found clear evidence

to suggest PKS 0735+178 showed different types of colour behaviour on each night and possible evidence of a roughly 15 minute time lag between the g and z_s bands. On the first night, the source showed redder-when-brighter (RWB) behaviour but on the second night, the source appeared to be bluer-when-brighter (BWB). BWB chromatism may arise from synchrotron cooling of internal shock accelerated electrons, where higher energy electrons cool faster, making bluer light appear more variable than redder light (Kirk et al., 1998). Alternatively, in a one-component synchrotron model, the increase in the energy output of the blazar increases the average particle energy and thus the frequency, making the blazar appear bluer-when-brighter (Fiorucci et al., 2004). When in faint states or periods of jet quiescence, redder emission and variability from the accretion disk may become visible, leading to RWB behaviour.

The possible time lag can also be used to constrain emissions processes. Time lags between x-ray or gamma-ray and optical have been observed in numerous studies (Liodakis et al., 2018), but inter-band lags within the optical waveband are much less commonly observed. The internal shock model predicts time lags across all synchrotron emission frequencies and therefore within the optical waveband, where the rate of synchrotron cooling is frequency-dependent. This means variability at higher energy should precede that at lower energies, producing a blue-leading intraband time lag (Kirk et al., 1998). In our observations with TCS we detect the opposite; a red-leading intraband time lag, something previously unseen across optical frequencies in the literature. To observe such a feature, observations are required in multiple optical wavebands at high cadence (i.e. minutes), requiring simultaneous, multi-optical-band imagers. While some INOV campaigns use such instruments (Wu et al., 2009), many do not (Sagar et al., 2004; Goyal et al., 2012; Negi et al., 2022). We find the uncertainty on the lag likelihood is strongly affected by the observing cadence and scatter in the light curves; a result of using a small telescope to carry out these observations.

Observations with HiPERCAM on GTC allowed us to probe PKS 0735+178 at a much higher cadence, while also lowering photometric uncertainties. Observations fully sampled the intranight variability of the target, constraining any colour changes and intraband time lags with higher statistical significance, while also allowing us to test for variability on much shorter timescales. The results would provide evidence for the causes of blazar intranight variability, such as geometric processes occurring within the

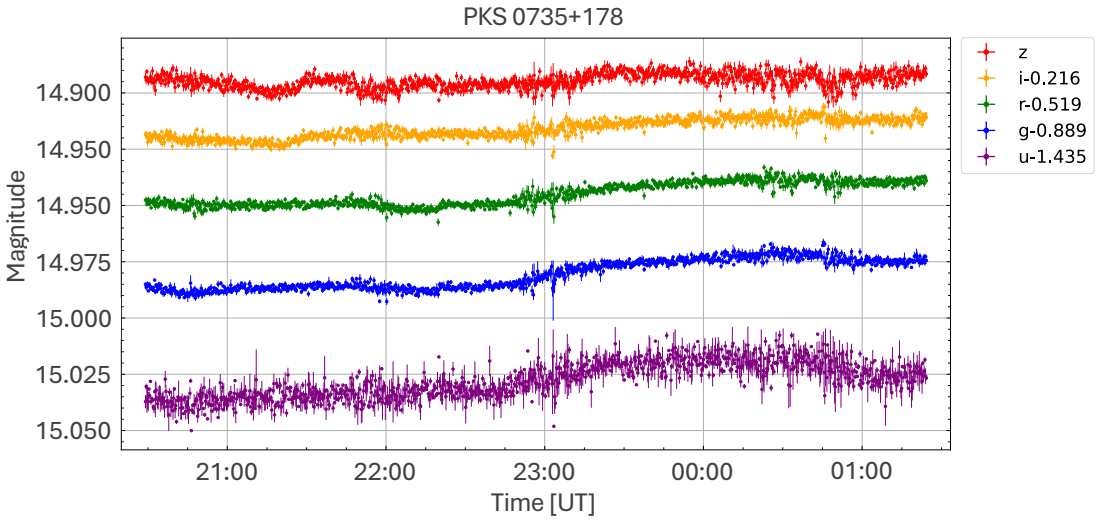

FIGURE 6.2: Preliminary light curve of the blazar PKS 0735+178 taken with the simultaneous imager HiPERCAM mounted on GTC. The data were resampled to achieve a 15.20 second cadence across each of the five wavebands.

jet (Doppler factor changes of emission regions), or intrinsic jet energy changes (shock-in-jet or other acceleration models). If the GTC observations confirmed the presence of a red-leading lag it would require a re-examination of emission models and processes and may point toward magnetic reconnection occurring in the jet.

The preliminary data reduction utilised the HiPERCAM reduction pipeline [1]. The data were first stitched to combine the four CCD images per exposure. Following this, the data were debiased, flat-fielded, and de-fringed using the built-in HiPERCAM pipeline functions. These fits files were then reduced using standard differential aperture photometry techniques explored in Chapter 2. No WCS coordinates were fitted to the data. Instead, the robust object tracking allowed one to specify approximate pixel coordinates before refinement through object detection.

A preliminary light curve consisting of data from all bands is shown in Figure 6.2. The data in this instance are resampled at a rate of twice the longest exposure time (2×7.60 seconds). This was to produce evenly sampled data which was consistent across wavebands, allowing for spectral analysis. This is presented in Figure 6.3 and shows strong evidence for significant BWB behaviour, indicating that strong spectral evolution is apparent over very short timescales.

[1] https://github.com/HiPERCAM/hipercam

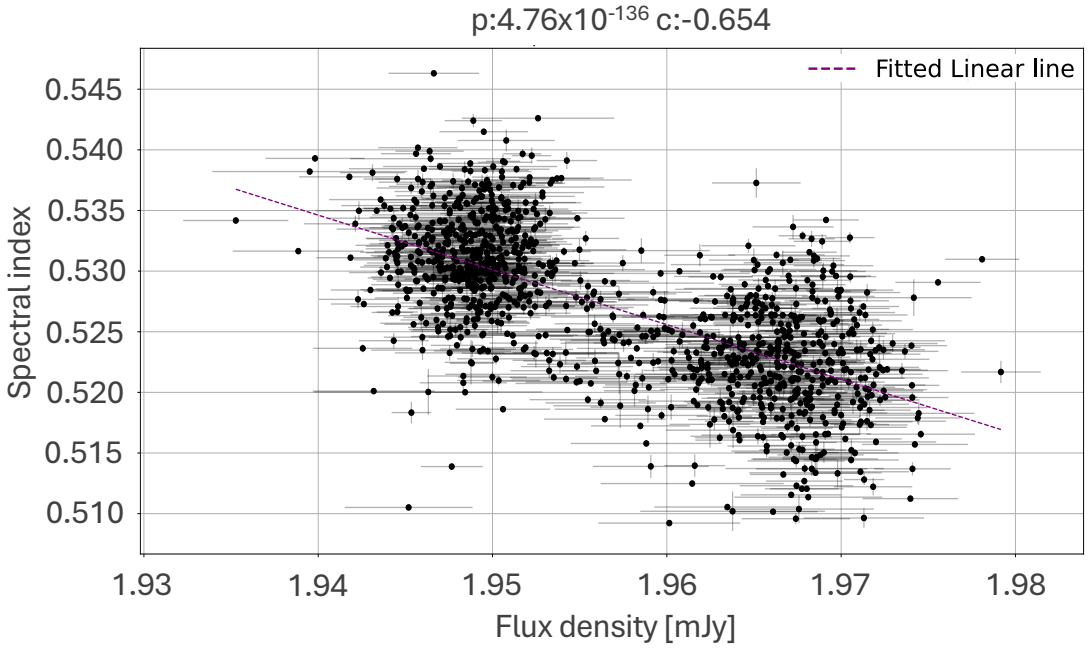

FIGURE 6.3: Preliminary spectral index vs. r-band flux of the blazar PKS 0735+178 taken with the simultaneous imager HiPERCAM mounted on GTC. The Spearman rank correlation coefficients on top of the figure indicate a strong BWB trend was observed over the 5-hour campaign.

While initial reduction and analysis have taken place, chosen processes and techniques must be scrutinised and refined to ensure the data is as accurate as possible. Firstly, given Figure 6.2 shows the z-band light curve to be the most variable, one must ensure the de-fringing has been adequately applied as this band is most affected. This should be possible to test by looking at example frames before and after the de-fringing step of the HIPERCAM reduction pipeline, but also by comparing the counts from r-band frames.

Furthermore, ensuring appropriately positioned and sized apertures is essential given the FWHM of the object on the CCD varies with the rapidly evolving sky conditions. While procedures were implemented into the reduction of the frames to fit an optimally sized aperture to the centre of the object, it must be checked that this does not deviate over time. If optimising the aperture size for the sky conditions in each frame, it would also be important to ensure no correlation between it and the magnitude of the source, likewise with the position of the source on the CCD.

The influence of variable seeing on the data should be mitigated by following the procedure outlined by McHardy et al. (2023). Any correlation between magnitude residuals

and the seeing variability could be used as a corrective factor on the light curve. This was required in their data on account of an anticorrelation between magnitude residuals and seeing, something that can be tested for in the data of PKS 0735+178.

6.2.2 Detecting EVPA rotations – A novel approach using Gaussian processing

Optical EVPA rotations are believed to occur as a result of changes to the relativistic jets' magnetic field structure (Zhang et al., 2016; Marscher & Jorstad, 2021) and can therefore provide valuable insight into the underlying mechanisms behind observed photo-polarimetric variability. EVPA rotations have been known to occur over a wide variety of sizes and timescales, making their automated detection very difficult using the current methodology. The results presented in Chapter 4 utilised the rotation detection procedure outlined in Blinov et al. (2015). Their definition was interpreted in this work to be three or more consecutive mono-directional swings in the EVPA totalling at least 90° and with each swing satisfying the condition $\Delta\theta > \sqrt{\sigma_{i+1}^2 + \sigma_i^2}$, where σ_{i+1} and σ_i are the associated errors of the EVPA measurements.

Low/irregular cadence can result in poorly sampled or entirely missed rotation events. The observed blazar flux at a given moment is made up of several emissions from different processes and regions, contributing to the composite spectrum at different ratios at different times. It is therefore possible that rotations may overlap or occur entirely within another, obscuring behaviour. Any unwrapping pipeline would need to account for this "intra-rotation" variability over a range of timescales, consisting of a generalised methodology which can be applied to all blazars with minimal personalisation and interpolation.

During this PhD, a novel approach was designed to detect EVPA rotations over short (days to weeks), intermediate (weeks to months), and long (months to years) timescales, accounting for gaps in observation cadence and the influence of EVPA variability within a larger rotation. The first step in this method consisted of fitting the EVPA points. To do this, the GaussianProcessRegressor module was used from the sklearn package. Gaussian processes automate the process of fitting data filled with inherent randomness using a range of different distributions and assigning a probability to each, over using a fixed function. One specifies a kernel to model the variability of the data (the covariance

function), providing the Gaussian process with priors for learning. Different kernels exist to produce the priors, and in this work the Rational Quadratic Kernel was used. This kernel offered a good degree of flexibility over the others tested, enabling sensitivity to both short- and long-timescale trends while also accounting for data uncertainties. To ensure a good fit for each set of data, the EVPA error specified within the kernel was multiplied by some factor. This had the effect of changing the dependence of the modelling on the priors, thus producing various degrees of fitting. After this, finding point-to-point swings and whole rotations consisted of the methodology detailed in 4.1.4. However, in order to find rotations over different timescales as previously mentioned one could alter the multiplicative factor. This would give the effect of under- and over-fitting the EVPA data, increasing sensitivity to shorter- and longer-duration variability, respectively. To automate this process as much as possible, a factor resulting in a good general fit was found by trial and error, and from this two additional values ten times smaller and larger were calculated to produce the over- and under-fit.

Following this process, the data for the blazar PG 1553+113 is shown in Figure 6.4. This figure shows the EVPA evolution over the full RINGO3 campaign fitted with three different smoothness factors to change the variability sensitivity. The upper panel shows the least smooth fit, sensitive to short-term variability. The middle panel shows a moderately smooth fit, sensitive to intermediate-term variability. Finally, the bottom panel shows the smoothest fit, sensitive to long-term variability. The highlighted portions of each curve show the detected rotations from the modelled data. The parameters of these rotations (MJD start/end/duration, EVPA start/end/size, and direction) are given in Table 6.1. Also given in this table is an indication of the possibility of individual rotations detected multiple times. If a rotation of similar start MJD, end MJD, and duration (within 30 days) was detected at different sensitivities then this match is given in the final column.

This method gives promising results. Under the previous method, no rotations were detected for this source despite variability in the EVPA data. Allowing for a small amount of interpolation between points as well as varying degrees of smoothing of the data and associated uncertainties, one can begin to more easily pick out potential rotations for deeper analysis on a variety of timescales. This source, in particular, seems to demonstrate rotations on a wide variety of timescales, ranging in duration from roughly 30 to 1000 days, and from roughly 90° to 400°.

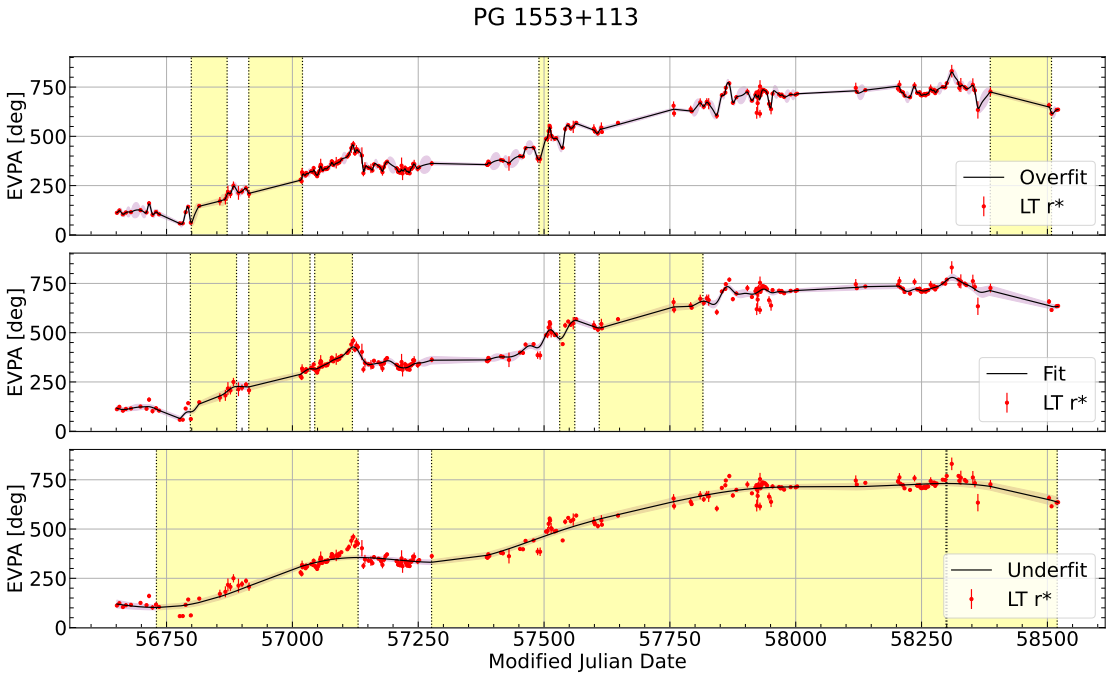

FIGURE 6.4: Figure showing the EVPA rotations detected in the data for PG 1553+113 during the RINGO3 monitoring campaign. Each panel shows a fit to the EVPA data of differing variability sensitivity (from top to bottom; high, intermediate, and low). Shaded regions show the rotation periods detected.

TABLE 6.1: EVPA rotations detected in the RINGO3 data for PG 1553+113. The rotations were detected through a novel approach, utilising fitting the data through Gaussian processing and smoothing the curve to different degrees to find rotations at different timescales.

Rotation Number	Source	Factor	MJD Start	MJD End	Duration	EVPA Start	EVPA End	EVPA Difference	Type	Matching Rotation Number
0	PG 1553+113	0.025	56799.17	56870.3	71.13	59.66	206.22	146.56	Positive	4
1	PG 1553+113	0.025	56913.35	57020.05	106.7	210.25	305.73	95.48	Positive	5
2	PG 1553+113	0.025	57489.89	57508.61	18.72	382	518.4	136.4	Positive	
3	PG 1553+113	0.025	58386.52	58508.19	121.67	725.12	616.52	-108.59	Negative	
4	PG 1553+113	0.25	56797.3	56889.02	91.72	98.39	227.22	128.83	Positive	0
5	PG 1553+113	0.25	56913.35	57035.02	121.67	224.59	316.85	92.27	Positive	1
6	PG 1553+113	0.25	57044.38	57119.26	74.87	315.62	426.73	111.11	Positive	
7	PG 1553+113	0.25	57531.07	57561.02	29.95	469.75	562.19	92.44	Positive	
8	PG 1553+113	0.25	57609.69	57815.6	205.91	524	659.5	135.5	Positive	
9	PG 1553+113	2.5	56729.91	57130.49	400.58	102.19	355.45	253.27	Positive	
10	PG 1553+113	2.5	57276.5	58298.54	1022.04	331.44	731.14	399.7	Positive	
11	PG 1553+113	2.5	58300.41	58519.42	219.01	731.14	637.34	-93.8	Negative	

To take this process further, one could consider alternative methods of fitting the data. Additional methods would have to fit well both the long-term stochastic behaviour seen in blazar light curves without disregarding shorter timescale photo-polarimetric flaring variability. If Gaussian processing appears optimal, one could consider different kernels to better fit the data and account for uncertainties. Furthermore, better automation of the specification of the smoothness factors could further ease the process of detecting EVPA rotations.

6.2.3 Using machine learning to distinguish blazar activity states

Accurately distinguishing between different blazar activity states is fundamental in assessing the origin of observed behaviour in relativistic jets. During this PhD, work began on trying to categorise blazar activity using machine learning (ML) clustering algorithms better to define the observed activity states during blazar monitoring campaigns.

The clustering was performed using the AGGLOMERATIVE CLUSTERING function in the SKLEARN Python package (Pedregosa et al., 2011b) and "hierarchical clustering". Hierarchical clustering consists of the successive splitting or joining of groups into nested clusters. The AGGLOMERATIVE CLUSTERING function uses the former approach, starting with each observation as its own node before attempting to join them together using the "linkage" criteria. The criteria selected in this work used a variance-minimising approach by minimising the sum of the squared differences in each node. This process can be visualised through a dendrogram. Figure 6.5 shows the dendrogram associated with the clustering of RINGO3 optical b-band flux, γ-ray flux, and polarisation data for OJ287. The x-axis shows the index number assigned to each node (the brackets around the numbers indicate this point is already in a node, done so to aid clarity on the x-axis), while the y-axis shows the distance between data points/nodes. The solid lines indicate the joining of nodes, with longer vertical lines indicating a decreased probability of those points/nodes being part of the same cluster. To statistically determine the optimum number of nodes in the data, and therefore the number of clusters, a silhouette coefficient was calculated. This was done at each iteration of the clustering procedure as $(b-a)/\max(a,b)$ where a is the mean intra-cluster distance and b is the mean nearest-cluster distance. The clustering iteration with the largest silhouette coefficient was chosen as the optimal number of clusters and is shown in the figure as a horizontal dashed line.

Figure 6.6 shows the results of the clustering of the OJ287 photo-polarimetric RINGO3 data. The left panels show these clusters assigned to the normalised data. The data are normalised in the process of clustering, so by plotting these values one can perform a visual check on the data. The right panels show the γ-ray, optical flux, and polarisation light curves with the assigned clusters. From this process, it is apparent that four photo-polarimetric states occurred in the OJ287 data during the RINGO3 monitoring campaign.

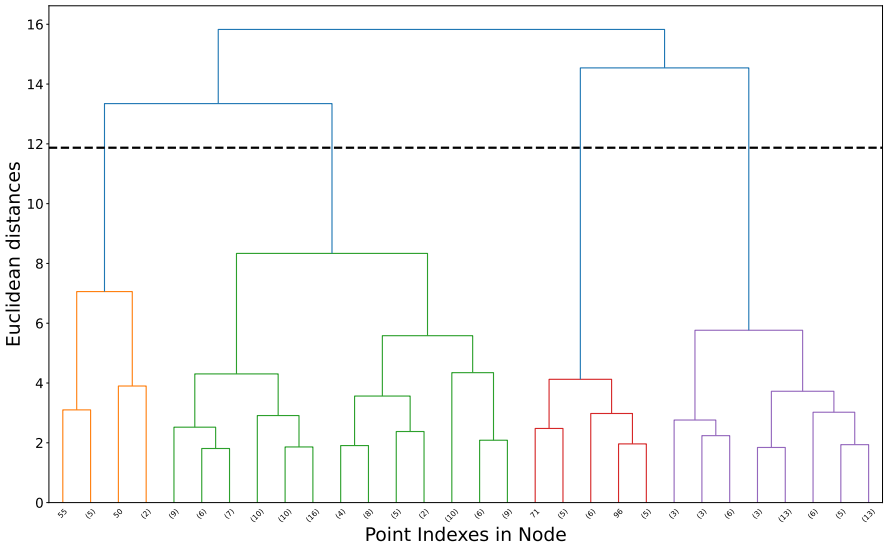

FIGURE 6.5: Figure showing the determination of the number of clusters associated with the data via a dendrogram.

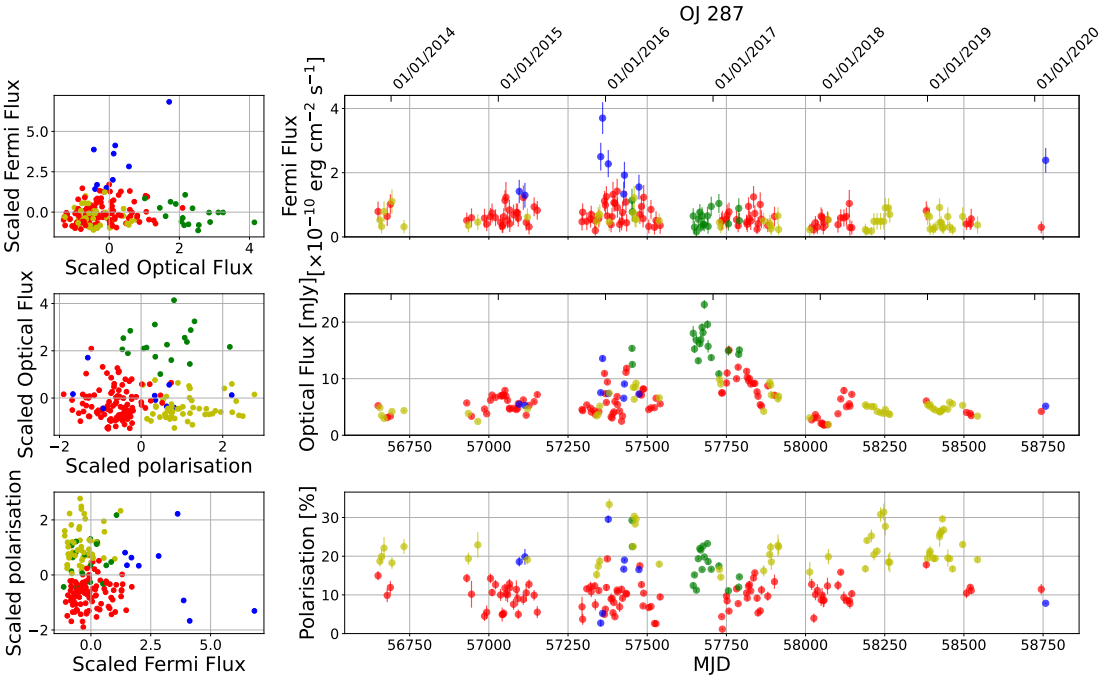

FIGURE 6.6: Figure showing the results associated with identifying activity states in RINGO3 OJ287 photo-polarimetric data using machine learning clustering. The left panels show the normalised data trends coloured with the different states identified. The right panels show the γ-ray and optical flux light curves, respectively, coloured by the different identified activity states.

There are multiple applications to this work. Firstly, if applied to a large sample of blazars, one could begin to see which sources/source types are more likely to display certain behaviour types and therefore better select sources for further observations.

Secondly, this method provides a better estimation of the activity state of a source at a given time. This would be useful to apply to the work determining the activity states during EVPA rotations.

Appendix A – RINGO3 light curves

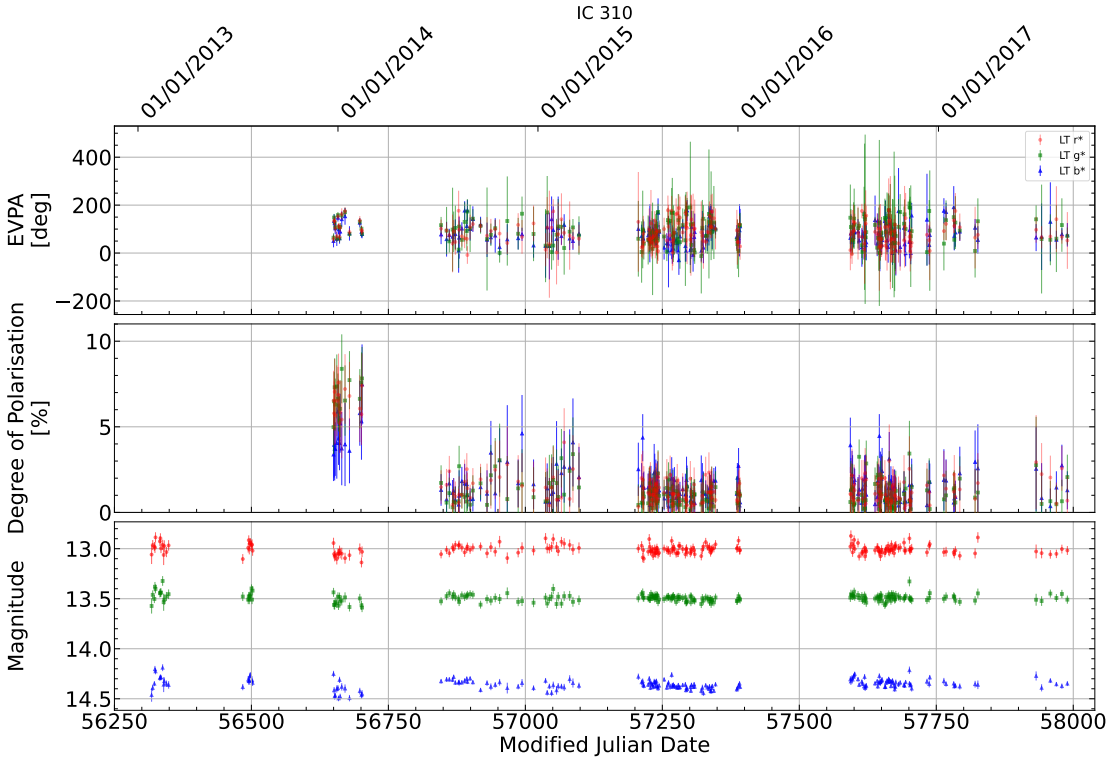

FIGURE A.1: Plots showing the full RINGO3 *r*g*b** data set for the source IC 310. The top, middle. and lower panels show the evolution of EVPA, degree of polarisation, and magnitude with time.

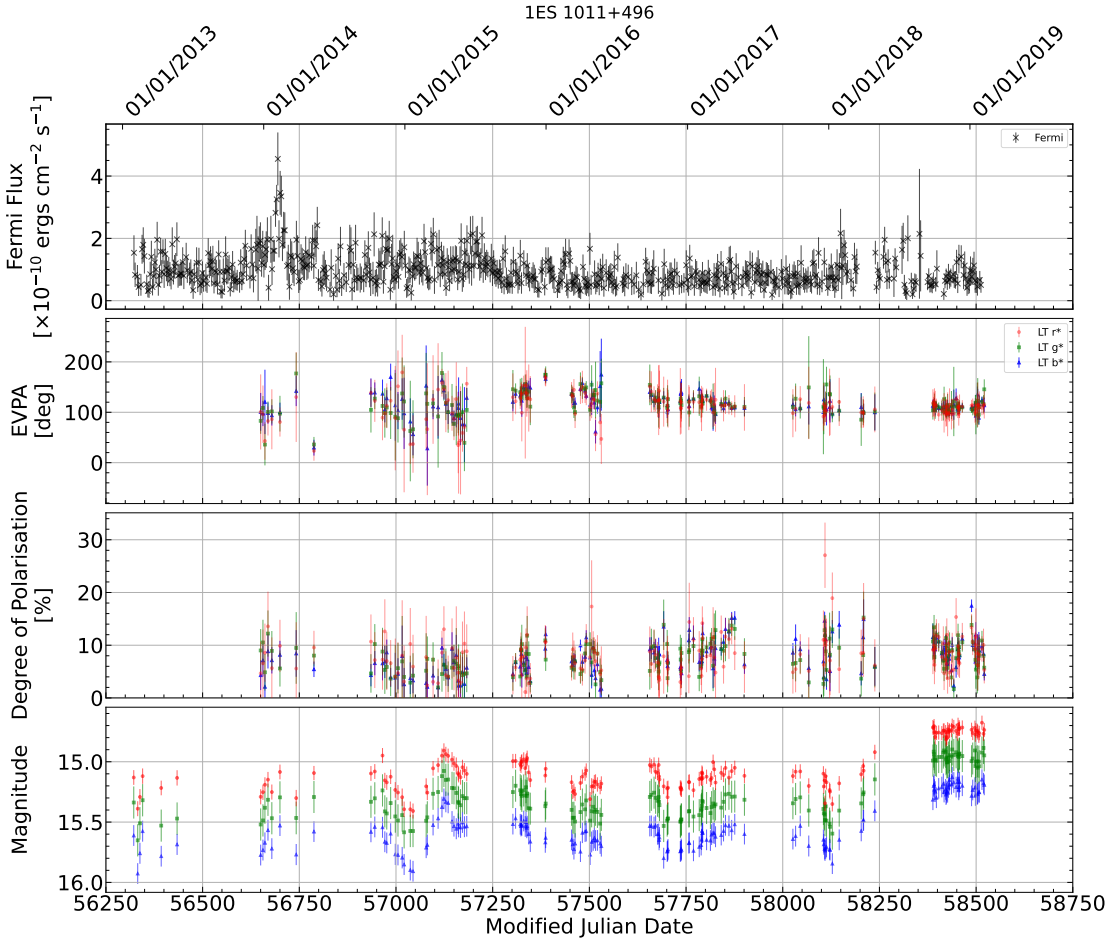

FIGURE A.2: Plots showing the full RINGO3 *r*g*b** data set for the source 1ES 1011+496 in addition to Fermi γ-ray data from the Fermi LAT Light Curve Repository (Abdollahi et al., 2023) taken over the same period. From top to bottom, the panels show the evolution of γ-ray flux, EVPA, degree of polarisation, and magnitude with time.

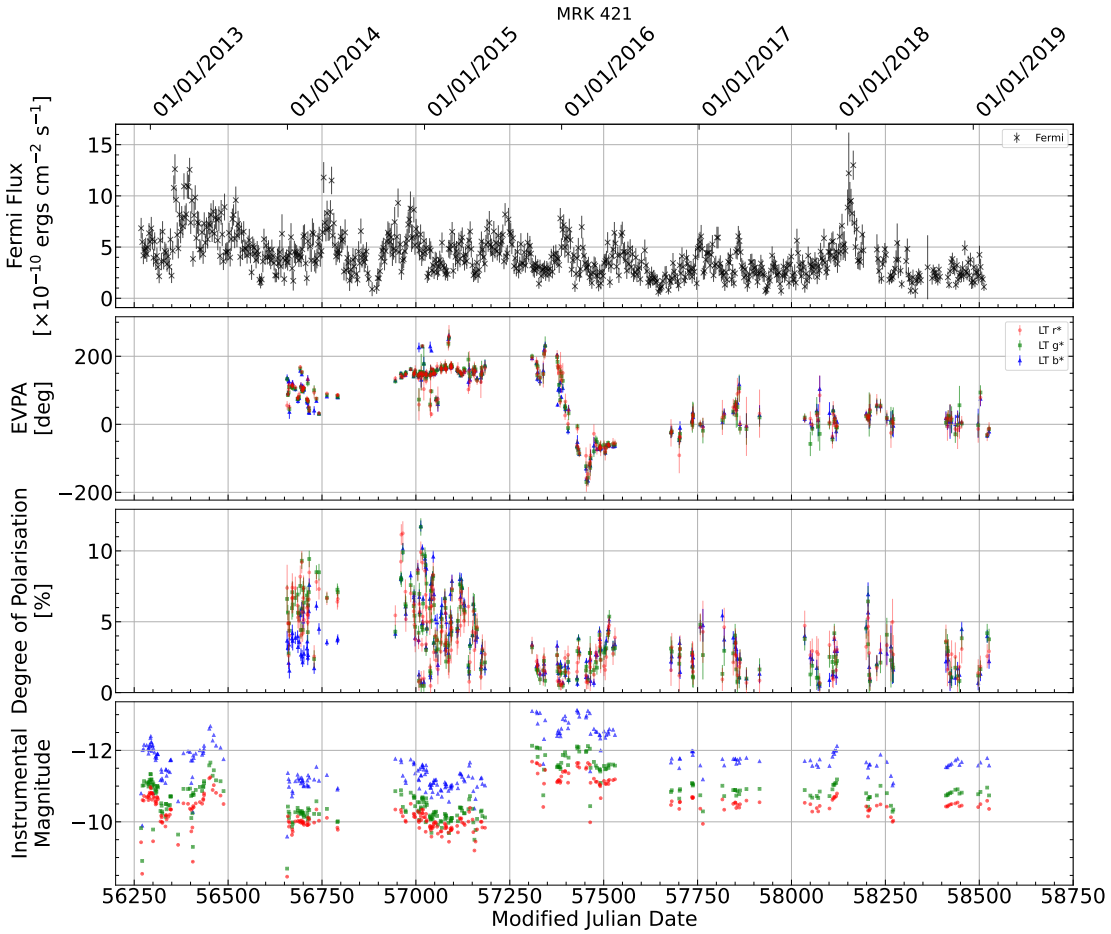

FIGURE A.3: As Fig. A.2, but for MRK 421. Furthermore, the lower panel shows the uncalibrated instrumental magnitude due to the lack of calibration stars in the frames.

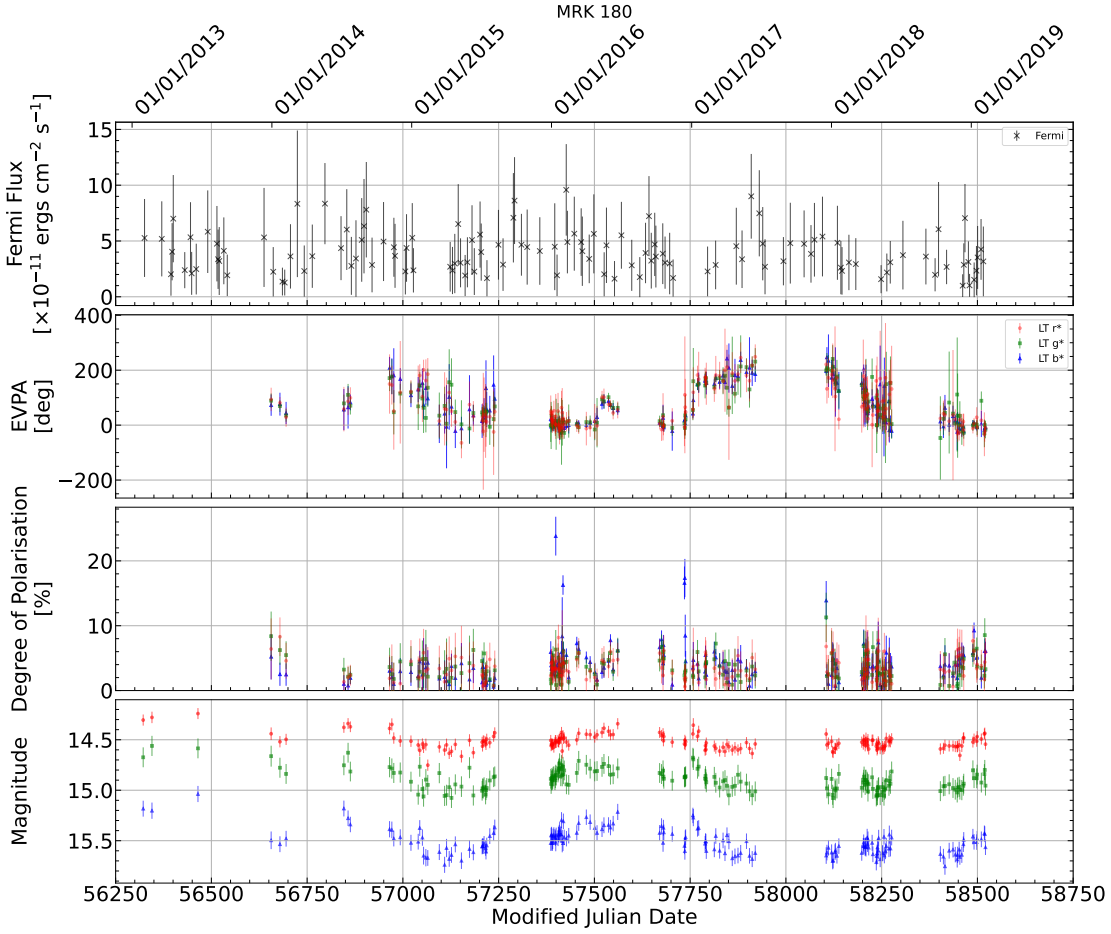

FIGURE A.4: As Fig. A.2, but for MRK 180.

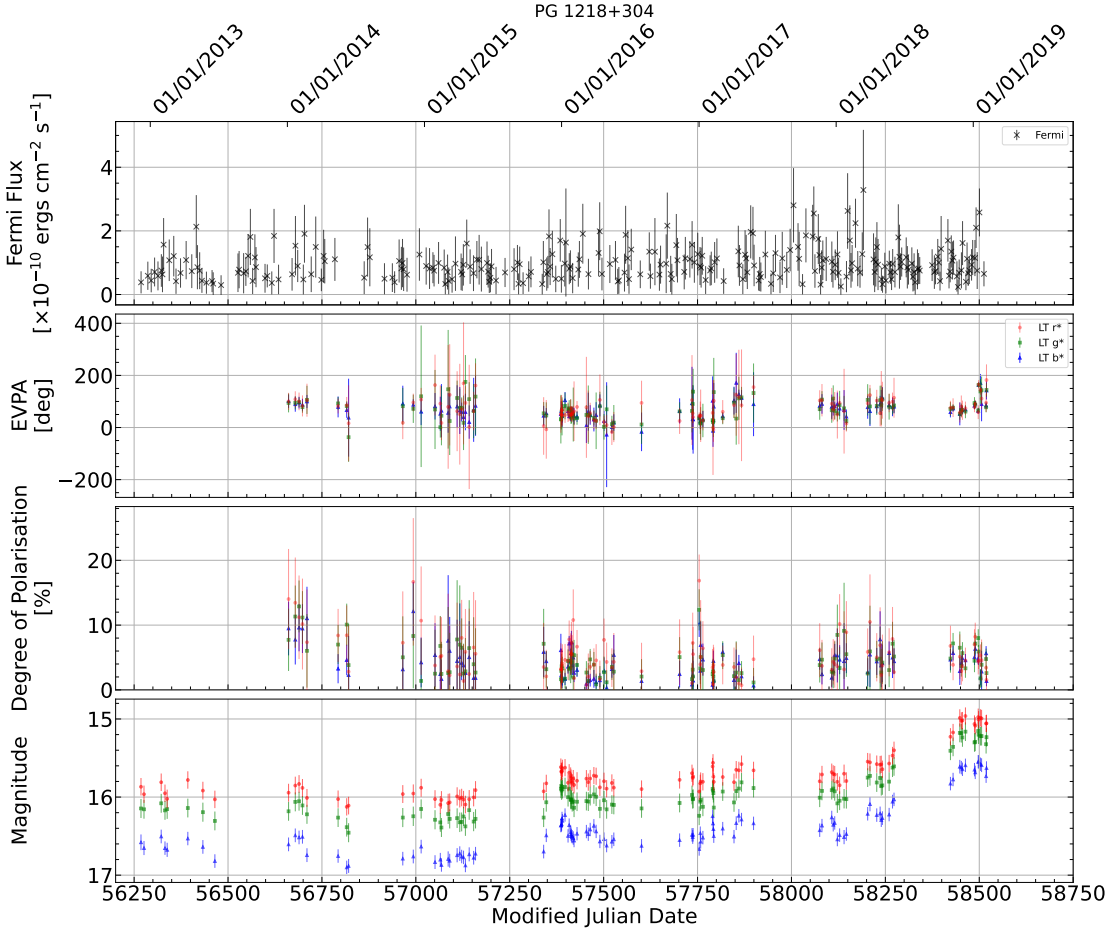

FIGURE A.5: As Fig. A.2, but for PG 1218+304.

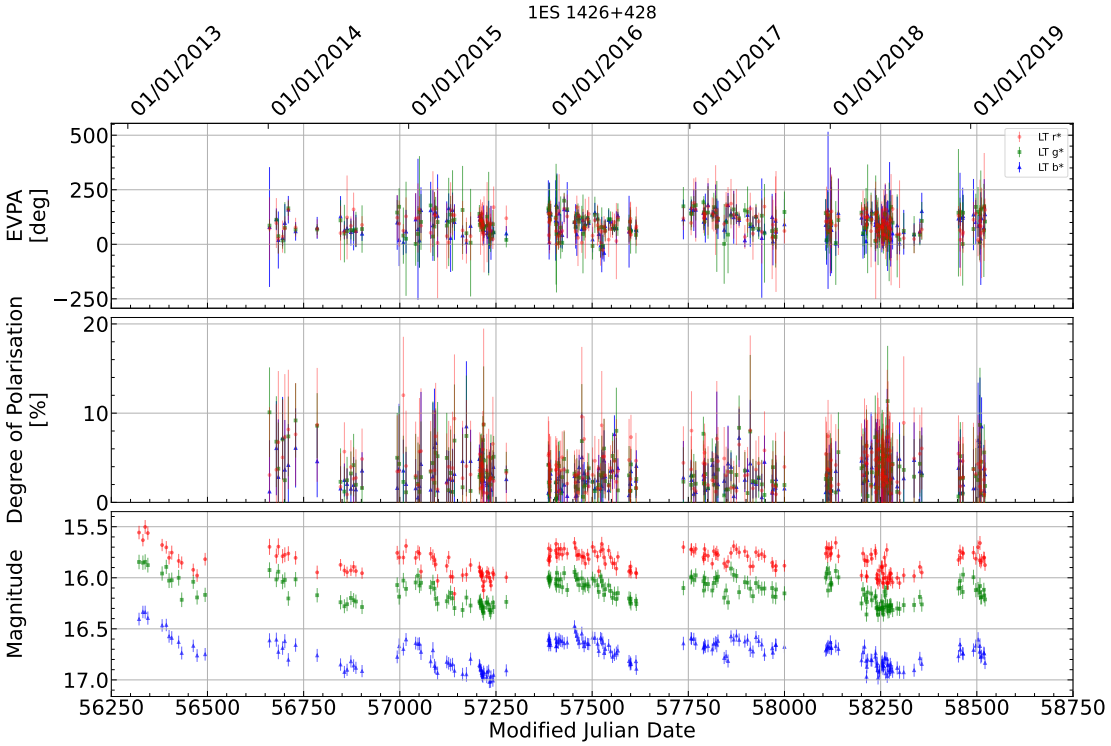

FIGURE A.6: As Fig. A.1, but for 1ES 1426+428.

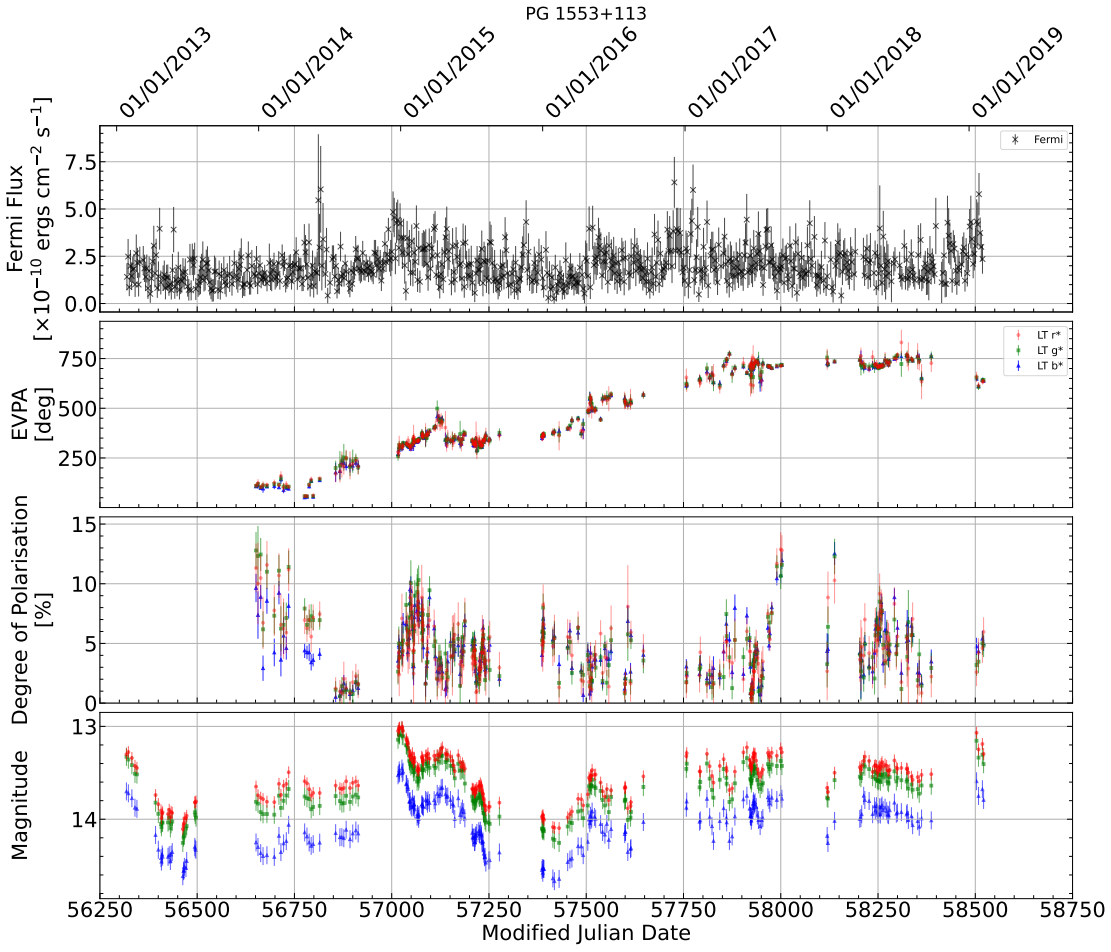

FIGURE A.7: As Fig. A.2, but for PG 1553+113.

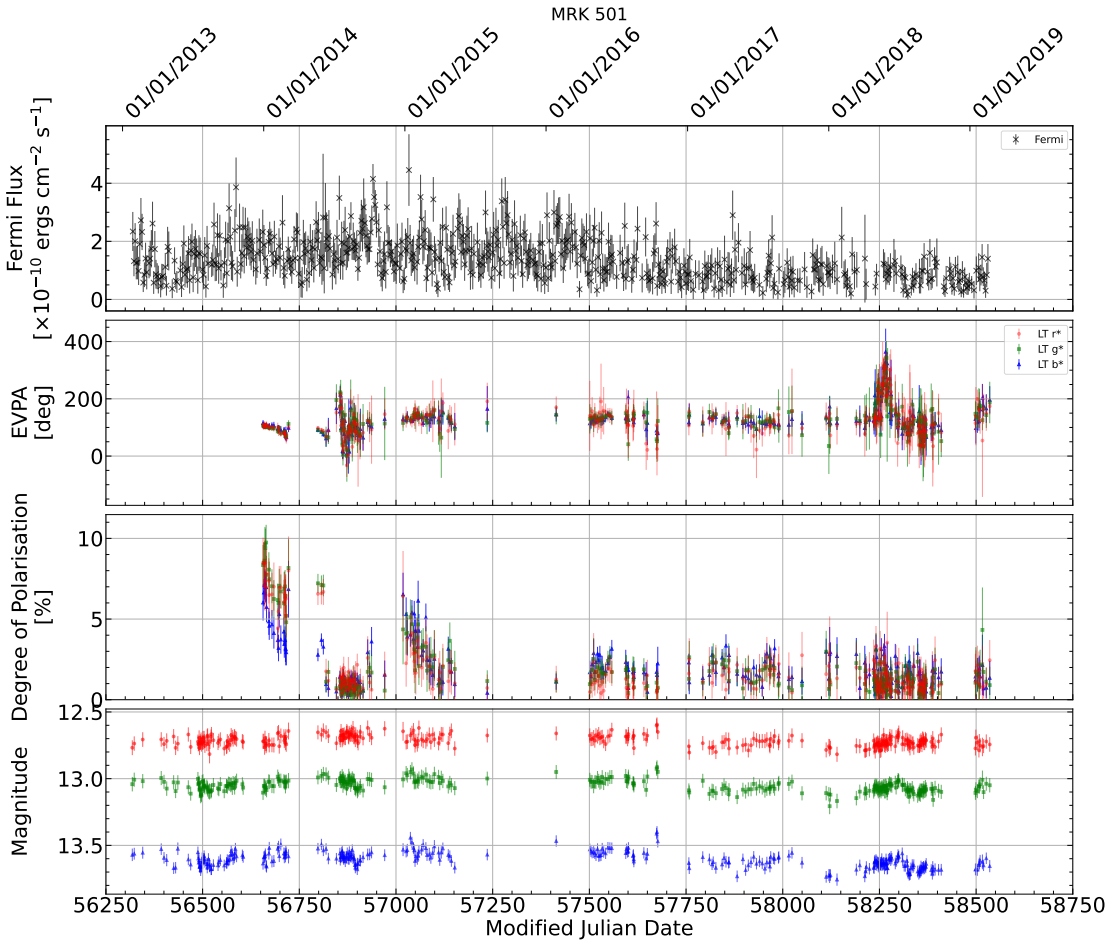

FIGURE A.8: As Fig. A.2, but for MRK 501.

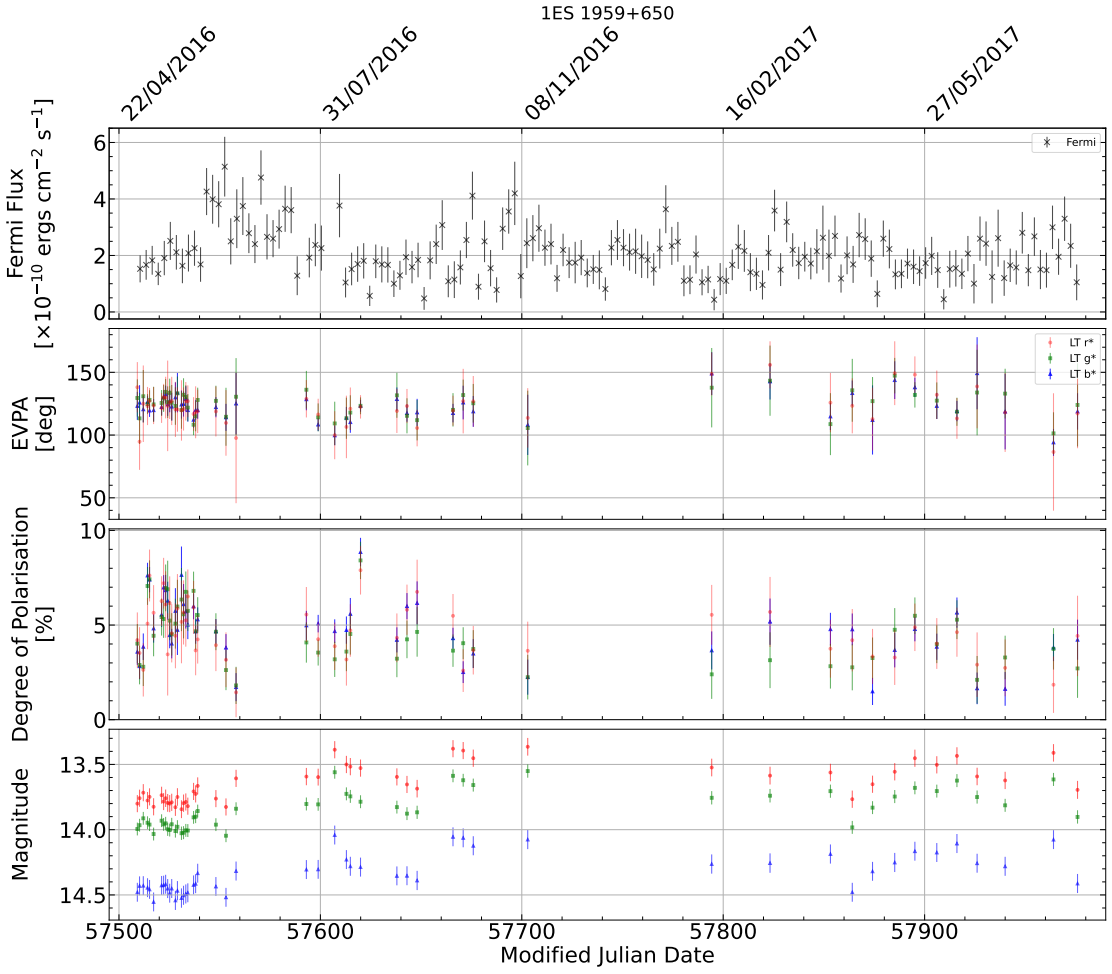

FIGURE A.9: As Fig. A.2, but for 1ES 1959+650.

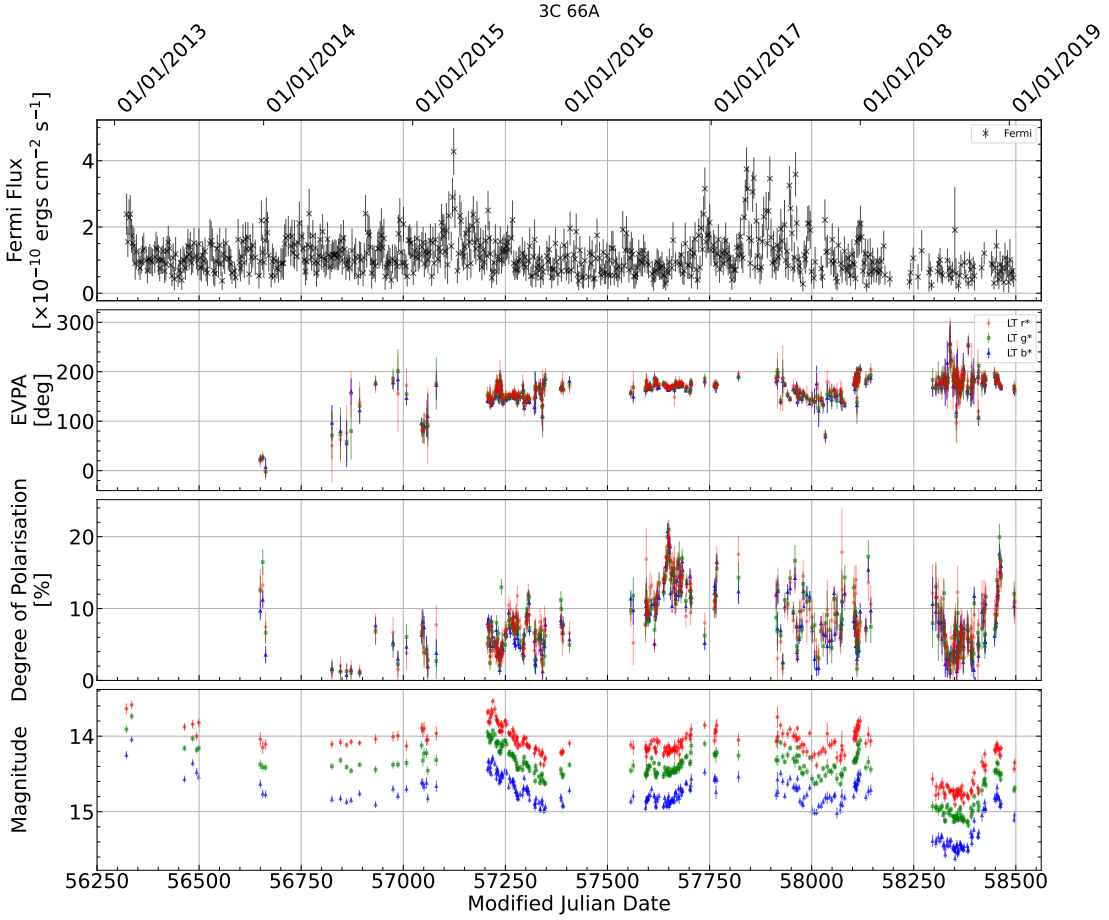

FIGURE A.10: As Fig. A.2, but for 3C 66A.

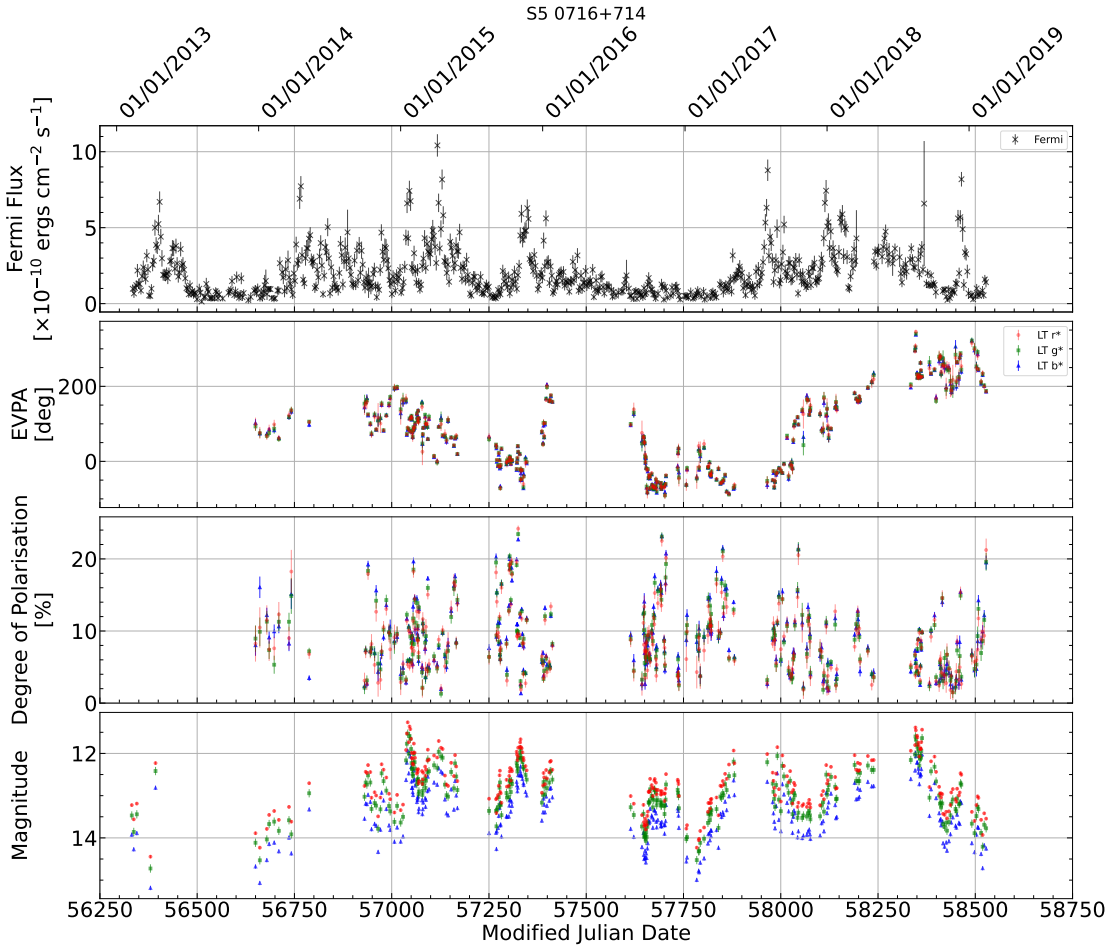

FIGURE A.11: As Fig. A.2, but for S5 0716+714.

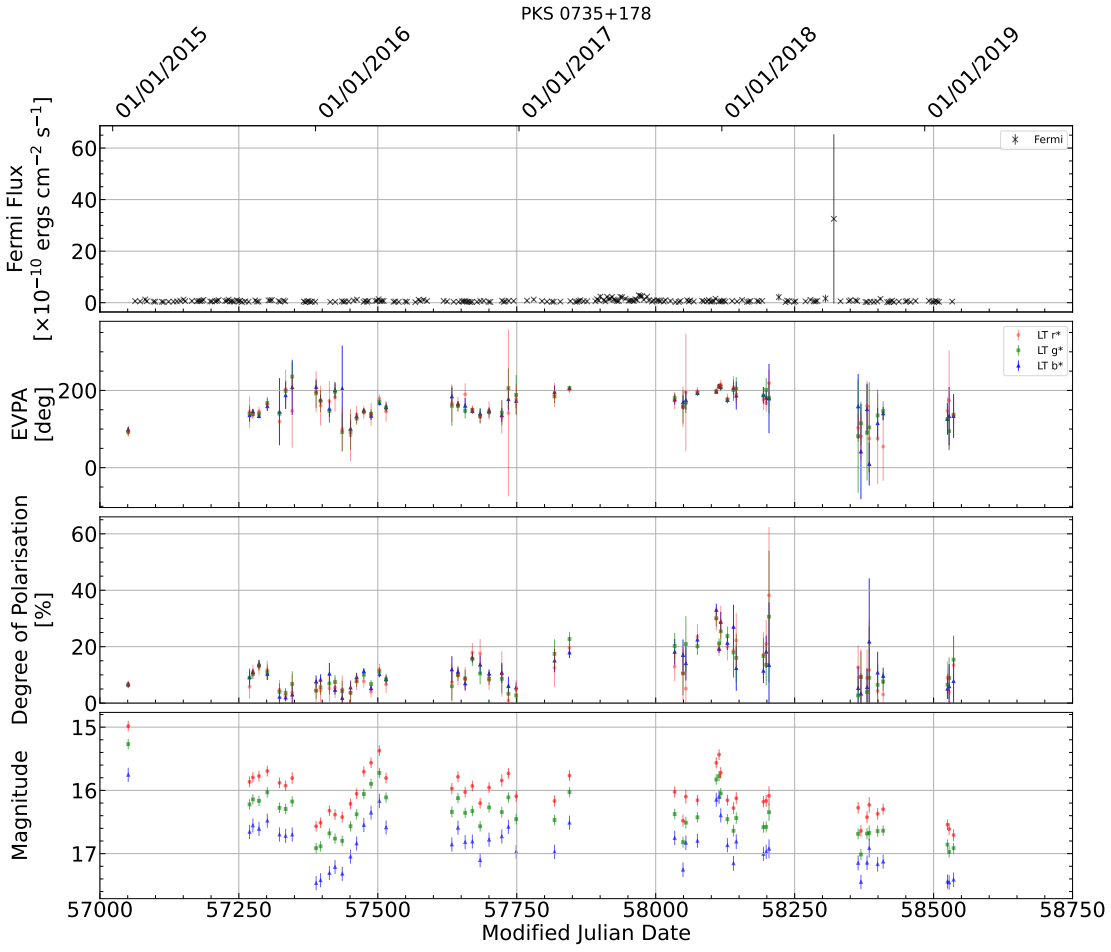

FIGURE A.12: As Fig. A.2, but for PKS 0735+178.

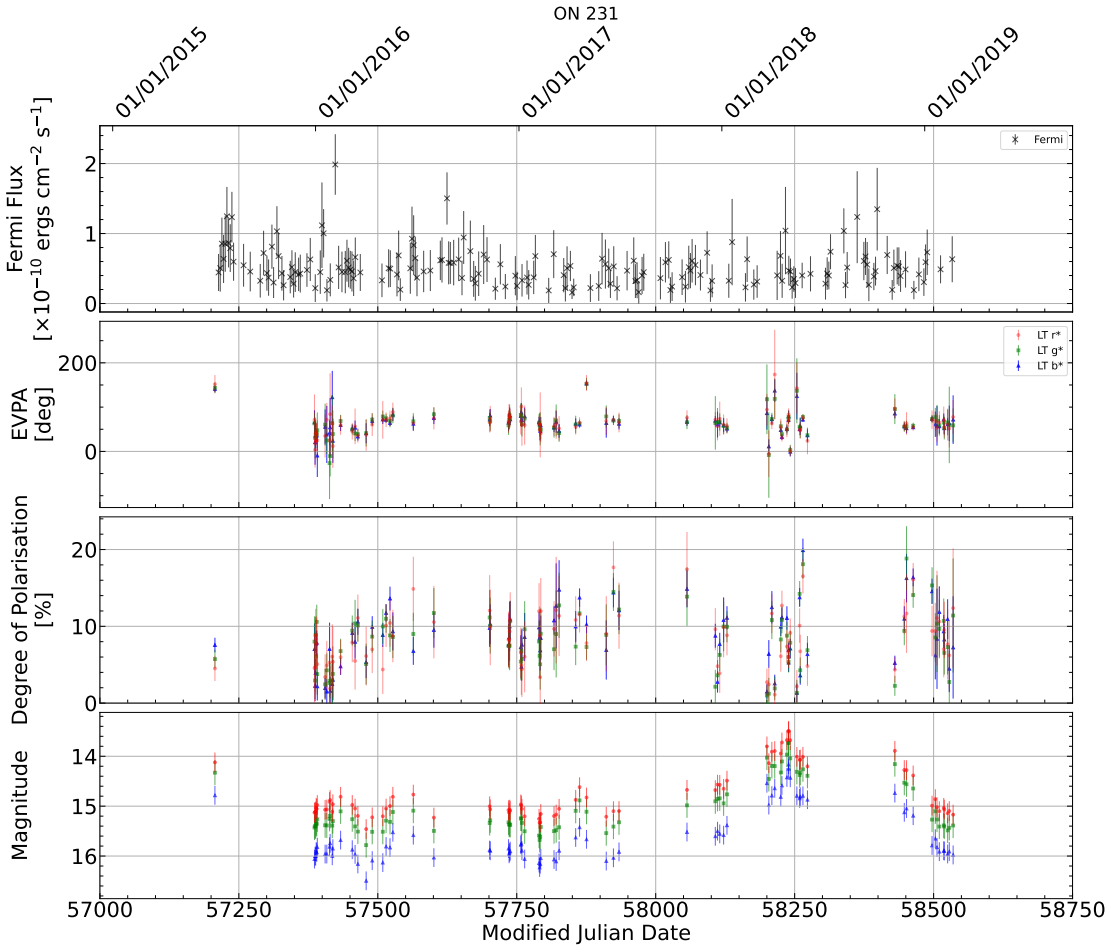

FIGURE A.13: As Fig. A.2, but for ON 231.

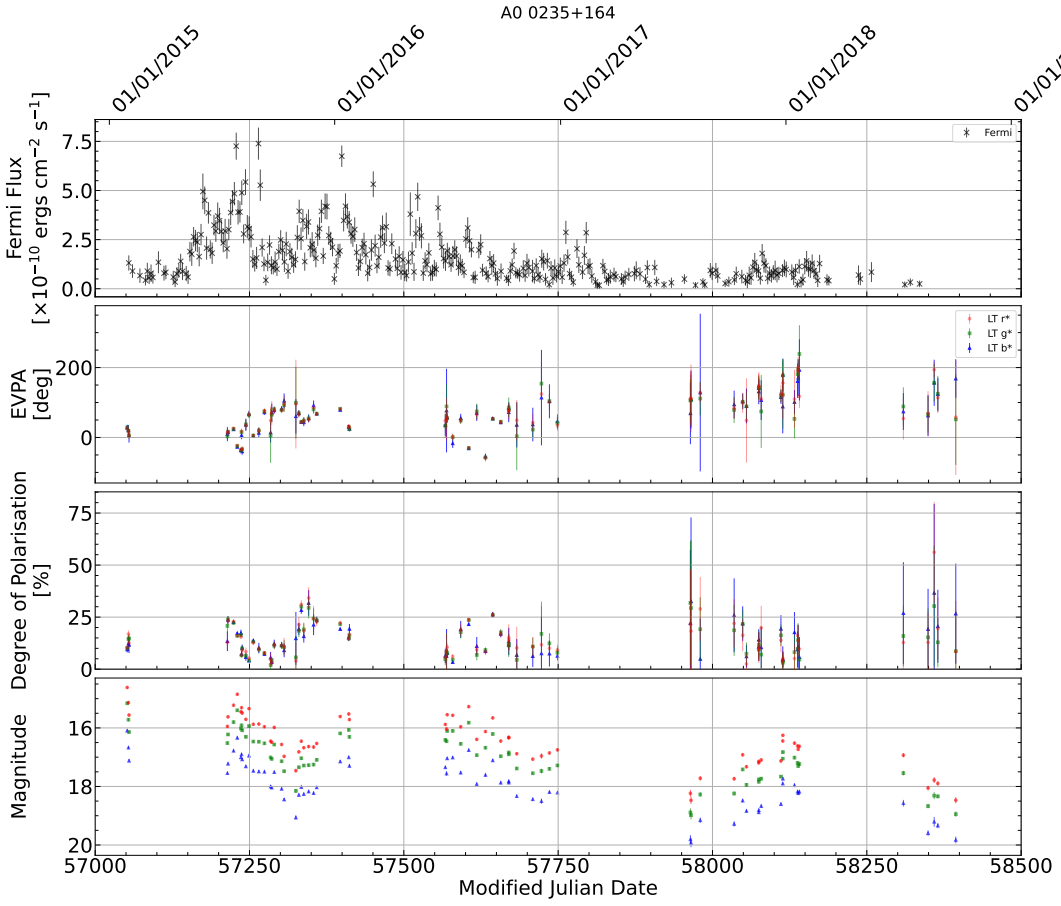

FIGURE A.14: As Fig. A.2, but for A0 0235+164.

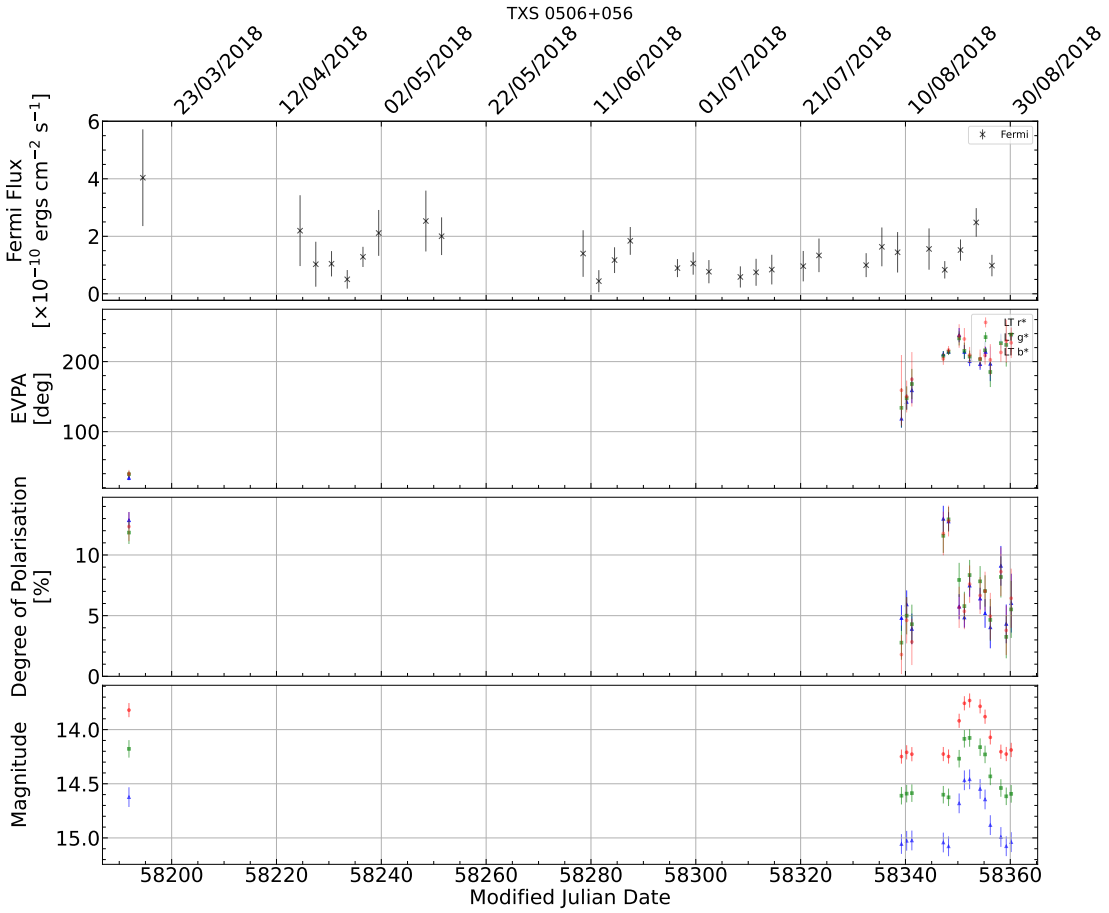

FIGURE A.15: As Fig. A.2, but for TXS 0506+056.

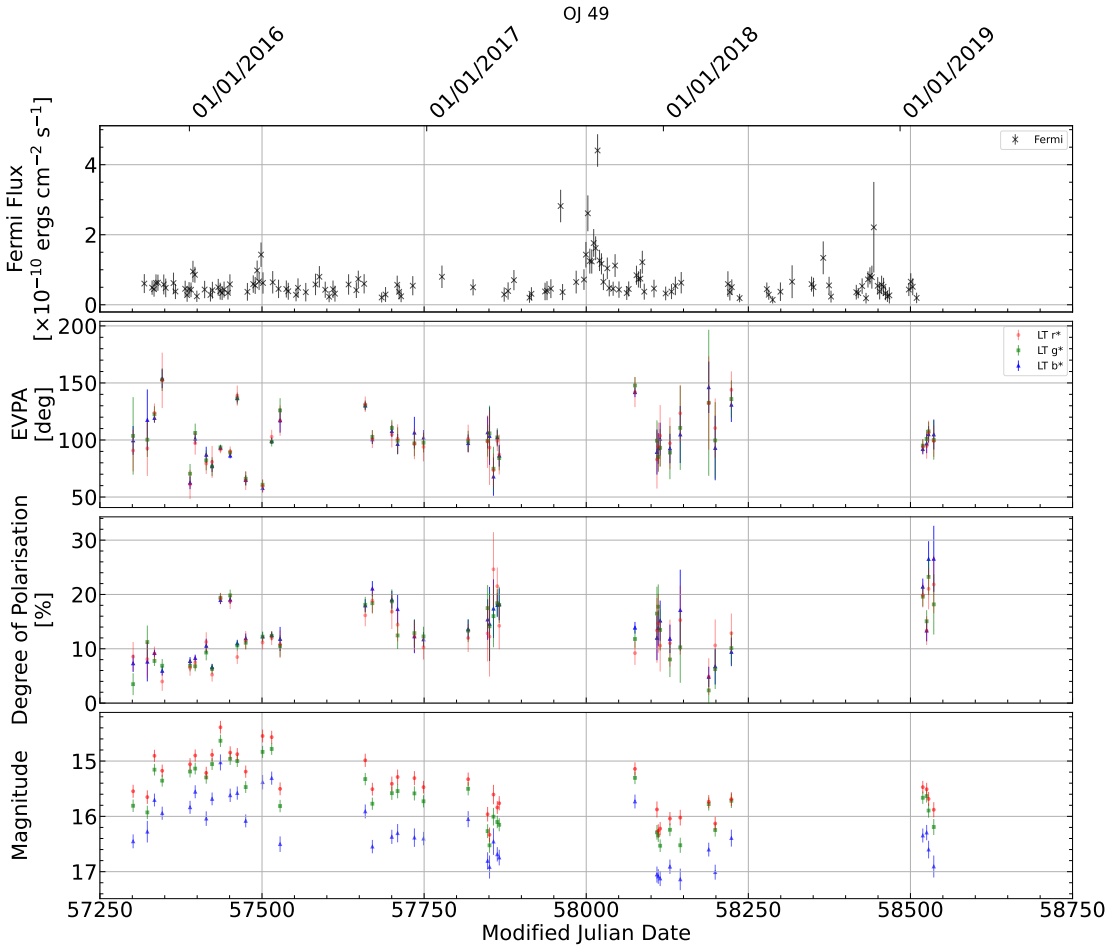

FIGURE A.16: As Fig. A.2, but for OJ 49.

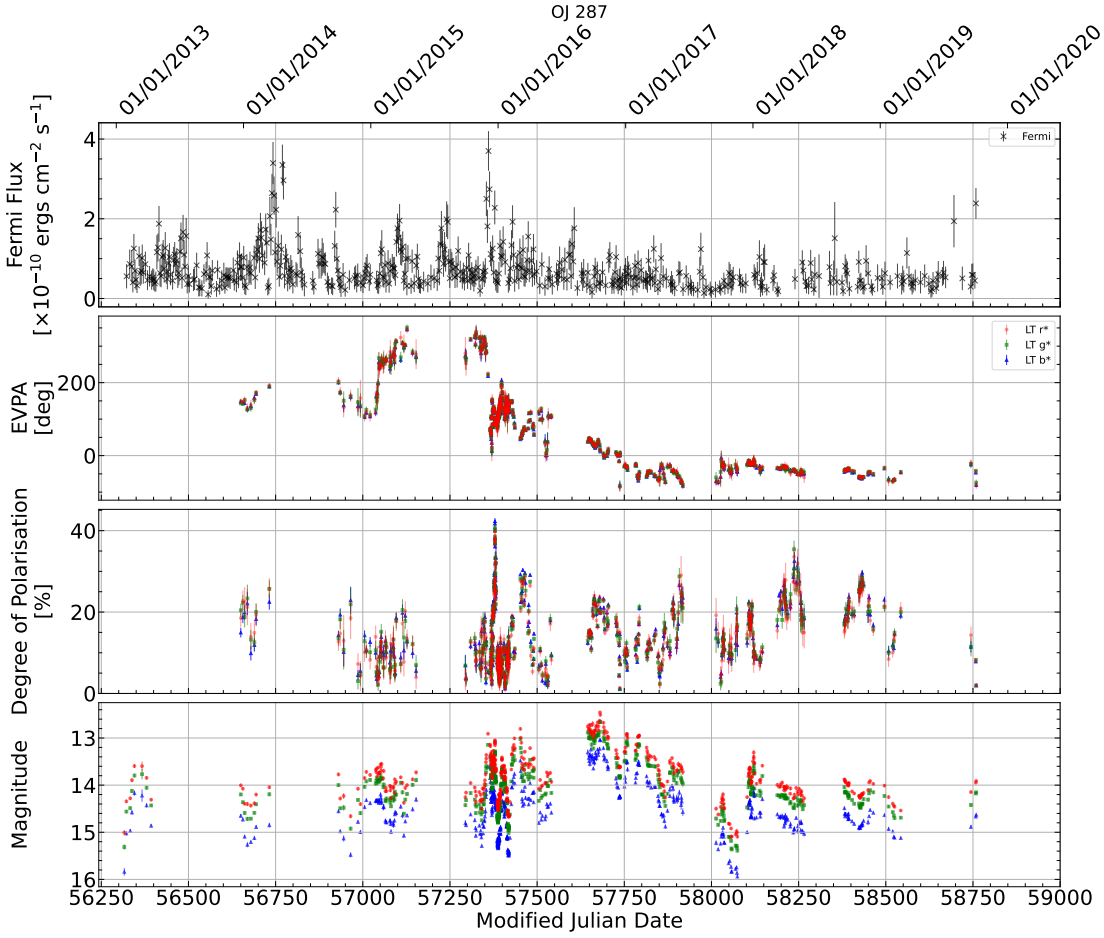

FIGURE A.17: As Fig. A.2, but for OJ 287.

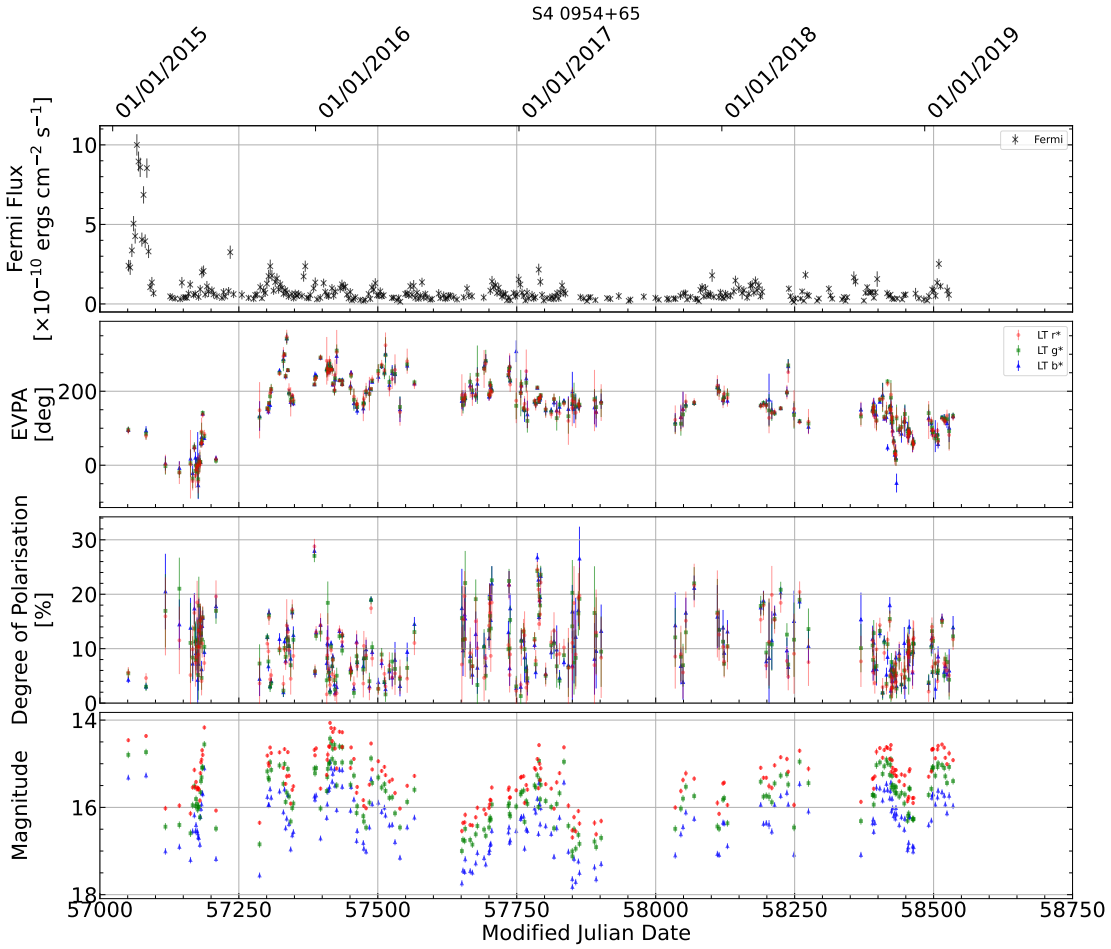

FIGURE A.18: As Fig. A.2, but for S4 0954+65.

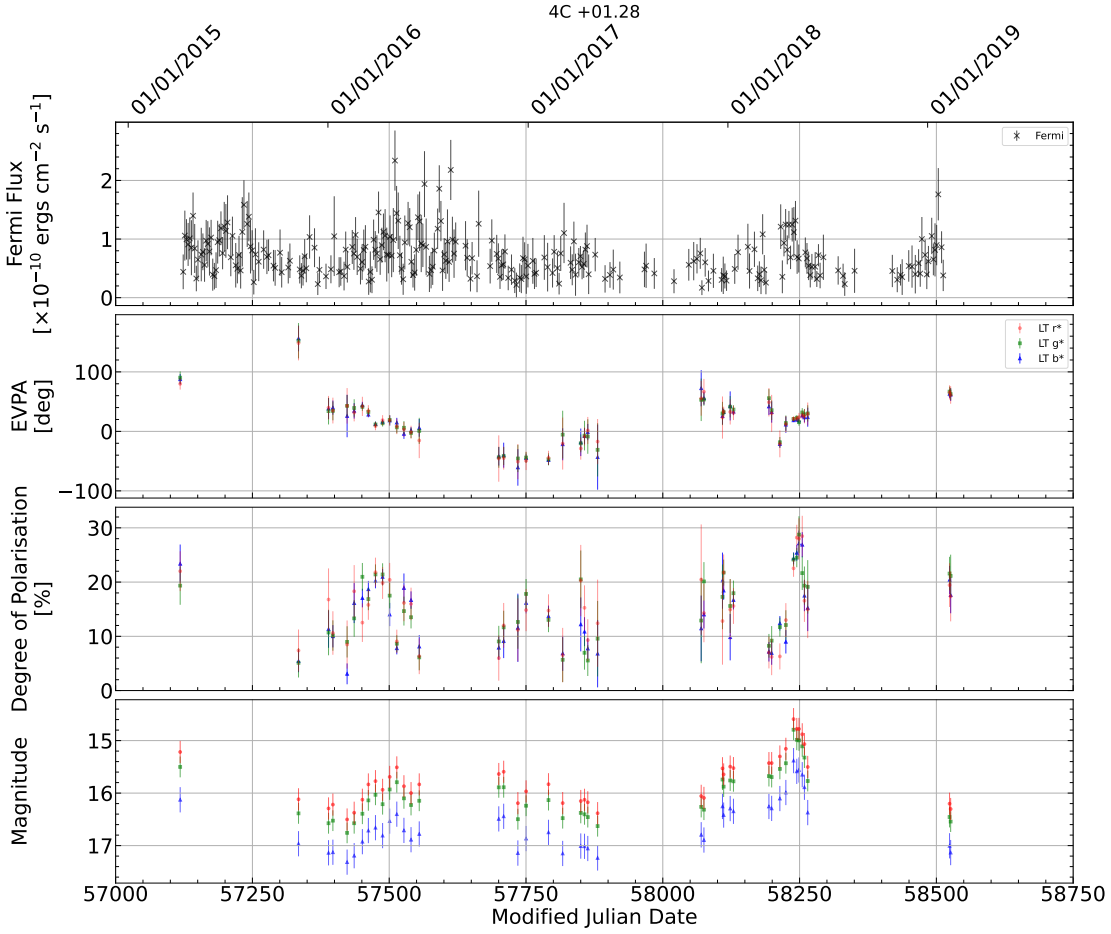

FIGURE A.19: As Fig. A.2, but for 4C+01.28.

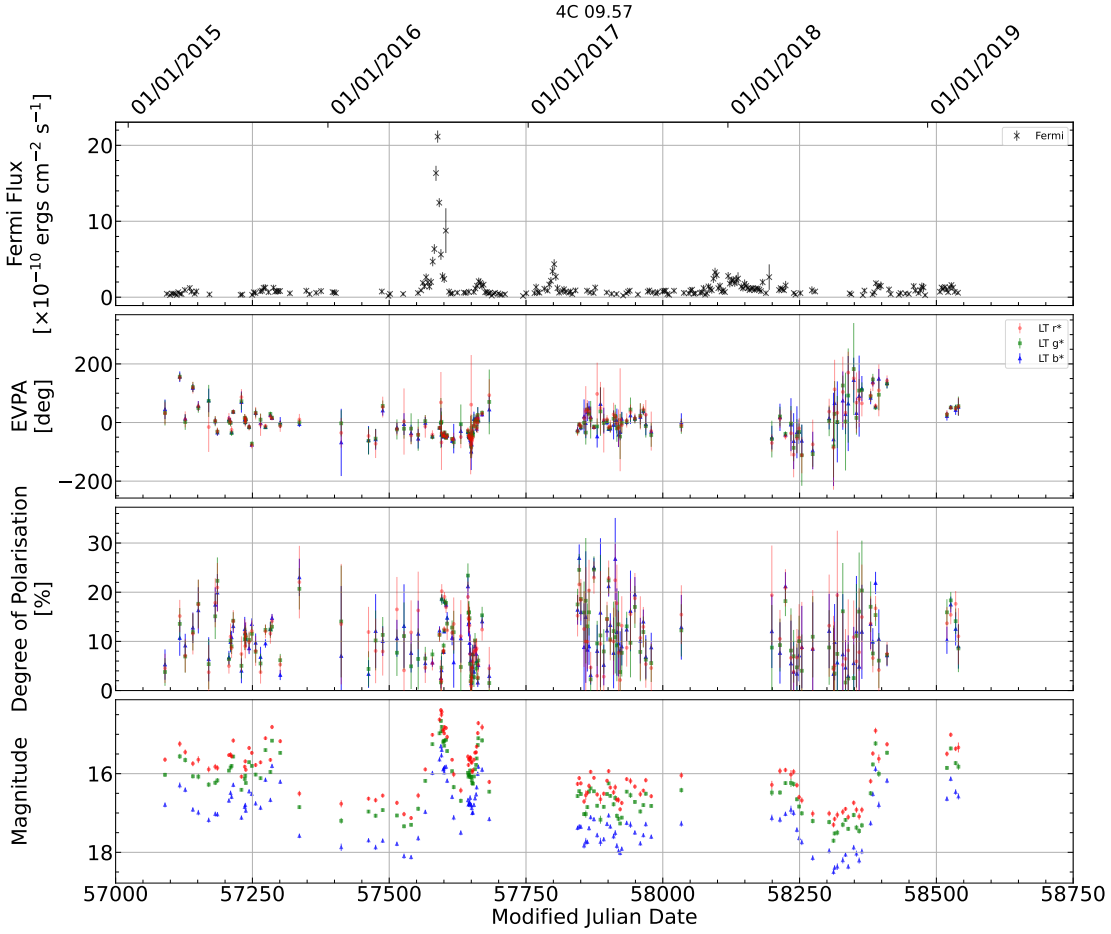

FIGURE A.20: As Fig. A.2, but for 4C 09.57.

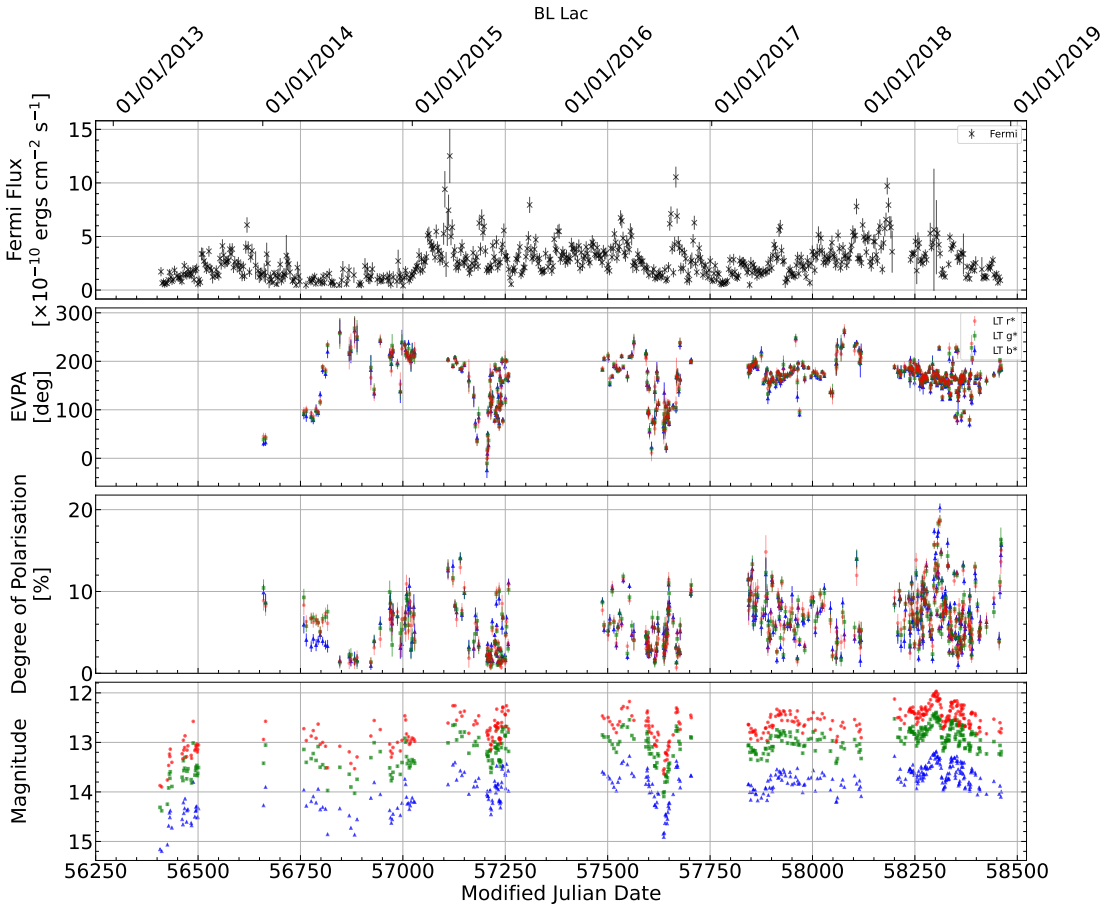

FIGURE A.21: As Fig. A.2, but for BL Lacertae.

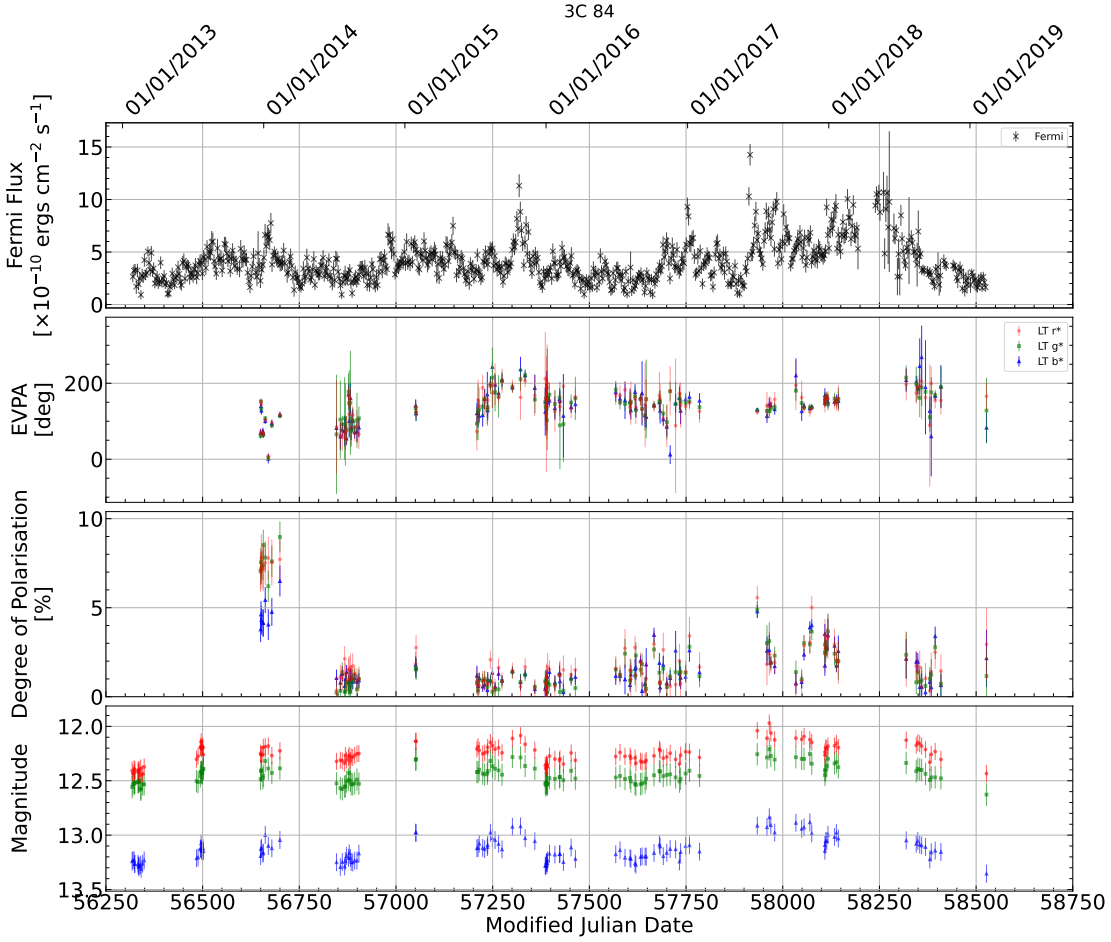

FIGURE A.22: As Fig. A.2, but for 3C 84.

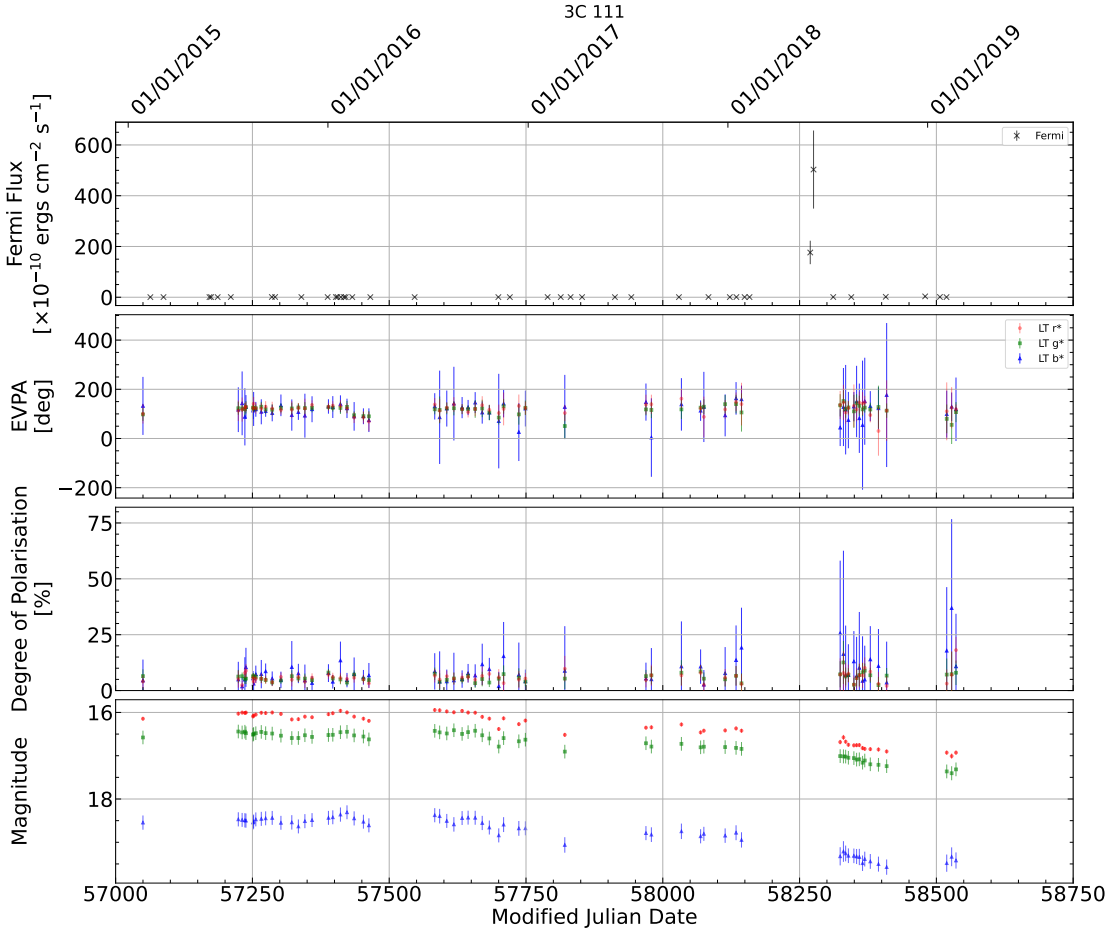

FIGURE A.23: As Fig. A.2, but for 3C 111.

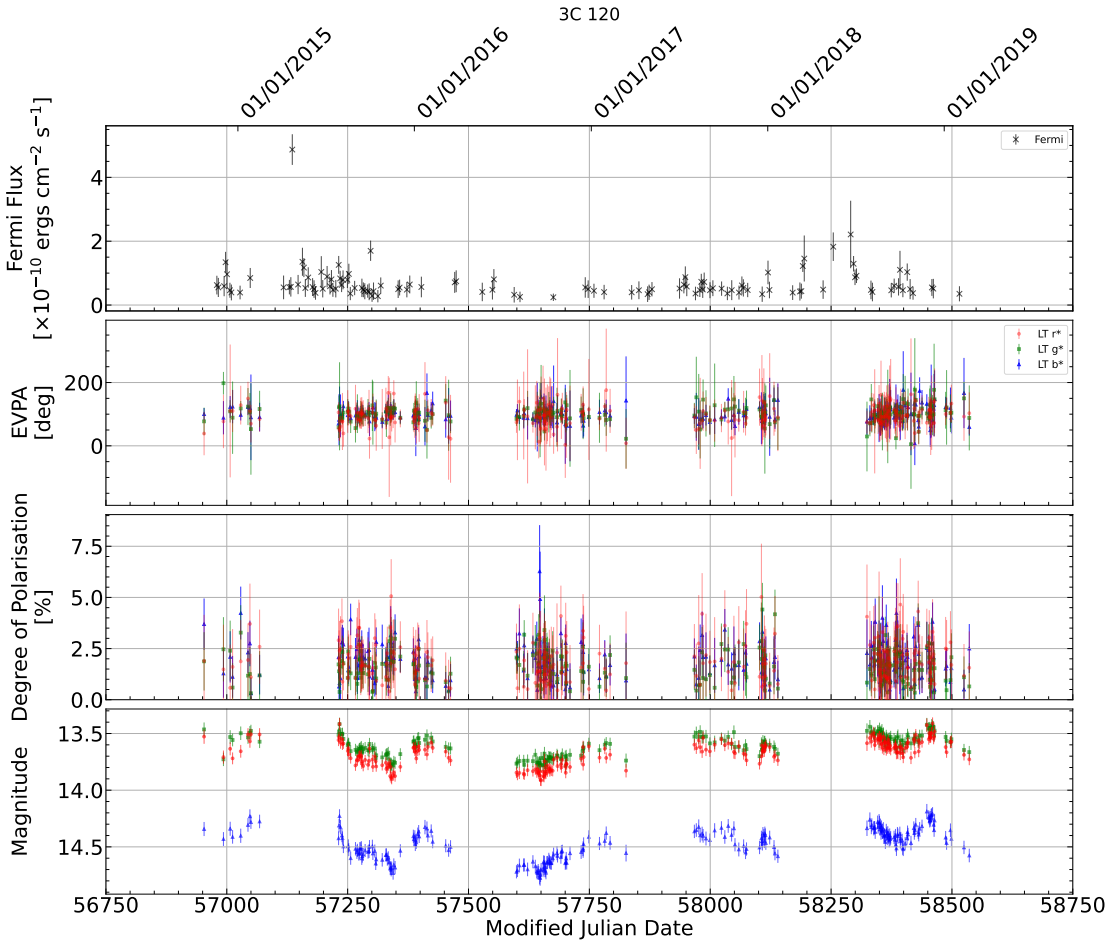

FIGURE A.24: As Fig. A.2, but for 3C 120.

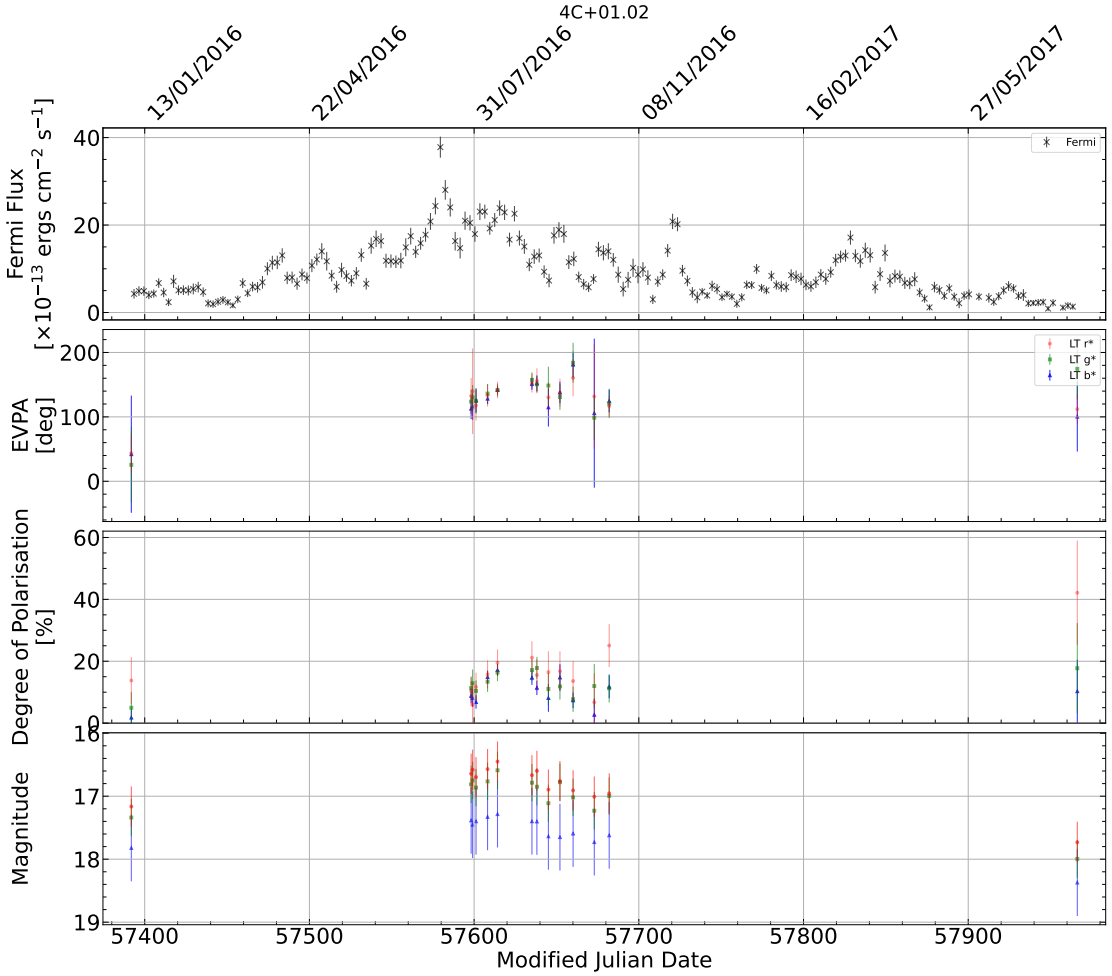

FIGURE A.25: As Fig. A.2, but for 4C+01.02.

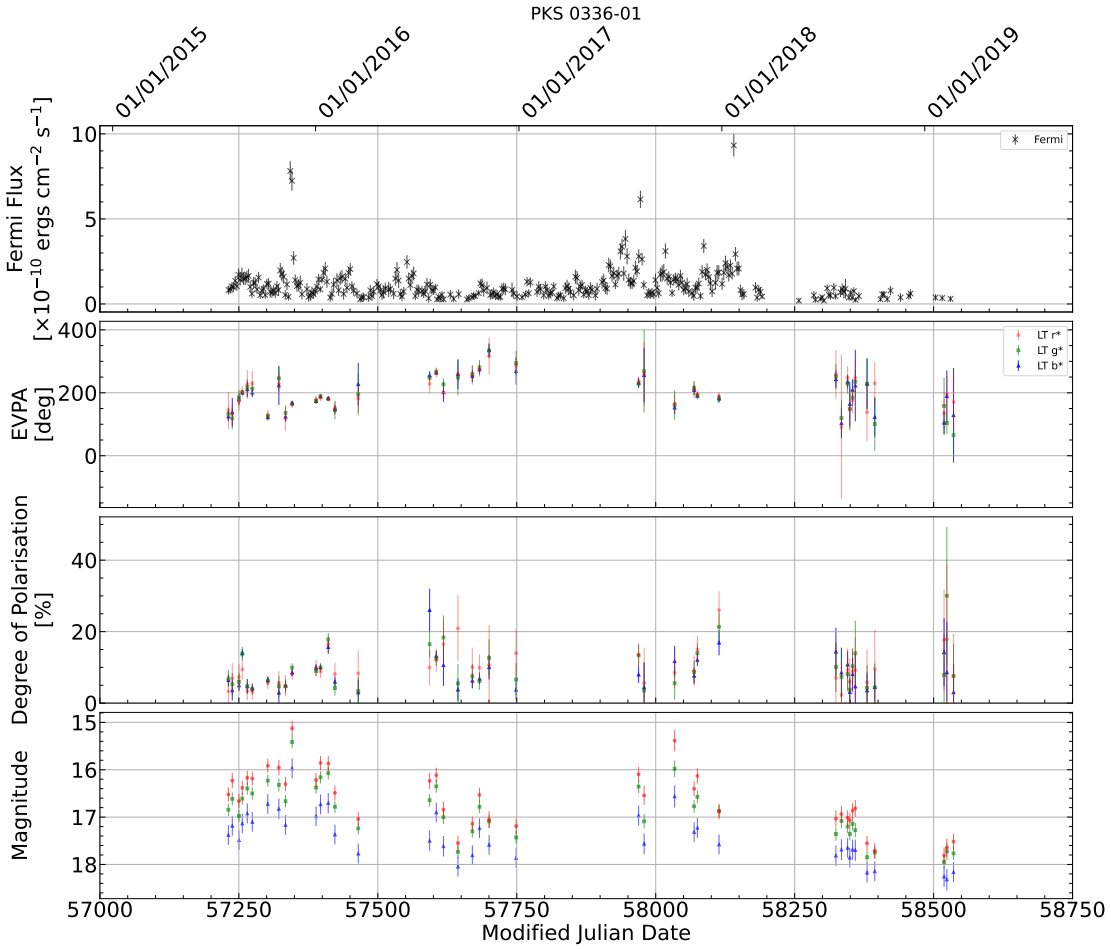

FIGURE A.26: As Fig. A.2, but for PKS 0336-01.

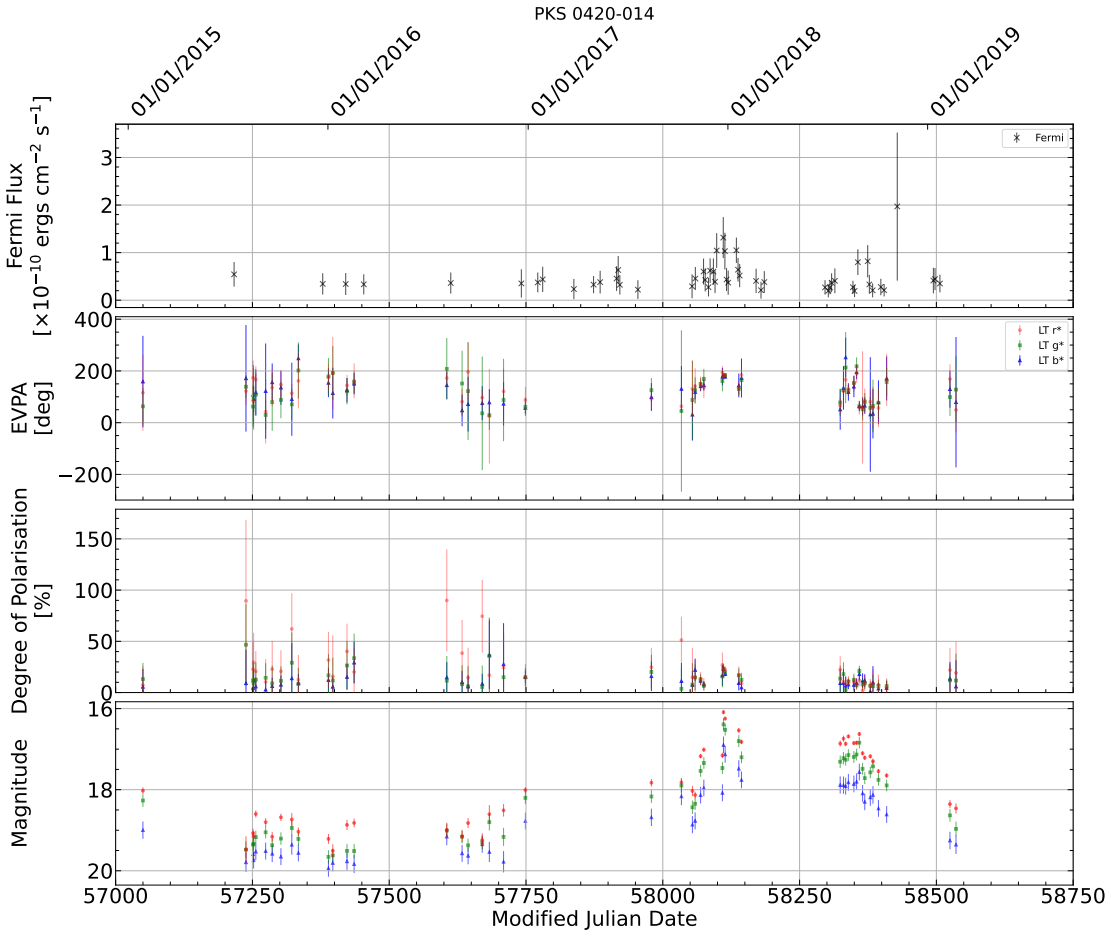

FIGURE A.27: As Fig. A.2, but for PKS 0420-014.

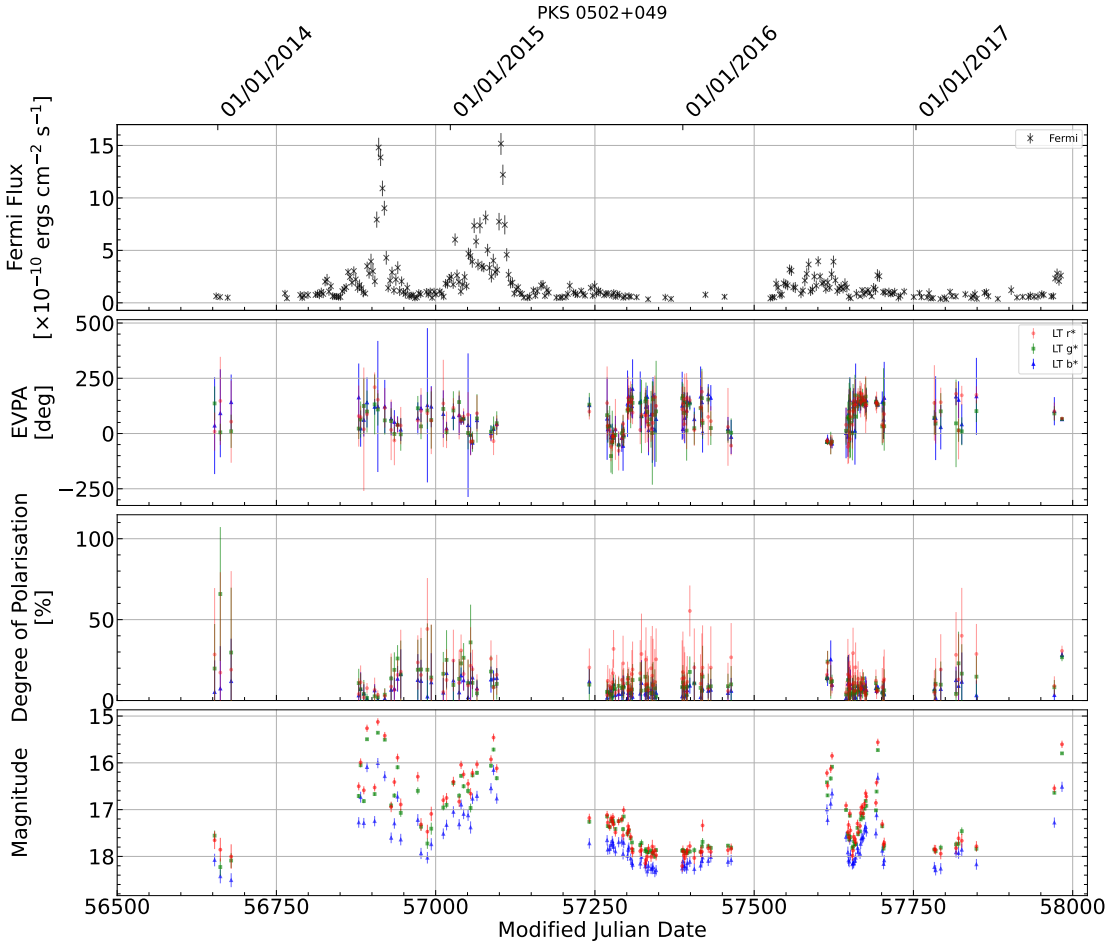

FIGURE A.28: As Fig. A.2, but for PKS 0502+049.

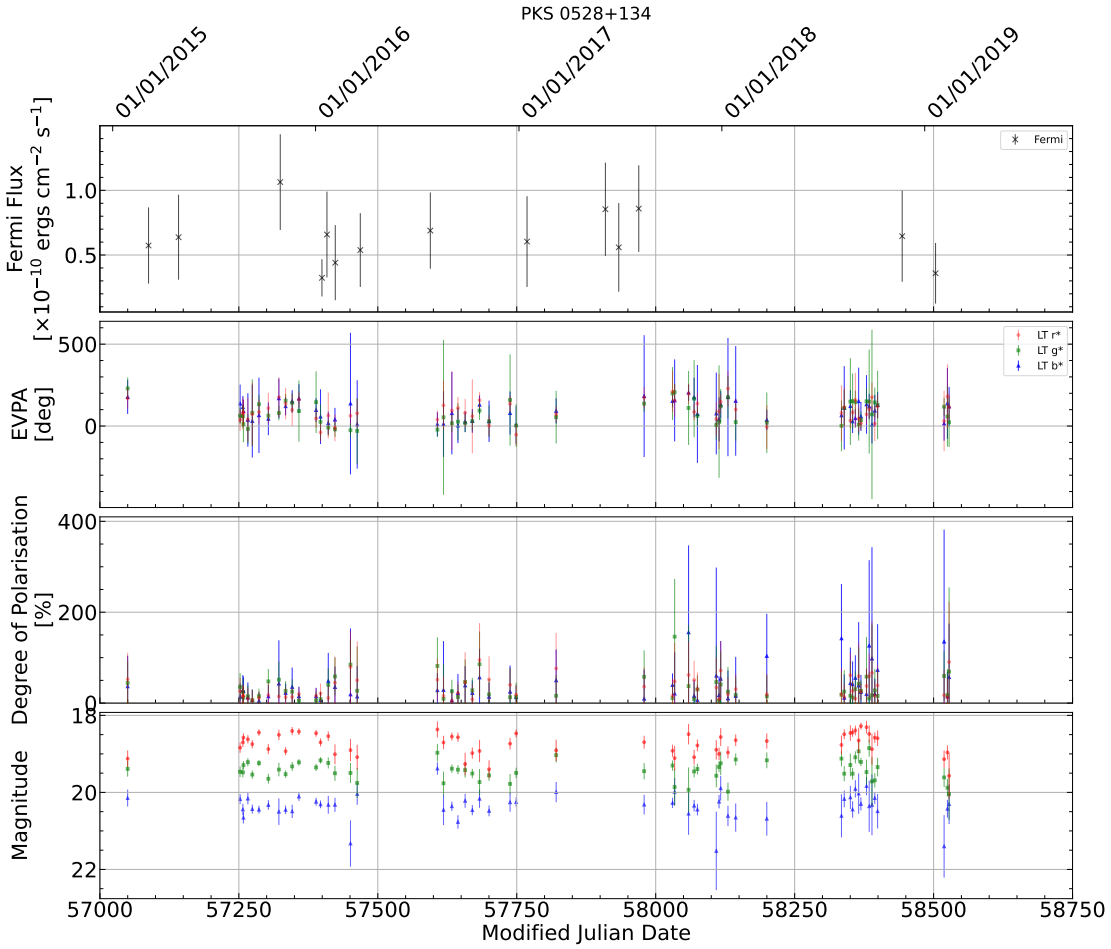

FIGURE A.29: As Fig. A.2, but for PKS 0528+134.

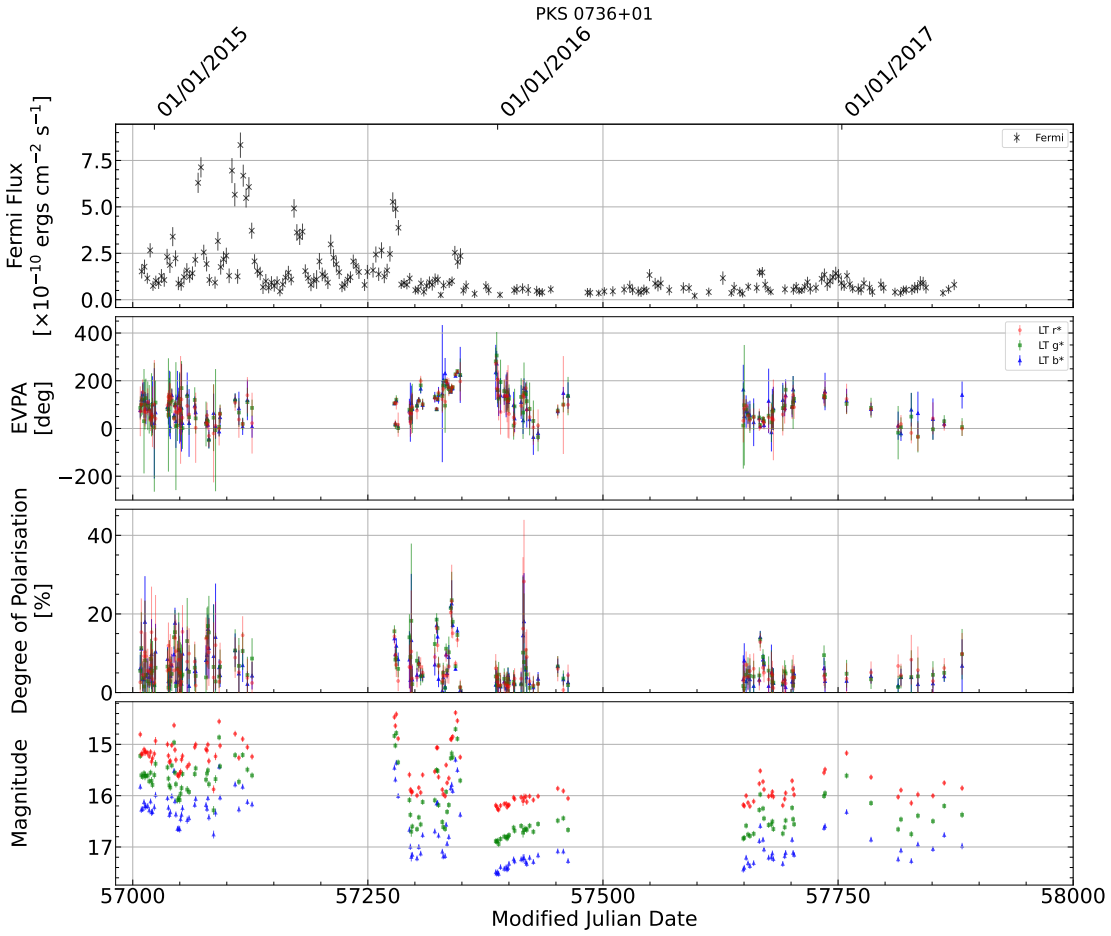

FIGURE A.30: As Fig. A.2, but for PKS 0736+01.

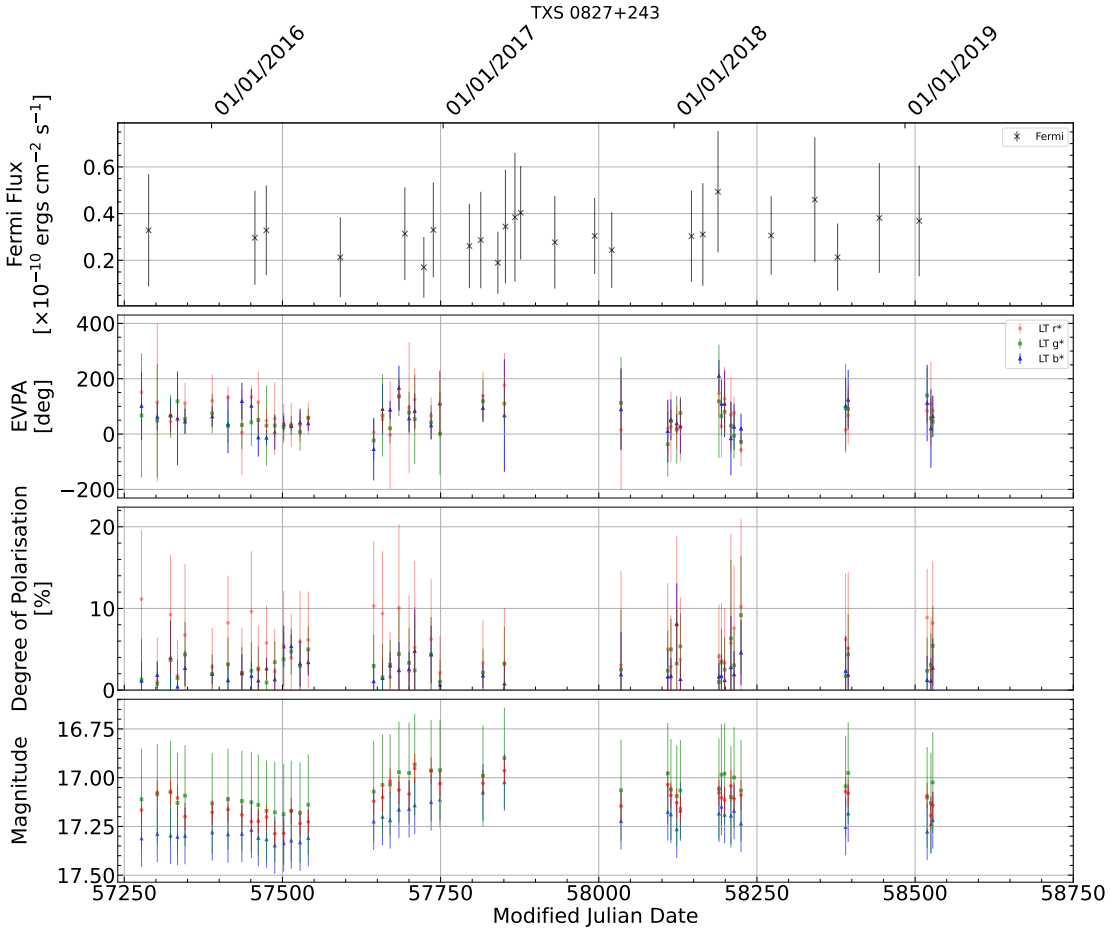

FIGURE A.31: As Fig. A.2, but for TXS 0827+243.

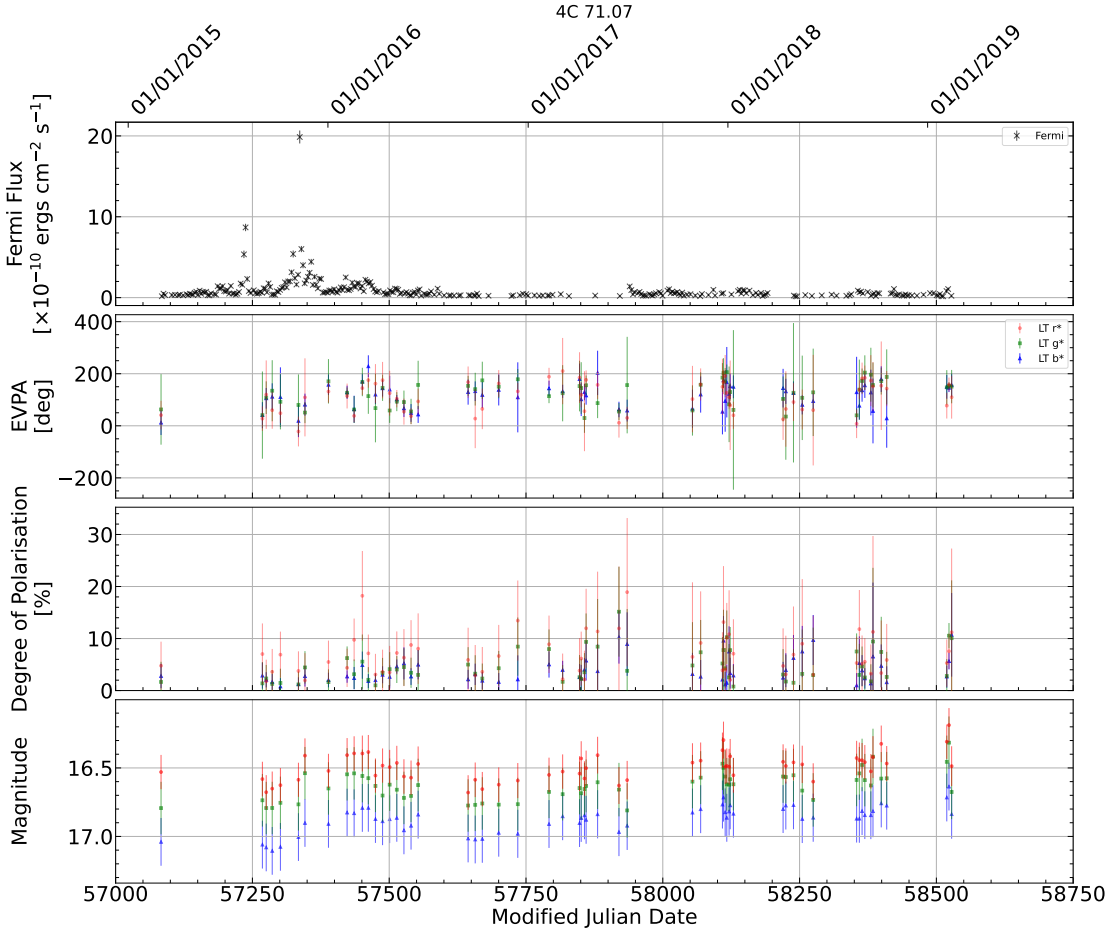

FIGURE A.32: As Fig. A.2, but for 4C 71.07.

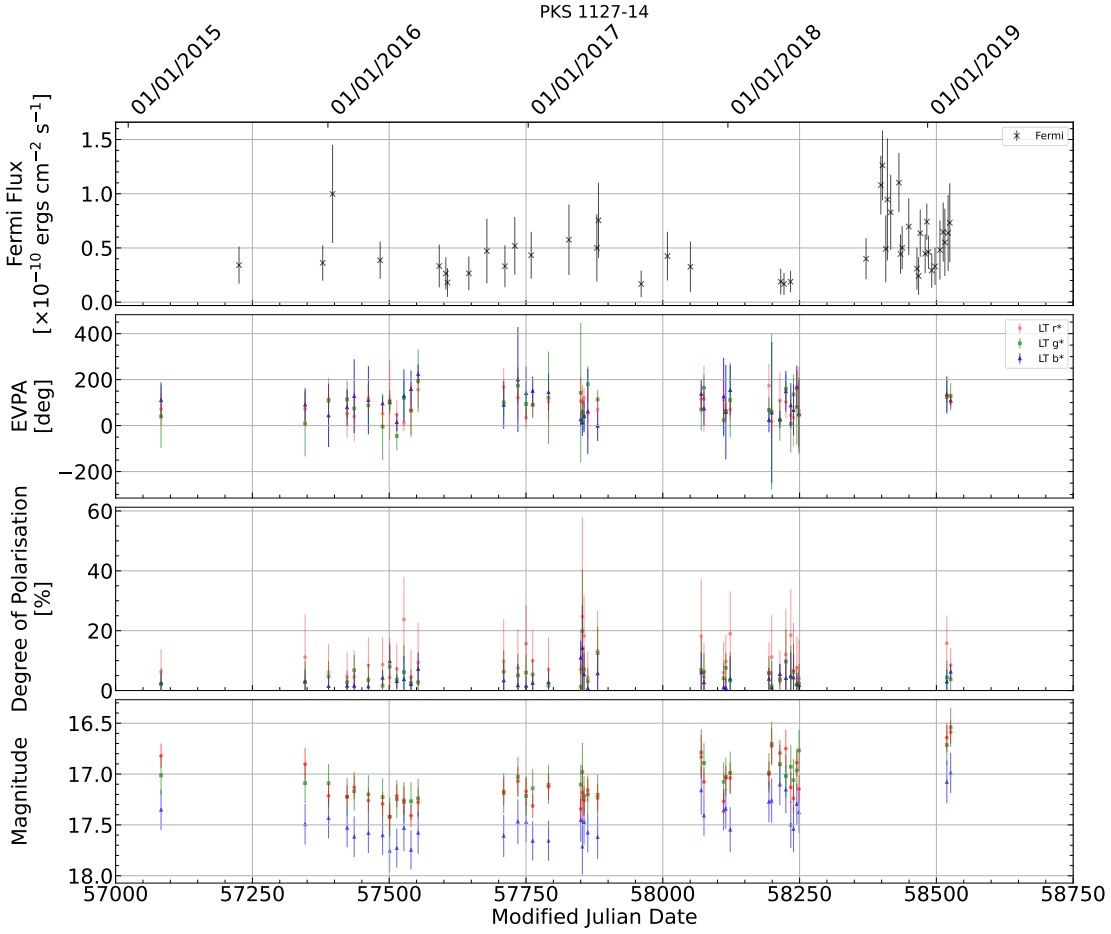

FIGURE A.33: As Fig. A.2, but for PKS 1127-14.

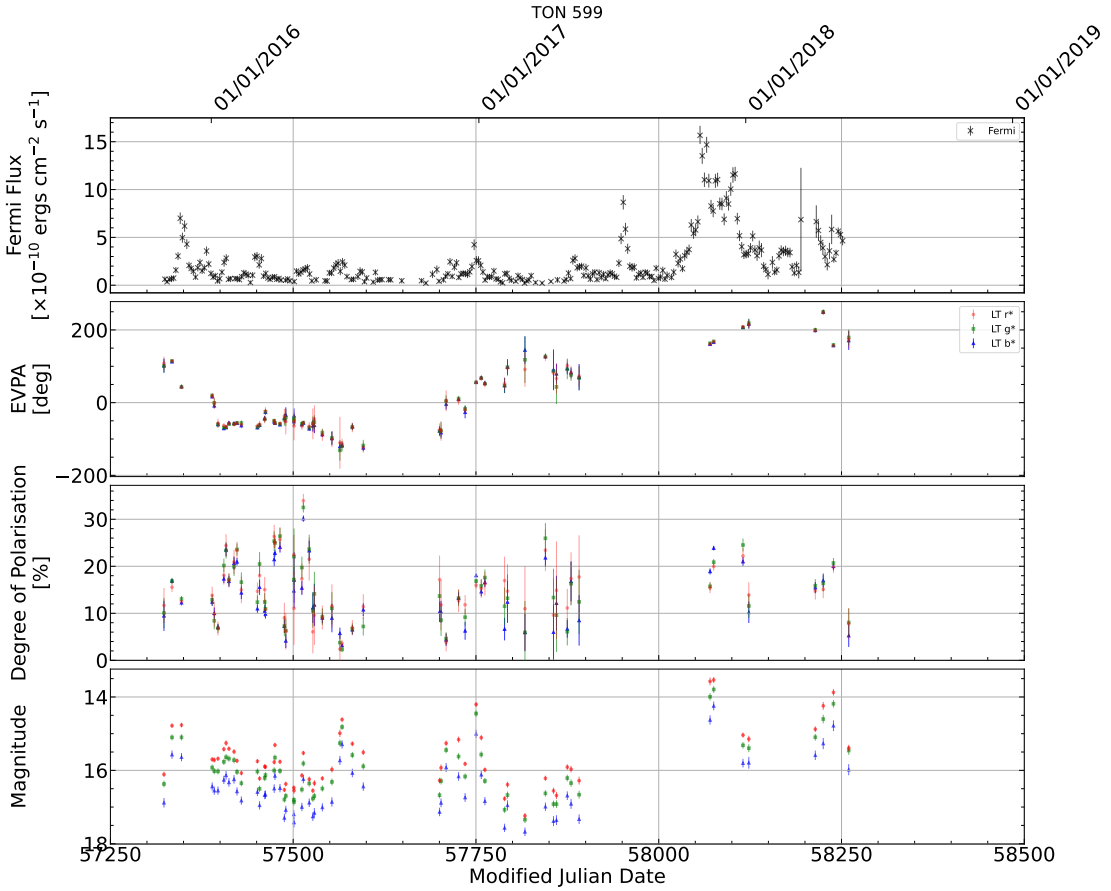

FIGURE A.34: As Fig. A.2, but for TON 599.

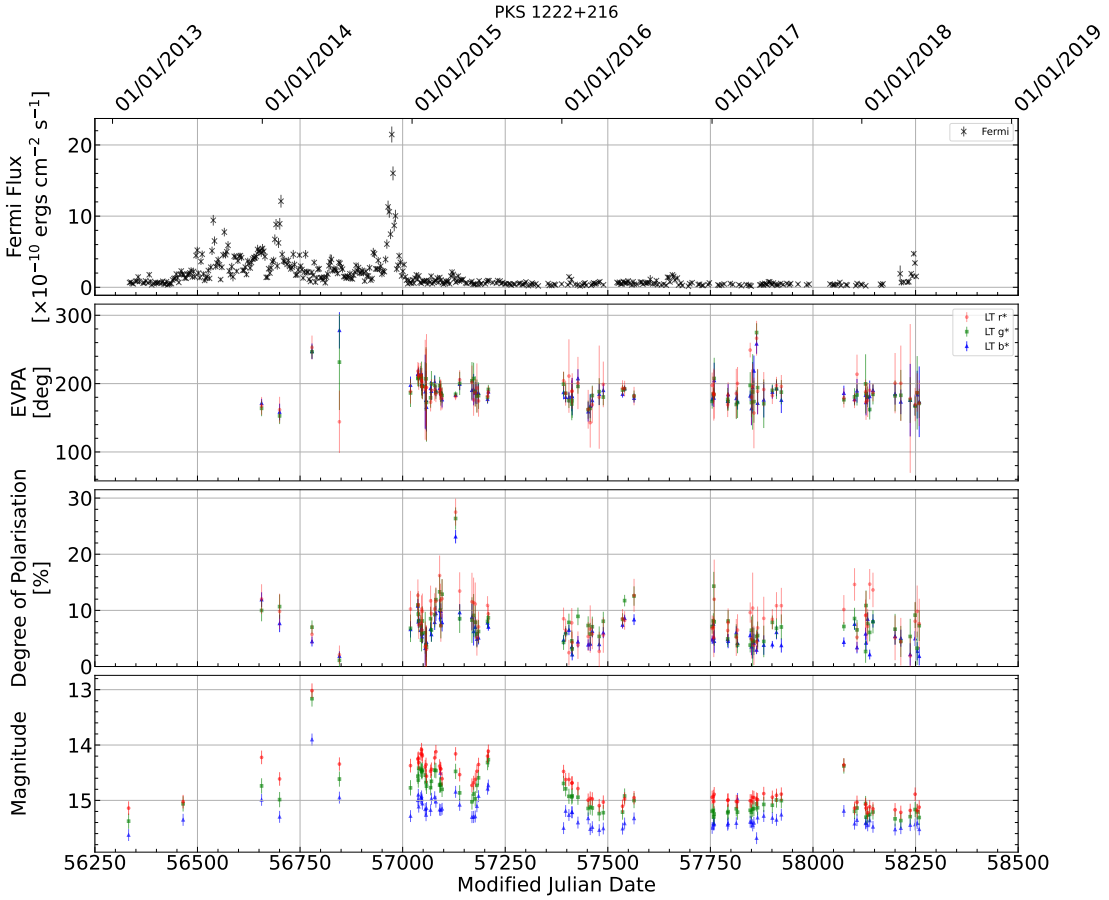

FIGURE A.35: As Fig. A.2, but for PKS 1222+216.

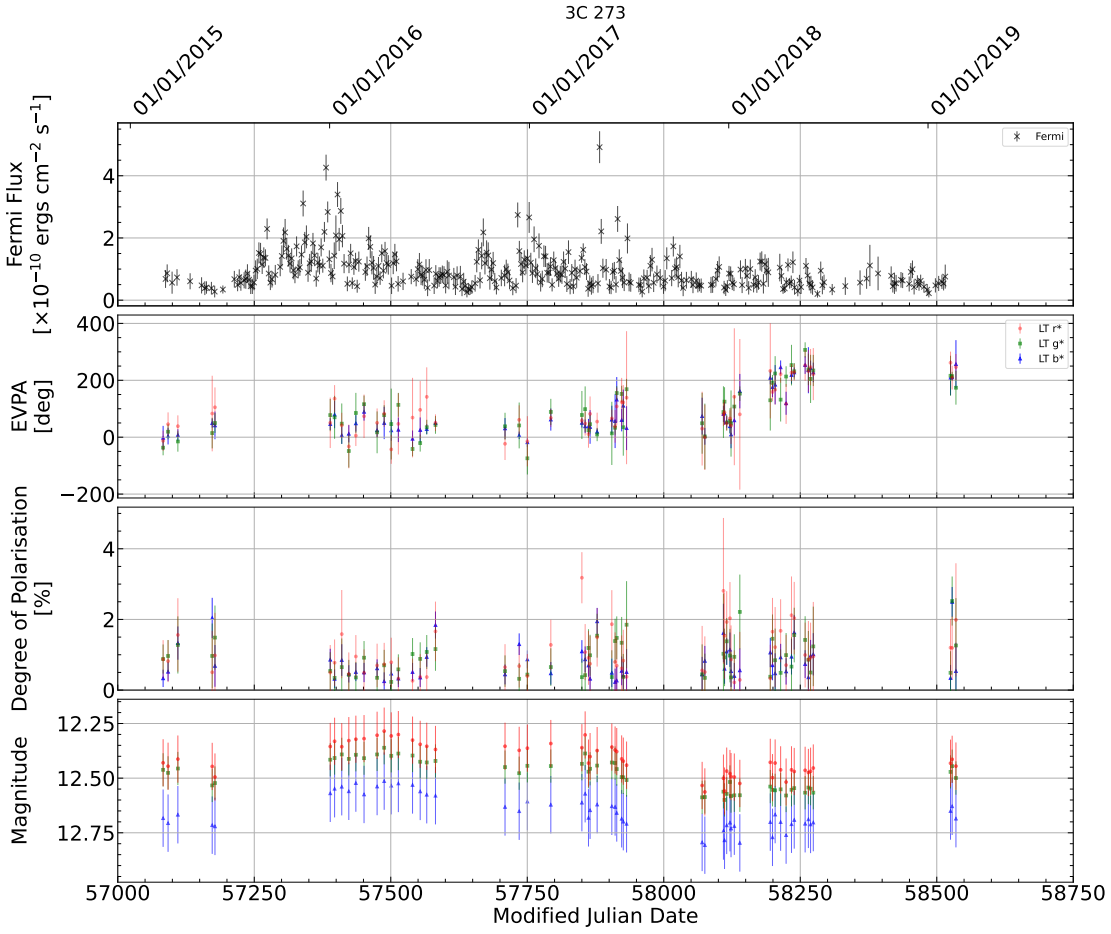

FIGURE A.36: As Fig. A.2, but for 3C 273.

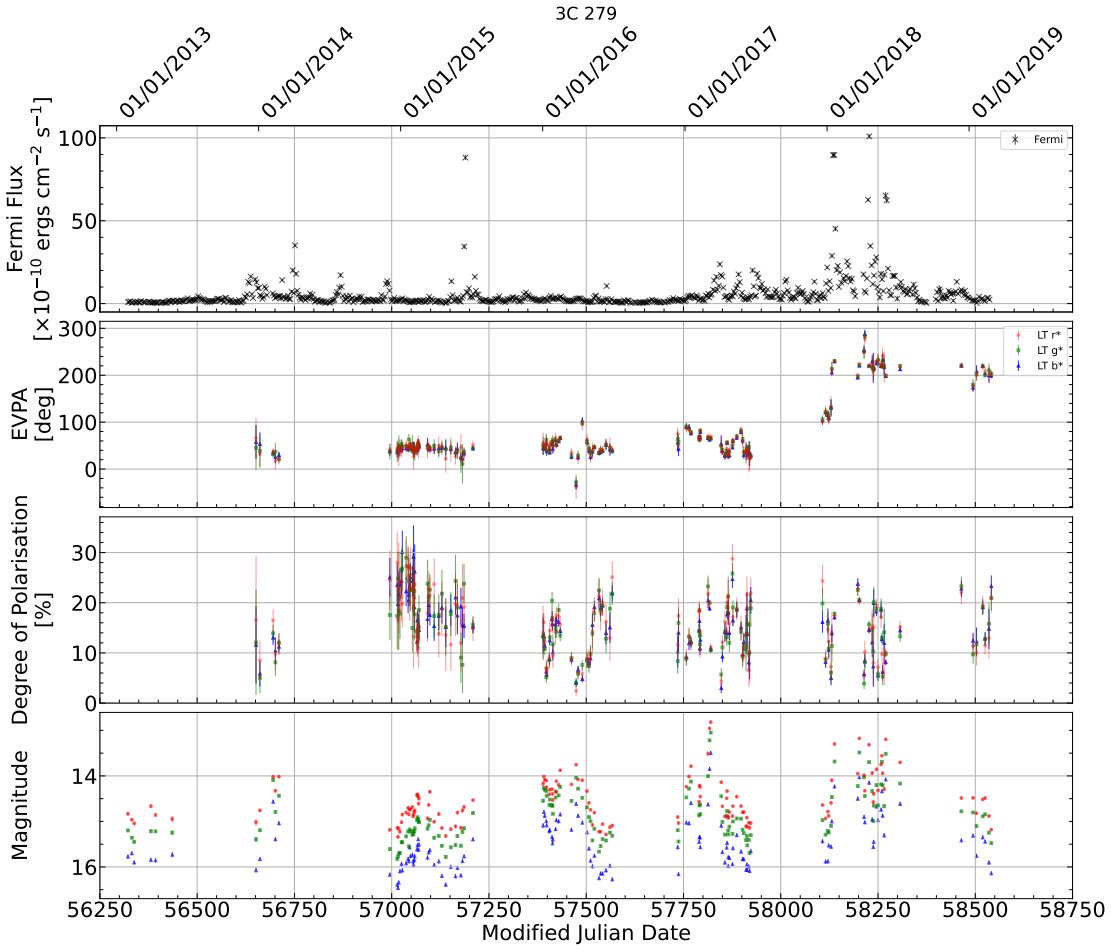

FIGURE A.37: As Fig. A.2, but for 3C 279.

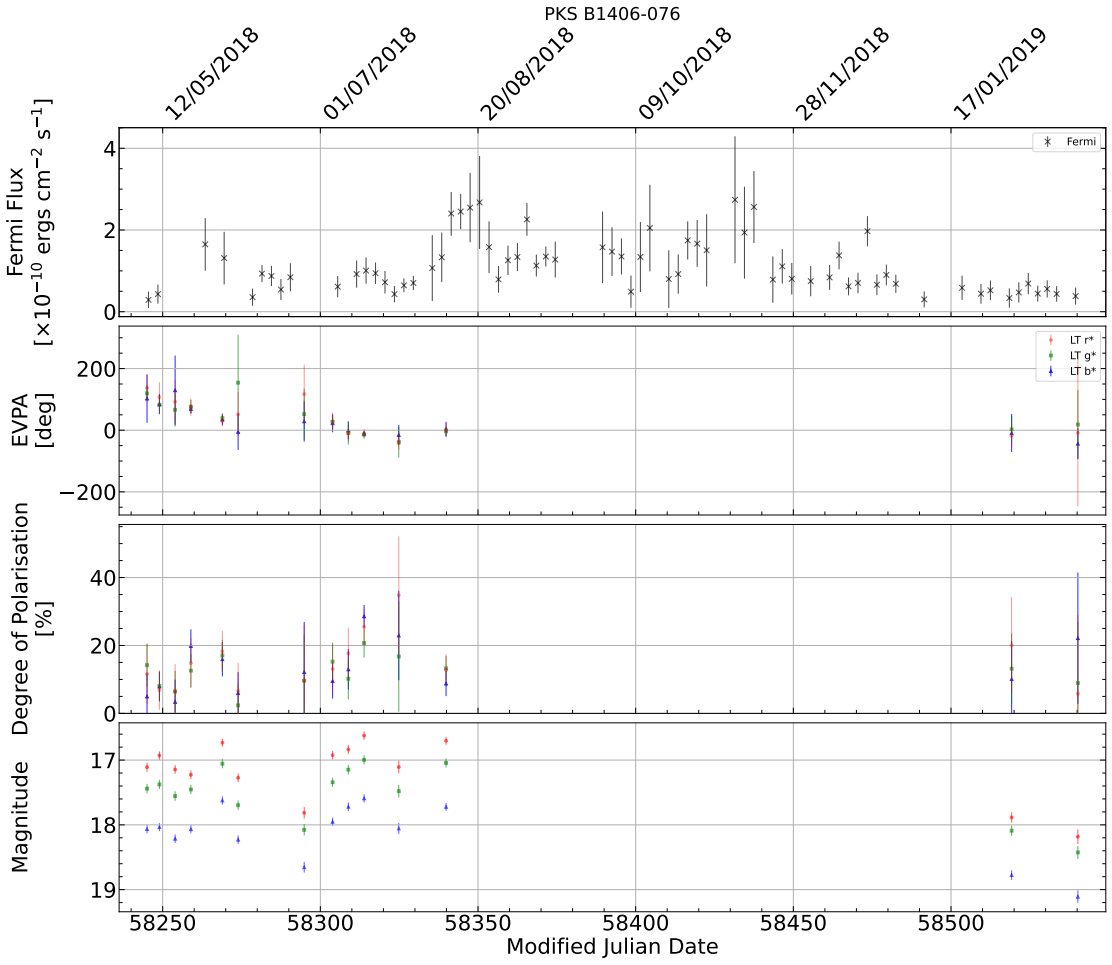

FIGURE A.38: As Fig. A.2, but for PKS B1406-076.

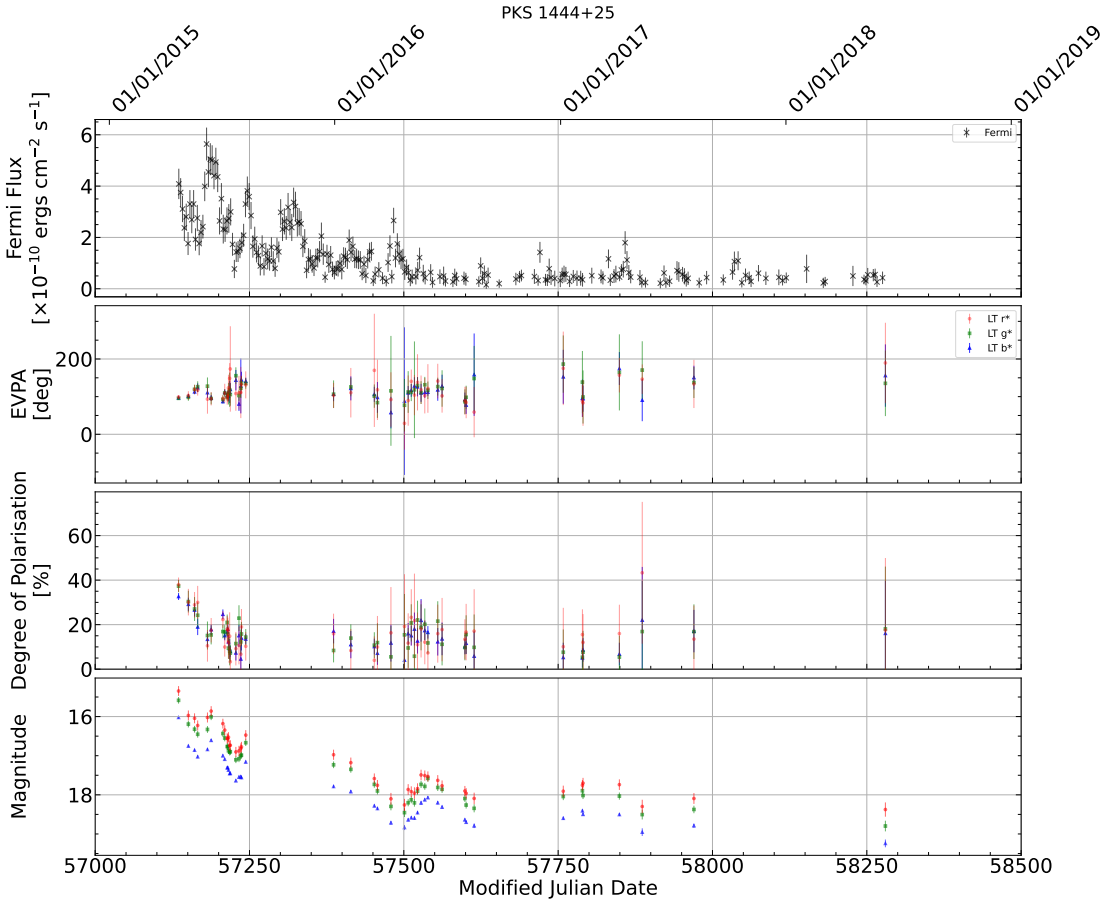

FIGURE A.39: As Fig. A.2, but for PKS 1444+25.

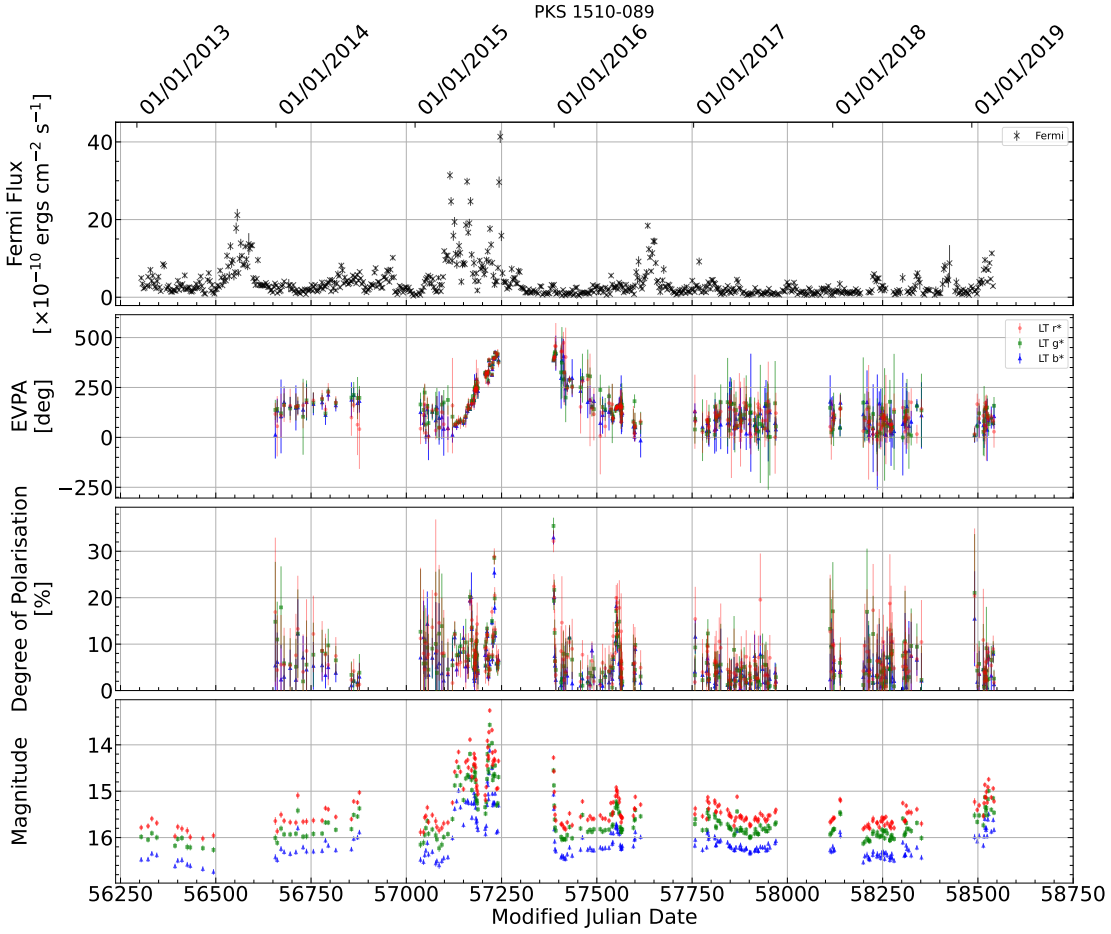

FIGURE A.40: As Fig. A.2, but for PKS 1510-089.

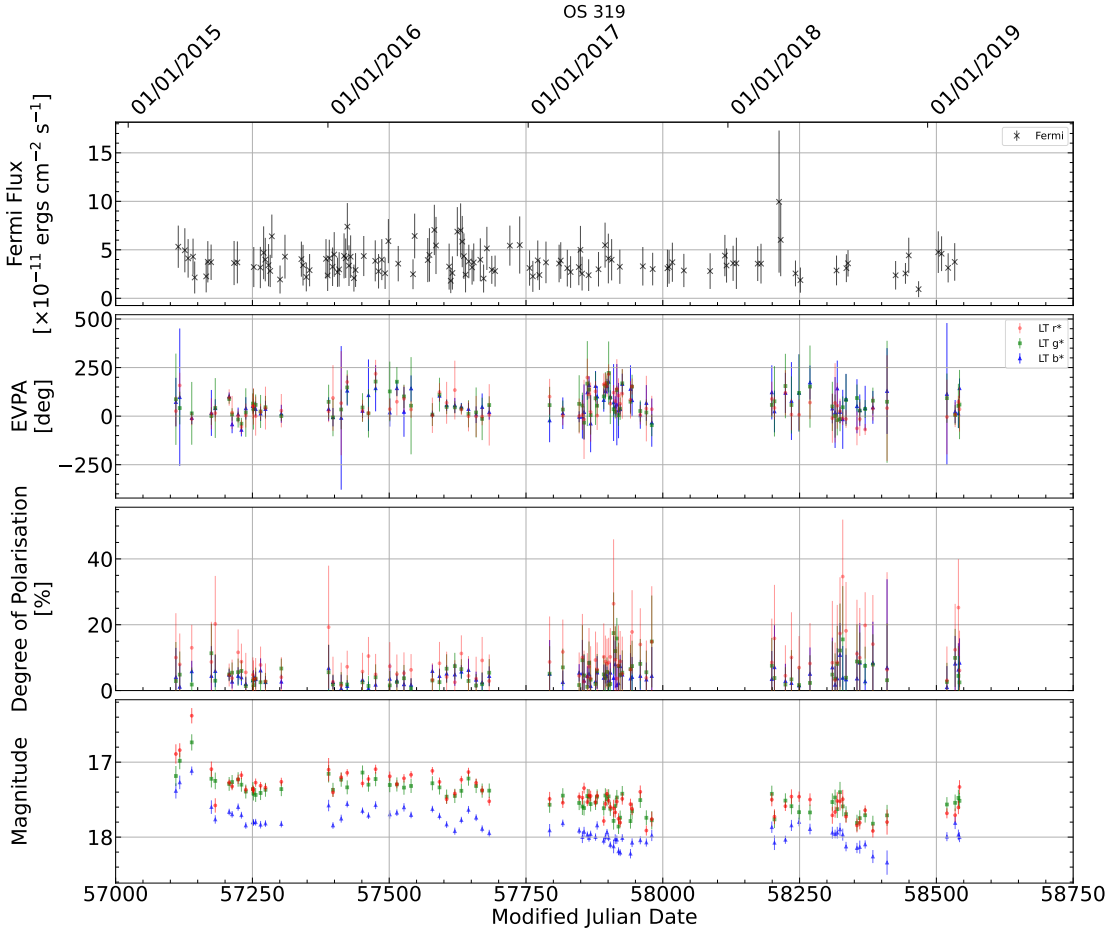

FIGURE A.41: As Fig. A.2, but for OS 319.

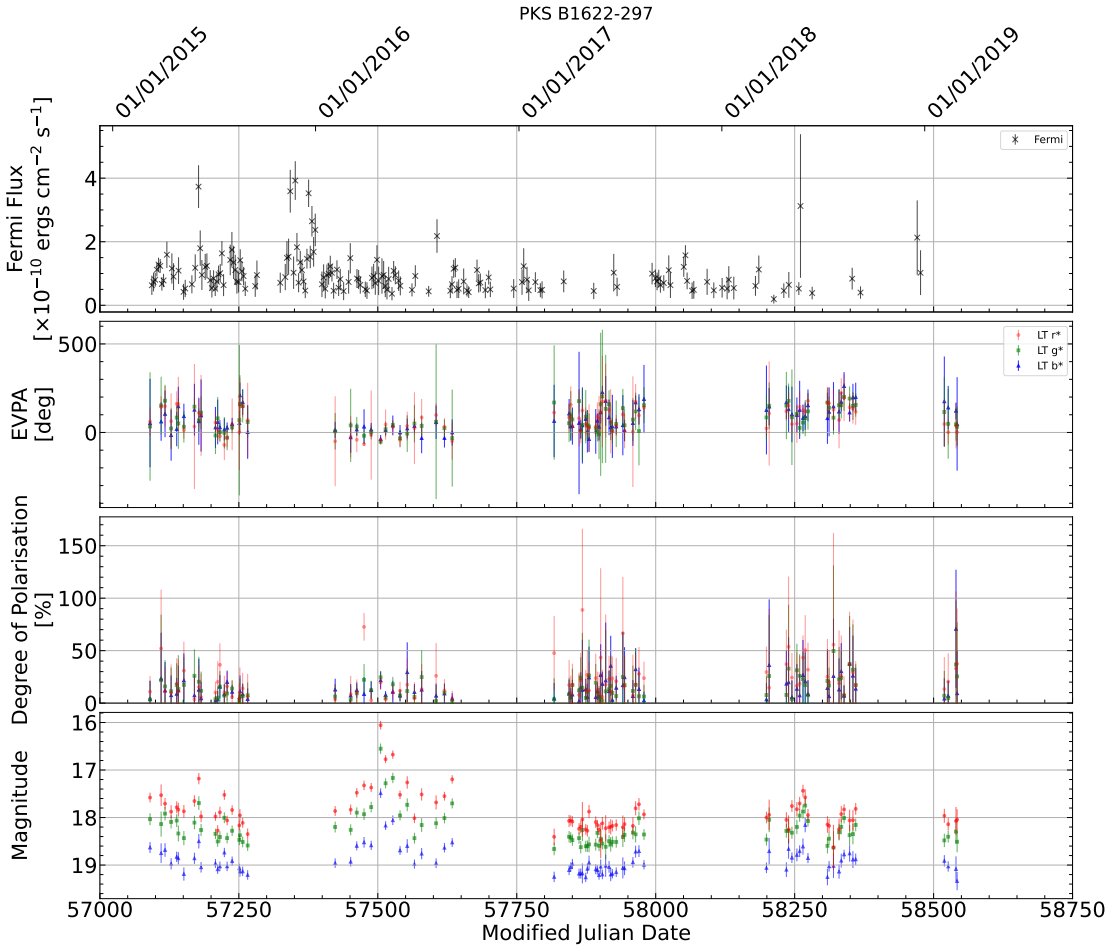

FIGURE A.42: As Fig. A.2, but for PKS B1622-297.

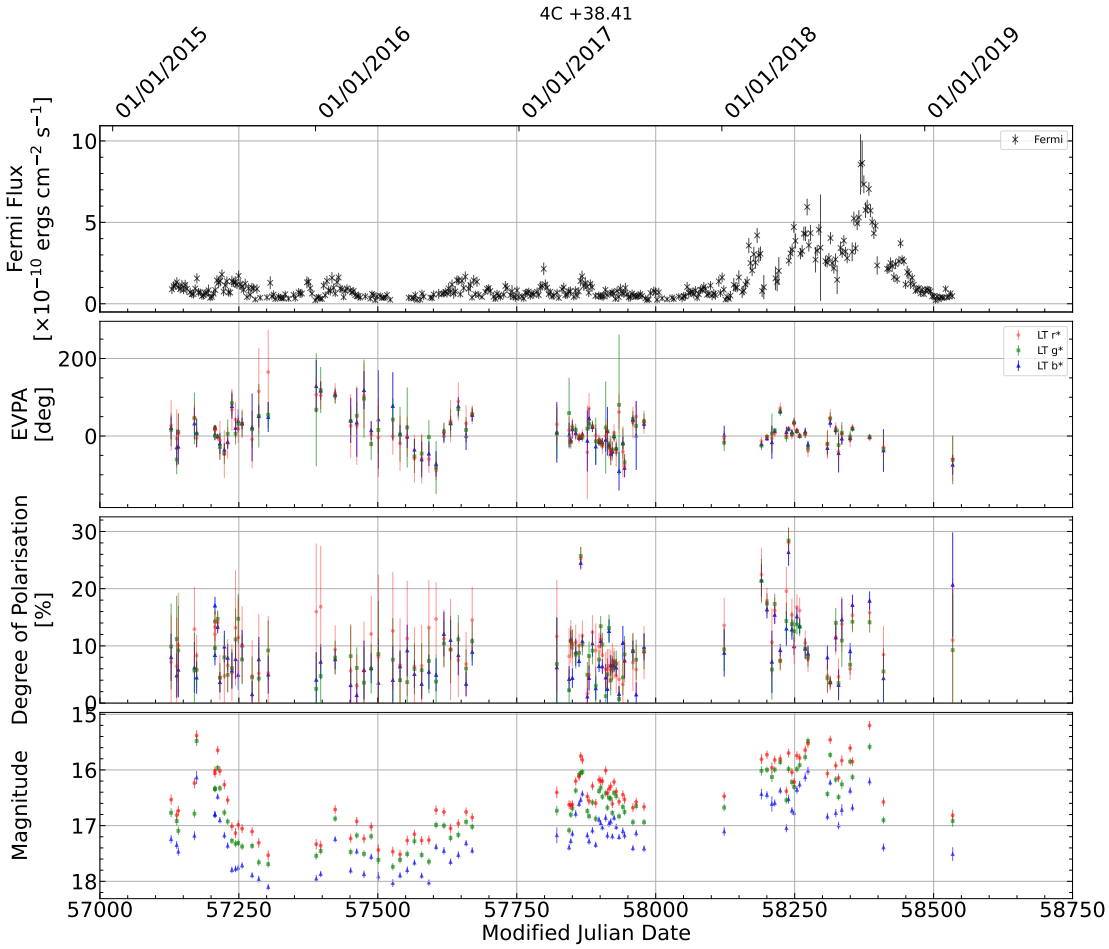

FIGURE A.43: As Fig. A.2, but for 4C+38.41.

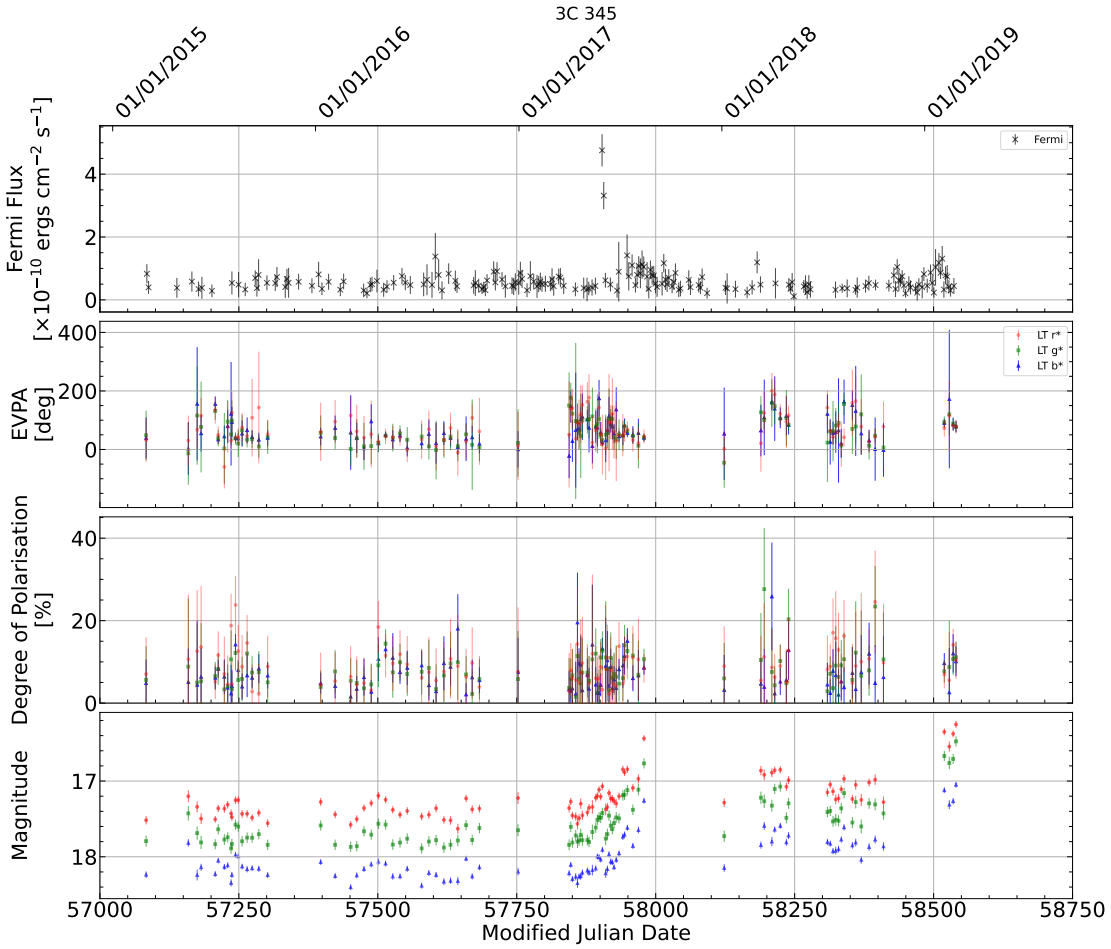

FIGURE A.44: As Fig. A.2, but for 3C 345.

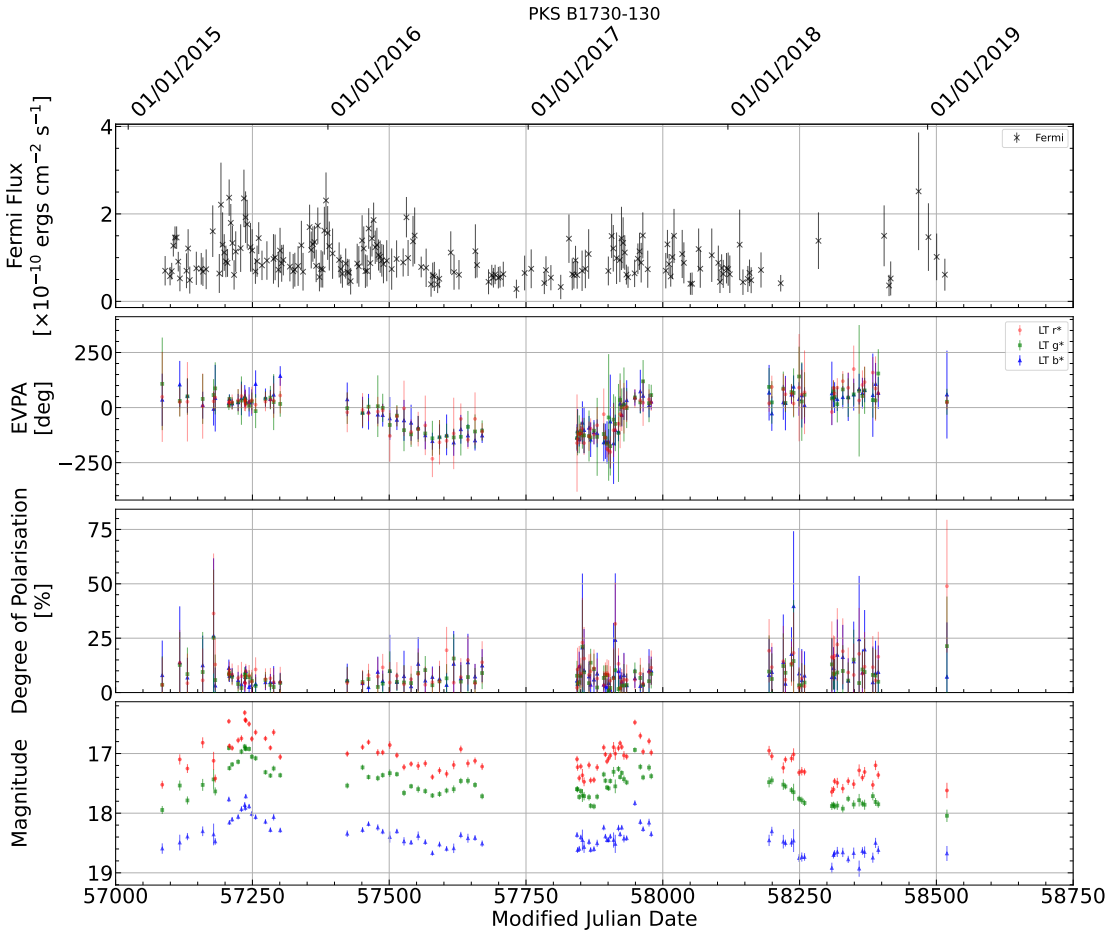

FIGURE A.45: As Fig. A.2, but for PKS B1730-130.

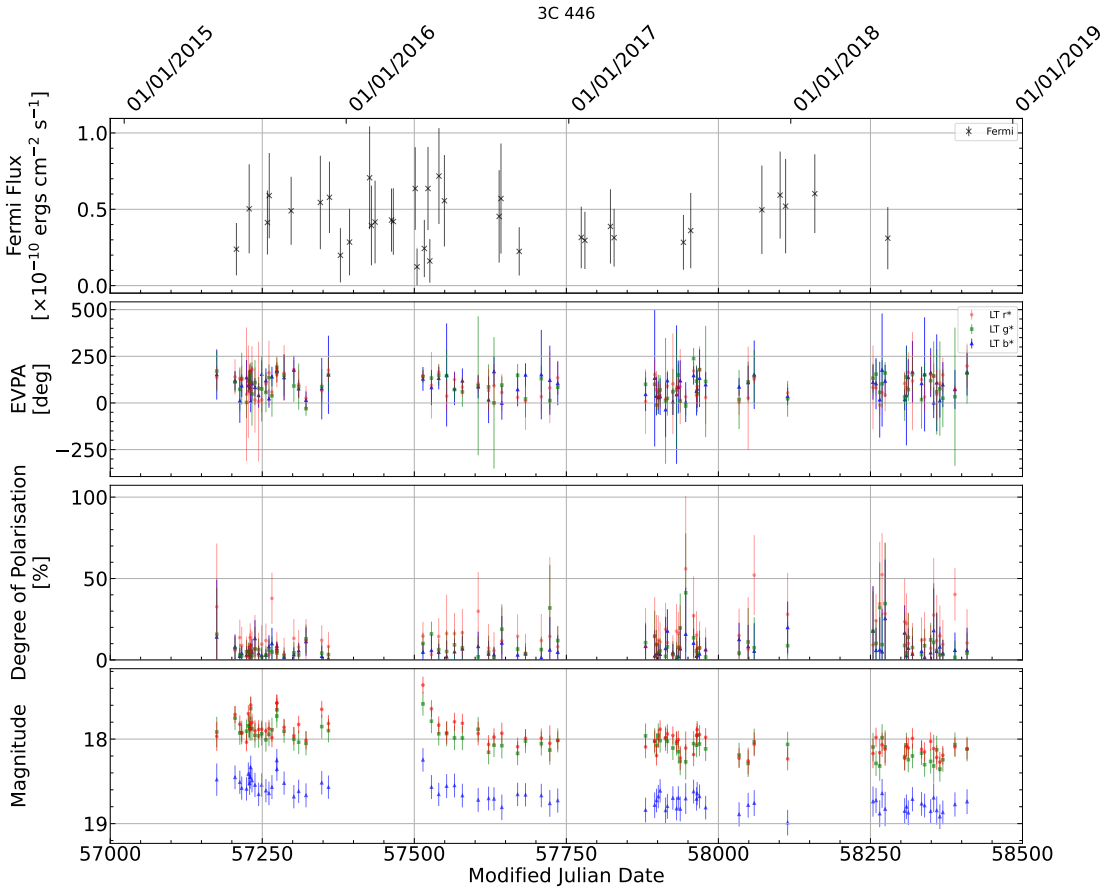

FIGURE A.46: As Fig. A.2, but for 3C 446.

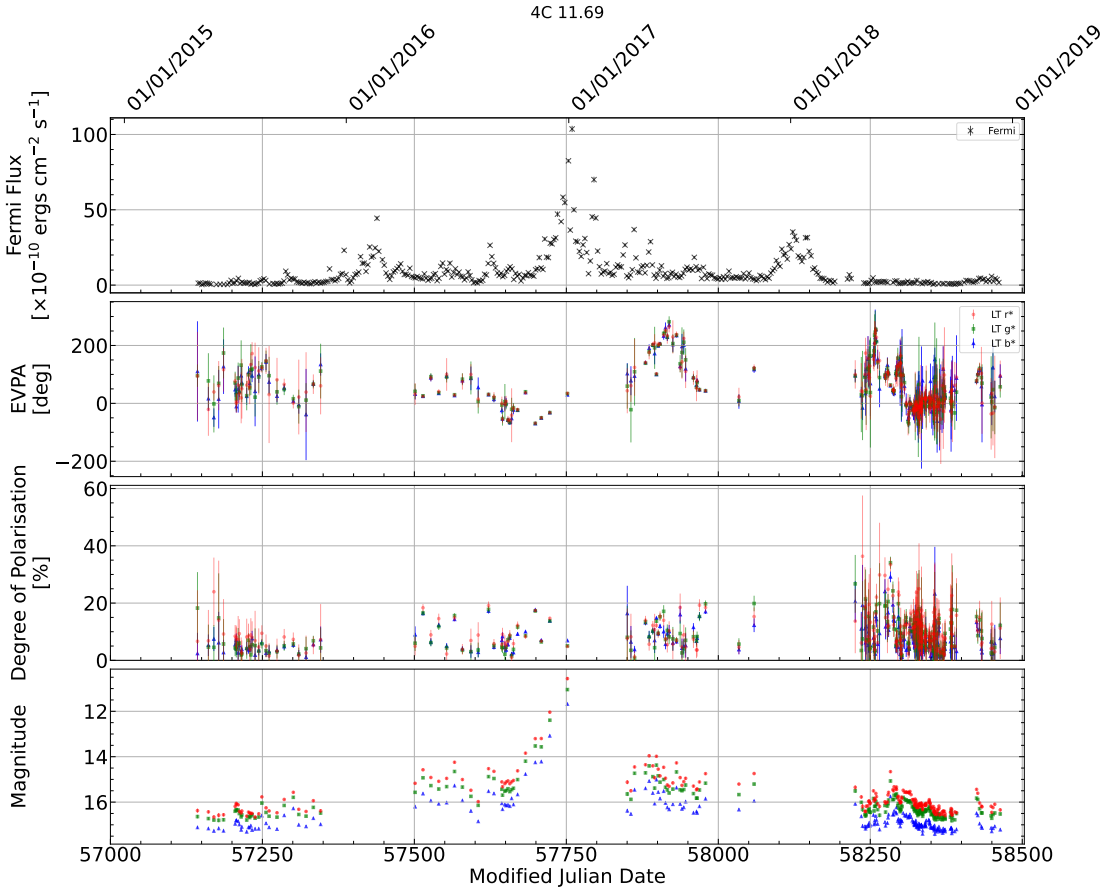

FIGURE A.47: As Fig. A.2, but for 4C 11.69.

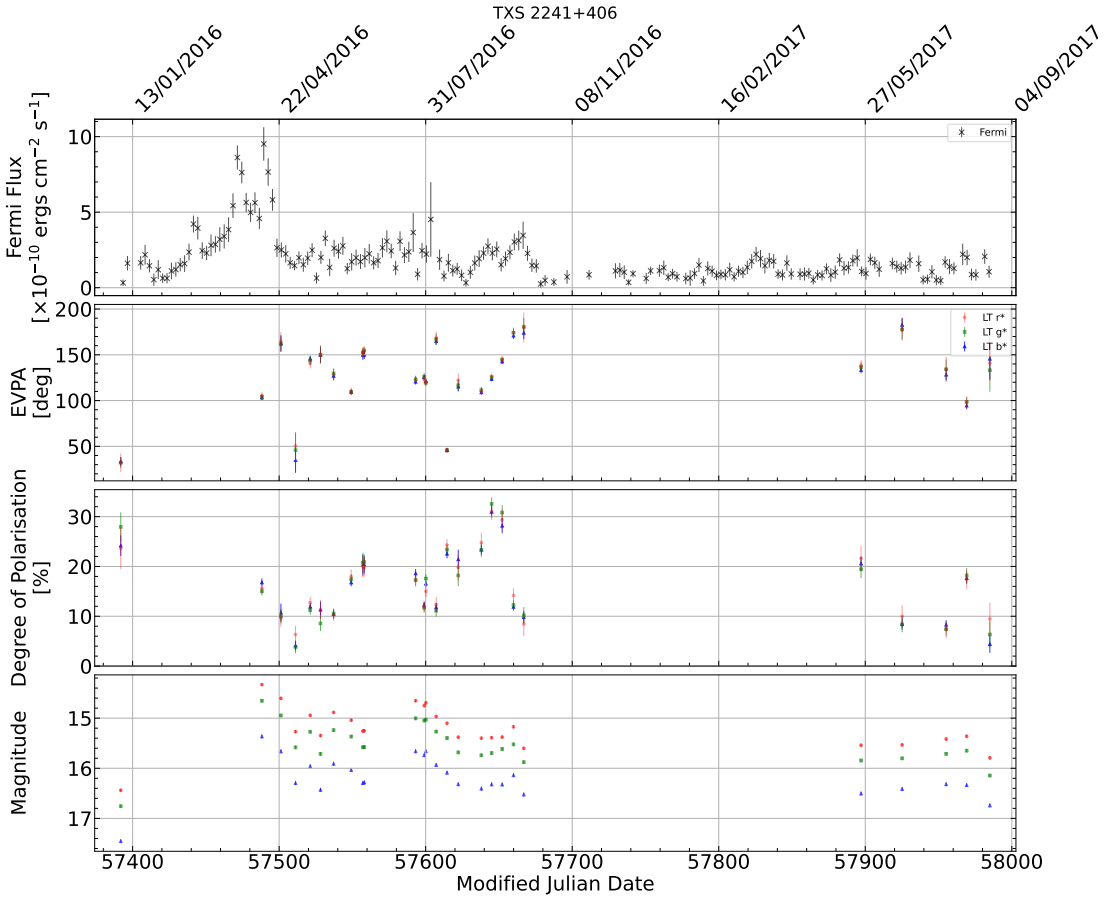

FIGURE A.48: As Fig. A.2, but for TXS 2241+406.

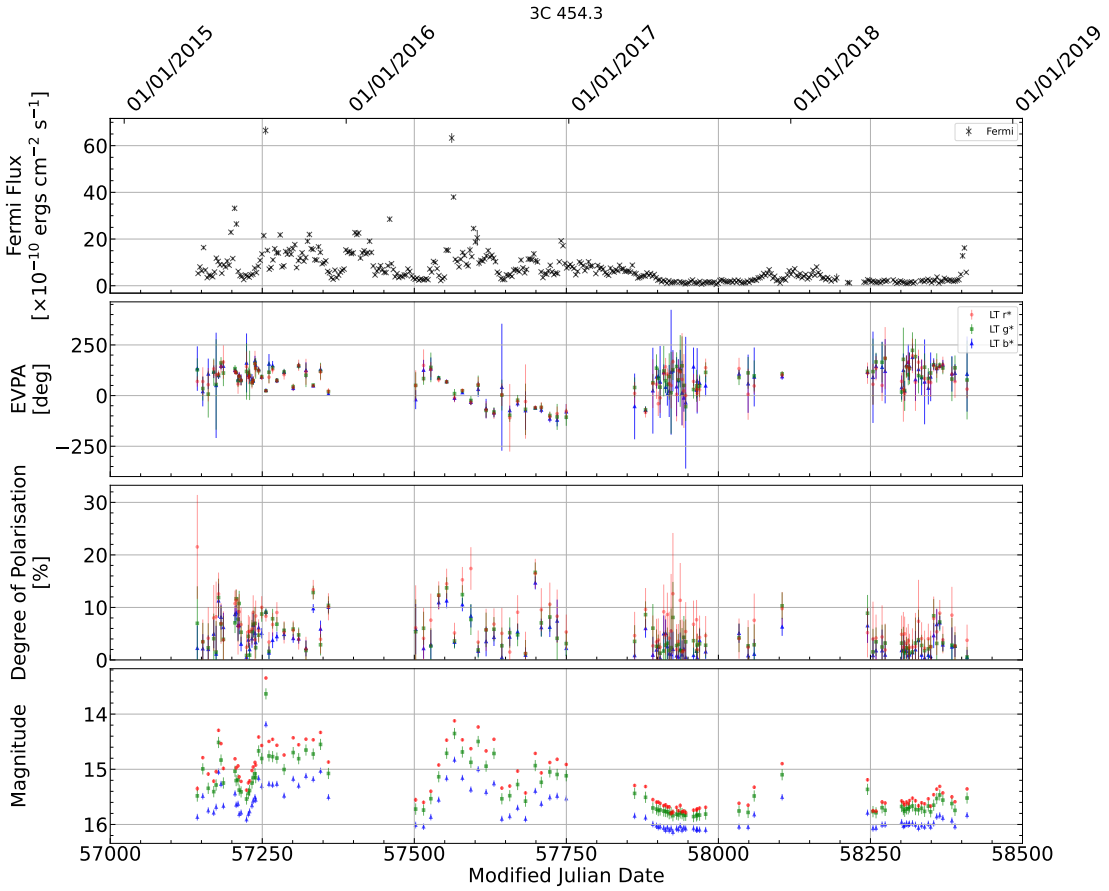

FIGURE A.49: As Fig. A.2, but for 3C 454.3.

Appendix B – MOPTOP light curves

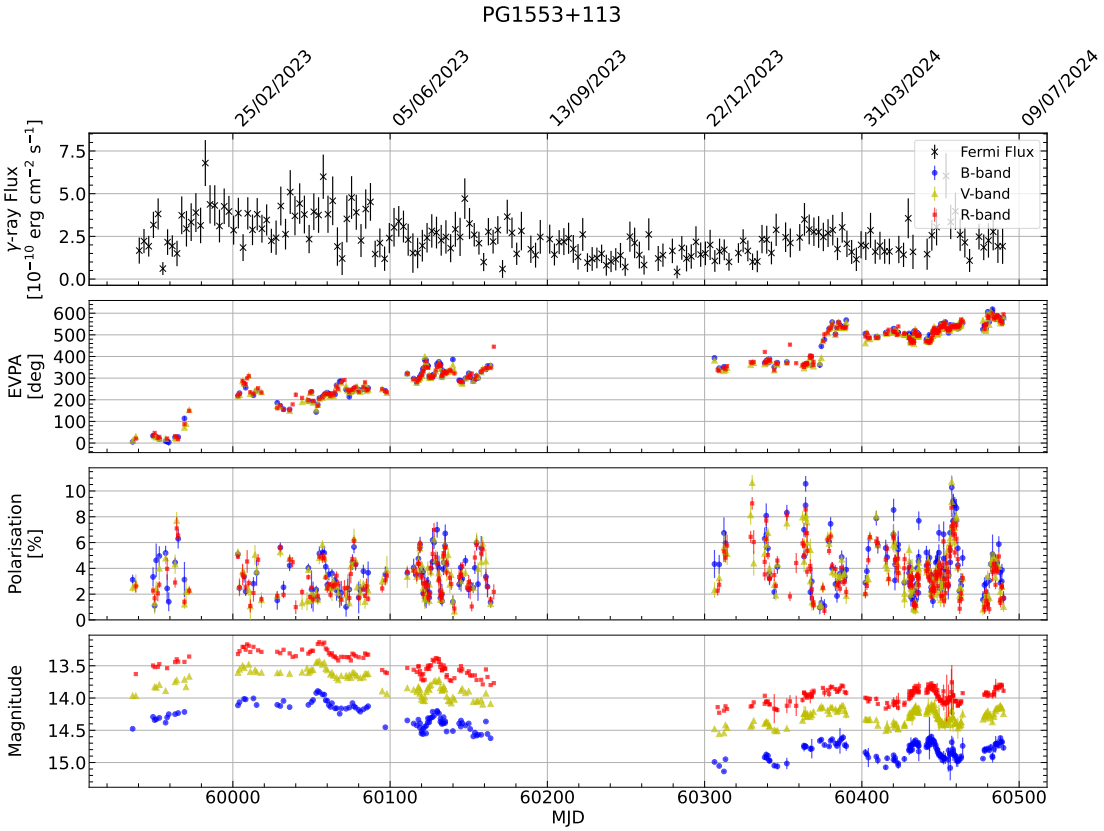

FIGURE B.1: Plots showing the full MOPTOP *BVR* data set for the source PG 1553+113 in addition to Fermi γ-ray data from the Fermi LAT Light Curve Repository (Abdollahi et al., 2023) taken over the same period. From top to bottom, the panels show the evolution of γ-ray flux, EVPA, degree of polarisation, and magnitude with time.

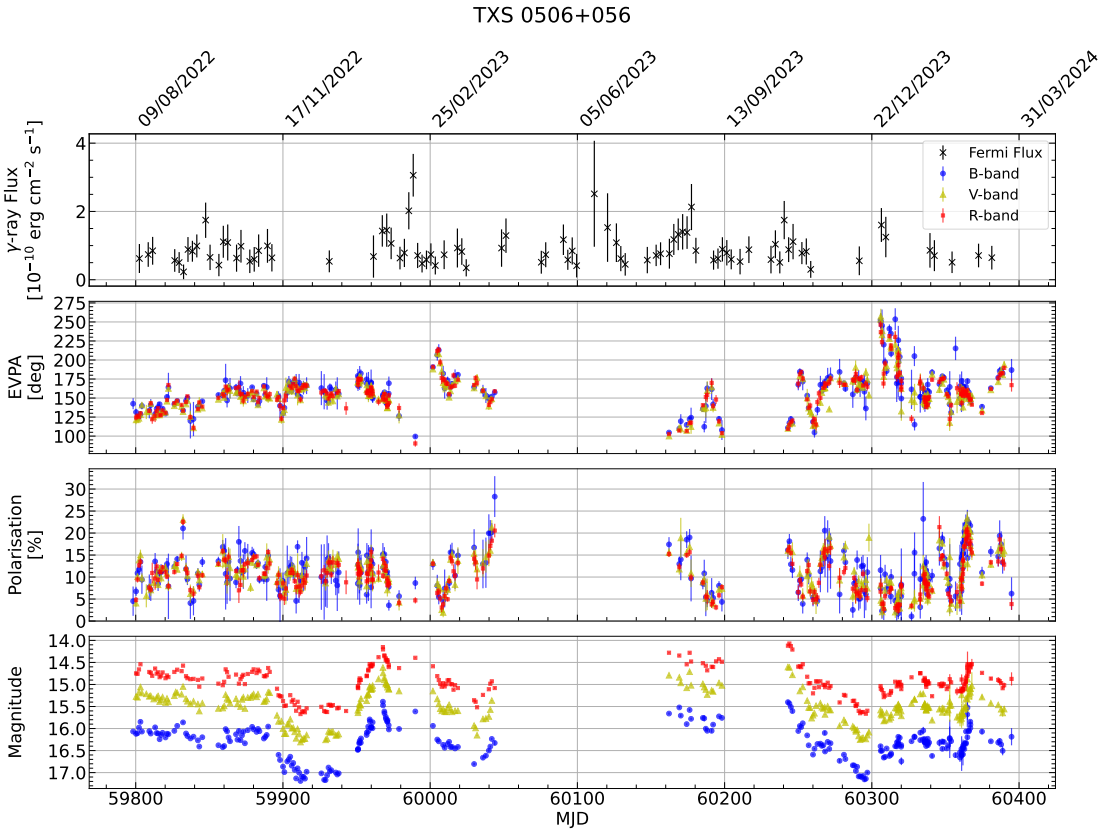

FIGURE B.2: As Fig. B.1, but for TXS 0506+056.

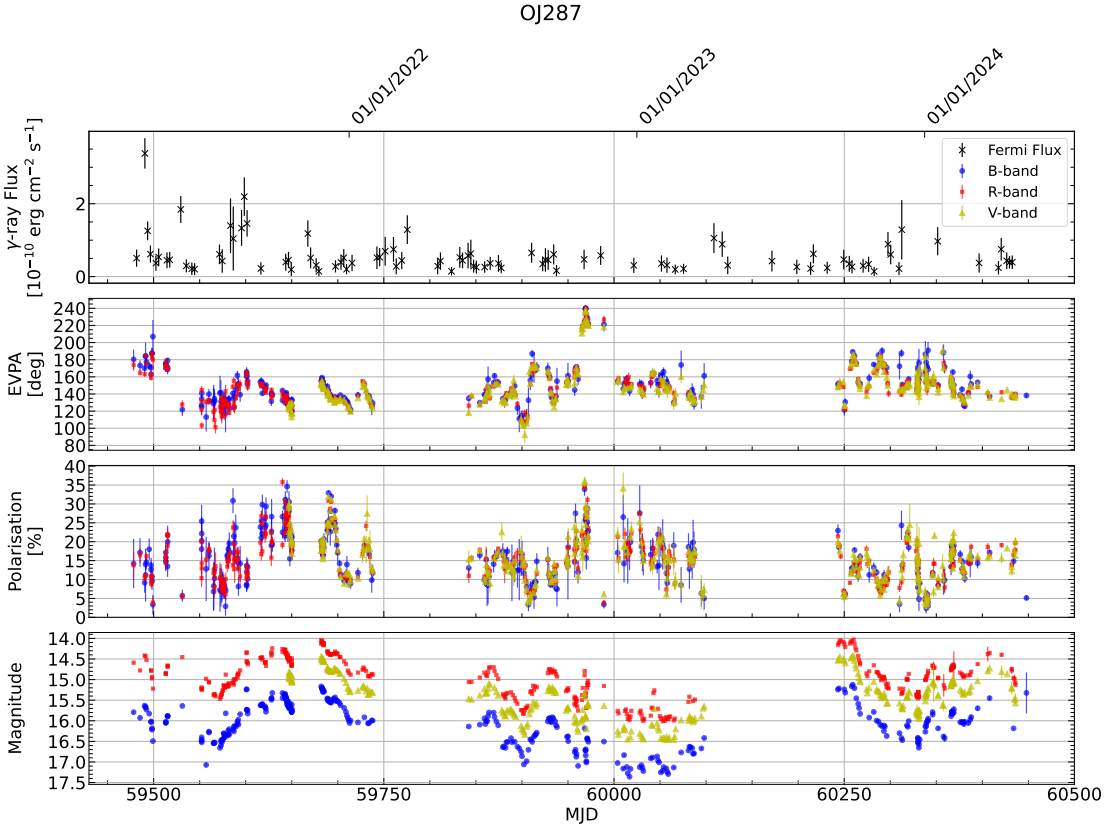

FIGURE B.3: As Fig. B.1, but for OJ 287.

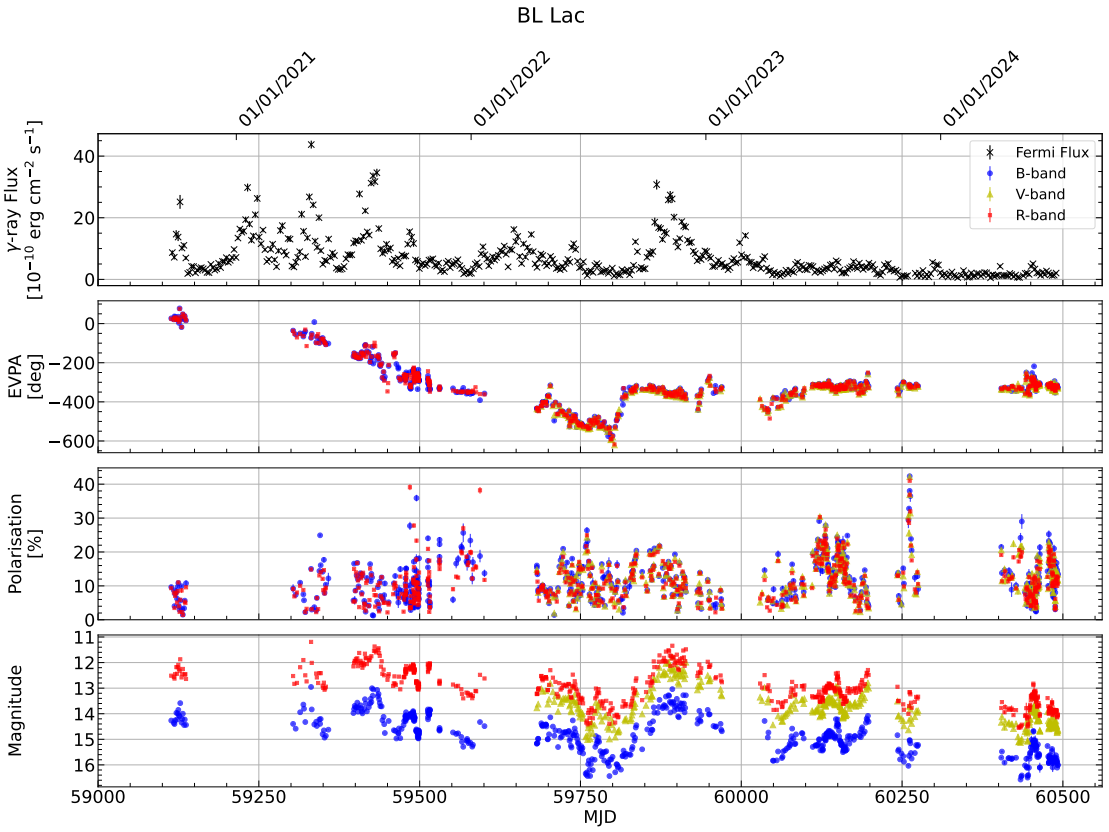

FIGURE B.4: As Fig. B.1, but for BL Lac.

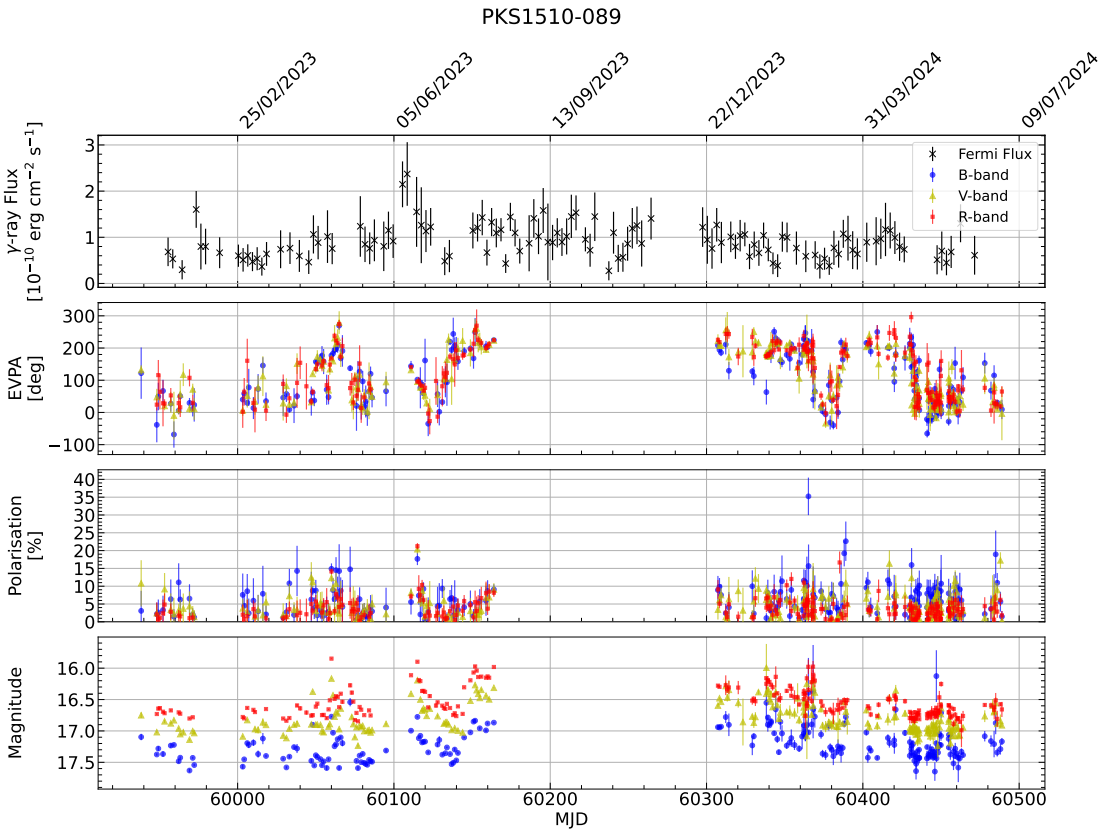

FIGURE B.5: As Fig. B.1, but for PKS 1510-089.

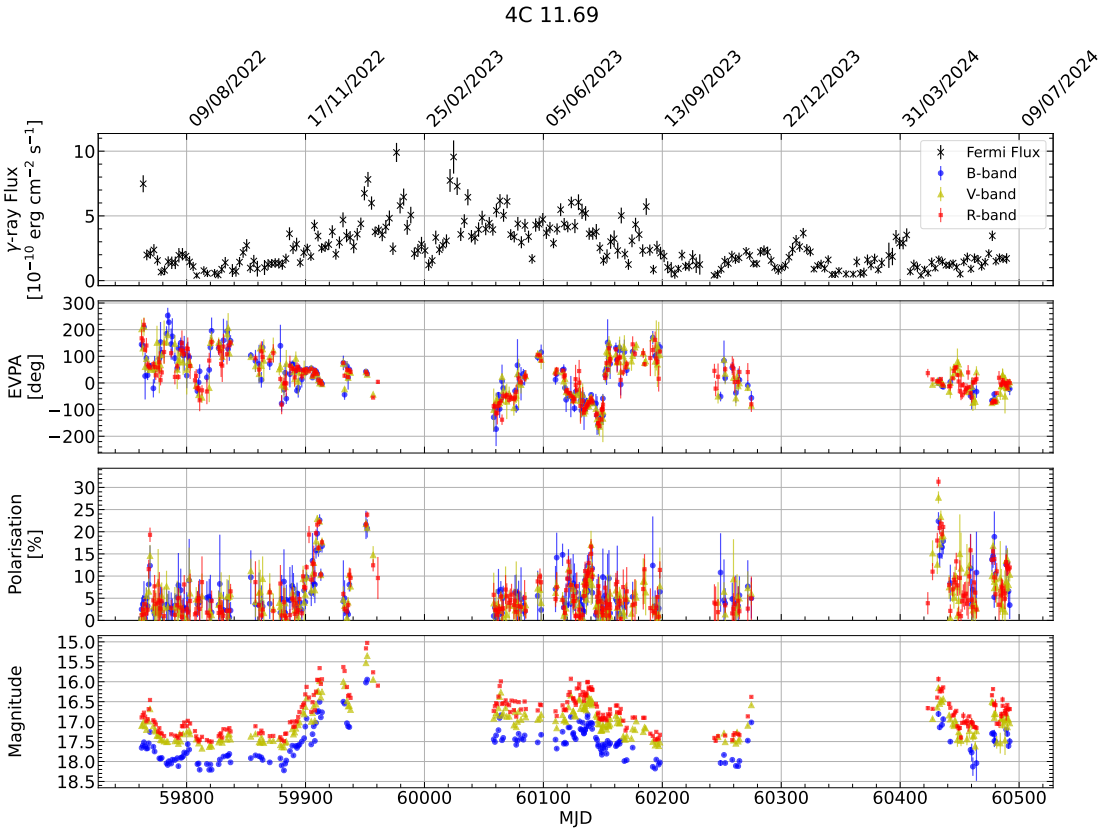

FIGURE B.6: As Fig. B.1, but for 4C 11.69.

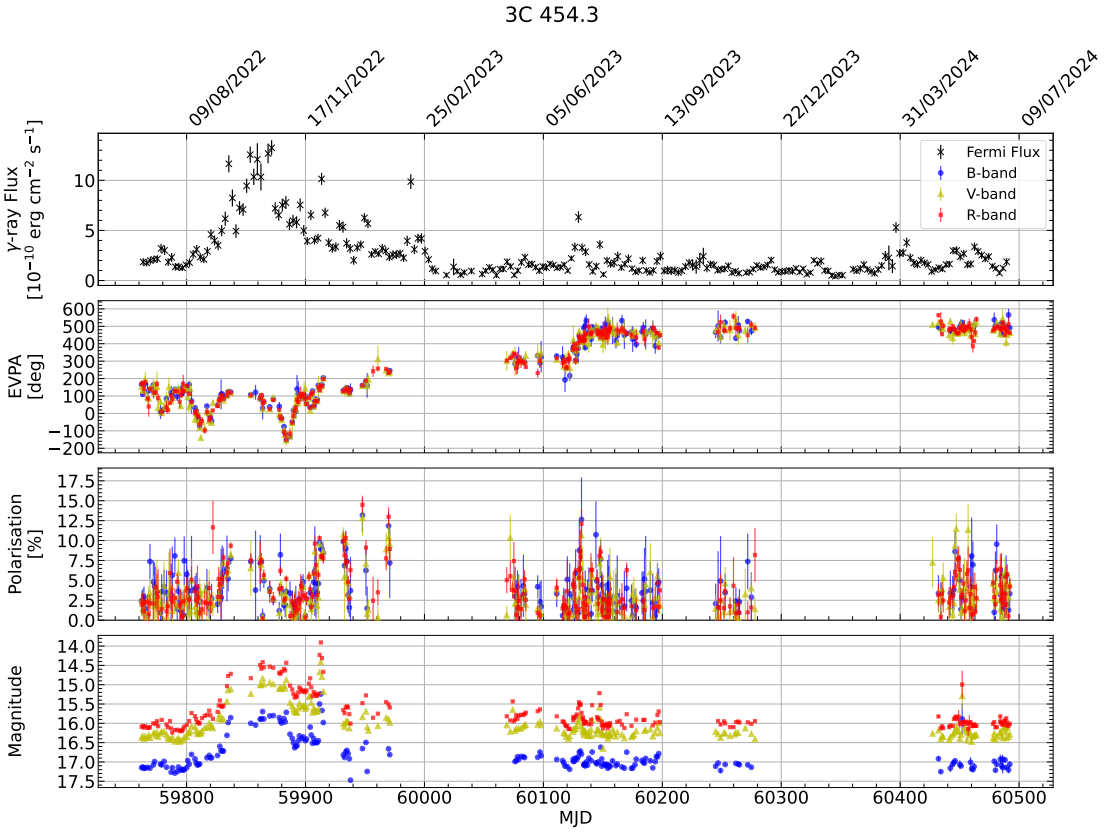

FIGURE B.7: As Fig. B.1, but for 3C 454.3.

Appendix C – Figures and tables

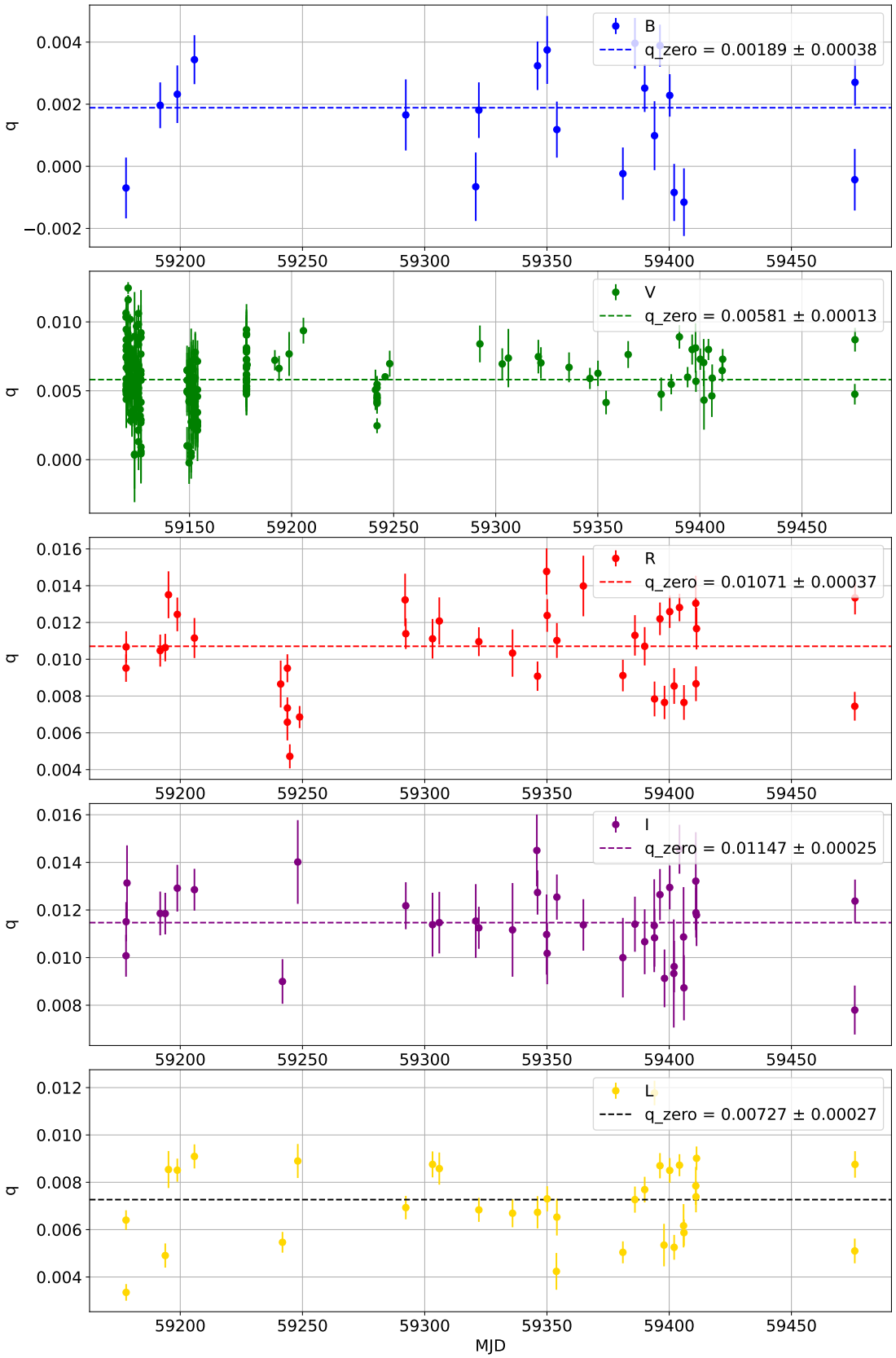

FIGURE C.1: q values of zero-polarised standard stars for each MOPTOP filter during the first dual-camera configuration epoch (epoch 1). The average values are taken as the q_0 value for that epoch.

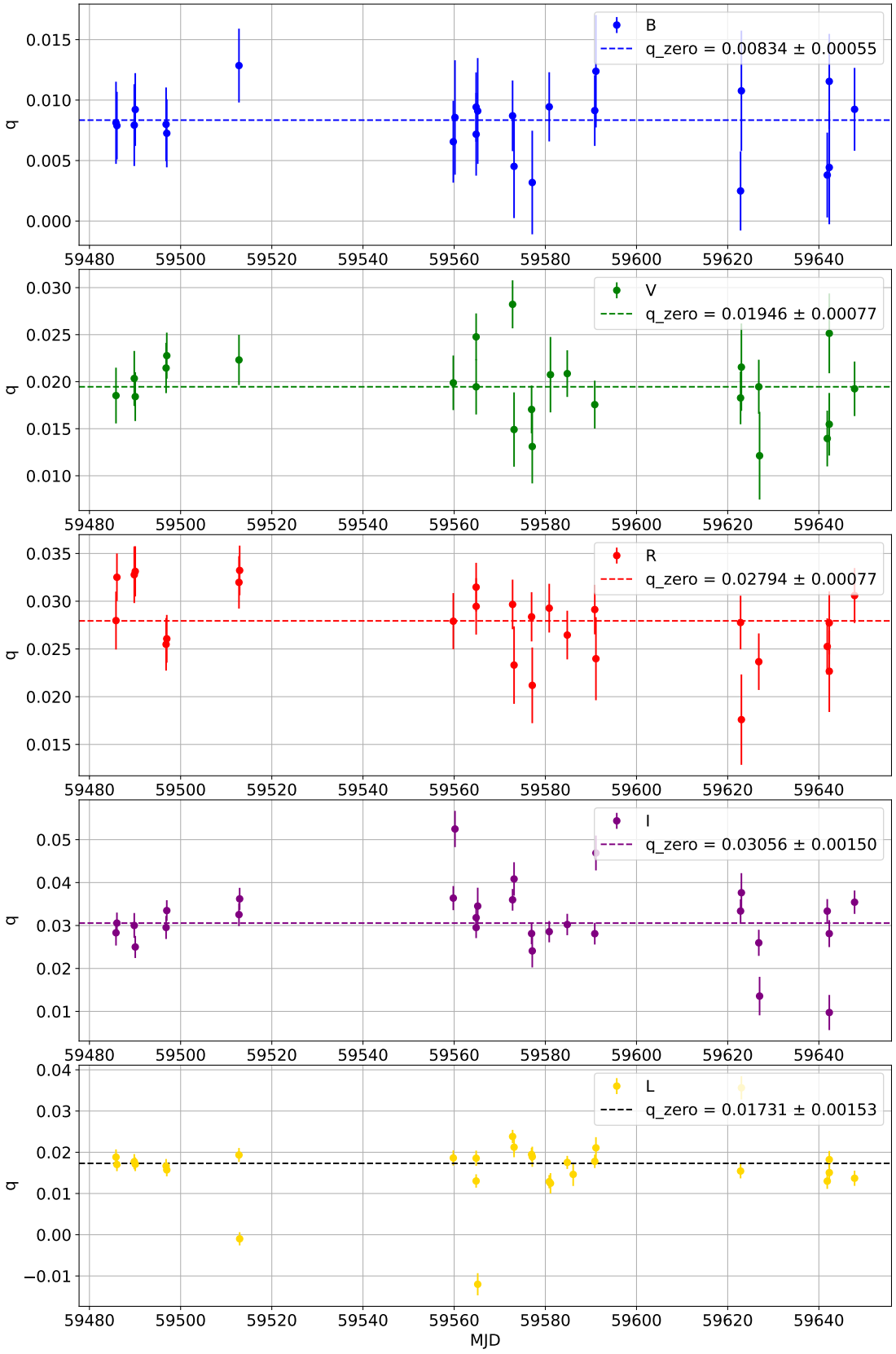

FIGURE C.2: q values of zero-polarised standard stars for each MOPTOP filter during the first single-camera configuration epoch (epoch 2). The average values are taken as the q_0 value for that epoch.

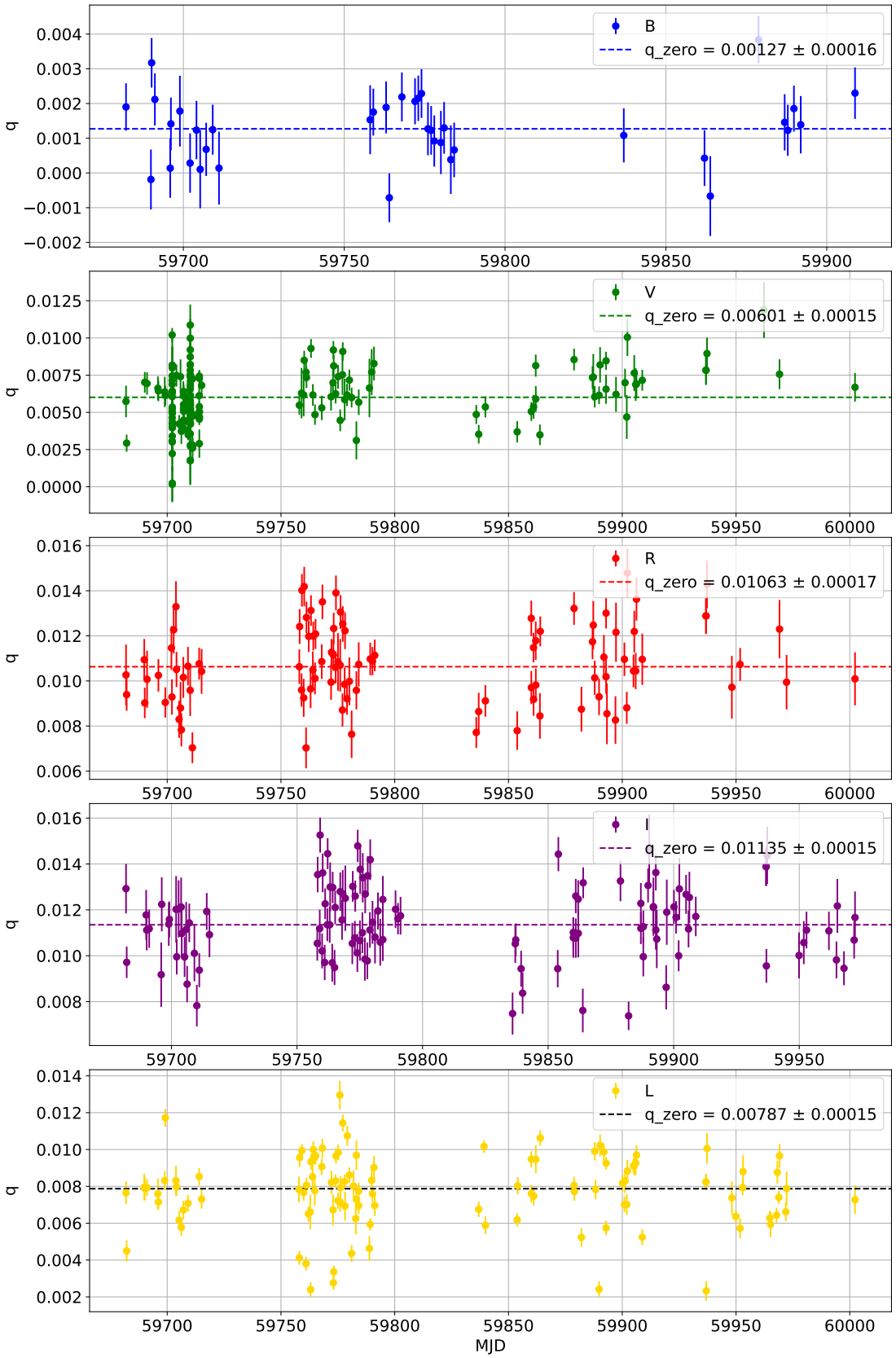

FIGURE C.3: q values of zero-polarised standard stars for each MOPTOP filter during the second dual-camera configuration epoch (epoch 3). The average values are taken as the q_0 value for that epoch.

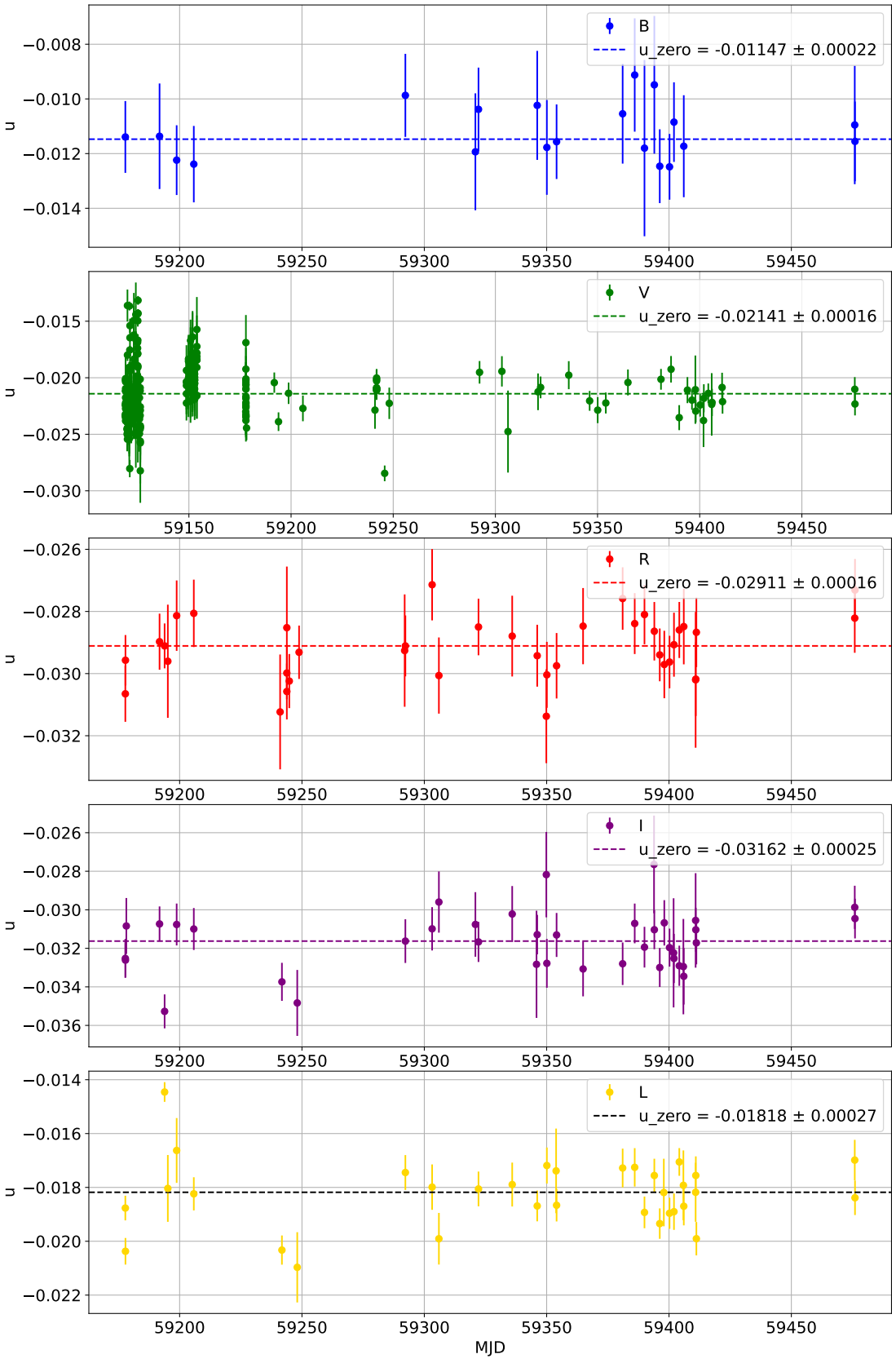

FIGURE C.4: u values of zero-polarised standard stars for each MOPTOP filter during the first dual-camera configuration epoch (epoch 1). The average values are taken as the u_0 value for that epoch.

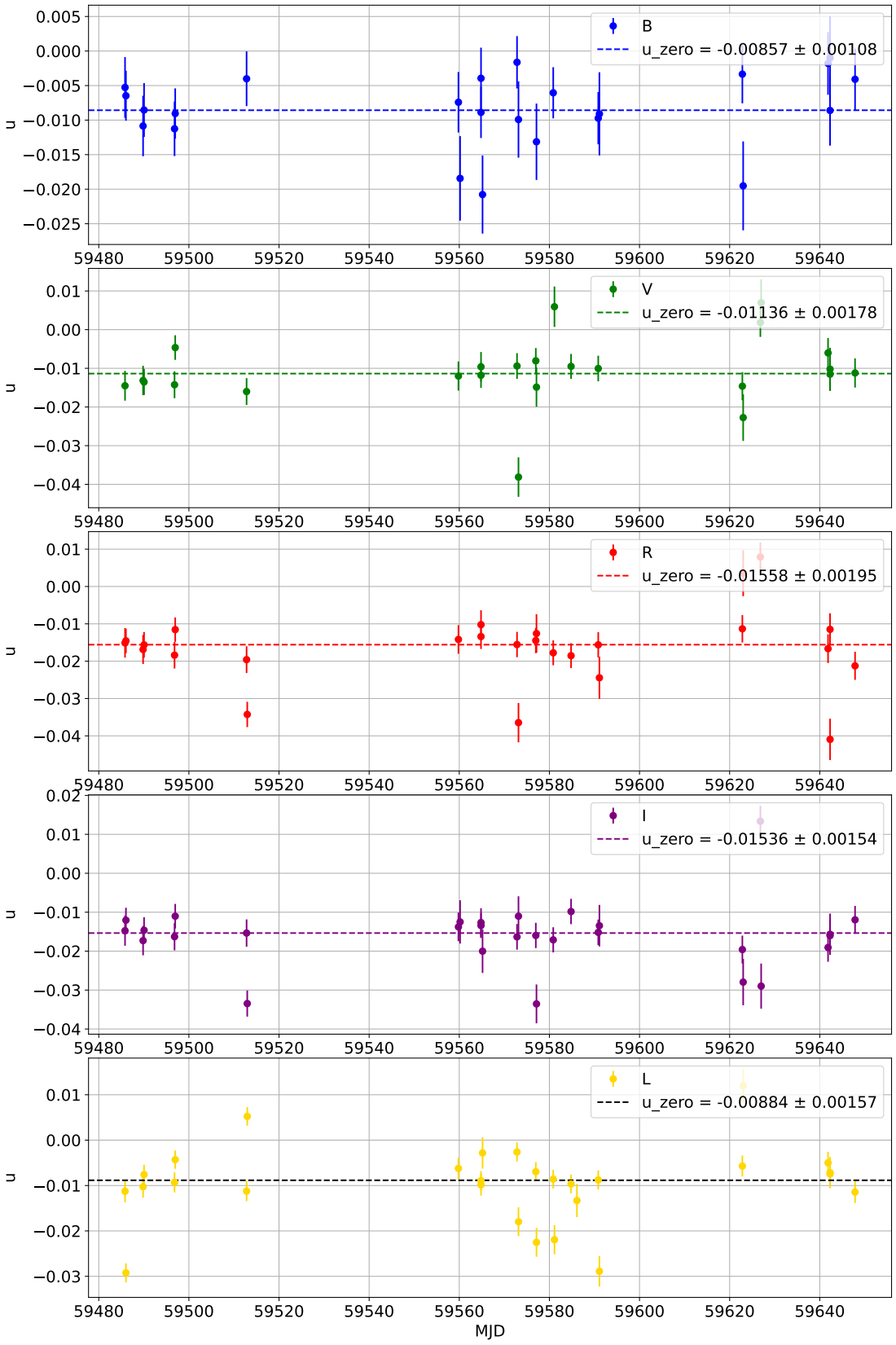

FIGURE C.5: u values of zero-polarised standard stars for each MOPTOP filter during the first single-camera configuration epoch (epoch 2). The average values are taken as the u_0 value for that epoch.

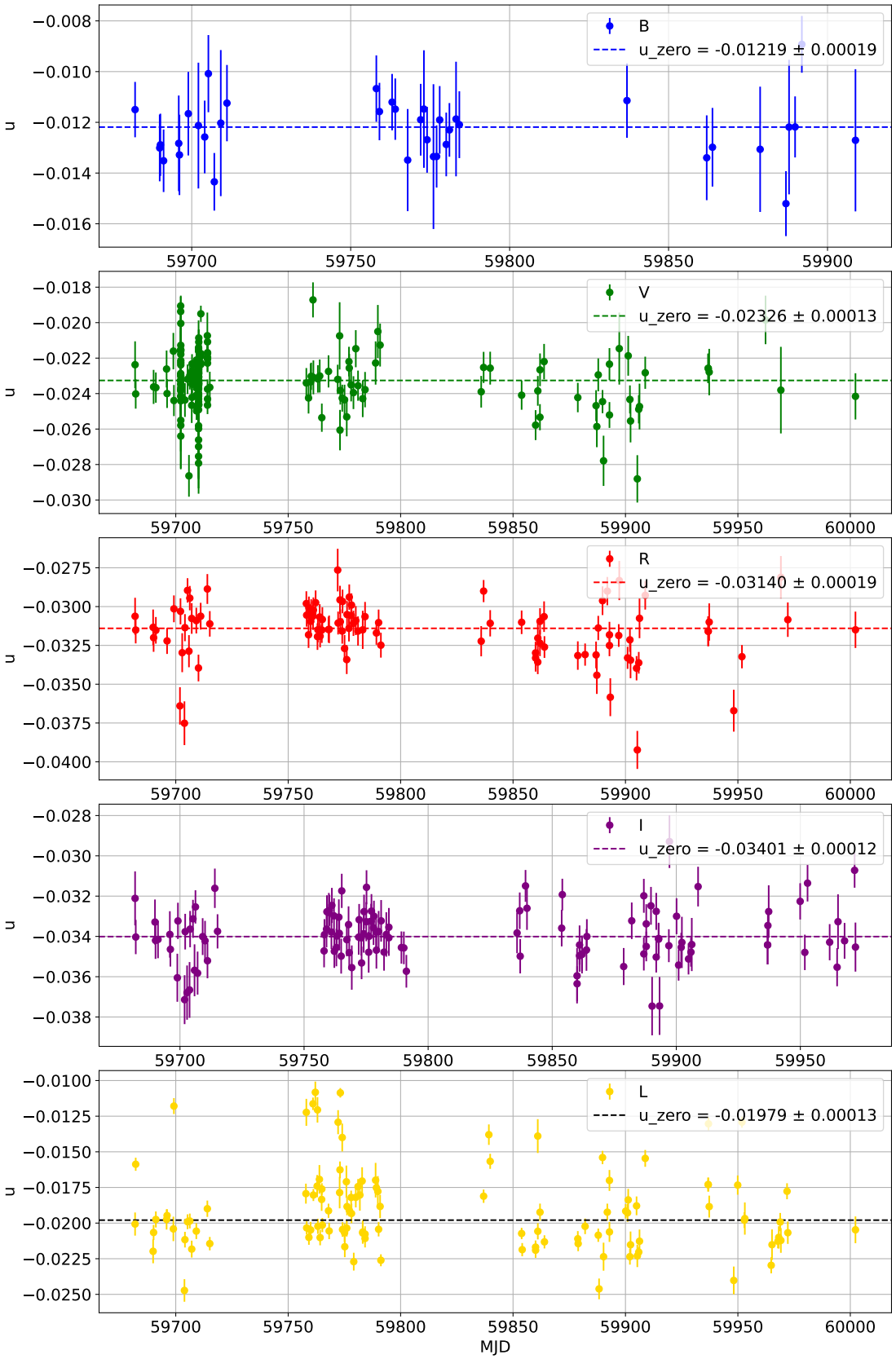

FIGURE C.6: u values of zero-polarised standard stars for each MOPTOP filter during the second dual-camera configuration epoch (epoch 3). The average values are taken as the u_0 value for that epoch.

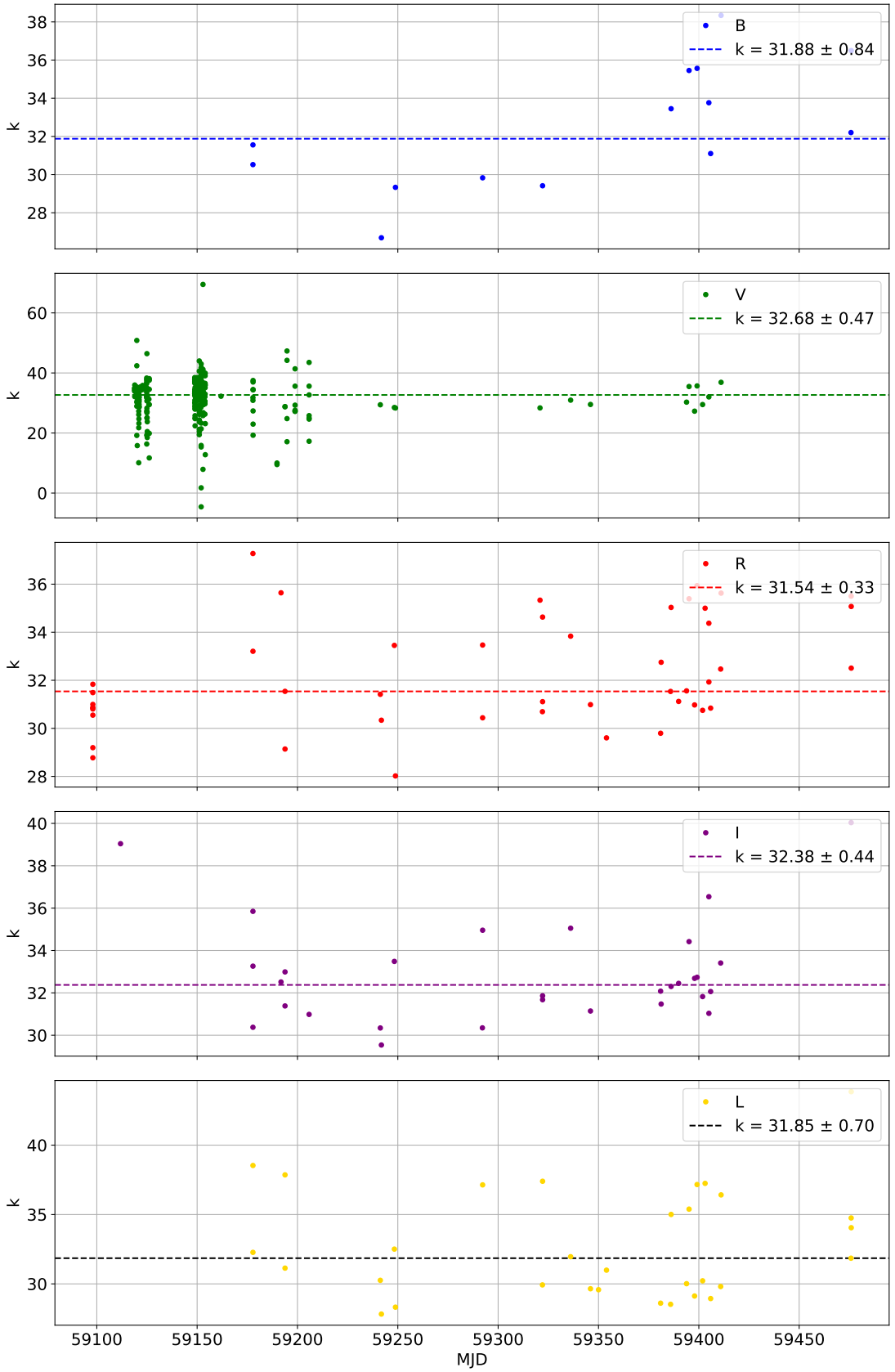

FIGURE C.7: k values of polarised standard stars for each MOPTOP filter during the first dual-camera configuration epoch (epoch 1). The average values are taken as the k value for that epoch.

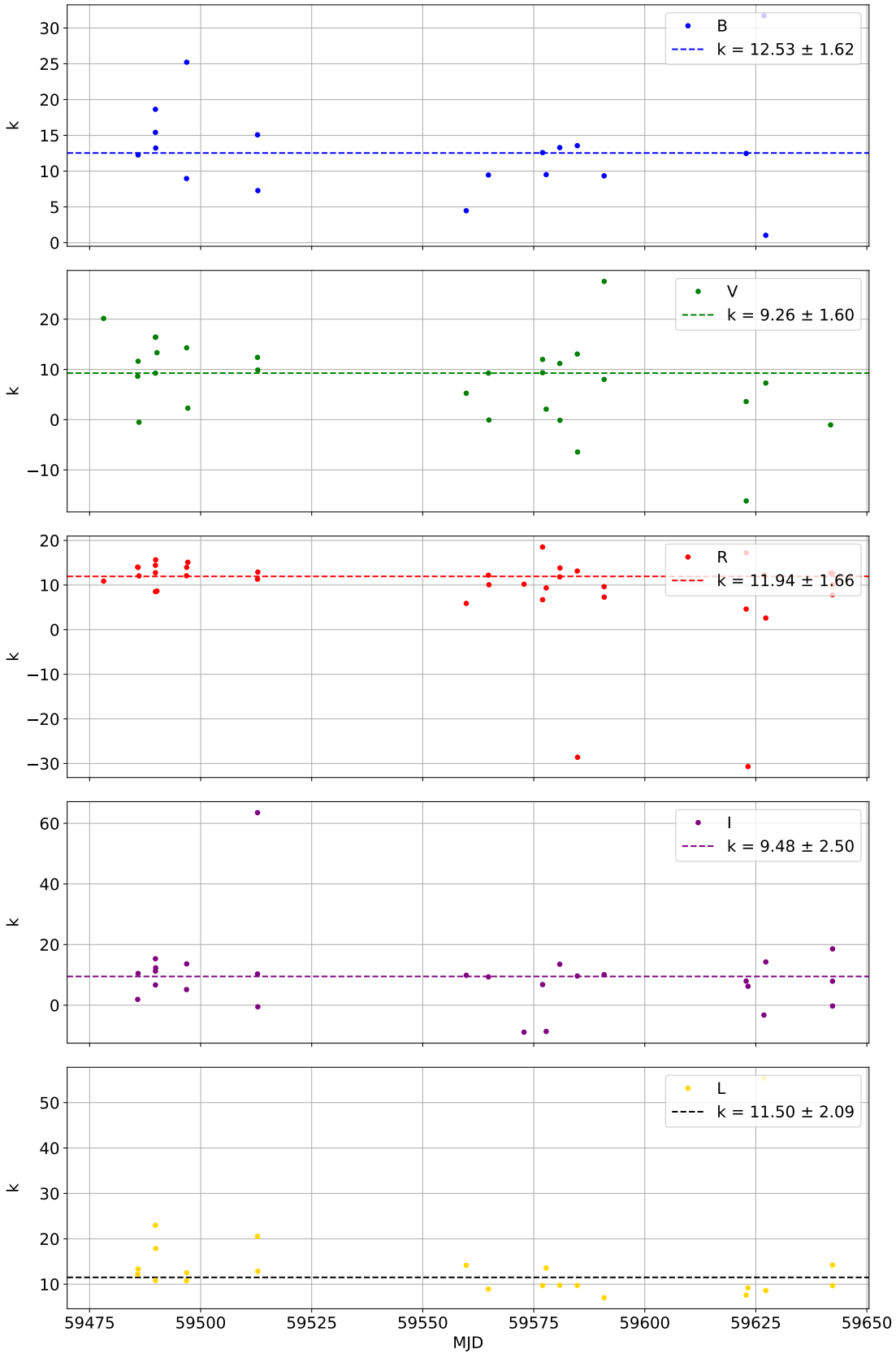

FIGURE C.8: k values of polarised standard stars for each MOPTOP filter during the first single-camera configuration epoch (epoch 2). The average values are taken as the k value for that epoch.

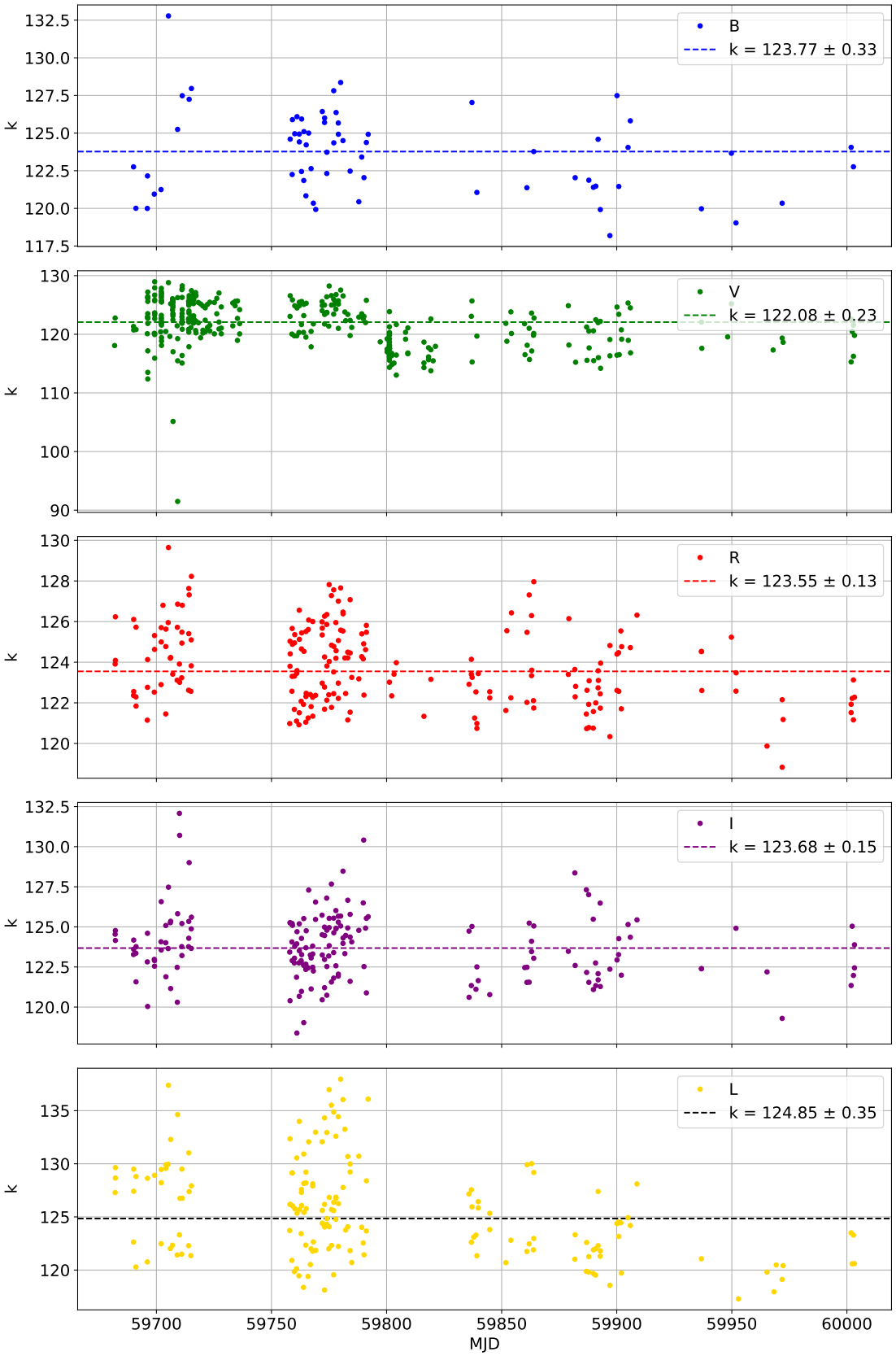

FIGURE C.9: k values of polarised standard stars for each MOPTOP filter during the second dual-camera configuration epoch (epoch 3). The average values are taken as the k value for that epoch.

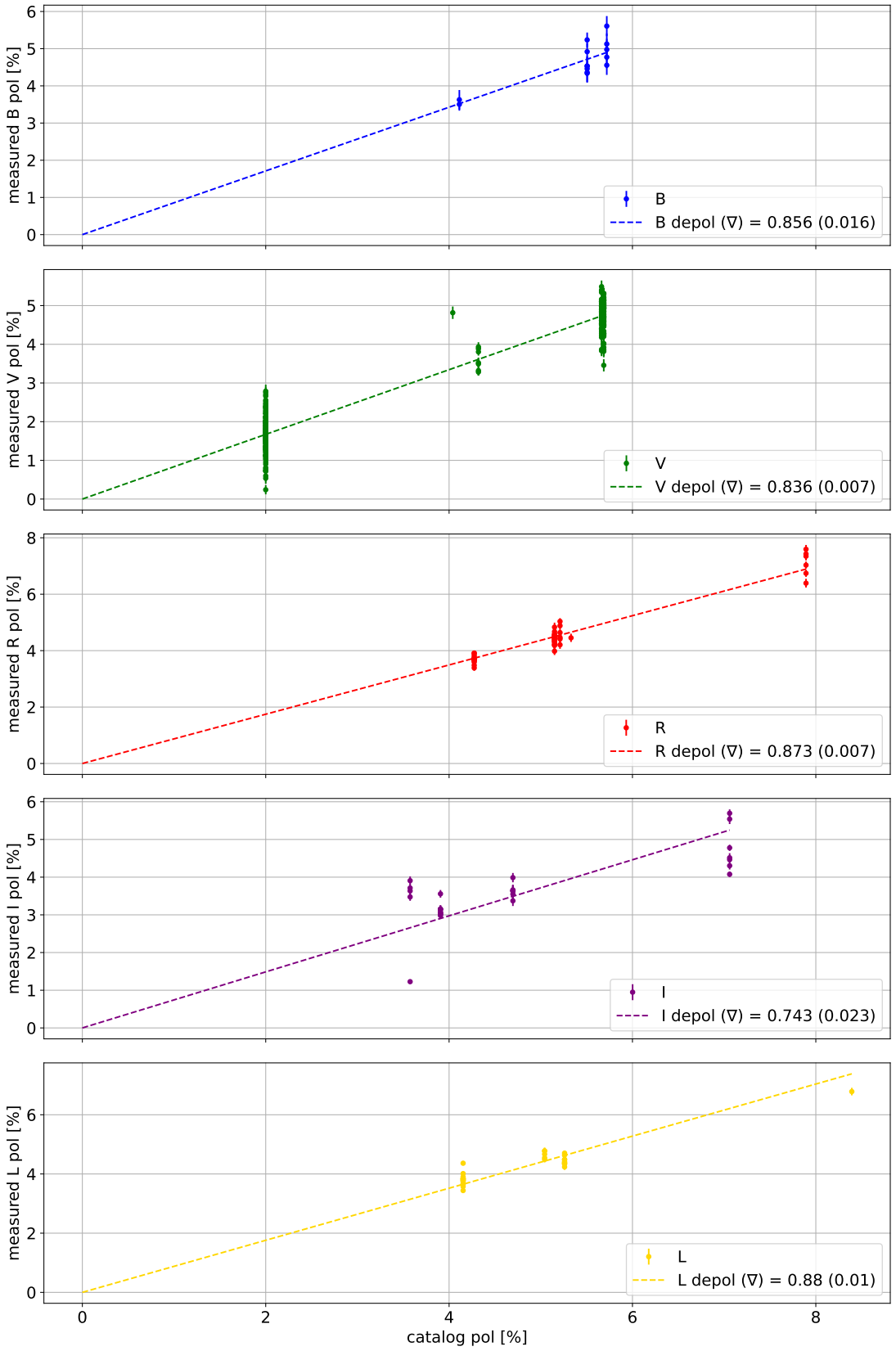

FIGURE C.10: Observed polarisation vs. known polarisation for polarised standard stars observed with MOPTOP during the first dual-camera configuration epoch (epoch 1). The gradient of a fitted linear regression is taken as the instrumental depolarisation value for that epoch for each filter.

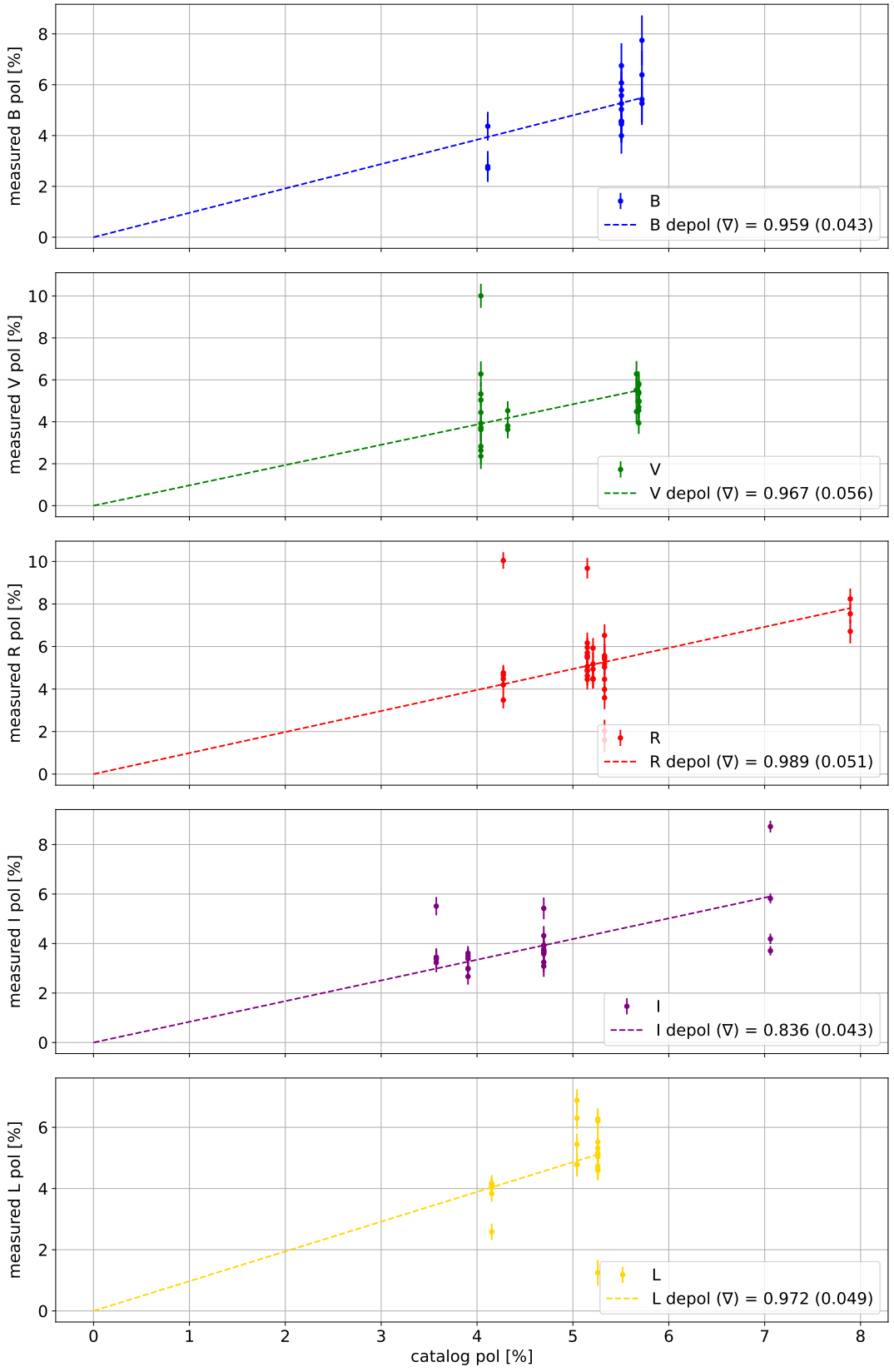

FIGURE C.11: Observed polarisation vs. known polarisation for polarised standard stars observed with MOPTOP during the first single-camera configuration epoch (epoch 2). The gradient of a fitted linear regression is taken as the instrumental depolarisation value for that epoch for each filter.

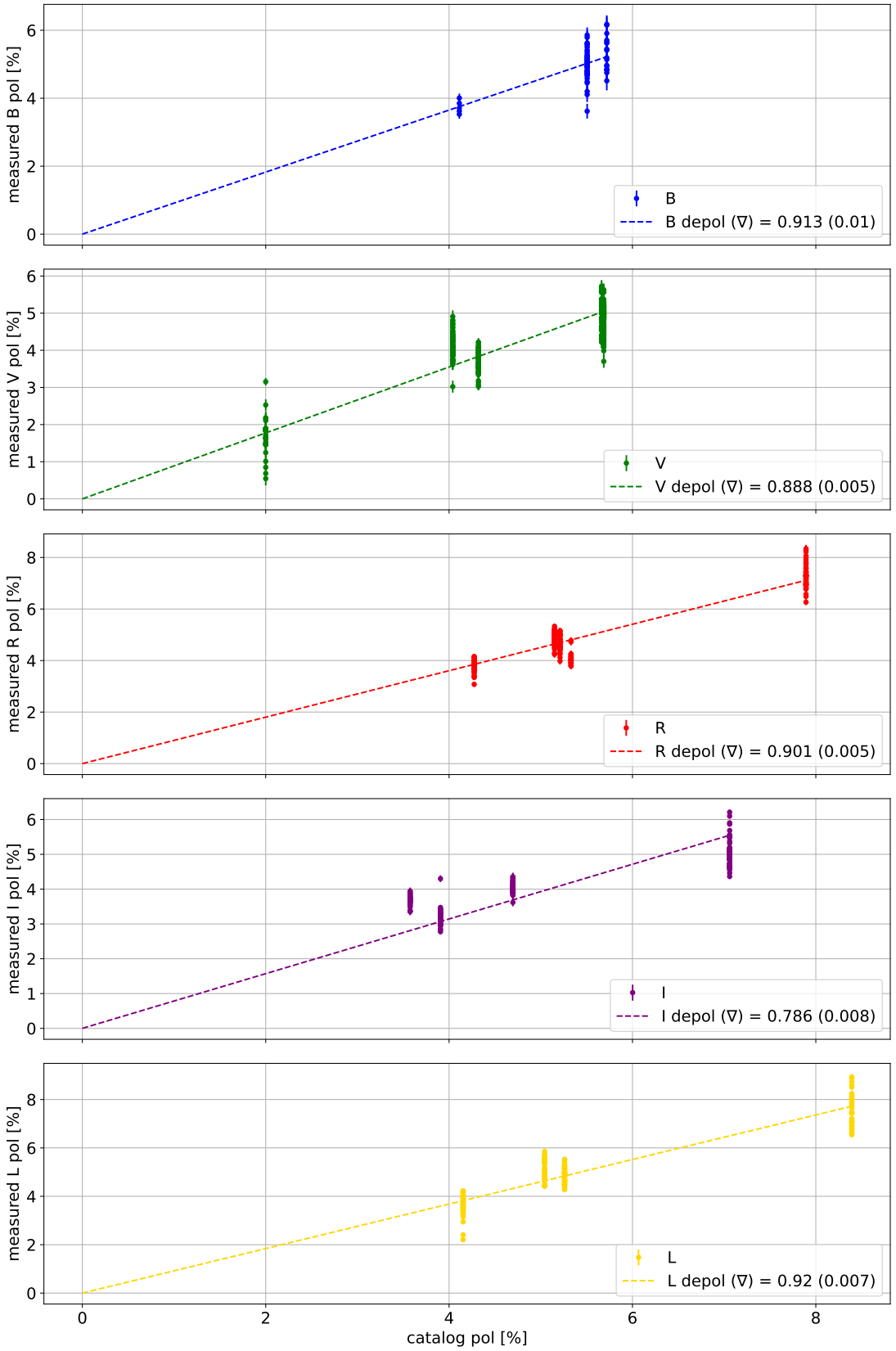

FIGURE C.12: Observed polarisation vs. known polarisation for polarised standard stars observed with MOPTOP during the second dual-camera configuration epoch (epoch 3). The gradient of a fitted linear regression is taken as the instrumental depolarisation value for that epoch for each filter.

TABLE C.1: Table showing the full RINGO3 sample of blazars. Each source's RA and Dec coordinates, redshift and classification are given. The observation range and total number of observations for each source are also given. [a]:De Jaeger et al. (2023),[b]:NASA Extragalactic Database.

Source	α_{2000}	δ_{2000}	z	Type	Obs Range (days)	Obs Num
IC 310	03:16:42.979	41:19:29.630	0.0189[b]	HBL	1671.389	206
1ES 1011+496	10:15:04.139	49:26:00.709	0.212[a]	HBL	2199.087	170
MRK 421	11:04:27.314	38:12:31.798	0.030[a]	HBL	2257.825	276
MRK 180	11:36:26.408	70:09:27.307	0.045[a]	HBL	2199.099	171
PG 1218+304	12:21:21.943	30:10:37.162	0.184[a]	HBL	2250.953	110
1ES 1426+428	14:28:32.609	42:40:21.050	0.129[b]	HBL	2199.153	219
PG 1553+113	15:55:43.044	11:11:24.366	0.360[a]	HBL	2203.096	258
MRK 501	16:53:52.217	39:45:36.609	0.033[a]	HBL	2216.996	322
1ES 1959+650	19:59:59.853	65:08:54.651	0.047[a]	HBL	466.798	50
3C 66A	02:22:39.611	43:02:07.797	0.444[a]	IBL	2174.985	288
S5 0716+714	07:21:53.448	71:20:36.362	0.127[a]	IBL	2195.973	289
PKS 0735+178	07:38:07.394	17:42:18.999	0.424[a]	IBL	1484.923	52
ON 231	12:21:31.690	28:13:58.500	0.102[a]	IBL	1328.167	82
A0 0235+164	02:38:38.930	16:36:59.275	0.940[a]	LBL	1342.253	68
TXS 0506+056	05:09:25.965	05:41:35.334	0.336[a]	LBL	168.321	15
OJ 49	08:31:48.877	04:29:39.087	0.174[a]	LBL	1234.701	40
OJ 287	08:54:48.875	20:06:30.643	0.306[a]	LBL	2443.209	357
S4 0954+65	09:58:47.245	65:33:54.822	0.367[a]	LBL	1483.938	197
4C +01.28	10:58:29.605	01:33:58.824	0.890[a]	LBL	1408.104	43
4C 09.57	17:51:32.819	09:39:00.728	0.322[a]	LBL	1450.053	124
BL Lac	22:02:43.291	42:16:39.978	0.069[a]	LBL	2053.721	385
3C 84	03:19:48.160	41:30:42.114	0.0176[b]	FR I (LSP)	2208.98	130
3C 111	04:18:21.277	38:01:35.801	0.0485[b]	FR II (LSP)	1485.896	60
3C 120	04:33:11.096	05:21:15.618	0.033[b]	Sy1 (LSP)	1582.801	233
4C+01.02	01:08:38.771	01:35:00.317	2.099[a]	FSRQ	574.356	14
PKS 0336-01	03:39:30.938	-01:46:35.804	0.850[a]	FSRQ	1304.652	40
PKS 0420-014	04:23:15.801	-01:20:33.065	0.916[a]	FSRQ	1485.98	47
PKS 0502+049	05:05:23.185	04:59:42.725	0.954[a]	FSRQ	1330.225	116
PKS 0528+134	05:30:56.417	13:31:55.150	2.070[a]	FSRQ	1477.952	56
PKS 0736+01	07:39:18.033	01:37:04.618	0.189[a]	FSRQ	873.873	126
TXS 0827+243	08:30:52.086	24:10:59.820	0.939[a]	FSRQ	1250.715	42
4C 71.07	08:41:24.365	70:53:42.173	2.17[b]	FSRQ	1444.89	58
PKS 1127-14	11:30:07.053	-14:49:27.388	1.184[b]	FSRQ	1443.054	37
TON 599	11:59:31.834	29:14:43.827	0.729[a]	FSRQ	936.607	59
PKS 1222+216	12:24:54.458	21:22:46.385	0.435[b]	FSRQ	1926.76	80
3C 273	12:29:06.700	02:03:08.599	0.158[a]	FSRQ	1452.054	57
3C 279	12:56:11.166	-05:47:21.532	0.536[a]	FSRQ	2219.08	138
PKS B1406-076	14:08:56.481	-07:52:26.666	1.493[a]	FSRQ	295.188	14
PKS 1444+25	14:43:56.892	25:01:44.491	0.939[a]	FSRQ	1144.988	47
PKS 1510-089	15:12:50.533	-09:05:59.830	0.361[b]	FSRQ	2237.968	237
OS 319	16:13:41.065	34:12:47.912	1.399[a]	FSRQ	1432.163	83
PKS B1622-297	16:26:06.021	-29:51:26.971	0.815[a]	FSRQ	1452.065	84
4C +38.41	16:35:15.493	38:08:04.501	1.814[a]	FSRQ	1406.139	90
3C 345	16:42:58.810	39:48:37.000	0.593[a]	FSRQ	1457.133	99
PKS B1730-130	17:33:02.706	-13:04:49.548	0.902[a]	FSRQ	1434.059	90
3C 446	22:25:47.259	-04:57:01.391	1.404[a]	FSRQ	1233.687	78
4C 11.69	22:32:36.409	11:43:50.904	1.037[a]	FSRQ	1320.565	175
TXS 2241+406	22:44:12.731	40:57:13.619	1.171[a]	FSRQ	593.119	26
3C 454.3	22:53:57.748	16:08:53.561	0.859[a]	FSRQ	1265.622	105

TABLE C.2: Spearman correlation coefficients for RINGO3 optical flux vs. Fermi γ-ray flux, where c is the correlation coefficient and p is the corresponding p value. The number of optical data points (per camera) used in these correlation calculations is also shown. Note there are no Fermi data available for 1ES 1426+428.

Source	Type	r^* c	r^* p	g^* c	g^* p	b^* c	b^* p	Points
1ES 1011+496	HSP	-0.111	0.149	-0.087	0.260	-0.105	0.171	170
MRK 180	HSP	0.117	0.129	0.109	0.158	0.136	0.076	171
PG 1218+304	HSP	0.043	0.655	0.002	0.985	0.027	0.778	110
PG 1553+113	HSP	0.483	1.88×10^{-16}	0.480	2.79×10^{-16}	0.472	1.05×10^{-15}	258
MRK 501	HSP	0.366	1.22×10^{-11}	0.392	3.02×10^{-13}	0.365	1.36×10^{-11}	322
1ES 1959+650	HSP	-0.185	0.197	-0.144	0.318	-0.139	0.335	50
3C 66A	ISP	0.438	6.00×10^{-15}	0.418	1.23×10^{-13}	0.439	5.23×10^{-15}	288
S5 0716+714	ISP	0.705	3.25×10^{-44}	0.710	4.28×10^{-45}	0.720	6.92×10^{-47}	286
ON 231	ISP	-0.128	0.250	-0.178	0.110	-0.127	0.256	82
A0 0235+164	LSP	0.674	2.90×10^{-10}	0.674	3.04×10^{-10}	0.660	8.97×10^{-10}	68
TXS 0506+056	LSP	0.569	0.034	0.670	0.009	0.670	0.009	14
OJ 287	LSP	0.267	3.51×10^{-10}	0.255	2.10×10^{-9}	0.230	7.18×10^{-8}	534
S4 0954+65	LSP	0.472	2.56×10^{-12}	0.476	1.48×10^{-12}	0.465	5.96×10^{-12}	197
4C 09.57	LSP	0.458	8.77×10^{-8}	0.452	1.35×10^{-7}	0.454	1.15×10^{-7}	124
BL Lacertae	LSP	0.679	2.85×10^{-53}	0.690	1.05×10^{-55}	0.700	4.47×10^{-58}	385
PKS 0502+049	LSP (FSRQ)	0.823	8.61×10^{-30}	0.824	6.35×10^{-30}	0.829	1.48×10^{-30}	116
PKS 0736+01	LSP (FSRQ)	0.845	1.54×10^{-35}	0.837	2.65×10^{-34}	0.852	1.04×10^{-36}	126
PKS 1222+216	LSP (FSRQ)	0.440	4.46×10^{-5}	0.407	1.83×10^{-4}	0.400	2.35×10^{-4}	80
3C 279	LSP (FSRQ)	0.466	8.65×10^{-9}	0.479	2.78×10^{-9}	0.465	9.23×10^{-9}	138
PKS 1510-089	LSP (FSRQ)	0.611	1.20×10^{-25}	0.614	5.94×10^{-26}	0.586	2.77×10^{-23}	237
OS 319	LSP (FSRQ)	0.218	0.048	0.354	0.001	0.266	0.015	83
PKS B1622-297	LSP (FSRQ)	0.272	0.012	0.223	0.042	0.231	0.034	84
4C +38.41	LSP (FSRQ)	0.667	6.79×10^{-13}	0.639	1.28×10^{-11}	0.643	8.01×10^{-12}	90
3C 345	LSP (FSRQ)	0.089	0.379	0.036	0.727	0.024	0.817	99
PKS B1730-130	LSP (FSRQ)	0.029	0.783	0.060	0.573	0.074	0.488	90
3C 446	LSP (FSRQ)	0.318	4.52×10^{-3}	0.332	2.99×10^{-3}	0.261	2.12×10^{-2}	78
4C 11.69	LSP (FSRQ)	0.762	2.24×10^{-42}	0.761	2.63×10^{-42}	0.760	3.71×10^{-42}	217
3C 454.3	LSP (FSRQ)	0.891	4.31×10^{-37}	0.887	2.42×10^{-36}	0.869	3.31×10^{-33}	105

TABLE C.3: Full table of Spearman rank coefficient values for the colour-magnitude correlations along with linear fit gradients.

Source	Type	Line Colour	c	p	Linear Fit Gradient	Points
IC 310	HSP	r^* (b^*-g^*)	-0.182	8.80×10^{-3}	-0.149	206
IC 310	HSP	g^* (b^*-r^*)	-0.288	2.72×10^{-5}	-0.429	206
IC 310	HSP	b^* (g^*-r^*)	-0.113	0.105	-0.126	206
1ES 1011+496	HSP	r^* (b^*-g^*)	-0.035	0.653	-0.008	170
1ES 1011+496	HSP	g^* (b^*-r^*)	-0.251	9.51×10^{-4}	-0.055	170
1ES 1011+496	HSP	b^* (g^*-r^*)	-0.230	2.53×10^{-3}	-0.047	170
MRK 180	HSP	r^* (b^*-g^*)	-0.249	1.01×10^{-3}	-0.289	171
MRK 180	HSP	g^* (b^*-r^*)	-0.527	1.29×10^{-13}	-0.404	171
MRK 180	HSP	b^* (g^*-r^*)	-0.362	1.12×10^{-6}	-0.178	171
PG 1218+304	HSP	r^* (b^*-g^*)	-0.553	3.90×10^{-10}	-0.090	110
PG 1218+304	HSP	g^* (b^*-r^*)	-0.735	6.11×10^{-20}	-0.151	110
PG 1218+304	HSP	b^* (g^*-r^*)	-0.455	5.96×10^{-7}	-0.062	110
1ES 1426+428	HSP	r^* (b^*-g^*)	-0.153	0.024	-0.073	219
1ES 1426+428	HSP	g^* (b^*-r^*)	-0.266	6.84×10^{-5}	-0.153	219
1ES 1426+428	HSP	b^* (g^*-r^*)	-0.186	5.73×10^{-3}	-0.071	219
PG 1553+113	HSP	r^* (b^*-g^*)	-0.020	0.743	-0.004	258
PG 1553+113	HSP	g^* (b^*-r^*)	-0.378	3.51×10^{-10}	-0.064	258
PG 1553+113	HSP	b^* (g^*-r^*)	-0.490	5.14×10^{-17}	-0.059	258
MRK 501	HSP	r^* (b^*-g^*)	-0.265	1.47×10^{-6}	-0.214	322
MRK 501	HSP	g^* (b^*-r^*)	-0.527	2.32×10^{-24}	-0.588	322
MRK 501	HSP	b^* (g^*-r^*)	-0.356	4.56×10^{-11}	-0.235	322
1ES 1959+650	HSP	r^* (b^*-g^*)	0.003	0.983	-0.011	50
1ES 1959+650	HSP	g^* (b^*-r^*)	-0.088	0.543	-0.015	50
1ES 1959+650	HSP	b^* (g^*-r^*)	-0.021	0.888	-0.004	50
3C 66A	ISP	r^* (b^*-g^*)	-0.083	0.159	-0.021	288
3C 66A	ISP	g^* (b^*-r^*)	-0.195	9.01×10^{-4}	-0.048	288
3C 66A	ISP	b^* (g^*-r^*)	-0.159	6.90×10^{-3}	-0.026	288
S5 0716+714	ISP	r^* (b^*-g^*)	-0.599	3.33×10^{-29}	-0.039	286
S5 0716+714	ISP	g^* (b^*-r^*)	-0.639	3.38×10^{-34}	-0.061	286
S5 0716+714	ISP	b^* (g^*-r^*)	-0.522	2.18×10^{-21}	-0.022	286
ON 231	ISP	r^* (b^*-g^*)	-0.429	5.77×10^{-5}	-0.056	82
ON 231	ISP	g^* (b^*-r^*)	-0.487	3.49×10^{-6}	-0.072	82
ON 231	ISP	b^* (g^*-r^*)	-0.291	8.05×10^{-3}	-0.016	82
A0 0235+164	LSP	r^* (b^*-g^*)	0.205	0.094	0.012	68
A0 0235+164	LSP	g^* (b^*-r^*)	0.164	0.182	0.014	68

Continued on next page

Table C.3 – continued from previous page

Source	Type	Line Colour	c	p	Linear Fit Gradient	Points
A0 0235+164	LSP	b^* (g^*-r^*)	0.053	0.666	0.002	68
TXS 0506+056	LSP	r^* (b^*-g^*)	-0.732	2.92×10^{-3}	-0.128	14
TXS 0506+056	LSP	g^* (b^*-r^*)	-0.881	3.11×10^{-5}	-0.179	14
TXS 0506+056	LSP	b^* (g^*-r^*)	-0.648	0.012	-0.051	14
OJ 287	LSP	r^* (b^*-g^*)	-0.405	1.52×10^{-22}	-0.048	534
OJ 287	LSP	g^* (b^*-r^*)	-0.494	2.92×10^{-34}	-0.080	534
OJ 287	LSP	b^* (g^*-r^*)	-0.381	7.65×10^{-20}	-0.031	534
S4 0954+65	LSP	r^* (b^*-g^*)	-0.474	1.89×10^{-12}	-0.054	197
S4 0954+65	LSP	g^* (b^*-r^*)	-0.598	1.74×10^{-20}	-0.091	197
S4 0954+65	LSP	b^* (g^*-r^*)	-0.454	2.18×10^{-11}	-0.036	197
4C 09.57	LSP	r^* (b^*-g^*)	-0.458	8.67×10^{-8}	-0.048	124
4C 09.57	LSP	g^* (b^*-r^*)	-0.421	1.11×10^{-6}	-0.055	124
4C 09.57	LSP	b^* (g^*-r^*)	-0.082	0.368	-0.007	124
BL Lacertae	LSP	r^* (b^*-g^*)	-0.485	3.77×10^{-24}	-0.047	385
BL Lacertae	LSP	g^* (b^*-r^*)	-0.637	3.51×10^{-45}	-0.098	385
BL Lacertae	LSP	b^* (g^*-r^*)	-0.676	8.55×10^{-53}	-0.050	385
PKS 0502+049	LSP (FSRQ)	r^* (b^*-g^*)	0.791	4.14×10^{-26}	0.126	116
PKS 0502+049	LSP (FSRQ)	g^* (b^*-r^*)	0.825	5.64×10^{-30}	0.254	116
PKS 0502+049	LSP (FSRQ)	b^* (g^*-r^*)	0.592	2.50×10^{-12}	0.128	116
PKS 0736+01	LSP (FSRQ)	r^* (b^*-g^*)	0.103	0.251	0.009	126
PKS 0736+01	LSP (FSRQ)	g^* (b^*-r^*)	-0.816	2.35×10^{-31}	-0.139	126
PKS 0736+01	LSP (FSRQ)	b^* (g^*-r^*)	-0.871	3.72×10^{-40}	-0.147	126
PKS 1222+216	LSP (FSRQ)	r^* (b^*-g^*)	0.691	1.28×10^{-12}	0.274	80
PKS 1222+216	LSP (FSRQ)	g^* (b^*-r^*)	0.769	7.98×10^{-17}	0.402	80
PKS 1222+216	LSP (FSRQ)	b^* (g^*-r^*)	0.390	3.51×10^{-4}	0.116	80
3C 279	LSP (FSRQ)	r^* (b^*-g^*)	-0.089	0.300	-0.018	138
3C 279	LSP (FSRQ)	g^* (b^*-r^*)	-0.374	6.18×10^{-6}	-0.098	138
3C 279	LSP (FSRQ)	b^* (g^*-r^*)	-0.389	2.36×10^{-6}	-0.079	138
PKS 1510-089	LSP (FSRQ)	r^* (b^*-g^*)	0.630	1.27×10^{-27}	0.097	237
PKS 1510-089	LSP (FSRQ)	g^* (b^*-r^*)	0.566	1.76×10^{-21}	0.112	237
PKS 1510-089	LSP (FSRQ)	b^* (g^*-r^*)	0.141	0.030	0.014	237
OS 319	LSP (FSRQ)	r^* (b^*-g^*)	-0.164	0.138	-0.063	83
OS 319	LSP (FSRQ)	g^* (b^*-r^*)	0.227	0.039	0.156	83
OS 319	LSP (FSRQ)	b^* (g^*-r^*)	0.349	1.23×10^{-3}	0.227	83
PKS B1622-297	LSP (FSRQ)	r^* (b^*-g^*)	0.400	1.67×10^{-4}	0.157	84
PKS B1622-297	LSP (FSRQ)	g^* (b^*-r^*)	0.476	4.85×10^{-6}	0.292	84
PKS B1622-297	LSP (FSRQ)	b^* (g^*-r^*)	0.269	0.013	0.114	84

Continued on next page

Table C.3 – continued from previous page

Source	Type	Line Colour	c	p	Linear Fit Gradient	Points
4C +38.41	LSP (FSRQ)	r^* (b^*-g^*)	0.548	2.26×10^{-8}	0.085	90
4C +38.41	LSP (FSRQ)	g^* (b^*-r^*)	0.261	0.013	0.060	90
4C +38.41	LSP (FSRQ)	b^* (g^*-r^*)	-0.092	0.391	-0.027	90
3C 345	LSP (FSRQ)	r^* (b^*-g^*)	0.331	8.12×10^{-4}	0.063	99
3C 345	LSP (FSRQ)	g^* (b^*-r^*)	-0.210	0.037	-0.041	99
3C 345	LSP (FSRQ)	b^* (g^*-r^*)	-0.464	1.35×10^{-6}	-0.103	99
PKS B1730-130	LSP (FSRQ)	r^* (b^*-g^*)	0.307	3.20×10^{-3}	0.108	90
PKS B1730-130	LSP (FSRQ)	g^* (b^*-r^*)	0.426	2.78×10^{-5}	0.178	90
PKS B1730-130	LSP (FSRQ)	b^* (g^*-r^*)	0.152	0.153	0.066	90
3C 446	LSP (FSRQ)	r^* (b^*-g^*)	0.080	0.484	0.044	78
3C 446	LSP (FSRQ)	g^* (b^*-r^*)	0.243	0.032	0.167	78
3C 446	LSP (FSRQ)	b^* (g^*-r^*)	0.160	0.161	0.131	78
4C 11.69	LSP (FSRQ)	r^* (b^*-g^*)	0.558	3.51×10^{-19}	0.045	217
4C 11.69	LSP (FSRQ)	g^* (b^*-r^*)	0.723	2.16×10^{-36}	0.106	217
4C 11.69	LSP (FSRQ)	b^* (g^*-r^*)	0.545	3.38×10^{-18}	0.060	217
3C 454.3	LSP (FSRQ)	r^* (b^*-g^*)	0.939	1.02×10^{-49}	0.161	105
3C 454.3	LSP (FSRQ)	g^* (b^*-r^*)	0.953	2.87×10^{-55}	0.304	105
3C 454.3	LSP (FSRQ)	b^* (g^*-r^*)	0.884	7.10×10^{-36}	0.146	105

TABLE C.4: Correlation strengths for the spectral index vs. g^* band flux correlations. The source name and subclass are given in columns one and two. The best fit determined as given by AIC and BIC values is shown in column three. Columns four and five give the Spearman rank strength and significance correlation coefficients after having linearised the dataset if better fitted with a logarithmic curve. Column six gives the colour trend of the object given the fit and Spearman rank coefficients. Column seven gives the average spectral index, and column 8 gives the number of data points.

Source	Type	Fit	c	p	Trend	$\alpha_{\rm av}$	Points
IC 310	HSP	linear	-0.288	2.72×10^{-5}	BWB	1.134	206
1ES 1011+496	HSP	linear	-0.251	9.51×10^{-4}	BWB	-0.233	170
MRK 180	HSP	linear	-0.527	1.29×10^{-13}	BWB	0.578	171
PG 1218+304	HSP	log	-0.735	6.11×10^{-20}	BSWB	0.091	110
1ES 1426+428	HSP	linear	-0.266	6.84×10^{-5}	BWB	0.426	219
PG 1553+113	HSP	linear	-0.378	3.51×10^{-10}	BWB	-0.211	258
MRK 501	HSP	linear	-0.527	2.32×10^{-24}	BWB	0.416	322
1ES 1959+650	HSP	linear	-0.088	0.543	-	0.093	50
3C 66A	ISP	linear	-0.195	9.01×10^{-4}	BWB	0.065	288
S5 0716+714	ISP	log	-0.639	3.38×10^{-34}	BSWB	0.123	286
ON 231	ISP	log	-0.487	3.49×10^{-6}	BSWB	0.336	82
A0 0235+164	LSP	linear	0.164	0.182	-	1.431	68
TXS 0506+056	LSP	linear	-0.881	3.11×10^{-5}	BWB	0.271	14
OJ 287	LSP	log	-0.494	2.92×10^{-34}	BSWB	0.149	534
S4 0954+65	LSP	log	-0.598	1.74×10^{-20}	BSWB	0.576	197
4C 09.57	LSP	linear	-0.421	1.11×10^{-6}	BWB	0.750	124
BL Lac	LSP	log	-0.637	3.51×10^{-45}	BSWB	0.931	385
PKS 0502+049	LSP (FSRQ)	log	0.825	5.64×10^{-30}	RSWB	-0.172	116
PKS 0736+01	LSP (FSRQ)	log	-0.816	2.35×10^{-31}	BSWB	0.774	126
PKS 1222+216	LSP (FSRQ)	log	0.769	7.98×10^{-17}	RSWB	-0.154	80
3C 279	LSP (FSRQ)	log	-0.374	6.18×10^{-6}	BSWB	0.524	138
PKS 1510-089	LSP (FSRQ)	log	0.566	1.76×10^{-21}	RSWB	0.136	237
OS 319	LSP (FSRQ)	linear	0.227	0.039	RWB	-0.290	83
PKS B1622-297	LSP (FSRQ)	log	0.476	4.85×10^{-6}	RSWB	0.599	84
4C +38.41	LSP (FSRQ)	log	0.261	0.013	RSWB	0.048	90
3C 345	LSP (FSRQ)	linear	-0.210	0.037	BWB	0.243	99
PKS B1730-130	LSP (FSRQ)	log	0.426	2.78×10^{-5}	RSWB	1.077	90
3C 446	LSP (FSRQ)	linear	0.243	0.032	RWB	0.120	78
4C 11.69	LSP (FSRQ)	log	0.723	2.16×10^{-36}	RSWB	0.469	217
3C 454.3	LSP (FSRQ)	log	0.953	2.87×10^{-55}	RSWB	-0.167	105

TABLE C.5: Full table of Spearman rank coefficient values for the optical colour vs. γ-ray flux correlations along with linear fit gradients.

Source	Type	Line Colour	c	p	Linear Fit Gradient	Points
1ES 1011+496	HSP	(b*-g*)	0.116	0.133	4.70×10^{7}	170
1ES 1011+496	HSP	(b*-r*)	-0.029	0.704	-3.55×10^{7}	170
1ES 1011+496	HSP	(g*-r*)	-0.130	0.092	-8.25×10^{7}	170
MRK 180	HSP	(b*-g*)	-0.097	0.207	-1.69×10^{8}	171
MRK 180	HSP	(b*-r*)	-0.090	0.239	-2.95×10^{8}	171
MRK 180	HSP	(g*-r*)	-0.037	0.634	-1.25×10^{8}	171
PG 1218+304	HSP	(b*-g*)	-0.132	0.168	-1.72×10^{8}	110
PG 1218+304	HSP	(b*-r*)	-0.008	0.931	-1.57×10^{8}	110
PG 1218+304	HSP	(g*-r*)	0.102	0.291	1.49×10^{7}	110
PG 1553+113	HSP	(b*-g*)	-0.012	0.849	-9.98×10^{6}	258
PG 1553+113	HSP	(b*-r*)	-0.148	0.017	-7.65×10^{7}	258
PG 1553+113	HSP	(g*-r*)	-0.197	1.49×10^{-3}	-6.66×10^{7}	258
MRK 501	HSP	(b*-g*)	-0.116	0.037	-7.45×10^{7}	322
MRK 501	HSP	(b*-r*)	-0.128	0.021	-1.10×10^{8}	322
MRK 501	HSP	(g*-r*)	-0.064	0.254	-3.58×10^{7}	322
1ES 1959+650	HSP	(b*-g*)	-0.160	0.268	-6.80×10^{7}	50
1ES 1959+650	HSP	(b*-r*)	-0.297	0.037	-1.04×10^{8}	50
1ES 1959+650	HSP	(g*-r*)	-0.258	0.071	-3.62×10^{7}	50
3C 66A	ISP	(b*-g*)	-0.113	0.056	-6.15×10^{7}	288
3C 66A	ISP	(b*-r*)	-0.102	0.085	-1.69×10^{8}	288
3C 66A	ISP	(g*-r*)	-0.075	0.202	-1.07×10^{8}	288
S5 0716+714	ISP	(b*-g*)	-0.606	4.75×10^{-30}	-1.18×10^{8}	286
S5 0716+714	ISP	(b*-r*)	-0.605	5.94×10^{-30}	-1.83×10^{8}	286
S5 0716+714	ISP	(g*-r*)	-0.458	3.12×10^{-16}	-6.47×10^{7}	286
ON 231	ISP	(b*-g*)	-0.198	0.074	-3.29×10^{8}	82
ON 231	ISP	(b*-r*)	-0.030	0.789	8.15×10^{7}	82
ON 231	ISP	(g*-r*)	0.281	0.011	4.10×10^{8}	82
A0 0235+164	LSP	(b*-g*)	0.314	9.04×10^{-3}	9.72×10^{7}	68
A0 0235+164	LSP	(b*-r*)	0.378	1.49×10^{-3}	1.71×10^{8}	68
A0 0235+164	LSP	(g*-r*)	0.224	0.066	7.40×10^{7}	68
TXS 0506+056	LSP	(b*-g*)	-0.648	0.012	-3.90×10^{8}	14
TXS 0506+056	LSP	(b*-r*)	-0.537	0.048	-4.70×10^{8}	14
TXS 0506+056	LSP	(g*-r*)	-0.150	0.610	-8.01×10^{7}	14
OJ 287	LSP	(b*-g*)	0.162	1.78×10^{-4}	1.79×10^{8}	534
OJ 287	LSP	(b*-r*)	0.145	7.71×10^{-4}	2.41×10^{8}	534

Continued on next page

Table C.5 – continued from previous page

Source	Type	Line Colour	c	p	Linear Fit Gradient	Points
OJ 287	LSP	(g*-r*)	0.070	0.105	6.11×10^{7}	534
S4 0954+65	LSP	(b*-g*)	-0.111	0.122	-1.31×10^{8}	197
S4 0954+65	LSP	(b*-r*)	-0.187	8.39×10^{-3}	-2.38×10^{8}	197
S4 0954+65	LSP	(g*-r*)	-0.175	0.014	-1.08×10^{8}	197
4C 09.57	LSP	(b*-g*)	-0.254	4.46×10^{-3}	-1.28×10^{8}	124
4C 09.57	LSP	(b*-r*)	-0.242	6.83×10^{-3}	-1.49×10^{8}	124
4C 09.57	LSP	(g*-r*)	-0.102	0.259	-2.17×10^{7}	124
BL Lac	LSP	(b*-g*)	-0.458	2.11×10^{-21}	-9.95×10^{7}	385
BL Lac	LSP	(b*-r*)	-0.538	2.49×10^{-30}	-1.90×10^{8}	385
BL Lac	LSP	(g*-r*)	-0.534	8.38×10^{-30}	-9.02×10^{7}	385
PKS 0502+049	LSP (FSRQ)	(b*-g*)	0.617	1.57×10^{-13}	3.21×10^{8}	116
PKS 0502+049	LSP (FSRQ)	(b*-r*)	0.694	5.66×10^{-18}	5.80×10^{8}	116
PKS 0502+049	LSP (FSRQ)	(g*-r*)	0.537	5.05×10^{-10}	2.58×10^{8}	116
PKS 0736+01	LSP (FSRQ)	(b*-g*)	-0.060	0.504	7.84×10^{6}	126
PKS 0736+01	LSP (FSRQ)	(b*-r*)	-0.737	8.08×10^{-23}	-4.92×10^{8}	126
PKS 0736+01	LSP (FSRQ)	(g*-r*)	-0.723	1.20×10^{-21}	-5.00×10^{8}	126
PKS 1222+216	LSP (FSRQ)	(b*-g*)	0.249	0.026	4.54×10^{7}	80
PKS 1222+216	LSP (FSRQ)	(b*-r*)	0.394	2.96×10^{-4}	3.69×10^{8}	80
PKS 1222+216	LSP (FSRQ)	(g*-r*)	0.361	1.02×10^{-3}	3.23×10^{8}	80
3C 279	LSP (FSRQ)	(b*-g*)	-0.049	0.566	-8.70×10^{6}	138
3C 279	LSP (FSRQ)	(b*-r*)	-0.189	0.026	-1.10×10^{7}	138
3C 279	LSP (FSRQ)	(g*-r*)	-0.169	0.047	-2.34×10^{6}	138
PKS 1510-089	LSP (FSRQ)	(b*-g*)	0.557	9.58×10^{-21}	9.62×10^{7}	237
PKS 1510-089	LSP (FSRQ)	(b*-r*)	0.535	5.85×10^{-19}	1.11×10^{8}	237
PKS 1510-089	LSP (FSRQ)	(g*-r*)	0.187	3.92×10^{-3}	1.46×10^{7}	237
OS 319	LSP (FSRQ)	(b*-g*)	-0.060	0.590	-5.74×10^{8}	83
OS 319	LSP (FSRQ)	(b*-r*)	-0.062	0.579	-3.94×10^{8}	83
OS 319	LSP (FSRQ)	(g*-r*)	0.006	0.956	1.80×10^{8}	83
PKS B1622-297	LSP (FSRQ)	(b*-g*)	0.089	0.423	1.32×10^{8}	84
PKS B1622-297	LSP (FSRQ)	(b*-r*)	0.163	0.138	4.29×10^{8}	84
PKS B1622-297	LSP (FSRQ)	(g*-r*)	0.134	0.223	2.96×10^{8}	84
4C +38.41	LSP (FSRQ)	(b*-g*)	0.344	8.91×10^{-4}	2.03×10^{8}	90
4C +38.41	LSP (FSRQ)	(b*-r*)	0.327	1.64×10^{-3}	1.73×10^{8}	90
4C +38.41	LSP (FSRQ)	(g*-r*)	0.132	0.214	-2.93×10^{7}	90
3C 345	LSP (FSRQ)	(b*-g*)	0.103	0.309	1.54×10^{8}	99
3C 345	LSP (FSRQ)	(b*-r*)	0.236	0.019	1.93×10^{8}	99
3C 345	LSP (FSRQ)	(g*-r*)	0.138	0.175	3.90×10^{7}	99

Continued on next page

Table C.5 – continued from previous page

Source	Type	Line Colour	c	p	Linear Fit Gradient	Points
PKS B1730-130	LSP (FSRQ)	(b*-g*)	0.011	0.920	1.08×10^{8}	90
PKS B1730-130	LSP (FSRQ)	(b*-r*)	-0.138	0.196	-9.61×10^{7}	90
PKS B1730-130	LSP (FSRQ)	(g*-r*)	-0.102	0.337	-2.04×10^{8}	90
3C 446	LSP (FSRQ)	(b*-g*)	0.085	0.457	7.58×10^{8}	78
3C 446	LSP (FSRQ)	(b*-r*)	0.117	0.309	7.78×10^{8}	78
3C 446	LSP (FSRQ)	(g*-r*)	0.010	0.928	2.03×10^{7}	78
4C 11.69	LSP (FSRQ)	(b*-g*)	0.404	6.18×10^{-10}	2.69×10^{7}	217
4C 11.69	LSP (FSRQ)	(b*-r*)	0.545	3.58×10^{-18}	6.65×10^{7}	217
4C 11.69	LSP (FSRQ)	(g*-r*)	0.443	7.89×10^{-12}	3.96×10^{7}	217
3C 454.3	LSP (FSRQ)	(b*-g*)	0.887	2.29×10^{-36}	6.68×10^{7}	105
3C 454.3	LSP (FSRQ)	(b*-r*)	0.901	4.85×10^{-39}	1.13×10^{8}	105
3C 454.3	LSP (FSRQ)	(g*-r*)	0.845	9.54×10^{-30}	4.61×10^{7}	105

TABLE C.6: As Table C.4 but for spectral index vs. γ-ray flux.

Source	Type	Fit	c	p	Trend	$\alpha_{\rm av}$	Points
1ES 1011+496	HSP	linear	0.034	0.707	-	-0.242	127
MRK 180	HSP	linear	0.002	0.984	-	0.570	82
PG 1218+304	HSP	linear	0.004	0.975	-	0.098	83
PG 1553+113	HSP	log	-0.136	0.056	-	-0.200	199
MRK 501	HSP	linear	-0.165	0.017	BWB	0.405	209
1ES 1959+650	HSP	log	-0.344	0.032	BSWB	0.120	39
3C 66A	ISP	log	-0.060	0.436	-	0.056	169
S5 0716+714	ISP	log	-0.615	5.79×10^{-22}	BSWB	0.125	198
ON 231	ISP	linear	0.043	0.765	-	0.351	50
A0 0235+164	LSP	linear	0.308	0.024	RWB	1.438	54
TXS 0506+056	LSP	linear	-0.714	0.111	-	0.235	6
OJ 287	LSP	linear	0.165	0.024	RWB	0.093	188
S4 0954+65	LSP	log	-0.188	0.045	BSWB	0.564	115
4C 09.57	LSP	log	-0.259	0.023	BSWB	0.752	77
BL Lac	LSP	log	-0.607	1.65×10^{-23}	BSWB	0.944	220
PKS 0502+049	LSP (FSRQ)	log	0.677	1.65×10^{-10}	RSWB	-0.056	69
PKS 0736+01	LSP (FSRQ)	log	-0.677	4.53×10^{-10}	BSWB	0.729	66
PKS 1222+216	LSP (FSRQ)	log	0.299	0.020	RSWB	-0.140	60
3C 279	LSP (FSRQ)	linear	-0.158	0.090	-	0.541	116
PKS 1510-089	LSP (FSRQ)	log	0.528	1.04×10^{-13}	RSWB	0.118	172
OS 319	LSP (FSRQ)	linear	-0.006	0.963	-	-0.248	59
PKS B1622-297	LSP (FSRQ)	linear	0.153	0.247	-	0.682	59
4C +38.41	LSP (FSRQ)	log	0.291	7.60×10^{-3}	RSWB	0.052	83
3C 345	LSP (FSRQ)	linear	0.095	0.435	-	0.255	70
PKS B1730-130	LSP (FSRQ)	linear	-0.031	0.804	-	1.089	65
3C 446	LSP (FSRQ)	linear	0.132	0.377	-	0.158	47
4C 11.69	LSP (FSRQ)	log	0.634	7.50×10^{-16}	RSWB	0.516	129
3C 454.3	LSP (FSRQ)	log	0.897	6.57×10^{-37}	RSWB	-0.155	101

TABLE C.7: DCF peak lag values with correlation strengths after computing on the RINGO3 optical and γ-ray fluxes. A negative lag implies the γ-ray emission is leading the optical. An asterisk in the 3σ lag column suggests the potential significance of the detected lag, warranting further analysis.

Source	Type	Peak [days]	ΔPeak [days]	c	3σ lag
1ES 1011+496	HSP	166.29	12.94	-0.270	no
MRK 180	HSP	-68.19	12.86	0.203	no
PG 1218+304	HSP	220.10	20.46	0.165	no
PG 1553+113	HSP	-20.91	8.54	0.493	no
MRK 501	HSP	-216.70	6.89	0.373	no
1ES 1959+650	HSP	29.75	9.34	-0.537	yes*
3C 66A	ISP	-90.40	7.55	0.367	no
S5 0716+714	ISP	-1.93	7.68	0.569	no
ON 231	ISP	118.09	16.2	0.520	yes*
A0 0235+164	LSP	-7.37	19.74	0.581	no
TXS 0506+056	LSP	2.91	1.50	-0.188	no
OJ 287	LSP	-40.01	4.58	-0.284	no
S4 0954+65	LSP	-1.29	7.53	0.315	no
4C 09.57	LSP	-8.27	11.69	0.692	no
BL Lac	LSP	-7.02	5.33	0.517	no
PKS 0502+049	LSP (FSRQ)	1.92	11.47	0.576	no
PKS 0736+01	LSP (FSRQ)	-0.08	6.94	0.506	no
PKS 1222+216	LSP (FSRQ)	187.68	24.08	0.729	no
3C 279	LSP (FSRQ)	-48.85	16.08	0.348	no
PKS 1510-089	LSP (FSRQ)	-55.41	9.44	0.659	yes*
OS 319	LSP (FSRQ)	79.00	17.25	0.247	no
PKS B1622-297	LSP (FSRQ)	-129.82	17.29	0.559	yes*
4C +38.41	LSP (FSRQ)	-5.84	15.62	0.639	no
3C 345	LSP (FSRQ)	89.44	14.72	-0.254	no
PKS B1730-130	LSP (FSRQ)	-1.52	15.93	0.489	no
3C 446	LSP (FSRQ)	-118.37	15.82	0.263	no
4C 11.69	LSP (FSRQ)	6.23	6.09	0.708	no
3C 454.3	LSP (FSRQ)	-0.12	12.05	0.653	no

TABLE C.8: Spearman correlation coefficients for MOPTOP optical flux vs. Fermi γ-ray flux. c is the Spearman rank correlation strength coefficient and p is the corresponding significance value. The number of optical data points for each filter used in these correlation calculations is also shown.

Source	Type	Filter	p	c	Points
PG1553+113	HSP	B	6.94×10^{-4}	0.391	72
PG1553+113	HSP	V	2.15×10^{-5}	0.464	77
PG1553+113	HSP	R	4.72×10^{-5}	0.441	79
TXS 0506+056	LSP	B	0.017	0.327	53
TXS 0506+056	LSP	V	0.046	0.277	52
TXS 0506+056	LSP	R	0.043	0.282	52
OJ287	LSP	B	0.657	-0.062	54
OJ287	LSP	V	0.187	-0.208	42
OJ287	LSP	R	0.858	-0.024	56
BL Lac	LSP	B	7.32×10^{-73}	0.905	193
BL Lac	LSP	V	3.30×10^{-41}	0.858	138
BL Lac	LSP	R	2.93×10^{-74}	0.903	199
PKS1510-089	LSP (FSRQ)	B	0.453	0.096	63
PKS1510-089	LSP (FSRQ)	V	0.061	0.232	66
PKS1510-089	LSP (FSRQ)	R	0.033	0.269	63
4C 11.69	LSP (FSRQ)	B	9.28×10^{-15}	0.713	87
4C 11.69	LSP (FSRQ)	V	1.07×10^{-15}	0.690	102
4C 11.69	LSP (FSRQ)	R	1.13×10^{-15}	0.677	107
3C 454.3	LSP (FSRQ)	B	3.72×10^{-12}	0.640	94
3C 454.3	LSP (FSRQ)	V	4.74×10^{-13}	0.635	104
3C 454.3	LSP (FSRQ)	R	5.29×10^{-14}	0.664	100

TABLE C.9: Correlation strengths for the spectral index vs. MOPTOP V band flux correlations. The source name and subclass are given in columns one and two. The best fit determined as given by AIC and BIC values is shown in column three. Columns four and five give the Spearman rank strength and significance correlation coefficients after having linearised the dataset if better fitted with a logarithmic curve. Column six gives the colour trend of the object given the fit and Spearman rank coefficients. Column seven gives the average spectral index, and column 8 gives the number of data points.

Source	Type	Fit	c	p	Trend	$\alpha_{\rm av}$	Points
PG1553+113	HSP	linear	-0.599	1.22×10^{-18}	BWB	1.145	177
TXS 0506+056	LSP	log	-0.612	8.62×10^{-24}	BSWB	2.564	218
OJ287	LSP	log	-0.541	1.23×10^{-13}	BSWB	1.961	161
BL Lac	LSP	log	-0.794	2.97×10^{-75}	BSWB	3.911	341
PKS1510-089	LSP (FSRQ)	linear	-0.056	0.490	-	0.656	154
4C 11.69	LSP (FSRQ)	log	0.665	1.59×10^{-20}	RSWB	1.024	150
3C 454.3	LSP (FSRQ)	log	0.738	2.72×10^{-28}	RSWB	1.878	157

TABLE C.10: As Table C.9 but for spectral index vs. γ-ray flux.

Source	Type	Fit	c	p	Trend	$\alpha_{\rm av}$	Points
PG1553+113	HSP	linear	-0.334	5.09×10^{-13}	BWB	1.096	69
TXS 0506+056	LSP	linear	-0.195	0.131	-	2.491	61
OJ287	LSP	linear	0.072	0.620	-	1.928	50
BL Lac	LSP	log	-0.697	5.57×10^{-21}	BSWB	3.875	135
PKS1510-089	LSP (FSRQ)	linear	0.345	7.99×10^{-3}	RWB	0.692	58
4C 11.69	LSP (FSRQ)	linear	0.476	6.30×10^{-6}	RWB	0.952	82
3C 454.3	LSP (FSRQ)	linear	0.623	7.27×10^{-11}	RWB	1.843	89

TABLE C.11: DCF peak lag values with correlation strengths after computing on the MOPTOP optical and γ-ray fluxes. A negative lag implies the γ-ray emission is leading the optical. An asterisk in the 3σ lag column suggests the potential significance of the detected lag, warranting further analysis.

Source	Type	Peak [days]	ΔPeak [days]	c	3σ lag
PG1553+113	HSP	-20.64	1.96	0.530	yes*
TXS 0506+056	LSP	-0.82	2.27	0.318	no
OJ287	LSP	-50.61	2.52	0.320	no
BL Lac	LSP	-2.79	2.29	0.704	yes*
PKS1510-089	LSP (FSRQ)	-40.62	2.47	0.392	yes*
4C 11.69	LSP (FSRQ)	-0.07	2.98	0.476	no
3C 454.3	LSP (FSRQ)	-7.15	3.13	0.720	yes*

TABLE C.12: Spearman correlation coefficients for optical magnitude vs. degree of polarisation, where c is the correlation strength coefficient and p is the corresponding significance value. The number of optical data points (per camera) used in these correlation calculations is also shown.

Source	Type	r^* c	r^* p	g^* c	g^* p	b^* c	b^* p	Points
IC 310	HSP	-0.243	9.02×10^{-4}	-0.230	1.72×10^{-3}	-0.084	0.258	184
1ES 1011+496	HSP	0.190	0.015	0.137	0.080	0.238	2.14×10^{-3}	164
MRK 180	HSP	-0.011	0.892	0.190	0.014	0.155	0.045	168
PG 1218+304	HSP	-0.123	0.219	-0.067	0.506	-0.064	0.520	102
1ES 1426+428	HSP	-0.088	0.211	-0.201	3.75×10^{-3}	-0.290	2.33×10^{-5}	206
PG 1553+113	HSP	0.055	0.402	0.089	0.176	0.146	0.026	233
MRK 501	HSP	-0.063	0.306	0.189	1.96×10^{-3}	0.234	1.15×10^{-4}	266
1ES 1959+650	HSP	-0.294	0.038	-0.376	7.17×10^{-3}	-0.360	0.010	50
3C 66A	ISP	-0.012	0.838	0.050	0.406	0.091	0.126	282
S5 0716+714	ISP	0.035	0.554	0.008	0.891	-0.002	0.977	281
ON 231	ISP	-0.107	0.340	-0.108	0.335	0.005	0.961	82
A0 0235+164	LSP	-0.085	0.492	-0.114	0.357	-0.190	0.120	68
TXS 0506+056	LSP	0.226	0.436	0.200	0.493	-0.051	0.864	14
OJ 287	LSP	0.303	1.19×10^{-12}	0.295	4.86×10^{-12}	0.284	3.04×10^{-11}	526
S4 0954+65	LSP	-0.138	0.053	-0.209	3.16×10^{-3}	-0.200	4.91×10^{-3}	197
4C 09.57	LSP	0.007	0.936	0.069	0.449	0.080	0.378	124
BL Lac	LSP	0.259	7.03×10^{-7}	0.234	7.88×10^{-6}	0.236	6.32×10^{-6}	357
PKS 0502+049	LSP (FSRQ)	-0.236	0.011	0.069	0.464	0.327	3.36×10^{-4}	116
PKS 0736+01	LSP (FSRQ)	0.463	4.71×10^{-8}	0.495	3.90×10^{-9}	0.551	2.20×10^{-11}	126
PKS 1222+216	LSP (FSRQ)	0.243	0.032	0.168	0.142	0.312	5.40×10^{-3}	78
3C 279	LSP (FSRQ)	-0.337	7.81×10^{-5}	-0.352	3.54×10^{-5}	-0.414	7.97×10^{-7}	132
PKS 1510-089	LSP (FSRQ)	0.196	3.14×10^{-3}	0.299	4.67×10^{-6}	0.325	6.03×10^{-7}	226
OS 319	LSP (FSRQ)	-0.292	7.35×10^{-3}	-0.361	8.10×10^{-4}	-0.208	0.060	83
PKS B1622-297	LSP (FSRQ)	-0.195	0.075	0.115	0.296	0.128	0.244	84
4C +38.41	LSP (FSRQ)	0.229	0.030	0.378	2.39×10^{-4}	0.474	2.41×10^{-6}	90
3C 345	LSP (FSRQ)	0.154	0.128	0.351	3.73×10^{-4}	0.115	0.258	99
PKS B1730-130	LSP (FSRQ)	-0.344	8.87×10^{-4}	-0.274	8.89×10^{-3}	-0.285	6.49×10^{-3}	90
3C 446	LSP (FSRQ)	-0.352	1.55×10^{-3}	-0.299	7.92×10^{-3}	-0.261	0.021	78
4C 11.69	LSP (FSRQ)	0.075	0.272	0.226	7.77×10^{-4}	0.383	5.38×10^{-9}	217
3C 454.3	LSP (FSRQ)	0.386	4.74×10^{-5}	0.489	1.17×10^{-7}	0.608	6.27×10^{-12}	105

TABLE C.13: As Table C.12 but for γ-ray flux vs. degree of polarisation.

Source	Type	r^* c	r^* p	g^* c	g^* p	b^* c	b^* p	Points
IC 310	HSP	-	-	-	-	-	-	184
1ES 1011+496	HSP	0.121	0.124	-0.011	0.885	-0.072	0.362	164
MRK 421	HSP	0.199	3.51×10^{-3}	0.246	2.88×10^{-4}	0.195	4.29×10^{-3}	213
MRK 180	HSP	-0.095	0.222	0.016	0.834	-0.027	0.724	168
PG 1218+304	HSP	0.187	0.059	-0.016	0.872	-0.094	0.349	102
1ES 1426+428	HSP	-	-	-	-	-	-	206
PG 1553+113	HSP	0.016	0.803	-0.025	0.701	0.006	0.932	233
MRK 501	HSP	0.105	0.087	0.097	0.115	0.020	0.750	266
1ES 1959+650	HSP	-0.078	0.589	0.002	0.989	-0.002	0.989	50
3C 66A	ISP	-0.077	0.195	-0.087	0.145	-0.044	0.460	282
S5 0716+714	ISP	-0.124	0.038	-0.151	0.011	-0.166	5.21×10^{-3}	281
ON 231	ISP	0.141	0.207	0.085	0.445	0.090	0.420	82
A0 0235+164	LSP	0.030	0.806	0.055	0.656	-0.027	0.827	68
TXS 0506+056	LSP	-0.329	0.250	-0.146	0.619	-0.188	0.519	14
OJ 287	LSP	-0.118	6.74×10^{-3}	-0.120	5.75×10^{-3}	-0.117	7.00×10^{-3}	526
S4 0954+65	LSP	0.078	0.277	0.058	0.415	0.056	0.430	197
4C 09.57	LSP	0.030	0.741	0.087	0.339	0.087	0.335	124
BL Lac	LSP	0.079	0.138	0.076	0.152	0.087	0.101	357
PKS 0502+049	LSP (FSRQ)	-0.140	0.135	0.110	0.239	0.274	2.94×10^{-3}	116
PKS 0736+01	LSP (FSRQ)	0.422	8.55×10^{-7}	0.457	7.64×10^{-8}	0.460	5.94×10^{-8}	126
PKS 1222+216	LSP (FSRQ)	-0.000	0.997	0.185	0.105	0.201	0.077	78
3C 279	LSP (FSRQ)	-0.151	0.085	-0.173	0.047	-0.239	5.88×10^{-3}	132
PKS 1510-089	LSP (FSRQ)	0.146	0.028	0.290	9.15×10^{-6}	0.291	8.99×10^{-6}	226
OS 319	LSP (FSRQ)	0.193	0.080	-0.052	0.641	0.096	0.390	83
PKS B1622-297	LSP (FSRQ)	-0.075	0.499	0.041	0.711	0.067	0.547	84
4C +38.41	LSP (FSRQ)	0.196	0.064	0.356	5.71×10^{-4}	0.362	4.60×10^{-4}	90
3C 345	LSP (FSRQ)	0.053	0.599	0.140	0.166	0.152	0.134	99
PKS B1730-130	LSP (FSRQ)	0.047	0.660	-0.041	0.699	-0.063	0.558	90
3C 446	LSP (FSRQ)	-0.133	0.245	-0.181	0.112	0.082	0.473	78
4C 11.69	LSP (FSRQ)	-0.040	0.558	0.078	0.252	0.257	1.27×10^{-4}	217
3C 454.3	LSP (FSRQ)	0.388	4.38×10^{-5}	0.467	5.24×10^{-7}	0.568	2.55×10^{-10}	105

TABLE C.14: Spearman rank coefficients for the RINGO3 polarisation colour correlations.

Source	Type	Line Colour	c	p	Linear Fit Grad	Points
IC 310	HSP	g^* (b^*-r^*)	-0.219	2.79×10^{-3}	-0.293	184
1ES 1011+496	HSP	g^* (b^*-r^*)	0.256	9.47×10^{-4}	0.249	164
MRK 421	HSP	g^* (b^*-r^*)	0.002	0.982	-0.063	213
MRK 180	HSP	g^* (b^*-r^*)	0.125	0.106	0.278	168
PG 1218+304	HSP	g^* (b^*-r^*)	0.035	0.723	-0.063	102
1ES 1426+428	HSP	g^* (b^*-r^*)	0.080	0.254	0.058	206
PG 1553+113	HSP	g^* (b^*-r^*)	-0.100	0.126	-0.086	233
MRK 501	HSP	g^* (b^*-r^*)	-0.010	0.865	-0.232	266
1ES 1959+650	HSP	g^* (b^*-r^*)	0.259	0.069	0.238	50
3C 66A	ISP	g^* (b^*-r^*)	0.038	0.520	0.030	282
S5 0716+714	ISP	g^* (b^*-r^*)	0.191	1.33×10^{-3}	0.040	281
ON 231	ISP	g^* (b^*-r^*)	0.180	0.105	0.151	82
A0 0235+164	LSP	g^* (b^*-r^*)	-0.010	0.936	-0.082	68
TXS 0506+056	LSP	g^* (b^*-r^*)	-0.196	0.503	-0.094	14
OJ 287	LSP	g^* (b^*-r^*)	0.126	3.72×10^{-3}	0.030	526
S4 0954+65	LSP	g^* (b^*-r^*)	0.181	0.011	0.091	197
4C 09.57	LSP	g^* (b^*-r^*)	0.032	0.725	0.032	124
BL Lac	LSP	g^* (b^*-r^*)	0.037	0.483	0.025	357
PKS 0502+049	LSP (FSRQ)	g^* (b^*-r^*)	-0.152	0.103	-0.145	116
PKS 0736+01	LSP (FSRQ)	g^* (b^*-r^*)	0.297	7.27×10^{-4}	0.196	126
PKS 1222+216	LSP (FSRQ)	g^* (b^*-r^*)	-0.142	0.215	-0.092	78
3C 279	LSP (FSRQ)	g^* (b^*-r^*)	-0.003	0.975	0.025	132
PKS 1510-089	LSP (FSRQ)	g^* (b^*-r^*)	-0.105	0.116	-0.068	226
OS 319	LSP (FSRQ)	g^* (b^*-r^*)	-0.237	0.031	-0.643	83
PKS B1622-297	LSP (FSRQ)	g^* (b^*-r^*)	0.001	0.994	-0.057	84
4C +38.41	LSP (FSRQ)	g^* (b^*-r^*)	0.144	0.176	0.104	90
3C 345	LSP (FSRQ)	g^* (b^*-r^*)	0.026	0.800	-0.162	99
PKS B1730-130	LSP (FSRQ)	g^* (b^*-r^*)	-0.054	0.612	-0.333	90
3C 446	LSP (FSRQ)	g^* (b^*-r^*)	0.001	0.990	-0.268	78
4C 11.69	LSP (FSRQ)	g^* (b^*-r^*)	-0.247	2.43×10^{-4}	-0.212	217
3C 454.3	LSP (FSRQ)	g^* (b^*-r^*)	0.029	0.769	-0.031	105

TABLE C.15: EVPA rotations found in the RINGO3 dataset. Shown are the starts of the rotations as MJD and EVPA, and the duration and size of the rotation. Also shown are the average γ-ray flux and optical polarisation and magnitude values during the full monitoring campaign and the rotation event.

Source	Type	MJD Start	ΔMJD [days]	EVPA Start [°]	ΔEVPA [°]	γ-ray av [erg cm^{-2} s^{-1}]	γ-ray rot [erg cm^{-2} s^{-1}]	Pol av [%]	Pol rot [%]	Opt av	Opt rot
MRK 421	HSP	56712.14	3.89	131.47	-91.83	3.86×10^{-10}	4.85×10^{-10}	3.27	6.11	-	-
...	...	56998.15	10.02	159.54	-101.72	...	5.38×10^{-10}	...	5.34	-	-
MRK 180	HSP	57120.94	31.93	118.63	-183.27	2.88×10^{-11}	2.72×10^{-11}	3.28	3.61	14.53	14.59
MRK 501	HSP	56867.89	5.02	121.64	-154.16	1.10×10^{-10}	1.93×10^{-10}	1.30	1.11	12.72	12.67
S5 0716+714	ISP	56979.09	27.93	82.49	113.72	1.55×10^{-10}	1.96×10^{-10}	8.18	7.61	12.72	12.97
...	...	57078.94	7.01	25.66	90.25	...	2.57×10^{-10}	...	8.96	...	12.38
...	...	57275.20	3.96	21.36	-92.57	...	7.48×10^{-11}	...	10.07	...	12.89
...	...	57324.11	7.15	40.89	-90.57	...	3.33×10^{-10}	...	10.89	...	12.08
...	...	57391.89	7.11	67.95	133.12	...	2.60×10^{-10}	...	6.65	...	12.51
...	...	57653.21	3.97	10.28	-93.87	...	9.32×10^{-11}	...	8.35	...	13.22
...	...	57702.27	34.88	-90.86	125.74	...	7.66×10^{-11}	...	9.97	...	12.90
...	...	58030.24	12.97	-20.50	138.82	...	1.86×10^{-10}	...	8.36	...	12.91
...	...	58334.22	13.02	200.71	144.91	...	2.97×10^{-10}	...	6.51	...	11.73
OJ 287	LSP	57428.07	23.88	150.84	-103.51	5.93×10^{-11}	7.44×10^{-11}	11.79	11.60	13.90	13.94
...	...	57511.86	13.01	126.76	-128.76	...	4.86×10^{-11}	...	6.78	...	13.90
S4 0954+65	LSP	57051.12	91.86	93.50	-113.55	5.91×10^{-11}	1.35×10^{-10}	8.88	11.12	15.29	15.31
...	...	57336.12	7.16	347.19	-175.67	...	6.85×10^{-11}	...	9.82	...	15.23
...	...	58213.90	24.56	144.10	107.26	...	7.15×10^{-11}	...	13.18	...	15.23
...	...	58425.23	4.97	131.40	-100.41	...	4.65×10^{-11}	...	5.81	...	15.03
BL Lac	LSP	57150.21	30.92	192.94	-157.56	2.56×10^{-10}	2.86×10^{-10}	6.23	5.55	12.57	12.60
...	...	57205.19	2.92	-0.92	92.36	...	2.60×10^{-10}	...	2.48	...	12.84
...	...	57620.08	16.92	177.69	-119.79	...	1.82×10^{-10}	...	4.46	...	13.08
...	...	58342.52	5.99	195.81	-112.02	...	3.18×10^{-10}	...	6.20	...	12.40
...	...	58373.12	10.34	180.38	-100.60	...	2.56×10^{-10}	...	5.72	...	12.48
3C 279	LSP (FSRQ)	58123.21	15.02	104.87	125.94	2.90×10^{-10}	2.31×10^{-09}	15.26	14.11	14.60	14.46
PKS B1622-297	LSP (FSRQ)	57207.90	15.99	56.18	-126.38	7.51×10^{-11}	1.01×10^{-10}	17.31	16.52	17.97	17.93
4C +38.41	LSP (FSRQ)	57604.87	40.01	-88.68	177.82	8.14×10^{-11}	7.47×10^{-11}	9.36	10.03	16.47	16.97
4C 11.69	LSP (FSRQ)	57698.93	52.91	-68.67	103.53	1.76×10^{-10}	1.65×10^{-09}	8.49	8.15	16.04	14.01
3C 454.3	LSP (FSRQ)	57527.17	38.92	128.63	-140.08	3.70×10^{-10}	8.61×10^{-10}	5.33	10.30	15.34	14.90

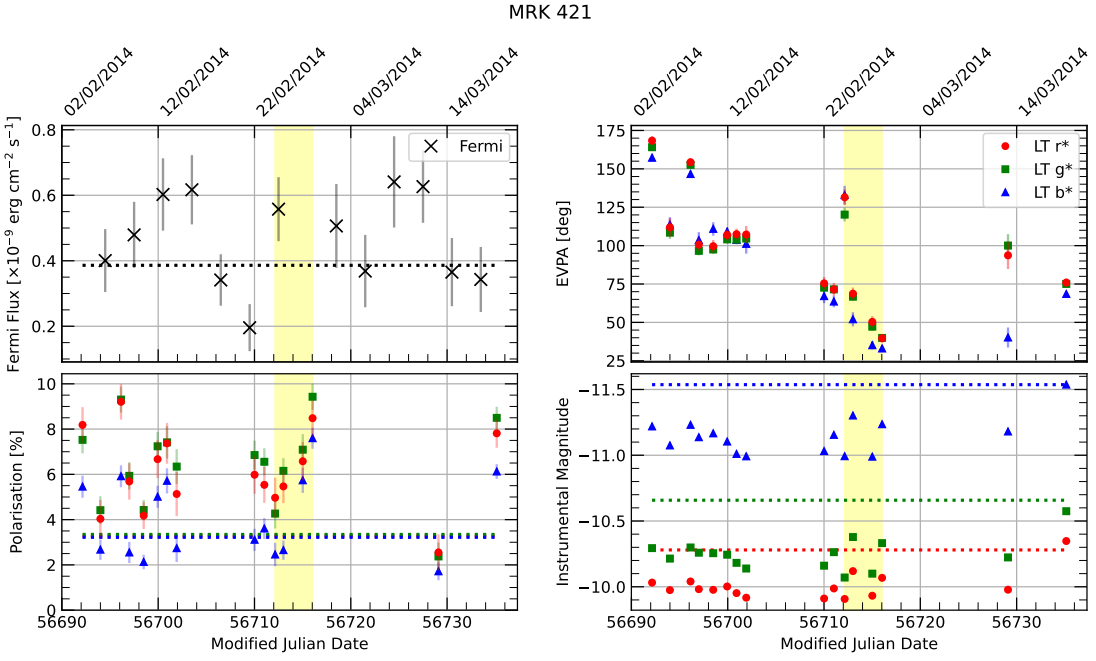

FIGURE C.13: MRK 421 light curve during the EVPA rotation at MJD 56712.14. The top left panel shows the γ-ray flux, the bottom left shows the optical polarisation, the top right shows the EVPA rotation, and the bottom right shows the optical instrumental magnitude. In the γ-ray flux, polarisation, and instrumental magnitude panels, dotted lines are plotted to show the respective average states in relevant filters over the full duration of RINGO3 observations.

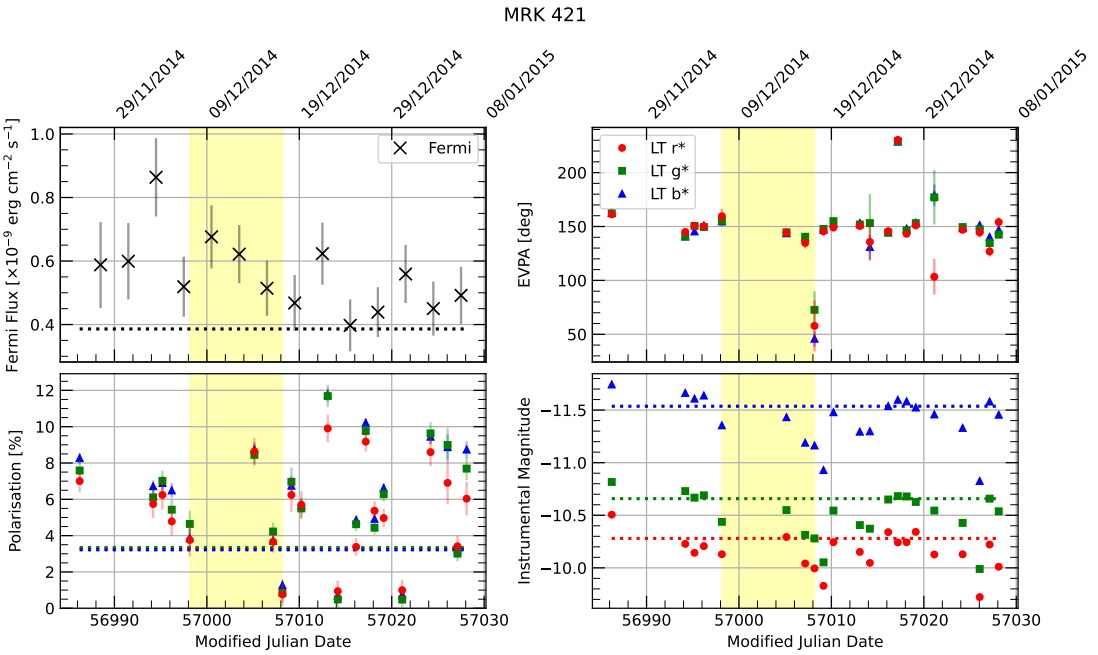

FIGURE C.14: As Fig. C.14 but for MRK 421 during the EVPA rotation at MJD 56998.15.

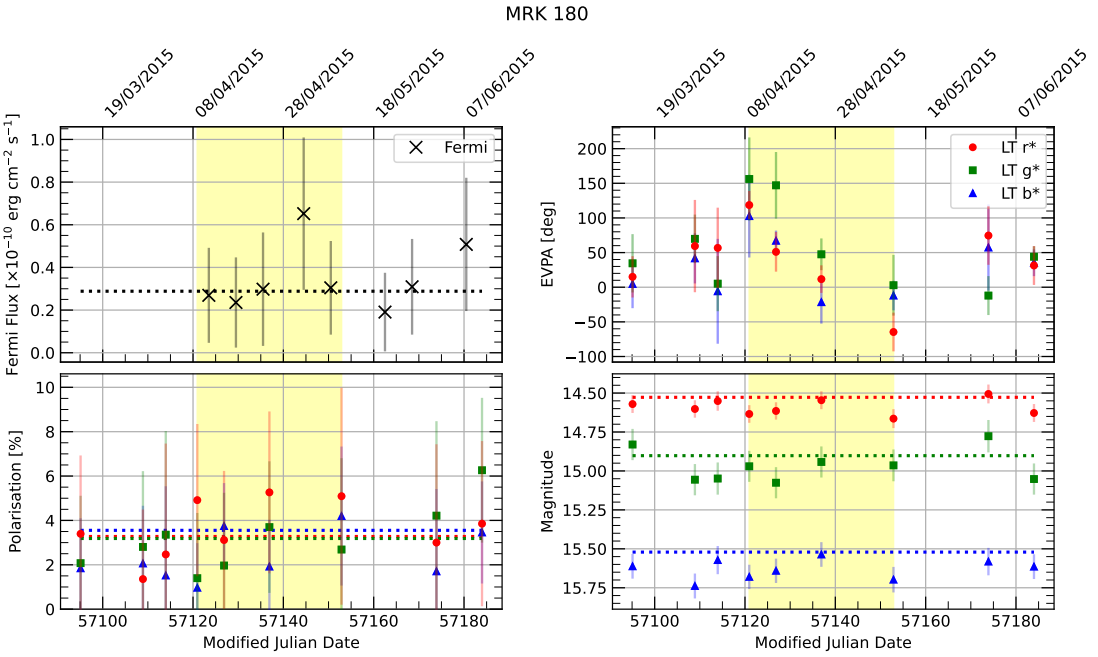

FIGURE C.15: MRK 180 light curve during the EVPA rotation at MJD 57120.94. The top left panel shows the γ-ray flux, the bottom left shows the optical polarisation, the top right shows the EVPA rotation, and the bottom right shows the optical magnitude. In the γ-ray flux, polarisation, and instrumental magnitude panels, dotted lines are plotted to show the respective average states in relevant filters over the full duration of RINGO3 observations.

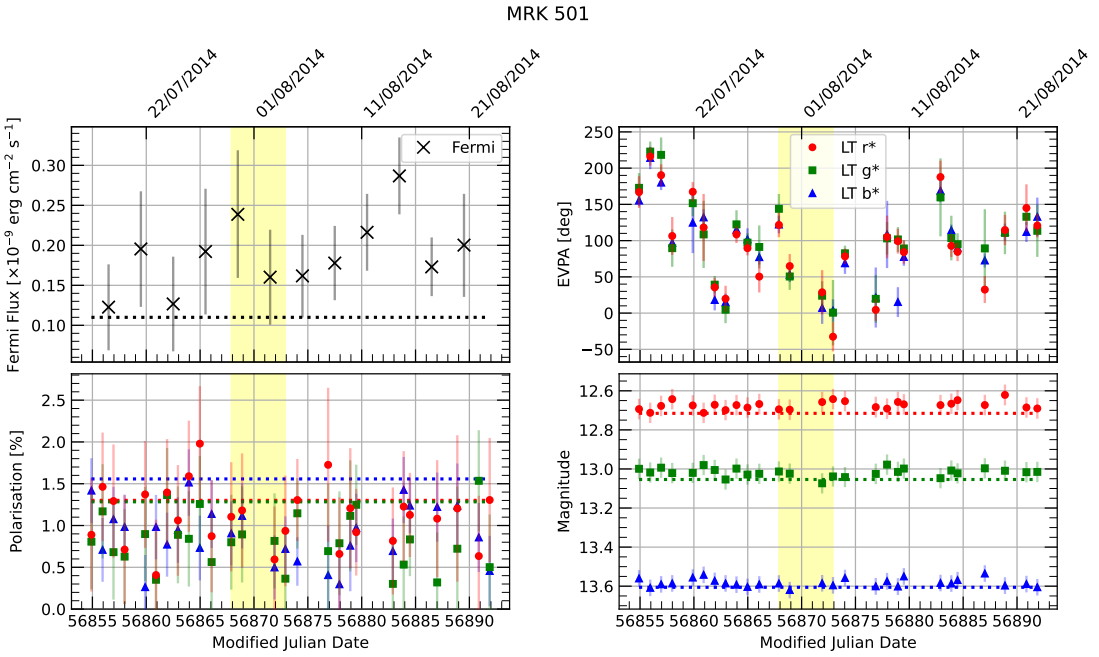

FIGURE C.16: As Fig. C.15 but for MRK 501 during the EVPA rotation at MJD 56867.89.

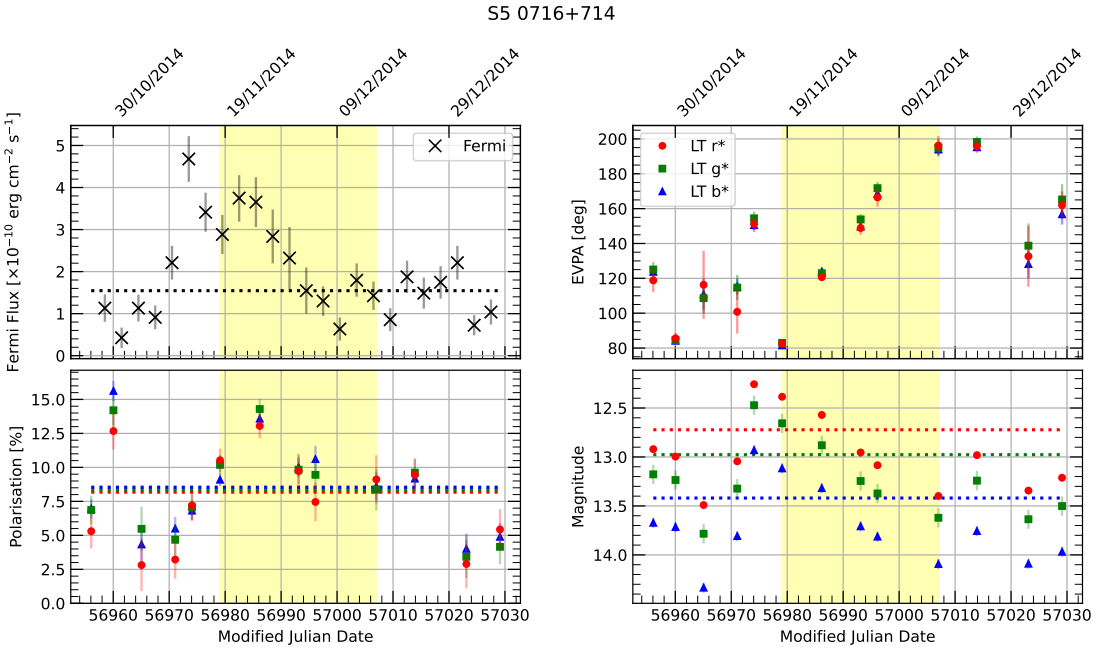

FIGURE C.17: As Fig. C.15 but for S5 0716+714 during the EVPA rotation at MJD 56979.09.

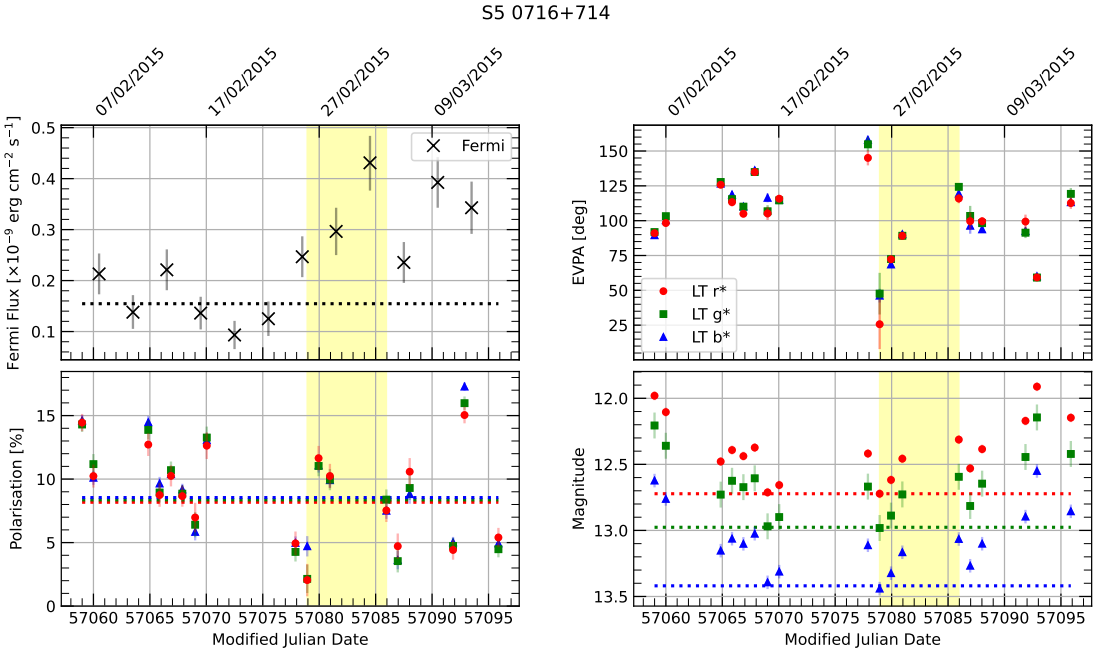

FIGURE C.18: As Fig. C.15 but for S5 0716+714 during the EVPA rotation at MJD 57078.94.

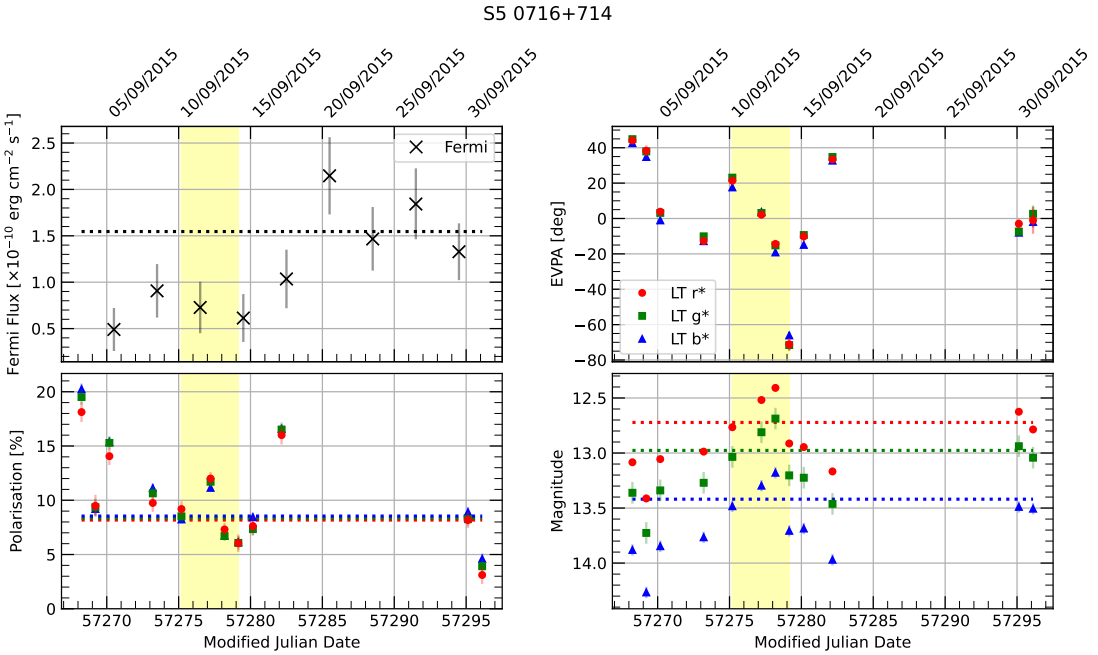

FIGURE C.19: As Fig. C.15 but for S5 0716+714 during the EVPA rotation at MJD 57275.20.

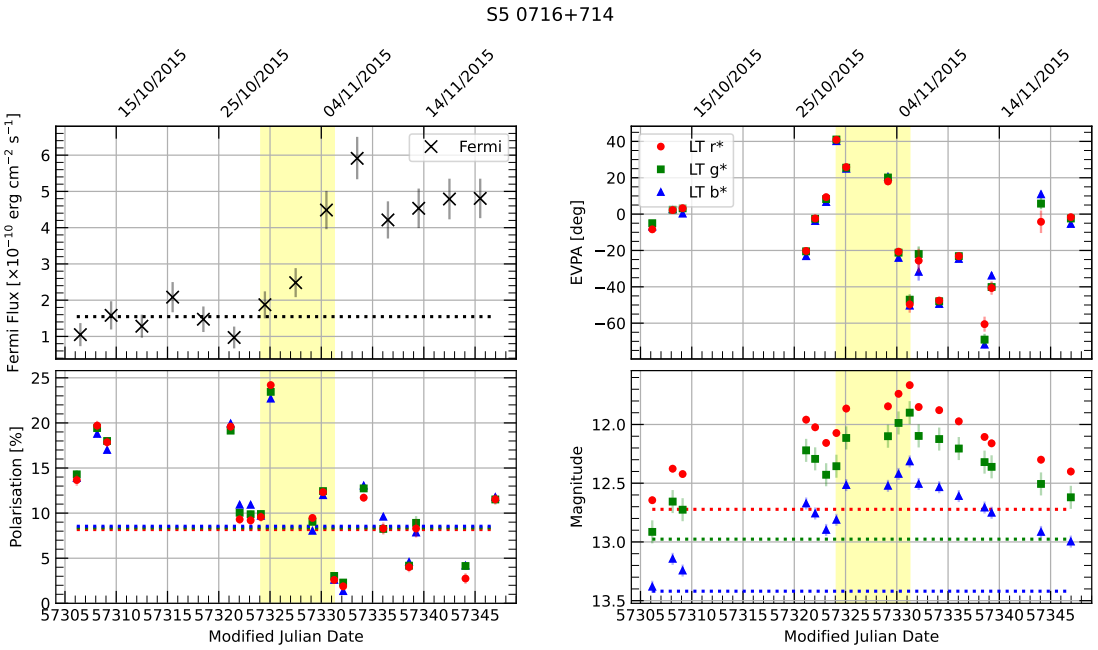

FIGURE C.20: As Fig. C.15 but for S5 0716+714 during the EVPA rotation at MJD 57324.11.

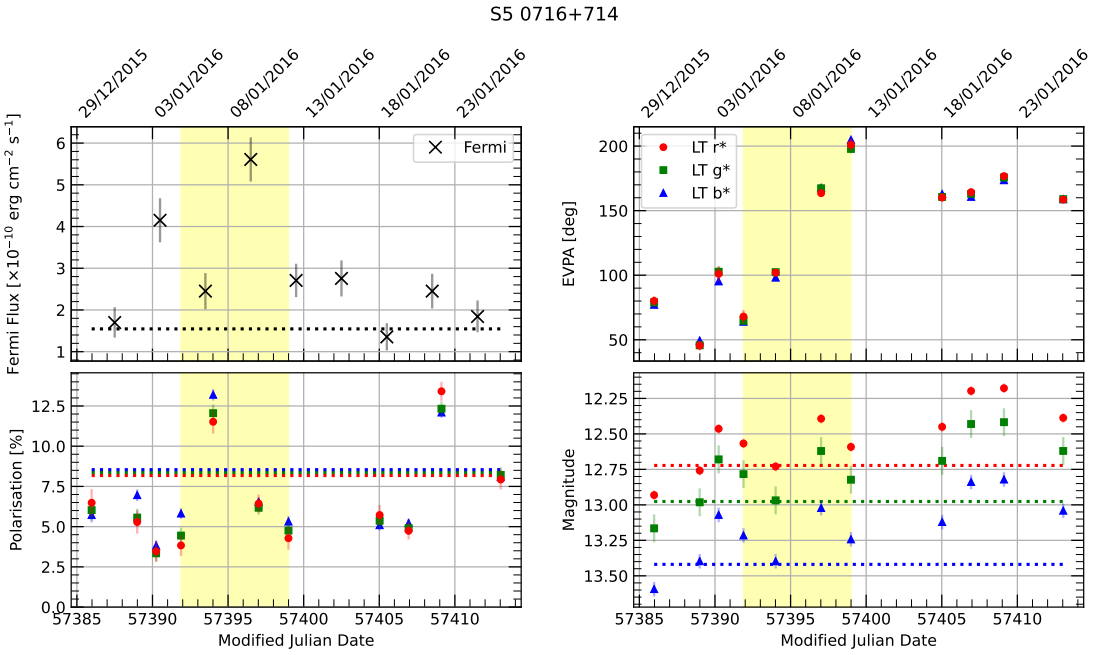

FIGURE C.21: As Fig. C.15 but for S5 0716+714 during the EVPA rotation at MJD 57391.89.

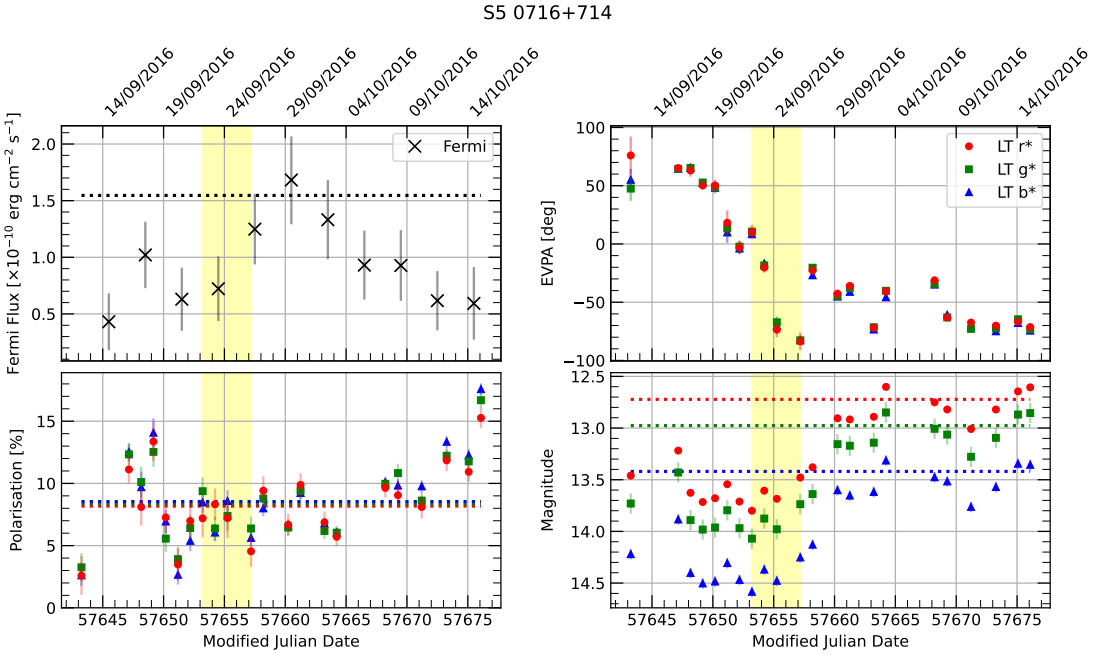

FIGURE C.22: As Fig. C.15 but for S5 0716+714 during the EVPA rotation at MJD 57653.21.

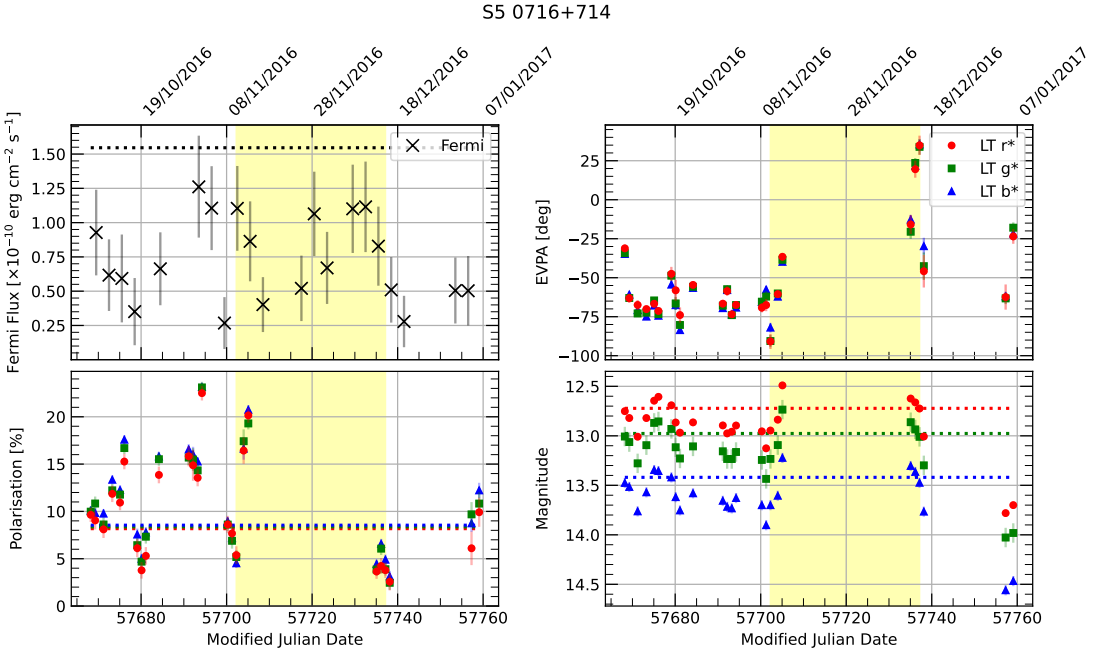

FIGURE C.23: As Fig. C.15 but for S5 0716+714 during the EVPA rotation at MJD 57702.27.

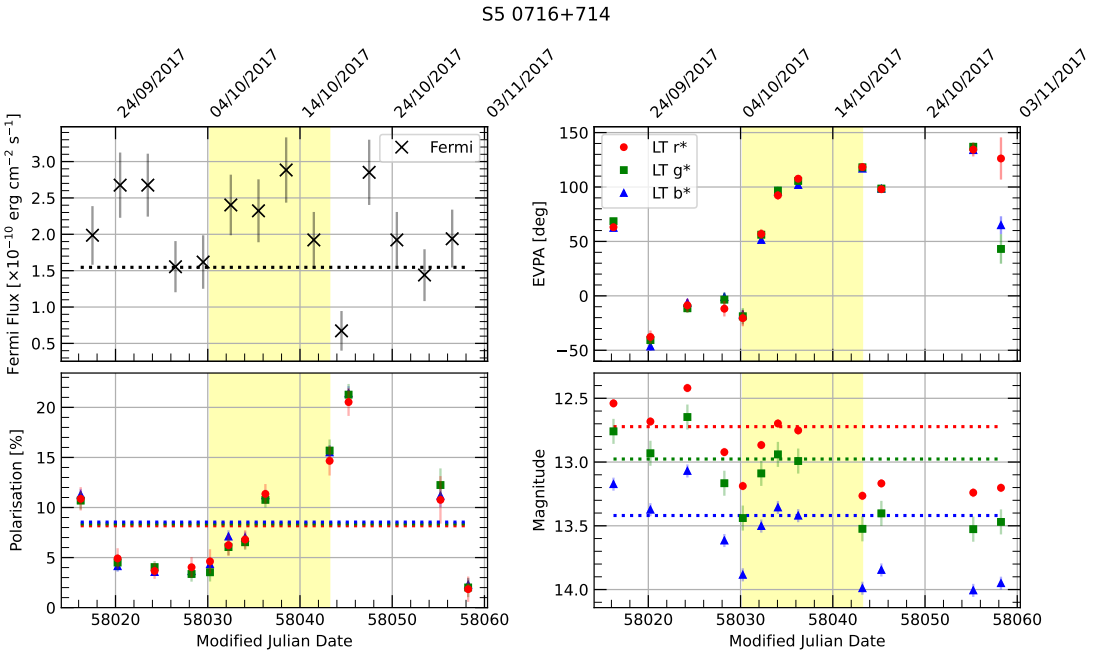

FIGURE C.24: As Fig. C.15 but for S5 0716+714 during the EVPA rotation at MJD 58030.24.

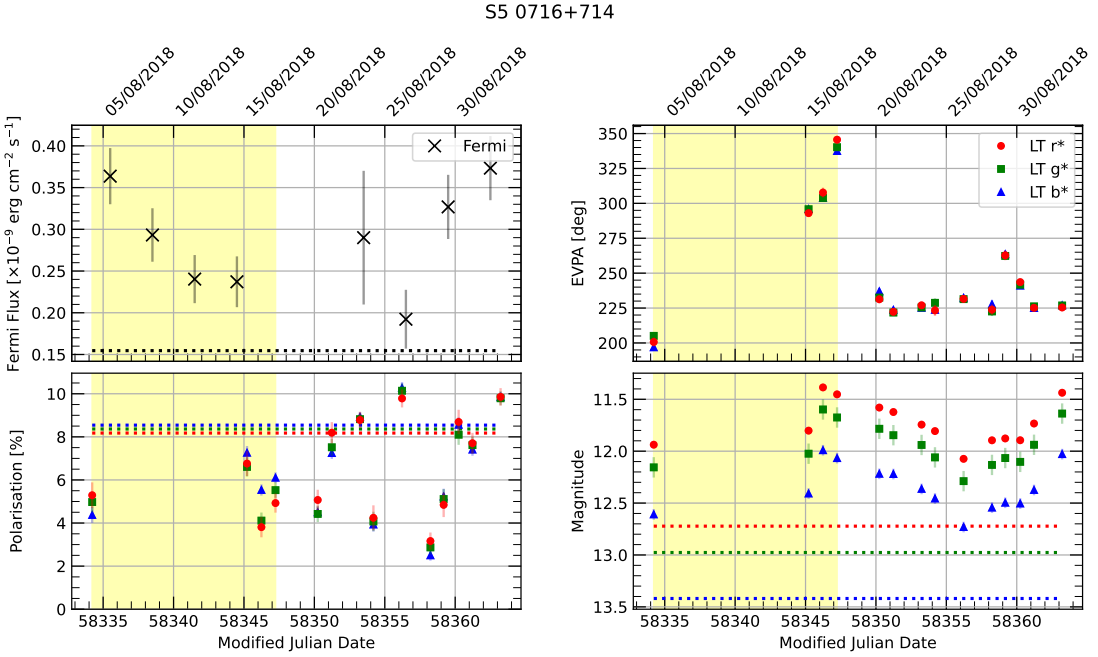

FIGURE C.25: As Fig. C.15 but for S5 0716+714 during the EVPA rotation at MJD 58334.22.

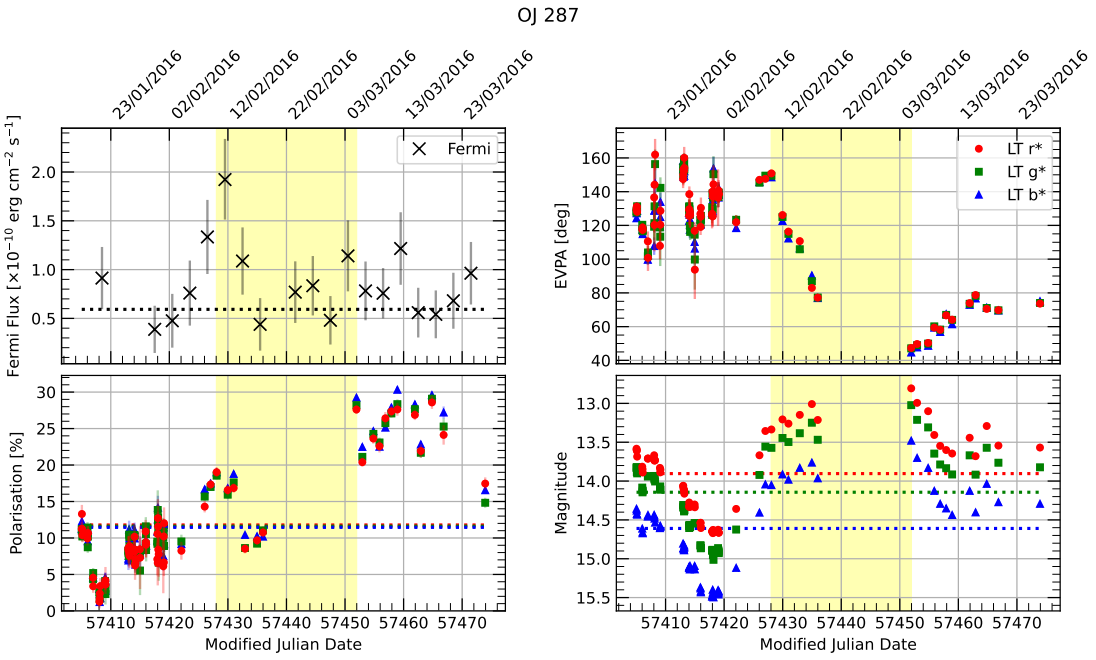

FIGURE C.26: As Fig. C.15 but for OJ 287 during the EVPA rotation at MJD 57428.07.

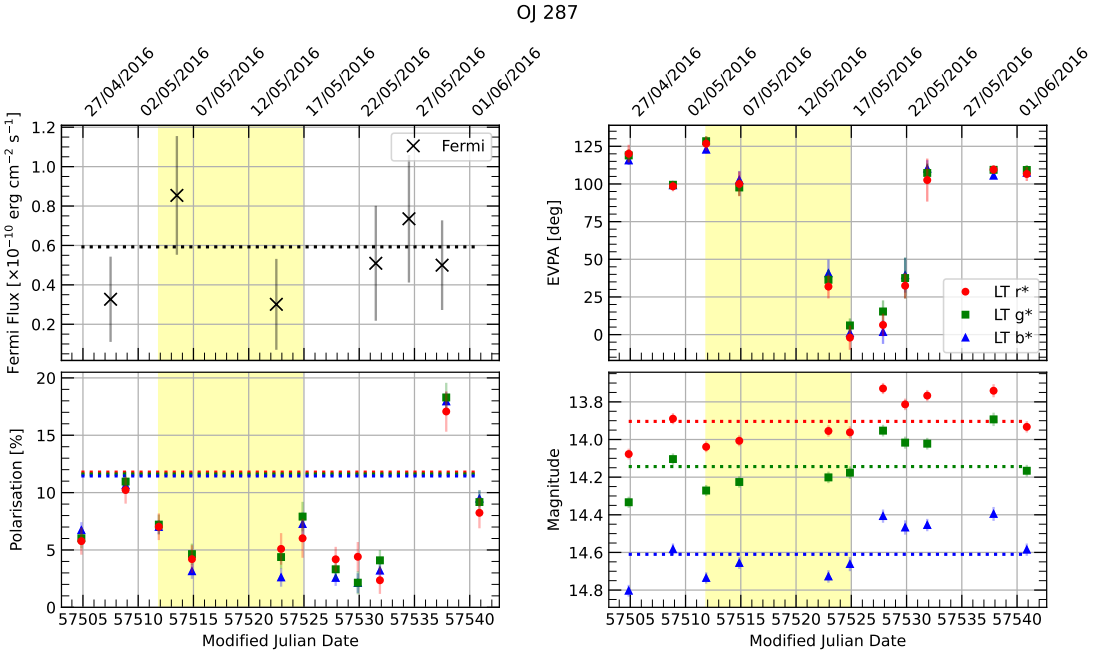

FIGURE C.27: As Fig. C.15 but for OJ 287 during the EVPA rotation at MJD 57511.86.

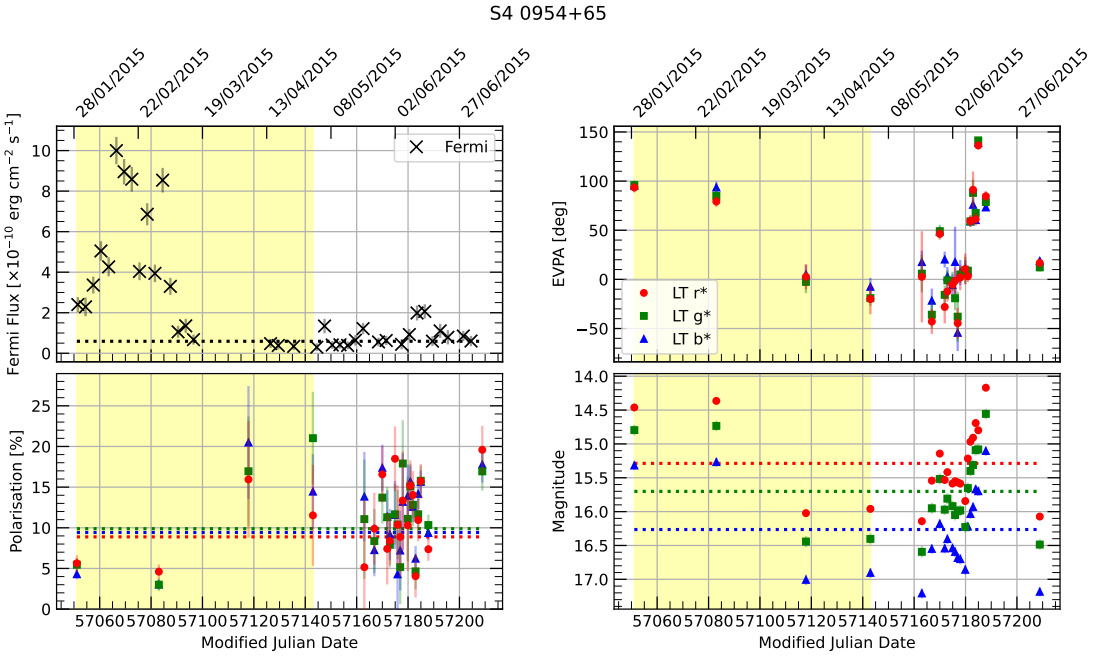

FIGURE C.28: As Fig. C.15 but for S4 0954+65 during the EVPA rotation at MJD 57051.12.

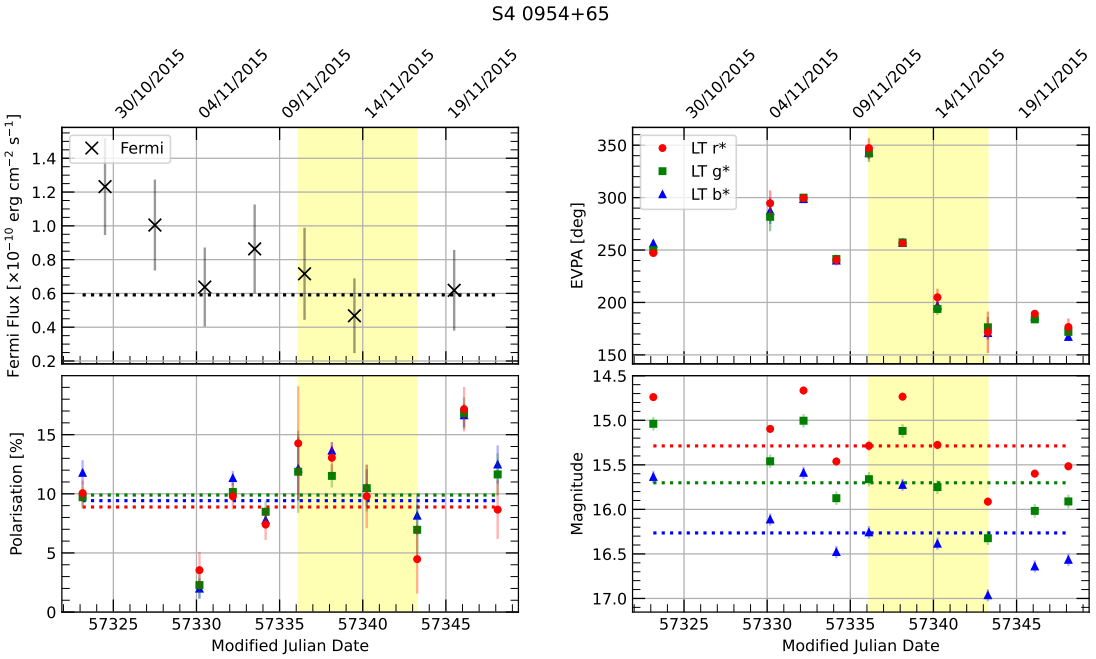

FIGURE C.29: As Fig. C.15 but for S4 0954+65 during the EVPA rotation at MJD 57336.12.

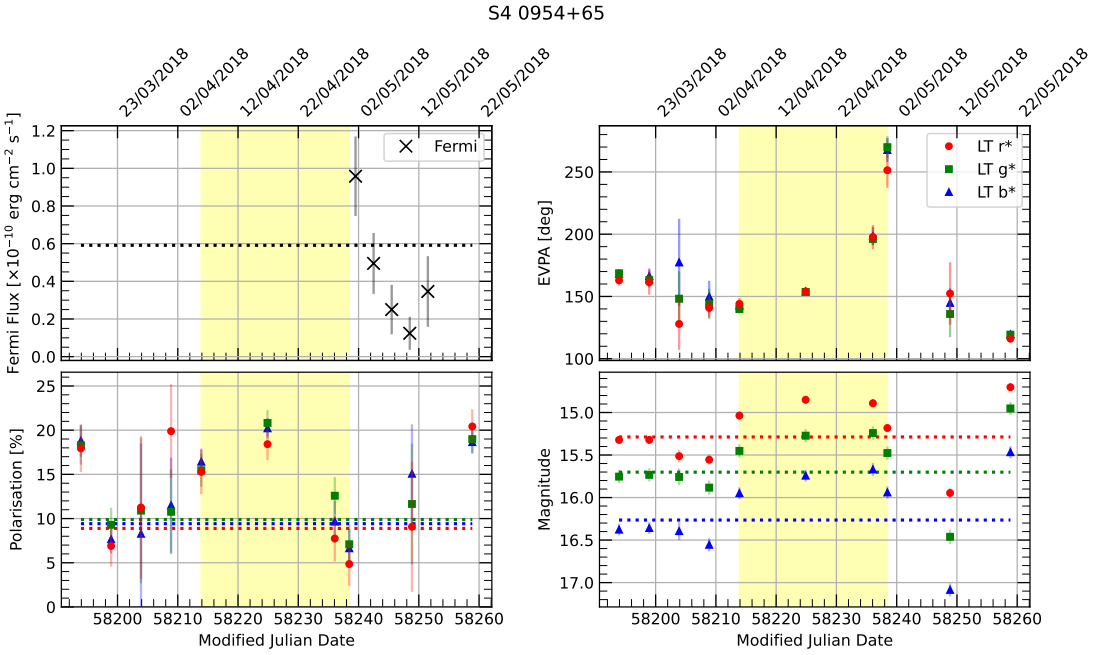

FIGURE C.30: As Fig. C.15 but for S4 0954+65 during the EVPA rotation at MJD 58213.90.

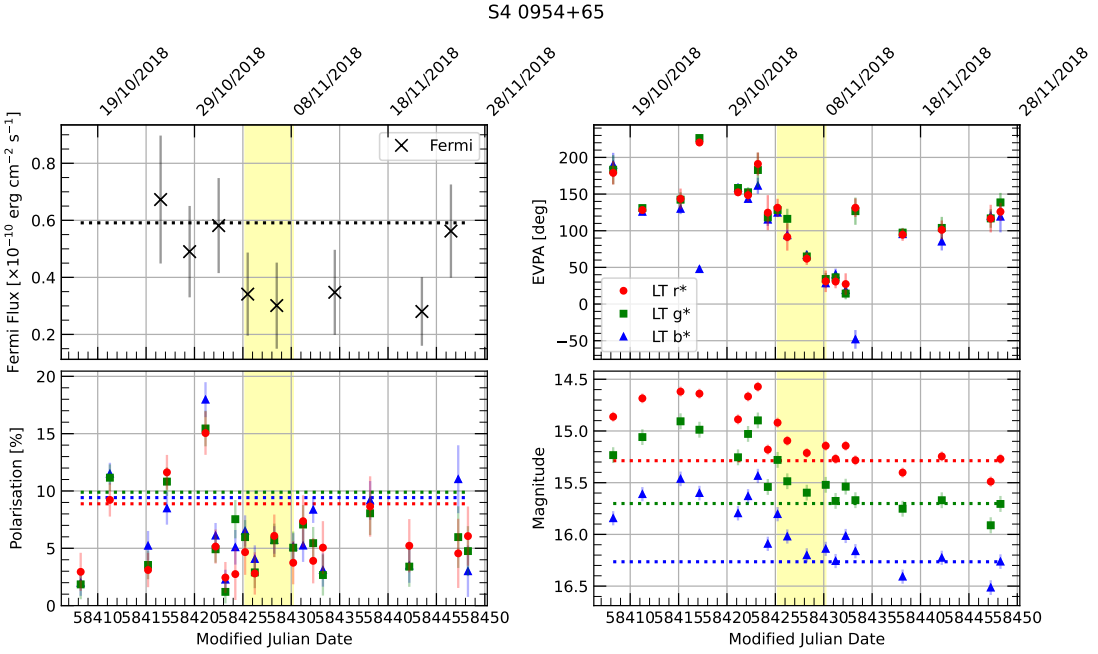

FIGURE C.31: As Fig. C.15 but for S4 0954+65 during the EVPA rotation at MJD 58425.23.

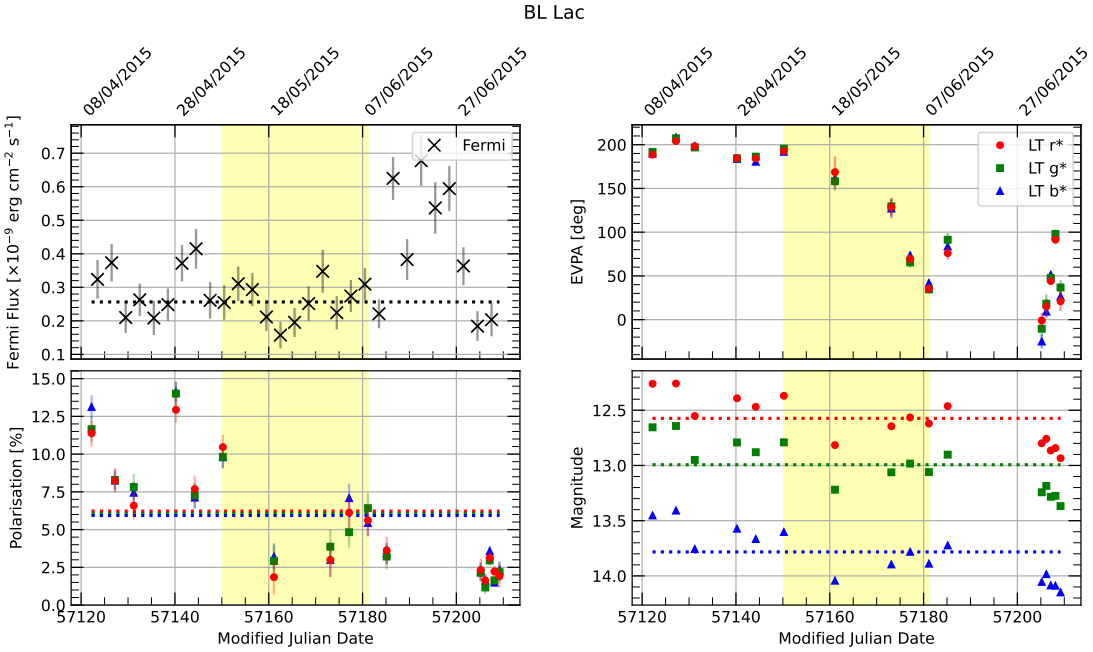

FIGURE C.32: As Fig. C.15 but for BL Lac during the EVPA rotation at MJD 57150.21.

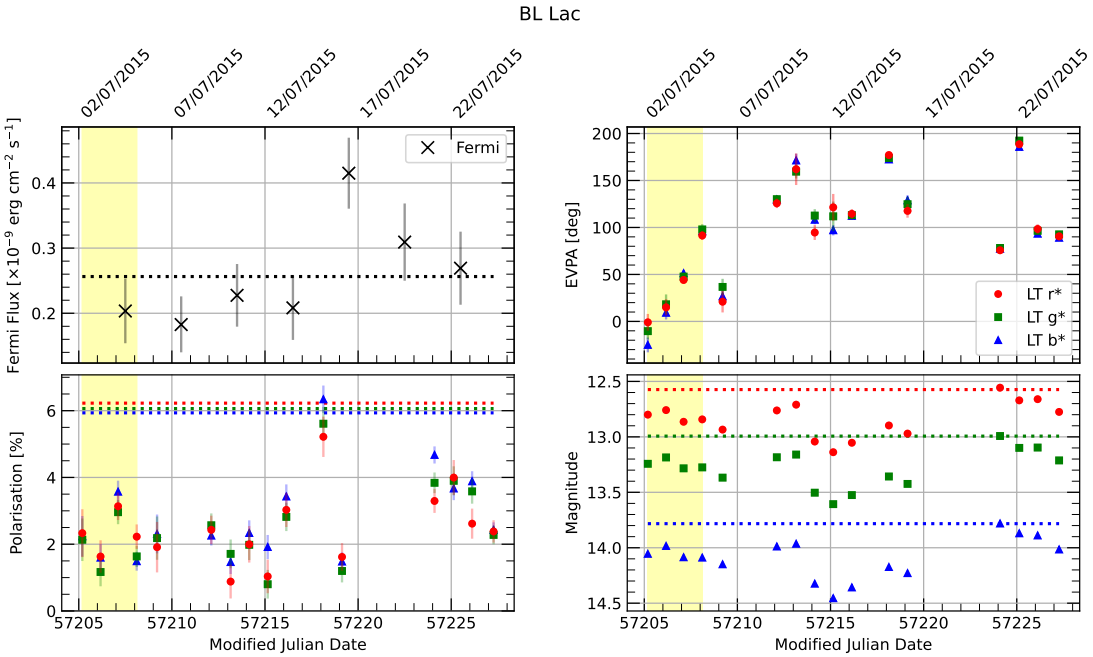

FIGURE C.33: As Fig. C.15 but for BL Lac during the EVPA rotation at MJD 57205.19.

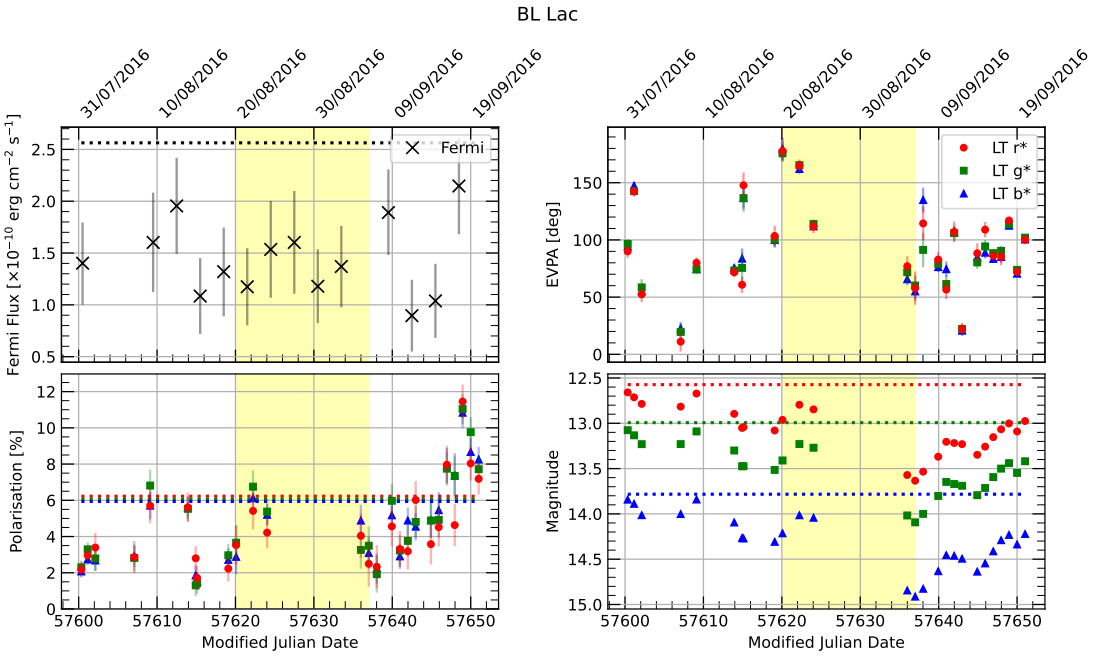

FIGURE C.34: As Fig. C.15 but for BL Lac during the EVPA rotation at MJD 57620.08.

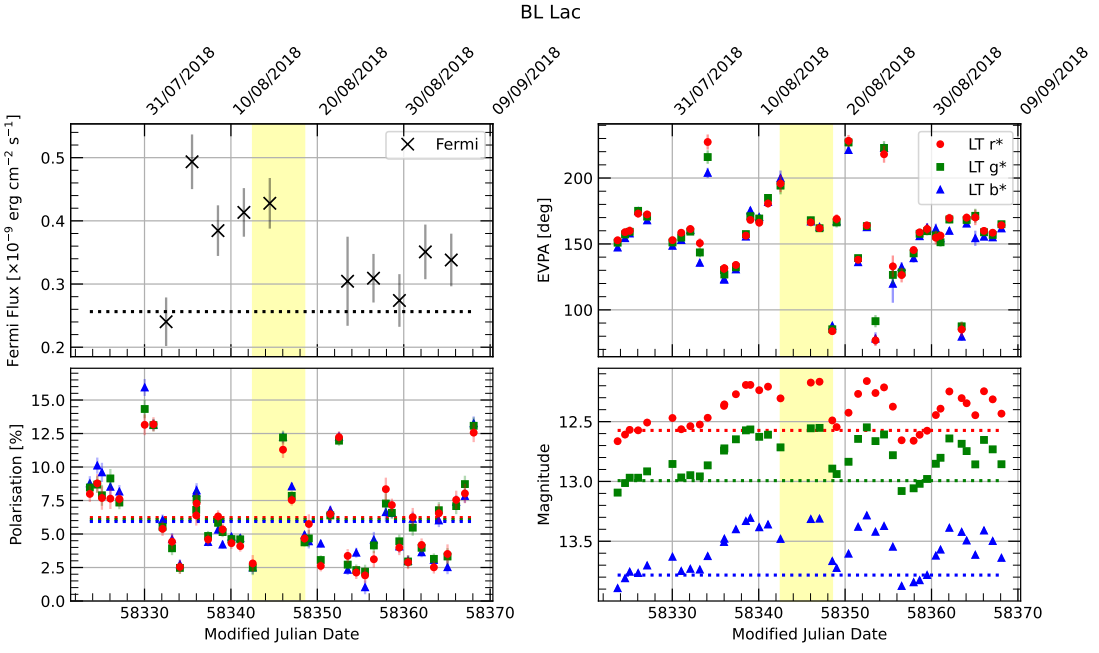

FIGURE C.35: As Fig. C.15 but for BL Lac during the EVPA rotation at MJD 58342.52.

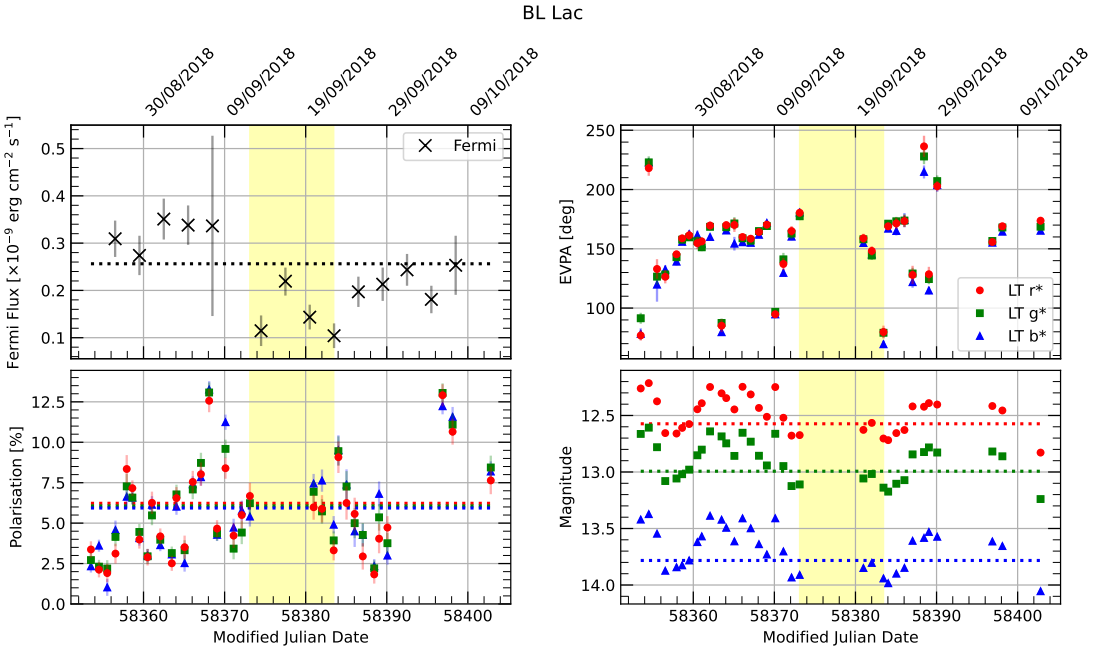

FIGURE C.36: As Fig. C.15 but for BL Lac during the EVPA rotation at MJD 58373.12.

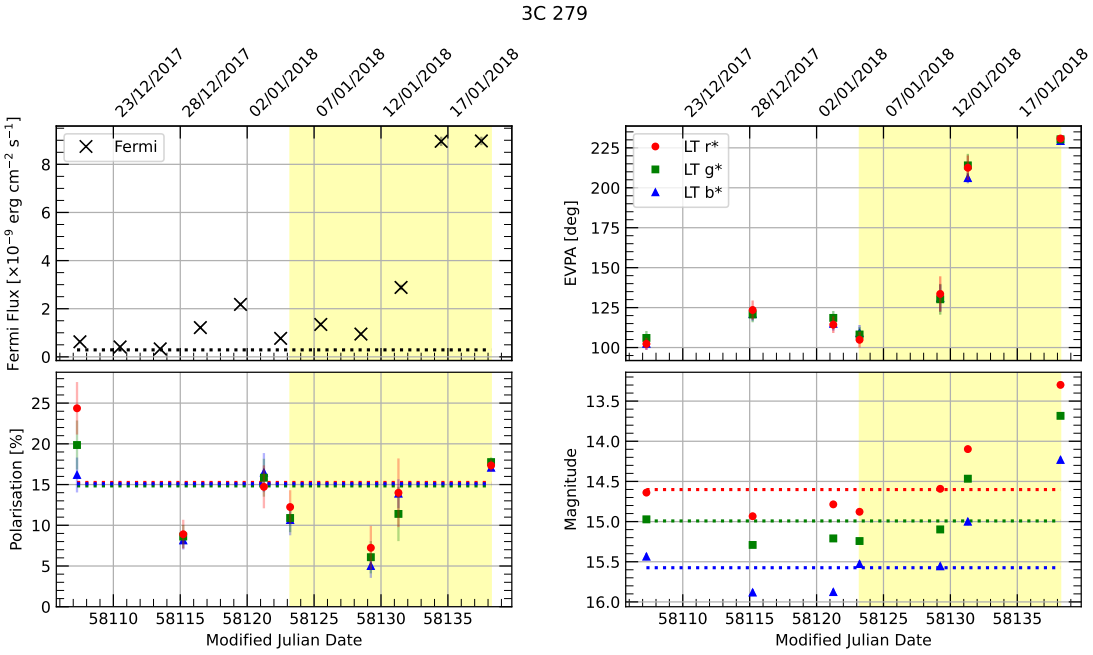

FIGURE C.37: As Fig. C.15 but for 3C 279 during the EVPA rotation at MJD 58123.21.

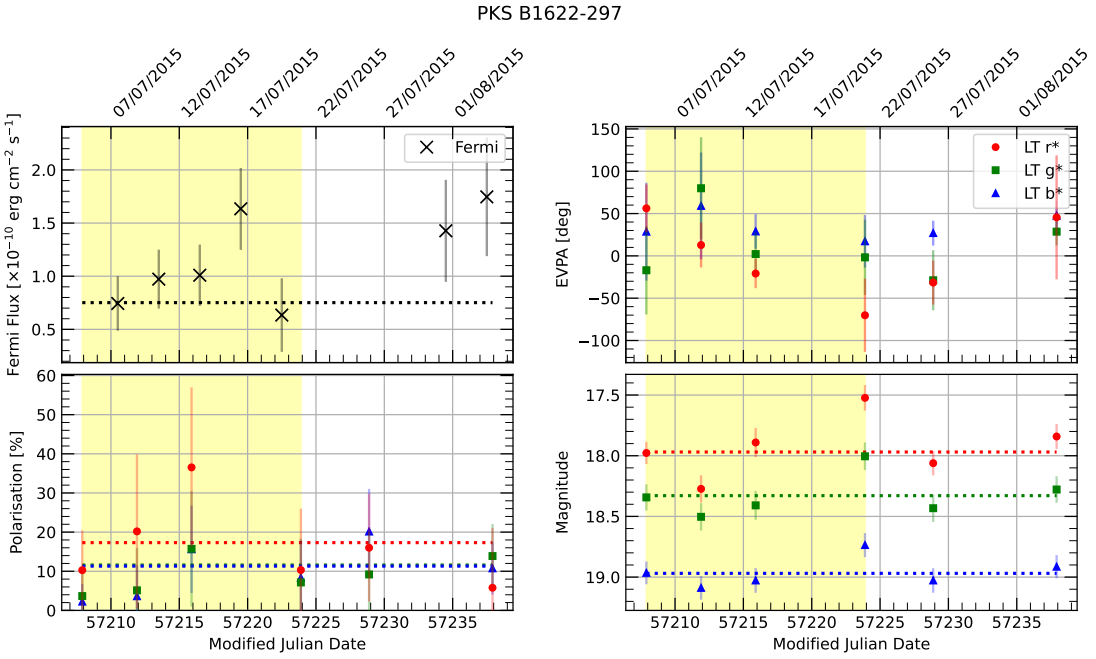

FIGURE C.38: As Fig. C.15 but for PKS B1622-297 during the EVPA rotation at MJD 57207.90.

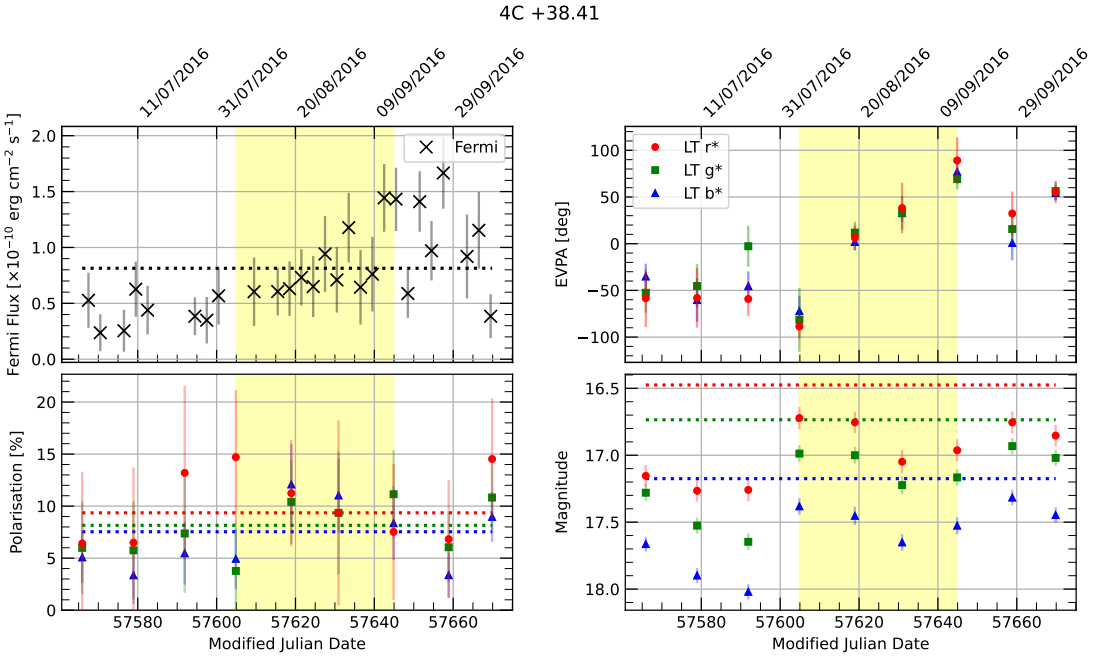

FIGURE C.39: As Fig. C.15 but for 4C +38.41 during the EVPA rotation at MJD 57604.87.

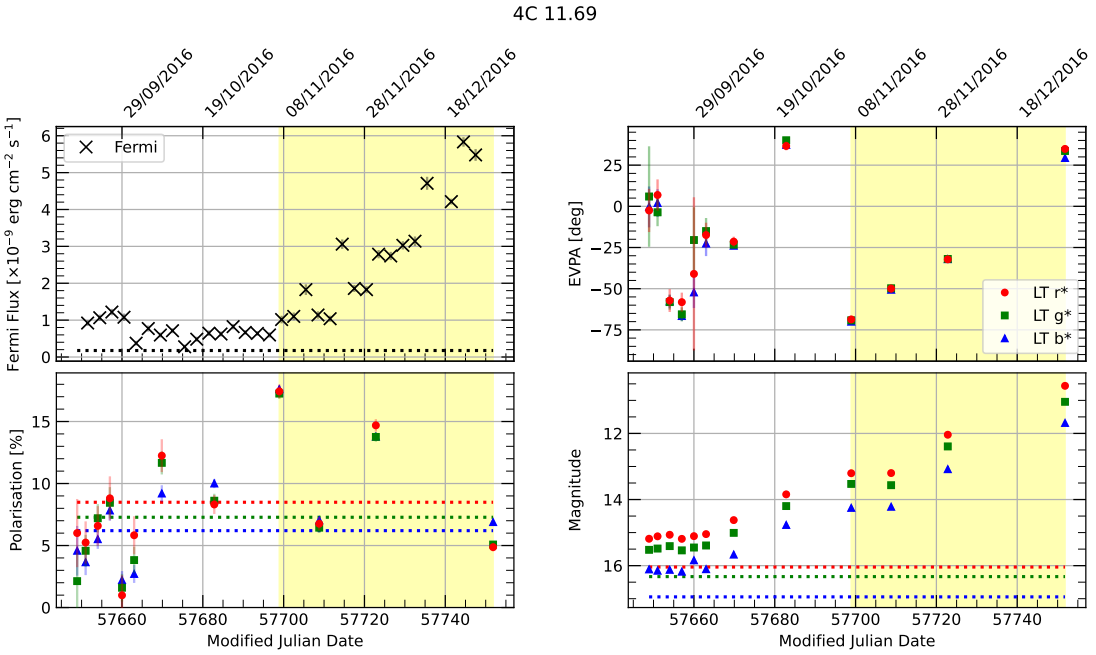

FIGURE C.40: As Fig. C.15 but for 4C 11.69 during the EVPA rotation at MJD 57698.93.

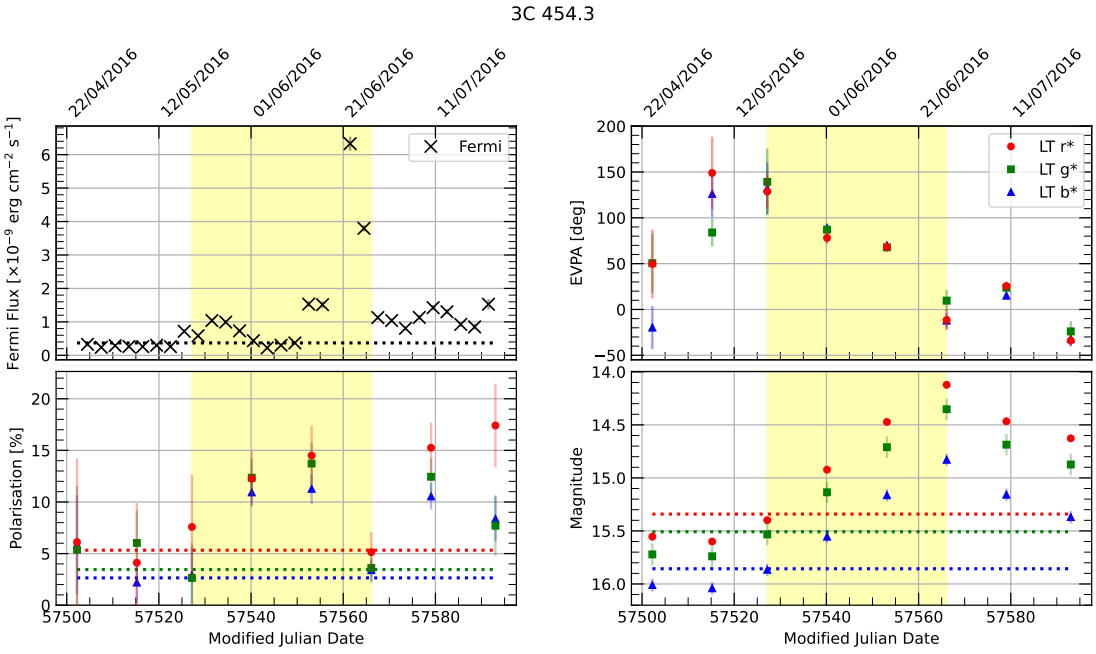

FIGURE C.41: As Fig. C.15 but for 3C 454.3 during the EVPA rotation at MJD 57527.17.

TABLE C.16: Spearman correlation coefficients for optical magnitude vs. degree of polarisation, where c is the correlation strength coefficient and p is the corresponding significance value. The number of optical data points (per filter) used in these correlation calculations is also shown.

Source	Type	Filter	p	c	Points
PG1553+113	HSP	B	1.45×10^{-5}	-0.281	231
PG1553+113	HSP	V	2.08×10^{-4}	-0.226	265
PG1553+113	HSP	R	1.29×10^{-4}	-0.226	281
TXS 0506+056	LSP	B	0.01	0.156	258
TXS 0506+056	LSP	V	2.28×10^{-3}	0.188	262
TXS 0506+056	LSP	R	5.82×10^{-4}	0.211	262
OJ287	LSP	B	3.45×10^{-7}	0.284	312
OJ287	LSP	V	0.02	0.136	289
OJ287	LSP	R	1.71×10^{-5}	0.219	380
BL Lac	LSP	B	1.03×10^{-6}	-0.203	570
BL Lac	LSP	V	0.05	-0.097	403
BL Lac	LSP	R	1.40×10^{-7}	-0.212	603
PKS1510-089	LSP (FSRQ)	B	1.55×10^{-4}	0.259	209
PKS1510-089	LSP (FSRQ)	V	6.18×10^{-8}	0.360	213
PKS1510-089	LSP (FSRQ)	R	6.52×10^{-10}	0.402	219
4C 11.69	LSP (FSRQ)	B	6.15×10^{-7}	0.359	183
4C 11.69	LSP (FSRQ)	V	4.29×10^{-11}	0.415	232
4C 11.69	LSP (FSRQ)	R	6.57×10^{-17}	0.500	245
3C 454.3	LSP (FSRQ)	B	2.23×10^{-3}	0.218	194
3C 454.3	LSP (FSRQ)	V	6.83×10^{-5}	0.257	235
3C 454.3	LSP (FSRQ)	R	6.18×10^{-11}	0.411	233

TABLE C.17: As Table C.16 but for γ-ray flux vs. polarisation correlations.

Source	Type	Filter	p	c	Points
PG1553+113	HSP	B	0.839	0.024	72
PG1553+113	HSP	V	0.250	-0.133	77
PG1553+113	HSP	R	0.292	-0.120	79
TXS 0506+056	LSP	B	0.627	0.068	53
TXS 0506+056	LSP	V	0.469	0.103	52
TXS 0506+056	LSP	R	0.901	0.018	52
OJ287	LSP	B	0.141	-0.203	54
OJ287	LSP	V	0.418	-0.128	42
OJ287	LSP	R	0.101	-0.221	56
BL Lac	LSP	B	2.21×10^{-3}	-0.219	193
BL Lac	LSP	V	0.146	-0.124	138
BL Lac	LSP	R	2.09×10^{-4}	-0.260	199
PKS1510-089	LSP (FSRQ)	B	0.156	0.181	63
PKS1510-089	LSP (FSRQ)	V	0.127	0.190	66
PKS1510-089	LSP (FSRQ)	R	0.018	0.296	63
4C 11.69	LSP (FSRQ)	B	0.258	0.122	87
4C 11.69	LSP (FSRQ)	V	0.569	0.057	102
4C 11.69	LSP (FSRQ)	R	7.07×10^{-3}	0.259	107
3C 454.3	LSP (FSRQ)	B	0.092	0.175	94
3C 454.3	LSP (FSRQ)	V	8.86×10^{-3}	0.255	104
3C 454.3	LSP (FSRQ)	R	4.87×10^{-5}	0.395	100

TABLE C.18: Spearman rank coefficients for the MOPTOP polarisation colour correlations.

Source	Type	Line colour	p	c	Linear fit grad	Points
PG1553+113	HSP	V-R	0.132	0.114	0.064	177
PG1553+113	HSP	B-R	0.357	0.070	0.104	177
PG1553+113	HSP	B-V	0.959	0.004	0.028	177
TXS 0506+056	LSP	V-R	0.014	0.166	0.060	218
TXS 0506+056	LSP	B-R	0.111	0.108	0.053	218
TXS 0506+056	LSP	B-V	0.976	0.002	-0.016	218
OJ287	LSP	V-R	0.056	0.151	0.054	161
OJ287	LSP	B-R	0.540	0.049	0.018	161
OJ287	LSP	B-V	0.288	-0.084	-0.038	161
BL Lac	LSP	V-R	5.27×10^{-6}	0.244	0.029	341
BL Lac	LSP	B-R	1.47×10^{-7}	0.280	0.076	341
BL Lac	LSP	B-V	8.07×10^{-4}	0.181	0.044	341
PKS1510-089	LSP (FSRQ)	V-R	0.016	0.195	0.163	154
PKS1510-089	LSP (FSRQ)	B-R	0.450	0.061	0.122	154
PKS1510-089	LSP (FSRQ)	B-V	0.053	-0.156	-0.242	154
4C 11.69	LSP (FSRQ)	V-R	0.262	-0.092	-0.058	150
4C 11.69	LSP (FSRQ)	B-R	6.68×10^{-7}	-0.393	-0.252	150
4C 11.69	LSP (FSRQ)	B-V	1.42×10^{-5}	-0.346	-0.166	150
3C 454.3	LSP (FSRQ)	V-R	0.970	-0.003	-0.017	157
3C 454.3	LSP (FSRQ)	B-R	3.78×10^{-3}	-0.230	-0.161	157
3C 454.3	LSP (FSRQ)	B-V	2.62×10^{-3}	-0.239	-0.128	157

TABLE C.19: EVPA rotations found in the MOPTOP dataset. Shown are the starts of the rotations as MJD and EVPA, and the duration and size of the rotation. Also shown are the average γ-ray flux and optical polarisation and magnitude values during the full monitoring campaign and the rotation event.

Source	Type	MJD Start	ΔMJD [days]	EVPA Start [°]	ΔEVPA [°]	γ-ray av [erg cm^{-2} s^{-1}]	γ-ray rot [erg cm^{-2} s^{-1}]	Pol av [%]	Pol rot [%]	Opt av	Opt rot
PG1553+113	HSP	59963.29	43.84	31.25	245.67	2.47×10^{-10}	3.26×10^{-10}	3.38	3.12	13.86	13.35
...	...	60364.26	16.87	360.96	186.80	...	2.74×10^{-10}	...	4.54	...	13.93
BL Lac	LSP	59684.24	18.93	-430.80	112.15	3.36×10^{-10}	4.98×10^{-10}	12.07	10.88	13.24	12.84
...	...	59797.98	10.04	-590.17	127.18	...	2.61×10^{-10}	...	9.64	...	13.77
...	...	59932.82	18.00	-436.43	169.22	...	7.96×10^{-10}	...	7.75	...	12.26
...	...	60196.93	47.89	-250.52	-112.31	...	3.09×10^{-10}	...	14.90	...	13.15
PKS1510-089	LSP (FSRQ)	60047.15	3.86	33.97	115.49	7.37×10^{-11}	8.35×10^{-11}	3.00	4.47	16.64	16.60
...	...	60368.25	5.97	207.27	-182.51	...	6.89×10^{-11}	...	4.15	...	16.49
...	...	60436.04	5.12	14.27	134.18	...	7.00×10^{-11}	...	2.63	...	16.70
4C 11.69	LSP (FSRQ)	59936.84	123.39	47.84	-162.19	2.52×10^{-10}	3.32×10^{-10}	4.52	6.33	16.71	16.61
...	...	60150.16	4.96	-81.57	211.49	...	3.44×10^{-10}	...	5.76	...	16.57
3C 454.3	LSP (FSRQ)	59800.11	6.96	157.46	-155.70	2.40×10^{-10}	2.39×10^{-10}	2.80	2.78	15.84	15.99
...	...	59872.92	10.94	76.11	-226.22	...	7.74×10^{-10}	...	3.30	...	14.88
...	...	59883.86	5.98	-150.10	136.07	...	6.85×10^{-10}	...	3.25	...	14.96
...	...	59936.85	139.35	119.24	218.53	...	4.27×10^{-10}	...	4.00	...	15.49
...	...	60127.10	4.95	302.97	113.60	...	2.59×10^{-10}	...	3.54	...	15.88

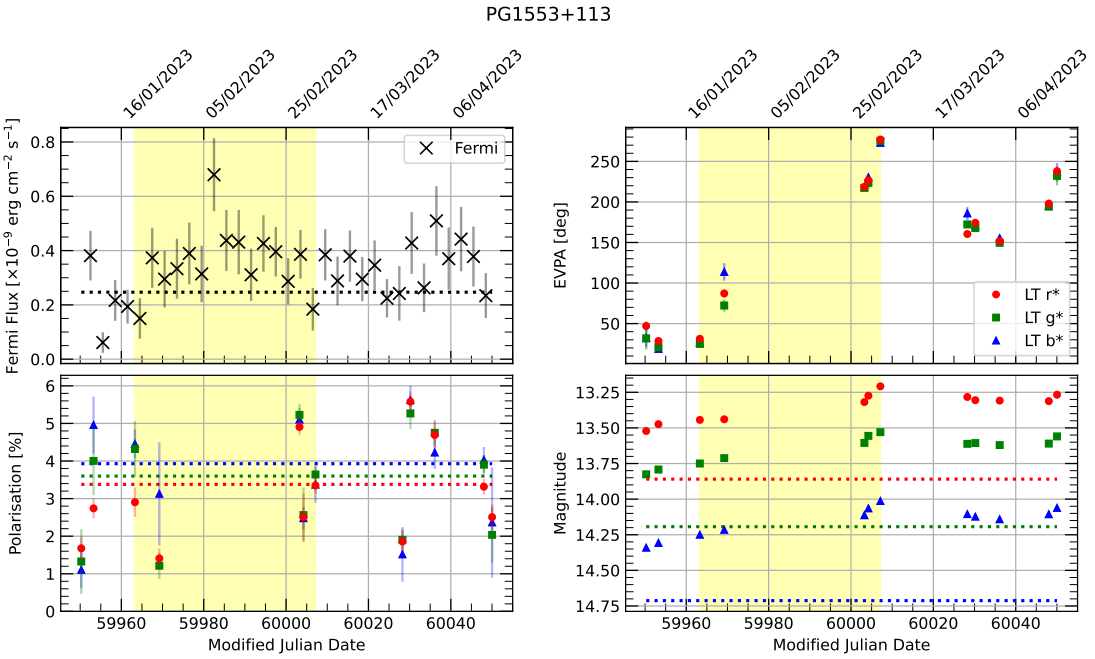

FIGURE C.42: PG 1553+113 light curve during the EVPA rotation at MJD 59963.29. The top left panel shows the γ-ray flux, the bottom left shows the optical polarisation, the top right shows the EVPA rotation, and the bottom right shows the optical instrumental magnitude. In the γ-ray flux, polarisation, and instrumental magnitude panels, dotted lines are plotted to show the respective average states in relevant filters over the full duration of MOPTOP observations.

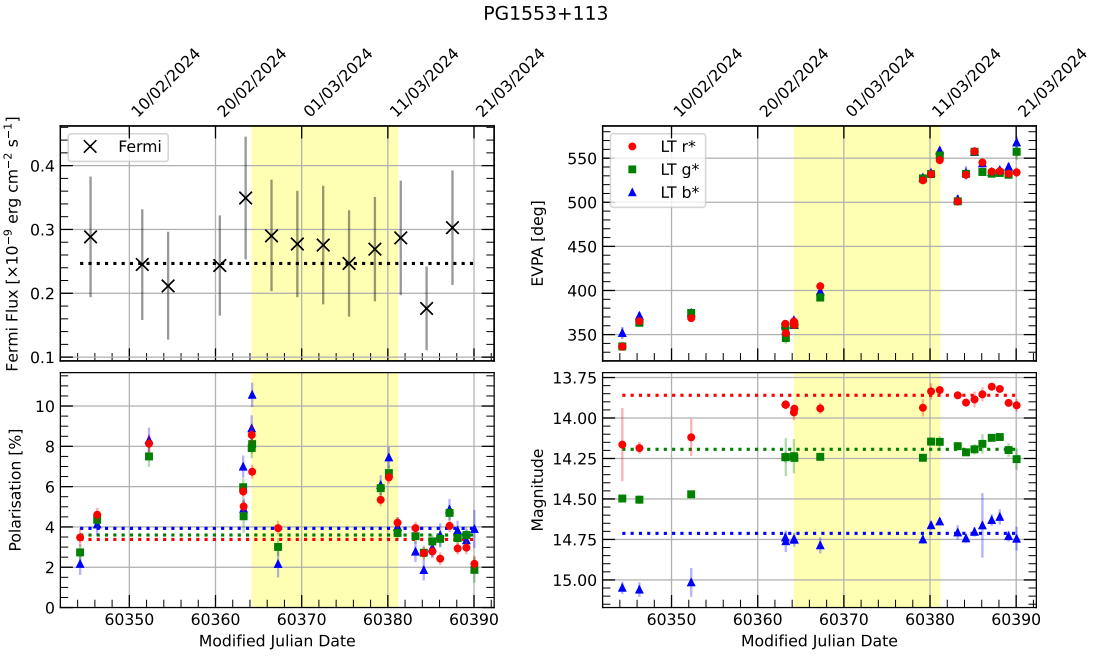

FIGURE C.43: As Fig. C.42 but for PG1553+113 during the EVPA rotation at MJD 60364.26.

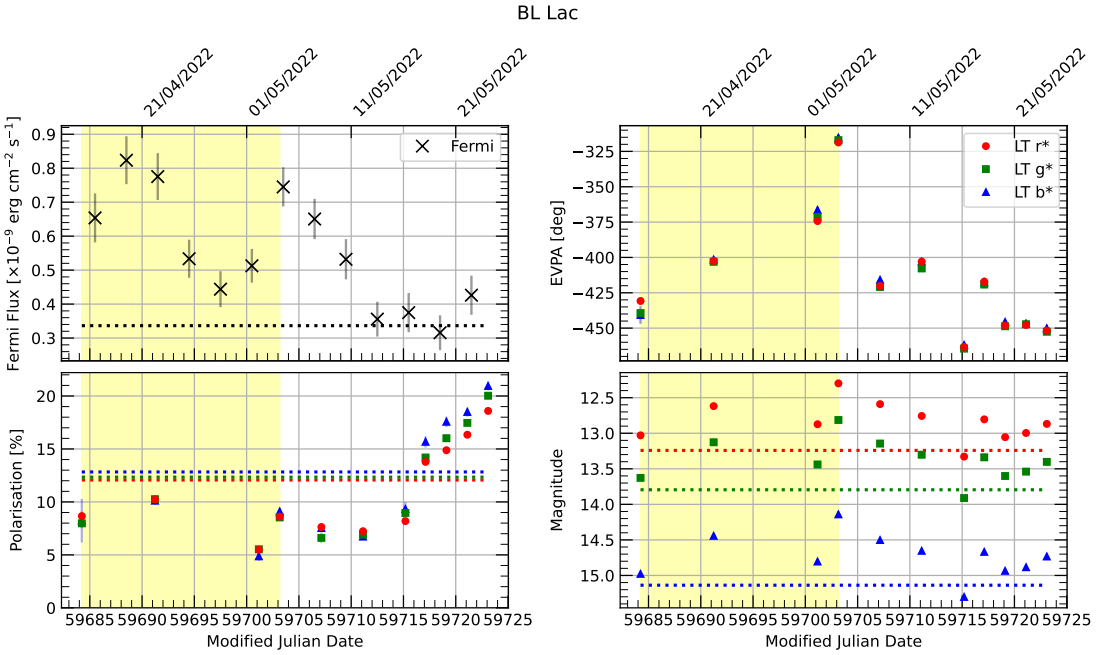

FIGURE C.44: As Fig. C.42 but for BL Lac during the EVPA rotation at MJD 59684.24.

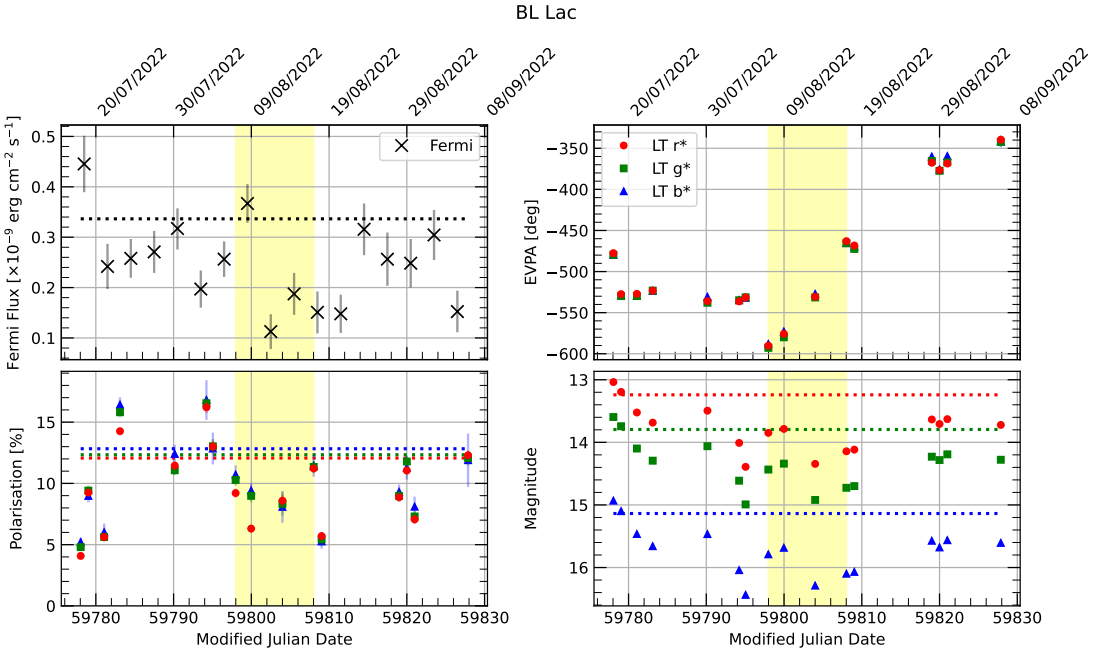

FIGURE C.45: As Fig. C.42 but for BL Lac during the EVPA rotation at MJD 59797.98.

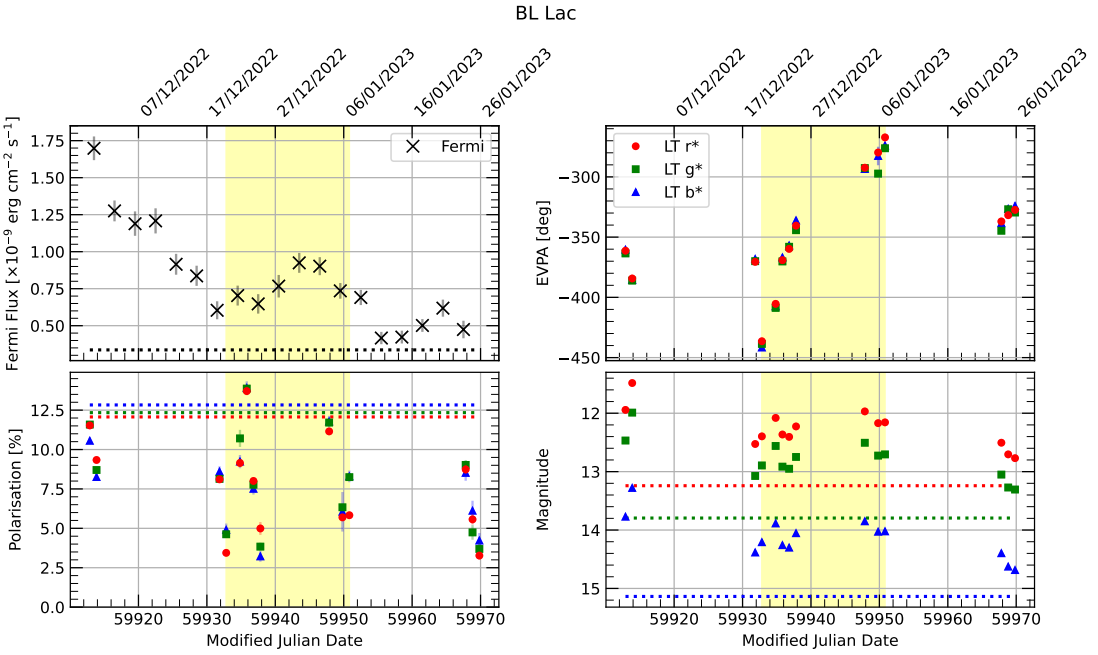

FIGURE C.46: As Fig. C.42 but for BL Lac during the EVPA rotation at MJD 59932.82.

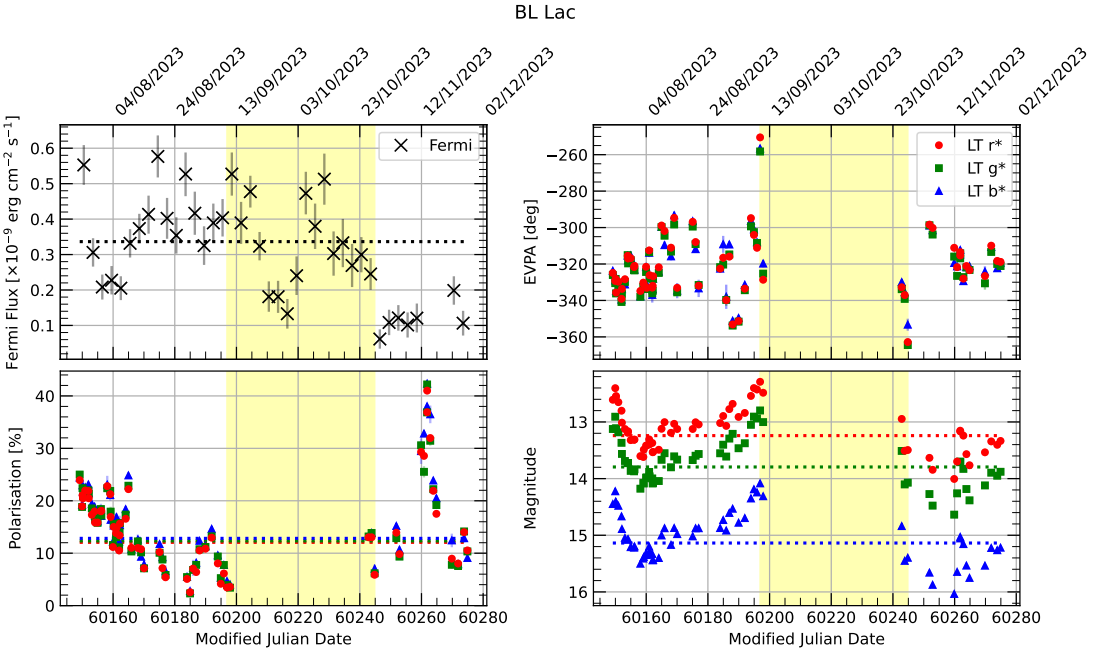

FIGURE C.47: As Fig. C.42 but for BL Lac during the EVPA rotation at MJD 60196.93.

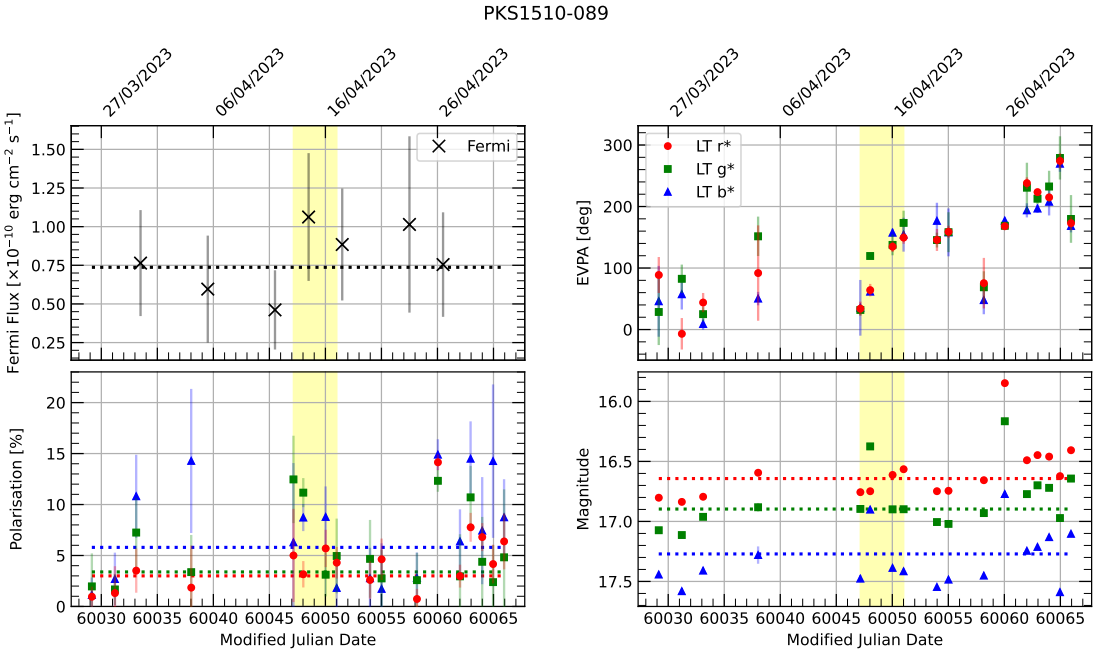

FIGURE C.48: As Fig. C.42 but for PKS 1510-089 during the EVPA rotation at MJD 60047.15.

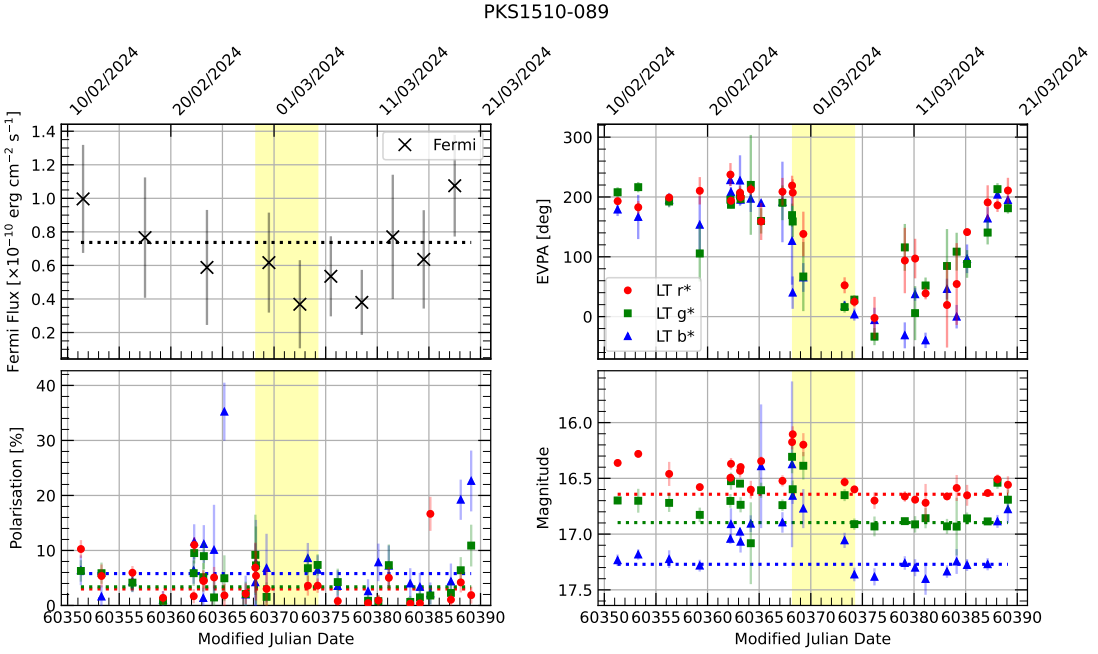

FIGURE C.49: As Fig. C.42 but for PKS 1510-089 during the EVPA rotation at MJD 60368.25.

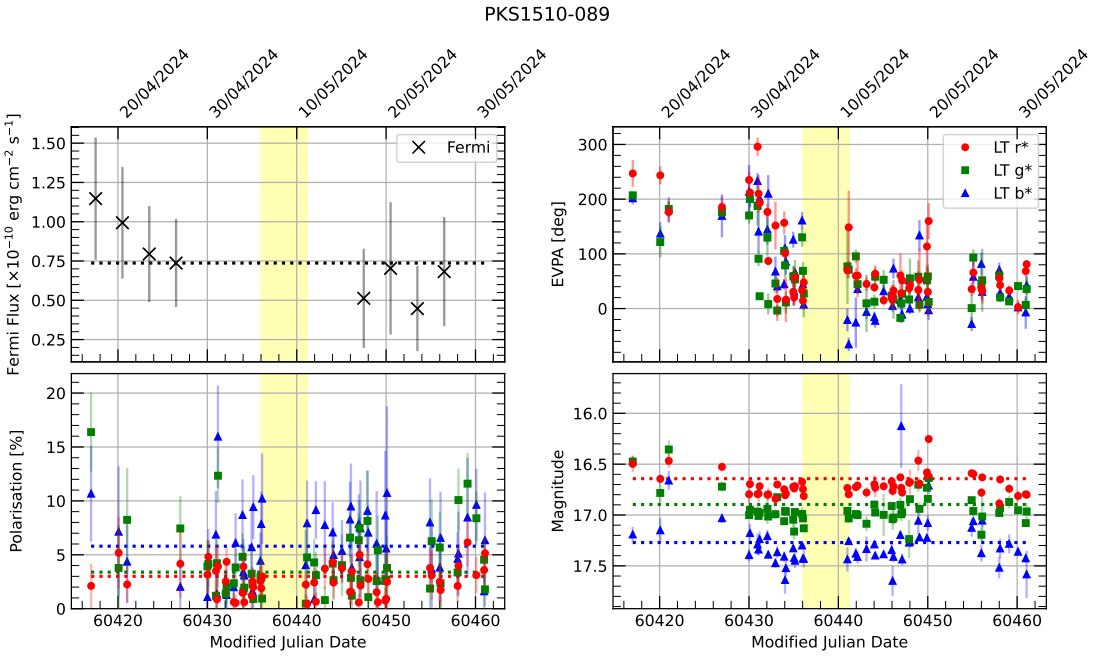

FIGURE C.50: As Fig. C.42 but for PKS 1510-089 during the EVPA rotation at MJD 60436.04.

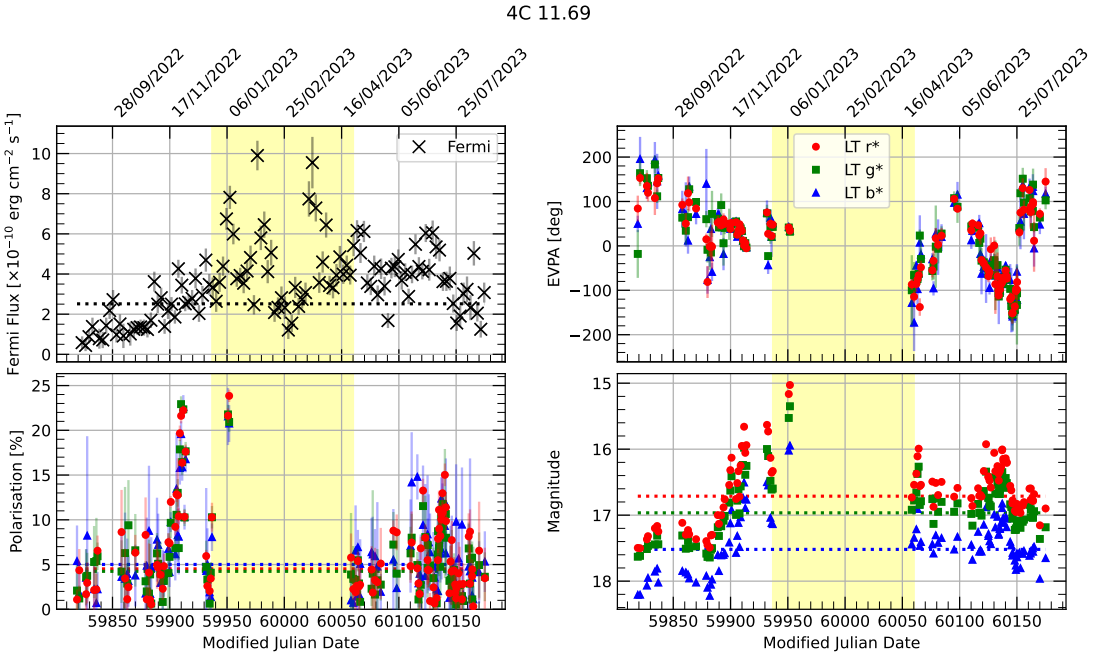

FIGURE C.51: As Fig. C.42 but for 4C 11.69 during the EVPA rotation at MJD 59936.84.

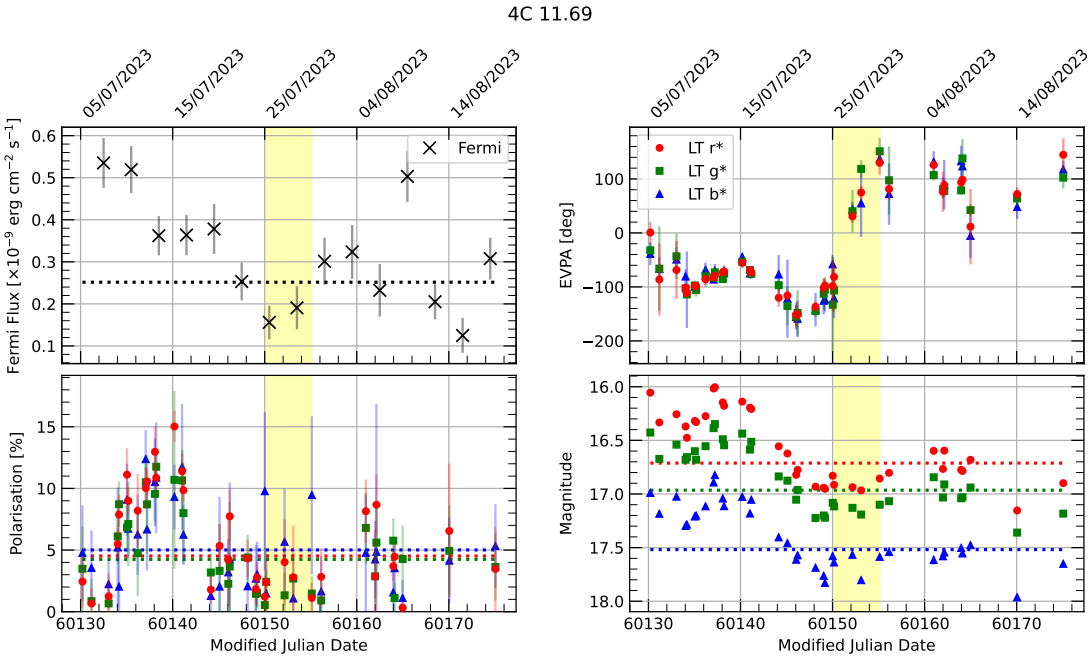

FIGURE C.52: As Fig. C.42 but for 4C 11.69 during the EVPA rotation at MJD 60150.16.

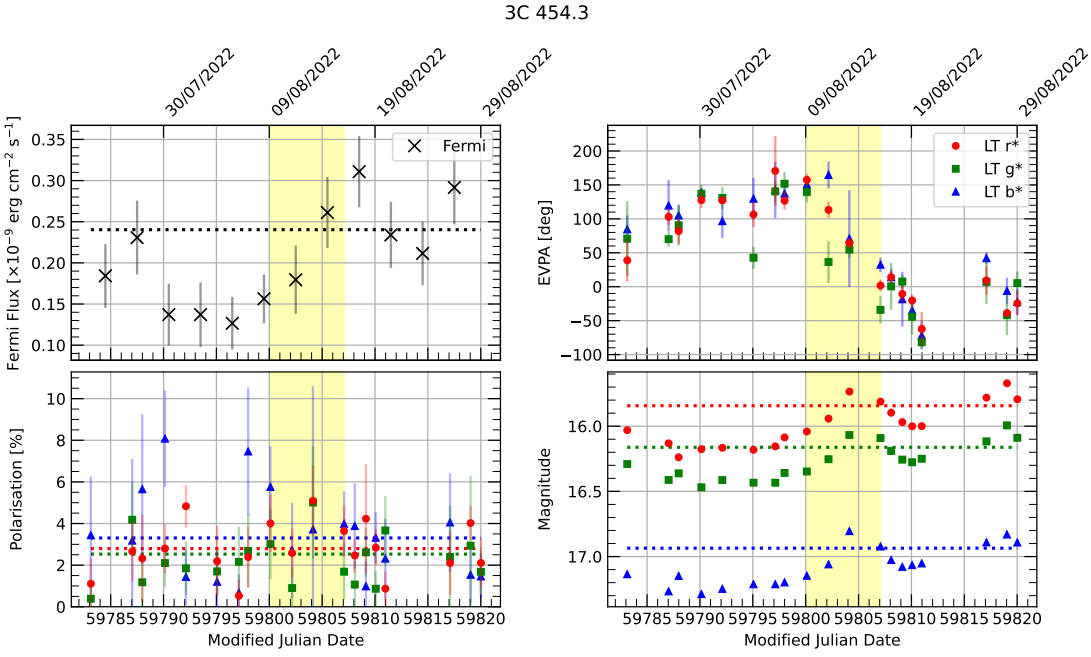

FIGURE C.53: As Fig. C.42 but for 3C 454.3 during the EVPA rotation at MJD 59800.11.

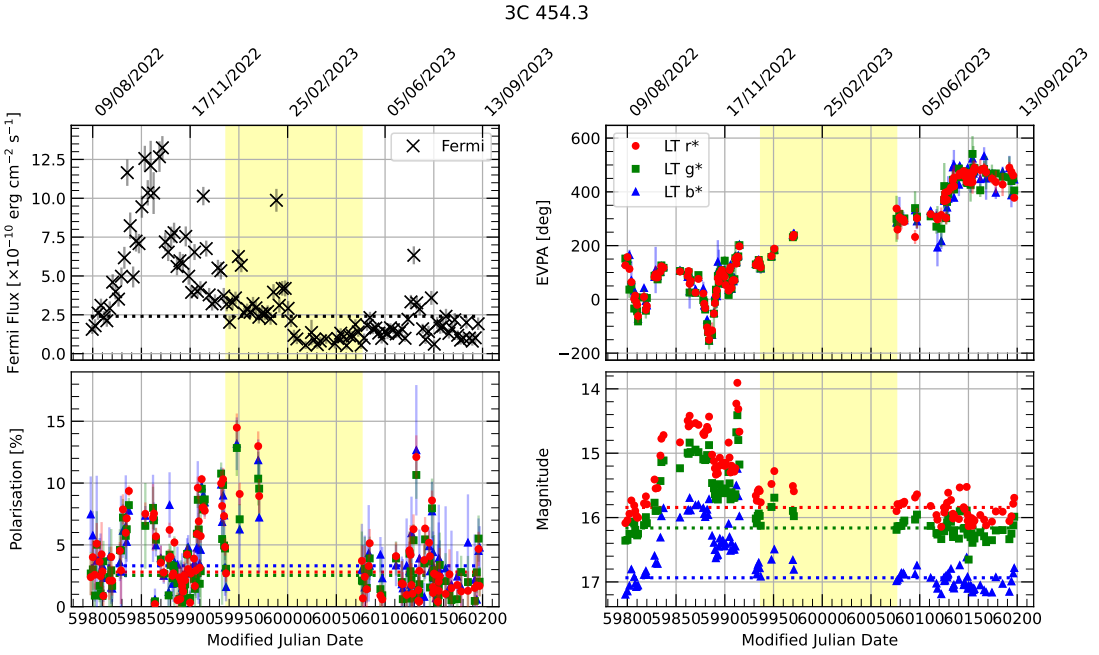

FIGURE C.54: As Fig. C.42 but for 3C 454.3 during the EVPA rotation at MJD 59872.92.

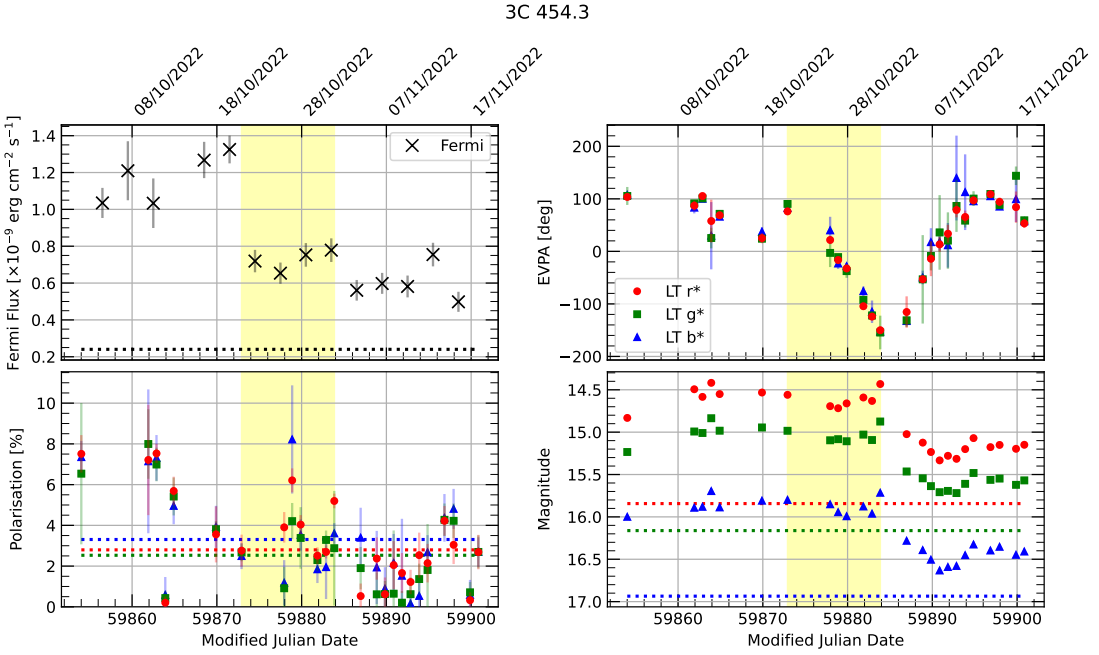

FIGURE C.55: As Fig. C.42 but for 3C 454.3 during the EVPA rotation at MJD 59883.86.

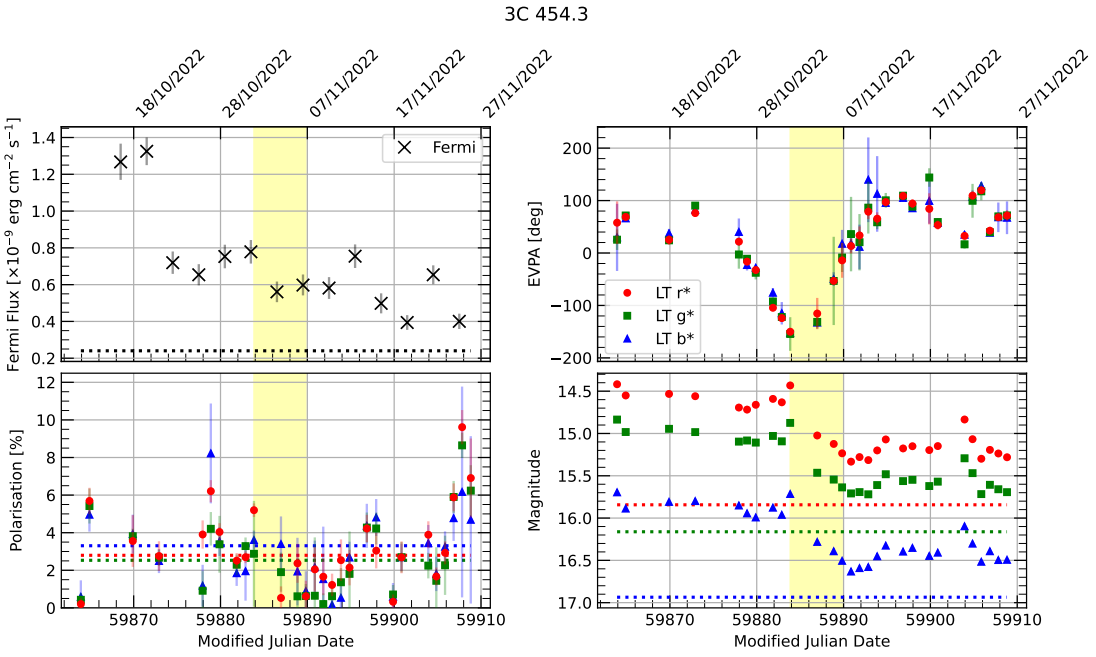

FIGURE C.56: As Fig. C.42 but for 3C 454.3 during the EVPA rotation at MJD 59936.85.

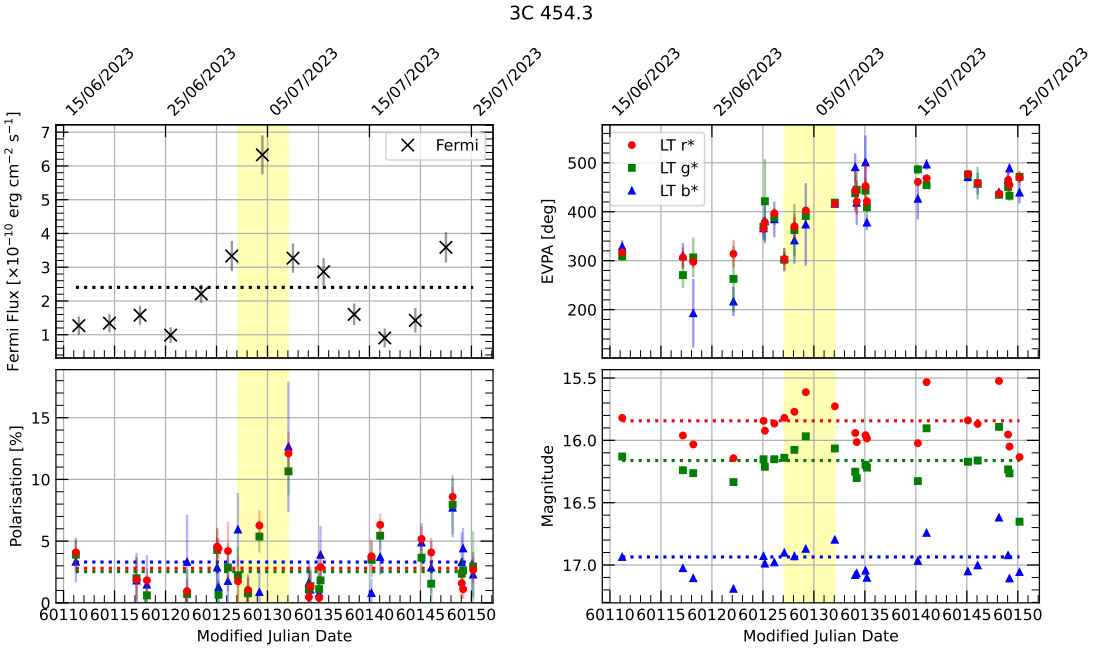

FIGURE C.57: As Fig. C.42 but for 3C 454.3 during the EVPA rotation at MJD 60127.10.

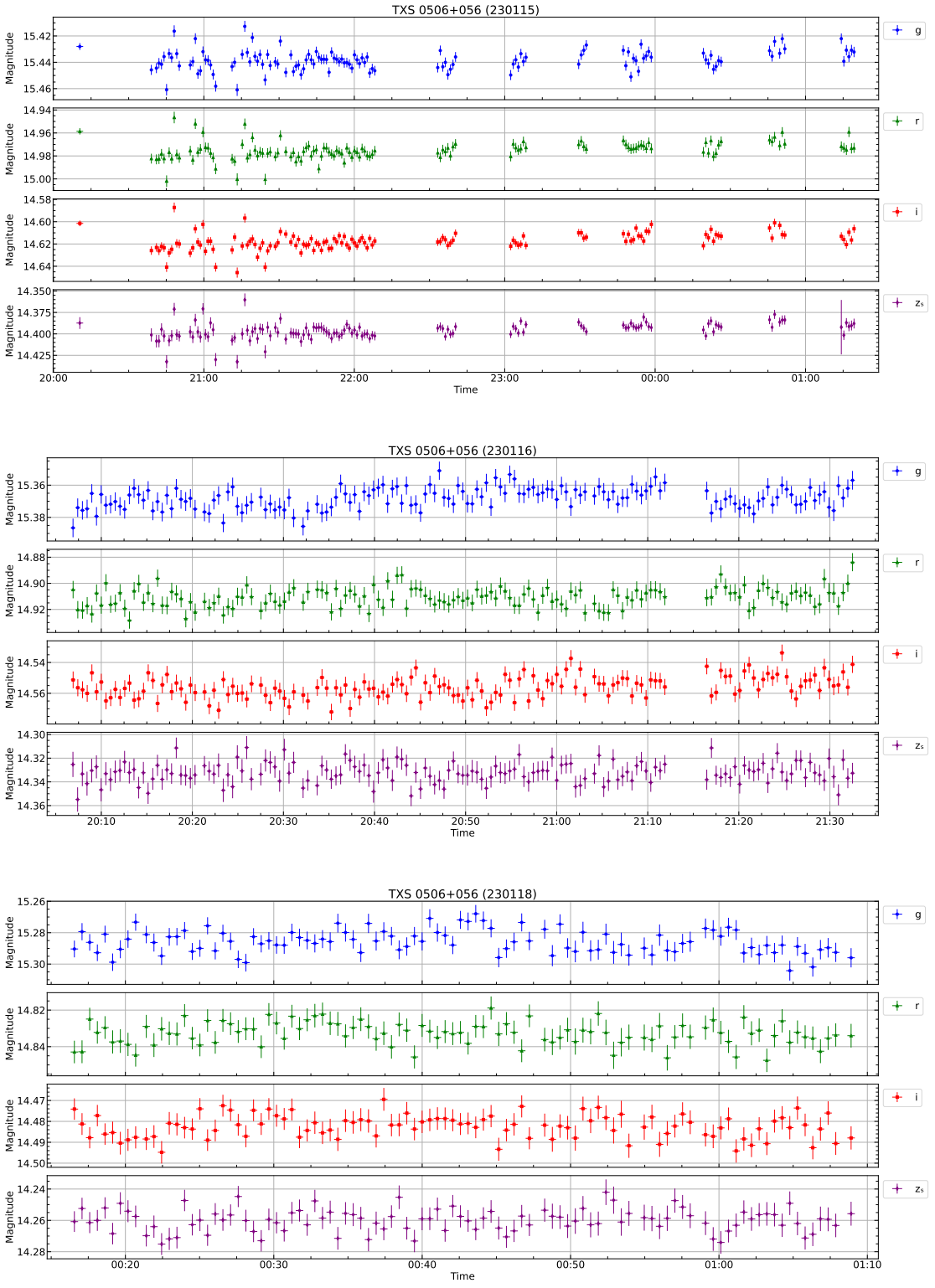

FIGURE C.58: Light curves of TXS 0506+056 on the nights of 2023 January 15, 2023 January 16, and 2023 January 18. The panels of each of the three plots correspond to g, r, i, and z_s filters, from top to bottom.

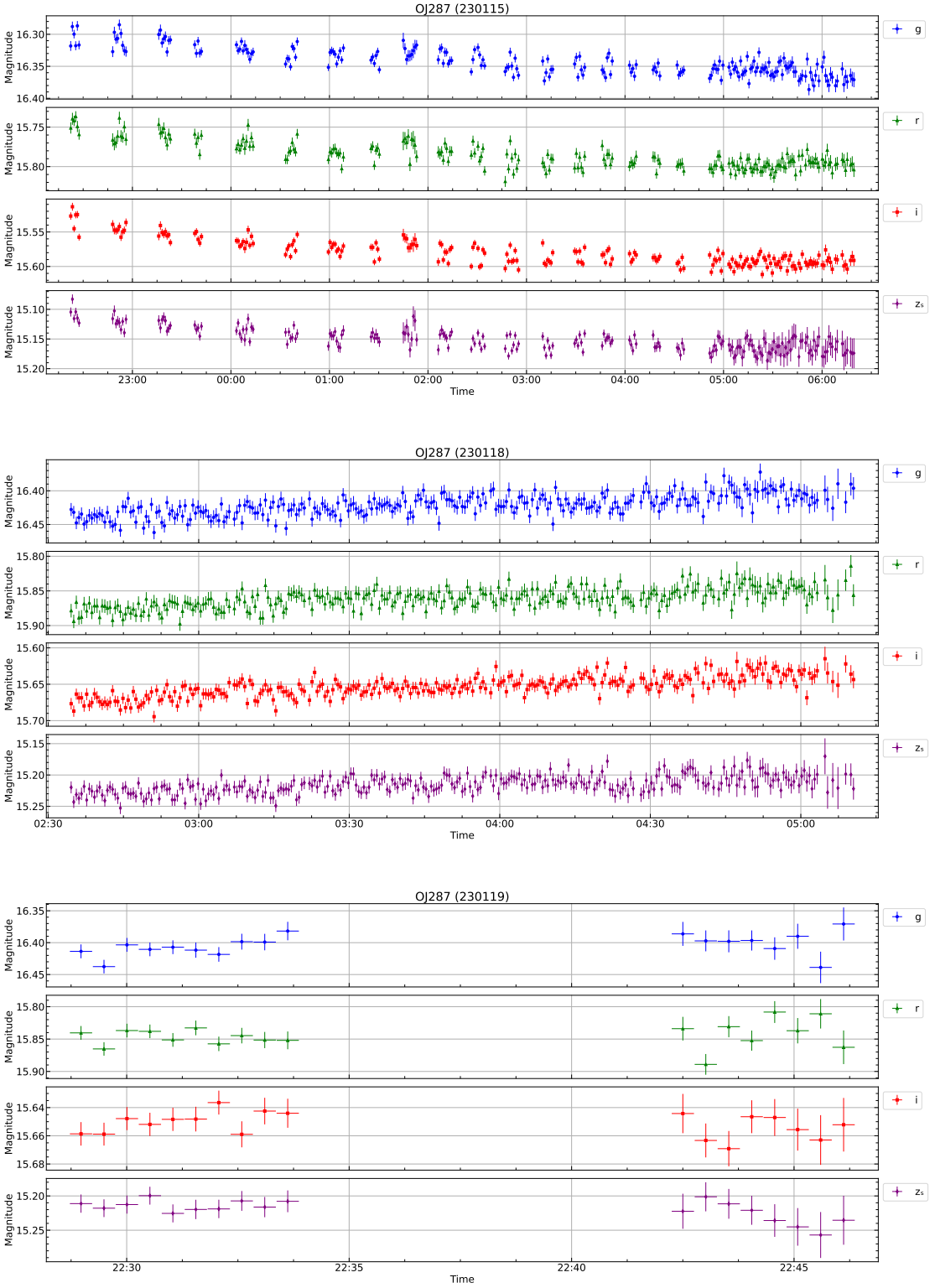

FIGURE C.59: As Fig. C.58, but for OJ287 on the nights of 2023 January 15, 2023 January 18, and 2023 January 19.

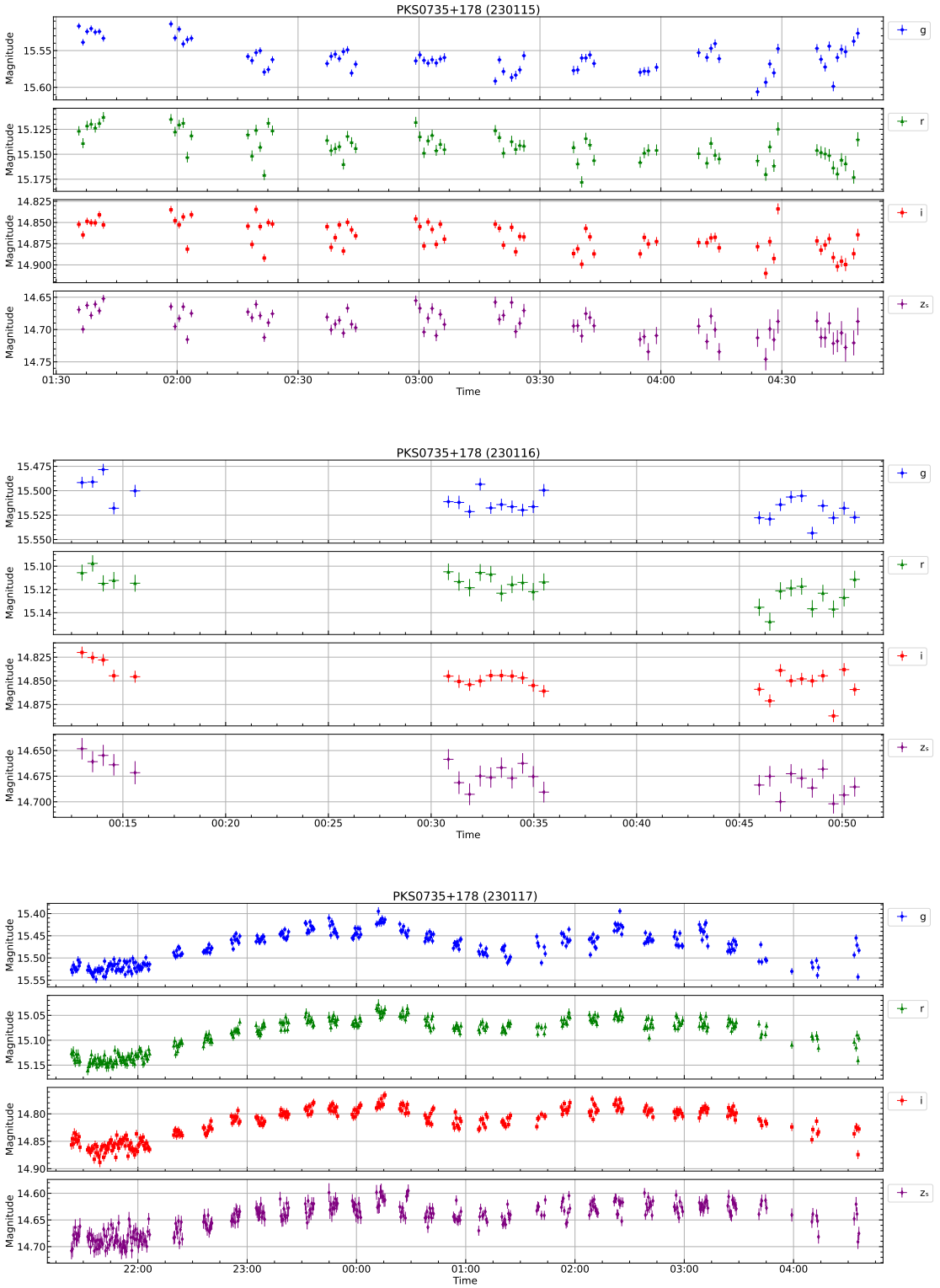

FIGURE C.60: As Fig. C.58, but for PKS 0735+178 on the nights of 2023 January 15, 2023 January 16, and 2023 January 17.

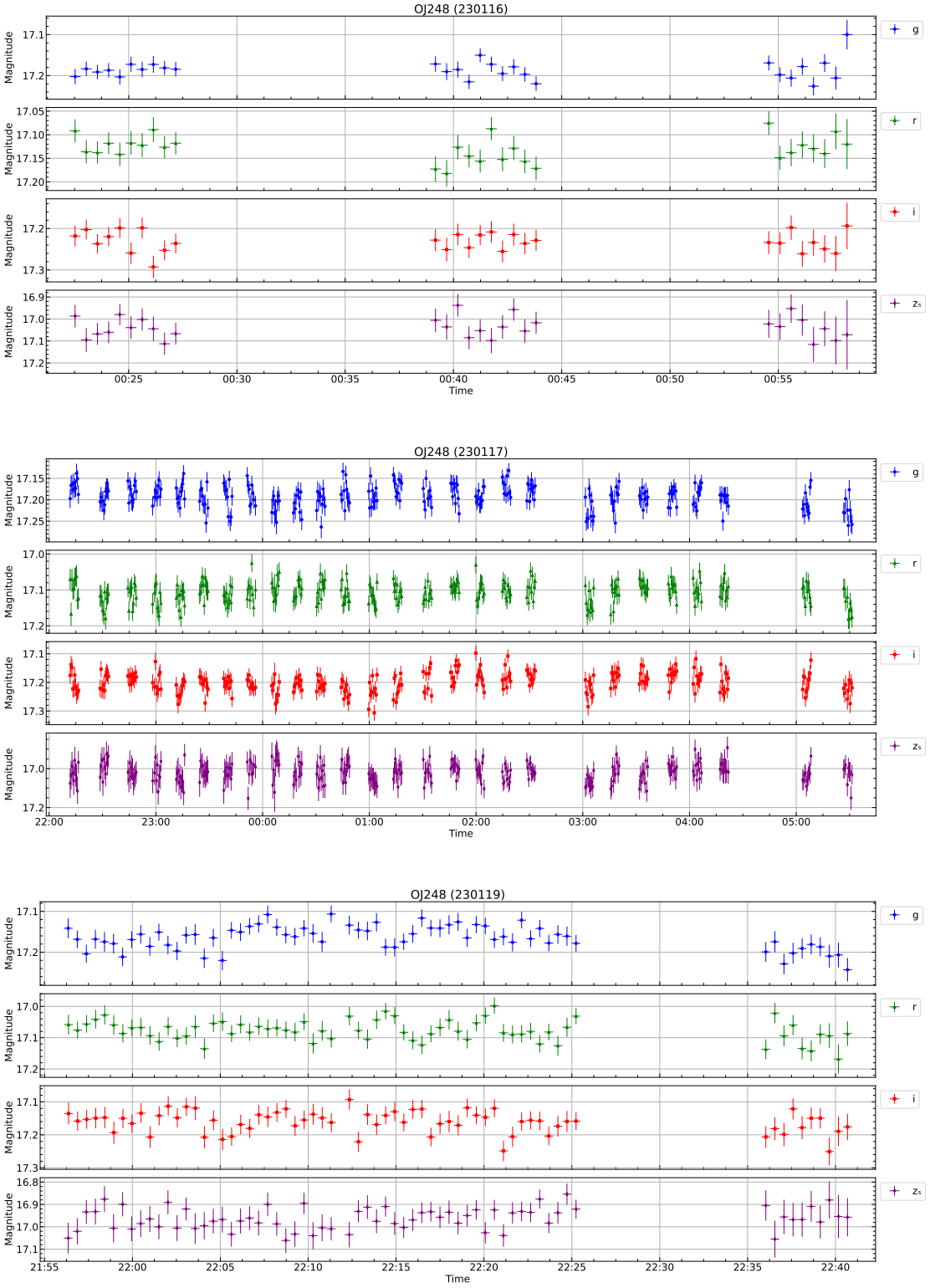

FIGURE C.61: As Fig. C.58, but for OJ248 on the nights of 2023 January 16, 2023 January 17, and 2023 January 19.

TABLE C.20: Variability analysis results. From left to right, the source name, date of observation and filter is given. VA represents the variability amplitude with error as described in section 5.1.1.1, $F_{\rm var}$ is the fractional variability with error as described in section 5.1.1.2, χ^2 is the Chi-squared value given with the critical value as described in section 5.1.1.3 and $F_{\rm enh}$ is the enhanced F-test value with the critical value as described in section 5.1.1.4. The final column describes whether or not the source was deemed variable in a particular filter on a given night. Of the three variability tests ($F_{\rm var}$, χ^2 and $F_{\rm enh}$), if all three showed variability the source was deemed variable (V), two meant possibly variable (PV), and one or none meant likely not variable (NV).

Source	Date	Filter	VA $\pm$ ΔVA(%)	$F_{\rm var} \pm \Delta F_{\rm var}$	$\chi^2(\chi^2_{\rm crit})$	$F_{\rm enh}(F_{\rm crit})$	Variable?
TXS 0506+056	2023 Jan 15	g	4.79 $\pm$ 0.63	0.04 $\pm$ 0.10	487.23 (181.99)	0.67 (1.54)	NV
...	...	r	5.50 $\pm$ 0.71	0.05 $\pm$ 0.11	420.57 (181.99)	0.91 (1.54)	NV
...	...	i	5.82 $\pm$ 0.64	0.05 $\pm$ 0.09	575.73 (181.99)	1.02 (1.54)	NV
...	...	$z_{\rm s}$	7.18 $\pm$ 1.09	0.06 $\pm$ 0.12	303.86 (181.99)	1.23 (1.54)	NV
TXS 0506+056	2023 Jan 16	g	3.46 $\pm$ 0.83	0.02 $\pm$ 0.30	195.04 (213.97)	1.17 (1.48)	NV
...	...	r	4.34 $\pm$ 0.98	0.02 $\pm$ 0.33	185.92 (213.97)	1.05 (1.48)	NV
...	...	i	3.76 $\pm$ 0.77	0.03 $\pm$ 0.20	255.78 (213.97)	1.48 (1.48)	PV
...	...	$z_{\rm s}$	4.21 $\pm$ 1.47	< 0	138.42 (213.97)	1.13 (1.48)	NV
TXS 0506+056	2023 Jan 15	g	3.53 $\pm$ 0.87	0.03 $\pm$ 0.24	151.25 (147.01)	0.65 (1.63)	NV
...	...	r	2.72 $\pm$ 0.95	< 0	87.88 (147.01)	0.93 (1.63)	NV
...	...	i	2.42 $\pm$ 0.80	0.01 $\pm$ 0.67	100.20 (147.01)	0.59 (1.63)	NV
...	...	$z_{\rm s}$	3.15 $\pm$ 1.13	< 0	95.45 (147.01)	1.34 (1.63)	NV
OJ287	2023 Jan 15	g	10.05 $\pm$ 1.22	0.12 $\pm$ 0.06	1575.69 (281.37)	1.45 (1.40)	V
...	...	r	8.17 $\pm$ 0.97	0.09 $\pm$ 0.07	1212.16 (281.37)	1.74 (1.40)	V
...	...	i	9.79 $\pm$ 0.82	0.11 $\pm$ 0.05	2472.15 (281.37)	1.82 (1.40)	V
...	...	$z_{\rm s}$	10.29 $\pm$ 1.74	0.11 $\pm$ 0.08	962.74 (281.37)	1.59 (1.40)	V
OJ287	2023 Jan 18	g	8.84 $\pm$ 1.64	0.07 $\pm$ 0.13	569.87 (369.03)	0.94 (1.34)	NV
...	...	r	8.22 $\pm$ 1.89	0.06 $\pm$ 0.15	489.41 (369.03)	1.04 (1.34)	NV
...	...	i	7.88 $\pm$ 1.85	0.08 $\pm$ 0.10	796.89 (369.03)	1.23 (1.34)	NV
...	...	$z_{\rm s}$	8.13 $\pm$ 3.07	0.06 $\pm$ 0.16	445.58 (369.03)	0.86 (1.34)	NV
OJ287	2023 Jan 19	g	6.53 $\pm$ 3.74	0.06 $\pm$ 0.40	23.90 (42.31)	1.22 (3.07)	NV
...	...	r	7.87 $\pm$ 2.39	0.08 $\pm$ 0.29	25.79 (42.31)	0.66 (3.07)	NV
...	...	i	2.95 $\pm$ 1.67	< 0	11.46 (42.31)	0.26 (3.07)	NV
...	...	$z_{\rm s}$	5.31 $\pm$ 3.88	< 0	7.76 (42.31)	0.56 (3.07)	NV
PKS 0735+178	2023 Jan 15	g	9.20 $\pm$ 0.75	0.12 $\pm$ 0.06	1194.61 (116.09)	6.17 (1.76)	V
...	...	r	6.46 $\pm$ 0.76	0.09 $\pm$ 0.08	564.00 (116.09)	4.01 (1.76)	V
...	...	i	7.57 $\pm$ 0.93	0.11 $\pm$ 0.06	833.54 (116.09)	5.54 (1.76)	V
...	...	$z_{\rm s}$	9.28 $\pm$ 1.84	0.13 $\pm$ 0.09	405.05 (116.09)	5.35 (1.76)	V
PKS 0735+178	2023 Jan 16	g	6.44 $\pm$ 0.88	0.08 $\pm$ 0.13	138.44 (52.62)	5.63 (2.59)	PV
...	...	r	4.91 $\pm$ 1.07	0.06 $\pm$ 0.22	61.50 (52.62)	3.88 (2.59)	PV
...	...	i	6.64 $\pm$ 0.91	0.08 $\pm$ 0.14	109.87 (52.62)	6.12 (2.59)	PV
...	...	$z_{\rm s}$	5.18 $\pm$ 1.47	0.06 $\pm$ 0.28	46.23 (52.62)	2.45 (2.59)	NV
PKS 0735+178	2023 Jan 17	g	15.35 $\pm$ 1.10	0.22 $\pm$ 0.03	6815.45 (383.68)	16.00 (1.33)	V
...	...	r	13.31 $\pm$ 1.36	0.22 $\pm$ 0.03	5214.03 (383.68)	21.84 (1.33)	V
...	...	i	12.22 $\pm$ 1.15	0.19 $\pm$ 0.04	4846.07 (383.68)	16.31 (1.33)	V
...	...	$z_{\rm s}$	11.26 $\pm$ 1.89	0.18 $\pm$ 0.07	1711.95 (383.68)	8.24 (1.33)	V
OJ248	2023 Jan 16	g	12.32 $\pm$ 4.33	0.08 $\pm$ 0.34	27.81 (56.89)	0.29 (2.46)	NV
...	...	r	10.07 $\pm$ 4.01	0.04 $\pm$ 0.89	27.86 (56.89)	0.31 (2.46)	NV
...	...	i	9.18 $\pm$ 6.73	< 0	20.36 (56.89)	0.09 (2.46)	NV
...	...	$z_{\rm s}$	16.11 $\pm$ 10.51	< 0	19.79 (56.89)	0.43 (2.46)	NV
OJ248	2023 Jan 17	g	12.83 $\pm$ 3.24	0.09 $\pm$ 0.19	398.02 (340.74)	0.28 (1.35)	NV
...	...	r	15.15 $\pm$ 3.97	0.07 $\pm$ 0.30	317.50 (340.74)	0.17 (1.35)	NV
...	...	i	20.52 $\pm$ 3.95	0.12 $\pm$ 0.20	405.82 (340.74)	0.20 (1.35)	NV
...	...	$z_{\rm s}$	24.78 $\pm$ 8.55	< 0	192.61 (340.74)	0.22 (1.35)	NV
OJ248	2023 Jan 19	g	13.30 $\pm$ 3.65	0.11 $\pm$ 0.24	104.02 (107.26)	0.51 (1.81)	NV
...	...	r	16.52 $\pm$ 5.49	0.09 $\pm$ 0.41	77.57 (107.26)	0.36 (1.81)	NV
...	...	i	15.17 $\pm$ 5.42	0.07 $\pm$ 0.53	70.36 (107.26)	0.24 (1.81)	NV
...	...	$z_{\rm s}$	19.26 $\pm$ 7.83	< 0	54.00 (107.26)	0.56 (1.81)	NV

TABLE C.21: Colour variability statistics for each source on a given night. p and c refer to the Spearman rank correlation coefficients (significance and strength respectively), $F_{\rm enh}$ is the enhanced F-test value with the critical value as described in section 5.1.1.4, and the final column describes whether or not the colour of the source was deemed variable on the given night. If $p < 0.05$ and $F_{\rm enh} > F_{\rm crit}$ the source was deemed variable (V), otherwise not variable (NV).

Source	Date	p	c	$F_{\rm enh}$ ($F_{\rm crit}$)	Variable?
TXS 0506+056	2023 Jan 15	4.1×10^{-3}	0.25	1.11 (1.50)	NV
...	2023 Jan 16	0.34	0.08	1.41 (1.45)	NV
...	2023 Jan 18	0.21	-0.13	1.43 (1.58)	NV
OJ287	2023 Jan 15	0.07	-0.12	0.88 (1.53)	NV
...	2023 Jan 18	0.45	-0.04	0.78 (1.31)	NV
...	2023 Jan 19	0.39	-0.22	0.70 (2.79)	NV
PKS 0735+178	2023 Jan 15	4.6×10^{-3}	0.33	4.66 (1.72)	V
...	2023 Jan 16	0.7	-0.08	1.84 (2.40)	NV
...	2023 Jan 17	3.9×10^{-10}	-0.35	3.13 (1.31)	V
OJ248	2023 Jan 16	0.22	-0.24	0.41 (2.29)	NV
...	2023 Jan 17	0.25	0.07	1.15 (1.47)	NV
...	2023 Jan 19	0.35	-0.12	0.69 (1.90)	NV

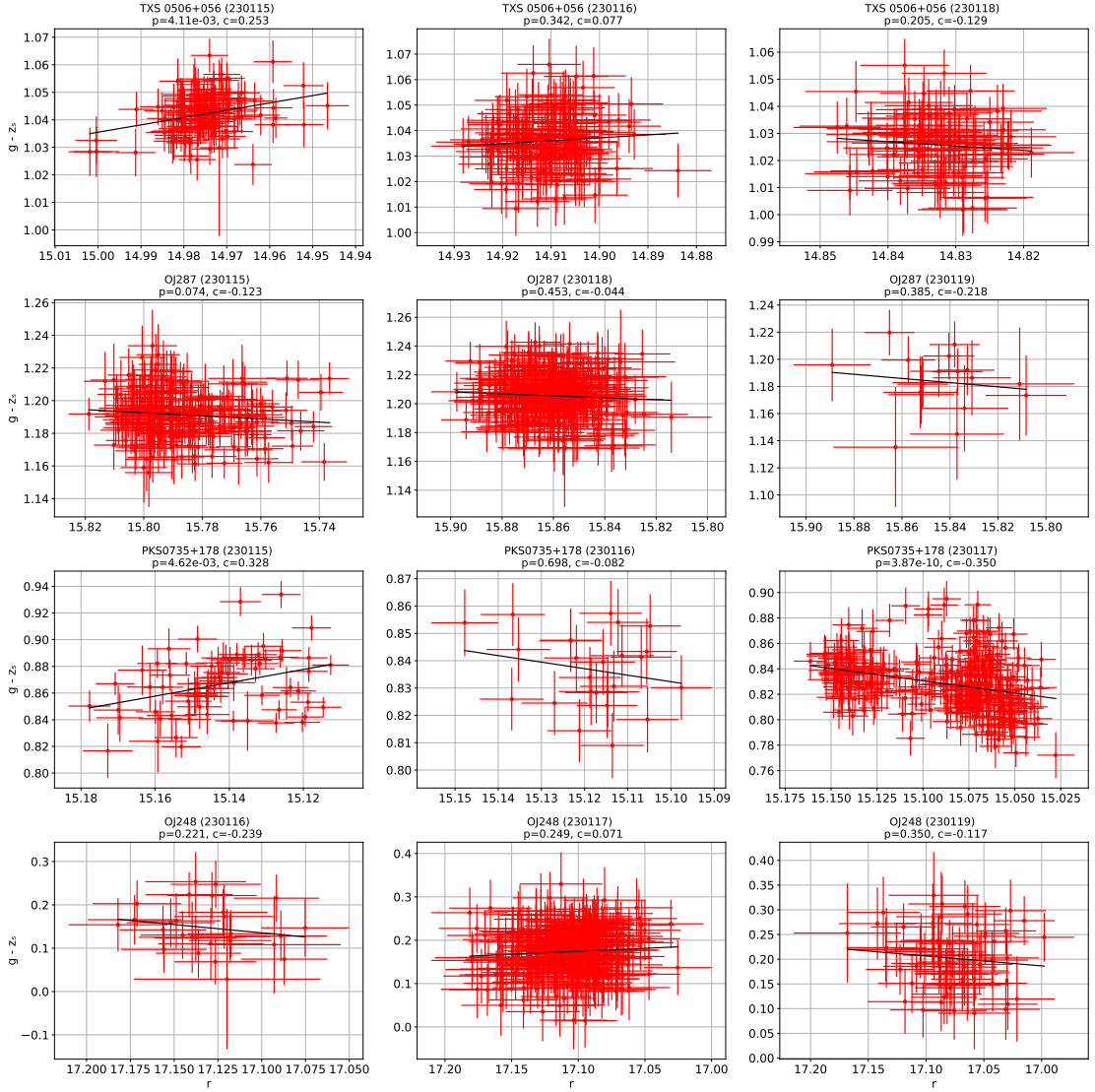

FIGURE C.62: Colour-magnitude (r vs. g-z_s magnitudes) diagrams for each of the four blazars (different rows) on different nights (different columns) as indicated above each plot. Also present above each plot are the corresponding Spearman rank correlation coefficients and significance values.

Bibliography

Abdo A. A., et al., 2009, ApJ, 699, 976

Abdo A. A., et al., 2010a, Nature, 463, 919

Abdo A. A., et al., 2010b, ApJ, 716, 30

Abdo A. A., et al., 2010c, ApJ, 721, 1425

Abdollahi S., et al., 2023, arXiv

Abdurro'uf et al., 2022, ApJS, 259, 35

Abramowicz M. A., Fragile P. C., 2013, Living Reviews in Relativity, 16, 1

Acharya S., Borse N. S., Vaidya B., 2021, MNRAS, 506, 1862

Acharya S., Vaidya B., Kalpa Dihingia I., Agarwal S., Shukla A., 2023, A&A, 671, A161

Ackermann M., et al., 2012, ApJ, 751, 159

Ackermann M., et al., 2015, ApJ, 813, L41

Agol E., 1997, PhD thesis, University of California, Santa Barbara

Agudo I., et al., 2025, The Astrophysical Journal Letters, 985, L15

Aharonian F. A., 2000, preprint, 5, 377 (arXiv:astro-ph/0003159)

Akaike H., 1974, IEEE Transactions on Automatic Control, 19, 716

Angelakis E., et al., 2016, MNRAS, 463, 3365

Arnold D., 2017, PhD thesis, Liverpool John Moores University

Arnold D. M., Steele I. A., Bates S. D., Mottram C. J., Smith R. J., 2012, in SPIE Conference Series. , doi:10.1117/12.927000

Attridge J. M., Roberts D. H., Wardle J. F. C., 1999, ApJ, 518, L87

Atwood W. B., et al., 2009, The Astrophysical Journal, 697, 1071

Bachev R., 2015, Monthly Notices of the Royal Astronomical Society: Letters, 451, L21

Bachev R., Semkov E., Strigachev A., Gupta A. C., Gaur H., Mihov B., Boeva S., Slavcheva-Mihova L., 2012, Monthly Notices of the Royal Astronomical Society, 424, 2625

Bachev R., et al., 2023, MNRAS, 522, 3018

Baghel J., Kharb P., Silpa S., Ho L. C., Harrison C. M., 2023, in Liodakis I., Aller M. F., Krawczynski H., Lähteenmäki A., Pearson T. J., eds, IAU Symposium Vol. 375, The Multimessenger Chakra of Blazar Jets. pp 56–60 (arXiv:2304.11831), doi:10.1017/S1743921323000947

Balbus S. A., Hawley J. F., 1991, ApJ, 376, 214

Baring M. G., 1997, in Giraud-Heraud Y., Tran Thanh van J., eds, Very High Energy Phenomena in the Universe; Moriond Workshop. p. 97 (arXiv:astro-ph/9711177), doi:10.48550/arXiv.astro-ph/9711177

Baum S. A., Zirbel E. L., O'Dea C. P., 1995, ApJ, 451, 88

Beckmann V., Shrader C. R., 2012, Active Galactic Nuclei. Wiley-VCH

Begelman M. C., 1998, ApJ, 493, 291

Begelman M. C., Fabian A. C., Rees M. J., 2008, MNRAS, 384, L19

Bernardes D., Steele I., Jermak H., McCall C., 2024a, Research Notes of the American Astronomical Society, 8, 71

Bernardes D., Steele I., Jermak H., McCall C., 2024b, Research Notes of the American Astronomical Society, 8, 87

Bernardini F., Cackett E. M., 2014, MNRAS, 439, 2771

Bhatta G., et al., 2015, ApJ, 809, L27

Bian W.-H., Zhao Y.-H., 2003, PASJ, 55, 599

Blandford R., Meier D., Readhead A., 2019, ARA&A, 57, 467

Blinov D., Pavlidou V., 2019, Galaxies, 7, 46

Blinov D., et al., 2015, MNRAS, 453, 1669

Blinov D., et al., 2016, MNRAS, 457, 2252

Bloom S. D., Marscher A. P., 1996, ApJ, 461, 657

Bonning E., et al., 2012, ApJ, 756, 13

Boroson T. A., Green R. F., 1992, ApJS, 80, 109

Böttcher M., 2016, Galaxies, 4, 22

Böttcher M., Dermer C. D., 2010, ApJ, 711, 445

Böttcher M., Reimer A., Sweeney K., Prakash A., 2013, ApJ, 768, 54

Bradley L., 2023, astropy/photutils: 1.8.0, Zenodo, doi:10.5281/zenodo.7946442

Britzen S., et al., 2018, MNRAS, 478, 3199

Britzen S., et al., 2019, A&A, 630, A103

Britzen S., Zajaček M., Gopal-Krishna Fendt C., Kun E., Jaron F., Sillanpää A., Eckart A., 2023, ApJ, 951, 106

Brunthaler A., et al., 2000, A&A, 357, L45

Burrows D. N., et al., 2011, Nature, 476, 421

Böttcher M., 2019, Galaxies, 7

Camenzind M., Krockenberger M., 1992, A&A, 255, 59

Cantó J., Lizano S., Fernández-López M., González R. F., Hernández-Gómez A., 2013, MNRAS, 430, 2703

Castignani G., Haardt F., Lapi A., De Zotti G., Celotti A., Danese L., 2013, A&A, 560, A28

Castignani G., et al., 2017, A&A, 601, A30

Cavaliere A., D'Elia V., 2002, ApJ, 571, 226

Cerruti M., 2020, in Journal of Physics Conference Series. IOP, p. 012094 (arXiv:1912.03666), doi:10.1088/1742-6596/1468/1/012094

Chand K., G.-K., Omar A., Chand H., Mishra S., Bisht P. S., Britzen S., 2021, Monthly Notices of the Royal Astronomical Society: Letters, 511, 13

Chang Y. L., Arsioli B., Giommi P., Padovani P., Brandt C. H., 2019, A&A, 632, A77

Chatterjee R., et al., 2008, ApJ, 689, 79

Chatterjee K., et al., 2020, MNRAS, 499, 362

Chiaberge M., Capetti A., Celotti A., 1999, A&A, 349, 77

Chiu H.-Y., 1964, Physics Today, 17, 21

Clarke D., Neumayer D., 2002, A&A, 383, 360

Cohen M. H., et al., 1977, Nature, 268, 405

Cohen D. P., Romani R. W., Filippenko A. V., Cenko S. B., Lott B., Zheng W., Li W., 2014, ApJ, 797, 137

Covino S., et al., 2015, A&A, 578, A68

D'Ammando F., Orienti M., 2013, The Astronomer's Telegram, 4717, 1

Davis S. W., Tchekhovskoy A., 2020, ARA&A, 58, 407

De Diego J. A., 2014, AJ, 148, 93

De Jaeger T., et al., 2023, MNRAS, 519, 6349

De Young D. S., 1991, Science, 252, 389

De Young D. S., 1993, ApJ, 405, L13

Dermer C. D., 1995, ApJ, 446, L63

Dermer C. D., Schlickeiser R., 1993, ApJ, 416, 458

Dey L., et al., 2019, Universe, 5, 108

Dong L., Zhang H., Giannios D., 2020, MNRAS, 494, 1817

Drouart G., et al., 2012, A&A, 548, A45

Edelson R. A., Krolik J. H., 1988, ApJ, 333, 646

Edelson R., Turner T. J., Pounds K., Vaughan S., Markowitz A., Marshall H., Dobbie P., Warwick R., 2002, The Astrophysical Journal, 568, 610

Escudero Pedrosa J., et al., 2024, arXiv e-prints, p. arXiv:2405.10141

Fabian A. C., 2012, ARA&A, 50, 455

Fan J.-H., et al., 2008, PASJ, 60, 707

Fanaroff B. L., Riley J. M., 1974, MNRAS, 167, 31P

Fiorucci M., Ciprini S., Tosti G., 2004, A&A, 419, 25

Flewelling H. A., et al., 2020, ApJS, 251, 7

Foschini L., 2017, Frontiers in Astronomy and Space Sciences, 4, 6

Foschini L., et al., 2015, A&A, 575, A13

Fossati G., Maraschi L., Celotti A., Comastri A., Ghisellini G., 1998, MNRAS, 299, 433

Frank J., King A., Raine D. J., 2002, Accretion Power in Astrophysics: Third Edition. Cambridge University Press

Gabuzda D. C., 2021, Galaxies, 9, 58

Gaug M., et al., 2024, MNRAS, 534, 2344

Gaur H., 2014, Journal of Astrophysics and Astronomy, 35, 241

Gaur H., Gupta A. C., Wiita P. J., 2012, AJ, 143, 23

Gaur H., Gupta A. C., Wiita P. J., Uemura M., Itoh R., Sasada M., 2014, ApJ, 781, L4

Georganopoulos M., Kazanas D., 2003, ApJ, 594, L27

Ghisellini G., Madau P., 1996, MNRAS, 280, 67

Ghisellini G., Tavecchio F., Chiaberge M., 2005, A&A, 432, 401

Ghisellini G., Tavecchio F., Foschini L., Ghirlanda G., Maraschi L., Celotti A., 2010, MNRAS, 402, 497

Ghisellini G., Tavecchio F., Foschini L., Ghirlanda G., 2011, MNRAS, 414, 2674

Ghisellini G., Righi C., Costamante L., Tavecchio F., 2017, MNRAS, 469, 255

Ghosh K. K., Ramsey B. D., Sadun A. C., Soundararajaperumal S., 2000, ApJS, 127, 11

Giannios D., 2013, MNRAS, 431, 355

Giannios D., Uzdensky D. A., Begelman M. C., 2009, MNRAS, 395, L29

Gill R., Kole M., Granot J., 2021, Galaxies, 9, 82

Giommi P., et al., 2021, MNRAS, 507, 5690

Giustini M., Proga D., 2019, A&A, 630, A94

Goldoni P., et al., 2021, A&A, 650, A106

Gopal-Krishna 2024, A&A, 688, L16

Gopal-Krishna Wiita P. J., 1992, A&A, 259, 109

Goyal A., Gopal-Krishna Wiita P. J., Anupama G. C., Sahu D. K., Sagar R., Joshi S., 2012, A&A, 544, A37

Greene J. E., Ho L. C., 2005, ApJ, 630, 122

Greenhill L. J., Gwinn C. R., Antonucci R., Barvainis R., 1996, ApJ, 472, L21

Gu M. F., Lee C. U., Pak S., Yim H. S., Fletcher A. B., 2006, A&A, 450, 39

Guetta D., Ghisellini G., Lazzati D., Celotti A., 2004, A&A, 421, 877

Guo W.-J., Li Y.-R., Zhang Z.-X., Ho L. C., Wang J.-M., 2022, ApJ, 929, 19

Gupta A. C., et al., 2008, AJ, 136, 2359

Heidt J., Wagner S. J., 1996, A&A, 305, 42

Henden A. A., Levine S., Terrell D., Welch D. L., Munari U., Kloppenborg B. K., 2018, in American Astronomical Society Meeting Abstracts #232. p. 223.06

Hervet O., Boisson C., Sol H., 2016, A&A, 592, A22

Hinshaw G., et al., 2013, ApJS, 208, 19

Hofmann A., 2004, The Physics of Synchrotron Radiation. Cambridge Monographs on Particle Physics, Nuclear Physics and Cosmology, Cambridge University Press

Høg E., et al., 2000, A&A, 355, L27

Hopkins P. F., Hernquist L., Hayward C. C., Narayanan D., 2012, MNRAS, 425, 1121

Hovatta T., Lindfors E., 2019, New Astronomy Reviews, 87, 101541

Hovatta T., Valtaoja E., Tornikoski M., Lähteenmäki A., 2009, A&A, 494, 527

Hovatta T., et al., 2014, MNRAS, 439, 690

Huang B.-Q., Liu T., 2024, Universe, 10, 438

IceCube Collaboration 2021, GRB Coordinates Network, 31191, 1

IceCube Collaboration et al., 2018, Science, 361, eaat1378

Ikejiri Y., et al., 2011, PASJ, 63, 639

Jermak H., 2016, PhD thesis, Liverpool John Moores University

Jermak H., et al., 2016a, MNRAS, 462, 4267

Jermak H., Steele I. A., Smith R. J., 2016b, in Evans C. J., Simard L., Takami H., eds, Society of Photo-Optical Instrumentation Engineers (SPIE) Conference Series Vol. 9908, Ground-based and Airborne Instrumentation for Astronomy VI. p. 99084I, doi:10.1117/12.2232324

Jha V. K., Joshi R., Chand H., Wu X.-B., Ho L. C., Rastogi S., Ma Q., 2022, MNRAS, 511, 3005

Jormanainen J., et al., 2025, arXiv e-prints, p. arXiv:2501.08652

Jorstad S. G., et al., 2022, Nature, 609, 265

Kalita N., et al., 2023, ApJ, 943, 135

Khachikian E. Y., Weedman D. W., 1974, ApJ, 192, 581

Kiehlmann S., et al., 2013, in European Physical Journal Web of Conferences. p. 06003, doi:10.1051/epjconf/20136106003

King A., 2016, MNRAS, 456, L109

Kirk J. G., Rieger F. M., Mastichiadis A., 1998, A&A, 333, 452

Kocevski et al. F. L. A. T. C., 2021, The Astronomer's Telegram, 15110, 1

Koljonen K. I. I., et al., 2024, MNRAS, 532, 112

Komossa S., et al., 2022, Multiwavelength astrophysics of the blazar OJ 287 and the project MOMO, doi:10.48550/ARXIV.2207.11291, https://arxiv.org/abs/2207.11291

Kormendy J., Ho L. C., 2013, ARA&A, 51, 511

Kormendy J., Richstone D., 1995, ARA&A, 33, 581

Kouch P. M., et al., 2024, A&A, 689, A119

Kravtsov V., et al., 2024, arXiv e-prints, p. arXiv:2407.07592

Krawczynski H., 2004, New Astronomy Reviews, 48, 367

Kügler S. D., Nilsson K., Heidt J., Esser J., Schultz T., 2014, A&A, 569, A95

Kylafis N. D., Contopoulos I., Kazanas D., Christodoulou D. M., 2012, A&A, 538, A5

Laing R. A., 1996, in Hardee P. E., Bridle A. H., Zensus J. A., eds, Astronomical Society of the Pacific Conference Series Vol. 100, Energy Transport in Radio Galaxies and Quasars. p. 241

Lang D., Hogg D. W., Mierle K., Blanton M., Roweis S., 2010, AJ, 139, 1782

Larionov V. M., et al., 2008, A&A, 492, 389

Lehto H. J., Valtonen M. J., 1996, ApJ, 460, 207

Lico R., et al., 2022, A&A, 658, L10

Liodakis I., Pavlidou V., 2015, MNRAS, 451, 2434

Liodakis I., Romani R. W., Filippenko A. V., Kiehlmann S., Max-Moerbeck W., Readhead A. C. S., Zheng W., 2018, MNRAS, 480, 5517

Liodakis I., Romani R. W., Filippenko A. V., Kocevski D., Zheng W., 2019, The Astrophysical Journal, 880, 32

Liodakis I., Blinov D., Potter S. B., Rieger F. M., 2022a, MNRAS, 509, L21

Liodakis I., et al., 2022b, Nature, 611, 677

Liodakis I., et al., 2024, A&A, 689, A200

Liodakis I., et al., 2025, arXiv e-prints, p. arXiv:2505.13603

Lister M. L., et al., 2016, AJ, 152, 12

Lister M. L., et al., 2019, ApJ, 874, 43

MAGIC Collaboration et al., 2018, A&A, 617, A30

MacDonald N. R., Marscher A. P., Jorstad S. G., Joshi M., 2015, ApJ, 804, 111

Mannheim K., Biermann P. L., 1992, A&A, 253, L21

Maraschi L., Ghisellini G., Celotti A., 1992, ApJ, 397, L5

Marcotulli L., et al., 2020, ApJ, 889, 164

Marscher A. P., 2014, ApJ, 780, 87

Marscher A. P., Jorstad S. G., 2021, Galaxies, 9, 27

Marscher A. P., Jorstad S. G., Aller M. F., McHardy I., Balonek T. J., Teräsranta H., Tosti G., 2004, in Kaaret P., Lamb F. K., Swank J. H., eds, American Institute of Physics Conference Series Vol. 714, X-ray Timing 2003: Rossi and Beyond. AIP, pp 167–173, doi:10.1063/1.1781021

Marscher A. P., et al., 2008, Nature, 452, 966

Marscher A. P., et al., 2010, ApJ, 710, L126

Mastichiadis A., Kirk J. G., 2002, Publ. Astron. Soc. Australia, 19, 138

Mastichiadis A., Moraitis K., 2008, A&A, 491, L37

McCall C., Jermak H. E., Steele I. A., Kobayashi S., Knapen J. H., Sánchez-Alarcón P. M., 2024a, MNRAS, 528, 4702

McCall C., et al., 2024b, MNRAS, 532, 2788

McEnery J. E., Michelson P. F., Paciesas W. S., Ritz S., 2012, Optical Engineering, 51, 011012

McHardy I. M., et al., 2023, MNRAS, 519, 3366

Meegan C., et al., 2009, The Astrophysical Journal, 702, 791

Miller H. R., Carini M. T., Goodrich B. D., 1989, Nature, 337, 627

Mingaliev M., et al., 2017, Astronomische Nachrichten, 338, 700

Mirabel I. F., Rodríguez L. F., 1999, ARA&A, 37, 409

Mohan P., Mangalam A., 2015, ApJ, 805, 91

Mücke A., Protheroe R. J., 2001, Astroparticle Physics, 15, 121

Mücke A., Protheroe R. J., Engel R., Rachen J. P., Stanev T., 2003, Astroparticle Physics, 18, 593

Murray N., Chiang J., Grossman S. A., Voit G. M., 1995, ApJ, 451, 498

Myserlis I., Komossa S., Angelakis E., Gómez J. L., Karamanavis V., Krichbaum T. P., Bach U., Grupe D., 2018, A&A, 619, A88

Naghizadeh-Khouei J., Clarke D., 1993, A&A, 274, 968

Nalewajko K., Sikora M., 2012, A&A, 543, A115

Narayan R., Igumenshchev I. V., Abramowicz M. A., 2003, PASJ, 55, L69

Narita N., et al., 2019, Journal of Astronomical Telescopes, Instruments, and Systems, 5, 015001

Natarajan P., Pringle J. E., 1998, ApJ, 506, L97

Nava L., Nakar E., Piran T., 2016, MNRAS, 455, 1594

Negi V., Joshi R., Chand K., Chand H., Wiita P., Ho L. C., Singh R. S., 2022, MNRAS, 510, 1791

Netzer H., 2006, in , Physics of Active Galactic Nuclei at all Scales. Springer, pp 1–38

Nilsson K., et al., 2018, A&A, 620, A185

Olguín-Iglesias A., et al., 2016, MNRAS, 460, 3202

Otero-Santos J., Acosta-Pulido J. A., Becerra González J., Luashvili A., Castro Segura N., González-Martín O., Raiteri C. M., Carnerero M. I., 2022, MNRAS, 511, 5611

Paczynski B., 1996, ARA&A, 34, 419

Padovani P., 2011, MNRAS, 411, 1547

Padovani P., 2016, A&A Rev., 24, 13

Padovani P., Giommi P., 1995, MNRAS, 277, 1477

Padovani P., Oikonomou F., Petropoulou M., Giommi P., Resconi E., 2019, Monthly Notices of the Royal Astronomical Society: Letters, 484, L104

Paltani S., Courvoisier T. J. L., Walter R., 1998, A&A, 340, 47

Papadakis I. E., Samaritakis V., Boumis P., Papamastorakis J., 2004, A&A, 426, 437

Patat F., Romaniello M., 2006, PASP, 118, 146

Pecaut M. J., Mamajek E. E., 2013, ApJS, 208, 9

Pedregosa F., et al., 2011a, Journal of Machine Learning Research, 12, 2825

Pedregosa F., et al., 2011b, Journal of Machine Learning Research, 12, 2825

Pelletier G., Pudritz R. E., 1992, ApJ, 394, 117

Peterson B. M., 1997, An Introduction to Active Galactic Nuclei. Cambridge University Press

Petropoulou M., Giannios D., Sironi L., 2016, MNRAS, 462, 3325

Petrosian V., 2012, Space Sci. Rev., 173, 535

Piconcelli E., Guainazzi M., 2005, A&A, 442, L53

Piran T., 2004, Reviews of Modern Physics, 76, 1143

Plaszczynski S., Montier L., Levrier F., Tristram M., 2014, MNRAS, 439, 4048

Plavin A. V., Kovalev Y. Y., Kovalev Y. A., Troitsky S. V., 2023, MNRAS, 523, 1799

Poutanen J., Zdziarski A. A., Ibragimov A., 2008, Monthly Notices of the Royal Astronomical Society, 389, 1427

Prandini E., Ghisellini G., 2022, Galaxies, 10, 35

Raiteri C. M., et al., 2023, MNRAS, 522, 102

Rakshit S., Stalin C. S., Kotilainen J., 2020, ApJS, 249, 17

Ramírez A., de Diego J. A., Dultzin-Hacyan D., González-Pérez J. N., 2004, A&A, 421, 83

Reimer A., 2012, in Journal of Physics Conference Series. IOP, p. 012011, doi:10.1088/1742-6596/355/1/012011

Rice S. O., 1944, Bell System Technical Journal, 23, 282

Richards J. L., et al., 2011, ApJS, 194, 29

Romero G. E., Cellone S. A., Combi J. A., 1999, A&AS, 135, 477

Ruan J. J., Anderson S. F., Plotkin R. M., Brandt W. N., Burnett T. H., Myers A. D., Schneider D. P., 2014, ApJ, 797, 19

Rybicki G. B., Lightman A. P., 1979, Radiative processes in astrophysics. John Wiley & Sons, Inc.

Rybicki G. B., Lightman A. P., 1986, Radiative processes in astrophysics. Wiley-VCH

Sagar R., Stalin C. S., Gopal-Krishna Wiita P. J., 2004, MNRAS, 348, 176

Sasada M., et al., 2011, PASJ, 63, 489

Savchenko S. S., Larionova E. G., Grisnina T. S., 2021, The Astronomer's Telegram, 15021, 1

Schaefer B., Collett E., Smyth R., Barrett D., Fraher B., 2007, American Journal of Physics, 75, 163

Schleicher B., et al., 2019, Galaxies, 7

Schmidt G. D., Elston R., Lupie O. L., 1992, AJ, 104, 1563

Schwarz G., 1978, The Annals of Statistics, 6, 461

Shablovinskaya E., Malygin E., Oparin D., 2023, MNRAS, 519, 3798

Shakura N. I., Sunyaev R. A., 1976, MNRAS, 175, 613

Shishkina E. V., et al., 2024, A&A, 691, L18

Shrestha M., Steele I. A., Piascik A. S., Jermak H., Smith R. J., Copperwheat C. M., 2020, Monthly Notices of the Royal Astronomical Society, 494, 4676

Shrestha M., et al., 2025, ApJ, 982, L32

Sikora M., Begelman M. C., Rees M. J., 1994, ApJ, 421, 153

Sikora M., Rutkowski M., Begelman M. C., 2016, Monthly Notices of the Royal Astronomical Society, 457, 1352

Sillanpaa A., Haarala S., Valtonen M. J., Sundelius B., Byrd G. G., 1988, ApJ, 325, 628

Sillanpää A., Takalo L. O., Nilsson K., Kikuchi S., 1993, Ap&SS, 206, 55

Singh K. K., et al., 2018, Astroparticle Physics, 103, 122

Sironi L., Petropoulou M., Giannios D., 2015, MNRAS, 450, 183

Smith P. S., Sitko M. L., 1991, ApJ, 383, 580

Sobacchi E., Sormani M. C., Stamerra A., 2017, MNRAS, 465, 161

Sol H., Zech A., 2022, Galaxies, 10, 105

Sorcia M., et al., 2013, ApJS, 206, 11

Spada M., Ghisellini G., Lazzati D., Celotti A., 2001, MNRAS, 325, 1559

Spinrad H., Smith H. E., 1975, ApJ, 201, 275

Steele I. A., et al., 2004, in Oschmann Jr. J. M., ed., Society of Photo-Optical Instrumentation Engineers (SPIE) Conference Series Vol. 5489, Ground-based Telescopes. pp 679–692, doi:10.1117/12.551456

Steele I. A., Wiersema K., McCall C., Newsam A., Shrestha M., 2023, MNRAS, 518, 1214

Stickel M., Padovani P., Urry C. M., Fried J. W., Kuehr H., 1991, ApJ, 374, 431

Stokes G. G., 1851, Transactions of the Cambridge Philosophical Society, 9, 399

Subbu Ulaganatha Pandian K., Natarajan A., Stalin C. S., Pandey A., Muneer S., Natarajan B., 2022, arXiv e-prints, p. arXiv:2202.07353

Słowikowska A., Krzeszowski K., Żejmo M., Reig P., Steele I., 2016, MNRAS, 458, 759

Tavecchio F., Maraschi L., Ghisellini G., 1998, ApJ, 509, 608

Tchekhovskoy A., 2015, in Contopoulos I., Gabuzda D., Kylafis N., eds, Astrophysics and Space Science Library Vol. 414, The Formation and Disruption of Black Hole Jets. p. 45, doi:10.1007/978-3-319-10356-3˙3

Tchekhovskoy A., Narayan R., McKinney J. C., 2011, MNRAS, 418, L79

Toma K., 2021, arXiv e-prints, p. arXiv:2112.13531

Toma K., et al., 2009, ApJ, 698, 1042

Tommasi L., et al., 2001, A&A, 376, 51

Tordella D., Belan M., Massaglia S., De Ponte S., Mignone A., Bodenschatz E., Ferrari A., 2011, New Journal of Physics, 13, 043011

Uemura M., et al., 2017, Publications of the Astronomical Society of Japan, 69

Ulrich M. H., Maraschi L., Urry C. M., 1997, Annual Review of Astronomy and Astrophysics, 35, 445

Urry C. M., Padovani P., 1995, PASP, 107, 803

Urry C. M., et al., 1997, The Astrophysical Journal, 486, 799

Valtonen M. J., et al., 2006, ApJ, 646, 36

Valtonen M. J., Lehto H. J., Takalo L. O., Sillanpää A., 2011, ApJ, 729, 33

Valtonen M. J., et al., 2016, ApJ, 819, L37

Valtonen M. J., et al., 2019, ApJ, 882, 88

Valtonen M. J., et al., 2021, Galaxies, 10, 1

Valtonen M. J., et al., 2022, MNRAS, 514, 3017

Valtonen M. J., et al., 2023, MNRAS, 521, 6143

Varglund, I. Järvelä, E. Lähteenmäki, A. Berton, M. Ciroi, S. Congiu, E. 2022, A&A, 668, A91

Vaughan S., Edelson R., Warwick R. S., Uttley P., 2003, Monthly Notices of the Royal Astronomical Society, 345, 1271

Villata M., Raiteri C. M., 1999, A&A, 347, 30

Villata M., et al., 2002, Mem. Soc. Astron. Italiana, 73, 1191

Wandel A., Peterson B. M., Malkan M. A., 1999, ApJ, 526, 579

Wang W., Bu D.-F., Yuan F., 2022, MNRAS, 513, 5818

Whittet D. C. B., Martin P. G., Hough J. H., Rouse M. F., Bailey J. A., Axon D. J., 1992, ApJ, 386, 562

Wiersema K., et al., 2022, Advances in Space Research, 70, 3003

Wu J., Zhou X., Ma J., Wu Z., Jiang Z., 2009, in Wang W., Yang Z., Luo Z., Chen Z., eds, Astronomical Society of the Pacific Conference Series Vol. 408, The Starburst-AGN Connection. p. 278

Xiao H. B., Zhu J. T., Fan J. H., Pei Z. Y., Luo Z. J., Zhang S. H., 2022, MNRAS, 517, 4202

Yarza R., Wong G. N., Ryan B. R., Gammie C. F., 2020, ApJ, 898, 50

Yuan Q., et al., 2023, ApJ, 953, 47

Zeng W., et al., 2017, Galaxies, 5, 85

Zhang H., 2019, Galaxies, 7, 85

Zhang Y. H., et al., 2002, ApJ, 572, 762

Zhang H., Chen X., Böttcher M., 2014, ApJ, 789, 66

Zhang B.-K., Zhou X.-S., Zhao X.-Y., Dai B.-Z., 2015a, Research in Astronomy and Astrophysics, 15, 1784

Zhang H., Chen X., Böttcher M., Guo F., Li H., 2015b, ApJ, 804, 58

Zhang H., Deng W., Li H., Böttcher M., 2016, ApJ, 817, 63

Zhang H., Li H., Guo F., Taylor G., 2017, ApJ, 835, 125

Zhang H., Li X., Giannios D., Guo F., Liu Y.-H., Dong L., 2020, ApJ, 901, 149

Zhang B.-K., Zhao X.-Y., Wu Q., 2022a, ApJS, 259, 49

Zhang H., Li X., Giannios D., Guo F., Thiersen H., Böttcher M., Lewis T., Venters T., 2022b, ApJ, 924, 90

Zhang B.-K., Tang W.-F., Wang C.-X., Wu Q., Jin M., Dai B.-Z., Zhu F.-R., 2023, MNRAS, 519, 5263

Ziaeepour H., 2009, MNRAS, 397, 361